UNIVERSITY OF CALIFORNIA, SAN DIEGO

Parallel Finite Element Modeling of Earthquake Ground Response and Liquefaction

A dissertation submitted in partial satisfaction of the requirements

for the degree of Doctor of Philosophy

in

Structural Engineering

by

Jinchi Lu

Committee in charge:

Professor Ahmed Elgamal, Chair
Professor David J. Benson
Professor Petr Krysl
Professor Kincho H. Law
Professor J. Enrique Luco

2006

The dissertation of Jinchi Lu is approved, and it is acceptable in quality and form for publication on microfilm:

_____

_____

_____

_____

_____
Chair

University of California, San Diego

2006

Table of Contents

List of Figures

List of Tables

Acknowledgments

I would like to gratefully acknowledge my advisor, Professor Ahmed Elgamal, for all the support, encouragement and guidance, during the course of my studies. More importantly, his creative way of study and research have fundamentally influenced my thinking style. His ever-strong confidence has changed and will continue to influence my life philosophy.

Special thanks are also due to Professor Kincho H. Law of the Department of Civil & Environmental Engineering, Stanford University, for sharing his parallel sparse solver knowledge and codes for our use, and also for his continued encouragement and suggestions throughout this research. The work in this thesis would not have been possible without Professor Law's involvement. All developments in the area of parallel computing where accomplished based on his advice and guidance. My work herein is based on the research and the resulting parallel computing algorithms provided by Professor Law.

I also wish to express my gratitude to Professor Petr Krysl of UC San Diego for his many useful comments during debugging of the parallel code. The contributions of other dissertation committee members: Professors David Benson and J. Enrique Luco are also gratefully acknowledged.

In addition, I would like to thank Dr. Zhaohui Yang of UC San Diego for his unconditional assistance throughout this study, and Dr. Jun Peng of Stanford University for his help in the development of the parallel code. Dr. Yang has been instrumental in providing assistance in all areas of constitutive modeling and soil-model algorithms. Dr.

Peng has been very helpful in developing the parallel sparse solver and preparing this dissertation.

I also owe a debt of gratitude to all my friends at UC San Diego for their encouragement and support. Special thanks are extended to my colleagues Dr. Liangcai He, Dr. Teerawut Juirnarongrit, Mr. Linjun Yan, Dr. Mike Frasier, Mr. Quan Gu, Mr. Yuyi Zhang, Mr. Xianfei He, Mr. Yohsuke Kawamata, Mr. Chung-Sheng Lee, Dr. Constantin Christopoulos, and Dr. Warrasak Jakrapiyanan for their helpful comments and suggestions on my work. Sharing my student experience with many friends at UC San Diego will remain a wonderful memory for the rest of my life. I would also like to express my appreciations to Dr. Zhaohui Yang of University of Alaska at Anchorage for his strong encouragement and many helpful suggestions. Special thanks are also due to Mr. Jiddu Bezares for helping proofread this thesis.

This research was supported by the National Science Foundation (Grants No. CMS0084616 and CMS0200510), and by the Pacific Earthquake Engineering Research Center (PEER), under the National Science Foundation Award Number EEC-9701568. Support was also provided in part by Caltrans and by the National Science Foundation through the San Diego Supercomputer Center under grant BCS050006 using Datastar and Blue Horizon. This support is most appreciated.

Finally, I would like to thank my mother, my parents-in-law and my wife for their encouragement and unconditional support. I could not have achieved this work without my wife's support, sacrifices and understanding. Special appreciations go to my father, who passed away 12 years ago, for everything he gave and taught me since I was born.

Vita

1991	B.S., Department of Hydraulic Engineering, Chengdu University of Science & Technology (former Sichuan University), Chengdu, Sichuan Province, China
1994	M.S., Department of Hydraulic Engineering, Sichuan Union University (former Sichuan University), Chengdu, Sichuan Province, China
1994 - 1998	Lecturer, Department of Hydraulic Engineering, Sichuan Union University (former Sichuan University), Chengdu, Sichuan Province, China
1994 - 1995	Field Engineer and Technical Interpreter, Ertan Hydro-power Development Corp., Panzhihua City, Sichuan Province, China
1998 - 1999	Graduate Student, The University of Toledo, OH
1999 - 2006	Graduate Student Researcher, University of California, San Diego, CA
2006	Ph.D., University of California, San Diego, CA

Publications

1. **Lu, Jinchi**, Elgamal, Ahmed, Law, Kincho H., and Yang, Zhaohui.. "Parallel Computing for Seismic Geotechnical Applications." *Proceedings of ASCE GeoCongress 2006*, Atlanta, GA, February 26-March 1.

2. **Lu, Jinchi**, and Elgamal, Ahmed. (2005). "A 3D Finite Element User-Interface for Soil-Foundation Seismic Response." *Proceedings of the 2005 Caltrans Bridge Research Conference*, Sacramento, CA, October 31-November 1.

3. Elgamal, Ahmed, **Lu, Jinchi**, and Yang, Zhaohui. (2005). "Liquefaction-Induced Settlement of Shallow Foundations and Remediation: 3D Numerical Simulation." *Journal of Earthquake Engineering*, Vol. 9, Special Issue 1, 17-45.

4. Elgamal, Ahmed, **Lu, Jinchi**, and Yang, Zhaohui. (2005). "Application of Numerical Methods to the Analysis of Liquefaction." *Proceedings of the 11th International Association of Computer Methods and Advances in Geomechanics*, Torino, Italy, June 19-24.

5. Elgamal, Ahmed, Yang, Zhaohui, and **Lu, Jinchi**. (2005). "Modeling of Soil Liquefaction: Pressure Dependence Effects." *Proceedings of the International Symposium on Plasticity 2005*, Kauai, Hawaii, January.

6. **Lu, Jinchi**, Elgamal, Ahmed, and Yang, Zhaohui. (2005). "Pilot 3D Numerical Simulation of Liquefaction and Countermeasures." *Proceedings of ASCE Geo-Frontiers 2005*, Austin, TX, January 24-26.

7. Peng, Jun, **Lu, Jinchi**, Law, Kincho H., and Elgamal, Ahmed. (2004). "ParCYCLIC: Finite Element Modeling of Earthquake Liquefaction Response on Parallel Computers." *Proceedings of the 13th World Conference on Earthquake Engineering*, Vancouver, Canada, August 1-6.

8. **Lu, Jinchi**, Yang, Zhaohui, He, Liangcai, Peng, Jun, Elgamal, Ahmed, and Law, Kincho H. (2004). "Computational Modeling of Nonlinear Soil-Structure Interaction on Parallel Computers." *Proceedings of the 13th World Conference on Earthquake Engineering*, Vancouver, Canada, August 1-6.

9. **Lu, Jinchi**, Yang, Zhaohui, Adlier, Korhan, and Elgamal, Ahmed. (2004). "Numerical Analysis of Stone Column Reinforced Silty Soil." *Proceedings of the 15th Southeast Asian Geotechnical Conference*, Vol. 1, Bangkok, Thailand, November 23-26.

10. Peng, Jun, **Lu, Jinchi**, Law, Kincho H., and Elgamal, Ahmed. (2004). "Simulation of Earthquake Liquefaction Response on Parallel Computers." *Proceedings of the ASCE Structural Congress and Expositions*, Nashville, TN, May 22-26.

11. He, Liangcai, Yang, Zhaohui, **Lu, Jinchi**, and Elgamal, Ahmed. (2004). "A Three-Dimensional Finite Element Study to Obtain p-y Curves for Sand." *Proceedings of the 17th ASCE Engineering Mechanics (EM2004)*, Newark, DE, June 13-16.

12. **Lu, Jinchi**, He, Liangcai, Yang, Zhaohui, Abdoun, Tarek, and Elgamal, Ahmed. (2004). "Three-Dimensional Finite Element Analysis of Dynamic Pile Behavior in Liquefied Ground." *Proceedings of the 11th International Conference on Soil Dynamics and Earthquake Engineering*, D.Doolin, A.Kammerer, T. Nogami, R. B. Seed, and I. T. (eds.), Berkeley, CA, January 7-9, 1, 144-148.

13. **Lu, Jinchi**, Peng, Jun, Elgamal, Ahmed, Yang, Zhaohui, and Law, Kincho H. (2004). "Parallel Finite Element Modeling of Earthquake Liquefaction Response." *International Journal of Earthquake Engineering and Engineering Vibration*, 3(1), 23-37.

14. Peng, Jun, **Lu, Jinchi** , Law, Kincho H., and Elgamal, Ahmed. (2004). "ParCYCLIC: Finite Element Modeling of Earthquake Liquefaction Response on Parallel Computers." *International Journal for Numerical and Analytical Methods in Geomechanics*, 28(12), 1207-1232.

15. Elgamal, Ahmed, **Lu, Jinchi**, and Yang, Zhaohui. (2004). "Data Uncertainty for Numerical Simulation in Geotechnical Earthquake Engineering." *Proceedings of the International Workshop on Uncertainties in Nonlinear Soil Properties and their Impact on Modeling Dynamic Soil Response*, Pacific Earthquake Engineering Research Center (PEER), Berkeley, CA, March 18-19.

16. Yang, Zhaohui, **Lu, Jinchi**, and Elgamal, Ahmed. (2004). "A Web-Based Platform for Computer Simulation of Seismic Ground Response." *Advances in Engineering Software*, 35(5), 249-259.

17. **Lu, Jinchi**, Elgamal, Ahmed, Yang, Zhaohui, and Adalier, Korhan. (2003). "Stone Columns in Silty Soils: a Numerical Model." *Proceedings of the U.S.-Taiwan Liquefaction Workshop*, Taiwan, November 2.

18. Peng, Jun, **Lu, Jinchi**, Law, Kincho H., and Elgamal, Ahmed. (2003). "Simulation of Earthquake Liquefaction Response on Parallel Computers." *Blume Earthquake Engineering Research Center News Letter*, Issue 35, Stanford University, Stanford, CA, August.

19. **Lu, Jinchi**, Li, Chaoguo, and Zhang, Lin. (1998). "Investigation of Characteristics of Joints in a RCC High Arch Dam." *Research Report*, Sichuan Union University, Chengdu, China, *In Chinese*.

20. Yang, Zhaohui, Liu, Haowu, and **Lu, Jinchi**. (1997). "Neural Network Method for Concrete Strength Prediction and Design." *Journal of Hydroelectric Engineering*, 43(1), 33-40, *In Chinese*.

21. Li, Chaoguo, **Lu, Jinchi**, and Zhang, Lin. (1997). "Application of Methods of Synthetic Measure and Overloading in Experimental Analysis of Abutment Stability of Shapai RCC Arch Dam." *Journal of Sichuan Union University (Engineering Science Edition)*, 1(3), *In Chinese*.

22. Li, Chaoguo, Zhang, Lin, and **Lu, Jinchi**. (1997). "3D Geomechanical Model Tests for an RCC Arch Dam." *Research Report*, Sichuan Union University, Chengdu, China, *In Chinese*.

23. Li, Chaoguo, Zhang, Lin, and **Lu, Jinchi**. (1997). "Geomechanical Model Studies and Finite Element Analysis for a RCC Gravity Dam." *Research Report*, Sichuan Union University, Chengdu, China, *In Chinese*.

24. Yang, Zhaohui, and **Lu, Jinchi**. (1995). "Development of a Management Information System Applied in the Collection of Transportation Fees." *Application Research of Computers and Structures*, 12(2), 62-64, *In Chinese*.

25. **Lu, Jinchi**. (1994). "Three-dimensional Nonlinear Finite Element Analysis and Model Studies of Pubugou High Rockfill Dam on Deep Overburden and Its Foundation," *MS Thesis*, Dept. of Hydraulic Engineering, Sichuan Union University, Chengdu, China, *In Chinese*.

26. Yang, Zhaohui, **Lu, Jinchi**, and Zhao, Lin. (1993). "Development of an Examination System Based on FOXPRO and Auto CAD." *Application Research of Computers, Sup. 2*, *In Chinese*.

ABSTRACT OF THE DISSERTATION

Parallel Finite Element Modeling of Earthquake Ground Response and Liquefaction

by

Jinchi Lu

Doctor of Philosophy in Structural Engineering

University of California, San Diego, 2006

Professor Ahmed Elgamal, Chair

Parallel computing is gradually becoming a main stream tool in geotechnical simulations. The need for high fidelity and for modeling of fairly large 3-dimensional (3D) spatial configurations is motivating this direction of research. The main objective of this thesis is to develop a state-of-the-art nonlinear parallel finite element (FE) program for earthquake ground/structure response and liquefaction simulation. In the developed parallel code, ParCYCLIC, finite elements are employed within an incremental plasticity, coupled solid-fluid formulation. A constitutive model calibrated by physical tests represents the salient characteristics of sand liquefaction and associated accumulation of shear deformations. Key elements of the computational strategy employed in ParCYCLIC include the development of a parallel sparse direct solver, the deployment of an automatic domain decomposer, and the use of the Multilevel Nested Dissection

algorithm for ordering of the FE nodes. Conducted large-scale geotechnical simulations show that ParCYCLIC is efficiently scalable to a large number of processors.

Calibrated FE simulations are increasingly providing a reliable environment for modeling liquefaction-induced ground deformation. Effects on foundations and super-structures may be assessed, and associated remediation techniques may be explored, within a unified framework. Current capabilities of such a FE framework are demonstrated via a series of 3-dimensional (3D) simulations. High-fidelity 3D numerical studies using ParCYCLIC are shown to provide more accurate results.

Much time and effort is expended today in building an appropriate FE mesh and associated data files. User-friendly interfaces can significantly alleviate this problem allowing for high efficiency and much increased confidence. Pre- and post processing interfaces are developed to facilitate use of otherwise complex computational environments with numerous (often vaguely defined) input parameters. User-friendly interfaces are useful not only for simple model simulations on single-processor computers but also for large-scale modeling on a parallel machine.

Chapter 1 Introduction and Literature Survey

1.1 Introduction

Soil liquefaction is a complex phenomenon that causes much damage during earthquakes (Figure 1.1 and Figure 1.2). Large-scale FE simulations of earthquake-induced liquefaction effects often require a lengthy execution time. This is necessitated by the complex algorithms of coupled solid-fluid formulation, the associated highly nonlinear plasticity-based constitutive models, and the time domain step-by-step earthquake computations. In view of the finite memory size and the limitation of current operating systems (e.g. Linux, MS Windows, and so forth), large-scale earthquake simulations may not be feasible on single-processor computers. Utilization of parallel computers, which combine the resources of multiple processing and memory units, can potentially reduce the solution time significantly and allow simulations of large and complex models that may not fit into a single processing unit.

Parallel computing is a promising approach to alleviate the computational demand of FE analysis of large-scale systems. Because of the significant difference in the architecture between parallel computers and traditional sequential computers, application software such as FE programs must be re-designed in order to run efficiently on parallel computers.

This dissertation attempts to explore an effective computational strategy of parallel nonlinear FE analysis for modeling earthquake geotechnical problems including liquefaction effects.

1.2 Parallel Computing in FE Analysis

The concept of parallel computing has been successfully applied to various structural and geotechnical FE problems. Gummadi and Palazotto (1997) described a nonlinear FE formulation for beams and arches analyzed on a parallel machine. They employed the concept of loop splitting to parallelize the element stiffness matrix generation phase. Nikishkov et al. (1998) developed a semi-implicit parallel FE code ITAS3D using the domain decomposition method and a direct solver for an IBM SP2 computer. They reported that the parallel implementation could only be efficiently scalable to a moderate number of processors (e.g. 8). Rometo et al. (2002) attempted to perform nonlinear analysis for reinforced concrete three-dimensional frames using different types of parallel computers, including a cluster of personal computers. McKenna (1997) proposed a parallel object-oriented programming framework, which employs a dynamic load balancing scheme to allow element migration between sub-domains in order to optimize CPU usage. Krysl et al. (Krysl and Belytschko 1998; Krysl and Bittnar 2001) presented node-cut and element-cut partitioning strategies for the parallelization of explicit FE solid dynamics. They found that node-cut partitioning could yield higher parallel efficiency than element-cut partitioning.

Bielak et al (1999; 2000) modeled earthquake ground motions in large sedimentary basins using a 3D parallel linear FE program with an explicit integration procedure. They noted that the implementation of an implicit time integration approach is challenging on distributed memory computers, requiring significant global information exchange (Bao et al. 1998; Hisada et al. 1998; Bielak et al. 1999; Bielak et al. 2000). Yang (2002) developed a parallel FE algorithm (based on the Plastic Domain

Decomposition PDD approach), and attempted to achieve dynamic load balancing by using an adaptive partitioning-repartitioning scheme.

There remains a need for introducing parallel FE methods to solve geomechanical and coupled physical problems (Smith and Margetts 2002; Yang 2002). Proper parallel computation algorithms and strategies for solving earthquake liquefaction problems are still under development. Nonlinear modeling of large-scale solid-fluid coupled geotechnical problems still remains a challenge. Efforts have been focused on parallelizing portions of FE code. A complete and highly efficient parallel FE program for modeling earthquake ground response including liquefaction effects is still unavailable. However, the need for conducting large-scale simulations of earthquake liquefaction problems on parallel computers cannot be overstated.

The research reported herein focuses on the development of a state-of-the-art nonlinear parallel FE code for earthquake ground/foundation response and liquefaction simulation. The parallel code, ParCYCLIC, is implemented based on a serial code CYCLIC (Ragheb 1994; Parra 1996; Yang 2000), which is a nonlinear FE program developed to analyze liquefaction-induced seismic response (Parra 1996; Yang and Elgamal 2002). Extensive calibration of CYCLIC has been conducted with results from experiments and full-scale response of earthquake simulations involving ground liquefaction. In ParCYCLIC, the calibrated serial code for modeling of earthquake geotechnical phenomena is combined with advanced computational methodologies to facilitate the simulation of large-scale systems and broaden the scope of practical applications.

1.3 Review of Parallel Equation Solvers

Nonlinear FE computations of earthquake simulations involve the iterative solution of sparse symmetric systems of linear equations. Solving the linear system is often the most computationally intensive task, especially when an implicit time integration scheme is employed.

Research efforts in parallelization of FE programs have been focused on developing parallel equation solvers (Gummadi and Palazotto 1997; Adams 1998). Parallel sparse direct solution techniques have been developed (George et al. 1986; George et al. 1989; Heath et al. 1991; Law and Mackay 1993; Li and Demmel 1998; Amestoy et al. 2000). Various aspects of the parallel direct sparse solver implementations, including symbolic factorization, appropriate data structures, and numerical factorization, have been studied.

ParCYCLIC employs a direct sparse solution method proposed and developed by Law and Mackay (1993). This parallel sparse solver is based on a row-oriented storage scheme that takes full advantage of the sparsity of the stiffness matrix. In this sparse direct solver, a square-root free parallel LDL^T factorization is applied to symmetric matrices containing negative diagonal entries. A direct solver is preferred in ParCYCLIC over an iterative solver because even the best-known iterative solver (e.g. the Polynomial Preconditioned Conjugate Gradient method (PPCG)) may exhibit instabilities under certain conditions. For instance, in a nonlinear analysis, an iterative solver may diverge (Garatani et al. 2001; Gullerud and Dodds 2001; Romero et al. 2002). The direct solution method is a more stable approach to achieve solution convergence.

1.4 Numerical Modeling of Earthquake Site Response and Liquefaction

1.4.1 Introduction

Liquefaction of soils and associated deformations remain among the main causes of damage during earthquakes (Seed et al. 1990; Bardet et al. 1995; Sitar 1995; JGS 1996; Ansal et al. 1999). Indeed, dramatic unbounded deformations (flow failure) due to liquefaction in dams and other structures (Seed et al. 1975; Seed et al. 1989; Davis and Bardet 1996) have highlighted the significance of this problem in earthquake engineering. However, liquefaction often results in limited, albeit possibly high levels of deformation (Casagrande 1975; Youd et al. 1999). The deformation process in such situations is mainly a consequence of limited-strain cyclic deformations (Seed, 1979), commonly known as cyclic mobility (Castro and Poulos 1977) or cyclic liquefaction (Casagrande 1975).

A large number of computational models have been, and continue to be developed for simulation of nonlinear soil response (e.g., Desai and Christian 1977; Finn et al. 1977; Desai and Siriwardane 1984; Prevost 1985; Pastor and Zienkiewicz 1986; Prevost 1989; Bardet et al. 1993; Manzari and Dafalias 1997; Borja et al. 1999a, b; Jeremic et al. 1999; Zienkiewicz et al. 1999; Desai 2000; Li and Dafalias 2000; Park and Desai 2000; Shao and Desai 2000; Arduino et al. 2001). Currently, liquefaction still remains a topic that presents major challenges for such numerical techniques. The research presented in this thesis addresses primarily the area of cyclic mobility and

accumulation of liquefaction induced shear deformations. Effort is dedicated to the analysis of liquefaction-induced deformations in medium-dense cohesionless soils.

1.4.2 Mechanism of Liquefaction-induced Deformation

In saturated clean medium to dense sands (relative densities D_r of about 40% or above, Lambe and Whitman 1969), the mechanism of liquefaction-induced cyclic mobility may be illustrated by the undrained cyclic response, schematically illustrated in Figure 1.3. In this figure, the following aspects may be observed (Parra 1996): (i) as excess-pore pressure increases, cycle-by-cycle degradation in shear strength is observed, manifested by the occurrence of increasingly larger shear strain excursions for the same level of applied shear stress, and (ii) a regain in shear stiffness and strength at large shear strain excursions, along with an increase in effective confinement (shear-induced dilative tendency).

In the case of an acting initial shear stress (e.g., in a slope or embankment), cycle-by-cycle deformation accumulates according to the schematic of Figure 1.4 (Parra 1996). Inspection of Figure 1.4 shows that a net finite increment of permanent shear strain occurs in a preferred "down-slope" direction on a cycle-by-cycle basis. Realistic estimation of the magnitude of such increments is among the most important considerations in assessments of liquefaction-induced hazards (Iai 1998; Li and Dafalias 2000; Park and Desai 2000).

1.4.3 FE Formulation

CYCLIC is an advanced nonlinear FE program for earthquake ground response and liquefaction simulation (Ragheb 1994; Parra 1996; Yang 2000). In CYCLIC, the saturated soil system is modeled as a two-phase material based on the Biot (1962) theory for porous media. A numerical framework of this theory, known as *u-p* formulation, was implemented (Parra 1996; Yang 2000; Yang and Elgamal 2002). In the *u-p* formulation, displacement of the soil skeleton *u*, and pore pressure *p*, are the primary unknowns (Chan 1988; Zienkiewicz et al. 1990). The implementation of CYCLIC is based on the following assumptions: small deformation and rotation, constant density of the solid and fluid in both time and space, locally homogeneous porosity which is constant with time, incompressibility of the soil grains, and equal accelerations for the solid and fluid phases.

The *u-p* formulation as defined by Chan (1988) consists of: i) equation of motion for the solid-fluid mixture, and ii) equation of mass conservation for the fluid phase, incorporating the equation of motion for the fluid phase and Darcy's law. The FE governing equations can be expressed in matrix form as follows (Chan 1988):

$$\mathbf{M}\ddot{\mathbf{U}} + \int_{\Omega} \mathbf{B}^{\mathrm{T}} \boldsymbol{\sigma}' \, d\Omega + \mathbf{Q}\mathbf{p} - \mathbf{f}^{s} = \mathbf{0} \tag{1.1}$$

$$\mathbf{Q}^{\mathrm{T}}\dot{\mathbf{U}} + \mathbf{S}\dot{\mathbf{p}} + \mathbf{H}\mathbf{p} - \mathbf{f}^{p} = \mathbf{0} \tag{1.2}$$

where **M** is the mass matrix, **U** the displacement vector, **B** the strain-displacement matrix, $\boldsymbol{\sigma}'$ the effective stress tensor (determined by the soil constitutive model described below), **Q** the discrete gradient operator coupling the solid and fluid phases, **p** the pore pressure vector, **S** the compressibility matrix, and **H** the permeability matrix.

The vectors $\mathbf{f}^s$ and $\mathbf{f}^p$ represent the effects of body forces and prescribed boundary conditions for the solid-fluid mixture and the fluid phase respectively.

In Eq. (1.1) (equation of motion), the first term represents inertia force of the solid-fluid mixture, followed by the internal force due to soil skeleton deformation, and the internal force induced by pore-fluid pressure. In Eq. (1.2) (equation of mass conservation), the first two terms represent the rate of volume change for the soil skeleton and the fluid phase respectively, followed by the seepage rate of the pore fluid. Eqs. (1.1) and (1.2) are integrated in the time space using a single-step predictor multi-corrector scheme of the Newmark type (Chan 1988; Parra et al. 1996). In the current implementation, the solution is obtained for each time step using the modified Newton-Raphson approach (Parra 1996).

1.4.4 Soil Constitutive Model

The second term in Eq. (1.1) is defined by the soil stress-strain constitutive model. The FE program incorporates a soil constitutive model (Parra 1996; Yang and Elgamal 2002; Elgamal et al. 2003; Yang et al. 2003) based on the original multi-surface-plasticity theory for frictional cohesionless soils (Prevost 1985). This model was developed with emphasis on simulating the liquefaction-induced shear strain accumulation mechanism in clean cohesionless soils (Elgamal et al. 2002a; Elgamal et al. 2002b; Yang and Elgamal 2002; Elgamal et al. 2003; Yang et al. 2003). Special attention was given to the deviatoric-volumetric strain coupling (dilatancy) under cyclic loading, which causes increased shear stiffness and strength at large cyclic shear strain excursions (i.e., cyclic mobility).

The constitutive equation is written in incremental form as follows (Prevost 1985):

$$\dot{\boldsymbol{\sigma}}' = \boldsymbol{E} : (\dot{\boldsymbol{\varepsilon}} - \dot{\boldsymbol{\varepsilon}}^{p}) \tag{1.3}$$

where $\dot{\boldsymbol{\sigma}}'$ is the rate of effective Cauchy stress tensor, $\dot{\boldsymbol{\varepsilon}}$ the rate of deformation tensor, $\dot{\boldsymbol{\varepsilon}}^{p}$ the plastic rate of deformation tensor, and $\boldsymbol{E}$ the isotropic fourth-order tensor of elastic coefficients. The rate of plastic deformation tensor is defined by: $\dot{\boldsymbol{\varepsilon}}^{p} = \mathbf{P} \langle L \rangle$, where **P** is a symmetric second-order tensor defining the direction of plastic deformation in stress space, L the plastic loading function, and the symbol $\langle\ \rangle$ denotes the McCauley's brackets (i.e., $\langle L \rangle = \max(L, 0)$). The loading function L is defined as: $L = \mathbf{Q} : \dot{\boldsymbol{\sigma}}' / H'$ where H' is the plastic modulus, and **Q** a unit symmetric second-order tensor defining the yield-surface normal at the stress point (i.e., $\mathbf{Q} = \nabla f / \|\nabla f\|$), with the yield function f selected of the following form (Elgamal et al. 2003):

$$f = \frac{3}{2}(\boldsymbol{s} - (p' + p_0')\boldsymbol{\alpha}) : (\boldsymbol{s} - (p' + p_0')\boldsymbol{\alpha}) - M^2 (p' + p_0')^2 = 0 \tag{1.4}$$

in the domain of $p' \geq 0$. The yield surfaces in principal stress space and deviatoric plane are shown in Figure 1.5. In Eq. (1.4), $\boldsymbol{s} = \boldsymbol{\sigma}' - p' \boldsymbol{\delta}$ is the deviatoric stress tensor, p' the mean effective stress, p_0' a small positive constant (1.0 kPa in this document) such that the yield surface size remains finite at $p' = 0$ for numerical convenience (Figure 1.5), $\boldsymbol{\alpha}$ a second-order kinematic deviatoric tensor defining the surface coordinates, and M dictates the surface size. In the context of multi-surface plasticity, a number of similar surfaces with a common apex form the hardening zone (Figure 1.5).

Each surface is associated with a constant plastic modulus. Conventionally, the low-strain (elastic) moduli and plastic moduli are postulated to increase in proportion to the square root of p' (Prevost 1985).

The flow rule is chosen so that the deviatoric component of flow $\mathbf{P}' = \mathbf{Q}'$ (associative flow rule in the deviatoric plane), and the volumetric component P'' defines the desired amount of dilation or contraction in accordance with experimental observations. Consequently, P'' defines the degree of non-associativity of the flow rule and is given by (Parra 1996):

$$P'' = \frac{(\eta/\overline{\eta})^2 - 1}{(\eta/\overline{\eta})^2 + 1}\Psi \tag{1.5}$$

Where $\eta = ((3/2)\boldsymbol{s}:\boldsymbol{s})^{1/2}/p'$ is effective stress ratio, $\overline{\eta}$ a material parameter defining the stress ratio along the phase transformation (PT) surface (Ishihara et al. 1975), and Ψ a scalar function controlling the amount of dilation or contraction depending on the level of confinement and/or cumulated plastic deformation (Elgamal et al. 2003). The sign of $(\eta/\overline{\eta})^2 - 1$ dictates dilation or contraction. If the sign is negative, the stress point lies below the PT surface and contraction takes place (phase 0-1, Figure 1.6). On the other hand, the stress point lies above the PT surface when the sign is positive and dilation occurs under shear loading (phase 2-3, Figure 1.6). At low confinement levels, accumulation of plastic deformation may be prescribed (phase 1-2, Figure 1.6) before the onset of dilation (Elgamal et al. 2003).

A purely deviatoric kinematic hardening rule is chosen according to (Prevost 1985):

$$p' \dot{\boldsymbol{\alpha}} = b \boldsymbol{\mu} \tag{1.6}$$

Where $\boldsymbol{\mu}$ is a deviatoric tensor defining the direction of translation and b is a scalar magnitude dictated by the consistency condition. In order to enhance computational efficiency, the direction of translation $\boldsymbol{\mu}$ is defined by a new rule (Parra 1996; Elgamal et al. 2003), which maintains the original concept of conjugate-points contact by Mroz (1967). Thus, all yield surfaces may translate in stress space within the failure envelope.

1.4.5 Model Calibration

The employed model has been extensively calibrated for clean Nevada Sand at $D_r \approx 40\%$ (Parra 1996; Yang 2000). Calibration was based on results of monotonic and cyclic laboratory tests (Arulmoli et al. 1992, Figure 1.7), as well as data from level-ground and mildly inclined infinite-slope dynamic centrifuge-model simulations (VELACS Models 1 & 2, Dobry et al. 1995; Taboada 1995). Results of these tests were employed for calibration of model parameters, through FE simulations. The computed surface lateral displacement histories for VELACS Model 2 and the calibrated numerical response are shown in Figure 1.8 (sandy gravel *k*, where *k* is permeability).

The main modeling parameters include (Table 1.1) standard dynamic soil properties such as low-strain shear modulus and friction angle, as well as calibration constants to control the dilatancy effects (phase transformation angle, contraction and dilation parameters), and the level of liquefaction-induced yield strain (γ_y).

1.4.6 Role of Permeability

A coupled solid-fluid framework such as the one described above is needed in order to account for excess pore-pressure evolution and its distribution during and after seismic excitation. At any location, excess pore-pressure is dictated by the overall influence of shear loading throughout the entire ground domain under investigation. In this regard, permeability plays a critical role, locally and globally. In simple terms, local effects might dictate the extent of dilation-induced regain of shear stiffness and strength during a large shear strain excursion (and the resulting level of shear strain accumulation). For instance, the global distribution of pore-pressure with depth can be significantly affected by the natural layering of soil strata of different permeabilities, with the dramatic example being (Figure 1.9) the situation of alluvial deposits or man-made hydraulic fills (Scott and Zuckerman 1972; Adalier 1992).

Yang and Elgamal (2002) attempted to shed light on the significance of permeability. For instance, Figure 1.8 depicts the situation of a 10m-thick uniform soil profile, inclined by 4 degrees to simulate an infinite-slope response. This configuration is identical to that of the VELACS Model-2 centrifuge experiment (Dobry et al. 1995; Taboada 1995). Three numerical simulations were conducted, with a permeability coefficient k of 1.3 x 10^{-2} m/sec (gravel), 3.3 x 10^{-3} m/sec (VELACS Model-2 sandy gravel calibration simulation), and 6.6 x 10^{-5} m/sec (clean sand) respectively. It is seen that: i) as mentioned earlier, computed lateral deformations with the sandy gravel k value are close to the experimental response (part of the calibration process), and ii) the extent of lateral deformation in this uniform profile is inversely proportional to soil

permeability, i.e., a higher *k* results in lower levels of lateral deformation (the profile with the least *k* value had a lateral translation of about 2.5 times that with the highest *k* value).

Spatial variation of permeability in a soil profile is also potentially of primary significance in the development of liquefaction and associated deformations. Figure 1.10 shows an example of liquefaction (excess pore pressure ratio $r_u=u_e/\sigma'_v$ approaching and reaching 1.0, where u_e=excess pore pressure and σ'_v is effective vertical stress) with a low-permeability interlayer in a uniform soil profile.

Figure 1.10 and the observed deformations displayed (Yang and Elgamal 2002):

1) A very high pore-pressure gradient within the silt-k layer. Below this layer, the post-shaking re-consolidation process eventually results in a constant distribution. This constant value is equal to the initial effective confinement (overburden pressure) imposed by the thin layer and the layers above. Dissipation of this trapped fluid through the low-permeability interlayer may take a very long time in practical situations (if no sand boils develop).
2) After the shaking phase, void ratio continued to increase immediately beneath the silt-k layer, with large shear-strain concentration. Meanwhile, negligible additional shear strain was observed in the rest of the profile.

1.5 Thesis Scope and Layout

The main purposes of the current research are:

1) To develop a parallel nonlinear FE program for simulation of earthquake ground response and liquefaction based on an existing serial code.
2) To explore computational strategies employed in nonlinear parallel FE methods.
3) To explore large-scale FE simulations of geotechnical problems.

The thesis is composed of 9 chapters. Chapter 2 presents the software organization of ParCYCLIC. Chapter 3 describes the parallel sparse solver employed in ParCYCLIC. The parallel performance of ParCYCLIC is also discussed in Chapter 3. Chapter 4 presents numerical simulations of two centrifuge experiments. A calibrated parallel FE simulation exercise is described in Chapter 5 via a simple 3D series of shallow foundation models of settlement and remediation. These simulations are further addressed by large-scale models and the analysis results are presented in Chapter 6. Chapter 7 presents numerical modeling of a pile-supported wharf system. A series of user-friendly interfaces are presented and discussed in Chapter 8. Finally, Chapter 9 summarizes the results of this study and discusses directions for future work.

Table 1.1: Model parameters calibrated for D_r = 40% Nevada Sand (Elgamal et al. 2002b).

Main calibration experiment	Parameter	Value
Drained monotonic tests (Arulmoli et al. 1992)	Low-strain shear modulus G_r (at 80 kPa mean effective confinement)	33.3 MPa
	Friction angle ϕ	31.4 degrees
Undrained cyclic test (Arulmoli et al. 1992)	Liquefaction yield strain γ_y *(Figure 1.6, phase 1-2)*	1.0 %
RPI Centrifuge Model 1 (Dobry et al. 1995)	Contraction parameter c_1	0.17
	Contraction parameter c_2 *(Figure 1.6, phase 0-1)*	0.05
RPI Centrifuge Model 2 (Dobry et al. 1995)	Phase transformation angle ϕ_{PT}	26.5 degrees
	Dilation parameter d_1	0.4
	Dilation parameter d_2 *(Figure 1.6, phase 2-3)*	100.0

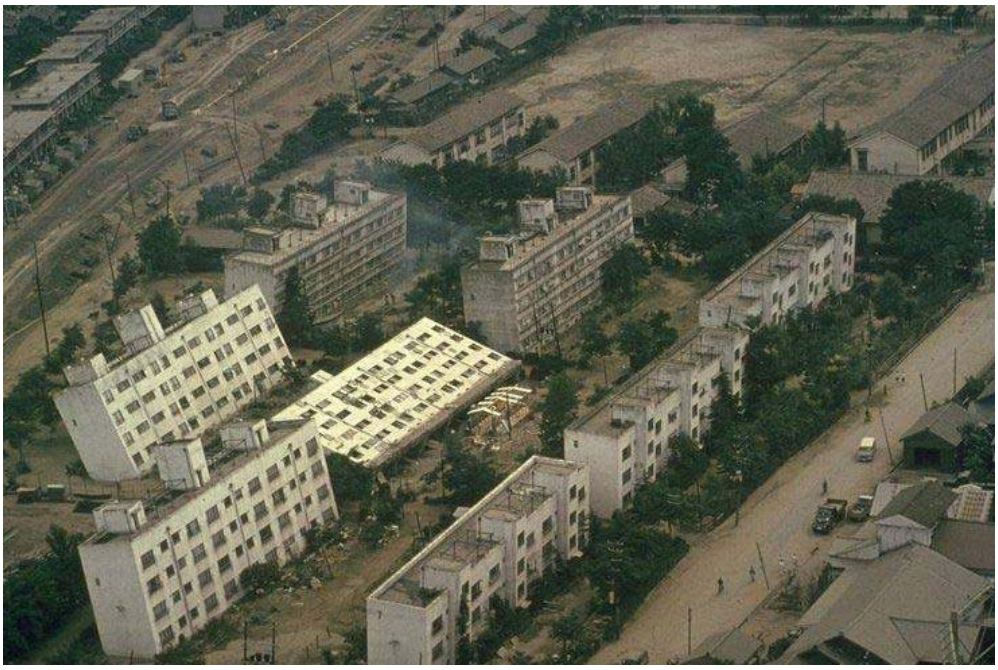

Figure 1.1: Tipped buildings caused by liquefaction-induced loss of bearing strength, 1964 Niigata, Japan Earthquake (Kramer 1996).

Figure 1.2: Liquefaction-induced lateral spreading effects on piles, 1964 Niigata, Japan Earthquake (Hamada 1991).

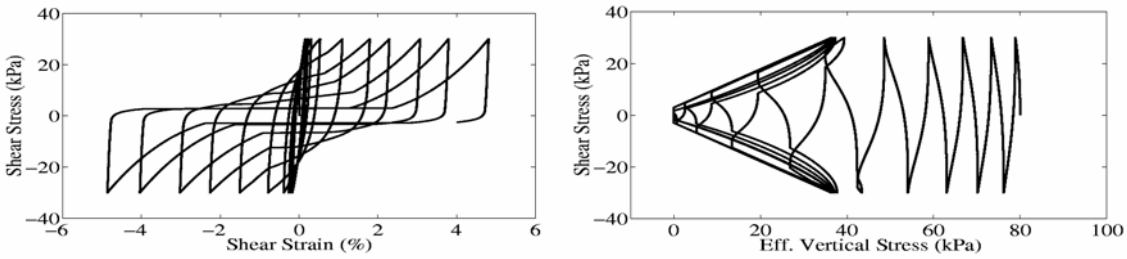

Figure 1.3: Schematic stress-strain and stress path response for medium-to-dense sand in stress-controlled, undrained cyclic shear loading (Parra 1996).

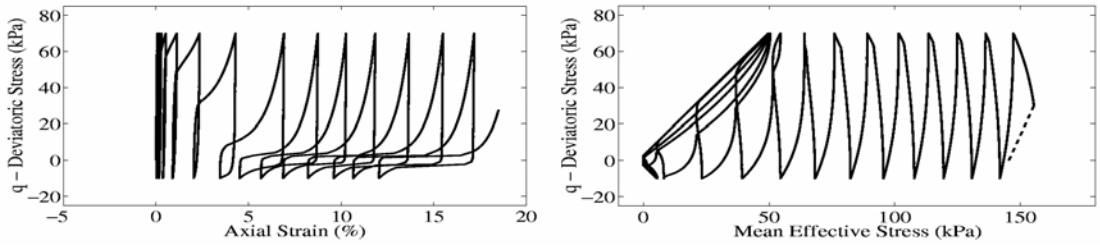

Figure 1.4: Schematic stress-strain and stress path response for medium-to-dense sand in stress-controlled, undrained cyclic shear loading with a static shear stress bias (Parra 1996).

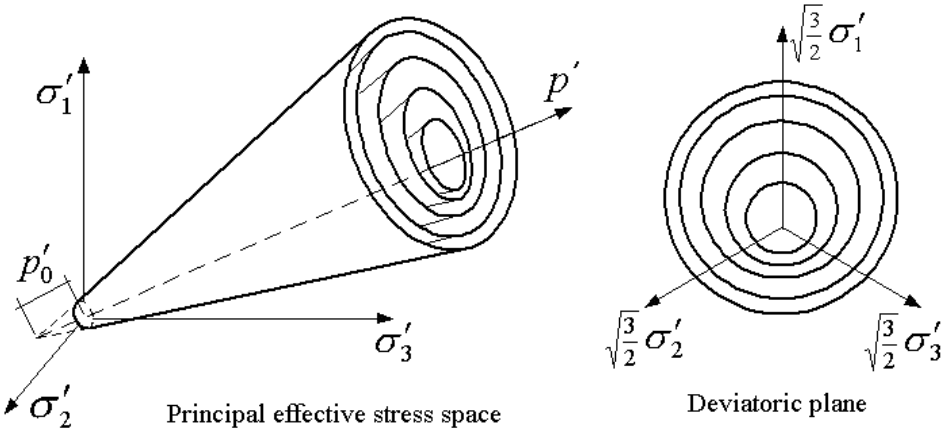

Figure 1.5: Conical yield surfaces for granular soils in principal stress space and deviatoric plane (Prevost 1985; Lacy 1986; Parra et al. 1996; Yang 2000).

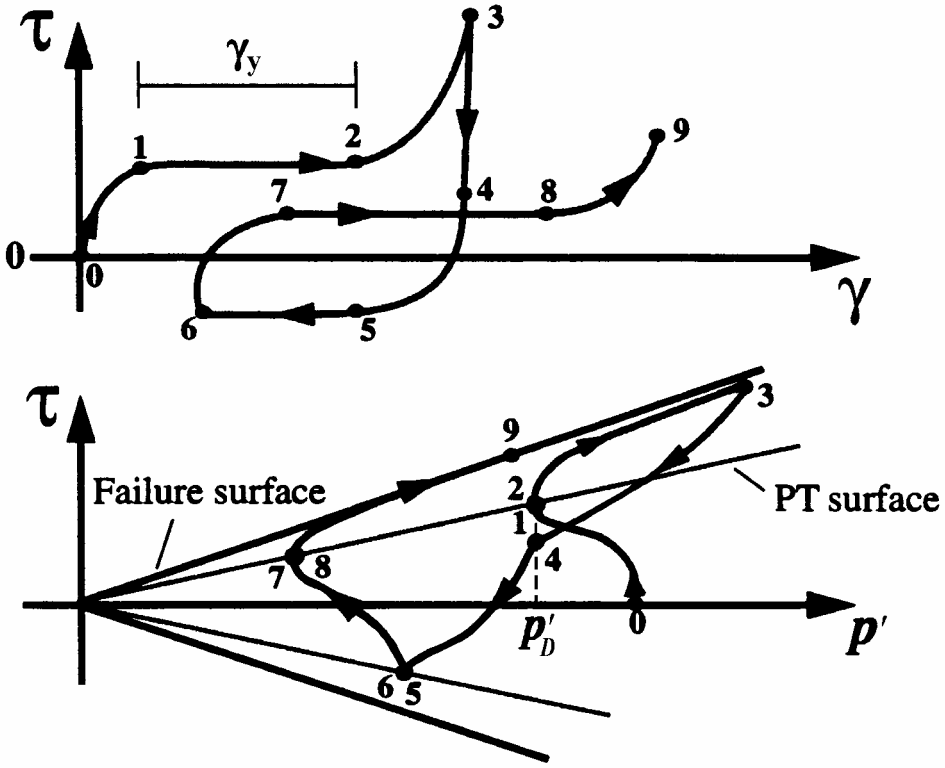

Figure 1.6: Shear stress-strain and effective stress path under undrained shear loading conditions (Parra 1996; Yang 2000).

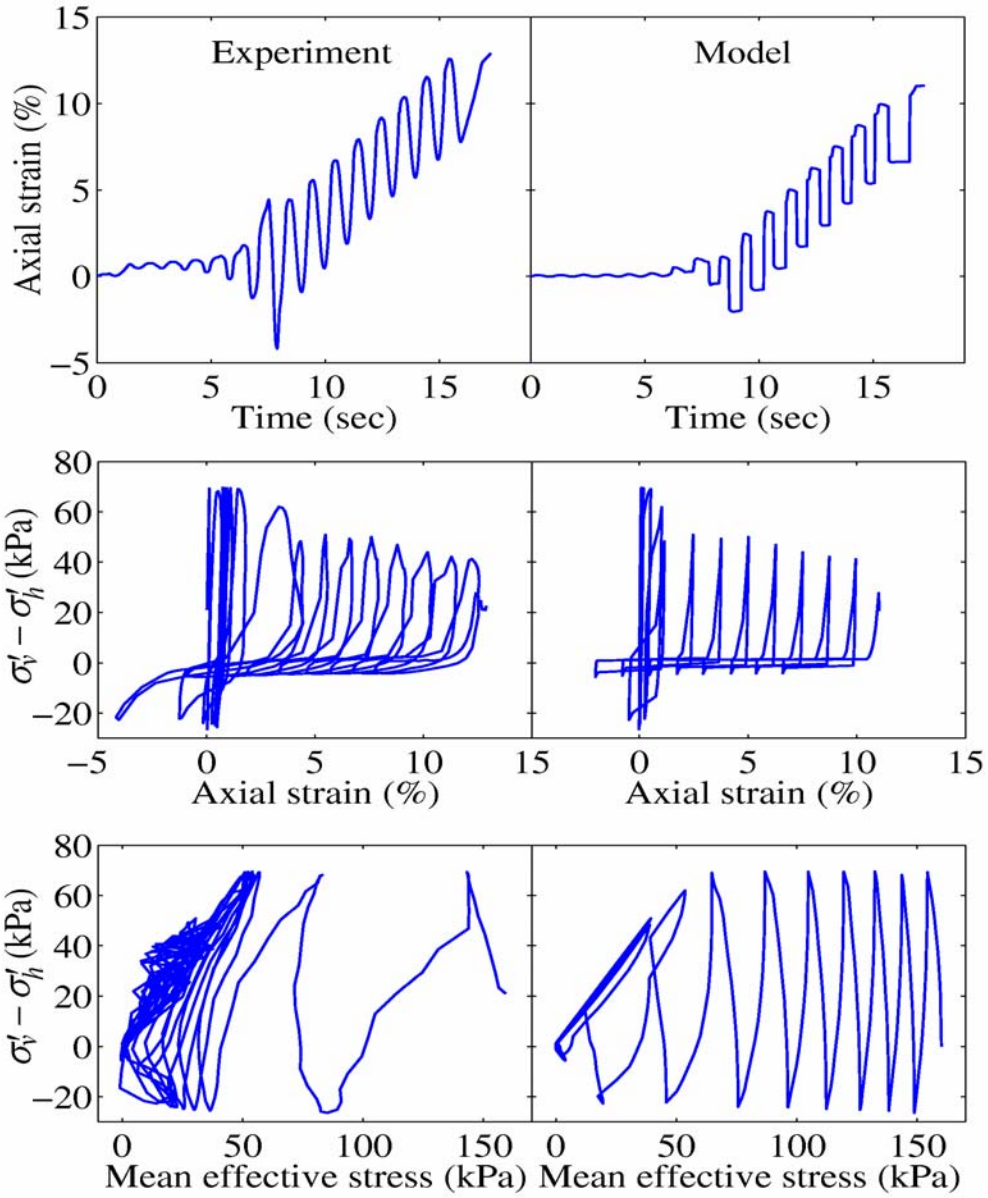

Figure 1.7: Recorded and computed results of anisotropically consolidated, undrained cyclic triaxial test (Nevada Sand at 40% relative density) with static shear stress bias (Arulmoli et al. 1992; Yang 2000).

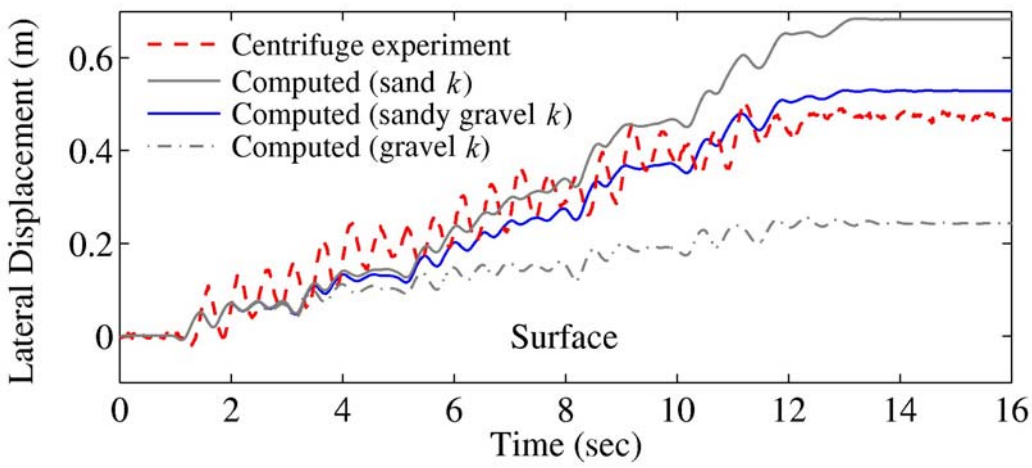

Figure 1.8: Recorded surface lateral displacement histories in uniform soil profile with different permeability coefficients (Yang and Elgamal 2002).

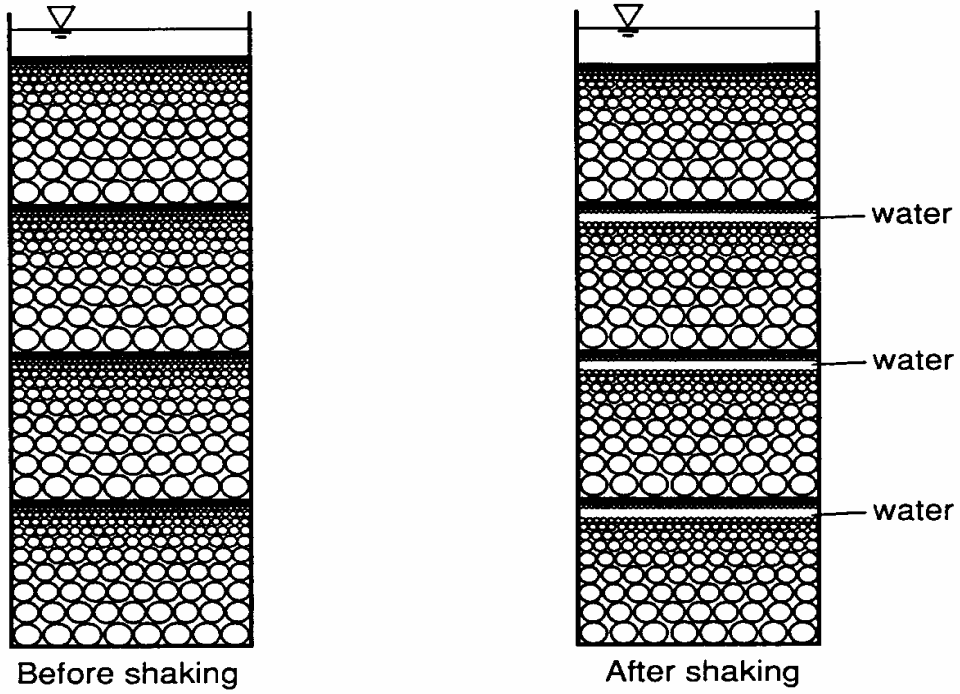

Figure 1.9: Recorded natural layering of soil strata of different permeabilities (Adalier 1992).

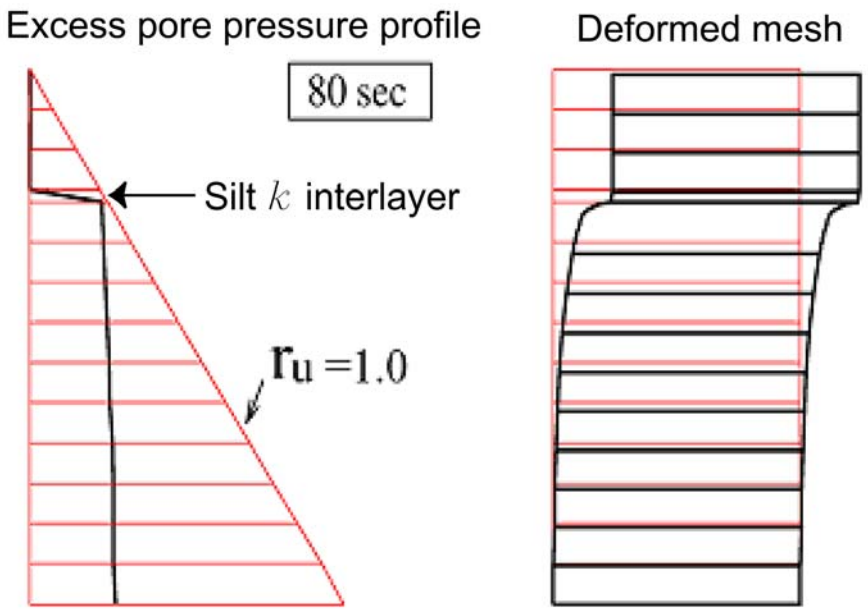

Figure 1.10: Excess pore-pressure profile and deformed mesh for uniform sand profile with a low-permeability interlayer (deformations are exaggerated for clarity)(Yang and Elgamal 2002).

Chapter 2 Parallel Software Organization

2.1 Parallel Computer Architectures

A parallel computer, as defined by Wilkinson and Allen (1999) , is a specially designed computer system containing multiple processors or several independent computers interconnected in some way. There are a number of different types of computers, and classifications are made on the basis of both instruction/data stream characteristics and memory architecture (Margetts 2002).

2.1.1 Instruction/Data Stream Classification

Flynn (1966) described four different types of computers:

1) SISD Single Instruction stream, Single Data stream
2) MISD Multiple Instruction stream, Single Data stream
3) SIMD Single Instruction stream, Multiple Data stream
4) MIMD Multiple Instruction stream, Multiple Data stream

This classification is commonly referred to as 'Flynn's Taxonomy'. The first term SISD describes traditional sequential von Neumann computers. A MISD computer would apply multiple instructions or operations on a single data stream. There has not been as much interest in this type of computer as in the other three types.

SIMD computers execute a single set of instructions on multiple data. The SIMD class can be further subdivided into vector processors and array processors. In a vector machine, each processor handles a different element of the vector. Examples of vector machines include the Fujitsu VPP300 and CRAY-YMP. In contrast, array processors

comprise a large number of very simple processors. This type of machine is not popular today and earlier examples include the ICL DAP and Connection Machine CM2 (Margetts 2002).

MIMD refers to essentially separate processors that work together to solve a problem. A MIMD computer may execute different instructions on multiple data streams. This architecture allows different parts of a program or even different programs to run simultaneously on different processors of the computer. Nearly all parallel machines used today are MIMD computers.

An important cross between the SIMD and the MIMD computers is the SPMD (Single-Program-Multiple-Data, see Section 2.2) programming paradigm (Mackay 1992). The SPMD paradigm executes the same program on multiple data streams. Most MIMD computers run in this mode, that is, each processor executes the same program. It differs from a SIMD computer, since each processor of a SIMD computer must execute the same instruction simultaneously. Although each processor on a MIMD computer executes the same program, each processor does not execute the same part of the program or same instruction simultaneously.

2.1.2 Memory Architecture

A much more useful way to classify modern parallel computers is by their memory model: distributed memory, shared memory, and hybrid distributed-shared memory. In a distributed memory computer (Figure 2.1), each processor has its own local memory. The processors synchronize and share data via message passing through an interconnecting network. Examples of such kind include CRAY T3E and IBM SP. In

a shared memory parallel computer (Figure 2.2), all processors have access to a pool of shared memory and the processors communicate and synchronize through the shared memory. An example of such a machine is CRAY T90.

A hybrid memory parallel computer is composed of a group of Symmetric Multiprocessors, or SMPs, communicated through the distributed network (Aoyama and Nakano 1999). SMP is a multiprocessor computer architecture where two or more identical processors are connected to a single shared main memory. SMPs know only about their own memory but not the memory on another SMP. The distributed memory component is the networking of multiple SMPs. Network communications are required to move data from one SMP to another. The hybrid distributed-shared memory architecture is used today by most of the largest and fastest machines, such as IBM DataStar (to be discussed in Section 2.1.3). Table 2.1 shows some examples of the top supercomputers worldwide as of June 2005.

Depending on the network type, the time for each processor in a shared memory computer to reach all memory locations may be the same (Uniform Memory Access – UMA, Figure 2.2a) or different (Non-Uniform Memory Access – NUMA, Figure 2.2b). In NUMA, time for memory access depends on location of data. Local access is faster than non-local access.

2.1.3 Parallel Computers Available to this Research

San Diego Supercomputer Center (SDSC) at University of California, San Diego (UCSD) is a one of the leading centers for high performance computing, worldwide. SDSC provides and supports a wide range of computing and data resources for the

research community. This research mainly uses two IBM SP machines: Blue Horizon and Datastar, available at SDSC.

Blue Horizon (SDSC 2003) is an IBM Scalable POWERparallel (SP) machine with 144 compute nodes, each with eight POWER3 RISC-based processors and with 4 GBytes of memory. Each processor on the node has equal shared access to the memory. Blue Horizon was decommissioned in June 2004.

Datastar (SDSC 2004) is SDSC's largest IBM terascale machine, built in a configuration especially suitable for data intensive computations. DataStar has 176 (8-way) P655+ and 11 (32-way) P690 compute nodes. The 8-way nodes have 16 GB, while most of the 32-way nodes have 128 GB of memory. One 32-way node has 256 GB of memory for applications requiring unusually large memory space. Both Blue Horizon and Datastar nodes are suitable for both shared-memory (e.g.OpenMP or Pthreads) and message-passing (e.g. MPI) programming models, as well as the mixture of the two.

Linux AMD cluster parallel computers provided by the Center for Advanced Computing (CAC) at the University of Michigan, and IBM SP machines provided by Texas Advanced Computing Center (TACC) at the University of Texas at Austin were also used for debugging and testing of the code.

2.2 Parallel Program Strategies

Programming models required to take advantage of parallel computers are significantly different from the traditional paradigm for a sequential program (Law 1986; Mackay 1992). Implementation of an engineering application, besides optimizing matrix manipulation kernels for the new computer environment, must take careful

consideration of the overall organization and the data structure of the program. In a parallel computing environment, for example, care must be taken to maintain all participating processors busy performing useful computations while minimizing communication among processors. To take advantage of parallel processing power, the algorithms and data structures of CYCLIC are re-designed and implemented in ParCYCLIC.

One common approach in developing application software for distributed memory parallel computers is to use the Single-Program-Multiple-Data (SPMD) paradigm (Law 1994; Herndon et al. 1995). The SPMD paradigm is related to the *divide and conquer* strategy (Neapolitan and Naimipour 1998) and is based on breaking a large problem into a number of smaller sub-problems, which may be solved separately on individual processors. In this parallel programming paradigm, all processors are assigned the same program code but run with different data sets comprising the problem. A FE domain is first decomposed using some well-known domain decomposition techniques. Each processor of the parallel machine then solves a partitioned domain, and data communications among sub-domains (a sub-domain denotes a collection of elements that would be assigned to a single processor) are performed through message passing. The Domain Decomposition Method (DDM) is attractive in FE computations on parallel computers because it allows individual sub-domain operations to be performed concurrently on separate processors. The SPMD model has been applied successfully in the development of many parallel FE programs from legacy serial codes (Aluru 1995; Herndon et al. 1995). Development of

ParCYCLIC was based on the SPMD model to parallelize the legacy serial code CYCLIC.

2.3 Computational Procedures

The computational procedure of ParCYCLIC is illustrated in Figure 2.3. The procedure can be divided into three phases, namely: preprocessing and input phase, nonlinear solution phase, and output and postprocessing phase. The first phase consists of initializing certain variables, allocating memories, and reading the input file. There is no inter-process communication involved in this phase – all the processors run the same code and read identical copies of the same input file. Since a mesh partitioning routine is incorporated in ParCYCLIC, the input file does not need to contain any information for processor assignment of nodes and elements. The input file for ParCYCLIC has essentially the same format as that of CYCLIC.

After the preprocessing and input phase, the nonlinear solution phase starts with using a domain decomposer to partition the FE mesh. Symbolic factorization is then performed to determine the nonzero pattern of the matrix factor. After symbolic factorization, storage spaces for the sparse matrix factor required by each processor are allocated. Since all processors need to know the nonzero pattern of the global stiffness matrix and symbolic factorization generally only takes a small portion of the total runtime, each processor carries out the domain decomposition and symbolic factorization based on the global data.

In the nonlinear analysis solution phase, the program essentially goes through a while loop until the number of increments reaches the pre-set limit. In the nonlinear

solution phase, the modified Newton-Raphson algorithm is employed, that is, the stiffness matrix at each iteration step uses the same tangential stiffness from the initial step of the increment. For large-scale FE modeling, the global matrix assembly and numerical factorization require substantial computation and message exchange. Although the modified iterative approach typically requires more steps per load increment as compared with a full Newton-Raphson scheme, substantial savings can be realized as a result of not having to assemble and factorize a new global stiffness matrix during each iteration step. In ParCYCLIC, there is one variation on the typical modified Newton-Raphson algorithm. As shown in Figure 2.3, a convergence test is performed at the end of each iteration step. If the solution has not converged after a certain number of iterations (e.g., 10 iterations) within a particular time step, the time step will be divided in half to expedite convergence. This process repeats until the solution converges.

The numerical solution scheme for the linear system of equations $Kx = f$ in ParCYCLIC is based on the row-oriented parallel sparse solver developed by Mackay and Law (Law and Mackay 1993). The direct solution of the linear system of equations consists of three steps: (1) parallel factorization of the symmetric matrix K into its matrix product LDL^T ; (2) parallel forward solution, $y = L^{-1} f$; and (3) parallel backward substitution, $x = L^{-T} D^{-1} y$. The parallel solver will be discussed in Chapter 3.

The final phase, output and postprocessing, consists of collecting the calculated node response quantities (e.g. displacement, acceleration, pore pressure, etc.) and element output (such as normal stress, normal strain, volumetric strain, shear strain,

mean effective stress, etc.) from different processors. The response quantities and timing results are then written into files for future processing and visualization.

For efficient usage, a supercomputer is usually imposed with the policy of a clock time limit for a running job (e.g. 18 hours clock time limit imposed on DataStar). Therefore, a restart option was implemented in ParCYCLIC. This option involves saving necessary node and element response quantities including nonlinear stress state information to physical storage (e.g. a disk) and reading from those restart files later. This restart functionality in ParCYCLIC allows a simulation to start from a preceding state (e.g., after 1000 or 2000 conducted time steps). Therefore, long runs exceeding the clock limit posed on a supercomputer are not a concern.

2.4 3D Simulation Capability Enhancement

The capacity of CYCLIC was extended from two-dimensional (2D) to 3D simulation by adding 3D brick elements (Figure 2.4). Inclusion of continuum 3D brick elements is a straightforward addition to CYCLIC. This effort is particularly useful in conjunction with the parallel and distributed computing capabilities developed.

In order to ensure numerical stability in case of nearly undrained and incompressible pore fluid condition, the Babuska-Brezzi condition should be met (Chan 1988). Consequently, the shape function of the solid phase should be one degree higher than that of the fluid phase. Therefore, 20-8 (Figure 2.4b, where 20 represents the number of nodes for the solid phase, 8 represents the number of nodes for the fluid phase) and 27-8 (Figure 2.4c) noded brick elements are also implemented in CYCLIC in addition to the 8-8 noded brick element (Figure 2.4a). Most analyses reported in this

thesis are undertaken using the 20-8 noded brick element. The procedure to construct the shape functions for a 27-8 noded brick element is included in Appendix A. A 3 x 3 Gauss-Legendre integration rule is used in the evaluation of the matrices related to the solid matrix, and a 2 x 2 rule for the matrices related to the fluid phase.

2.5 Message Exchange Using MPI

During the parallel execution of ParCYCLIC, processors in the program need to communicate with each another. The inter-processor communication of ParCYCLIC is implemented using MPI (Message Passing Interface) (Snir and Gropp 1998), which is a specification of a standard library for message passing. MPI was defined by the MPI Forum, a broadly based group of parallel computer vendors, library developers, and applications specialists. One advantage of MPI is its portability, which makes it suitable to develop programs to run on a wide range of parallel computers and workstation clusters. Another advantage of MPI is its performance, because each MPI implementation is optimized for the hardware it runs on. Generally, MPI code can be developed for an arbitrary number of processors. It is up to the user to decide, at run-time, how many processors should be invoked for the execution.

The MPI library consists of a large set of message passing primitives (functions) to support efficient parallel processes running on a large number of processors interconnected over a network. The implementation of ParCYCLIC employs only a small set of MPI message passing functions. There are two types of communications in ParCYCLIC: point-to-point communication and collective messages. The point-to-point communication in MPI involves transmittal of data between two processors. The

collective communications, on the other hand, transmit data among all processors in a group.

For the implementation of ParCYCLIC, point-to-point messages are used extensively during the global matrix assembly and matrix factorization phases. Figure 2.5 shows some sample code for the point-to-point messages in ParCYCLIC, which have the following features:

1) For most of the point-to-point communications, the blocking send (`MPI_Send`) is used to send out data, and the non-blocking receive (`MPI_Irecv`) is used to receive data. The purpose of this choice is to keep all processors busy performing useful computation and at the same time to ensure that all messages are delivered. A blocking send temporarily stores the message data in a buffer. The function does not return until the message has been safely delivered. A non-blocking receive tests the buffer for any incoming messages, and can concurrently perform computation not relying on the incoming messages.
2) The `MPI_Send` sends a message to the specific recipient by passing the receiver's node identification (denoted as `r_node` in Figure 2.5) as one of the parameters. The `MPI_Irecv`, on the other hand, receives a message from any source by denoting the sender as a wild card value of `MPI_ANY_SOURCE`. The sender knows whom the recipient is when sending a particular message, while the receiver listens to messages from all processors. After a message is received, the `MPI_SOURCE` field of the `MPI_Status` is retrieved to find the node identification of the sender. The

actual size of the received message is detected by calling the function `MPI_Get_count`.

3) Instead of sending messages with data type information (such as double, integer, byte, etc.), all data are sent as a byte stream, which is denoted as `MPI_BYTE`. Since messages have overhead cost, minimizing the number of messages improves the system performance. One way to reduce the number of messages is for the sender to combine messages. Each sender maintains a buffer for all the outgoing messages, and these messages will not be sent off to other processors unless the buffer is nearly full. Since the buffer may contain mixed types of data, the byte stream is a common format to represent the content of the buffer. The type information of the actual content can be retrieved during the unpacking of a message according to the pre-defined communication protocol.

There are three types of collective communications in the implementation of ParCYCLIC: barrier synchronization, gather-to-all, and broadcast. The barrier synchronization function, `MPI_Barrier`, blocks the caller until all processors within a group have finished calling it. The barrier synchronization can be used to ensure all the processors are at the same pace.

The gather-to-all function is employed for performing global operations (such as sum, max, logical, and etc.) across all the processors of a group. The gather-to-all function is applied in ParCYCLIC to gather global information. For example, since each processor is working on a portion of the domain, it only holds the solution for that portion. A gather-to-all function call is needed at the end of the numerical solution

phase to collect the global solution from each processor. The gather-to-all function, `MPI_Allreduce`, has the following syntax:

```
MPI_Allreduce(sendbuf, recvbuf, count,
      [MPI_INT, MPI_DOUBLE...],
      [MPI_MAX, MPI_MIN, MPI_SUM...], MPI_COMM_WORLD);
```

The third type of collective messages is broadcast, which sends a message to all members of a processors group. In ParCYCLIC, most communications in the forward and backward solution phases require sending the same message to more than one processor. Figure 2.6 shows some sample codes for broadcasting messages in ParCYCLIC. After knowing which processor belongs to the broadcast group, the `MPI_Comm_create` function can be invoked to create a communication group `MPI_Comm`. The group communication is then handled by a broadcast message to the `MPI_Comm`.

Table 2.1: Top supercomputers in June 2005, worldwide (TOP500 2005).

Rank	Manufa-cturer	Computer	Installation Site	Country	Proce-ssors	R_{max}* (GFlops)	R_{peak}** (GFlops)
1	IBM	BlueGene/L eServer Blue Gene Solution	DOE/NNSA/LLNL	United States	65536	136800	183500
2	IBM	BGW eServer Blue Gene Solution	IBM Thomas J. Watson Research Center	United States	40960	91290	114688
3	SGI	Columbia SGI Altix 1.5 GHz, Voltaire Infiniband	NASA/Ames Research Center/NAS	United States	10160	51870	60960
4	NEC	Earth-Simulator	The Earth Simulator Center	Japan	5120	35860	40960
5	IBM	MareNostrum JS20 Cluster, PPC 970, 2.2 GHz, Myrinet	Barcelona Supercomputer Center	Spain	4800	27910	42144
6	IBM	eServer Blue Gene Solution	ASTRON/Universit y Groningen	Nether-lands	12288	27450	34406
7	California Digital Corporation	Thunder Intel Itanium2 Tiger4 1.4GHz - Quadrics	Lawrence Livermore National Laboratory	United States	4096	19940	22938
8	IBM	Blue Protein eServer Blue Gene Solution	Computational Biology Research Center, AIST	Japan	8192	18200	22937
9	IBM	eServer Blue Gene Solution	Ecole Polytechnique Federale de Lausanne	Switzerlan d	8192	18200	22937
10	Cray Inc.	Red Storm, Cray XT3, 2.0 GHz	Sandia National Laboratories	United States	5000	15250	20000
Parallel computer available for this research							
43	IBM	DataStar eServer pSeries 655/690 (1.5/1.7 Ghz Power4+)	UCSD/San Diego Supercomputer Center	United States	1696	6385	10406

*R_{max} – Maximal LINPACK performance achieved (LINPACK Benchmark is a measure of a computer's floating-point rate of execution. It is determined by running a computer program that solves a dense system of linear equations)
**R_{peak} – Theoretical peak performance

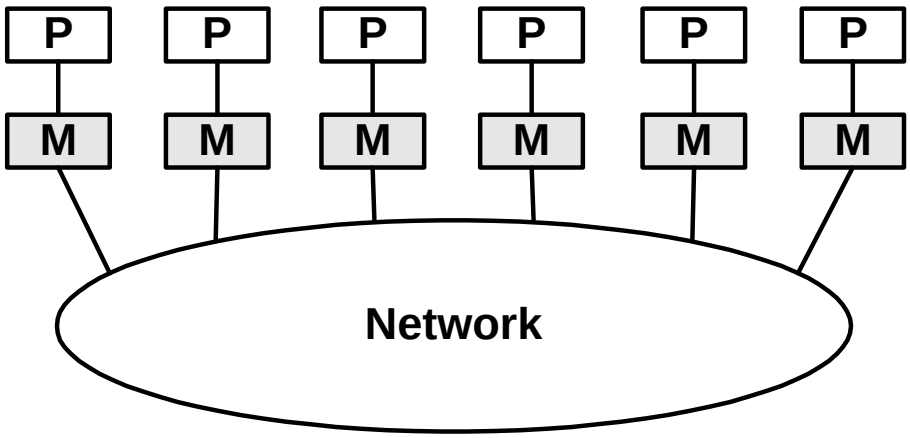

Figure 2.1: Distributed memory.

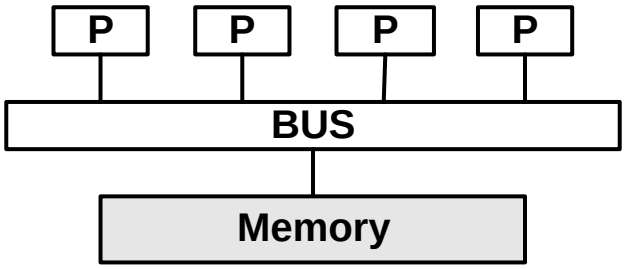

(a) Uniform Memory Access - UMA

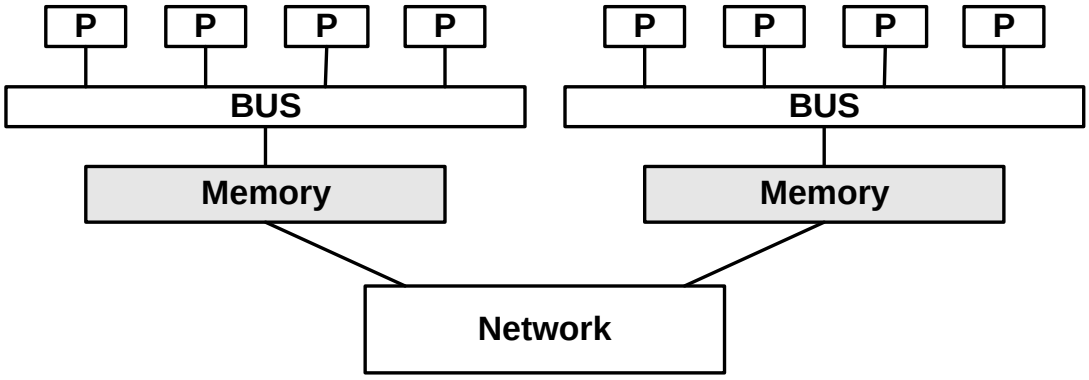

(b) Non-Uniform Memory Access – NUMA

Figure 2.2: Shared memory.

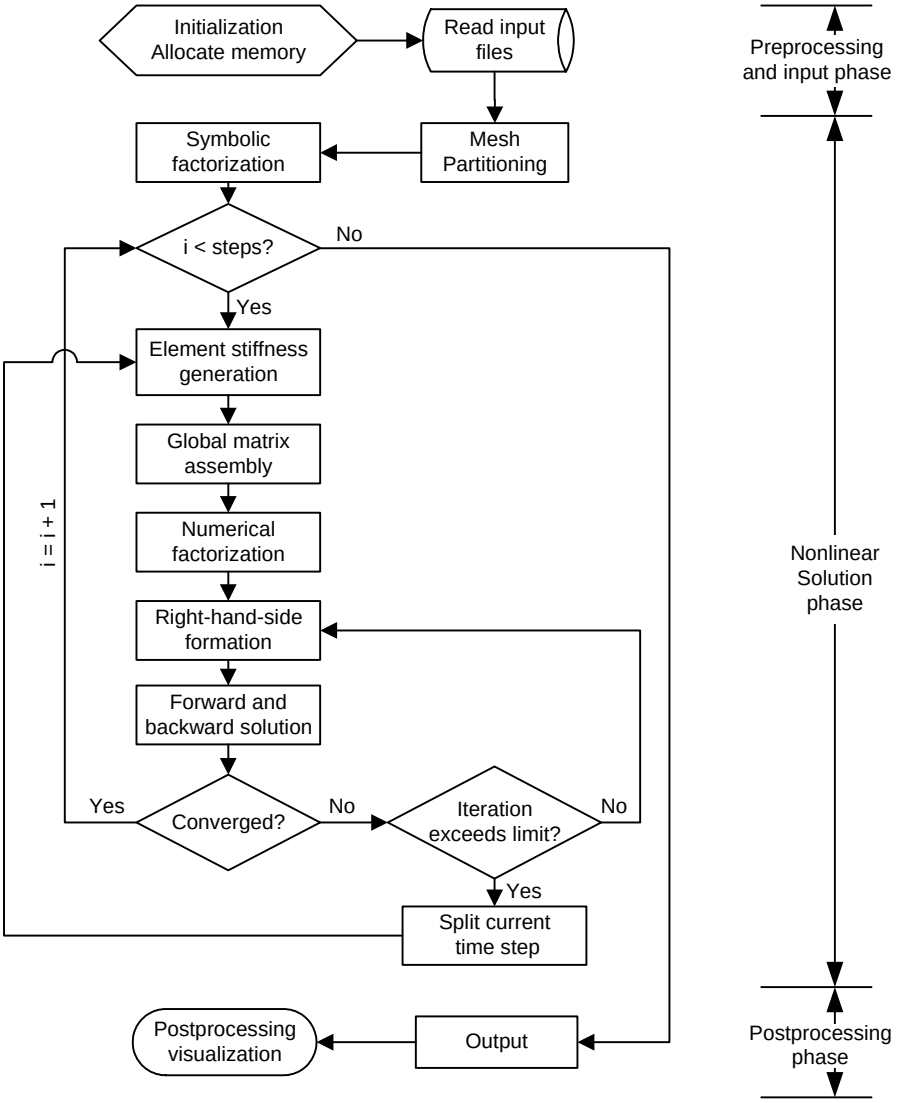

Figure 2.3: Flowchart of computational procedures in ParCYCLIC.

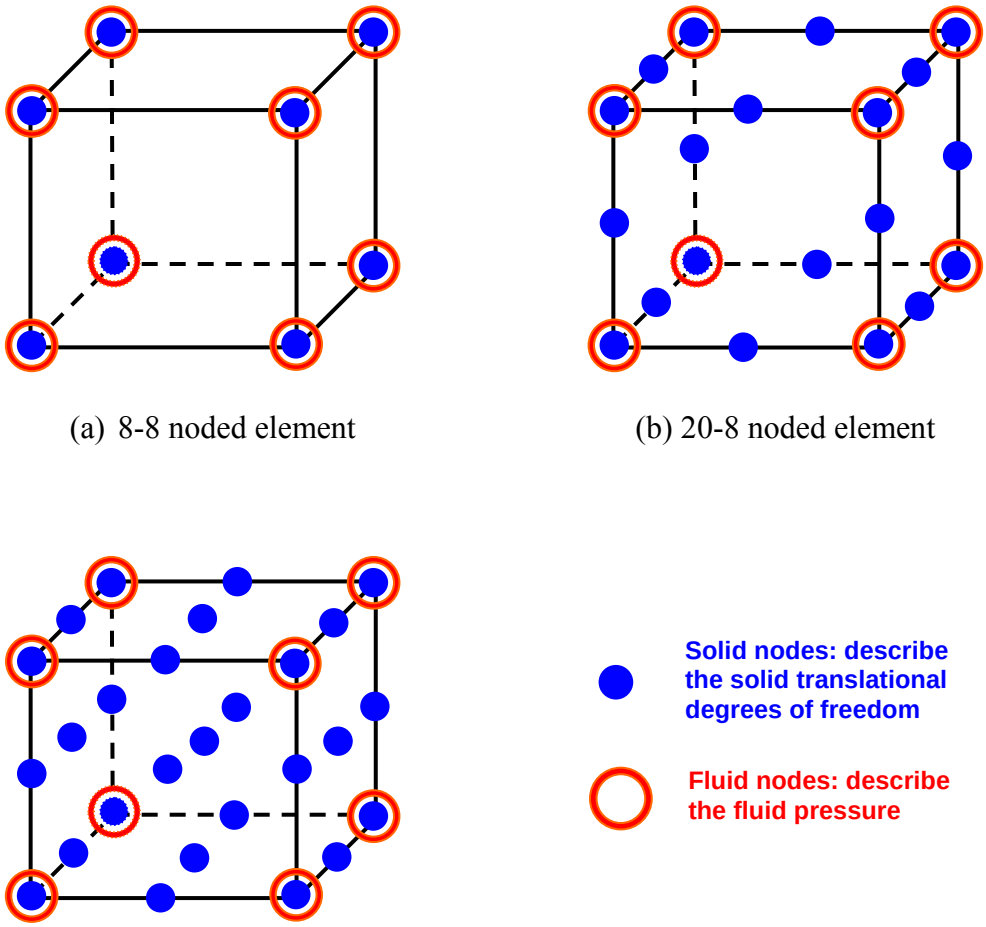

(a) 8-8 noded element

(b) 20-8 noded element

(c) 27-8 noded element

Figure 2.4: 3D solid-fluid coupled brick elements.

```
MPI_Request request;
MPI_Status status;
int mlen;
int s_node, r_node;

MPI_Send(sendbuf, len, MPI_BYTE, r_node, tag, MPI_COMM_WORLD);

MPI_Wait(&request, &status);

/* set up recbuf for the incoming message*/
...
MPI_Irecv(recbuf, length, MPI_BYTE, MPI_ANY_SOURCE, tag,
          MPI_COMM_WORLD, &request);

s_node = status.MPI_SOURCE;
MPI_Get_count(&status, MPI_BYTE, &mlen);
Unpack(recbuf, mlen);
```

Figure 2.5: Sample code for point-to-point message in ParCYCLIC.

```
int *sendlist, nshare;
MPI_Comm workers;
MPI_Group world_group, worker_group;

MPI_Comm_group(MPI_COMM_WORLD, &world_group);
MPI_Group_incl(world_group, nshare, sendlist, &worker_group);
MPI_Comm_create(MPI_COMM_WORLD, worker_group, &workers);

MPI_Bcast(buf, length, MPI_BYTE, my_pid, workers);
```

Figure 2.6: Sample code for broadcast message in ParCYCLIC.

Chapter 3 Parallel Sparse Direct Solver

3.1 Introduction

Nonlinear FE computations of earthquake simulations involve the iterative solution of a linear system of equations:

$$K x = f \tag{3.1}$$

Where x and f are respectively the displacement and loading vectors. K is the effective global stiffness matrix which is sparse and symmetric. Due to the solid-fluid coupled formulation (see Section 1.4.3), the resulting K is also indefinite and contains negative diagonal elements. To solve the system of linear equations, the symmetric matrix K is often factored into its matrix product LDL^T, where L is a lower triangular matrix and D is a diagonal matrix. The solution vector x is then computed by a forward solve $Ly = f$ or $y = L^{-1}f$, followed by a backward solve $DL^Tx = y$ or $x = L^{-T}D^{-1}y$.

A variable bandwidth or profile solver is perhaps the most commonly used direct solution method in FE analysis programs (George and Liu 1981; Mackay 1992). A profile solver uses a row storage (or skyline storage) scheme as the basic data structure (Hughes 1987), in which, for each row of the matrix factor L, the scheme stores the entries from the first nonzero coefficient of that row to the diagonal element. A profile solver is often limited for small sized problems.

A sparse matrix solver is employed for moderate to large sized problems, especially in 3D scenarios. Sparse matrix methods explicitly avoid the storage of and operations on the zero entries by first determining the nonzero structure of matrix factor L from that of K before numerical factorization proceeds (George and Liu 1981).

The solution strategy in ParCYCLIC is based on the parallel row-oriented sparse solver originally developed by Law and Mackay (1993). The original parallel sparse solver has been improved and enhanced, and incorporated into ParCYCLIC. This work is in conjunction with efforts of Prof. Kincho Law and Dr. Jun Peng of Stanford University.

This chapter describes the solution strategy employed in ParCYCLIC and the parallel performance of the code. Section 3.2 reviews the original parallel sparse solver. Section 3.3 describes an automatic domain decomposer. The parallel global matrix assembly is discussed in Section 3.4. In Section 3.5, we report the parallel performance of ParCYCLIC.

3.2 Overview of the Original Parallel Sparse Solver

The parallel sparse solver is based on a row-oriented storage scheme that takes full advantage of the sparsity of the stiffness matrix. The concept of the sparse solver is briefly described below (Mackay et al. 1991; Mackay 1992; Law and Mackay 1993).

3.2.1 Assignment of Sparse Stiffness Matrix

The notion of the elimination tree plays a significant role in sparse matrix study (Liu 1990). It is well known that the nonzero entries in the numerical factor L can be determined by the original nonzero entries of the stiffness matrix K (Law and Fenves 1986; Liu 1991) and a list vector, which is defined as

$$PARENT(j) = \min\{i \mid L_{ij} \neq 0\} \tag{3.2}$$

The array *PARENT* represents the row subscript of the first nonzero entry in each column of the lower triangular matrix factor L. The definition of the list array *PARENT* results in a monotonically ordered elimination tree of which each node has its numbering higher than its descendants. By topologically post-ordering the elimination tree, the nodes in any subtree can be numbered consecutively. The resulting sparse matrix factor is partitioned into block submatrices where the columns/row of each block corresponds to the node set of a branch in the elimination tree.

Figure 3.1 shows a simple square FE grid and its post-ordered elimination tree representation. One important feature of the elimination tree is that it describes the dependencies among the variables during the factorization process. That is, a column block may not be factored until all nodes below the nodes representing the column block have been factored. This implies that all the column blocks represented by the leaves of the elimination tree have no dependencies. These column blocks can be factored independently and concurrently.

The coefficients of a sparse matrix factor are distributively stored among the processors according to the column blocks. Figure 3.2 shows an example of the data assignment of a sparse matrix on four processors for the FE model shown in Figure 3.1. The strategy is to assign the rows corresponding to the nodes along each branch of the elimination tree (column block) to a processor or a group of processors. Beginning at the root of the elimination tree, the nodes belonging to this branch of the tree are assigned among the available processors in a rotating round robin fashion. As we traverse down the elimination tree, at each fork of the elimination tree, the group of processors is divided to match the number and size of the subtrees below the current

branch. A separate group of processors is assigned to each branch at the fork and the process is repeated for each subtree. The process of assigning groups of processors to each branch of the elimination tree continues until only one processor remains for the subtree. At this stage, all remaining nodes in the subtree are assigned to the single processor.

The matrix assignment strategy described partitions a sparse matrix into two basic sets: the principal diagonal block submatrices and the row segments outside the principal block submatrices. For the principal block submatrices, which have a profile structure, the processor assignment proceeds on a row group by row group basis with each row group corresponding to a node in the FE model. This strategy divides the diagonal block submatrices into two groups: one is assigned to a single processor and the other is shared by multiple processors. For the row segments outside the diagonal blocks, the rows are assigned to the processors sharing the node set (column block) in a rotating round robin fashion.

3.2.2 Data Structure for Matrix Coefficients

After symbolic factorization, all nonzero entries in the matrix factor are determined. The data structure for storing the matrix coefficients is directly set up for the factored matrix L. There are three different data structures for storing the coefficients: one for the principal block submatrices associated with the column blocks assigned to a single processor, one for the principal block submatrices associated with column blocks shared by multiple processors, and one for the row segments in column blocks. The following describes the details of these three different data structures. For

demonstration purpose, the data structure in Processor 0 for the square grid problem shown in Figure 3.2 is presented.

The data structure for the principal block submatrices assigned to a single processor is illustrated in Figure 3.3. It consists of an array of pointers `ipenv` which points to the beginning of the coefficients for each row, and an array of integers to indicate the corresponding global row numbers. The actual matrix coefficients are stored consecutively to facilitate efficient access.

The data structure for the principal block submatrices assigned to multiple processors is illustrated in Figure 3.4. The array of pointers `epenv` points to the beginning coefficients of each row just like `ipenv` does for the principal block submatrices assigned to a single processor. The global row numbers and the length of the rows are stored in another array for each row block. Because each row block ends with an element in the matrix diagonal, the row number and row length are sufficient to map a stored matrix coefficient to its location in the global matrix. For example, the matrix coefficient $\mathbf{X_7}$ belongs to the third row block, which has global row number of 25 and row length of 5. Since we know that $\mathbf{X_7}$ is the second to the last elements in the row block, the global column number for $\mathbf{X_7}$ can be calculated as being 24.

The third data structure stores the row segments, as illustrated in Figure 3.5. This data structure is essentially a linked list with each node corresponding to a row segment. Each node in the linked list contains four variables, namely the global row number, the starting global column number for the row segment, a pointer to the next node, and a pointer to the beginning of the matrix coefficients for the row segment. These variables can be used to find the global row number and column number of a

particular matrix coefficient. For example, in Figure 3.5, the node in the linked list corresponding to matrix coefficient $\mathbf{n_{15}}$ has row number 23 and starting column number 9. Since $\mathbf{n_{15}}$ is the second element in the row segment, its column number can be calculated as 10.

3.2.3 Parallel Numerical Factorization

Once the processor assignment and the assembly of the global stiffness matrix are completed, numerical calculation can proceed. In ParCYCLIC, the LDL^T factorization is performed. The parallel numerical factorization procedure is divided into two distinct phases. During the first phase, the column blocks assigned entirely to a single processor are factorized. The strategy is to carry out as much computation as possible in the local processor. Figure 3.6 shows the parallel factorization procedures in this phase with the factor of matrix coefficients in Processor 1 being highlighted. The operations in this phase are as follows:

1) For each column block assigned to a processor, perform a profile factorization on the principal block submatrix.
2) Update the off-diagonal row segments below the principal submatrix by a series of forward solutions.
3) After the column blocks are factorized, form dot products among row segments. These dot products are then fanned-out to update the remaining matrix coefficients in the same processor or saved in the buffer to be sent out to other processors during the parallel factorization phase.

In the second phase of the numerical factorization, the column blocks shared by more than one processor are factorized. Figure 3.7 shows the parallel factorization procedures in this phase with the factor of matrix coefficients in Processor 1 being highlighted. The operations in this phase proceed as follows:

1) For the column blocks shared by multiple processors, each processor fans-in the dot products generated in phase one of the numerical factorization. The principal block submatrix can be updated based on the received dot products.
2) Perform parallel factorization of column blocks. This step involves a parallel profile factorization of the principal block submatrix and updating the row segments shared by a group of processors. In this step, the processor responsible for the first row (say, row r) in the column block factorizes the row and broadcasts it to all other processors sharing the column block. The other processors receive the row factor and use it to update columns in them. The processor containing the next row, $r+1$, updates the row and broadcasts it to the other processors sharing the column block. The other processors continue receiving rows until it is time to factor a row they are responsible for. This process continues until the entire submatrix is factored and all the row segments in the column block are updated.
3) After all the row segments in the column block have been updated, the row segments of the column blocks are circulated among the shared processors. After a processor receives another processor's row segment, the processor forms dot products between the row segments belonging to the two different

processors. The row segment is then passed on to the next processor to update the matrix column blocks.

Note that in this parallel factorization strategy, the dot products between row segments are not fanned-in until the column block that needs the dot products is being factorized by the processors.

3.2.4 Parallel Numerical Solution

Following the parallel factorization is the parallel forward solution phase, which can be viewed symbolically as a procedure traversing the elimination tree from the leaves to the root. The solution vector x and the load vector f are divided into blocks just as the matrix is divided into column blocks determined by the elimination tree. The forward solution phase is also divided into two phases: a sequential phase and a parallel phase.

In the first phase, each processor calculates the blocks of f corresponding to the matrix blocks which reside entirely within a single processor. For each column block assigned to a processor, each processor performs a profile forward solve with the principal submatrix in the column block. Each processor also updates the shared portions of the solution vector based on the row segments that lie below the profile submatrices. The solution coefficients not assigned to this processor are stored in a buffer to be sent to other processors.

Phase two of the parallel forward solution begins as the processors work together on the variables in the shared column blocks. There are three steps involved in this phase as outlined below:

1) The first step is to send and receive solution coefficients generated in phase one of the forward solution. These coefficients are used to update the partially solved block of solution vector *f*.
2) The second step performs parallel forward solution based on the principal submatrices. As each value of *f* is calculated, for example *f* [*i*], it is broadcast to the other processors sharing the block. After receiving the value of *f* [*i*], the processor responsible for *f* [*i*+*1*] can complete the solution and broadcast the value to other processors sharing the column block. This process is repeated until the solution to the entire block is completed.
3) The third step is to use the values in this block to update other blocks using the row segments in this column block.

Following the forward solution phase is the backward substitution procedure, which is essentially a reverse of the forward solution. The first phase of backward substitution deals with the portion of the solution vector shared by multiple processors and is essentially a reverse of the second phase of the forward solution. In the second phase, each processor calculates the portion of the solution vector corresponding to the column blocks residing within a single processor; the processors perform the calculations independently without any processor communications and may complete the solution at different times. Once all the processors finish the backward substitution, a global gathering function is invoked to obtain the global solution from each processor. This step is essential because each processor only has part of the global solution vector that it is responsible for.

3.3 Mesh Partitioning Using Domain Decomposition

In a parallel FE program, a domain decomposer is needed to automatically partition the FE mesh into subdomains. To achieve high parallel efficiency of the parallel sparse solver, it is important that the FE mesh is partitioned in such a way that computational workloads are well balanced among processors and inter-processor communication is minimized. In particular, an automatic FE domain decomposer must meet three basic requirements in order to be successful (Farhat 1988): (1) it must be able to handle irregular geometry and arbitrary discretization in order to be general purpose; (2) it must yield a set of balanced subdomains in order to ensure that the overall computational load will be as evenly distributed as possible among the processors; and (3) it must minimize the amount of interface nodes in order to reduce the cost of synchronization and/or message passing between the processors.

3.3.1 METIS Graph Partitioning Software

To decompose a FE domain, ParCYCLIC employs METIS (Karypis and Kumar 1998a), a software package for partitioning large irregular graphs, partitioning large meshes, and computing fill-reducing ordering of sparse matrices. The algorithms in METIS are based on multilevel graph partitioning (Karypis and Kumar 1998b, c). The multilevel algorithm reduces the original graph partitioning problem to a sequence of bisection steps. That is, the algorithm first divides the graph into two pieces, and then recursively bisects the two sub-pieces independently. The multilevel partitioning method is quite different from traditional methods (Figure 3.8). Traditional graph partitioning algorithms compute a partition of a graph by operating directly on the

original graph. A multilevel partitioning algorithm, on the other hand, takes a different approach. First, the algorithm reduces the size of the graph by collapsing vertices and edges to produce a smaller graph. The graph partitioning is then performed on the collapsed graph, as shown in Figure 3.8. Finally, the partition is propagated back through the sequence to un-collapse the vertices and edges, with an occasional local refinement (Karypis and Kumar 1998a).

METIS provides both stand-alone programs (executable files) and library interfaces (functions). The library interfaces are incorporated in ParCYCLIC to perform the domain decomposition. In particular, we are interested in the usage of the METIS function of `METIS_NodeND()`, which is a function to compute fill-reducing orderings of sparse matrices using the multilevel nested dissection algorithm. The nested dissection paradigm is based on computing a vertex-separator for the graph corresponding to the matrix. The nodes in the separator are moved to the end of the matrix, and a similar process is applied recursively for each one of the other two parts. This routine is very useful for generating the ordering for the sparse solver so that the storage of the sparse matrix can be reduced.

The details of the above-mentioned function and its interface can be found in METIS manual (Karypis and Kumar 1997). The function has input parameters `xadj` and `adjncy`, which are two arrays used to represent the adjacency structure of a graph.

3.3.2 Graph Representation of Matrices

Graph theory plays a significant role in the study of sparse matrices (George and Liu 1981). A graph *G=(X, E)* consists of a finite set of *nodes* or *vertices* together with a

set of *edges*, which are unordered pairs of *vertices*. The structure of a matrix can be symbolically represented as a graph, where the row (or column) number of the matrix represents the vertices and the non-zero entries of the matrix corresponds to edges (Peng 2002). For example, if a_{12} is a non-zero entry of the matrix A, then we have an edge from vertex *1* to vertex *2* in the graph that represents the matrix.

The adjacency structure of a graph can be stored using a compressed storage format (CSR). The CSR format is a widely used scheme for storing sparse graphs (Karypis and Kumar 1997). In this format, the adjacency structure of a graph with n vertices and m edges is represented using two arrays `xadj` and `adjncy`. The `xadj` array is of size $n+1$, and the `adjncy` is of size of $2m$. The size of `adjncy` is $2m$ instead of m is because for each edge between vertices x and y, we actually store both (x, y) and (y, x).

The CSR storage of a graph is as follows. The adjacency list of vertex i is stored in array `adjncy` starting at index `xadj[`i`]` and ending at (but not including) `xadj[`$i+1$`]` (i.e., `adjncy[xadj[`i`]]` through and including `adjncy[xadj[`$i+1$`]-1]`). That is, for each vertex i, its adjacency list is stored in consecutive locations in the array `adjncy`, and the array `xadj` is used to indicate where the adjacent vertices of i begin and end. Figure 3.9a shows an example of a sparse matrix, with the number and * denoting the nonzero entries. Figure 3.9b is the graph representation of the matrix, and the Figure 3.9c illustrates the CSR storage of the adjacency structure of the graph.

3.3.3 Linking METIS routine

The `METIS_NodeND` function is incorporated into ParCYCLIC to compute the fill-reducing orderings of sparse matrices. The routine interfacing with `METIS` is called `multind()` and the `METIS_NodeND` method is incorporated in this routine, as shown in Figure 3.10. The inputs to the `multind()` function are the `xadj` and `adjncy` pair, and the outputs are `perm` and `invp` arrays, which store the computing ordering of the input graph.

In addition, two parameters are introduced: `numlevels`, `order` (Figure 3.10). The integer `numlevels` is the number of levels to partition, which is determined by the number of processors (power of 2 is suggested) used in the execution of ParCYCLIC. The objective of the partitioning is to minimize the total communication volume. Once the cuts are found by METIS routines, i.e., the FE mesh has been partitioned into subdomains, the internal nodes of each subdomain still need to be ordered to reduce the fill-ins of the matrix factors. The integer `order` stands for the type of the ordering scheme for the subdomains. In ParCYCLIC, there are many ordering routines implemented and added into `METIS` to perform this task, including Reverse Cuthill-McKee (George 1971), Minimum Degree (Tinney and Walker 1967), General Nested Dissection (Lipton et al. 1979), and Multilevel Nested Dissection (Karypis and Kumar 1998b). Users are allowed to choose different types of ordering routines for a specific problem. Otherwise, the default ordering routine is the Multilevel Nested Dissection ordering (`order` = 0), because it is stable and normally generates an ordering with the

least fill-ins of the matrix factors. After the matrix ordering is complete, symbolic factorization and parallel matrix assignment are performed.

3.4 Parallel Global Matrix Assembly and Right-Hand-Side Formation

3.4.1 Parallel Global Matrix Assembly

The generation of element stiffness matrices is one of the most natural tasks for parallel implementation. Since each element stiffness matrix can be generated independently of the other element stiffness matrices, each processor can work independently on the elements assigned to it. After the stiffness matrix of an element is generated, the processor that has the element assigned to it will be responsible to assemble the element coefficients to the matrix data structure described in the previous section. There are two methods for assigning elements to different processors. For the first method, each element is assigned to a particular processor with no duplication of element assignment. The second method allows duplicated assignment of elements to the processors but requires no inter-processor communication for global matrix assembly.

The first method (referred to herein as the first element assignment method), proposed by Mackay (1992), is to distribute the elements to different processors according to the processor assignment of the global nodal variables of the elements. This element assignment method can be summarized as follows (Mackay 1992):

1) If all the nodal variables of an element belong to a single processor, the element is assigned to that processor.

2) If one of the nodal variables of an element belongs to a column block assigned to a single processor, then the element is assigned to that processor.
3) If all nodal variables of an element are shared among multiple processors, the element is assigned to the processor which is assigned the lowest global number variable of the element stiffness matrix.

For the parallel global matrix assembly, coefficients of the element stiffness matrices that belong to the processor where the element stiffness matrix is formed are assembled into the global stiffness matrix directly. If the coefficients of the element stiffness matrix belong to the segment of the global stiffness matrix located in another processor, they are sent to that processor for assembly.

The first element assignment method ensures no duplication of element stiffness generation, but a substantial amount of messages is needed to exchange the stiffness matrix coefficients among the processors. To eliminate the messages for global matrix assembly, a second element assignment method (referred to herein as the second element assignment method) is introduced in ParCYCLIC (Law 2004). All the elements along a cut are assigned to a group of processors that share the cut. In this method, the same element may be assigned to more than one processor, and consequently the element stiffness generation will be duplicated. However, the duplication of work can be offset by not having to exchange messages. During the global matrix assembly phase, coefficients of the element stiffness matrices that belong to the processor where the element stiffness matrix is formed are assembled into the global stiffness matrix directly. If the coefficients of the element stiffness matrix belong to another processor, they are simply discarded.

Both methods for element assignment have been implemented in ParCYCLIC. For illustration purpose, Figure 3.11 shows the results of applying both methods to assign elements to four processors for the square grid model (more examples are shown in Figure 3.12 and Figure 3.13). Depending on the characteristics of the FE model, users can choose which method to use. For large FE models where the interfaces (cuts) are relatively small (in other words, most of the elements have all their nodes assigned to a single processor), method two is recommended. From the performance point of view, the performance overhead is small because the number of duplicated elements is only a small portion of the total number of elements. From the execution point of view, method two incurs no communication and thus it is easier to guarantee the completion of matrix assembly.

3.4.2 Parallel Formation of Right-Hand-Side Vector

In ParCYCLIC, The storage of soil constitutive model parameters, which are associated with the formation of the Right-Hand-Side (RHS) vector, is fairly large since each Gauss integration point of each element has to keep its own constitutive model parameters. Therefore, the above-mentioned first element assignment method is employed for the formation of the RHS vector. No sub-domain duplication occurs in this method and thus the storage requirement is minimized. After all processors finish their own RHS formation, a gather-to-all function (`MPI_Allreduce`) is called to obtain the global RHS vector.

3.4.3 Stress Update

In ParCYCLIC, formation of the RHS vector employs the first element assignment method while formation of the global matrix employs the second element assignment method. Therefore, care must be taken to ensure the correct stress update process. That is, in a processor, the stress-state variables of an element in a duplicated zone have to be updated in a timely manner. The stress calculation of this element is performed by another processor because a different element assignment method is employed. Therefore, global communication between processors is involved to ensure updating of the stress variables. For instance, take an example of the element 22-14-13-21 of Figure 3.11a, where its stress calculation is conducted by processor 2 because it belongs to processor 2. However, it also belongs to processor 0 in the second element assignment method (Figure 3.11b) used for the formation of the global matrix. Therefore, processor 2 has to send processor 0 the stress variables of this element upon stress update.

3.5 Parallel Performance

ParCYCLIC has been successfully ported on many different types of parallel computers and workstation clusters, including IBM SP machines, SUN supercomputers, and Linux workstation clusters. The following sections present the parallel performance of ParCYCLIC. Section 3.5.1 describes basic concepts of performance evaluation for parallel software, followed by performance results measured on the Blue Horizon machine (see Section 2.1.3).

3.5.1 Performance Evaluation

The performance of a parallel application is usually evaluated by using the speedup factor, S(n), defined as:

$$S(n) = \frac{t_s}{t_p} \tag{3.3}$$

Where t_s is the execution time on a single processor and t_p is the execution time on a multiprocessor. $S(n)$ gives the increase in speed in using a multiprocessor. The maximum speedup is n with n processors (linear speedup). Superlinear speedup, where $S(n) > n$, may be seen on occasion, but usually this is due to using a suboptimal sequential algorithm or some unique feature of the architecture that favors the parallel formation.

It is reasonable to expect that some parts (e.g., an initialization phase before concurrent processes are being set up) of the computation cannot be divided at all into concurrent tasks and must be performed serially (Figure 3.14). As shown in Figure 3.14, if the fraction of the computation that cannot be divided into concurrent tasks is f, and no overhead is incurred when the computation is divided into concurrent parts, the time to perform the computation with n processors is given by $ft_s + (1 - f)t_s/n$. Hence, the speedup factor is given by:

$$S(n) = \frac{t_s}{ft_s + (1-f)t_s/n} = \frac{n}{1+(n-1)f} \tag{3.4}$$

This equation is known as Amdahl's law (Amdahl 1968). As we can see from the equation, the fraction of the computation that is executed by concurrent processes needs

to be a substantial fraction of the overall computation if a significant increase in speed is to be achieved. With an infinite number of processors, the maximum speedup is limited to 1/*f*; i.e.,

$$\lim_{n\to\infty} S(n) = \frac{1}{f} \tag{3.5}$$

3.5.2 Performance for Solution of FE Grid Models

This section deals with the solution of a number of 2D plane strain FE grid models of sizes ranging from 150x150 to 300x300 elements, as well as 3D grid models of sizes ranging from 20x20x20 to 35x35x35 elements. The multilevel nested dissection (Karypis and Kumar 1997) for the grid problems is able to generate a very well-balanced workload distribution to be run on a parallel computer. Each processor is responsible for approximately the same number of elements and equations. When there is good load balance, each processor will complete its tasks at about the same time and synchronization costs will be minimized. Table 3.1 summarizes the execution times of the solution phase for these 2D and 3D grid models for one time step. Excellent parallel speedup is achieved for these grid models up to a certain number of processors, as shown in Table 3.2. However, the speedup tends to saturate or peak at a certain point and the performance does not continue to improve with increasing number of processors. This is due to the increased communication overhead as the number of processors continues to increase. It may be noted that some of the grid models, e.g. the 30x30x30 mesh and the 35x35x35 mesh, are too large to fit into the memory for a low

number of processors. The execution time for these situations is denoted as N/A in Table 3.2.

3.5.3 Performance for Solution of 3D Geotechnical FE Models

This section presents the results of simulating geotechnical models including a soil-pile interaction model and a stone column centrifuge test model. The soil-pile interaction model shown in Figure 3.15 is used to study the loads on a pile group subjected to earthquake-induced liquefaction and lateral spreading. A total of 29,120 3D brick elements constitute the FE mesh (Figure 3.15). In this soil-pile interaction model, a 3x3 pile group is embedded in a submerged mild infinite ground slope with an effective inclination angle of about 4° while subjected to strong base shaking. A three-layer soil profile is used in this model, with a nonliquefiable stratum placed below and above the liquefiable sand. As shown in Figure 3.15, a half mesh configuration is used due to geometrical symmetry.

Table 3.3 summarizes the timing results of the nonlinear analysis for one time step. Note that the results for one processor are not available because the model is too large to fit into the memory of a single processor. The parallel speedup (relative to 2 processors) and the execution times of the solution phase are illustrated in Figure 3.16. In a typical earthquake simulation where hundreds or even thousands of time steps may be performed, the solution phase actually dominates, and thus the reported speedup essentially represents that of the entire seismic analysis phase. The performance results demonstrate excellent parallel speedup up to 64 processors for this model.

Another example is the solution of a stone column centrifuge test model, as shown in Figure 3.17. The stone column technique is a ground improvement process where vertical columns of compacted aggregate are installed through the soils to be improved. A series of centrifuge tests were conducted at Rensselaer Polytechnic Institute to assess the performance of this ground improvement method (Adalier et al. 2003). Figure 3.17 shows one of the centrifuge test models used in the analysis. In this stone column model, a number of gravel columns are embedded into a fully-saturated silt soil stratum. The model is then subjected to earthquake excitation along the *x*-direction at the base. Again, a half mesh configuration is used due to geometrical symmetry.

Table 3.4 summarizes the timing results of the solution phase, the LDL^T numerical factorization and the forward and backward solve, as well as the total execution time for one time step. The speedup and the execution times for the solution phase are illustrated in Figure 3.18. Note that the stone column model, with a scale of 364,800 degrees of freedom (dofs), cannot fit into the memory of less than 4 processors. As shown in Table 3.4 and Figure 3.18, excellent parallel speedup is achieved for this model.

Table 3.1: Execution times of solution phase for FE grid models (time in seconds; supercomputer: Blue Horizon).

Number of process-ors	2D grid models				3D grid models			
	150x150[1]	200x200[2]	250x250[3]	300x300[4]	20x20x20[5]	25x25x25[6]	30x30x30[7]	35x35x35[8]
1	19.66	46.11	98.14	185.70	188.00	674.60	N/A	N/A
2	9.34	19.83	37.60	66.38	93.97	357.00	1016.78	N/A
4	4.57	9.73	17.70	28.68	47.26	187.10	492.82	1359.26
8	2.69	5.56	9.78	16.16	25.59	96.16	248.53	714.91
16	1.81	3.49	5.81	9.22	16.74	54.72	132.73	365.88
32	1.52	2.55	4.05	6.17	12.52	35.14	76.85	188.32
64	2.36	3.60	7.02	6.84	14.80	34.70	58.98	127.23
[1] 68,403 equations; 7,457,460 non-zeros [2] 121,203 equations; 14,189,580 non-zeros [3] 189,003 equations; 23,724,231 non-zeros [4] 271,803 equations; 35,706,300 non-zeros					[5] 37,044 equations; 27,214,674 non-zeros [6] 70,304 equations; 66,365,120 non-zeros [7] 119,164 equations; 138,930,582 non-zeros [8] 186,624 equations; 258,680,240 non-zeros			

Table 3.2: Speedup factors of the solution phase for FE grid models.

Number of processors	2D grid models				3D grid models			
	150x150	200x200	250x250	300x300	20x20x20	25x25x25	30x30x30[1]	35x35x35[2]
1	1.00	1.00	1.00	1.00	1.00	1.00	N/A	N/A
2	2.10	2.33	2.61	2.80	2.00	1.89	1.00	N/A
4	4.30	4.74	5.54	6.47	3.98	3.61	2.06	1.00
8	7.31	8.29	10.03	11.49	7.35	7.02	4.09	1.90
16	10.86	13.21	16.89	20.14	11.23	12.33	7.66	3.72
32	12.93	18.08	24.23	30.10	15.02	19.20	13.23	7.22
64	8.33	12.81	13.98	27.15	12.70	19.44	17.24	10.68
[1]Relative to 2 processors [2]Relative to 4 processors								

Table 3.3: Solution times for the soil-pile interaction model (time in seconds; supercomputer: Blue Horizon).

Number of processors	LDL^T factorization	Forward and backward solve	Solution phase	Total execution time
(130,020 equations; 29,120 elements; 96,845,738 non-zeros in factor *L*)				
2	332.67	1.41	370.42	455.91
4	166.81	0.78	187.72	286.97
8	85.20	0.45	97.71	186.67
16	50.73	0.29	59.39	147.55
32	27.80	0.23	34.61	124.30
64	18.41	0.26	24.40	116.21
128	18.47	0.83	25.95	124.40

Table 3.4: Solution times for the stone column centrifuge test model (time in seconds; supercomputer: Blue Horizon).

Number of processors	LDL^T factorization	Forward and backward solve	Solution phase	Total execution time
(364,800 equations; 84240 elements; 340,514,320 non-zeros in factor *L*)				
4	1246.08	2.76	1306.87	1769.00
8	665.66	1.56	702.09	1150.17
16	354.99	0.98	378.35	841.38
32	208.90	0.67	225.93	668.02
64	125.05	0.66	142.33	583.98

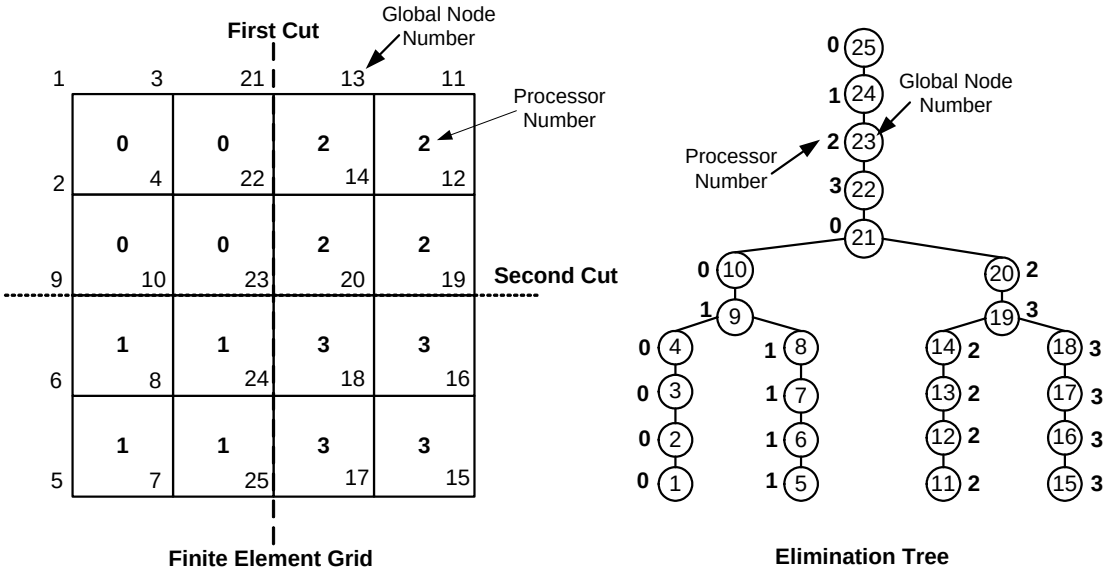

Figure 3.1: A FE grid and its elimination tree representation (Law and Mackay 1993).

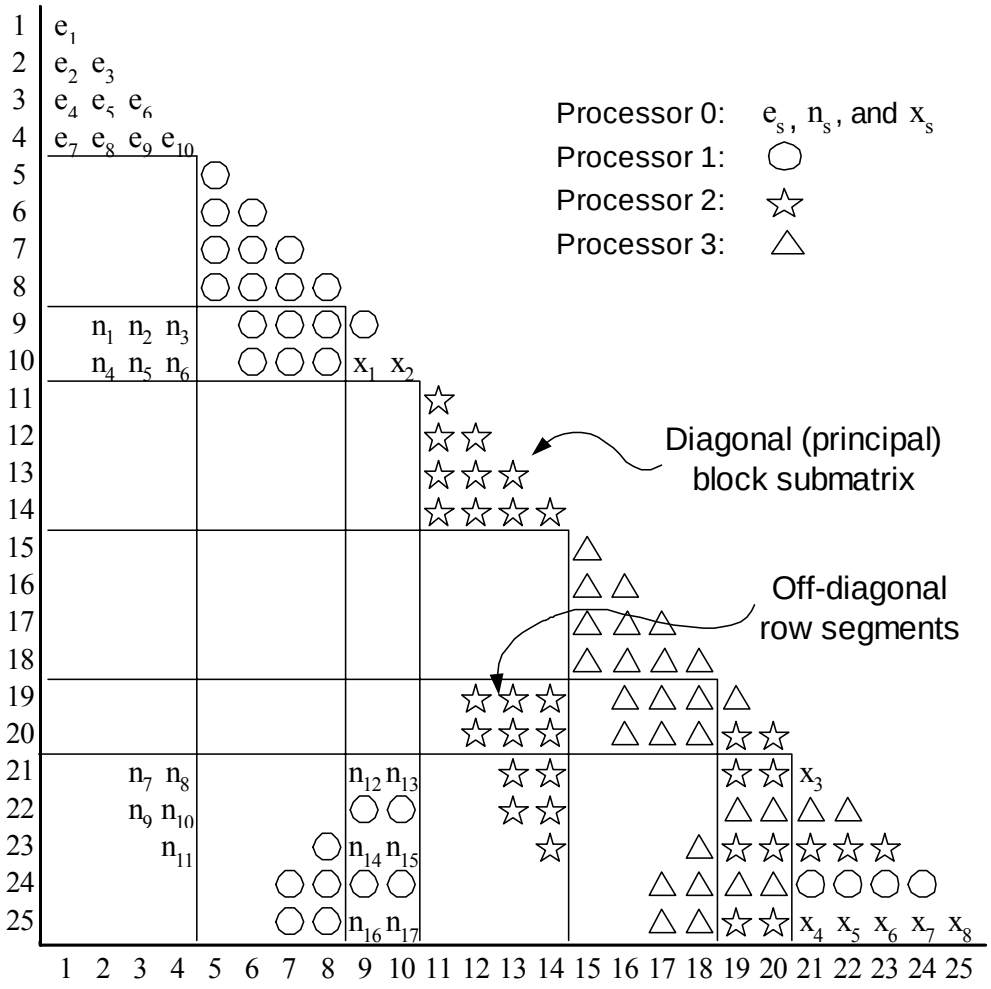

Figure 3.2: Matrix partitioning for parallel computations (Mackay 1992).

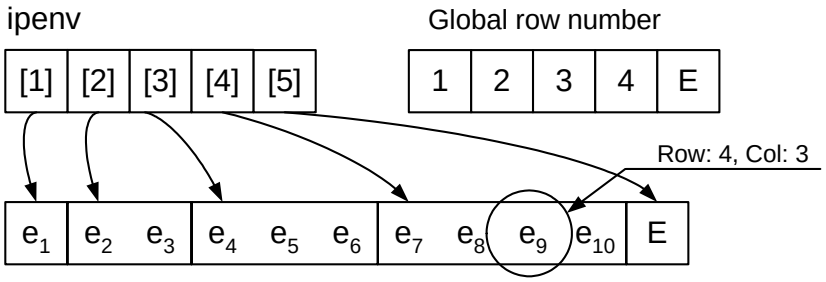

Figure 3.3: Data structure for principal block submatrix assigned to a single processor (Peng et al. 2004).

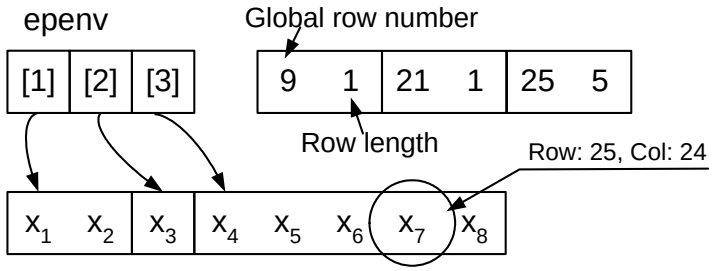

Figure 3.4: Data structure for principal block submatrix shared by multiple processors (Peng et al. 2004).

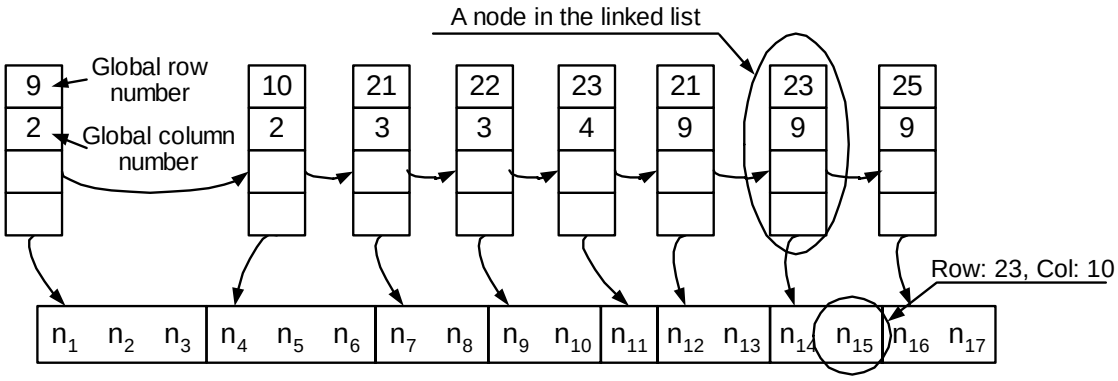

Figure 3.5: Data structure for row segments (Peng et al. 2004).

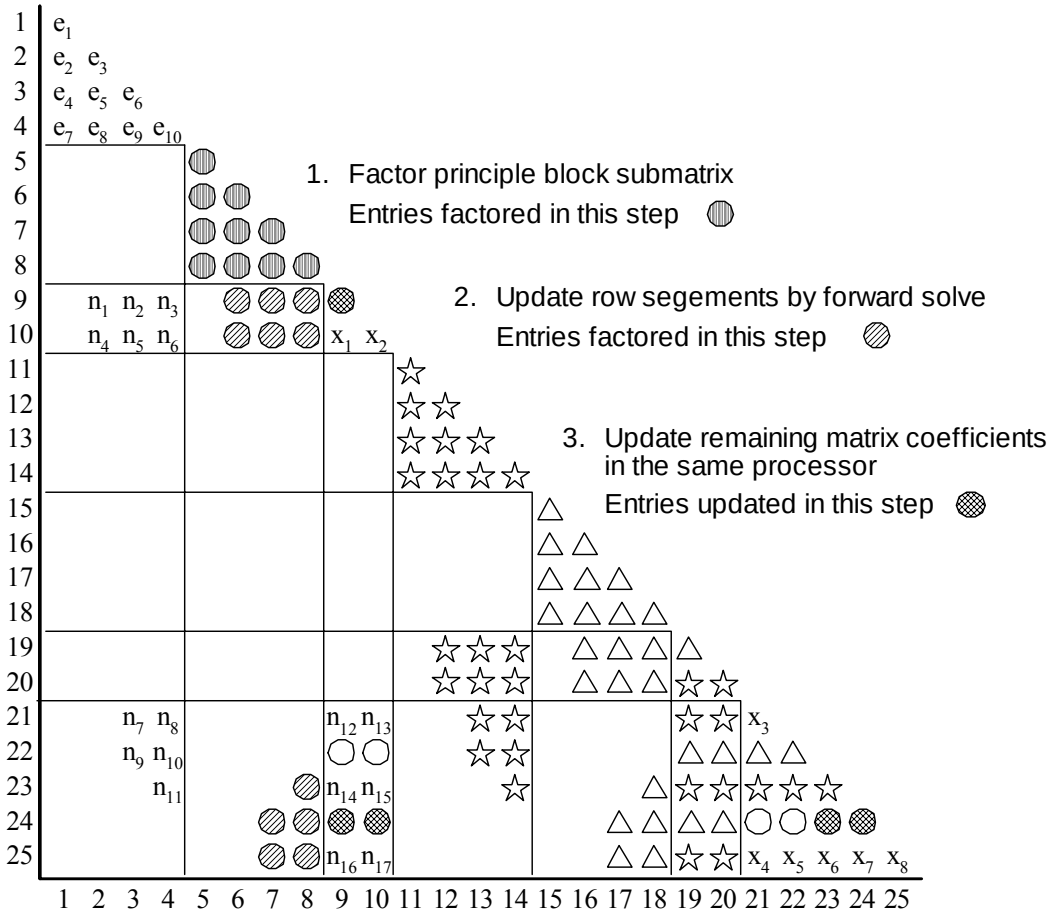

Figure 3.6: Phase one of parallel factorization (Mackay 1992).

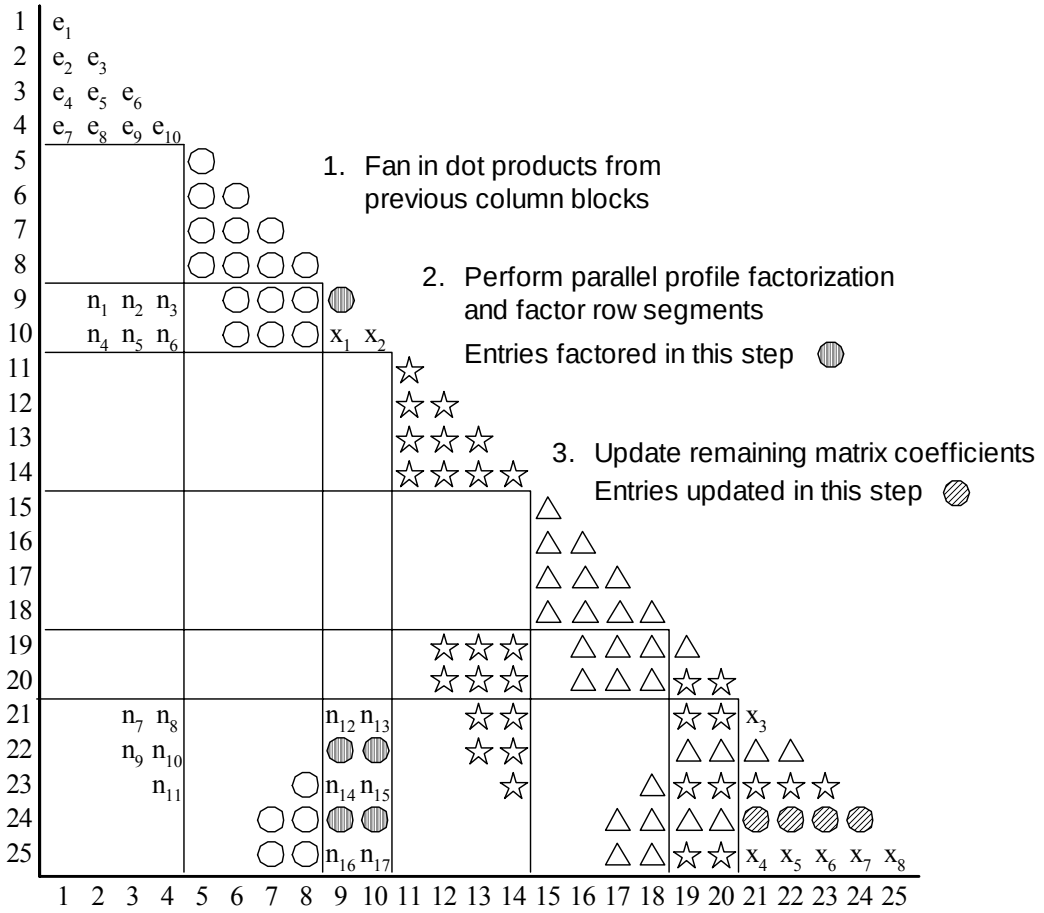

Figure 3.7: Phase two of parallel factorization (Mackay 1992).

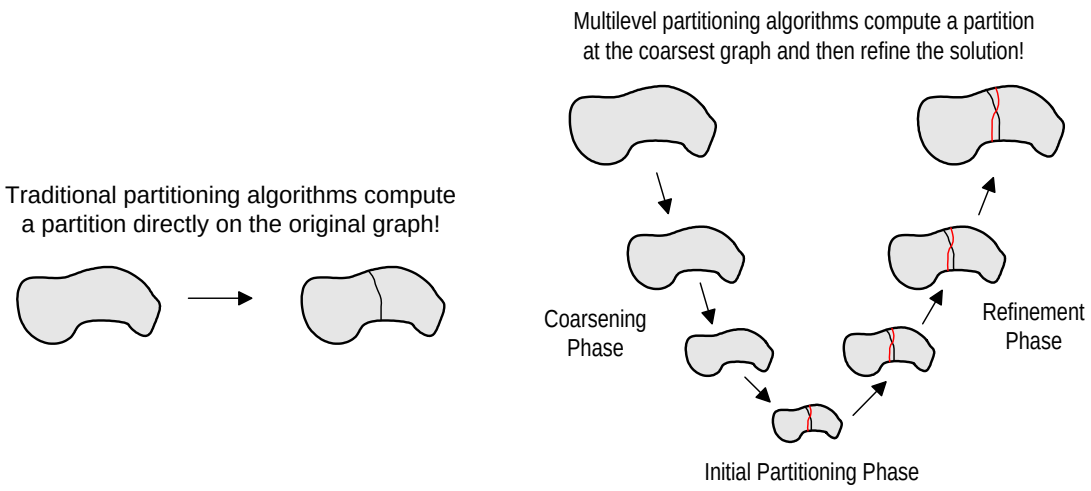

(a) (b)

Figure 3.8: (a) Traditional partitioning algorithms. (b) Multilevel partitioning algorithms (Karypis and Kumar 1997).

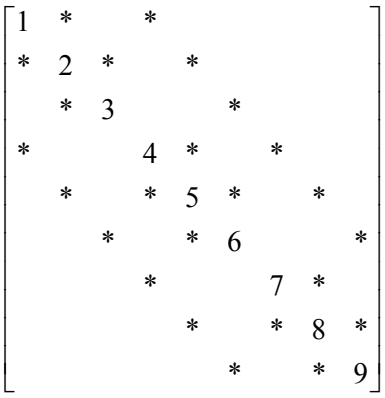

(a) A sample matrix

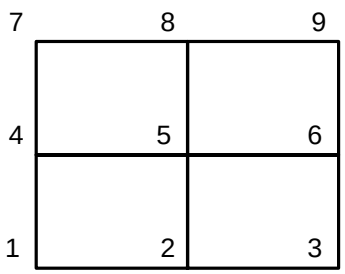

(b) Graph representation

```
xadj 0 2 5 7 10 14 17 19 22 24
adjncy 2 4 1 3 5 2 6 1 5 7 2 4 6 8 3 5 9 4 8 5 7 9 6 8
```

(c) CSR format

Figure 3.9: An example of the CSR format for storing sparse graphs.

```
void multinnd(int *neq, int* xadj, int* adjncy, int* perm,
     int* invp,int numlevels, int order)
{
    int numflag = 1;
    int options[10];
    options[0] = 0; /* use default values */

    METIS_NodeND(neq, xadj, adjncy, &numflag, options, perm, invp,
                 numlevels, order);

}
```

Figure 3.10: Pseudo-code for incorporating METIS_NodeND function.

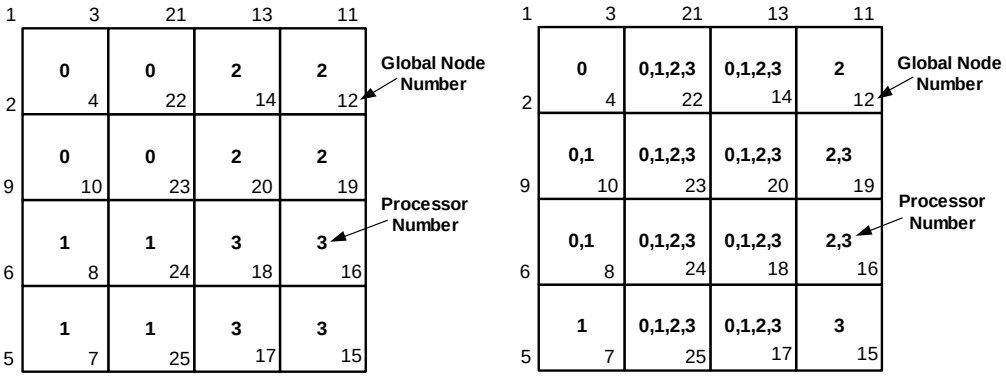

(a). Assignment of elements without duplication (b). Assignment of elements with duplication

Figure 3.11: Two methods of assigning elements to four processors.

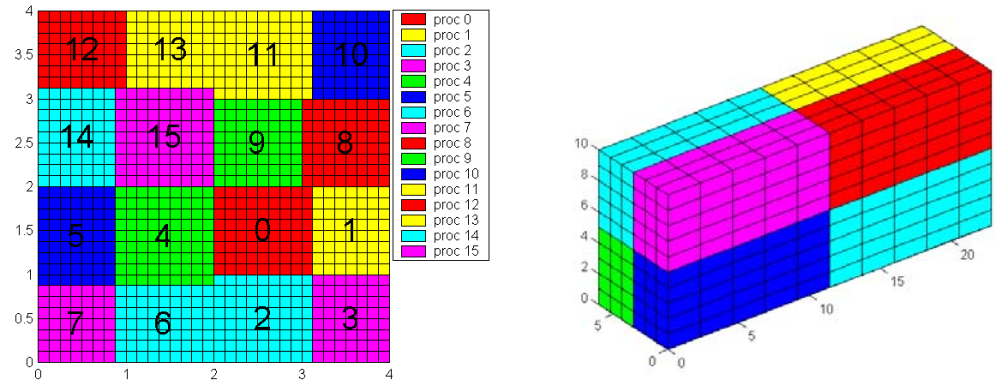

(a) A 2D 32x32 grid problem with 16 processors.

(b) A 3D 10x6x10 grid problem with 8 processors.

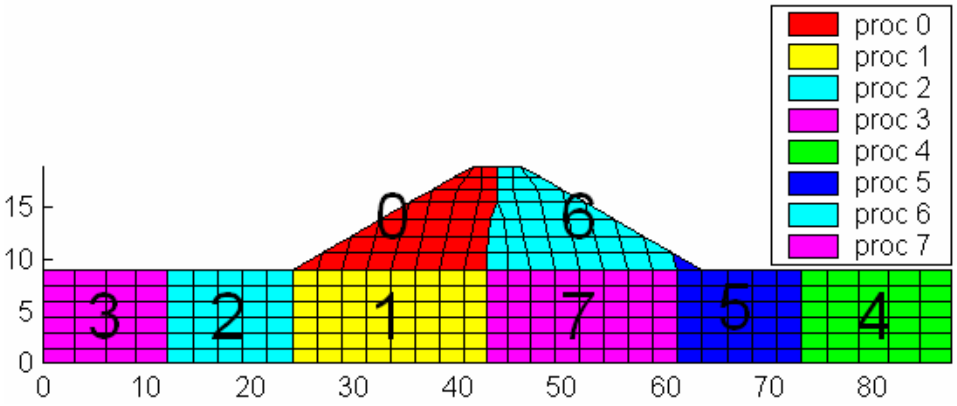

(e) A 2D earth dam model with 8 processors.

Figure 3.12: Mesh partitioning without element duplication.

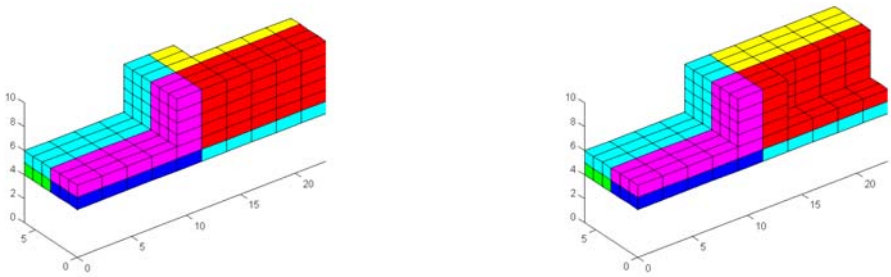

proc 0 proc 1

proc 2 proc 3

proc 4 proc 5

proc 6 proc 7

Figure 3.13: Mesh partitioning with element duplication.

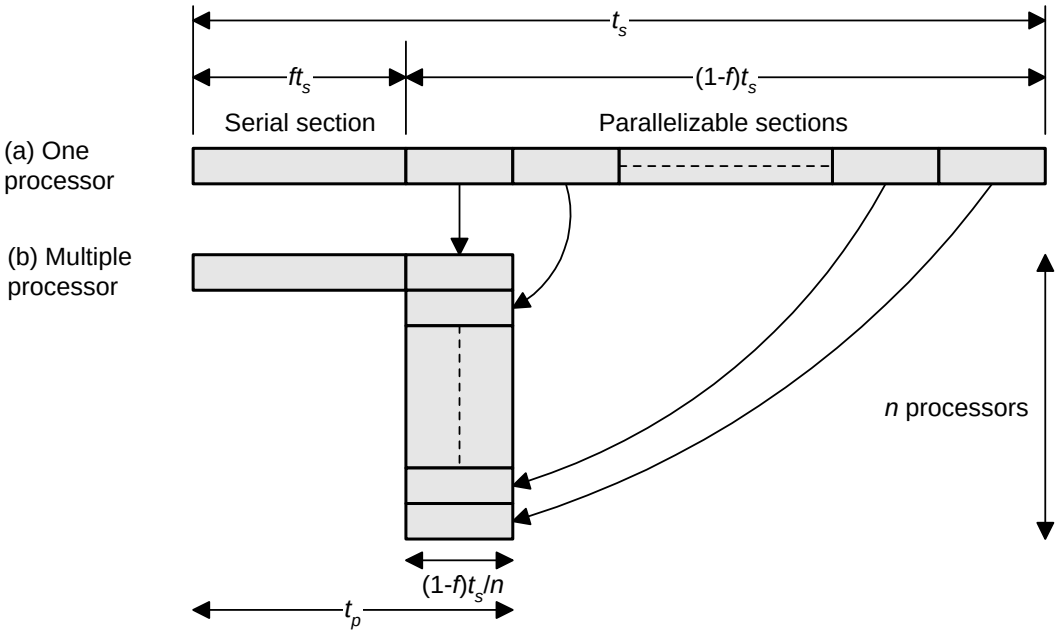

Figure 3.14: Parallelizing sequential problem -- Amdahl's law (Wilkinson and Allen 1999).

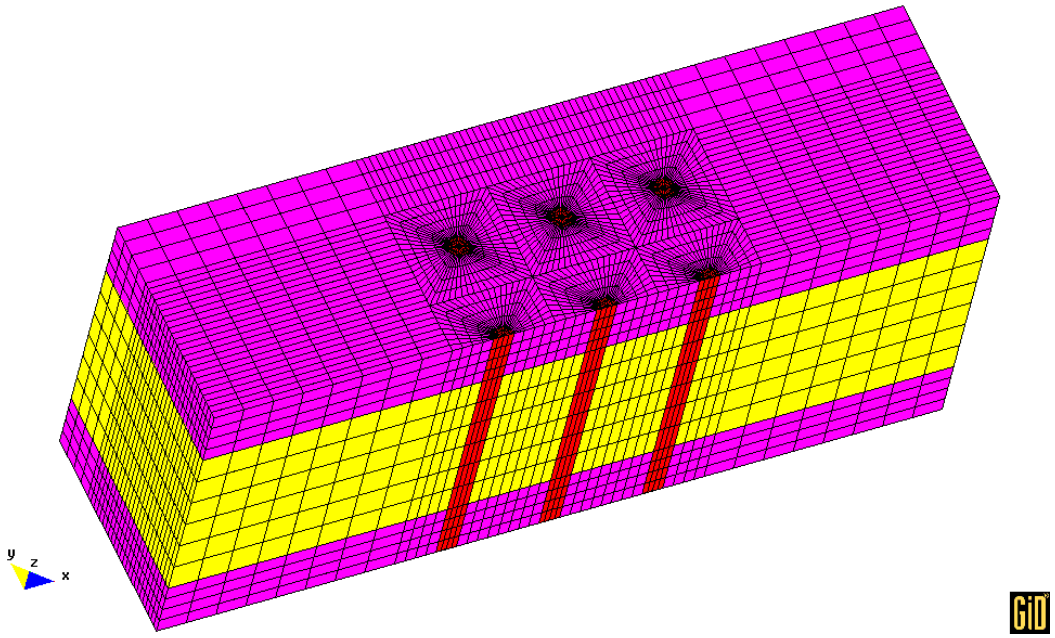

Figure 3.15: A soil-pile interaction FE model.

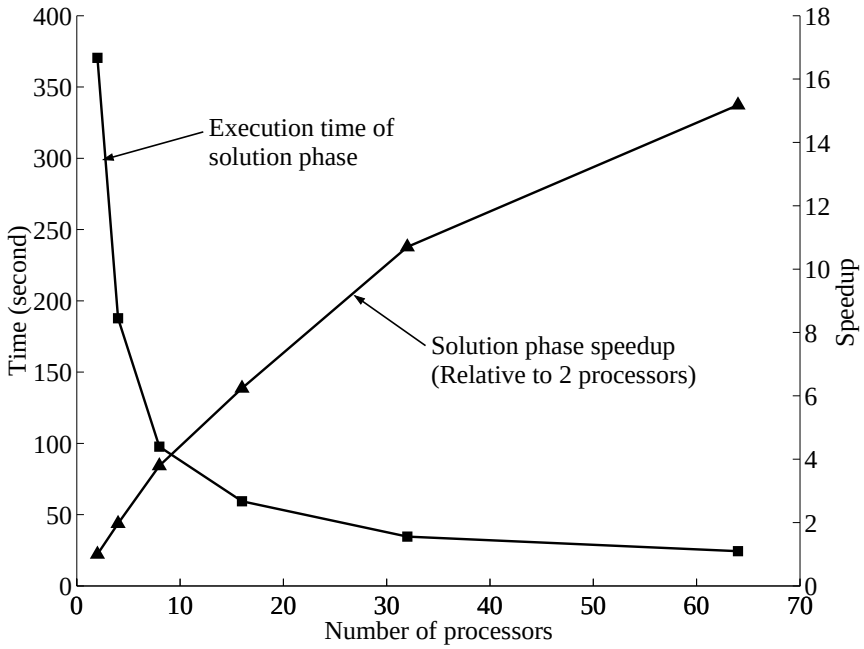

Figure 3.16: Execution times and speedup of the solution phase for the soil-pile interaction model (see Figure 3.15).

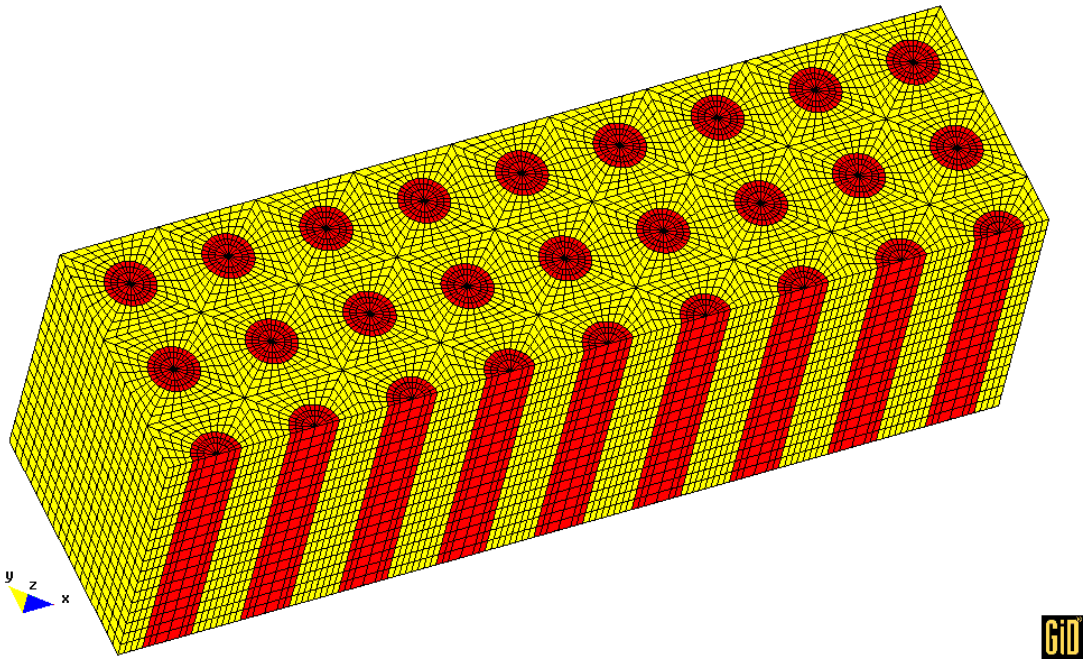

Figure 3.17: FE model of a stone column centrifuge test.

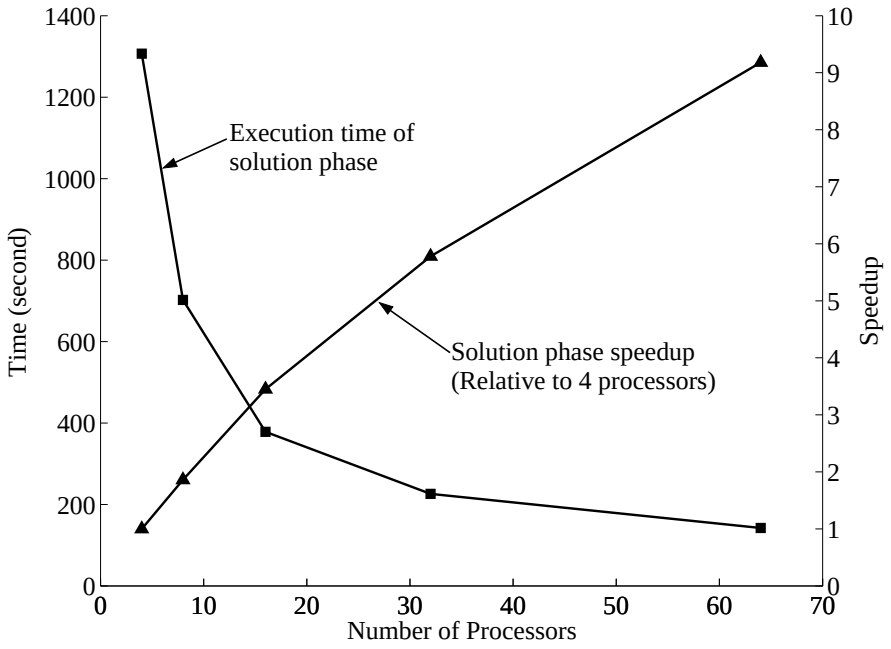

Figure 3.18: Execution times and speedup of the solution phase for the stone column centrifuge test model (see Figure 3.17).

Chapter 4 Numerical Analysis of Centrifuge Experiments

This chapter presents numerical simulations of a series of centrifuge test models. Section 4.1 presents numerical modeling of two site response centrifuge tests. Simulation of a centrifuge experiment of pile in lateral spreading is presented in Section 4.2.

4.1 Modeling of VELACS Centrifuge Experiments

In this section, numerical simulations of two centrifuge test models using ParCYCLIC are presented. Two centrifuge model tests (Figure 4.1) were conducted by Dobry and Taboada (1994b) to simulate the dynamic response of level and mildly sloping sand sites. The employed centrifuge models are (Taboada 1995): VELACS (VErification of Liquefaction Analysis by Centrifuge Studies) Model 1 representing a level site, subjected to a predominantly 2 Hz harmonic base excitation (Figure 4.2); and VELACS Model 2 representing a mildly inclined infinite slope with an effective inclination angle of about 4°, subjected to a predominantly 2 Hz harmonic base excitation (Figure 4.2).

These tests were performed in a laminated container that allows relative slip between laminates in order to simulate approximately one-dimensional (1D) shear response. Nevada sand was used at D_r in the range of 40-45%. The soil models were spun to a 50g gravitational field (Taboada 1995). At this gravitational field, the centrifuge models aim to simulate a prototype stratum of 22.86m long, 12.70m wide and 10m high. Water was used as the pore fluid, resulting in a prototype soil permeability

equal to 50 times that of the model soil (Tan and Scott 1985). The results of these tests were thoroughly documented in Taboada (1995), and further analyzed in Refs. (Dobry and Taboada 1994a; Taboada 1995; Elgamal et al. 1996)

As mentioned in Section 1.4.5, these VELACS centrifuge test models were employed for calibrating CYCLIC (Elgamal et al. 2002b). The simulations performed herein using ParCYCLIC could be viewed as a further calibration procedure with a highly refined 3D FE mesh. The calibrated main modeling parameters, as shown in Table 1.1, have been employed in the following 3D simulations.

4.1.1 Numerical Modeling

A grid mesh (Figure 4.3) with 60x30x16 elements (128,588 degrees of freedom in total) was used for the simulations. The boundary conditions were: (i) dynamic excitation was defined as the recorded base acceleration, (ii) at any given depth, displacement degrees of freedom of the downslope and upslope boundaries were tied together (both horizontally and vertically using the penalty method) to reproduce a one-dimensional (1D) shear beam effect (Parra 1996), (iii) along the longitudinal boundary, no out of plane motion was allowed, (iv) the soil surface was traction free, with zero prescribed pore pressure, and (v) the base and lateral boundaries were impervious.

A static application of gravity (model self weight) was performed before seismic excitation. The resulting fluid hydrostatic pressures and soil stress-states served as initial conditions for the subsequent dynamic analysis.

The simulations were conducted using 32 processors on the Blue Horizon machine at the San Diego Supercomputer Center (SDSC). The total execution time was

approximately 5 hours for the Model 1 simulation and 7 hours for the Model 2 simulation. Note that these simulations cannot fit into a single processor unit due to the limitation of memory size.

4.1.2 Computation Results

1. Level Site: Model 1

Figures 4.4-4.6 display the computed and recorded lateral accelerations, excess pore-pressures and lateral displacements for Model 1. In general, good agreement is achieved between the computed and the recorded responses. In Model 1, accelerations virtually disappeared at the free surface after about 4 seconds due to liquefaction, as shown in Figure 4.4. Liquefaction was reached down to a depth of 5.0m, as indicated by the pore-pressure ratio r_u approaching 1.0 (dashed lines in Figure 4.5, $r_u = u_e/\sigma_v$ where u_e is excess pore pressure, and σ_v initial effective vertical stress).

Relatively small lateral displacements were observed in this case (Figure 4.6). In fact, the cyclic shear strains were generally below 1% (Figure 4.7). These stress-strain histories (Figure 4.7) display the usual pattern of stiffness loss due to pore-pressure buildup (Figure 4.5).

The stress-paths of Figure 4.8 show the typical mechanism of cyclic decrease in effective confinement due to pore-pressure buildup (Figure 4.5). This data (Figure 4.5) was a main source for calibration of model pore-pressure buildup (shear-induced contraction) parameters (c_1 and c_2 in Table 1.1). Overall, it may be noted that the relatively small strains during liquefaction (Figure 4.7) led to soil response (Figure 4.8) predominantly below the PT surface (i.e. virtual absence of dilative tendency). The

infinite-slope model below displayed much larger accumulated strain levels and allowed for calibration of dilative model response above the PT surface.

2. Mild Slope: Model 2

Figures 4.9-4.11 show the computed and recorded lateral acceleration, excess pore pressure and displacement time histories for Model 2. The 4° inclination of Model 2 imposed a static shear stress component (due to gravity), causing accumulated cycle-by-cycle lateral deformation. Despite the relatively mild inclination, all response characteristics (Figure 4.9 and Figure 4.10) are much different from those of Model 1 (Figure 4.4 and Figure 4.5). Surface accelerations were sustained throughout the shaking phase (Figure 4.9), and lateral displacement reached a permanent value of about 0.4m (Figure 4.11). The recorded and computed excess pore pressure histories (Figure 4.10) both displayed a number of instantaneous sharp pore pressure drops after initial liquefaction. These drops coincided with the observed and computed acceleration spikes that occurred exclusively in the negative direction (Figure 4.9).

The cause of these observed asymmetric accelerations and sharp pore pressure drops may be inferred from the computed shear stress-strains (Figure 4.12) and effective stress paths (Figure 4.13). In these figures, the presence of dilative response prevailed, in terms of instantaneous regain in effective confinement and shear strength at large strains. This response characteristic was especially evident in the upper sections after initial liquefaction ($r_u = 1$). Thus dilation-induced regain in shear strength appears to be the main cause of the large acceleration spikes after liquefaction. The responses of Figure 4.12 and Figure 4.13 manifest the role of Model 2 in calibrating the constitutive

model response above the PT surface (PT angle and dilation parameters d_1 and d_2 in Table 1.1). In addition, reasonably good agreement between the computed and recorded lateral displacements along the soil column verified the calibrated yield strain γ_y (Table 1.1), an important parameter in dictating the extent of post-liquefaction cycle-by-cycle shear deformation.

As illustrated in Figure 4.14, the 3D simulations show that the centrifuge test models do behave approximately as a 1D shear beam.

4.2 Simulation of Pile-Soil Interaction in Liquefied Sloping Ground

Liquefaction and associated shear deformation is a major cause of earthquake-related damage to piles and pile-supported structures. Pile foundation damage due to lateral spreading (Figure 1.2) induced by liquefaction is documented in numerous reports and papers (Mizuno 1987; Matsui and Oda 1996; Tokimatsu and Aska 1998).

The recognition of the importance of lateral ground displacement on pile performance has led to the development of analytical models capable of evaluating the associated potential problems (Abdoun 1997). Modeling lateral ground displacement and pile response involves complex aspects of soil-structure interaction and soil behavior under large strains. Currently computational procedures for nonlinear soil-pile interaction response commonly employ a 1D pile-soil system, and simplify the effect of soil pressure by linear or nonlinear p-y springs. Much effort has not been devoted to the study of the piles in liquefaction-induced lateral spreading using the FE method.

This section presents a pilot 3D FE study of dynamic pile response in liquefied ground.

4.2.1 Pile-Soil Interaction Model

Figure 4.15 shows a RPI centrifuge test model (Abdoun 1997) to investigate the response of a single-pile foundation in liquefied gently sloping ground, subjected to dynamic base excitation. The experiment was conducted using a rectangular, flexible-wall laminar box container (as shown in Figure 4.15). The soil profile consists of a saturated loose liquefiable sand layer (relative density D_r = 40%, 6 m prototype thickness), underlain by a slightly cemented non-liquefiable sand layer with a thickness of 2 m (Abdoun and Doubry 2002). The prototype single pile in the middle of the soil domain is 0.6m in diameter, 8m in length, and is free at the top. The model was inclined at an angle of 2° and subjected to a predominantly 2Hz harmonic base excitation with a peak acceleration of 0.3g. The results of the test were documented in Abdoun (1997).

The centrifuge model was simulated using ParCYCLIC on Blue Horizon. The soil domain and the pile were discretized with 8-node brick elements, as shown in Figure 4.16. A half mesh configuration was used in view of geometrical symmetry. There are 63,492 degrees of freedom in this model (13,824 elements in total). The boundary conditions are same as described in Section 4.1.1.

With a mild inclination of 2°, the centrifuge test model attempted to simulate an infinite slope of an effective angle of about 4° subjected to shaking parallel to the slope (Dobry and Taboada 1994b). However, it was noted that, in the centrifuge test, the soil surface gradually lost the slope and became level during the shaking phase. To simulate such behavior (losing the surface slope), a lateral component of gravity varying with time was applied to the FE simulation. The load-time history of the applied lateral

gravity component was based on the shape of accumulated lateral displacement at ground surface (i.e., lateral gravity gradually decreases and becomes zero where the surface displacement stabilizes).

4.2.2 Computation Results

As shown from the results in Figures 4.17-4.19, good agreement is noted between the computed and the recorded acceleration, displacement, and pore pressure responses. Salient liquefaction response characteristics, including excess pore pressure generation and dissipation, acceleration spikes, pile lateral movement, and permanent soil lateral deformation, were captured with reasonable accuracy. At 2 m depth, accelerations virtually disappeared after about 4 seconds due to liquefaction (A4, Figure 4.17). Liquefaction was reached down to a depth of 5.0 m (Figure 4.19), as indicated by the pore-pressure ratio r_u approaching 1.0. The Nevada sand layer remained liquefied until the end of shaking and beyond. Thereafter, excess pore pressure started to dissipate.

The mild inclination of the centrifuge test model imposed a static shear stress component (due to gravity), causing accumulated cycle-by-cycle lateral deformation. The recorded and computed u_e histories both displayed a number of instantaneous sharp pore pressure drops after initial liquefaction (Figure 4.19). These drops coincided with the observed and computed acceleration spikes that occurred exclusively in the negative direction.

The permanent lateral displacement of the ground surface after shaking is approximately 0.8 m. All lateral displacements occurred in the top 6.0m within the liquefiable sand layer. The top graph of Figure 4.18 shows the recorded and computed

pile lateral displacement at the soil surface during and after shaking. Pile lateral displacement increased to 0.55 m, and decreased to approximately 0.35 m at the end of shaking, indicating relative movement between the pile and soil. The lower slightly cemented sand layer, as indicated in Figure 4.18, did not slide with respect to the base of the laminar box.

4.2.3 Parallel Performance

Table 4.1 summarizes timing measurements for performing the centrifuge test simulation after 5 seconds of excitation using 8, 16, 32 and 64 processors. Overall, significant decrease in both numerical factorization and the total execution time can be observed. Since there is no element duplication in the phases of the right-hand-side (RHS) formation and the stress update, these two procedures have scaled well (almost linearly), as shown in Table 4.1. As mentioned earlier, in the employed hybrid element assignment strategy, element duplication occurs in the stiffness matrix formation. As the number of processors increases, the ratio of the duplicated portion (i.e., number of duplicated elements) over the non-duplicated portion becomes larger, and thus the parallel speedup of LHS formation decreases.

Details of the timing measurements for the initialization phase are shown in Table 4.2. The initialization phase is essentially sequential and only consists of less than 2% of the total execution time. Most of the time in this phase was spent on the FE model input, formation of the adjacency structure, and the setup for matrix storage and the parallel solver indexing. The multilevel nested dissection ordering using METIS is relatively fast and less than 1 second is needed to order this FE model with

approximately 63,500 degrees of freedom. The times spent on the elimination tree setup and the symbolic factorization is insignificant compared to the total execution time.

Table 4.1: Timing measurements for simulation of the centrifuge model (time in seconds; supercomputer: Blue Horizon).

Number of processors	LHS formation	RHS formation	Stress update	Factorization	Forward & back solve	Total time
8	273.6	2446.8	254.4	2736.6	490.9	6406.2
16	164.1	1224.6	128.3	1491.4	341.4	3579.8
32	104.4	622.0	64.2	813.7	320.2	2157.4
64	85.4	445.1	40.6	629.3	517.7	2000.5

Table 4.2. Detailed timing results for the initialization phase (time in seconds; supercomputer: Blue Horizon).

Number of processors	8	16	32	64
FE model input	13.2			
Formation of adjacency structure	9.4			
Multilevel nested dissection ordering (using METIS)	0.8			
Elimination tree setup and postordering	0.2			
Symbolic factorization	1.4			
Solver inter-processor communication setup	2.0	3.2	5.2	7.4
Matrix storage and solver indexing setup	14.7	9.7	4.1	2.6
Total for initialization phase	45.0	41.8	38.5	39.8

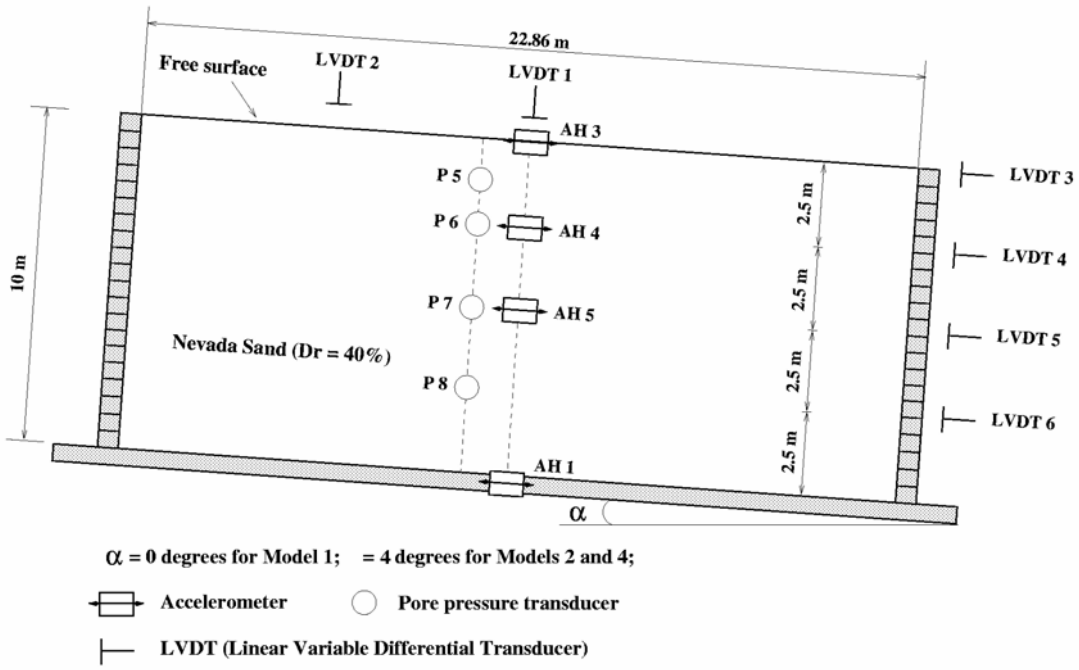

Figure 4.1: General configurations of RPI models 1 and 2 in laminar container (Taboada 1995).

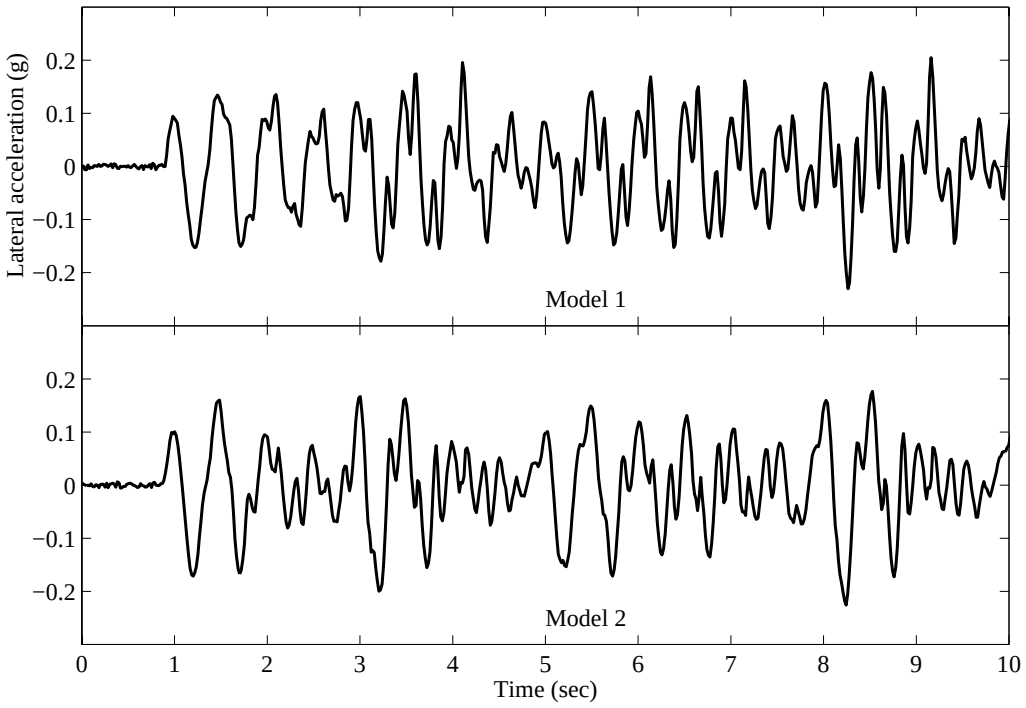

Figure 4.2: Base input motions for Models 1 & 2.

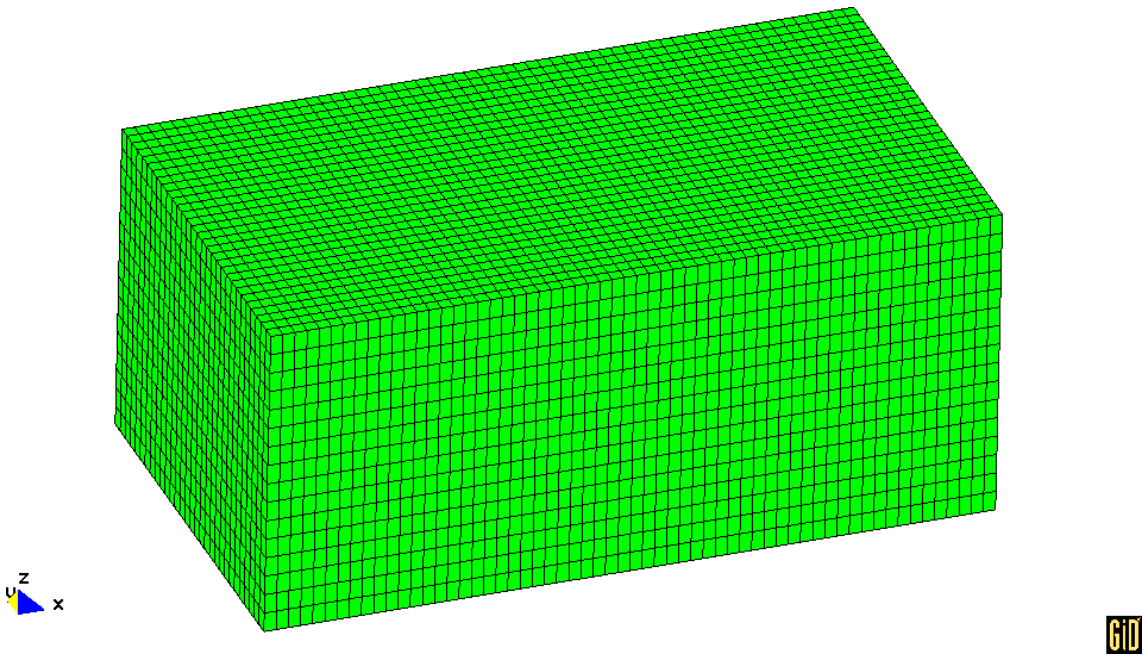

Figure 4.3: FE mesh employed for simulation of Models 1 & 2.

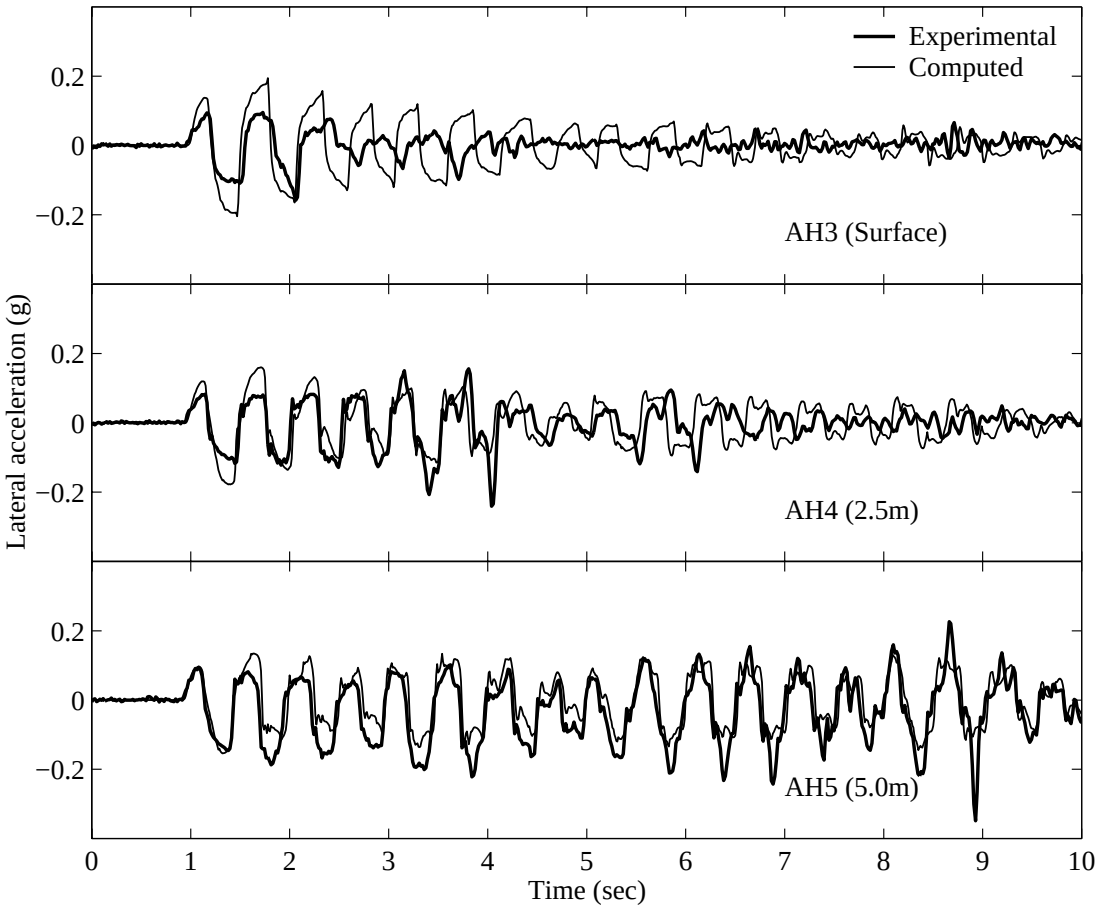

Figure 4.4: Model 1 recorded and computed acceleration time histories.

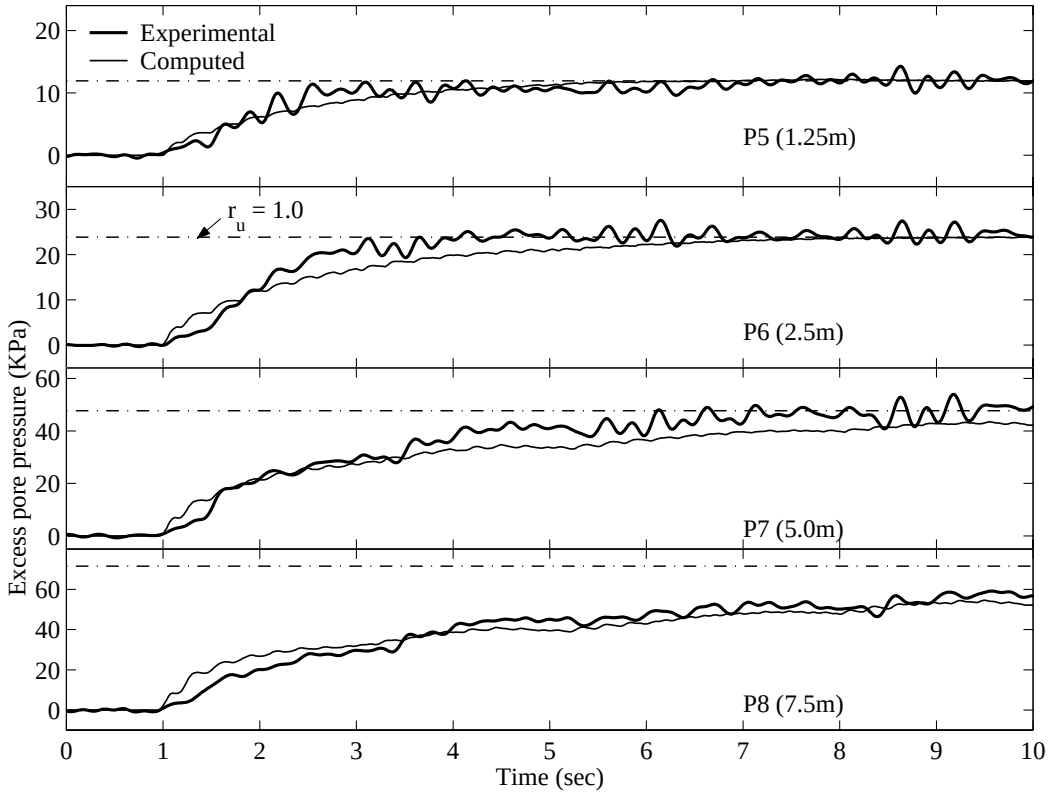

Figure 4.5: Model 1 recorded and computed excess pore pressure time histories.

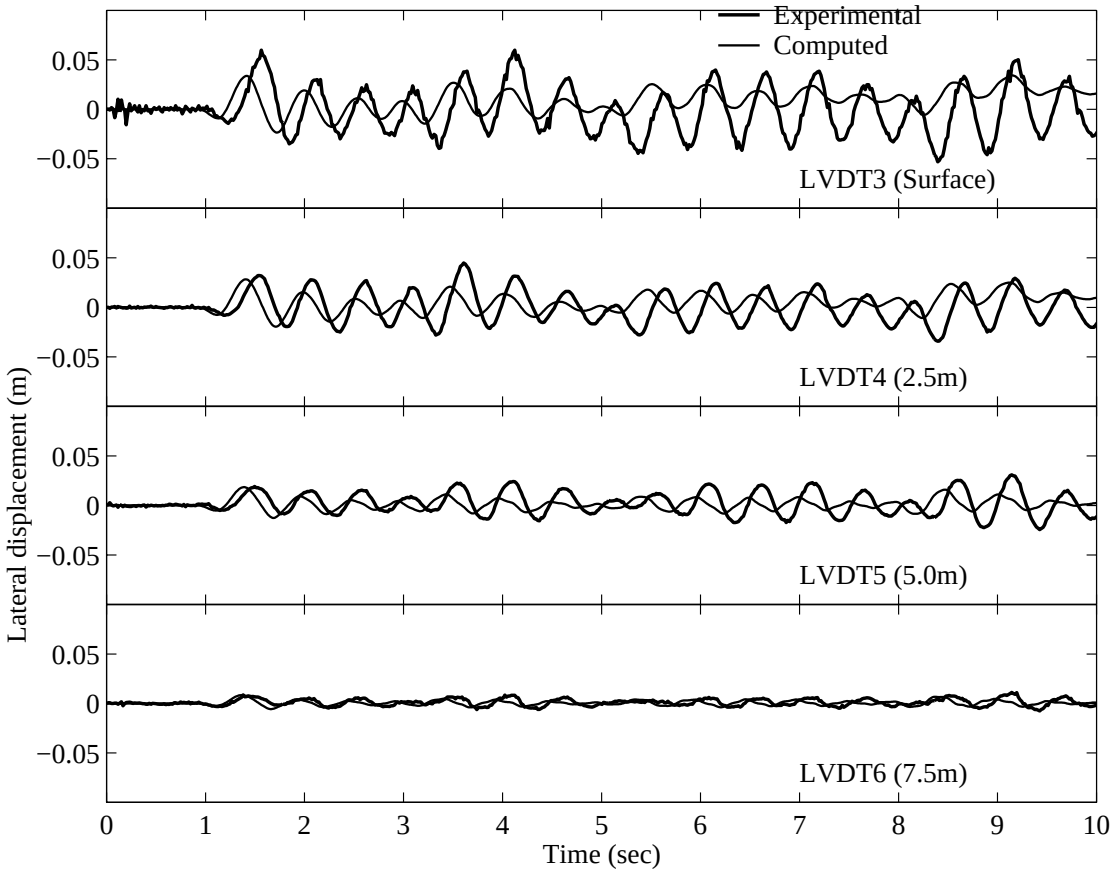

Figure 4.6: Model 1 recorded and computed lateral displacement time histories.

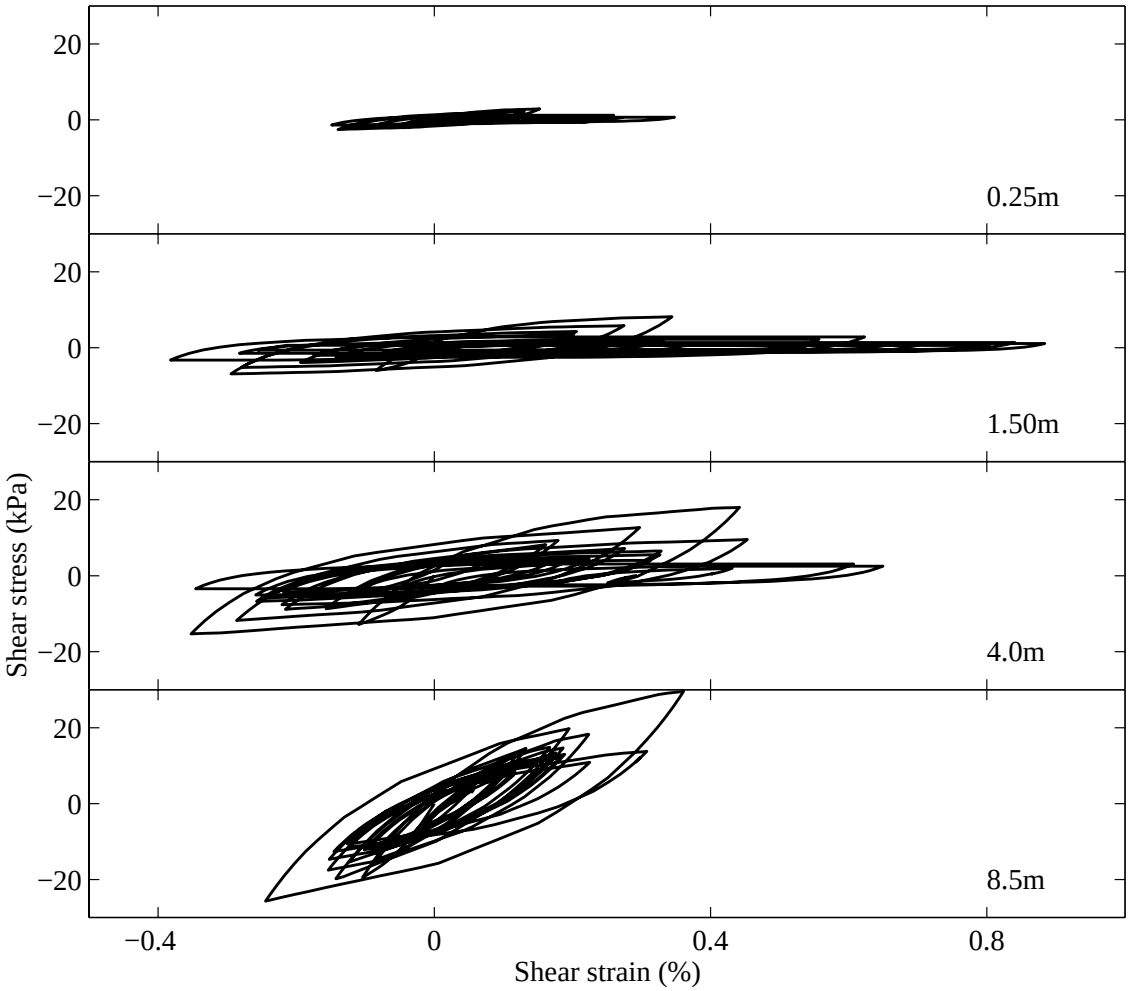

Figure 4.7: Model 1 computed shear stress-strain time histories.

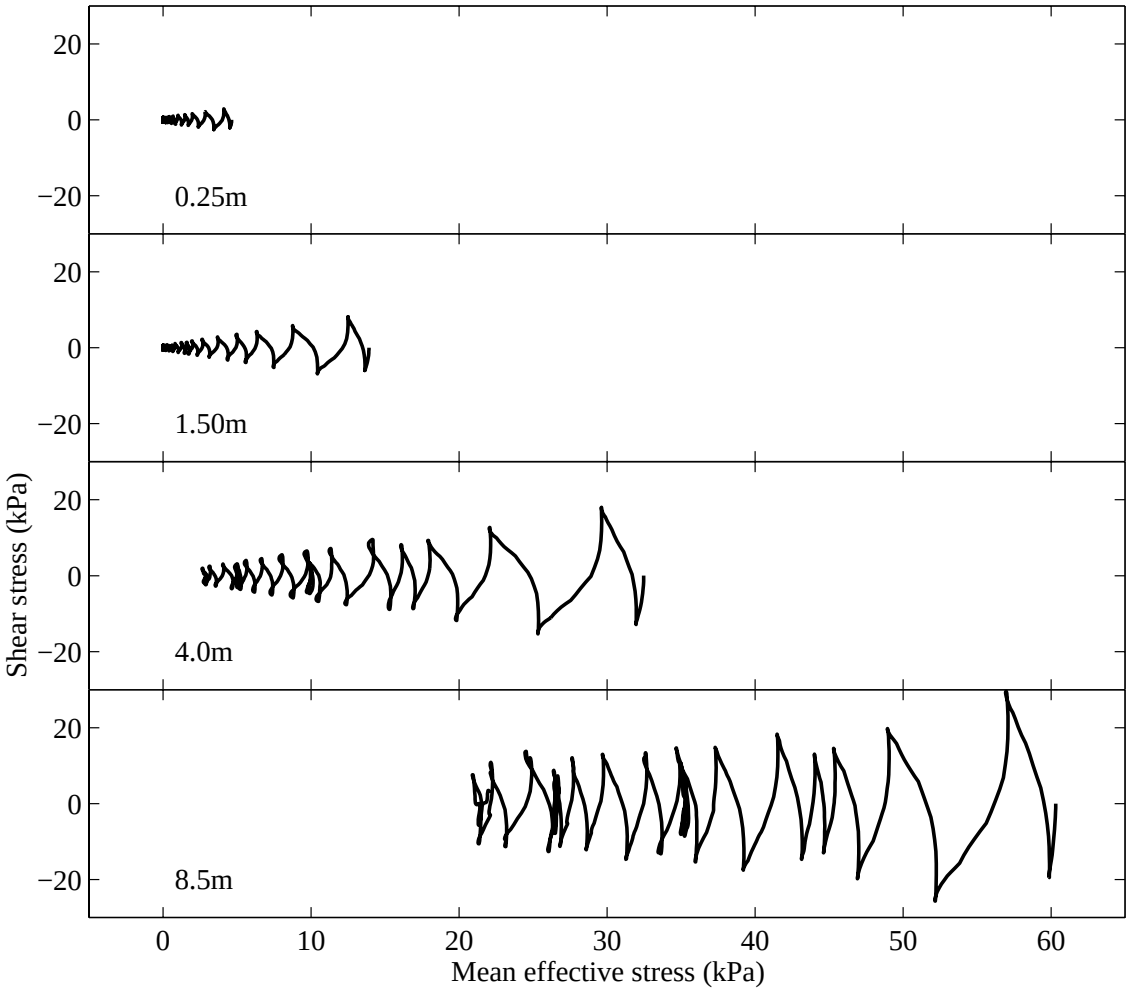

Figure 4.8: Model 1 computed effective stress path.

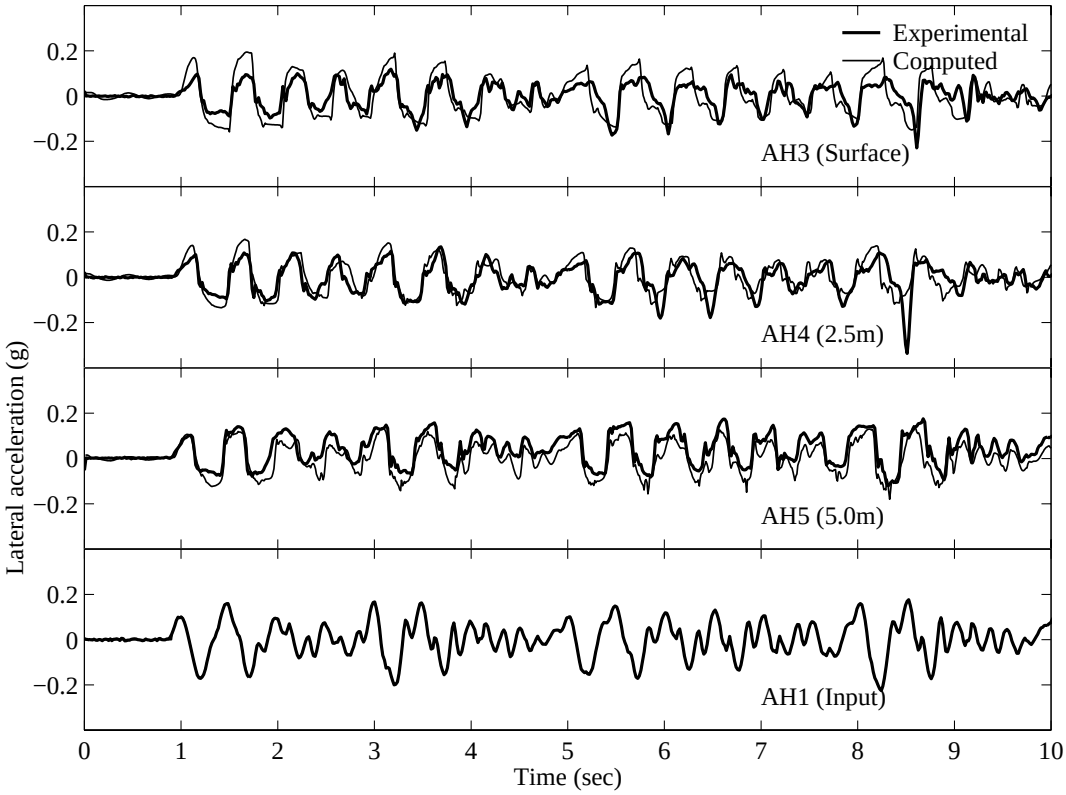

Figure 4.9: Model 2 recorded and computed acceleration time histories.

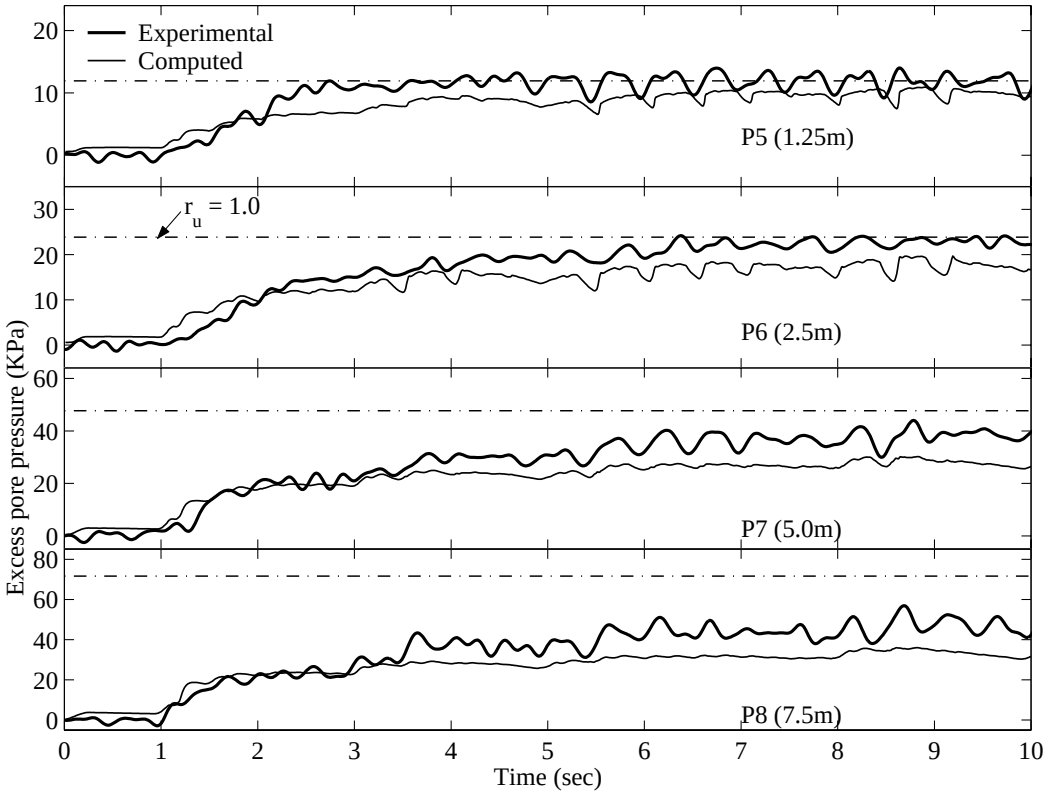

Figure 4.10: Model 2 recorded and computed excess pore pressure time histories.

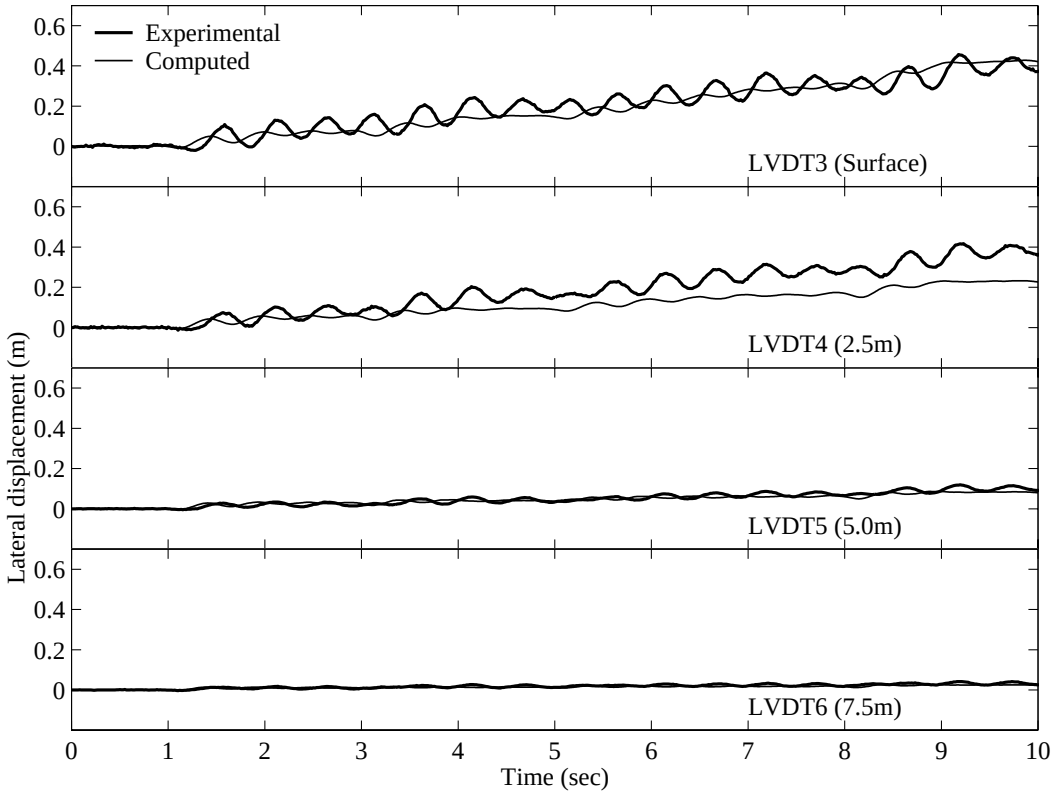

Figure 4.11: Model 2 recorded and computed lateral displacement histories.

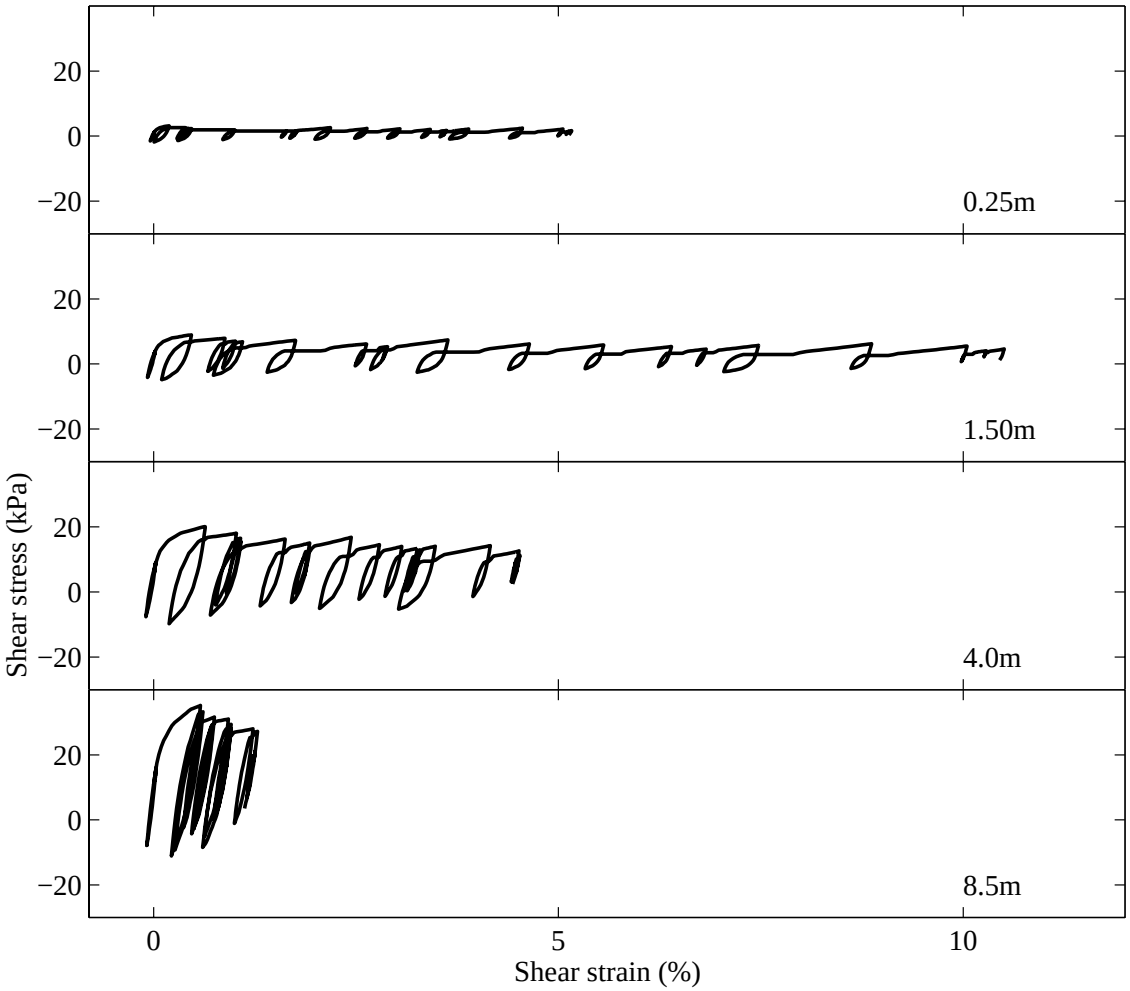

Figure 4.12: Model 2 computed shear stress-strain time histories.

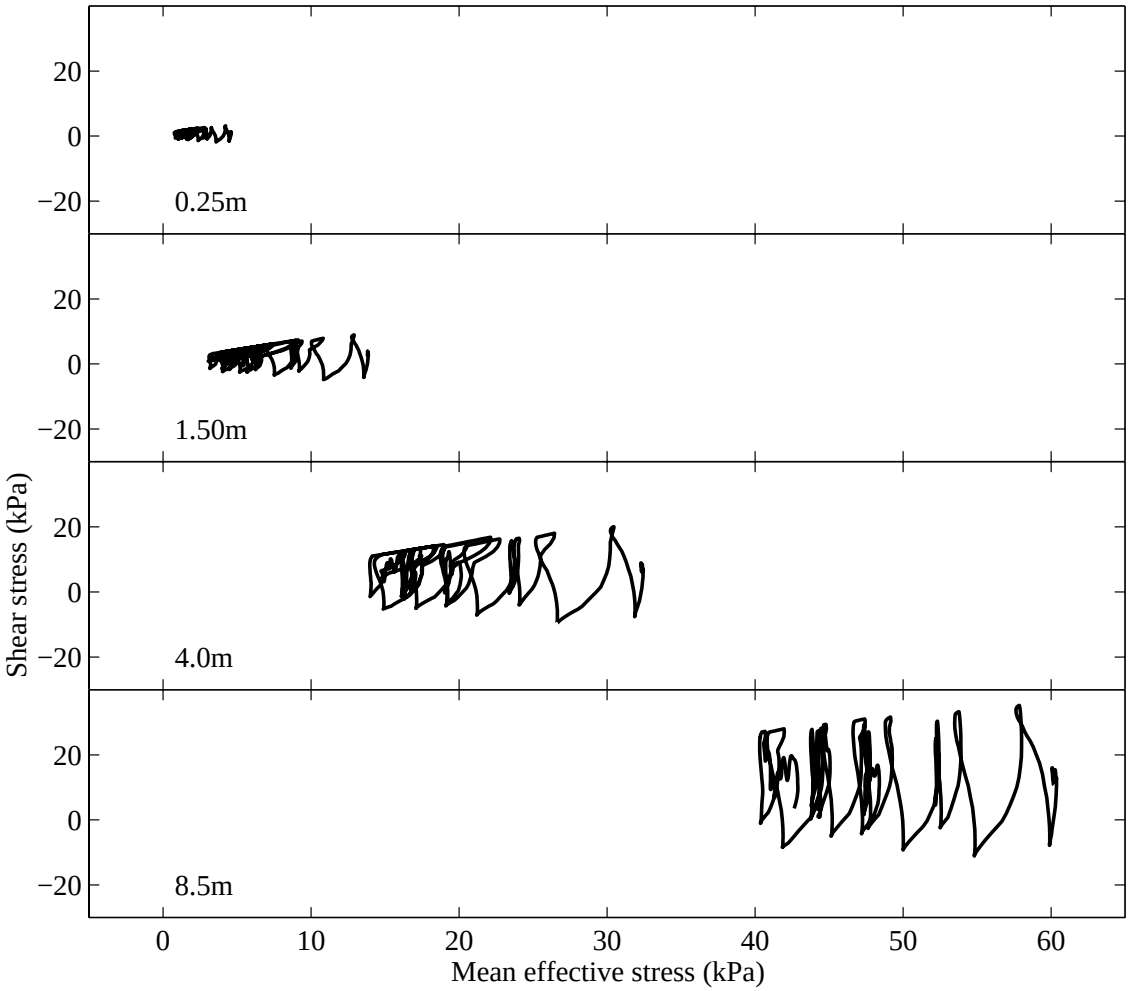

Figure 4.13: Model 2 computed effective stress path.

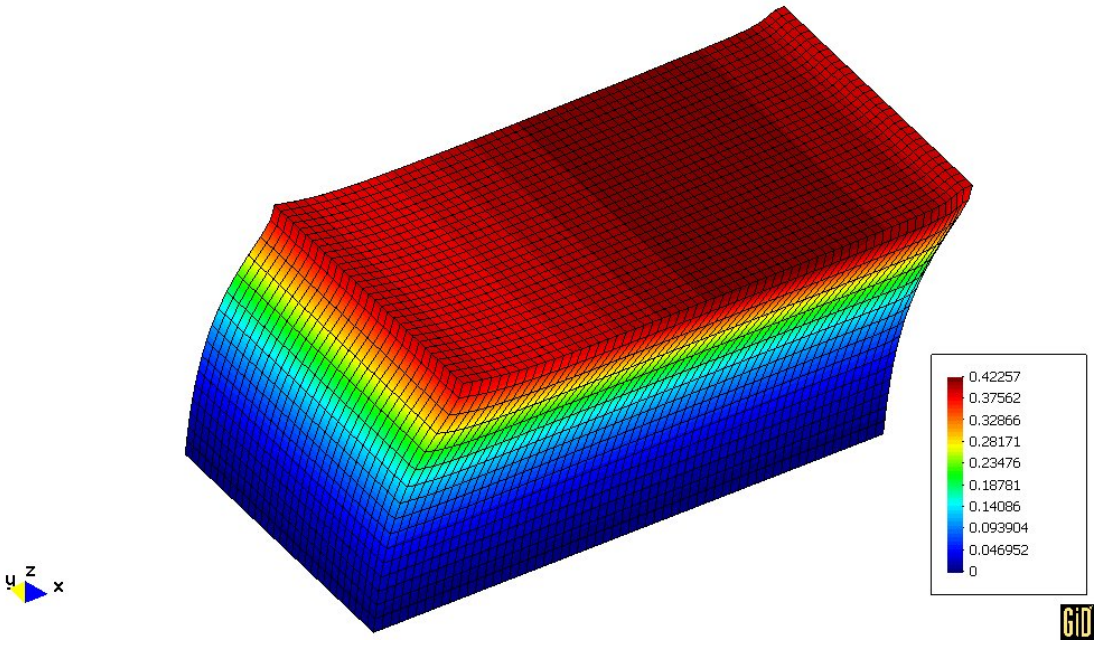

Figure 4.14: Deformed mesh (factor of 10) of Model 2 after 10 seconds of excitation (units: m).

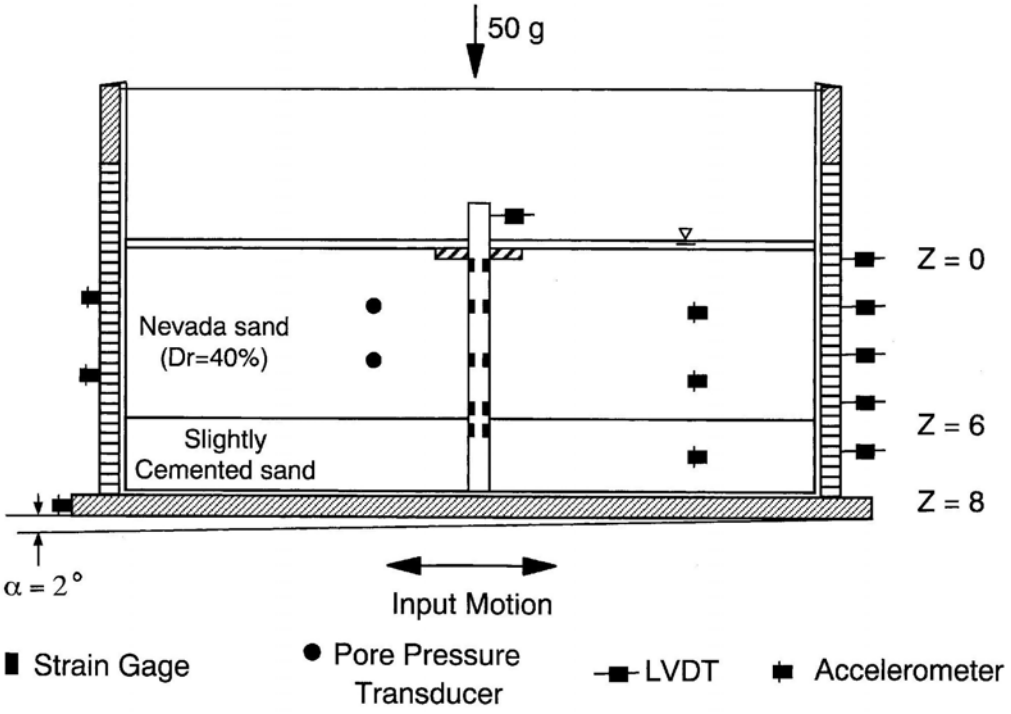

Figure 4.15:Lateral spreading pile centrifuge model in two-layer soil profile (Abdoun 1997).

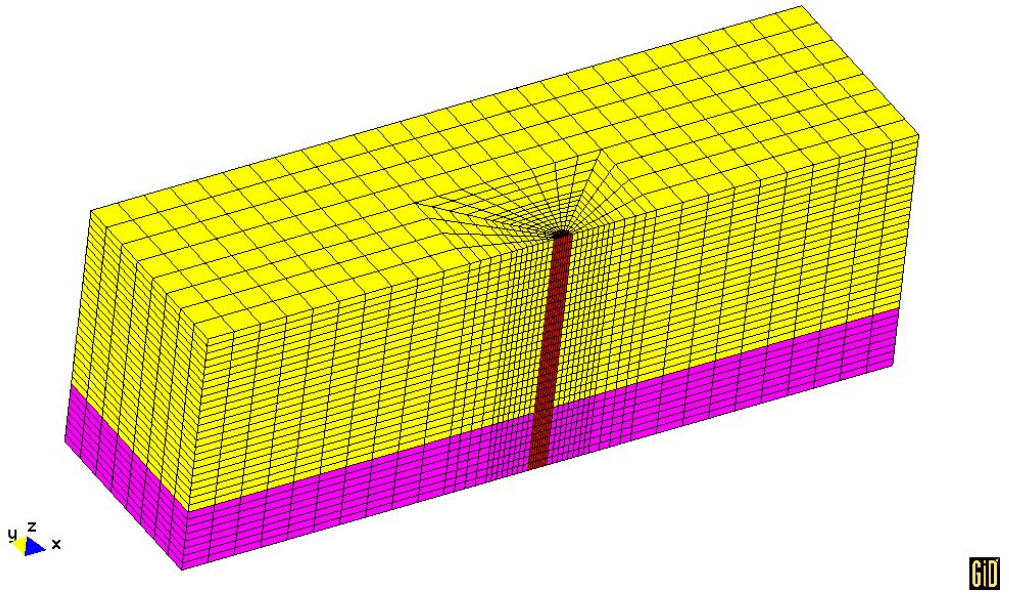

(a) FE mesh.

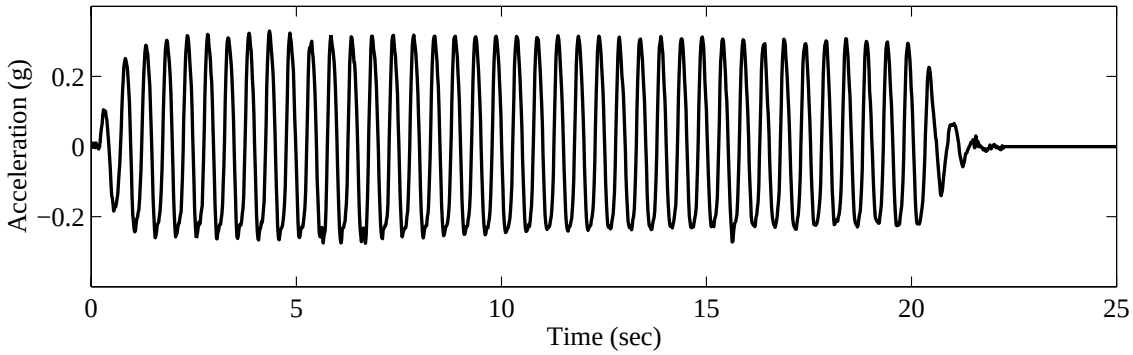

(b) Base input motion.

Figure 4.16. FE mesh and the input motion for the lateral spreading pile centrifuge test model.

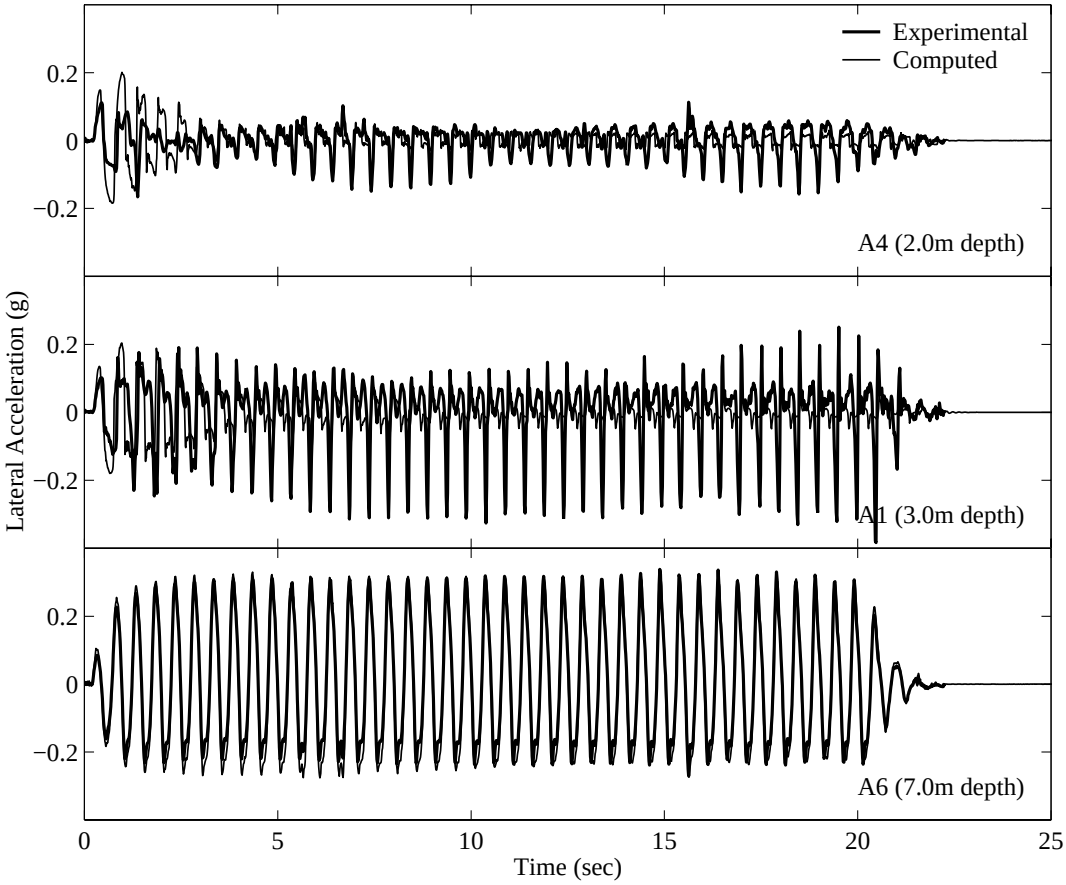

Figure 4.17. Computed and recorded lateral acceleration time histories.

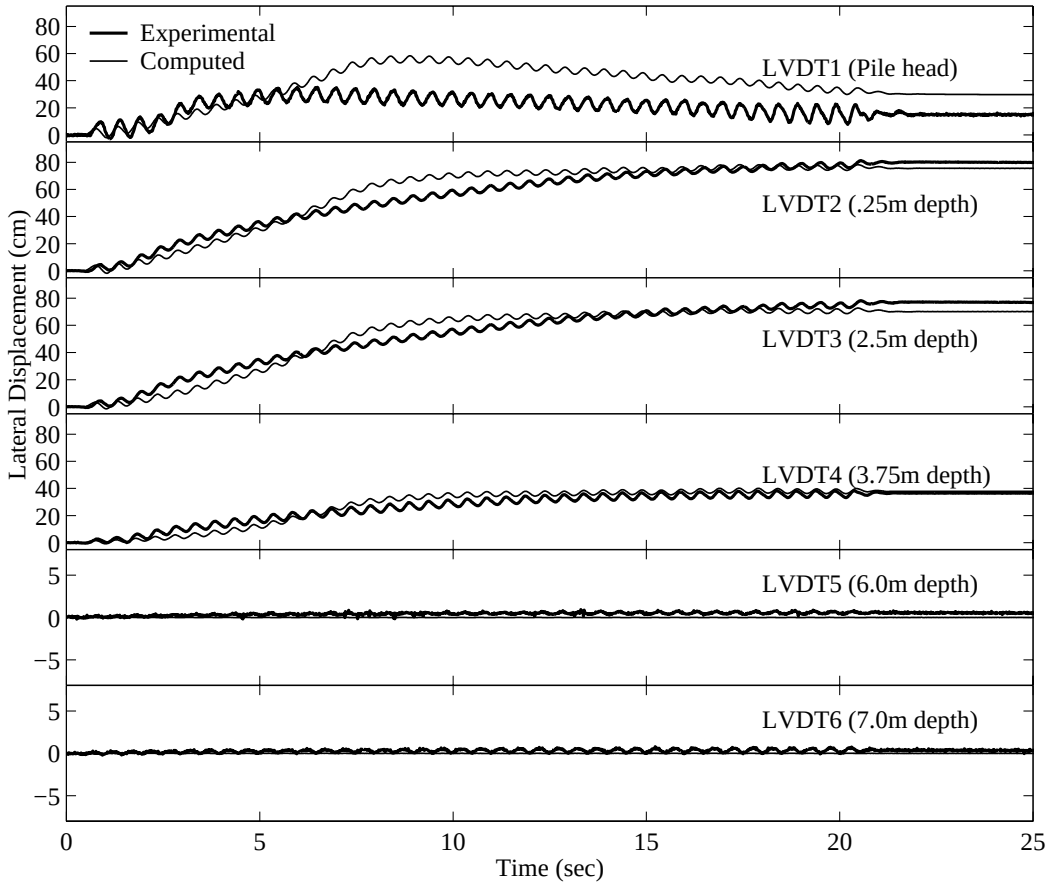

Figure 4.18. Computed and recorded pile head and soil lateral displacement time histories.

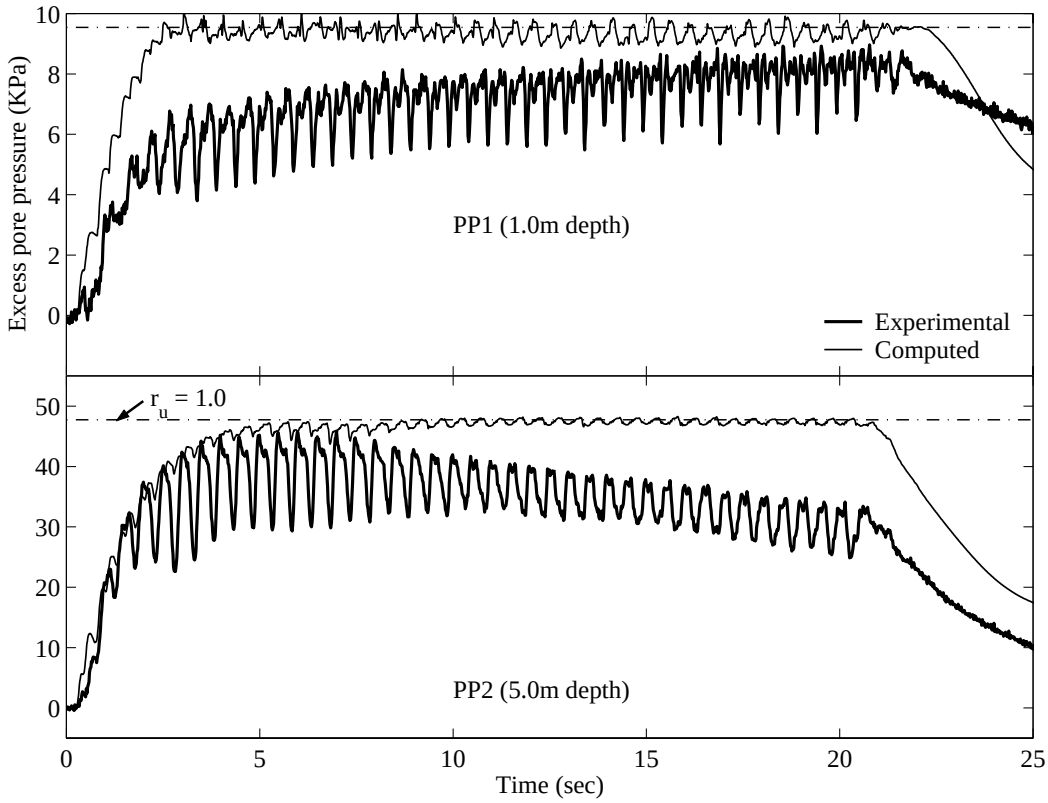

Figure 4.19. Computed and recorded excess pore pressure time histories.

Chapter 5 Liquefaction-Induced Settlement of Shallow Foundations and Remediation

Calibrated FE simulations are increasingly providing a reliable environment for modeling liquefaction-induced ground deformation. Effects on foundations and super-structures may be assessed and associated remediation techniques may be explored, within a unified framework. This chapter demonstrates current capabilities of such a FE framework via a simple 3-dimensional (3D) series of simulations. Ground liquefaction and settlement under the action of a surface load is investigated. Liquefaction hazard mitigation is explored by soil compaction and/or increase of permeability below and around the applied surface load.

5.1 Introduction

FE modeling along with other numerical simulation techniques has provided valuable insights into the response of ground and ground/foundation/structure systems. In the early 1990s, liquefaction behavior mechanisms and numerical simulation were addressed within a concerted effort, on the basis of more than 10 different centrifuge testing experimental setups (Arulanandan and Scott 1993, 1994). Overall, some success was achieved, but significant challenges were evident both numerically and experimentally. Following this effort, much research has been conducted with 3 main outcomes:

1) Our understanding and appreciation of the underlying liquefaction-induced deformation mechanisms has steadily increased in view of continued

experimentation and evidence from the increasing database of post-earthquake reconnaissance studies (e.g., JGS 1996, 1998; EERI 2000). Notable among such issues, are:

i) further appreciation of the significance of cyclic mobility in dictating deformations in clean cohesionless soils (e.g., Holzer et al. 1989; Zeghal and Elgamal 1994),

ii) the important contribution of permeability towards the process and extent of deformation accumulation (e.g., Yang and Elgamal 2002; Sharp et al. 2003),

iii) the influence of fines-content (non-plastic) and the associated potential detrimental effect (e.g., Bray et al. 2004),

iv) influence of permeability interfaces (e.g., Kokusho 1999; Malvick et al. 2004) and situations where major lateral deformations may accumulate along relatively narrow seams at such locations (e.g., in commonly encountered hydraulic-fill formations, and in alluvial deposits), and

v) the impact of an overlying structure and its foundation, and the effect thereof on the near field behavior and ensuing deformation pattern (e.g., Liu and Dobry 1997; Hausler 2002).

2) Continued development and calibration of the numerical simulation tools. Among the primary issues are:

i) calibration of soil model properties using acceleration and pore-pressure data from centrifuge and shake-table experiments, as well as

seismic records from in-situ downhole accelerometer/pore-pressure arrays (e.g., Elgamal et al. 2001),

ii) development of constitutive models that put more emphasis on cyclic mobility effects as observed from experimental data on clean sands (e.g., Iai 1991; Kramer and Elgamal 2001; Elgamal et al. 2003),

iii) pilot studies on engineering approaches to account for the effect of permeability interfaces in stratified layered soils (e.g., Yang and Elgamal 2002),

iv) steady improvements in procedures for modeling large-deformation scenarios (e.g., Manzari 2004),

v) emerging efforts to include uncertainty and sensitivity in the analysis framework (e.g., Conte et al. 2003; Gu and Conte 2003; Borja 2004), and most importantly,

vi) the increasing adoption and use of elaborate simulations which more accurately represent geometry and deformation mechanisms of complex geotechnical systems (e.g., Pecker et al. 2001; Ju 2004; Lu et al. 2004).

3) Advances in software and hardware. Among the issues impacting liquefaction simulation are:

i) wider availability of affordable personal computer workstations with large memory (e.g., 2 and 3 Gigabyte RAM), faster processors (3 Gigahertz), etc., allowing users to conduct higher fidelity analyses (2D and 3D),

ii) gradual developments in parallel computing hardware in the form of affordable networked PC workstations enabling the order of 1 million degree-of-freedom models (e.g., Jeremic 2004),

iii) wider availability of mesh generation and visualization software packages such as GiD (CIMNE 1999),

iv) recent availability of large-scale collaborative open-source codes for seismic analysis including advanced modeling capabilities for soil and structural elements (at the forefront of such efforts is the Berkeley framework OpenSees http://opensees.berkeley.edu, McKenna and Fenves 2001), and

v) facilitated development of user friendly interfaces that greatly simplify development of meshes, selection of material properties, execution of calculations, and visualization of results (e.g., Pro-shake code http://www.proshake.com, http://cyclic.ucsd.edu, http://cyclic.ucsd.edu/cyclictp, and http://cyclic.ucsd.edu/openseestp, Elgamal et al. 2004), as well as current efforts in archiving and database access (e.g., Peng et al. 2003).

In addition to the above, we are on the cusp of a new cycle of national and international collaborative developments within frameworks such as the Network of Earthquake Engineering Simulation (NEES http://www.nees.org), and the new Japan E-defense shaking-table facility (http://www.bosai.go.jp/sougou/sanjigen/3De/index.htm). These new experimental facilities and the associated numerical modeling efforts will eventually lead to consensus documents regarding liquefaction mechanisms and

appropriate computational simulation environments. Numerical simulation will rapidly become an integral component providing valuable insights for design purposes, where substantial safety and economical concerns are at stake.

In the following sections, an attempt is made to demonstrate current computational capabilities in the domain of ground modification for seismic liquefaction applications. In particular, valuable insights can now be gained in view of: i) availability of calibrated constitutive models, and ii) practical feasibility of conducting more accurate 3D analyses within a comparative framework. In order to demonstrate the above, a simple analysis framework will be adopted. The aim here is to assess potential, and derive conclusions, as to efficiency and availability for wide use. For that purpose, the problem of ground modification for mitigation of liquefaction effects due to surface loads will be addressed. Overall comparison of the numerically observed patterns with experimental observations is shown to demonstrate promise and value.

5.2 Shallow Foundations on Liquefiable Soil

Liquefaction-induced tilting and settlement of buildings on shallow foundations results in significant damage, disruption of function, and considerable replacement expense. This type of response was commonplace and well documented during Niigata, Japan 1964, Dagupan city, Philipines 1990, Chi-Chi, Taiwan 1999, and Koaleci, Turkey 1999 earthquakes (Kishida 1966; Ohsaki 1966; Seed and Idriss 1967; Yoshimi and Tokimatsu 1977; Tokimatsu et al. 1991; Adachi et al. 1992; Ishihara et al. 1993; Tokimatsu et al. 1994; EERI 2000, 2001).

Liu and Dobry (1997) conducted a centrifuge investigation related to the problem of shallow-foundation liquefaction-induced settlement. In prototype scale, they explored the response of an essentially rigid footing (about 4-5 m diameter) supported on liquefiable sand (D_r of about 50%, with 10 m to 12.5 m saturated layer thickness). In this study, the mitigation of liquefaction hazard was explored with emphasis on compaction and permeability variation of the immediate ground below the foundation. More recently Haulser (2002) conducted a multi-experiment centrifuge study where ground improvement by compaction was explored. Scenarios of different soil relative density, and compaction to different depths below the super-structure were explored.

Our numerical investigation addresses the effect of compaction with and without permeability increase. No direct comparisons are made with centrifuge studies, but observed trends are assessed and discussed. In this regard, the computational framework can be an environment for development of insights that must be further substantiated by experimental/full-scale observation.

5.3 Shallow Foundation Model

A 10 m saturated medium sand layer was studied (based on Nevada Sand at D_r of about 40%). Herein, the load (40 kPa, or about 2m of an equivalent soil overburden) was simply applied at ground level in the form of a distributed surficial vertical stress over a 2 m x 2 m area (Figure 5.1). More accurate loading patterns may be explored in future studies with no added complexity (e.g., imposing load that represents an actual building geometry by using additional super-structure elements, modeling of potential

embedment of the foundation below ground surface, and/or locating water table at some depth below ground surface).

In view of symmetry, a half-mesh (75 20-8 noded brick elements in total) is studied as shown in Figure 5.2. Length in the longitudinal direction is 26 m, with 13 m transversally (in this half-mesh configuration). At this preliminary stage, the employed mesh is crude geometrically, and further refinement is addressed later. The following (solid and fluid) boundary conditions were implemented: (i) lateral excitation was defined along the base in the longitudinal direction (x-axis), (ii) at any given depth, displacement degrees of freedom of the left and right boundaries were tied together (both horizontally and vertically using the penalty method) to reproduce a 1D shear wave propagation mechanism effect, (iii) the soil surface was traction free, with zero prescribed pore pressure, and (iv) the base and lateral boundaries were impervious.

The 7.5 m depth (NS direction) downhole acceleration record (Figure 5.3) from the Wildlife site during the 1987 Superstition Hills earthquake was employed as base excitation along the x-axis. During this event, much evidence of liquefaction was observed at Wildlife (Holzer et al. 1989; Youd and Holzer 1994). Selection of this excitation (recorded at 7.5 m depth) as one representative motion causing liquefaction is suitable for our demonstration purposes, but an appropriate ensemble of records should be used to develop more comprehensive conclusions.

A key component of this modeling effort lies in earlier calibration of the employed soil model (based on recorded response of Nevada Sand at D_r of about 40%) under situations of liquefaction and lateral spreading response (Parra 1996; Yang 2000; Elgamal et al. 2003; Yang et al. 2003). The compacted zone modeling parameters were

chosen mainly based on extrapolating the D_r = 40% calibration results, available empirical formulae (Kramer 1996), and engineering judgment (see Table 5.1, Figure 5.4 and Figure 5.5 for soil properties, configuration of multi-yield surfaces and shear stress-strain response, respectively). While more verification and further tuning are always possible and potentially helpful, the model currently reproduces salient liquefaction response characteristics, based on earlier calibration work over the past 10 years (Parra 1996; Yang 2000; Yang et al. 2003; Yang and Elgamal 2004).

5.4 Site Remediation

We attempt to explore the effect of including a compacted zone below the loaded area. Employing high permeability drains (e.g., wick drains) or replacing the original sand (permeability $k = 6.6 \times 10^{-5}$ m/s) under the load with a high permeability compacted gravel ($k = 1.0 \times 10^{-2}$ m/s) was also explored. In both cases, the treated zone was varied in depth and lateral extent.

Table 5.2 depicts the scope of our ground modification study (Figure 5.1). Specifically, a total of 8 simulations were performed. Case **MS**1D (Table 5.2) simulates a **M**edium **S**and site response situation (1D shear wave propagation) with no applied surface load. The result obtained provides a reference of free-field response for the remaining cases. Case **MS** is the same as **MS**1D with the surface load applied (Table 5.2 and Figure 5.1a). This is the case without any remediation, serving as the benchmark. Cases **DS**, **DS**L and **DS**L4 (Figure 5.1b, c and d) are studied to evaluate the effect of compaction (**D**ense **S**and) for different levels of soil depth and lateral extent.

Cases **DS** and **DS**L are both compacted to 2 m depth (Figure 5.1b and c) while a **L**arger 10 m lateral extent is compacted in Case **DSL** (compared to 2 m width in Case DS). Case DSL4 (Figure 5.1d) is the same as Case DSL with compaction up to 4 m. **G**ravel permeability is used for the compacted area in Cases **DG**, **DGL** and **DGL**4.

5.5 Simulated Foundation Settlement

Figure 5.6 displays the foundation settlement time histories for all conducted simulations. The final settlements are also listed in Table 5.2. It is seen that compaction to a larger depth and/or greater lateral extent had a minor effect on reducing foundation settlement (Cases DS, DSL and DSL4). However, higher permeability of the compacted area played a key role in decreasing settlement. In the case of DGL4 (dense gravel, 10 m wide and 4 m deep), the foundation final settlement (Table 5.2) was reduced to 0.02 m (compared to 0.23 m in Case DSL4).

Additional observations for compaction effects are (Table 5.2):

1) In the investigated scenario, the zone treated by compaction was virtually of no consequence. Such an outcome remains to be verified by additional simulations and experiments.

2) In fact, increasing the compacted area (case of 2 m depth, DSL) actually resulted in increased settlement which is a counter-intuitive outcome. It appears that the compacted area acted as an embedded block, ultimately resulting in marginally larger liquefaction-induced settlement.

3) As expected, compaction to depths greater than 4 m (e.g., compacting throughout the entire depth) was found to lower total settlement by about 50% (not shown).

Increased permeability effects are (Table 5.2):

1) High permeability right under the foundation only (DG) immediately reduced settlement by more than 50%.

2) Increasing the treated zone laterally (DGL), then also vertically (DGL4) eventually resulted in an order of magnitude of settlement reduction.

Details and insights regarding the underlying dynamic response mechanisms are discussed next.

5.6 Response Characteristics and Discussion

5.6.1 Site Response (Case MS1D)

Figure 5.7 and Figure 5.8 display lateral acceleration and excess pore pressure (u_e) time histories at different depths for Case MS1D. Figure 5.8 shows that the entire sand stratum was liquefied throughout (maximum excess pore-pressure u_e equals the initial overburden vertical effective stresses σ'_{v0}, i.e. the pore-pressure ratio $r_u = u_e / \sigma'_{v0} = 1.0$). Initial liquefaction was reached at 9 seconds near the surface (Figure 5.8), propagating downwards throughout the stratum after about 13 seconds of excitation (Figure 5.8). As liquefaction occurred, acceleration at relatively high levels of input excitation (during 10 s – 20 s) was clearly attenuated (Figure 5.7).

Once liquefaction was reached, r_u remained at 1.0 with reduction only taking place near the end of shaking, from the base upwards. The stress-paths and stress-strain history of Figure 5.9 show the typical mechanism of cyclic decrease in effective confinement due to pore-pressure buildup, along with the associated loss in shear stiffness and strength.

5.6.2 Benchmark Simulation (Case MS)

In the free field (not shown), the response was essentially the same as that of MS1D. Under the foundation, strong dilative response was observed. As shown in Figure 5.10, a number of instantaneous sharp pore pressure drops occurred. This dilative response is also observed in the stress paths as shown in Figure 5.11. In the soil section immediately below the foundation, u_e buildup was relatively slow (top graph of Figure 5.10). This pattern of response was caused mainly by the shear-induced dilative response during deformation of the saturated soil below the foundation (Liu and Dobry 1997; Adalier et al. 1998). As the rate of settlement decreased (MS in Figure 5.6), u_e under the foundation (top graph of Figure 5.10) built up rapidly and only started to dissipate after nearly reaching liquefaction at about 110 seconds (well after the end of shaking at 98 seconds). The permanent foundation settlement was 0.23 m (Table 5.2) in Case MS. Similar characteristics of u_e response were recorded during the centrifuge test of Liu and Dobry (corner of Figure 5.10).

5.6.3 Compaction Remediation

Cases DS, DSL and DSL4 were compacted to different lateral extents and soil depth levels (Table 5.2 and Figure 5.1). The response recorded away from the foundation (free-field) in all these cases was quite similar to that of Case MS (not shown). Under the foundation, the responses (e.g. lateral acceleration and excess pore pressure time histories) in cases DS, DSL and DSL4 were also quite comparable to Case MS.

Pore-pressure for DSL4 under the foundation is shown in Figure 5.12. Note the similarity to MS (Figure 5.10), with u_e rising near the end of shaking (even at 4 m and 6 m depth in DSL4), and the somewhat faster dissipation of u_e at 8 m depth.

5.6.4 Permeability Remediation

Cases DG, DGL and DGL4 are the cases with high permeability (gravel). Figure 5.13 and Figure 5.14 display u_e time histories at different depths under the foundation for cases DG and DGL4 respectively. Insignificant u_e was observed under the foundation up to the compacted depth. The dilative response, as seen in the stress paths (Figure 5.15), was also manifested by pore pressure reduction instants (lower 2 graphs of Figure 5.14).

5.7 Summary

A study was conducted to explore the influence of compaction and/or increased drainage on the liquefaction-induced settlement below an applied surface load. Within

the scope of conducted simulations, high drainage was found to be effective in reducing settlement. In this regard, crude mesh simulations appeared useful in providing valuable qualitative insights.

Such relatively simple simulations may be of great value in conducting "*what if*" scenarios, before execution of more elaborate numerical or physical model investigations. For instance, the reported study may be conveniently extended to explore the relative influence of changes in input excitation, permeability, shear stress-strain relationships, surcharge stress and configuration, and extent of liquefaction-countermeasure remediation/treatment.

Table 5.1: Model parameters for medium sand and dense soils

Parameters	Medium	Dense
Low-strain shear modulus G_r (at 80 kPa mean effective confinement)	78.5 MPa	135.0 MPa
Friction angle ϕ	31.4 degrees	40.0 degrees
(Figure 1.6, phase 1-2)		
Liquefaction yield strain γ_y	0.5 %	0
(Figure 1.6, phase 0-1)		
Contraction parameter c_1	0.065	0.02
Contraction parameter c_2	400.0	400.0
(Figure 1.6, phase 2-3)		
Phase Transformation angle ϕ_{PT}	26.5 degrees	26.0 degrees
Dilation parameter d_1	140.0	200.0
Dilation parameter d_2	1.0	1.0

Table 5.2: Preliminary crude mesh simulations

Simulation	Compacted area (m x m x m)	Compacted area permeability *k* (m/s)	Foundation settlement (m)
MS1D (Medium Sand, 1D)	(Site response simulation)		0.00
MS (Medium Sand)	Benchmark, no compaction (Fig. 1a)		0.23
DS (Dense Sand)	2 x 2 x 2 (Fig. 1b)	6.6×10^{-5}	0.22
DG (Dense Gravel)	2 x 2 x 2 (Fig. 1b)	1.0×10^{-2}	0.12
DSL (Dense Sand, Large area)	10 x 10 x 2 (Fig. 1c)	6.6×10^{-5}	0.26
DGL (Dense Gravel, Large area)	10 x 10 x 2 (Fig. 1c)	1.0×10^{-2}	0.07
DSL4 (Dense Sand, Large area, 4m depth)	10 x 10 x 4 (Fig. 1d)	6.6×10^{-5}	0.24
DGL4 (Dense Gravel, Large area, 4m depth)	10 x 10 x 4 (Fig. 1d)	1.0×10^{-2}	0.02

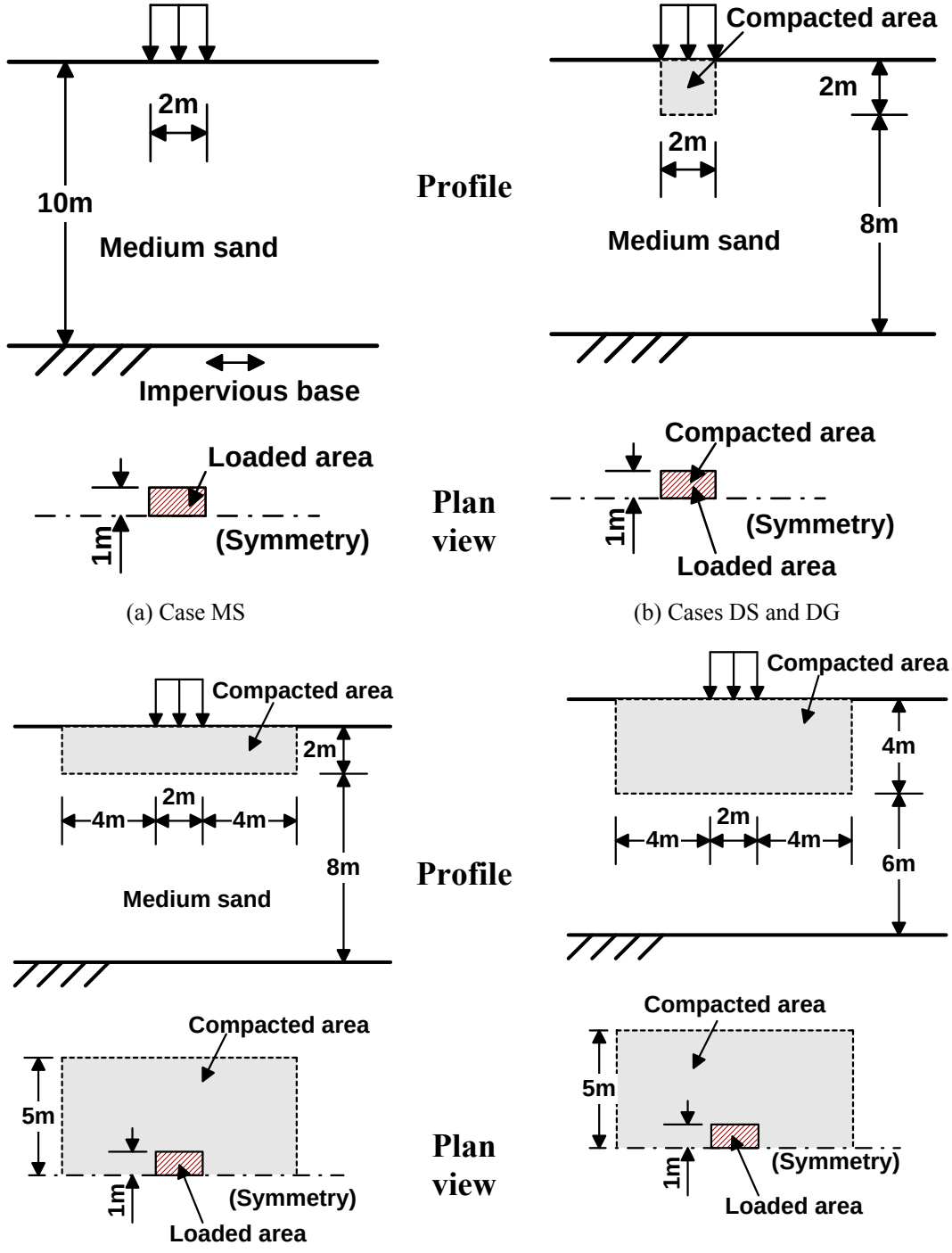

(a) Case MS

(b) Cases DS and DG

(c) Cases DSL and DGL

(d) Cases DSL4 and DGL4

Figure 5.1: A medium sand soil layer subjected to a surface load of 40 kPa.

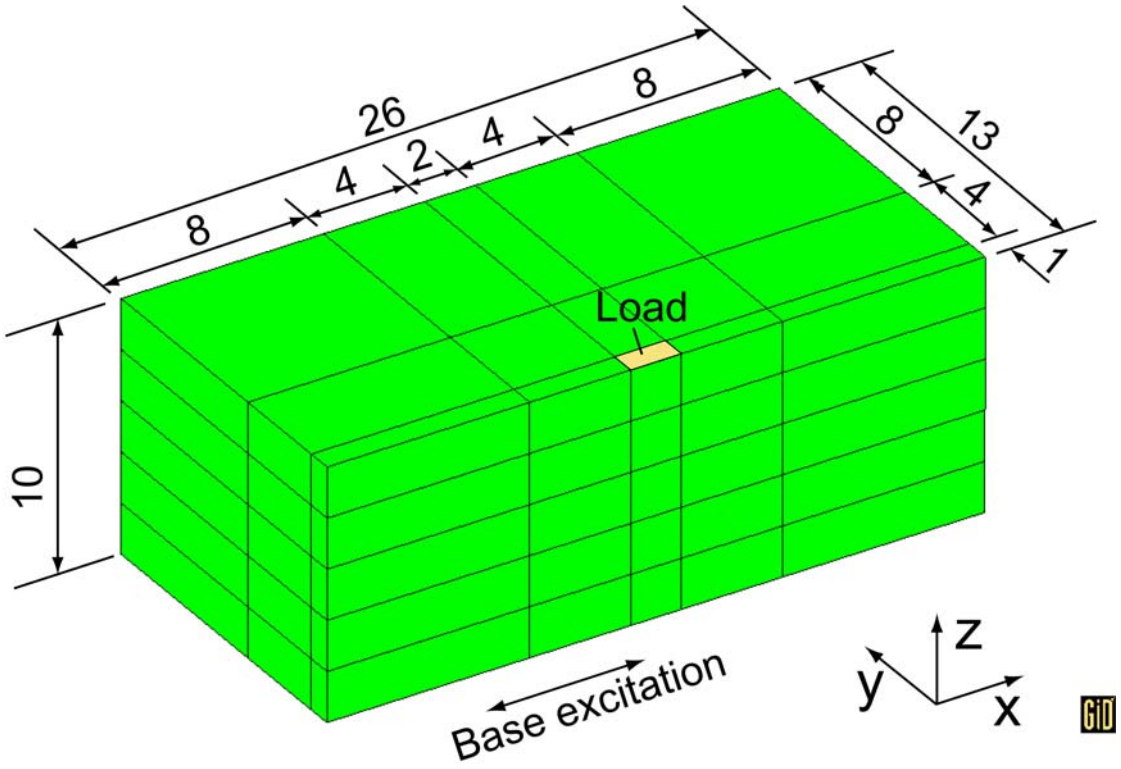

Figure 5.2: FE mesh of the shallow foundation model.

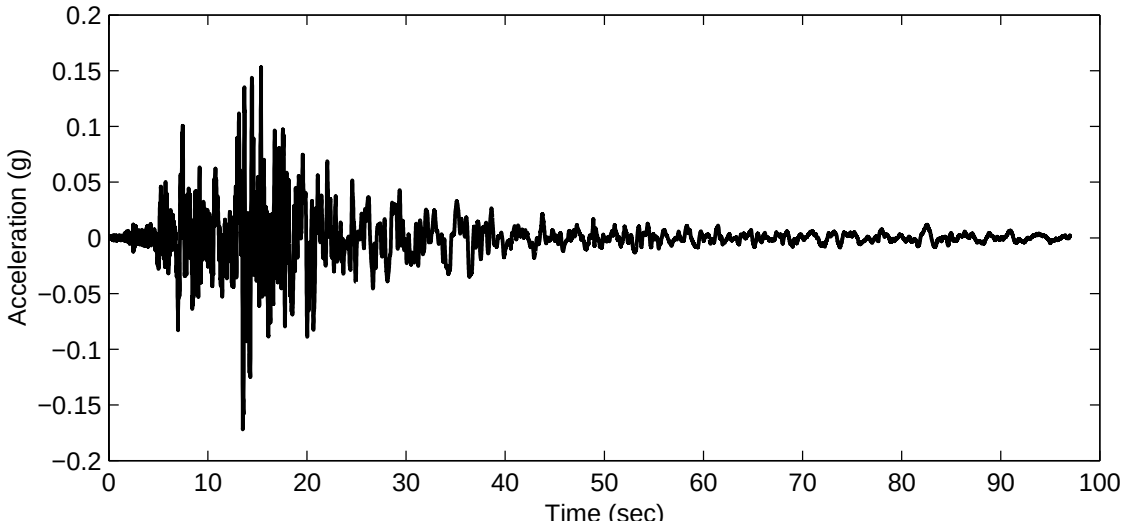

Figure 5.3: Base input motion.

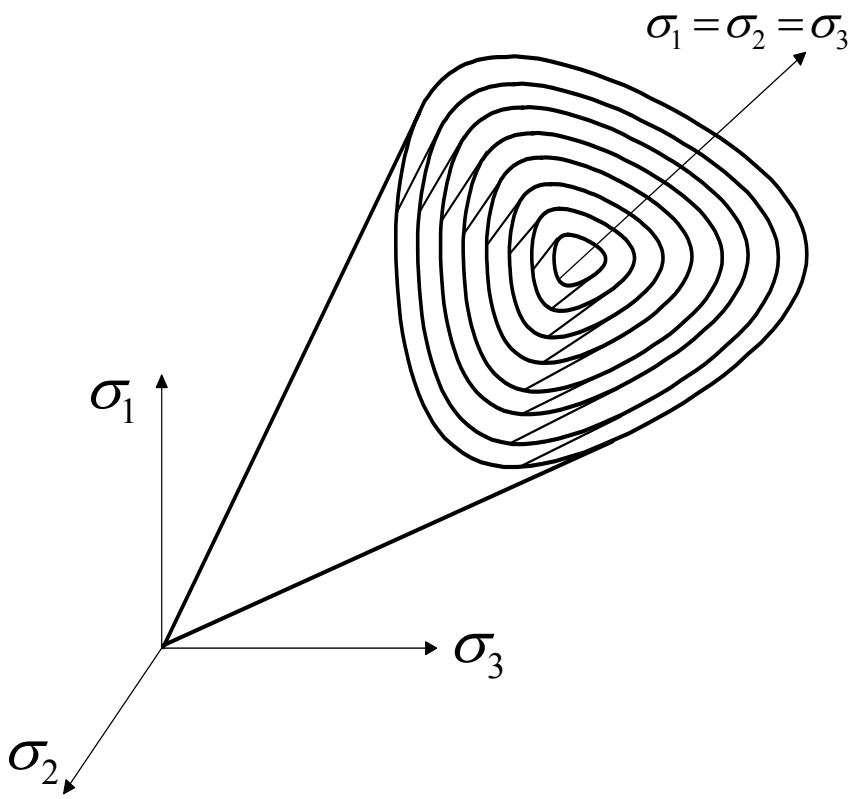

Figure 5.4: Configuration of multi Lade-Duncan yield surfaces in principal stress space (Yang and Elgamal 2004).

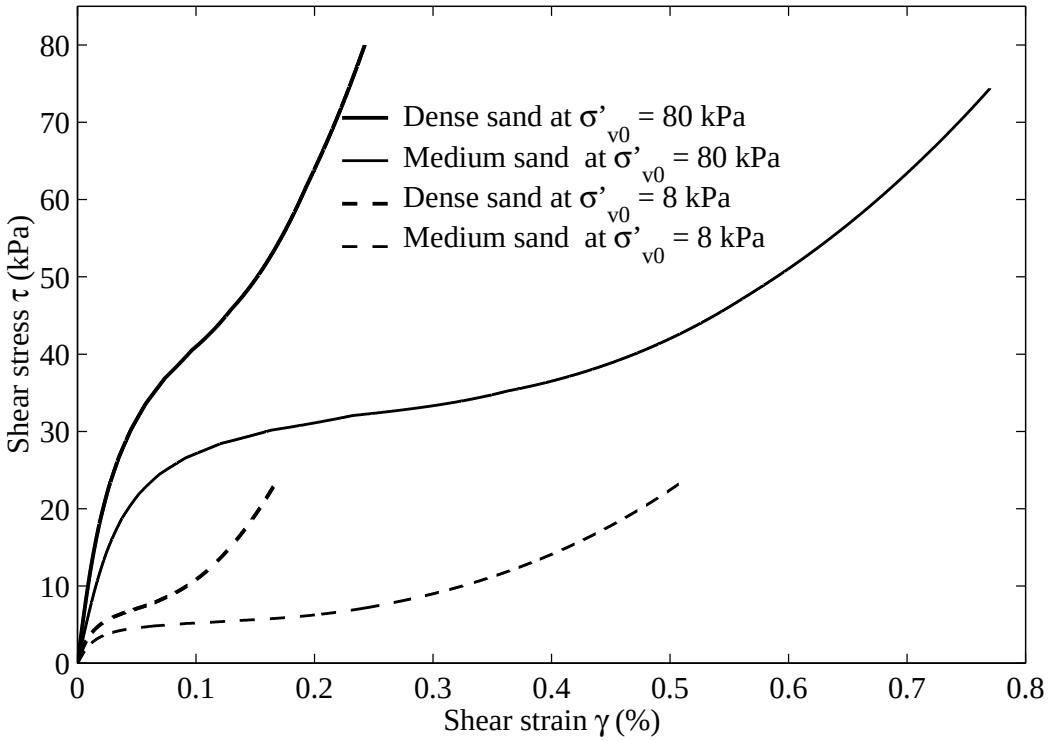

Figure 5.5: Model shear stress-strain response under undrained conditions (initial vertical effective confinement $\sigma'_{v0} =$ 80 and 8 kPa).

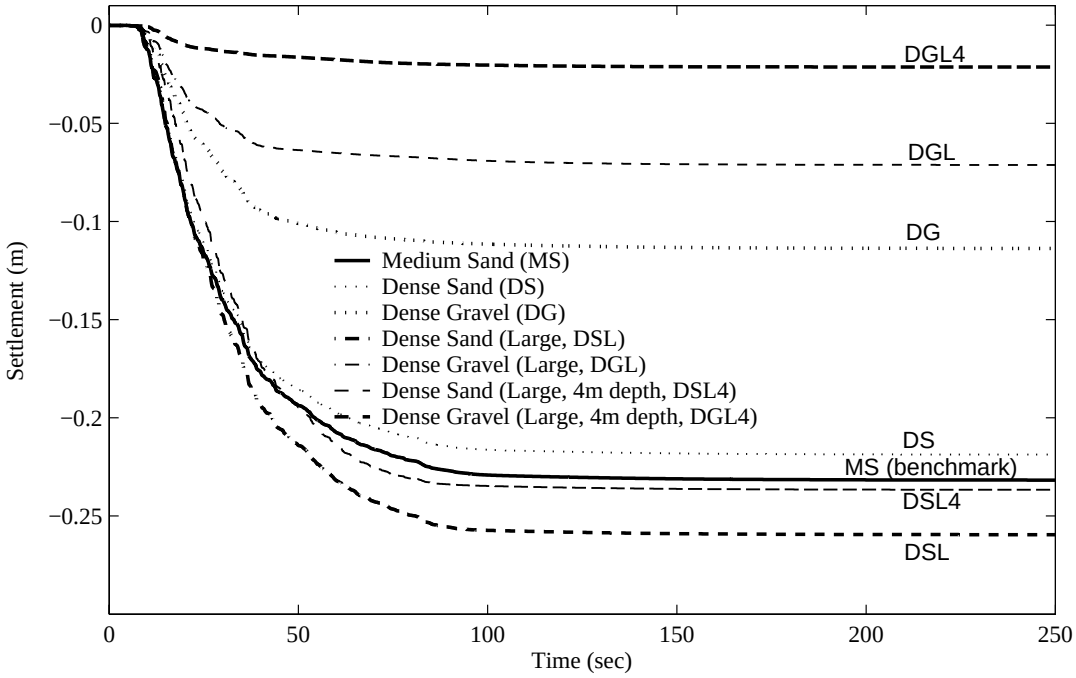

Figure 5.6: Foundation settlement time histories.

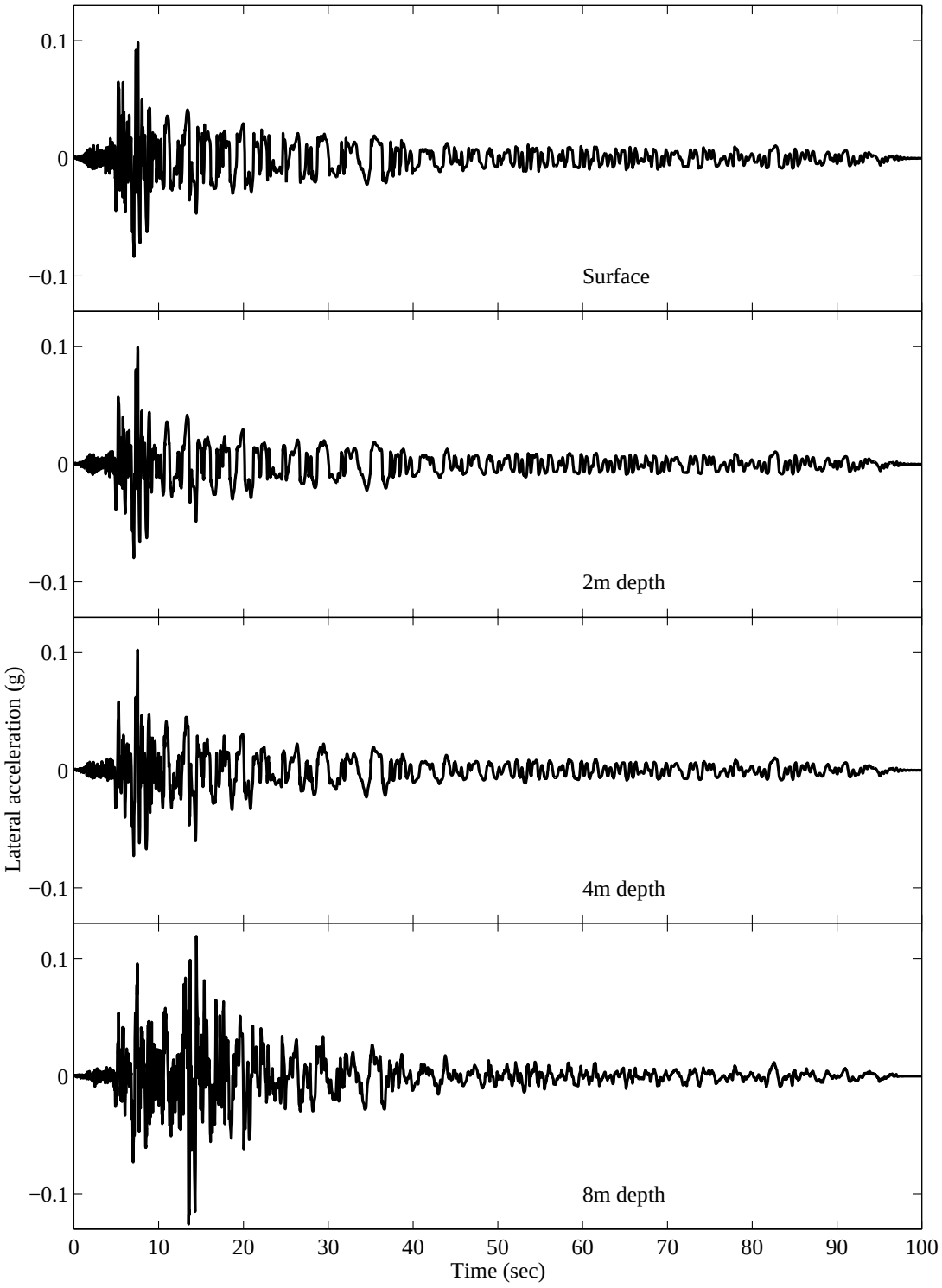

Figure 5.7: Lateral acceleration time histories for Case MS1D (site response situation).

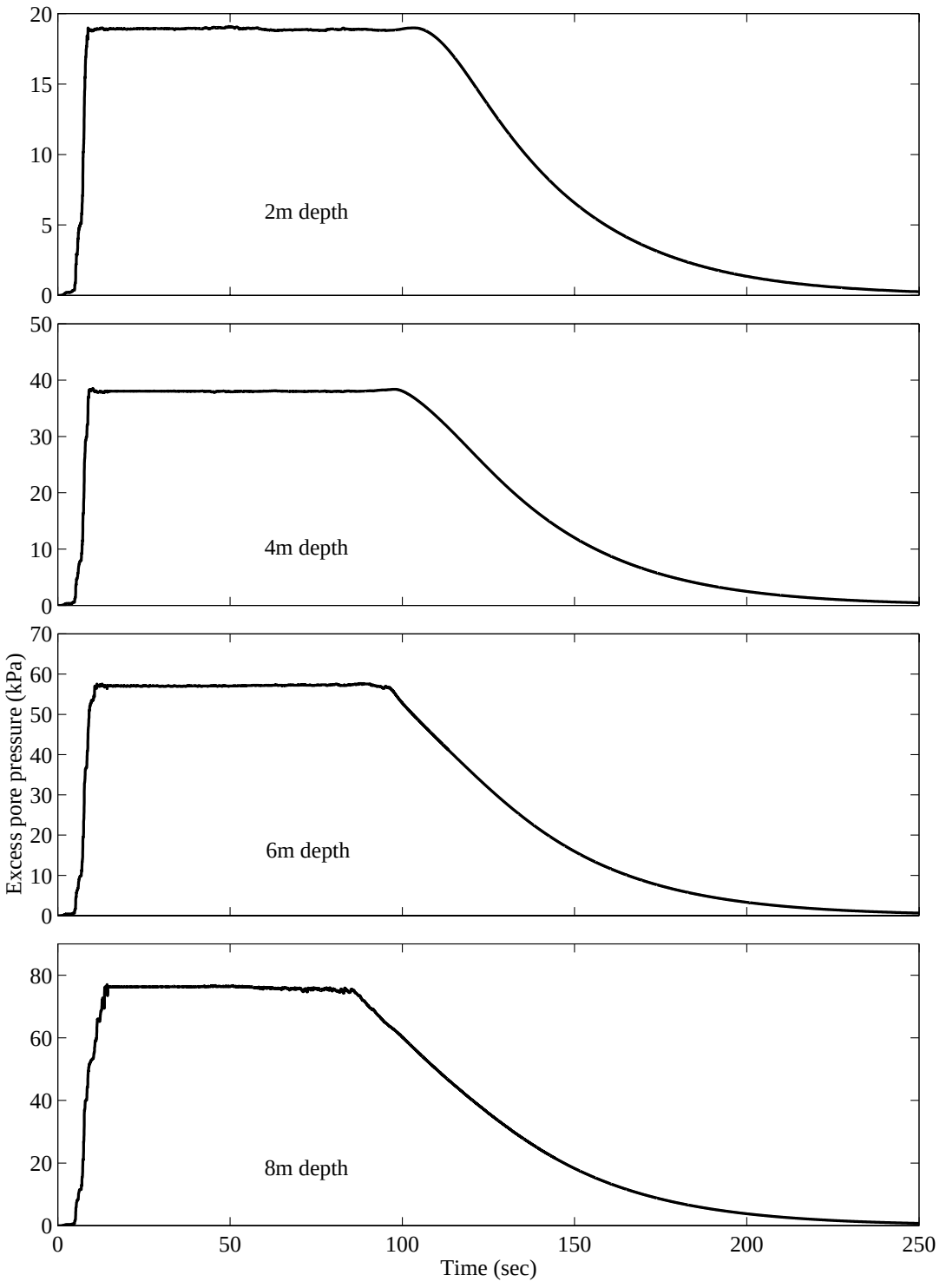

Figure 5.8: Excess pore pressure time histories for Case MS1D (site response situation).

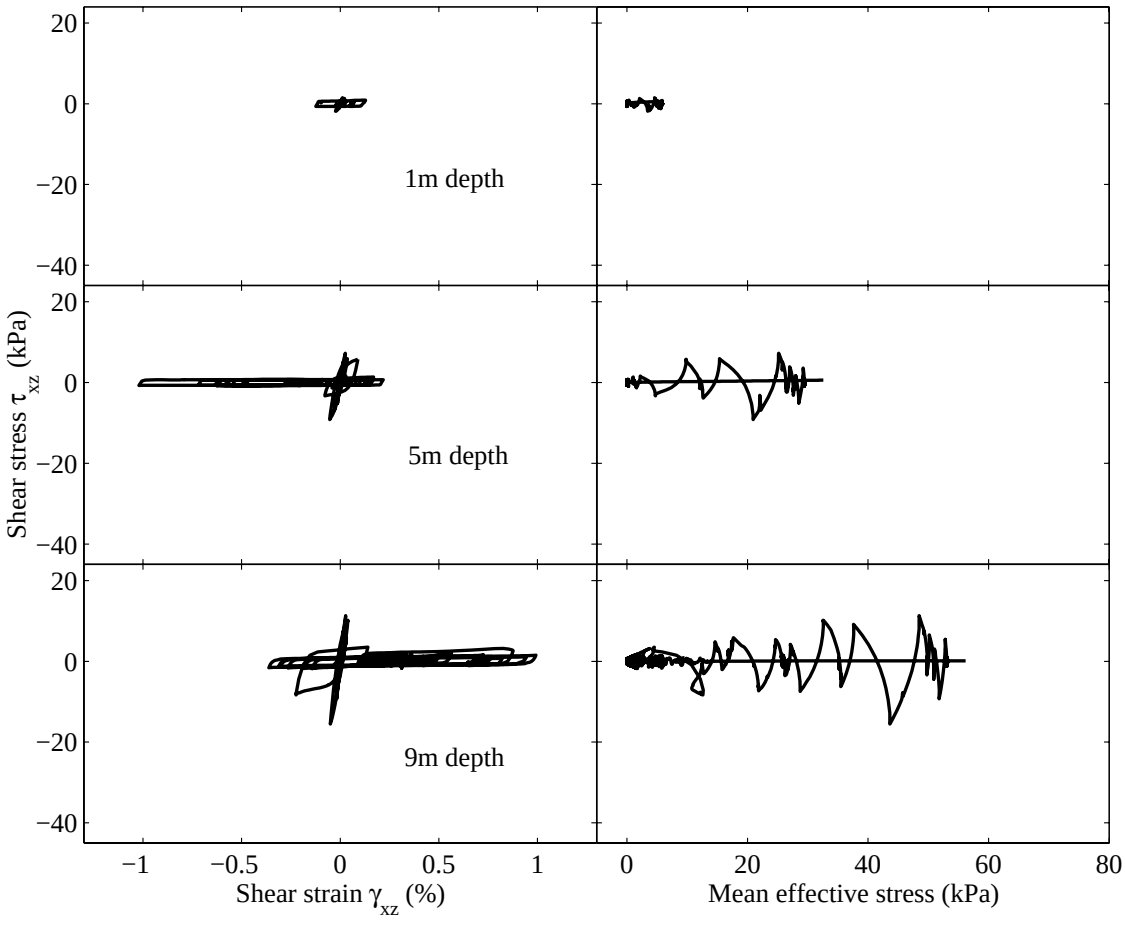

Figure 5.9: Shear stress-strain and stress path at different depths for Case MS1D (site response situation).

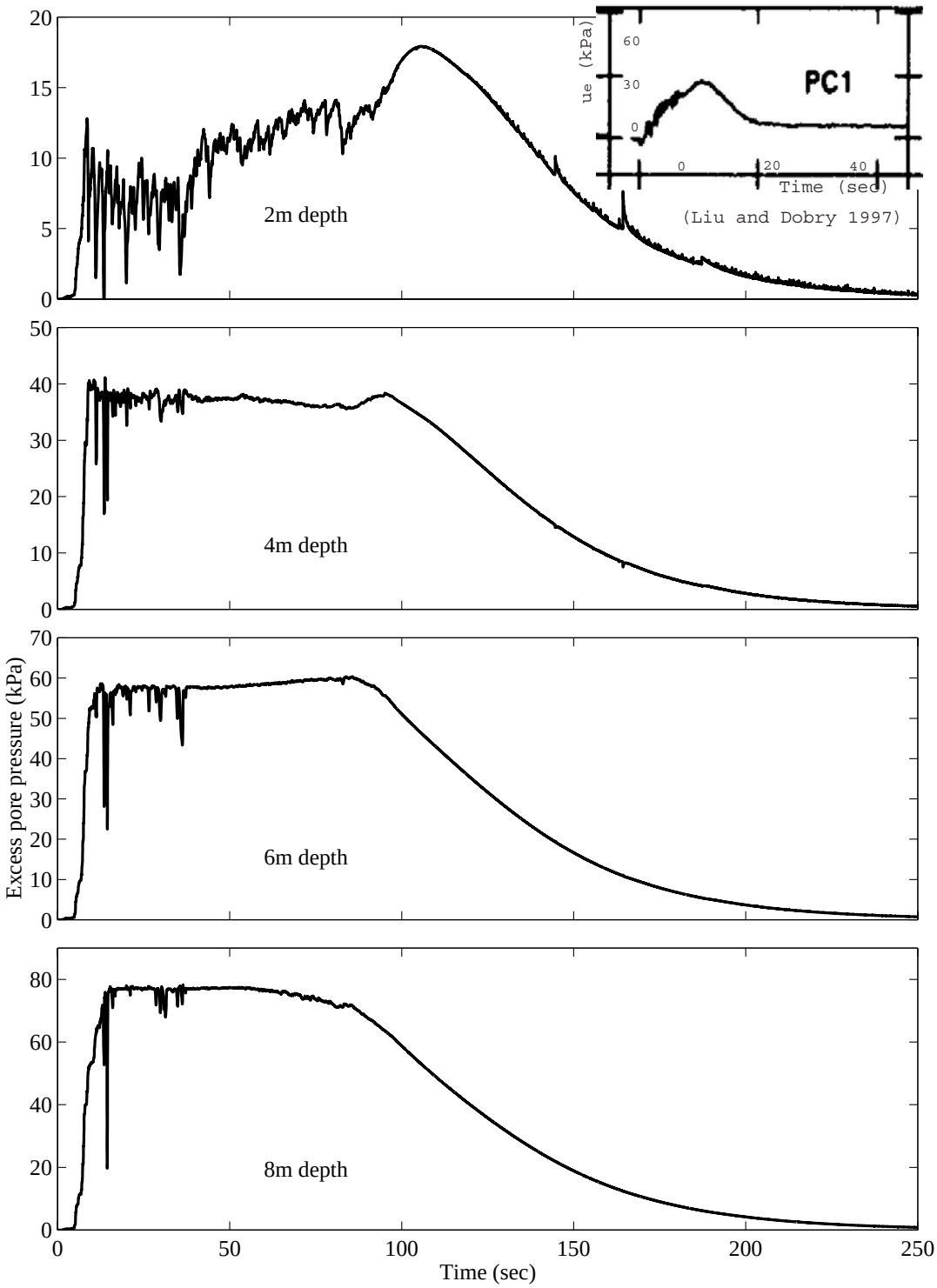

Figure 5.10: Excess pore pressure time histories at different depths under foundation for Case MS.

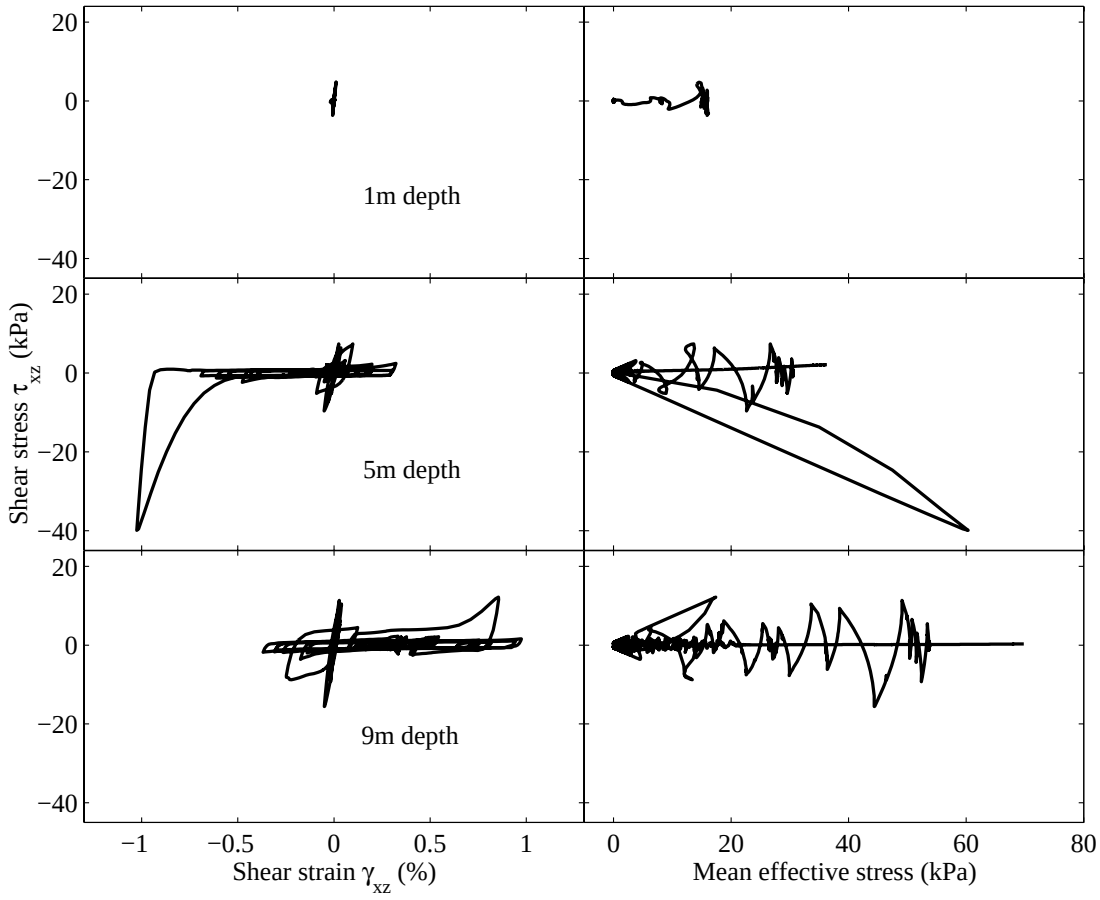

Figure 5.11: Shear stress-strain and stress path at different depths (under foundation) for Case MS.

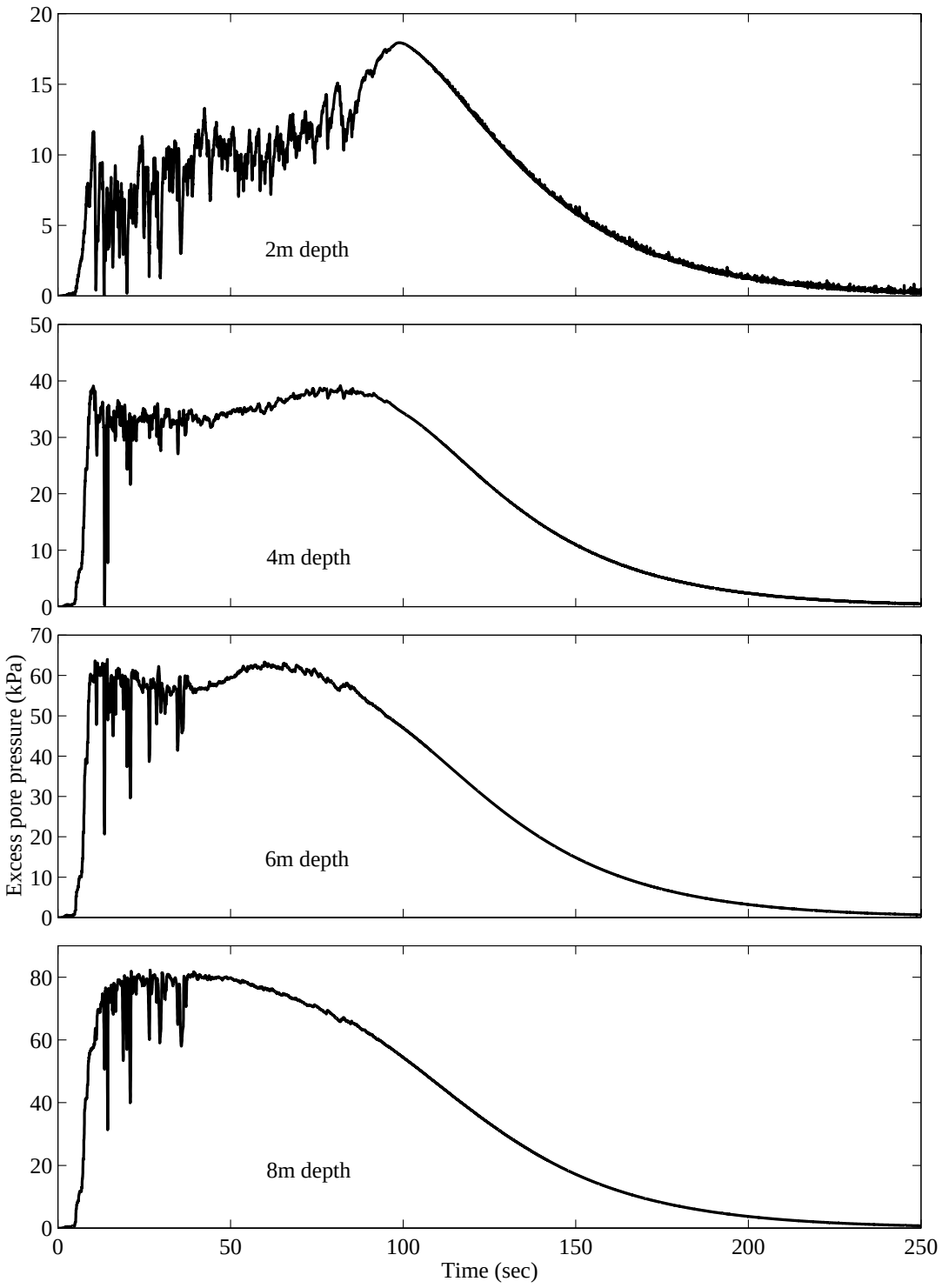

Figure 5.12: Excess pore pressure time histories at different depths (under foundation) for Case DSL4.

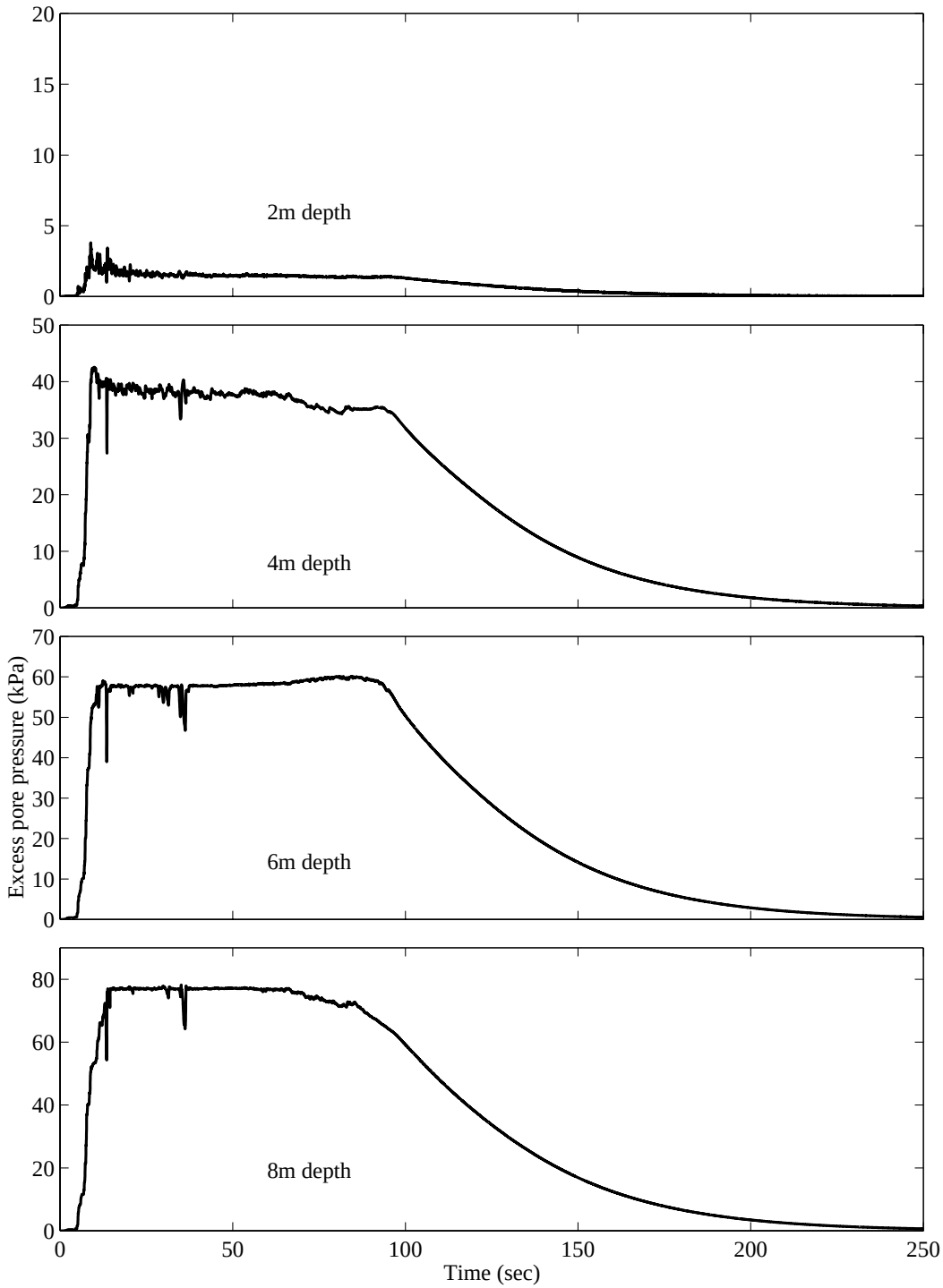

Figure 5.13: Excess pore pressure time history at different depths (under foundation) for Case DG.

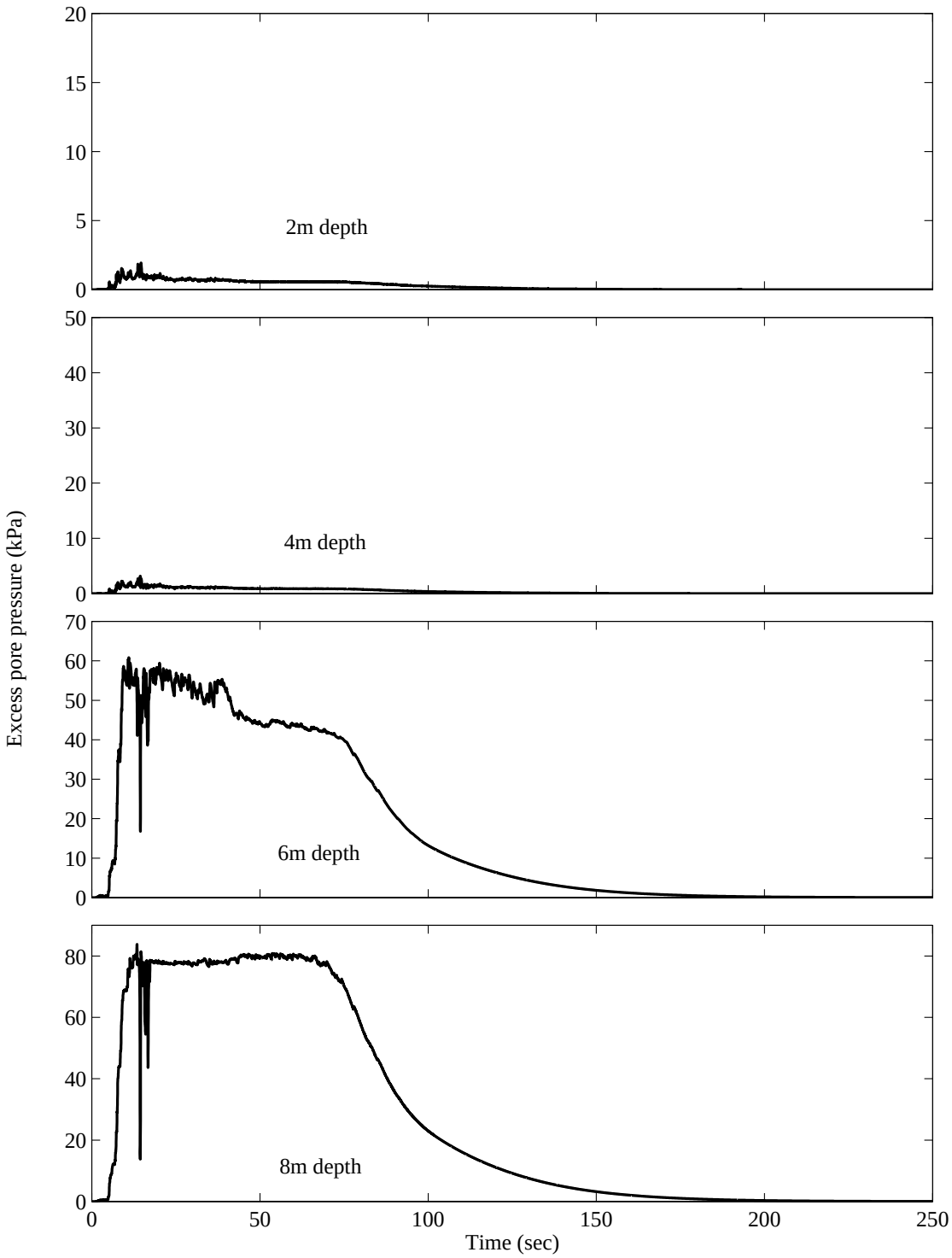

Figure 5.14: Excess pore pressure time histories at different depths (under foundation) for Case DGL4.

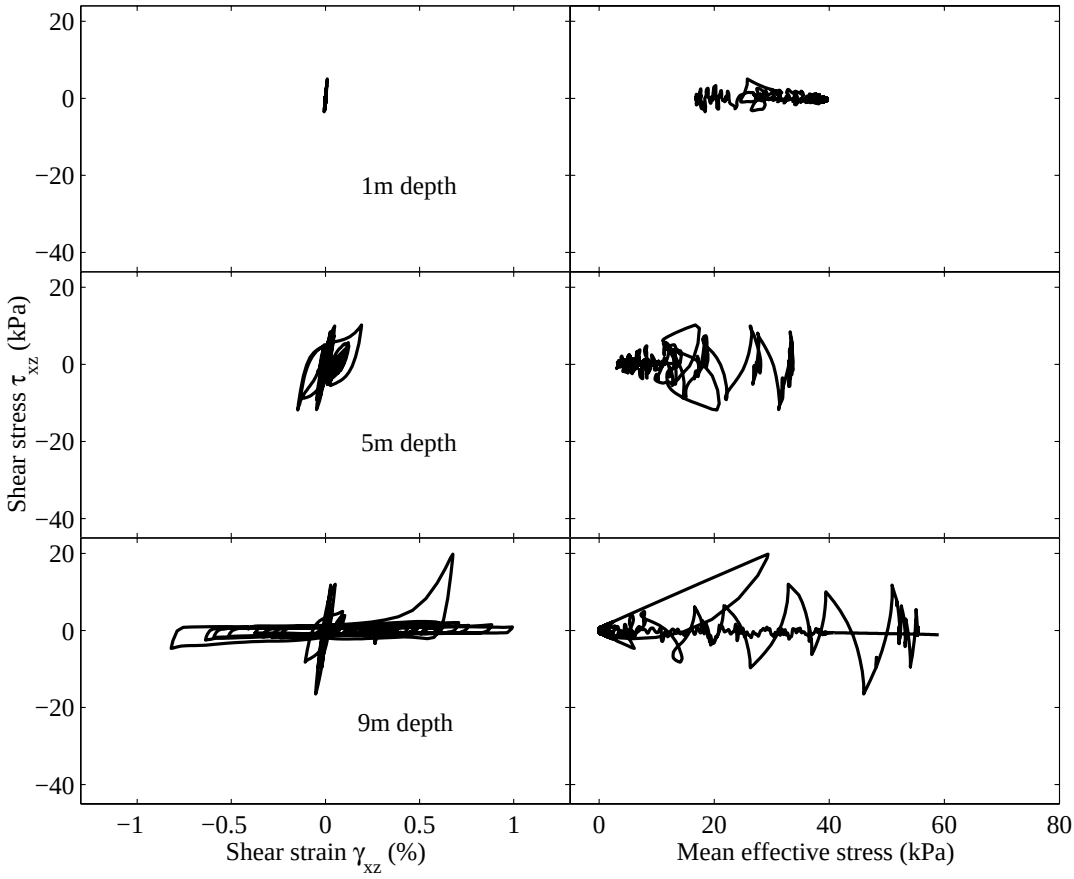

Figure 5.15: Shear stress-strain and stress path at different depths (under foundation) for Case DGL4.

Chapter 6 High Fidelity Simulations of Shallow Foundation Settlement

This chapter attempts to provide more accurate simulations of liquefaction-induced settlements through high-fidelity 3D numerical studies conducted on the supercomputer Datastar. Section 6.1 further explores simulations of Case DG, discussed in Chapter 5, with 3 finer meshes. Section 6.2 presents simulations of foundation settlement and remediation techniques for a larger shallow foundation (10 m x 10 m, compared to the 2 m x 2 m foundation employed in Chapter 5 and Section 6.1) using high-fidelity models. All simulations were performed using ParCYCLIC on the Datastar parallel machine at SDSC.

6.1 Mesh Refinement Studies of Shallow Foundation Settlement

In the studies of the shallow foundation settlement presented in the previous chapter (Chapter 5), the employed 75-element mesh in (Figure 5.2) is rather coarse. In order to satisfactorily reproduce the dynamic mechanisms of the shallow foundation settlement and associated remediation techniques, a high level of spatial resolution of modeling is necessary. Therefore, three refined meshes (500 elements, Figure 6.1b; 960 elements, Figure 6.1c; and 4480 elements, Figure 6.1d) were utilized for additional studies. The numbers of degrees of freedom (DOFs) are 1620, 8679, 15868 and 67716, respectively, for the above-mentioned meshes (Table 6.1).

Case DG (Figure 5.1b) was chosen as the case for this high fidelity simulation study. All configurations of Case DG are the same as in Chapter 5.

6.1.1 Comparisons of Computed Responses

Figure 6.2 shows the final deformed meshes for the 4 models. As expected, the deformed shape becomes smoother as we refine the model (Figure 6.2a, b, c and d). Figure 6.2d (4480-element mesh) illustrates that the boundary of the employed model is far enough. Figure 6.2 also indicates that high-fidelity 3D numerical studies provide more accurate estimates of liquefaction-induced settlements (on a relative scale).

Figure 6.3 displays the foundation settlement time histories for the 4 meshes. The foundation final settlement (Figure 6.3) was 0.19 m for the 500-element mesh, about 0.21 m for the 960-element mesh, and 0.22 m for the 4480-element mesh. With such a much more flexible system, the high fidelity 4480-element mesh results in an additional final settlement of less than 0.01 m compared to the 960 elements mesh (Figure 6.3), or 0.03 m compared to the 500 elements mesh (Figure 6.3). This shows the simulation results appear to have become essentially stable with the 500 elements mesh and beyond.

Comparison of the foundation lateral acceleration from these four meshes (Case DG) is shown in Figure 6.4. The responses are similar except for the more significant spiking in acceleration during 12 sec – 15 sec for the finer meshes (960-element mesh and 4480-element mesh in Figure 6.4). It is noted that the somewhat “noisy” acceleration response occurring in the 75 elements mesh (Figure 6.4), which is rather coarse, disappears in the finer meshes (500-element mesh, 960-element mesh and 4480-element mesh in Figure 6.4). This shows that it is advisable to verify analysis results with a finer mesh.

6.1.2 Analysis Results for the 4480-Element Mesh

Figure 6.5 displays the contour lines of the final vertical displacement for the 4480-element mesh. The settlement of the ground surface (Figure 6.5b) is almost symmetric with respect to the foundation. However, side view (Figure 6.5c) of the contour lines shows the settlement is not strictly symmetric, especially near the bottom of the soil domain. This is on account of the history dependent nature of the response due to seismic excitation (Figure 5.3).

Figure 6.6 shows excess pore pressure (u_e) time histories for Case DG for the 4480-element mesh. The u_e response (Figure 6.6) was mostly comparable to that obtained with the coarse mesh (Figure 5.13), with the exception of more pronounced dilative response peaks (lower 2 graphs of Figure 6.6).

Figure 6.7 shows the contour lines of the excess pore pressure ratio at different time frames. Initially the ground surface reaches liquefaction (excess pore pressure ratio = 1.0) and propagates downwards. At 10 sec (Figure 6.7a), the top half soil domain liquefied. The entire domain reached liquefaction at 20 sec (Figure 6.7b). The whole model remained liquefied until the end of the shaking at 100 sec (Figure 6.7d), where excess pore pressure started to dissipate. At 150 sec (Figure 6.7e), the excess pore pressure within the soil domain returned to 0.2 or less, indicating pore pressure had almost completely dissipated.

6.1.3 Parallel Performance

Case DG was analyzed using different numbers of processors ranging from 1-32. The total execution times for the above-mentioned different size meshes are displayed in Figure 6.8. The parallel speedup for each case is also shown in Figure 6.8. Except for the case of the 4480-element mesh where timing is based on the first 10 seconds of excitation only, all cases are measured for the whole 250 seconds of dynamic analysis.

In parallel FE simulations, the appropriate number of processors employed to run an analysis depends on the problem size. Running with more than that will incur additional communications and overheads and thus compromise the performance. As we can see from Figure 6.8, the appropriate numbers of processors for running 75-, 500-, 960- and 4480-element meshes may be 4, 8, 16 and 32, respectively (the number of processors employed to run ParCYCLIC has to be a power of 2, see Section 3.3 for more details).

The time measurements for the 4 meshes are listed in Table 6.1, which only shows the timing results for the cases of 4, 8, 16 and 32 processors employed for the analyses of the 75-, 500-, 960- and 4480-element meshes, respectively. As we can see, the time spent on the initialization phase is insignificant compared to the entire analysis. Most time during the initialization phase is spent on the FE model input and formation of the adjacency structure for the high fidelity 4480-element mesh. The multilevel nested dissection ordering using METIS is relatively fast and less than 2 seconds are needed to order the high fidelity 4480-element mesh with 67,716 degrees of freedom (Table 6.1).

The times spent on the LHS formation, the RHS formation and the numerical factorization per step are listed in Table 6.1. Numerical factorization dominates the entire nonlinear solution phase as the problem size becomes large.

6.2 Simulations of Settlement of a 10 m x 10 m Shallow Foundation

Chapter 5 and the previous section in this chapter studied the settlement of a 2 m x 2 m shallow foundation. For comparison, studies of settlement for a larger shallow foundation under similar scenarios would provide more insight. This section presents numerical simulations of settlement of a 10 m x 10 m shallow foundation.

6.2.1 Shallow Foundation Model

Figure 6.9 shows the shallow foundation model employed in this large size simulation. The soil profile is still a 10 m saturated medium sand layer and the surface load 40kPa (about 2 m of an equivalent soil overburden) as described in Chapter 5 and the previous section in this chapter.

In view of symmetry, a half-mesh (5,320 elements in total) is studied as shown in Figure 6.10. The model is chosen rather large in order to minimize boundary effects. The length is 80 m and the width is 30 m (in this half-mesh configuration). Thus, the whole soil domain modeled is actually 80 m long, 60 m wide and 30 m high. The following (solid and fluid) boundary conditions were employed: (i) lateral excitation was defined along the base in the longitudinal direction (x-axis), (ii) at any depth, displacement degrees of freedom of the left and right boundaries were tied together (both horizontally and vertically using the penalty method) to reproduce a 1D shear

wave propagation mechanism effect, (iii) the soil surface was traction free, with zero prescribed pore pressure, and (iv) the base and the lateral boundaries were impervious. Similar to Chapter 5, the 7.5 m depth (NS direction) downhole acceleration record from the Wildlife site during the 1987 Superstition Hills earthquake was employed as base excitation along the x-axis (Figure 5.3).

6.2.2 Site Remediation

1) Site Remediation by Compaction and Permeability

We attempted to explore the effect of different remediation methods below the large loaded area (10 m x 10 m). Specifically, 3 simulations were performed (Table 6.3). Case **LMS** (Figure 6.10a) simulates a **M**edium **S**and site with the surface load applied. This is the case without any remediation, serving as the benchmark. Case **LDG** (Figure 6.10b) is studied to evaluate the effect of compaction (**D**ense **G**ravel) to 4 m depth throughout the foundation lateral extent. The third simulation (Case **LSC**, see Table 6.3) is discussed below.

2) Site Remediation by Stone Columns

Remediation by the stone column technique is explored herein. Considerable data (e.g., Ashford et al. 2000) has shown that stone column installation is an effective means of ground improvement for mitigating liquefaction hazards. The stone column technique can combine the beneficial effects of densification, reinforcement, and provision for increased drainage. However, there is a great need for better understanding of stone column liquefaction hazard mitigation mechanisms (Adalier and Elgamal 2002; Adalier et al. 2003).

Case LSC (Figure 6.10c) investigates the response of the same system employed in Case LMS but with the inclusion of 25, 1.2 m x 1.2 m square, stone columns at pre-determined positions (2.2 m center-to-center). This configuration provided an area replacement ratio of 30% within the zone below the foundation. Note that the area replacement ratio is defined as the area of the stone column to the tributary area per stone column (Baez and Martin 1993).

Dense Sand properties (Table 5.1) are used for the stone columns in Case LSC. **G**ravel permeability is used for the compacted area in Cases **LDG** and **LSC**. Ground water table was at the soil surface in all cases.

6.2.3 Simulated Foundation Settlement

Figure 6.11 displays the final deformed mesh for all conducted simulations. The foundation settlement time histories are shown in Figure 6.12. The final settlements are also listed in Table 6.3. In the case of LDG (Dense Gravel, 10 m wide and 4 m high), the foundation final settlement was reduced to 0.21 m (25% reduction compared to 0.28 m in Case LMS). The foundation final settlement (below the center) was further reduced to 0.04 m at the foundation center in Case LSC.

6.2.4 Response Characteristics and Discussion

1. Benchmark Simulation (Case LMS)

Figure 6.13 displays the excess pore pressure time histories for Case LMS at free field. This situation is quite similar to the usual 1D shear beam response as shown in Case MS1D (Figure 5.8 of the previous chapter). The excess pore pressure time

histories at different depths under the foundation for Case LMS are shown in Figure 6.14. Strong dilative response was observed under the foundation as indicated by a number of instantaneous sharp pore pressure drops (Figure 6.14). This pattern of response was also discussed in Section 5.6.2.

2. Compaction and Permeability Remediation (Case LDG)

The response recorded away from the foundation (free-field) in Case LDG was quite similar to that of Case LMS (not shown). Figure 6.15 shows the excess pore pressure time histories under foundation for Case LDG. Insignificant u_e was observed under the foundation up to the compacted depth.

3. Stone Column Remediation (Case LSC)

Figure 6.16 displays the lateral acceleration time histories at different depths under the foundation (center location) for Case LSC. As we can seen in Figure 6.16, the lateral accelerations along the depths are not attenuated between 15 sec – 30 sec since the remediated zone (stone column area) was not liquefied (Figure 6.17).

Figure 6.18 shows the excess pore pressure ratio distribution for Case LSC at different time frames. At all time, the remediated zone (stone column area) remained unliquefied. At 10 sec (Figure 6.18b), the top half of the untreated soil domain liquefied. All of the untreated soil domain reached liquefaction at 20 sec (Figure 6.18c). The whole untreated model remained liquefied until the end of the shaking at 100 sec (Figure 6.18e), where excess pore pressure stated to dissipate. At 160 sec (Figure 6.18h),

the excess pore pressure for the whole soil domain went back to 0.2 or less, indicating that pore pressure is almost completely dissipated.

Table 6.1: Execution time measurements of Case DG with different mesh sizes (supercomputer: Datastar).

Case		75-element mesh	500-element mesh	960-element mesh	4480-element mesh*
Total number of equations		1,620	8,679	15,868	67,716
Number of processors used		4	8	16	32
Execution time measurements (time in seconds)					
Initialization phase	FE model input	0.1	0.5	0.9	24.1
	Formation of adjacency structure	0.3	2.1	4.1	17.4
	Multilevel nested dissection ordering (using METIS)	0.01	0.1	0.3	1.6
	Elimination tree setup and postordering	0.01	0.01	0.03	0.2
	Symbolic factorization	0.02	0.1	0.3	1.2
	Solver inter-processor communication setup	0.02	0.2	0.6	3.7
	Matrix storage and solver indexing setup	0.1	0.4	0.4	1.6
	Total for initialization phase	0.7	3.6	6.7	50.8
Nonlinear solution phase	LHS formation	297.5	1432.6	2072.6	148.4
	RHS formation	2001.6	7154.6	5886.7	584.3
	Stress update	320.3	1217	987.7	91.4
	Numerical Factorization	165.2	1912.3	2675.8	589.5
	Forward and backward solves	167	951.9	2030.9	330.2
	Total on solution phase	3240.2	13008	14538	1911.8
Total execution time		3241.3	13012	14546	1962.8

* Only the first 10 seconds of excitation are included in the case of the 4480-element mesh. All other cases include 250 seconds of excitation.

Table 6.2: Timing details of the nonlinear solution phase for Case DG with different mesh sizes (time in seconds; supercomputer: Datastar).

Case	Number of processors		LHS formation	RHS formation	Stress update	Numerical factorization	Forward and backward solves
75-element mesh	4	Time	297.5	2001.6	320.3	165.2	167.0
		Number of times performed	2228	79488	26126	2228	52245
		Time per step	**0.13**	**0.03**	**0.01**	**0.07**	**0.00**
500-element mesh	8	Time	1432.6	7154.6	1217.0	1912.3	951.9
		Number of times performed	2527	82274	26316	2527	54676
		Time per step	**0.57**	**0.09**	**0.05**	**0.76**	**0.02**
900-element mesh	16	Time	2072.6	5886.7	987.7	2675.8	2030.9
		Number of times performed	2682	83801	26414	2682	56011
		Time per step	**0.77**	**0.07**	**0.04**	**1.00**	**0.04**
4480-element mesh*	32	Time	148.4	584.3	91.4	589.5	330.2
		Number of times performed	57	3201	1028	57	2145
		Time per step	**2.60**	**0.18**	**0.09**	**10.34**	**0.15**

* Only the first 10 seconds of excitation are included in the case of the 4480-element mesh. All other cases include 250 seconds of excitation.

Table 6.3: Simulations of the 10 m x 10 m foundation model.

Simulation	Compacted area (m x m x m)	Compacted area permeability k (m/s)	Foundation settlement (m)
LMS (Large foundation, Medium Sand)	Benchmark, no compaction	6.6×10^{-5}	0.28
LDG (Large foundation, Dense Gravel)	10 x 10 x 4	1.0×10^{-2}	0.21
LSC (Large foundation, Stone Columns)	25 1.2 m x 1.2 m stone columns	1.0×10^{-2}	0.04

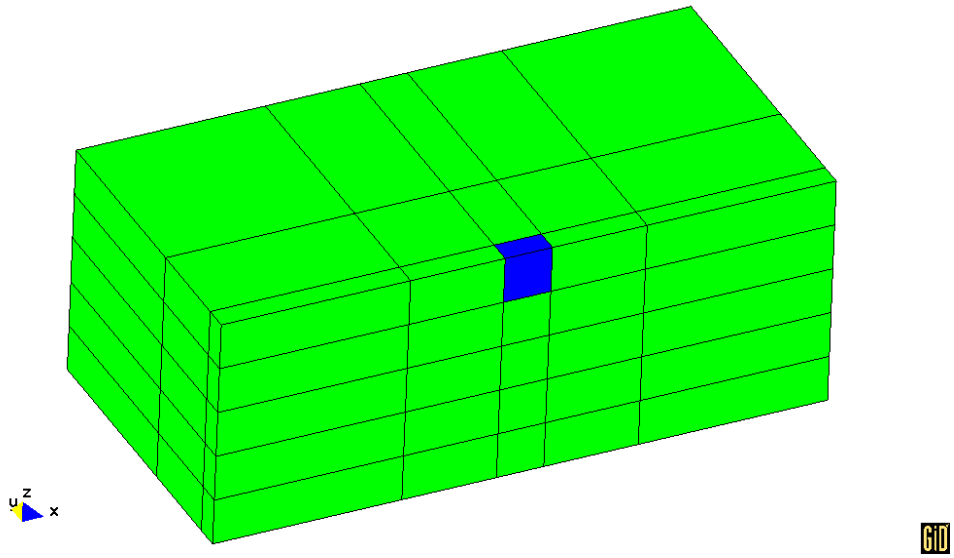

(a) 75-element mesh.

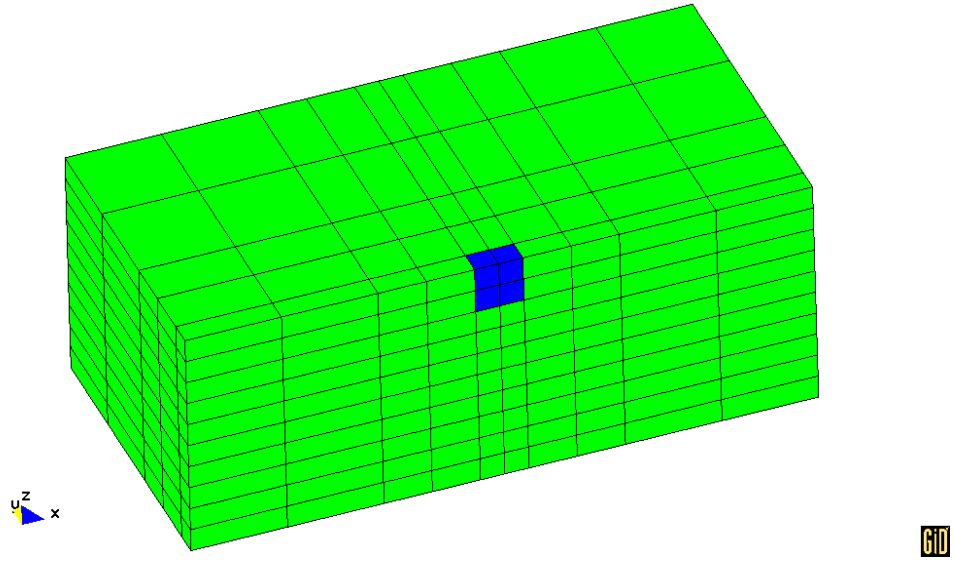

(b) 500-element mesh.

Figure 6.1: FE meshes for Case DG (dark zone represents remediated domain).

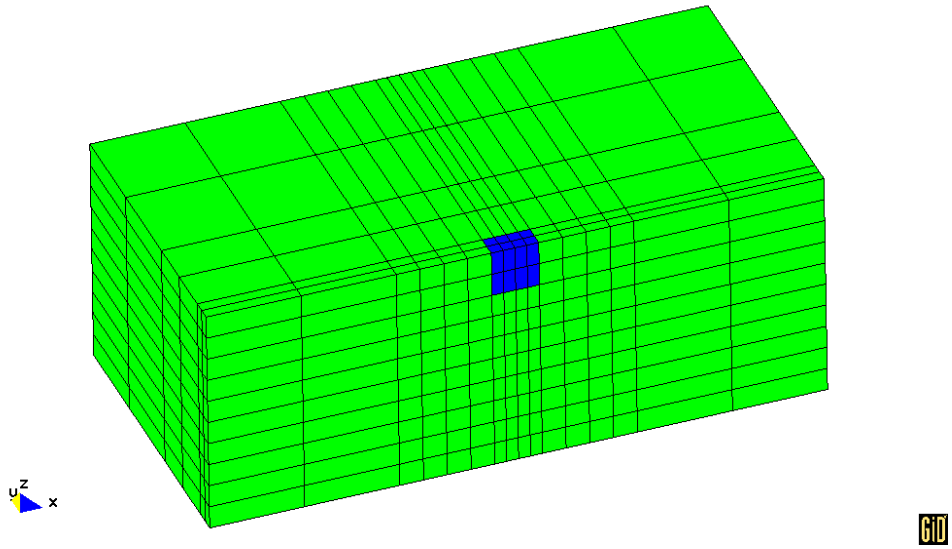

(c) 960-element mesh.

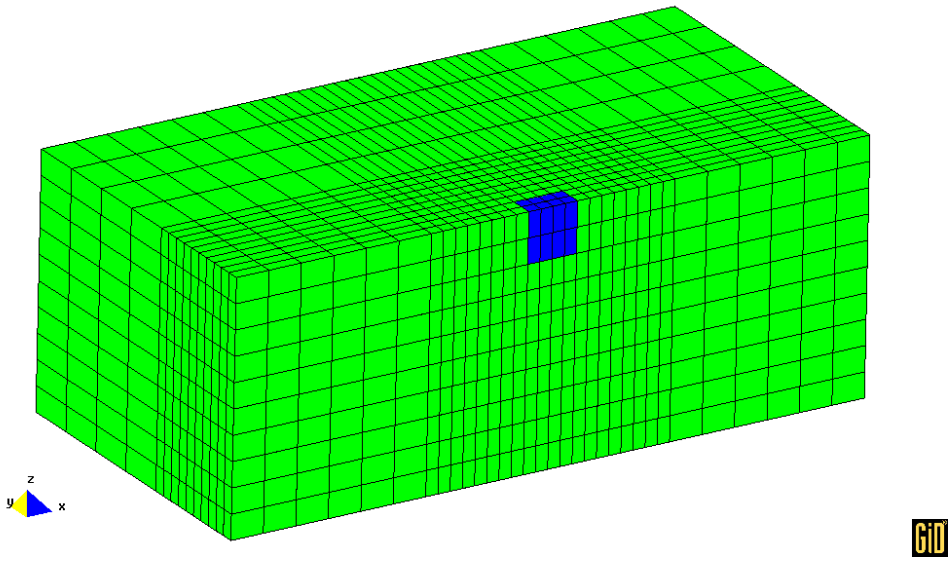

(d) 4480-element mesh.

Figure 6.1 (continued).

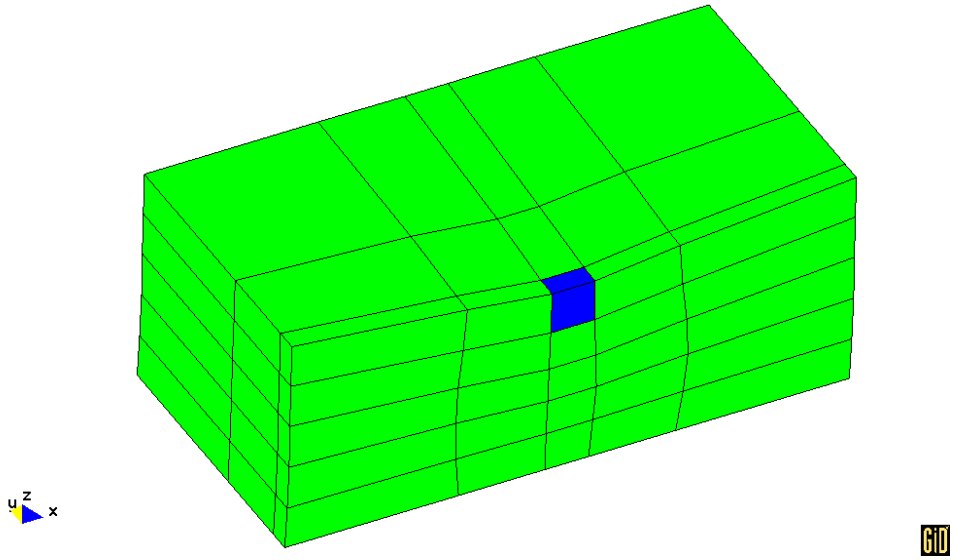

(a) 75-element mesh.

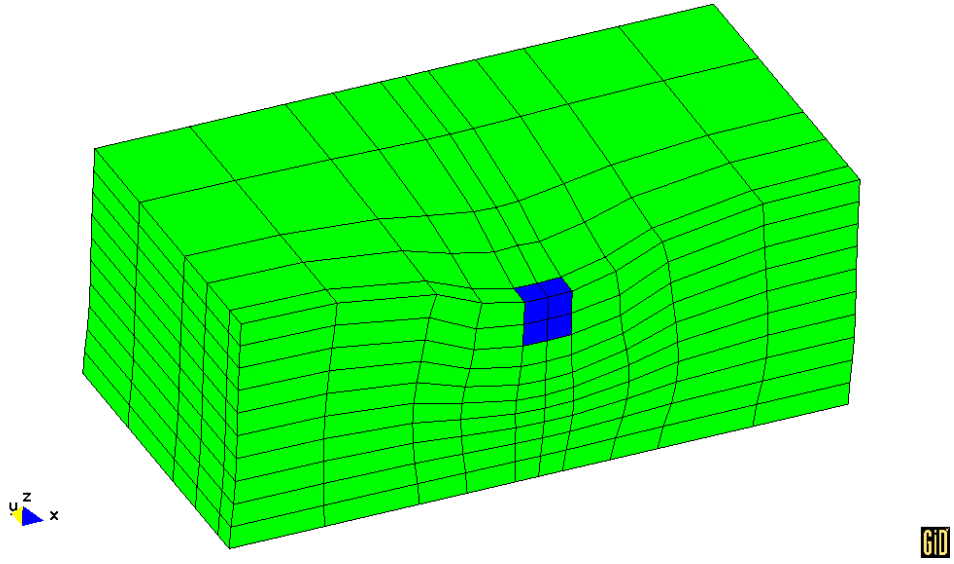

(b) 500-element mesh.

Figure 6.2: Final deformed mesh (factor of 10) for Case DG (dark zone represents remediated domain).

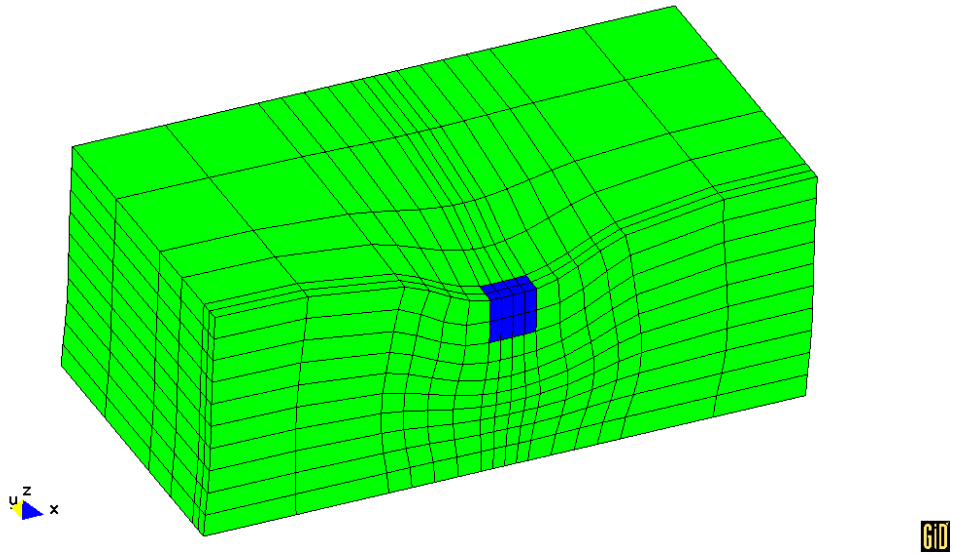

(c) 960-element mesh.

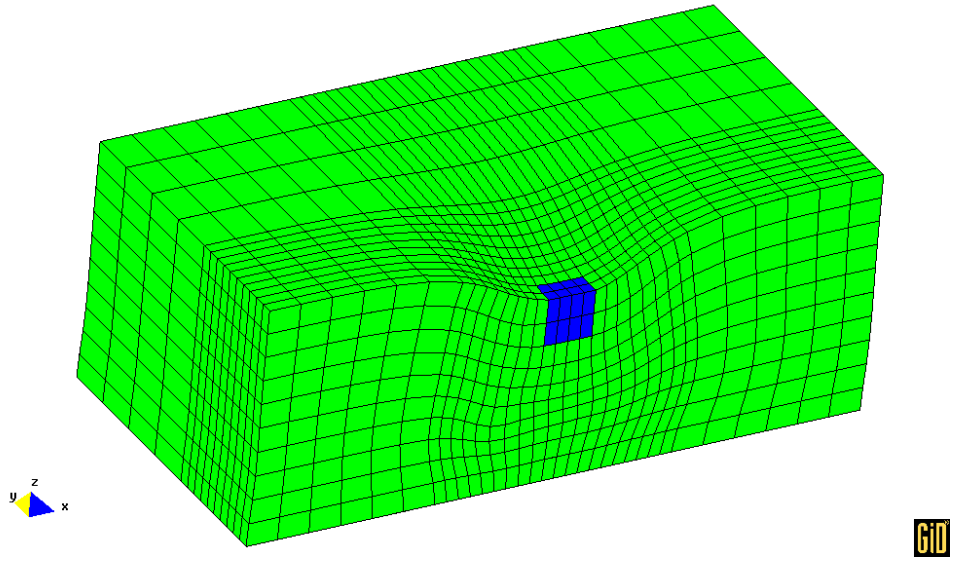

(d) 4480-element mesh.

Figure 6.2 (continued).

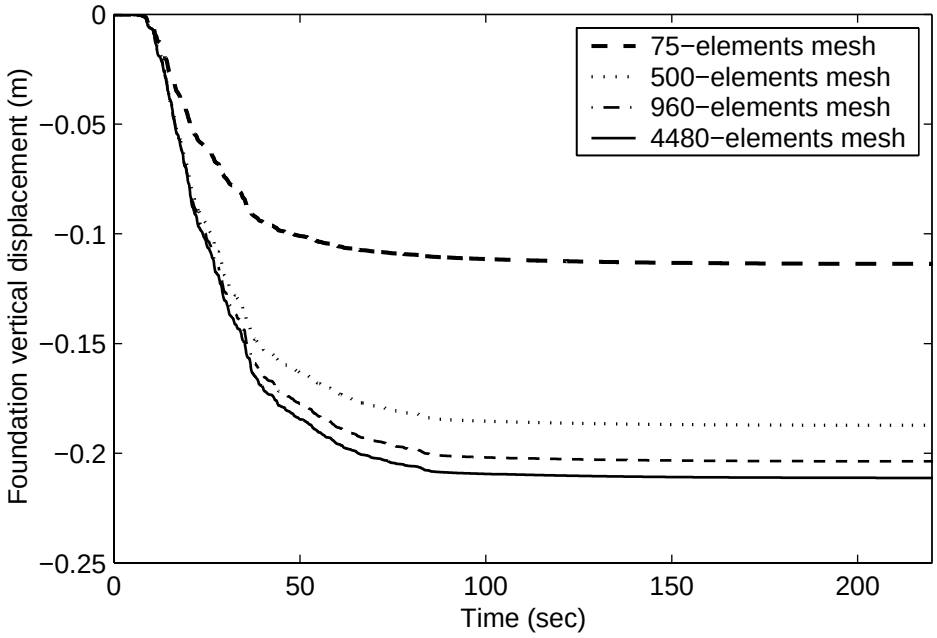

Figure 6.3: Vertical displacement time histories of the foundation for Case DG.

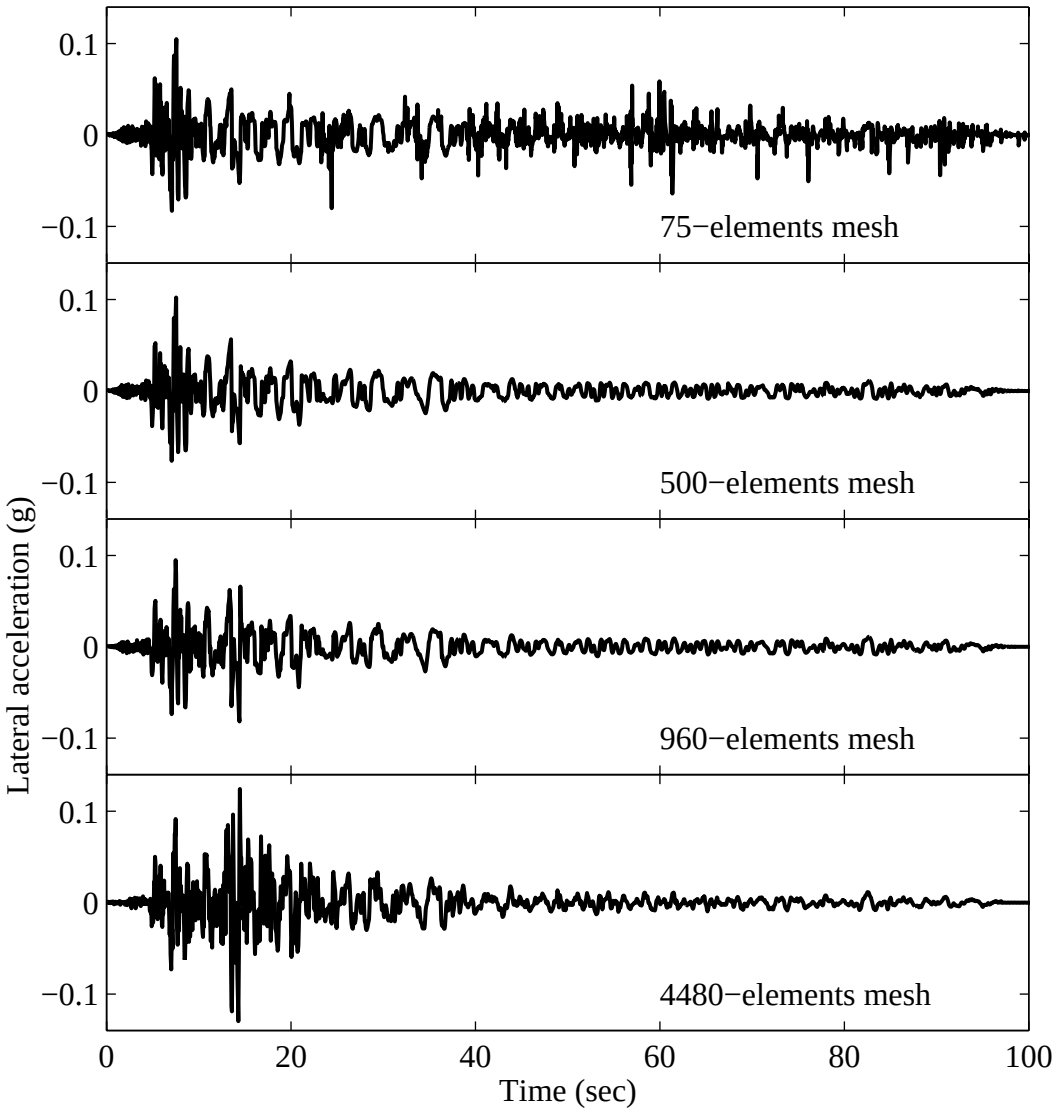

Figure 6.4: Foundation lateral acceleration time histories for Case DG with 4 different mesh sizes.

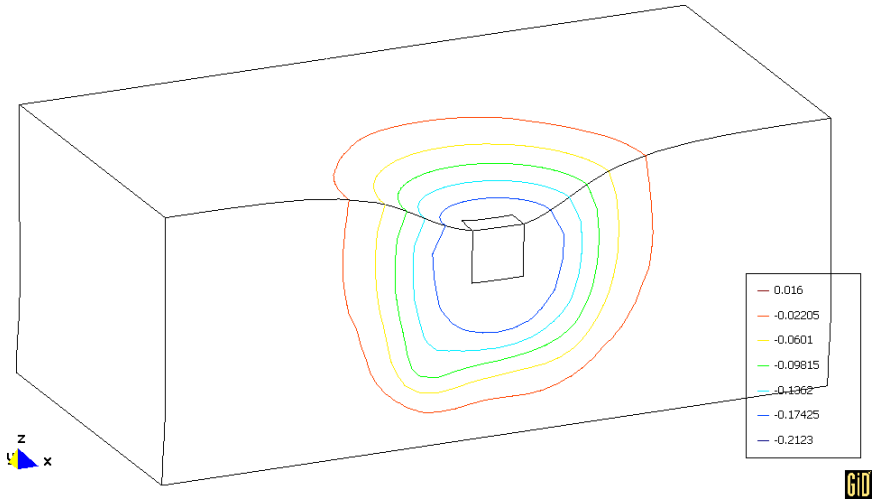

(a) 3D view.

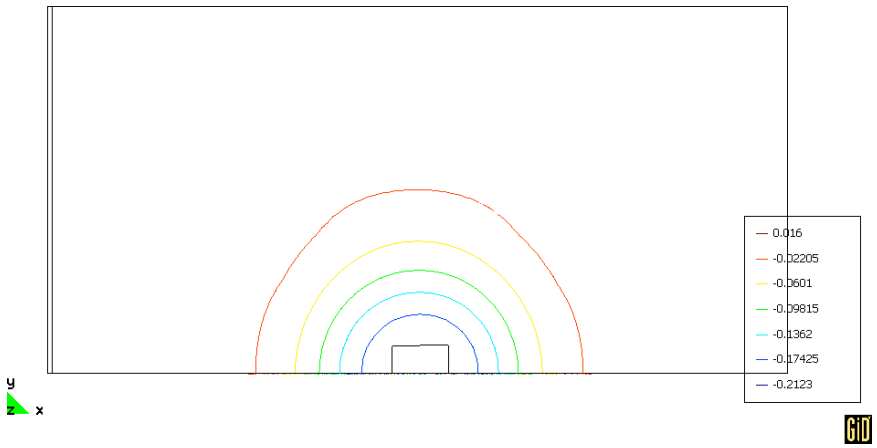

(b) Plan view.

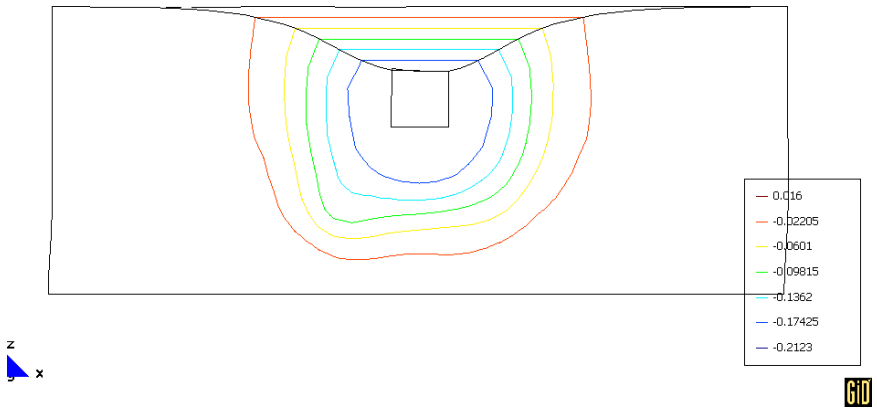

(c) Side view.

Figure 6.5: Contour lines of vertical displacement (unit: m, deformed mesh display: factor of 10) of Case DG for the 4480-element mesh.

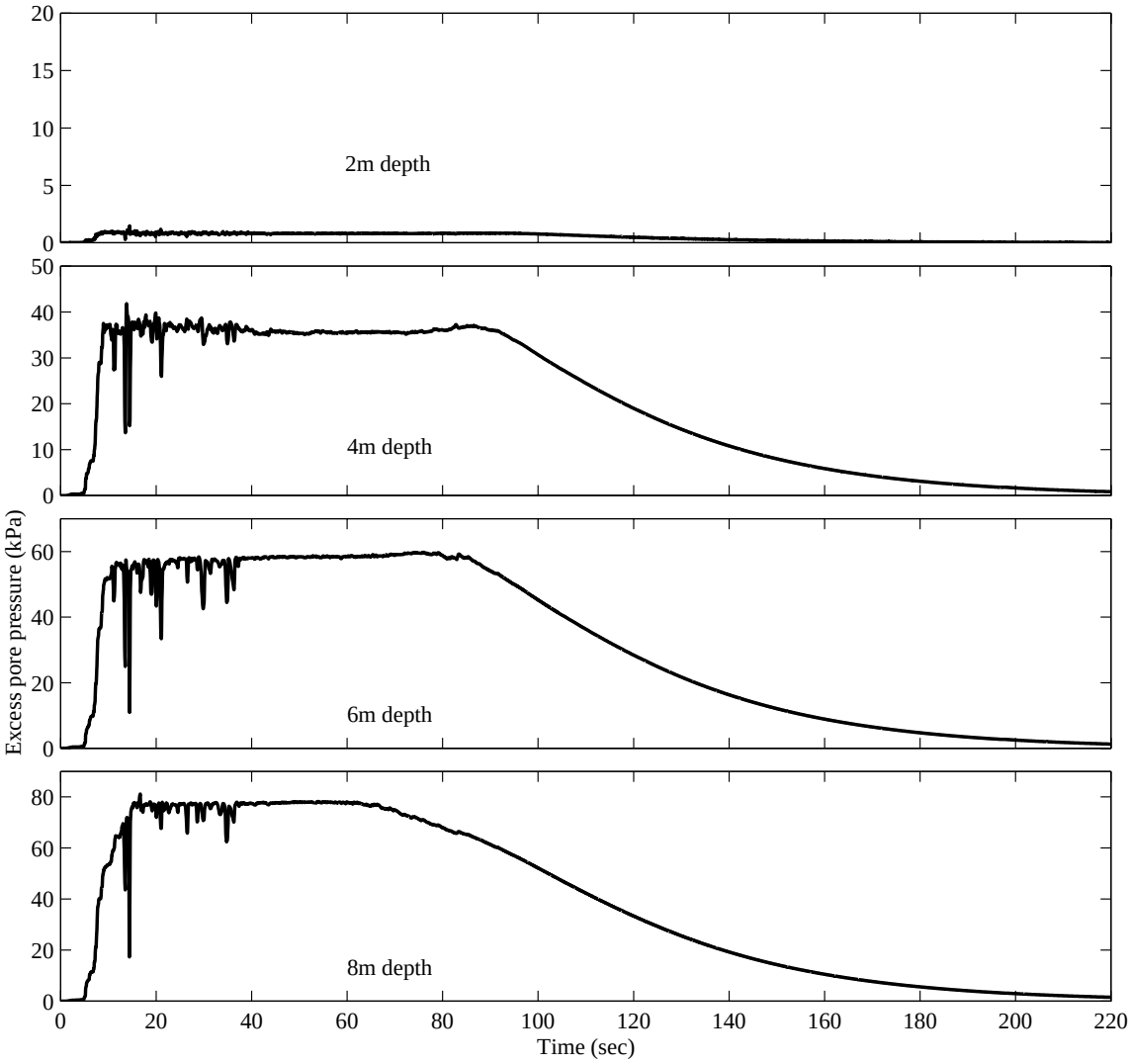

Figure 6.6: Excess pore pressure time histories at different depths (under foundation) of Case DG for the 4480-element mesh.

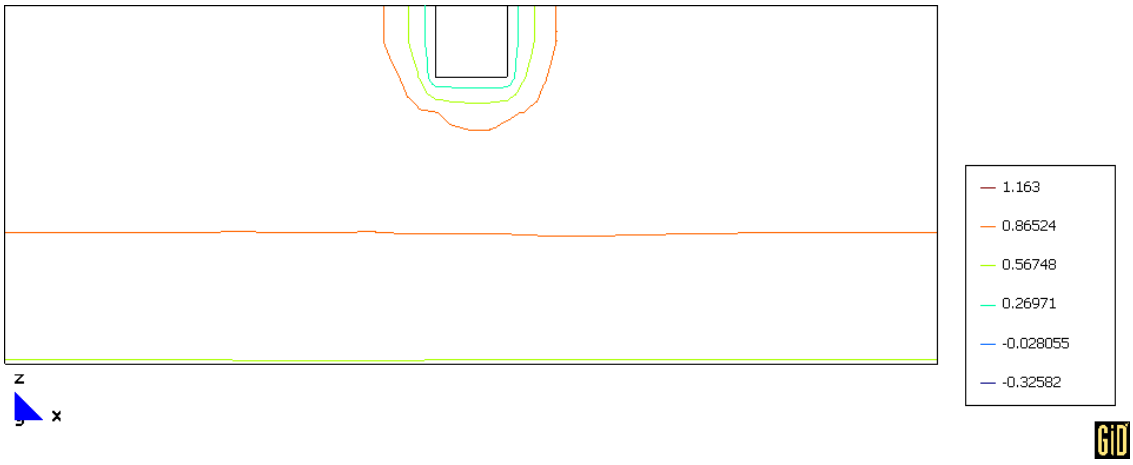

(a) At 10 sec.

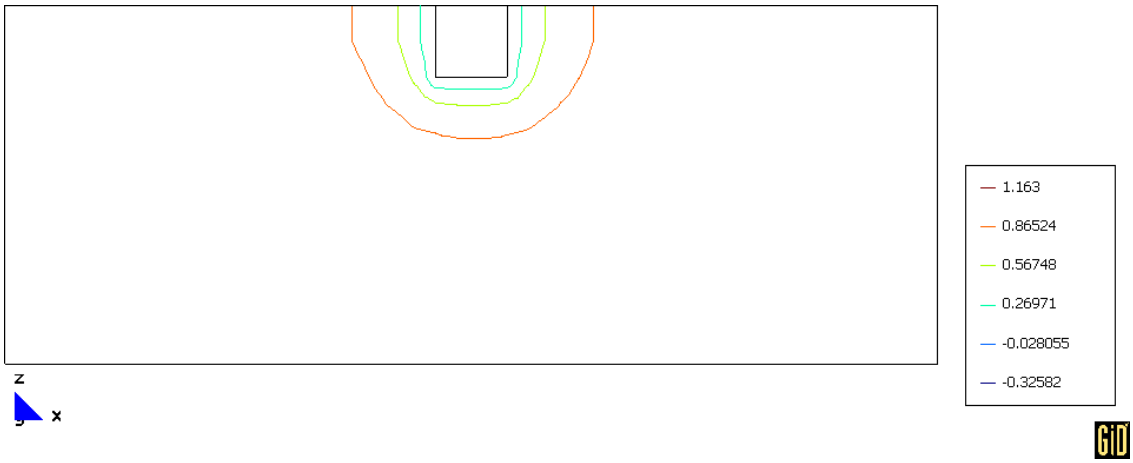

(b) At 20 sec.

Figure 6.7: Contour lines of excess pore pressure ratio at different time frames of Case DG for the 4480-element mesh (side view; small square box shows remediated area).

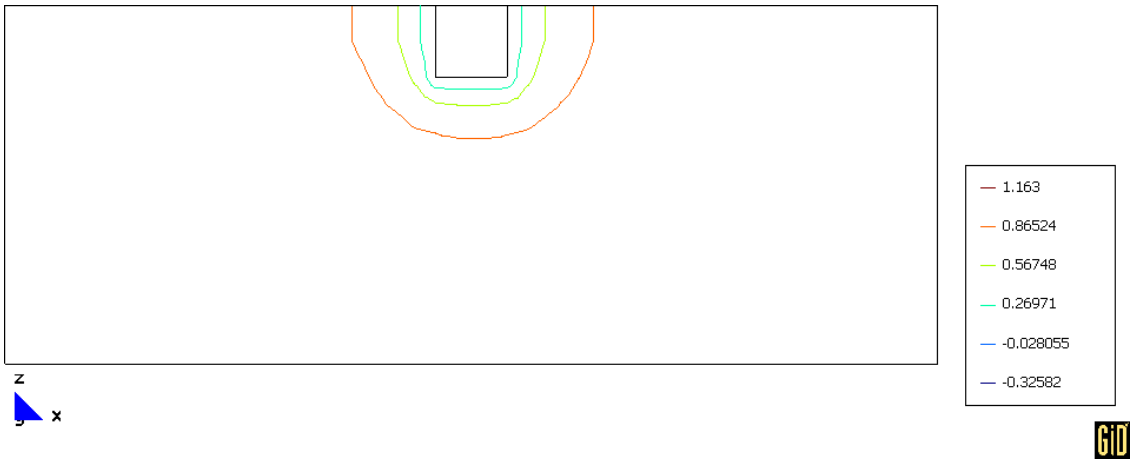

(c) At 60 sec.

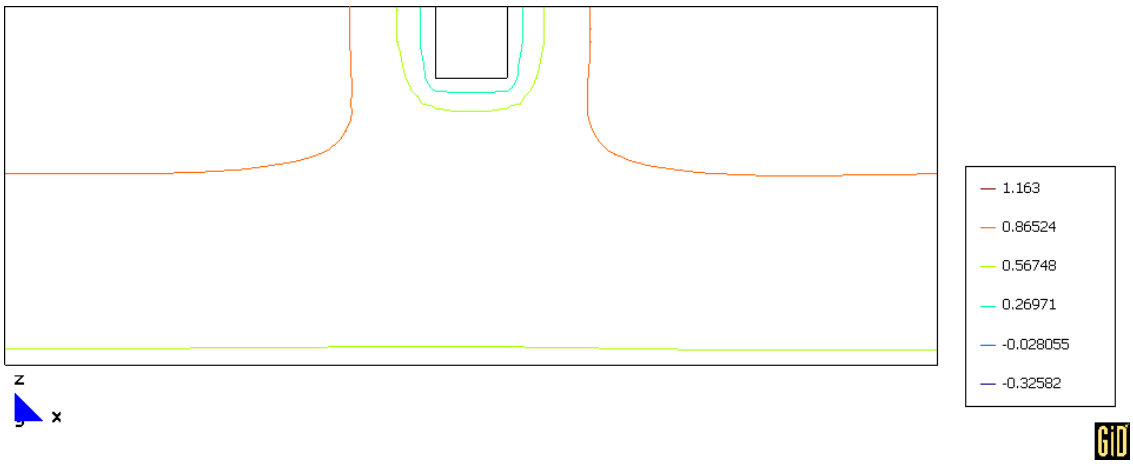

(d) At 100 sec.

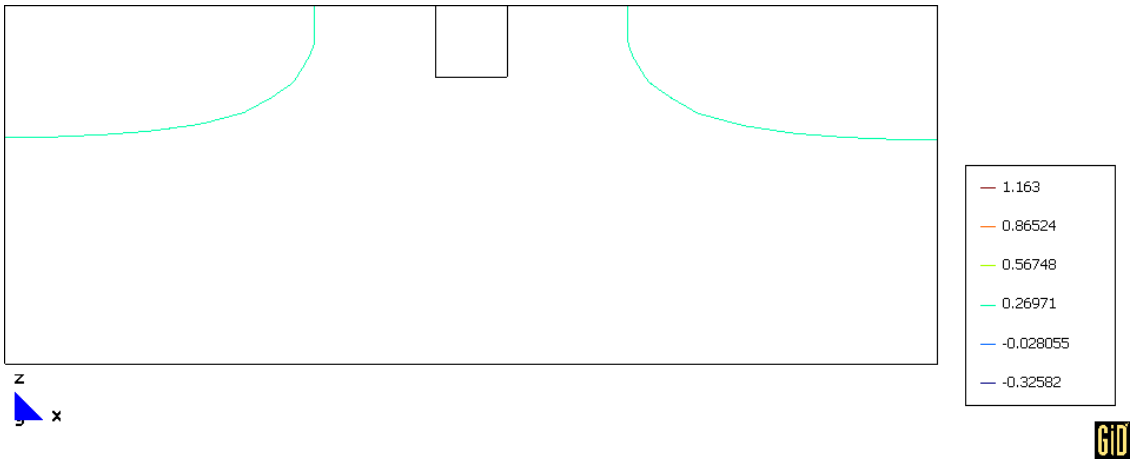

(e) At 150 sec.

Figure 6.7 (continued).

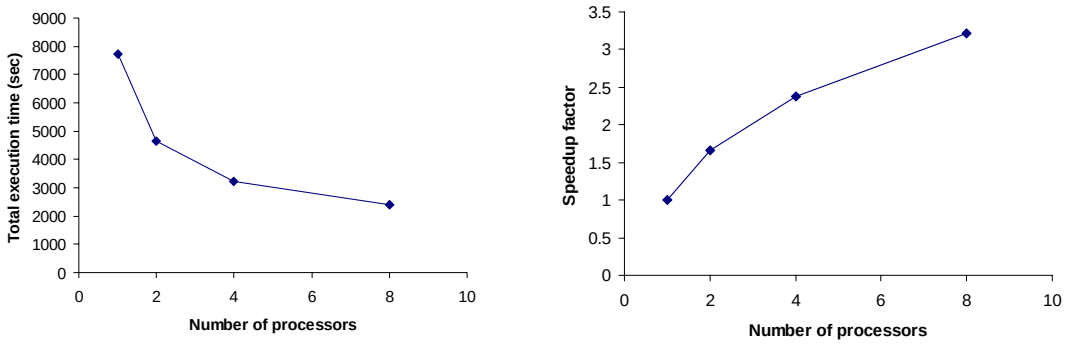

(a) 75-element mesh

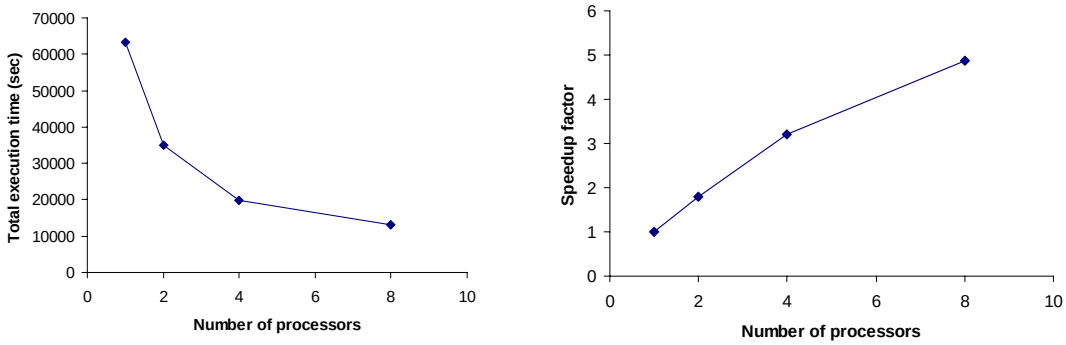

(b) 500-element mesh

Figure 6.8: Total execution time and parallel speedup for Case DG with different mesh sizes (supercomputer: Datastar).

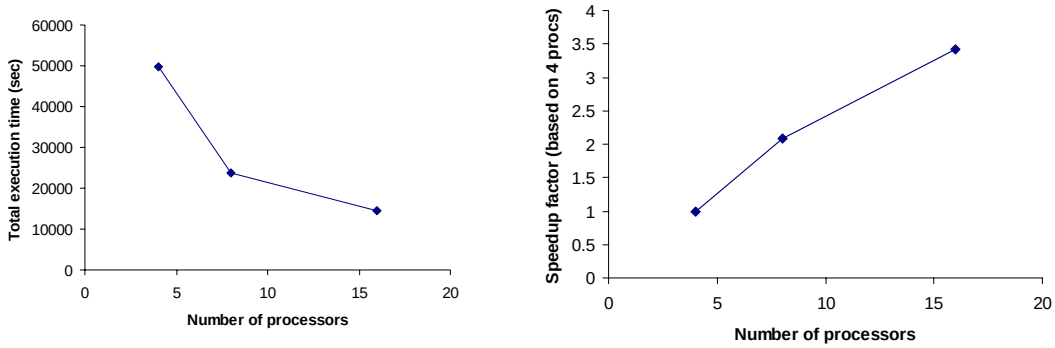

(c) 960-element mesh

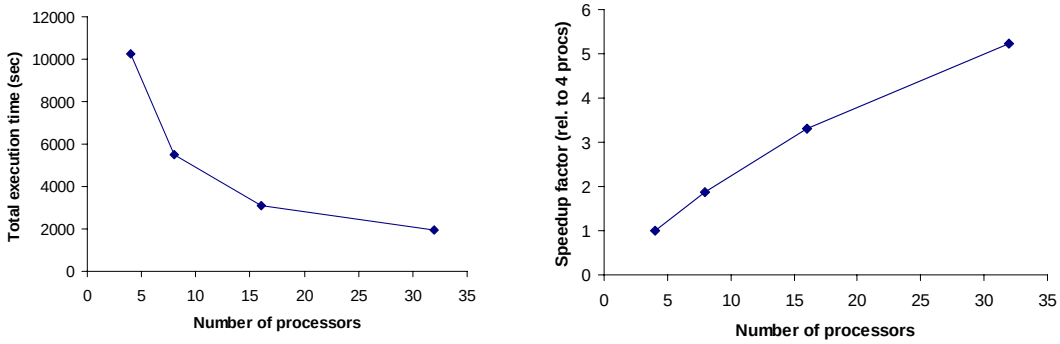

(d) 4480-element mesh (based on the first 10 seconds of excitation)

Figure 6.8: (continued).

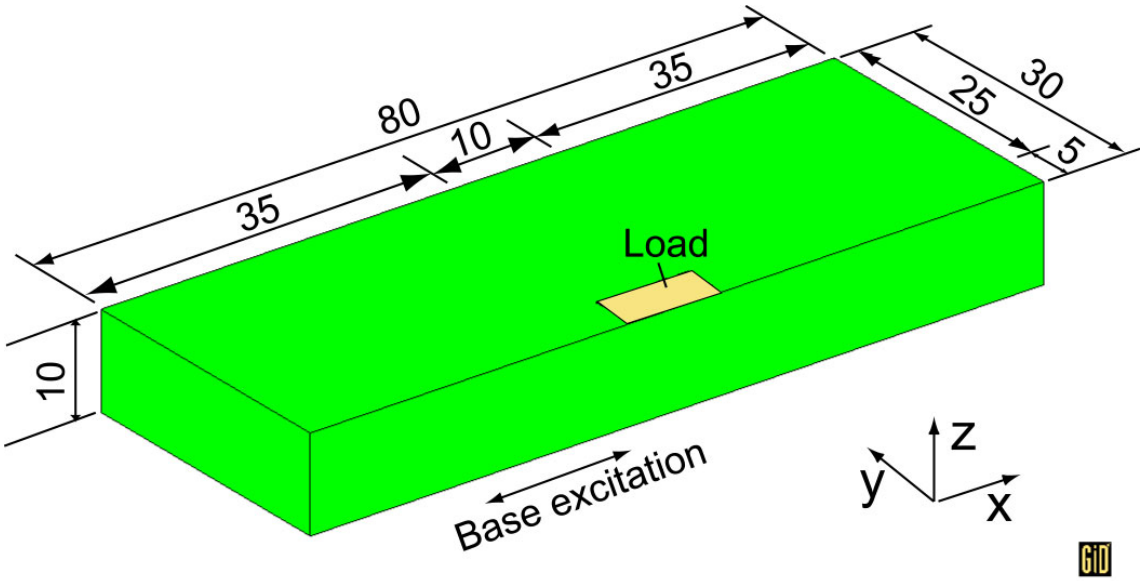

Figure 6.9: Model of a 10m x 10m shallow foundation.

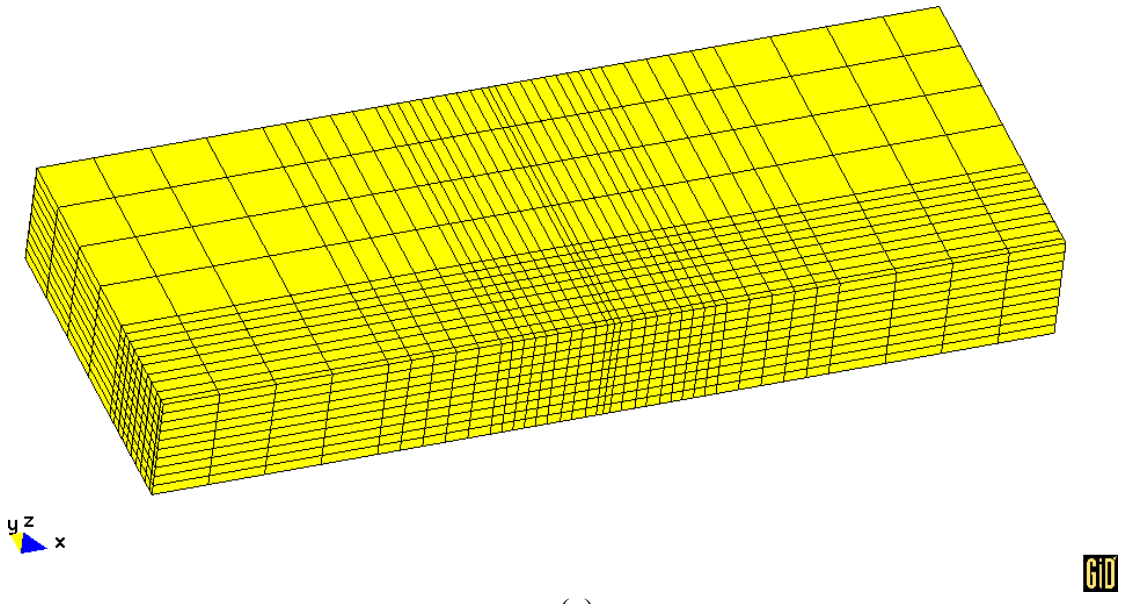

(a)

Figure 6.10: FE meshes (# of elements = 5,320) of the 10m x 10m shallow foundation model, a) Case LMS; b) Case LDG; c) Case LSC.

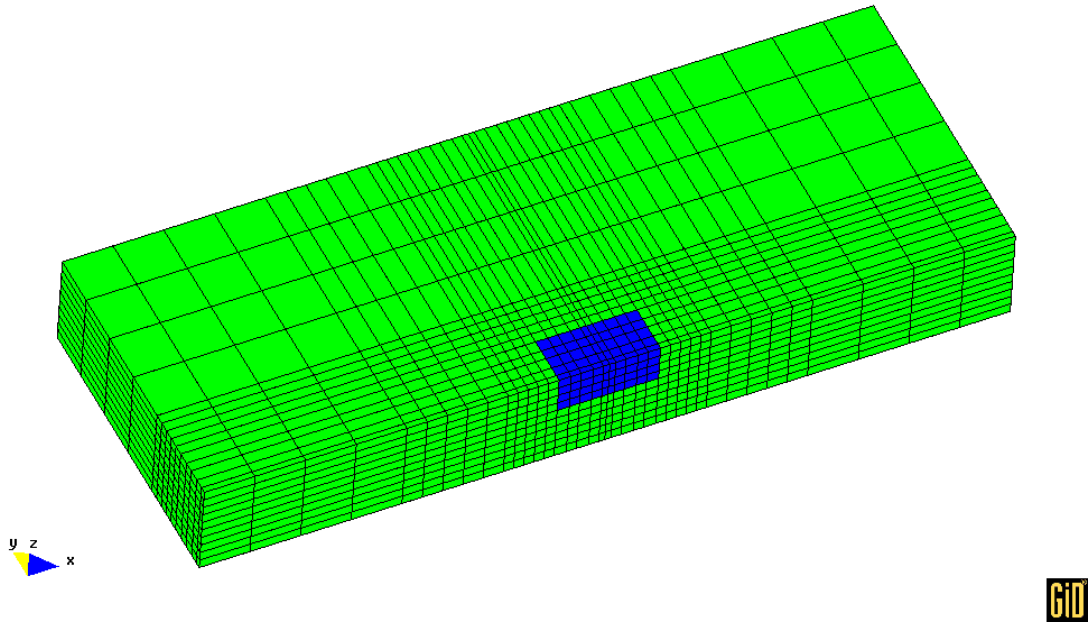

(b)

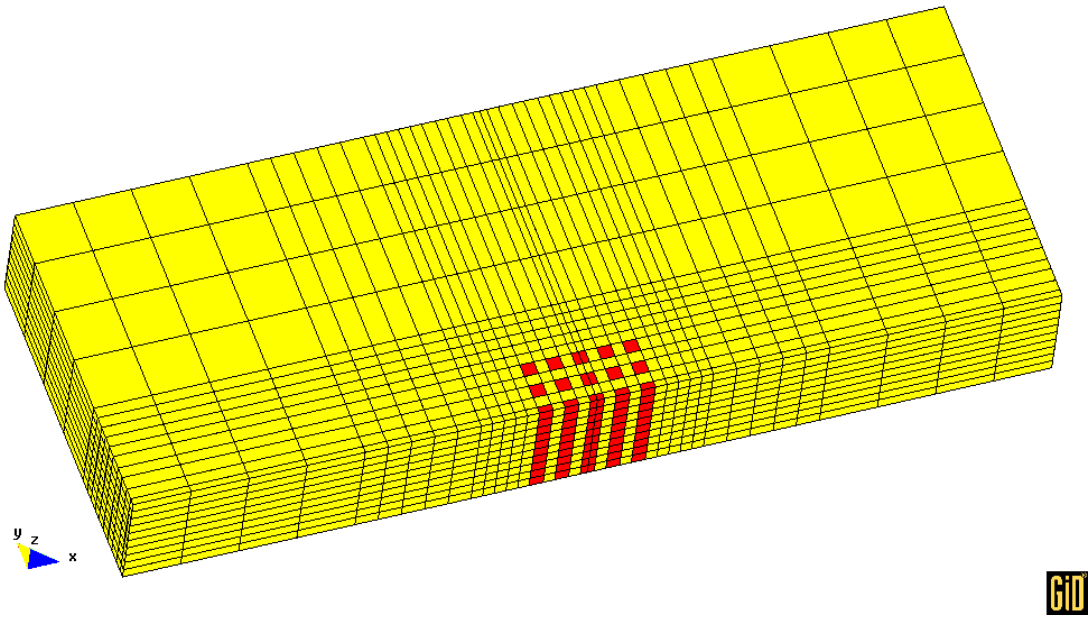

(c)

Figure 6.10: (continued).

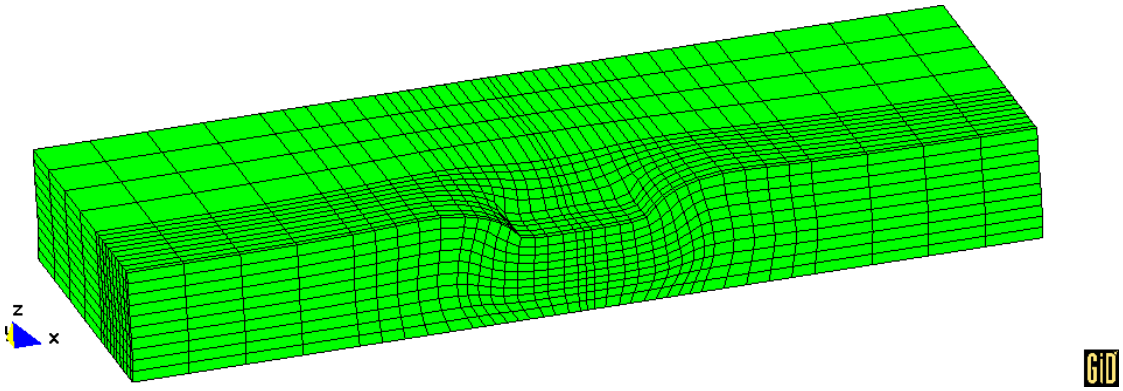

(a)

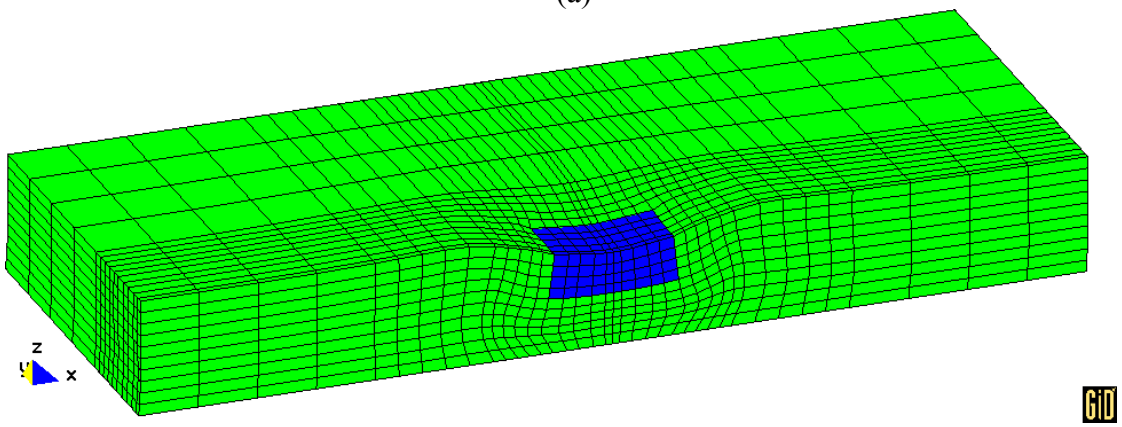

(b)

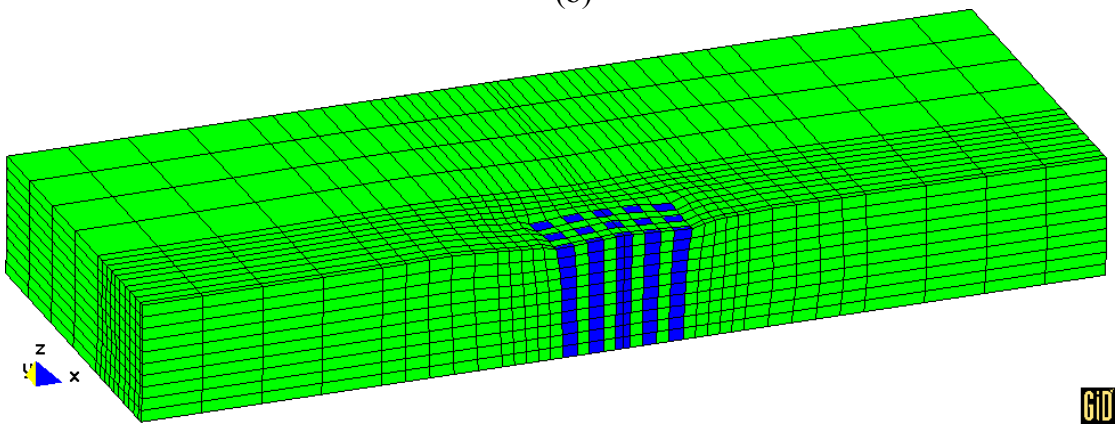

(c)

Figure 6.11: Final deformed mesh (factor of 10) of the 10m x 10m shallow foundation model (dark zone represents remediated domain), a) Case LMS; b) Case LDG; c) Case LSC.

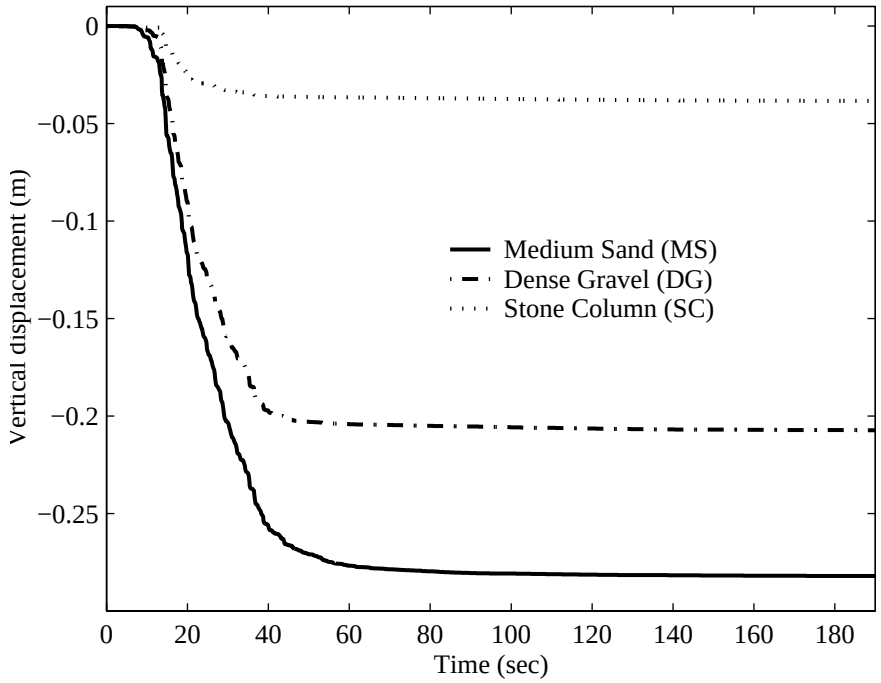

Figure 6.12: Foundation vertical displacement time histories below the center of the 10m x 10m shallow foundation model.

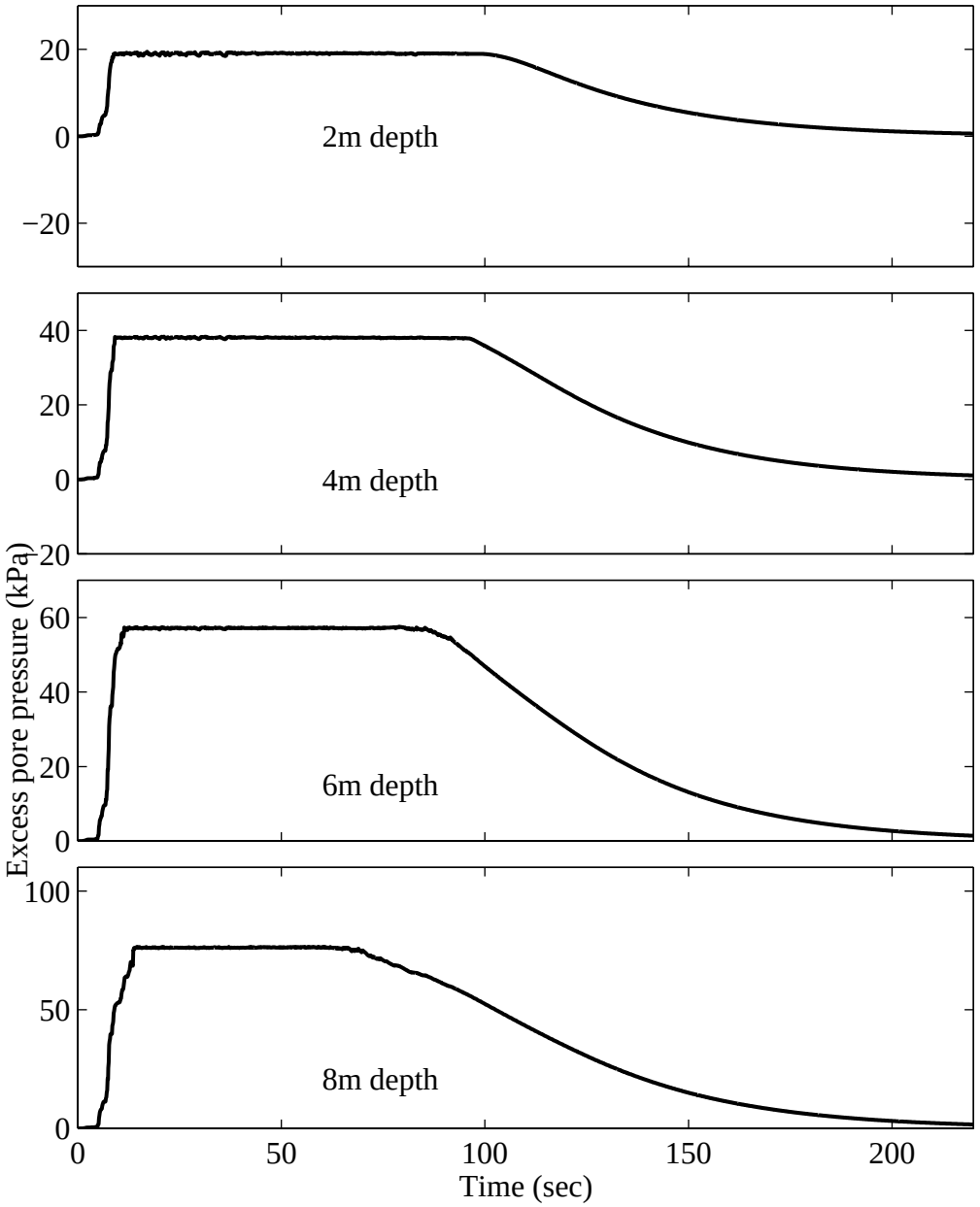

Figure 6.13: Excess pore pressure time histories for Case LMS in the free field.

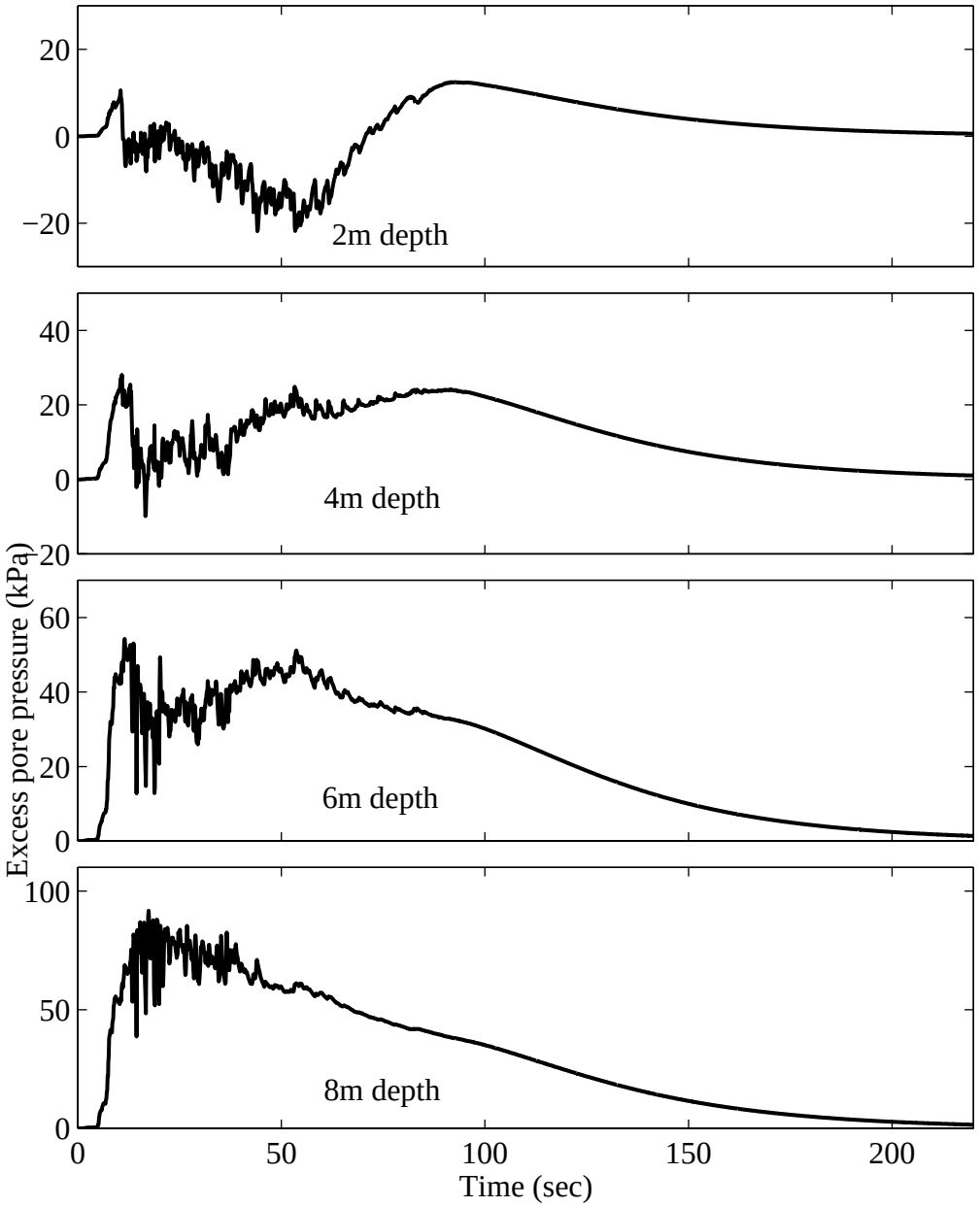

Figure 6.14: Excess pore pressure time histories for Case LMS under foundation.

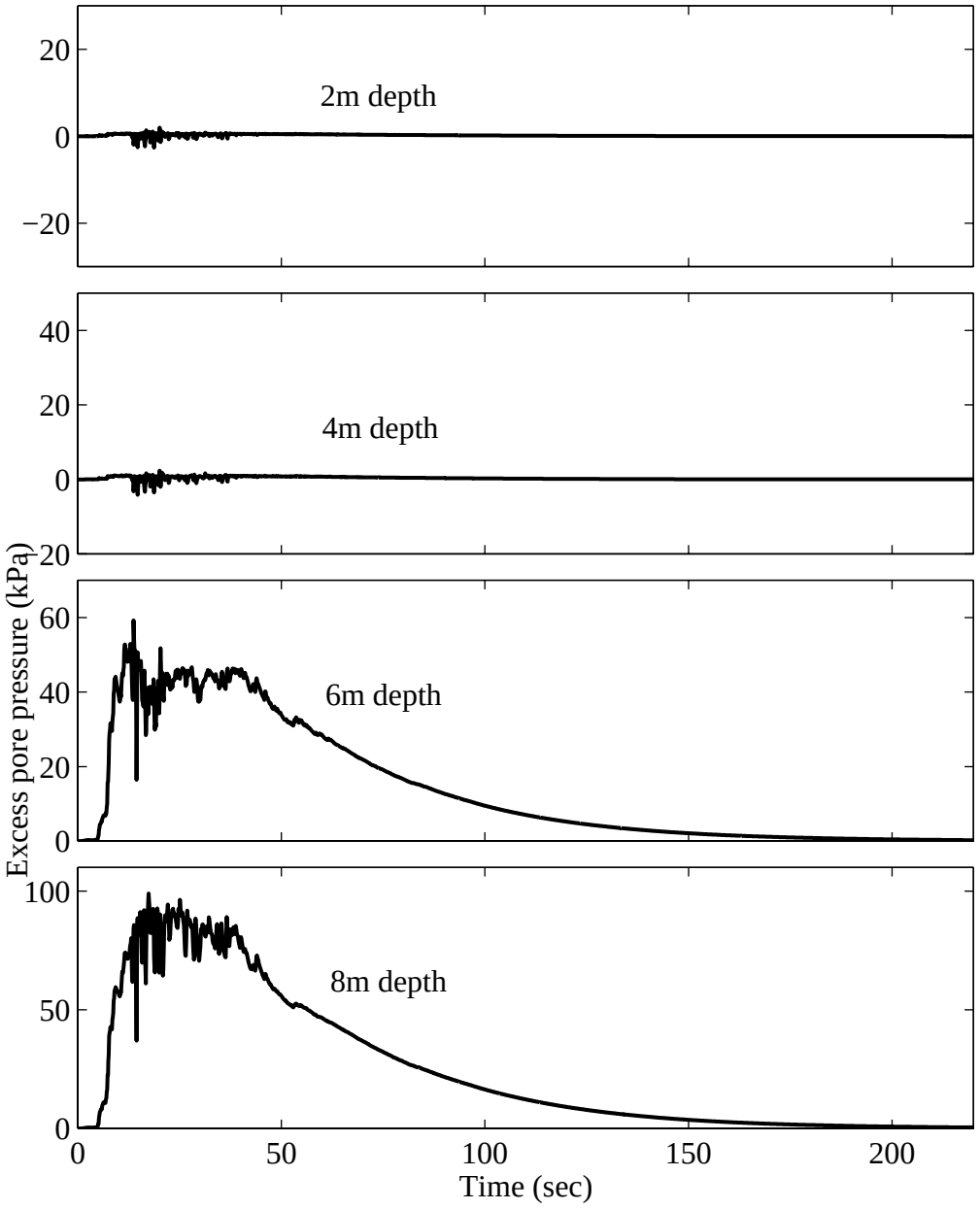

Figure 6.15: Excess pore pressure time histories for Case LDG under foundation.

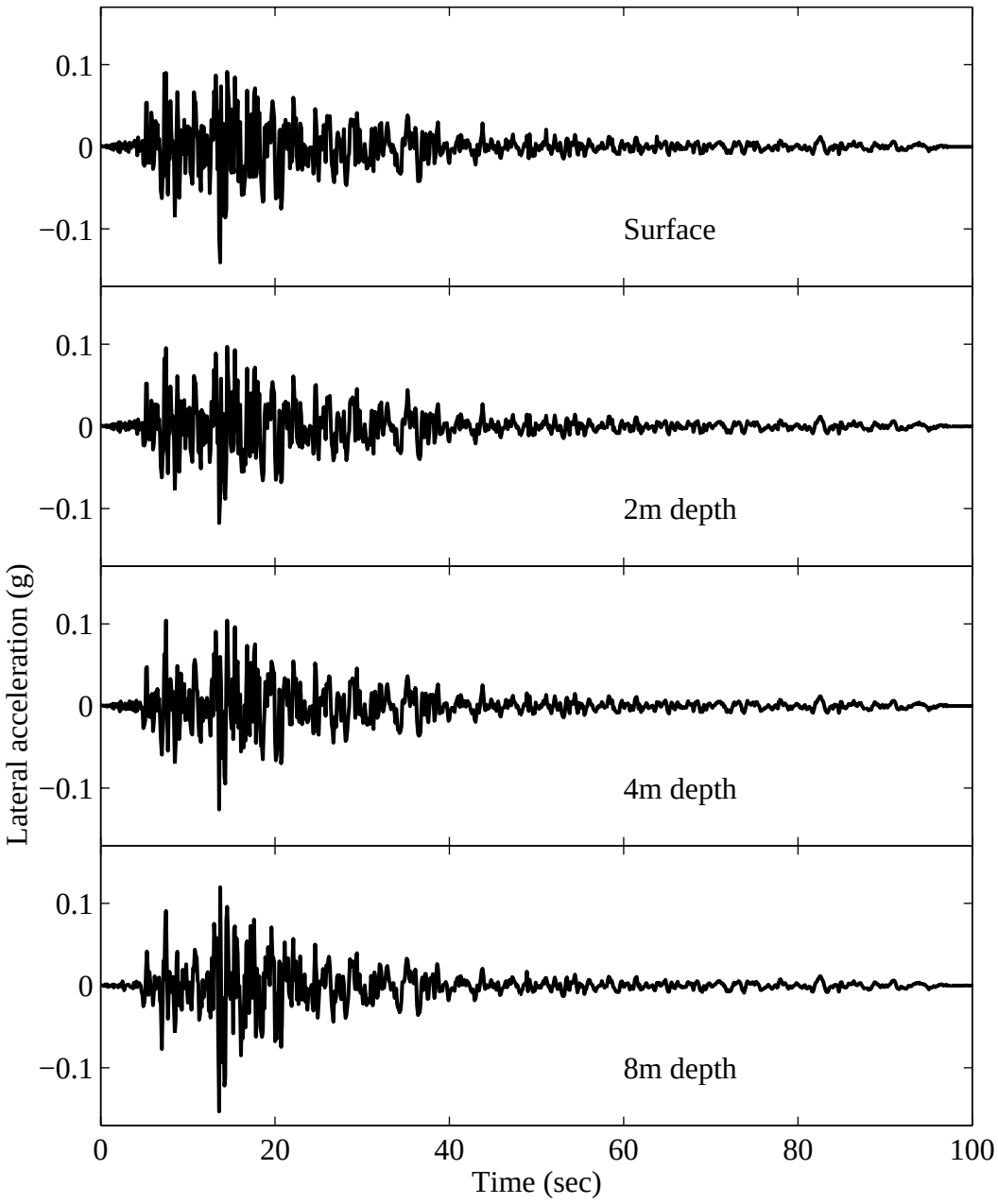

Figure 6.16: Lateral acceleration time histories for Case LSC under foundation.

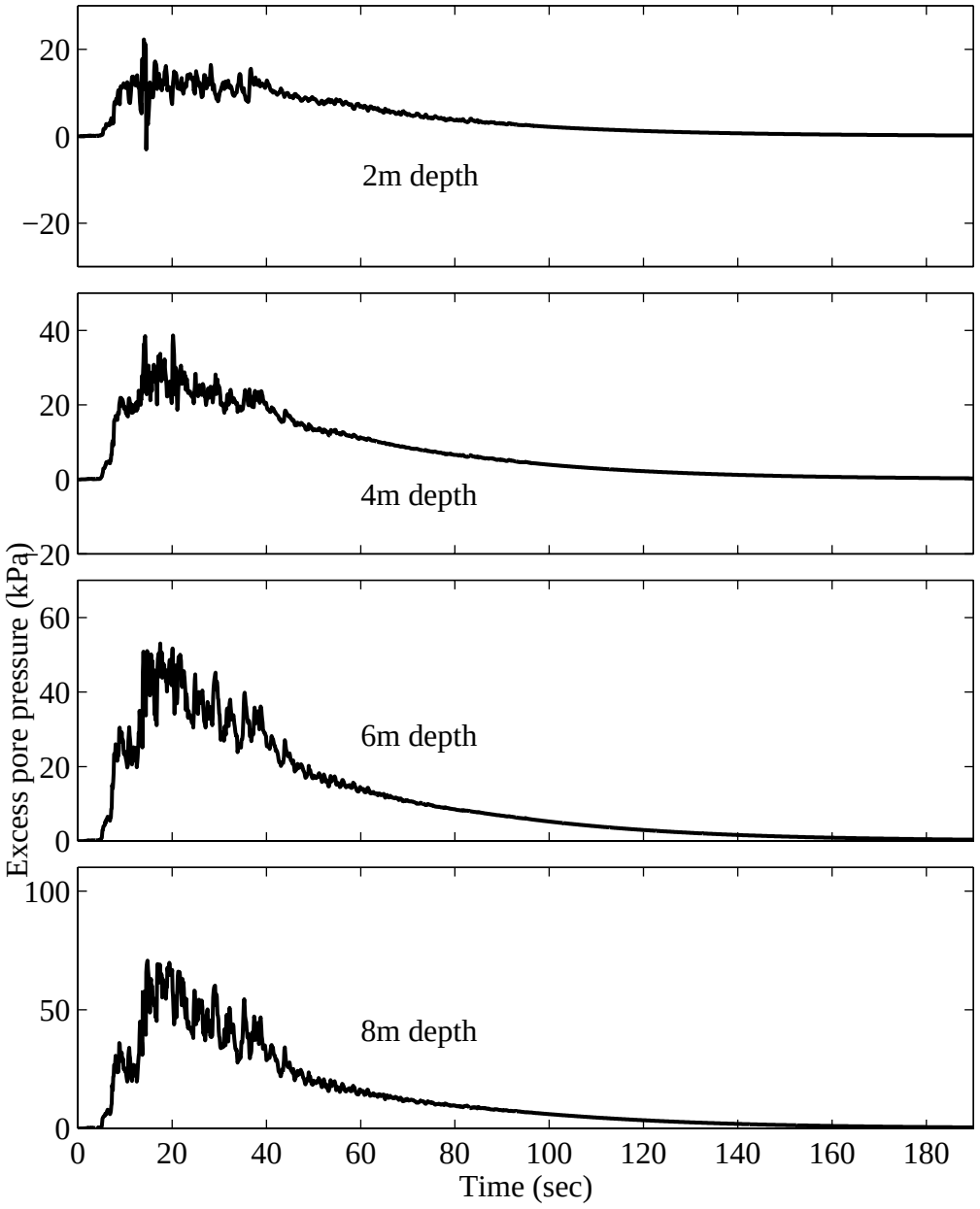

Figure 6.17: Excess pore pressure time histories for Case LSC under the foundation left edge.

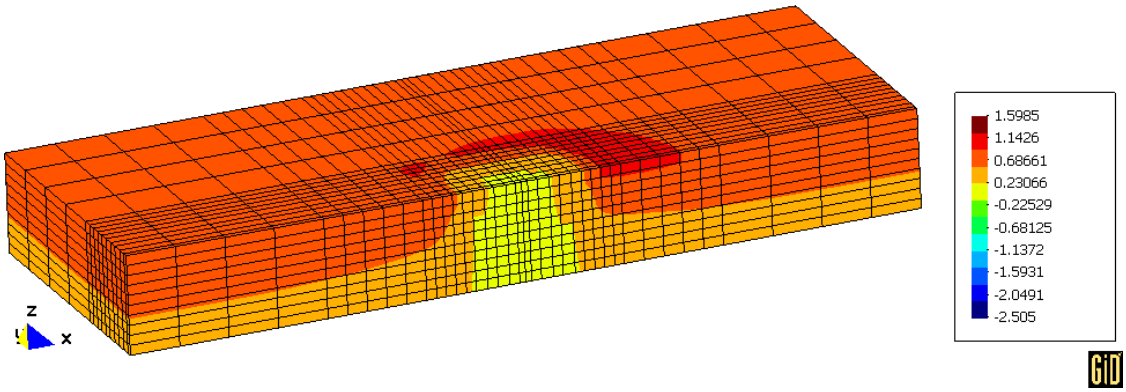

a) At 8 sec.

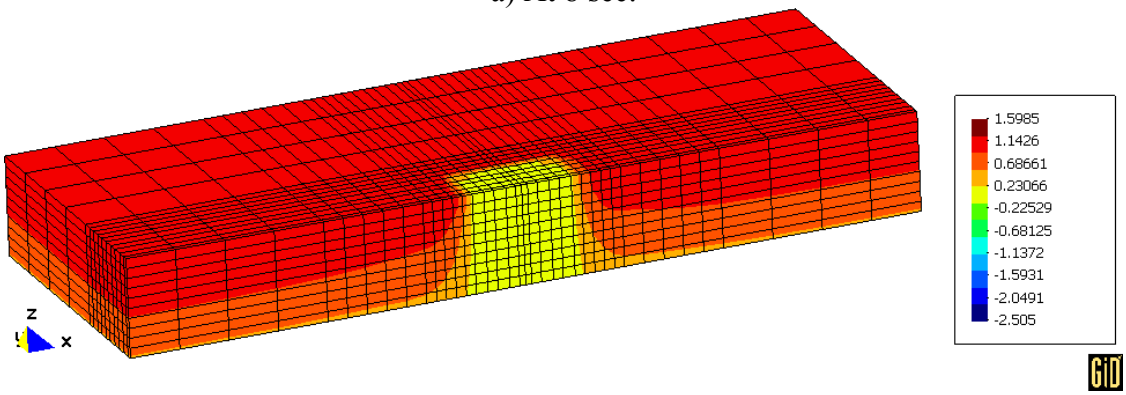

b) At 10 sec.

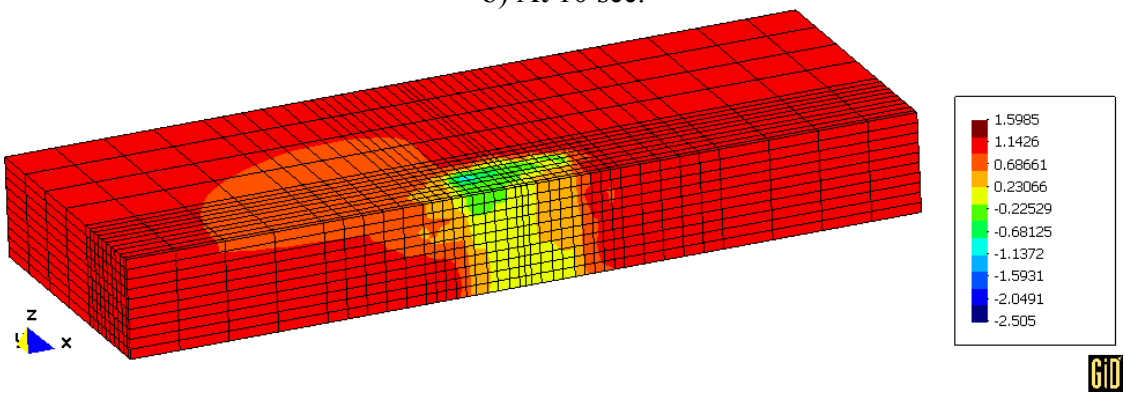

c) At 20 sec.

Figure 6.18: Excess pore pressure ratio color map for Case LSC at different time frames.

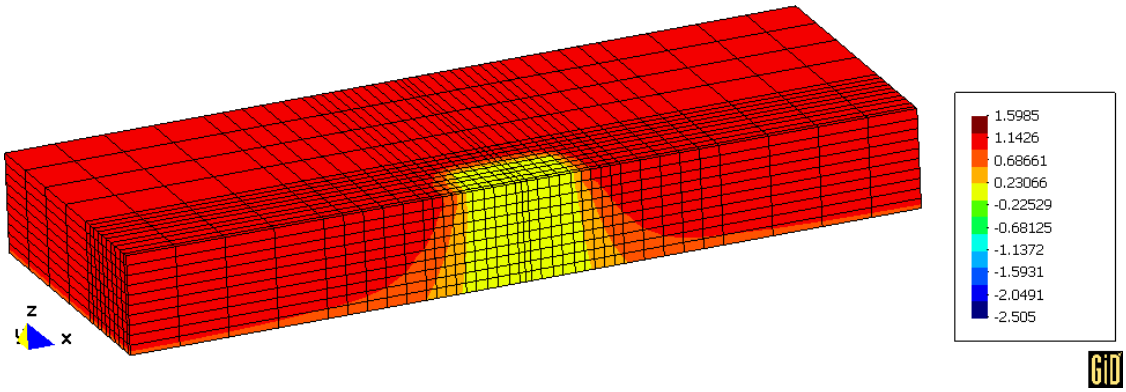

d) At 60 sec.

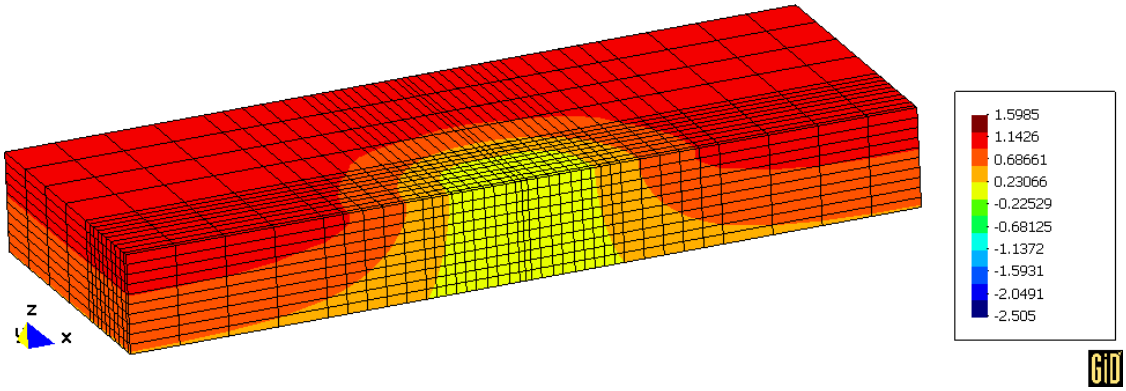

e) At 100 sec.

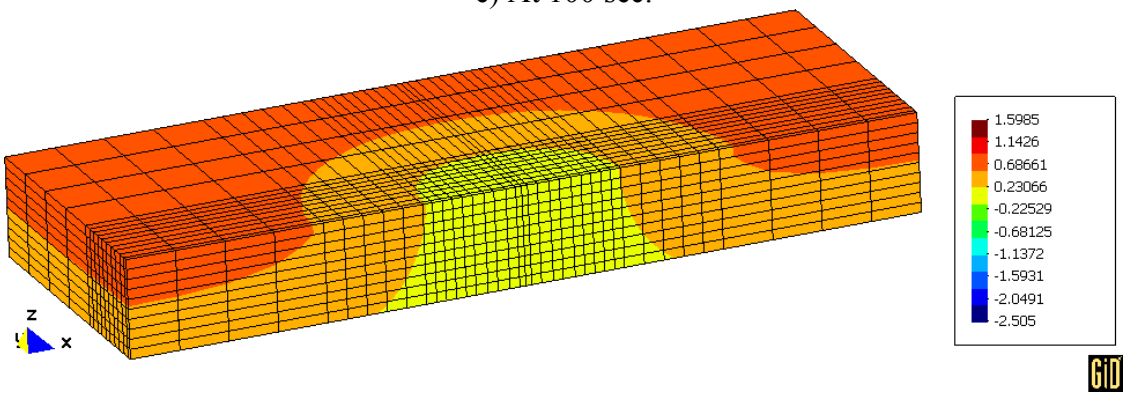

f) At 120 sec.

Figure 6.18: (continued).

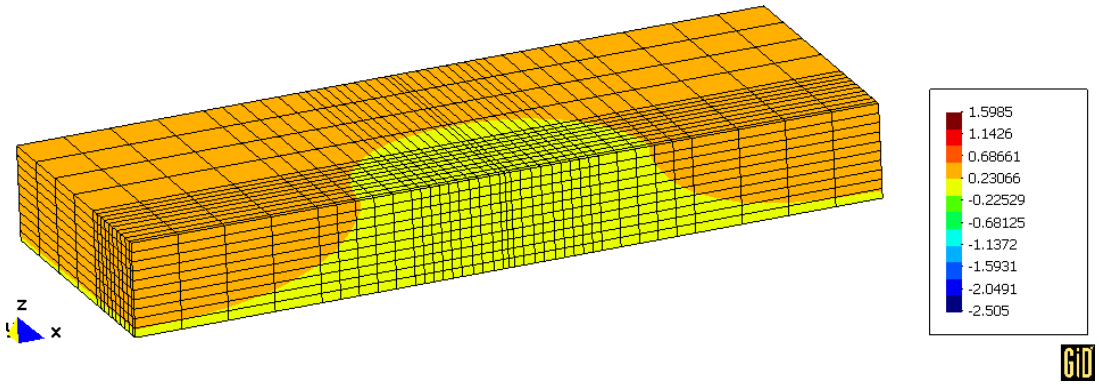

g) At 140 sec.

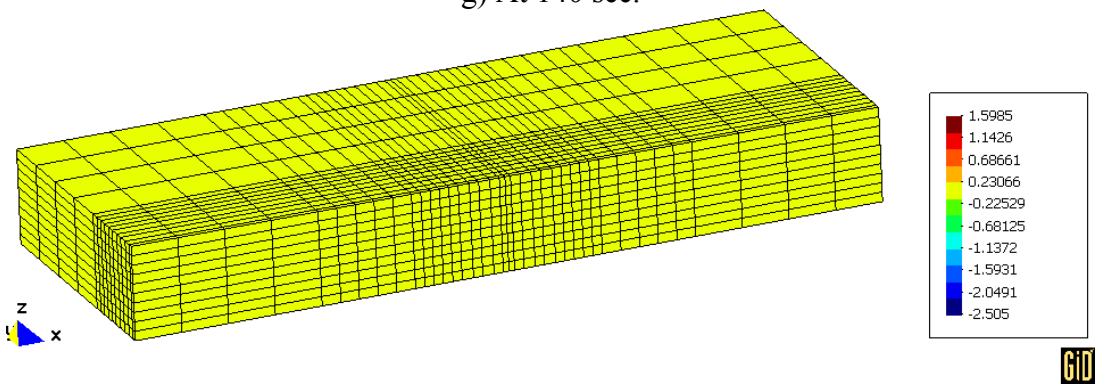

h) At 160 sec.

Figure 6.18: (continued).

Chapter 7 Numerical Simulation of a Pile-Supported Wharf System

The chapter presents numerical analyses of a pile-supported wharf system. All runs except 2D simulations were conducted using ParCYCLIC on the supercomputer Datastar.

7.1 Introduction

Pile-supported wharves are commonly used in the construction of port facilities, especially in land reclamation projects for new port construction. Seismic damage of such structures has generally been attributed to weak soils that are often prevalent in the marine environment (e.g. liquefiable sands, sensitive cohesive soils) and/or insufficient ductility of pile-wharf deck connections (McCullough et al. 2001a).

It has been extensively documented in seismic field case histories that pile-supported wharf damage has been noted primarily in cases where moderate to significant permanent ground deformations were observed (Werner 1998; PIANC 2001). In addition, much of the damage has occurred during levels of shaking that were much less than current design level motions (Dickenson and McCullough 2005).

The current standard-of-practice for the design of port structures (and their remediation) typically utilizes traditional limit-equilibrium methods, whereas more appropriate performance-based design methods are generally not used due to lack of available guidelines. In moving from a limit-equilibrium method of design to a performance-based method, there is a need for better understanding of the seismic performance of waterfront structures during design level earthquakes (McCullough et al.

2001b; Yan et al. 2004). In addition, the seismic response and performance of pile-supported wharves on sloping ground is not well documented due to a historical lack of instrumentation on port structures (Donahue et al. 2005).

This chapter addresses the seismic analysis of a simplified pile-supported wharf system with configurations typical of waterfront structures at the Port of Los Angeles. The primary objective of this numerical study is to investigate and shed light on the underlying dynamic response mechanisms, including soil-structure interaction, of a wharf with a typical geometric configuration. The analysis begins with 2D modeling, followed by 3D simulations with mesh refinement. In view of the numerous new details involved in this exercise, liquefaction was not addressed. However, the work reported herein can now be used to explore liquefaction scenarios as the next logical step. No additional developments are needed to undertake this task.

7.2 Pile-Supported Wharf Model

7.2.1 Pile Group System

The model configuration is based on typical geometries of pile-supported wharf structures of the Berth 100 Container Wharf at the Port of Los Angeles (Figure 7.1 and Figure 7.2). Figure 7.3 shows the idealized wharf model employed for this study. It is a slice in the wharf system (central section) that exploits symmetry (Figure 7.1).

There are 16 piles in 6 rows in this simplified model (Figure 7.3c; starting from the waterside, these rows of piles were labeled as Rows A, B, C, D, E and F). Each pile is 61-cm (24 inch) in diameter, octagonal, reinforced concrete pile. The length of the pile is 43 m. The cracked flexural rigidity (**EI**) of the pile is 159 MN-m^2. The moment

of inertia (**I**) of the pile can be calculated from the octagonal geometry and is 7.09 x 10^{-3} m^4. Therefore, the Young's Modulus (**E**) for the pile is 2.237 x 10^7 kPa (Table 7.2). The deck was assumed to be stiff in the simulation of the wharf model (with a thickness of 0.8 m).

7.2.2 Soil Domain

The soil domain was also simplified and the rock dike was ignored. As shown in Figure 7.3, the inclination angle of the slope is about 39 degrees. The model is 197.5 m long and 6.1 m wide. Height of the soil domain are 33 m and 53.5 m at the waterside (the far right side in Figure 7.3b) and the landside (the far left side in Figure 7.3b), respectively.

Two soil layers were assumed in this simplified model. The lower layer (25 m in height) is modeled as a very stiff clay (255 kPa of Cohesion) with the upper layer being a weaker medium-strength clay (44 kPa of Cohesion). This configuration provides support for the piles at depth, while allowing significant seismically induced lateral deformations to potentially accumulate within the shallow layer. The above two materials are referred to as Very Stiff Clay and Medium Clay respectively. The soil properties of these two materials are listed in Table 7.1. Water table level is 16.6 m above the level ground surface at the waterside.

7.2.3 Bedrock

The base of the model was assumed to be bedrock. However, the actual bedrock level at the Berth 100 Container Wharf site is much deeper.

7.3 Analysis Methods and Soil Constitutive Model

7.3.1 Analysis Methods

Both linear and nonlinear analyses were performed for the pile-supported wharf model. In a linear analysis, a static application of gravity (model self weight) was performed before seismic excitation. The resulting soil stress states served as initial conditions for the subsequent dynamic analysis.

In a nonlinear analysis, the following 4 runs were conducted in sequence for each study in order to achieve convergence and simulate the actual loading situation:

1) 1st run: Gravity was applied in this run; soil properties were used for piles and deck; all materials were prescribed as linear during this run.
2) 2nd run: Soil elements were changed to nonlinear (including pile elements within the soil); all elements kept the same properties as in the 1st run; surface loads on the ground surface at the waterside, due to water pressure, were applied.
3) 3rd run: Pile and deck properties were turned on and all others were kept the same (pile and deck are modeled as linear in this study).
4) 4th run: All materials were kept the same as in the 3rd run; and dynamic excitation was started.

7.3.2 Soil Constitutive Model for Clay

In a nonlinear analysis in CYCLIC/ParCYCLIC, clay material is modeled as a nonlinear hysteretic material (Parra 1996; Yang 2000; Yang et al. 2003) with a Von

Mises multi-surface (Iwan 1967; Mroz 1967) kinematic plasticity model (Figure 7.4). In this regard, focus is on reproduction of the soil hysteretic elasto-plastic shear response (including permanent deformation). In this material, plasticity is exhibited only in the deviatoric stress-strain response. The volumetric stress-strain response is linear-elastic and is independent of the deviatoric response. This constitutive model simulates monotonic or cyclic response of materials whose shear behavior is insensitive to the confinement change. Plasticity is formulated based on the multi-surface (nested surfaces) concept, with an associative flow rule (according to the well-known Provost approach). In the clay model, the nonlinear shear stress-strain back-bone curve is represented by the hyperbolic relation (Kondner 1963), defined by the two material constants, low-strain shear modulus and ultimate shear strength.

In addition to damping generated by the soil, a small level of viscous damping was included. Specifically, stiffness proportional damping was used with a multiplier of 0.003.

7.4 2D Plane Strain Modeling

In this section, the wharf model is further simplified as a 2D plane strain problem. Both linear and nonlinear analyses were conducted (Table 7.3) and the simulation results are presented.

7.4.1 FE Model

Figure 7.5 displays the FE mesh of the 2D plane strain model for a simplified wharf (Cases W2L & W2N, where “W” represents “wharf”, “2” for 2D, “L” for Linear

analysis, “N” for Nonlinear analysis, see Table 7.3). For comparison, modeling of the soil domain without the wharf structure was also performed. Figure 7.6 shows the FE mesh of the plane strain model without the wharf (Cases C2L & C2N, where “C” represents “Clay” material). Both meshes employ 9 node quadrilateral elements for all materials including the piles.

The pile diameter of 61 cm was still used for this simplified 2D plane strain simulation. Therefore, a reduction of pile properties was needed for the 2D simulations in order to be compatible with the 3D simulations. Specifically, 30% of Young’s Modulus and Mass Density were employed for Cases W2L & W2N above ground surface, with Mass Density of the soil used below ground surface for simplicity (Table 7.2).

The base of the FE model was assumed to be bedrock (the actual bedrock level is much deeper). In view of imparting the base excitation of a depth of 53.5 m (landside), the Rinaldi Receiving Station record in the 1994 Northridge Earthquake was scaled down by half and the resulting acceleration was employed as the base input motion (Figure 7.7). Both sides (waterside and landside) of the FE models (Figure 7.5 and Figure 7.6) were specified with the computed accelerations from the 1D shear beam simulations (Yang et al. 2004b) of the left and right soil boundaries.

Figure 7.8 and Figure 7.9 show the accelerations specified at sample locations/depths for both sides of the models for linear analyses while Figure 7.10 and Figure 7.11 are the specified accelerations for nonlinear analyses.

7.4.2 Linear Analysis Results

Figures 7.12-7.14 display the lateral acceleration time histories at different depths for locations A, B and C (corresponding to the top, center and bottom of the sloping ground, respectively, see Figure 7.5 and Figure 7.6), respectively for Case W2L. The lateral acceleration was amplified to about 1.8g at the surface (Figure 7.12) in this linear case. The free field responses are shown in Figure 7.15 and Figure 7.16. The responses of the case without the wharf (Case C2L) are quite similar and are thus listed in Appendix B (Figures B.1-B.5).

Figure 7.17 displays the lateral acceleration time histories for pile heads for Case W2L. Due to the stiff deck, all 6 rows of pile heads behave approximately the same. The peak lateral acceleration of the pile heads was about 1.8g (Figure 7.17).

Figure 7.18 shows the stress ratio distribution of the soil domain for Case W2L before and after shaking. The stress ratio (Yang 2000) is defined as a ratio of the octahedral shear stress (Desai and Siriwardane 1984) to the peak octahedral shear strength τ_f, which is given as:

$$\tau_f = \frac{2\sqrt{2}}{3} c \tag{7.1}$$

where c is the cohesion (kPa). The maximum stress ratio is 0.64 before the shaking (Figure 7.18a) and 0.66 (Figure 7.18b) at the end of the dynamic excitation. The stress ratio distribution for the case without the wharf (Case C2L) is shown in Figure B.6.

7.4.3 Nonlinear Analysis Results

Figures 7.19-7.21 display the lateral acceleration time histories at different depths for Locations A, B and C, respectively for Case W2N. Significant change is observed compared to the linear response, especially at location A (Figure 7.19) and location B (Figure 7.20). This response is associated with down-slope shear deformation with the soil deforming laterally towards to the waterside.

The free field responses at the landside and waterside for Case W2N are shown in Figure 7.22 and Figure 7.23. The waterside responses (Figure 7.22) are larger since the upper weak soil layer at the waterside is much less in thickness, compared to the landside (Figure 7.23). The lateral acceleration responses for the case without the wharf (Case C2N) are quite similar and are listed in Appendix B (Figures B.7-B.11).

The pile head lateral acceleration time histories for all piles are shown in Figure 7.24. The acceleration responses for all rows of piles are essentially the same due to the rigid deck. The peak lateral acceleration for pile heads is about 0.4g, which is much weaker than the linear case (Figure 7.17).

Figures 7.25-7.27 display the lateral displacement time histories at different depths for locations A, B and C, respectively for Case W2N. The slope deformed rapidly at 2.5-3.5 seconds due to a large pulse of the input motion (Figure 7.7). The final lateral displacements at the ground surface for the slope are 0.27 m, 0.3 m, and 0.16 m at locations A, B and C, respectively (the final lateral displacement at the ground surface for the free field is 0.1 m (not shown)). The pile head lateral displacement time histories for all piles are shown in Figure 7.28. As we can see from Figure 7.28, all rows of piles

behave similarly due to the stiff deck. The final lateral displacement for pile heads is about 0.28 m (Figure 7.28).

Figure 7.29 shows the final deformed mesh for Case W2N. As we can see, the majority of the deformation occurred within the upper clay layer. The lower soil layer shows insignificant lateral displacement.

Figure 7.30 shows the stress ratio distribution of the soil domain for Case W2N before and after shaking. The maximum stress ratio is 0.76 before the shaking (Figure 7.30a) and 0.82 (Figure 7.30b) at the end of the dynamic excitation.

Figures 7.31-7.33 display the shear stress-strain response at different depths for locations A, B and C, respectively for Case W2N. There are large accumulated permanent strain increments (Figures 7.31-7.33) at almost every location in the sloping ground area. These permanent strain increments correspond to the big "jumps" in the displacement time histories as shown in Figures 7.25-7.28. The shear stress-strain responses for the case without the wharf (Case C2N) are similar and are listed in Appendix B (see Figures B.12-B.14).

Figures 7.34-7.36 show the lateral displacement time histories at different depths for locations A, B and C, respectively for Case C2N. Again, the slope deformed rapidly at 2.5-3.5 second due to a large pulse of the input motion (Figure 7.7). The final lateral displacements at ground surface for the slope are 0.28 m, 0.4 m, and 0.3 m at locations A, B and C, respectively. Comparing the lateral displacement time histories for Cases W2N & C2N, we can see that the lateral displacements of the slope with the wharf included were reduced by 0.01 m, 0.1 m, and 0.14 m at locations A, B and C, respectively.

Figure 7.37 shows the final deformed mesh for Case C2N. As we can see, the majority of the deformation occurred within the upper layer. The area under the slope near the interface between the two soil layers actually deformed the most. The lower soil layer shows little movement due to the stiff clay.

Figure 7.38 displays the stress ratio distribution for Case C2N. The maximum stress ratio is 0.55 before the shaking (Figure 7.38a) and 0.82 (Figure 7.38b) at the end of the dynamic excitation.

7.5 3D Simulations

This section presents 3D simulations of the wharf model.

7.5.1 FE Model

Three mesh sizes (Figure 7.39) were employed for 3D simulation. These meshes are referred to as Cases W3L-C & W3N-C (Figure 7.39a), Cases W3L-M & W3N-M (Figure 7.39b) and Cases W3L-F & W3N-F (Figure 7.39c) respectively (where the three last letters of the case numbers "**C**", "**M**" and "**F**" represent "**C**oarse mesh", "**M**edium size mesh" and "**F**ine mesh", respectively (see Table 7.3). 20-node brick elements are used for all materials including piles and the deck. The total numbers of degrees of freedom (DOFs) for each mesh is listed in Table 7.3.

The boundary conditions are similar to the 2D plane strain simulations discussed in Section 7.4. The waterside and landside boundaries were specified with the computed accelerations from the 1D shear beam simulation (Figures 7.8-7.11). The other two side

boundaries were assumed to be roller-supported (i.e., simulating planes of symmetry). The base input motion is shown in Figure 7.7.

7.5.2 Linear Analysis Results

Figures 7.40-7.42 display the longitudinal acceleration time histories at different depths for locations A, B and C (see Figure 7.3b and Figure 7.3c), respectively, for Case W3L-F. The longitudinal acceleration was amplified to about 1.6g at the surface (Figure 7.40) in this linear case. The free field responses of the waterside and landside are shown in Figure 7.43 and Figure 7.44.

Figure 7.45 displays the longitudinal acceleration time histories of pile heads for the piles along the A-B-C line for Case W3L-F. All pile heads behave approximately the same due to the stiff deck. The peak longitudinal acceleration of the pile heads is about 1.8g (Figure 7.45).

Figure 7.46 shows the stress ratio distribution of the soil domain for Case W3L-F before and after shaking. The maximum stress ratios are about 2.38 before and after the shaking. The stress ratio distributions for coarser meshes (Cases W3L-M & W3L-C) are also shown in Figure 7.48 and Figure 7.47.

The responses of Cases W3L-C & W3L-M are quite similar and are thus listed in Appendix B (Figures B.15-B.19 for Case W3L-C and Figures B.20-B.24 for Case W3L-M).

7.5.3 Nonlinear Analysis Results

Figures 7.49-7.51 display the longitudinal acceleration time histories at different depths for locations A, B and C, respectively for Case W3N-F. Similar to 2D, significant reduction in the acceleration peaks occurred, especially at locations A (Figure 7.49) and B (Figure 7.50), indicative of lateral spreading. This response is associated with down-slope (seaward) shear deformations with the soil deforming laterally towards to the waterside.

The free field responses of the landside and waterside are shown in Figure 7.52 and Figure 7.53. Similar to 2D, the waterside responses (Figure 7.53) are larger since the upper weak soil layer at the waterside is of little thickness, compared to the landside (Figure 7.52).

The pile head longitudinal acceleration time histories for the 6 piles along the A-B-C line are shown in Figure 7.54. The acceleration responses for all 6 piles are essentially the same due to the rigid deck. The peak longitudinal acceleration for these pile heads is about 0.38g, which is much smaller than the linear case.

Figures 7.55-7.57 display the longitudinal displacement time histories at different depths for locations A, B and C, respectively for Case W3N-F. The final longitudinal displacements at the ground surface were 0.3 m, 0.32 m and 0.17 m at locations A, B and C, respectively (the final longitudinal displacement at the ground surface for the free field is 0.07 m (not shown)). The pile head longitudinal displacement time histories for the 6 piles along the A-B-C line are shown in Figure 7.58. Again, all rows of piles behave similarly. The final longitudinal displacement for pile heads is about 0.3 m.

Figure 7.59 shows the final deformed mesh for Case W3N-F. As we can see, the majority of the deformation occurs within the upper layer. The lower soil layer shows insignificant lateral displacement even in this fine mesh. A close-up view for the wharf section is shown in Figure 7.60. Figure 7.61 shows a close-up view of the contour lines of the longitudinal displacement for the slope section.

Figure 7.62 displays the final deformed mesh (and also the undeformed mesh) of the wharf (contour fill shows the vertical displacement). Compared to the original location, the deck moved downward at the landside (Row F) and upward at the waterside (Row A) (Figure 7.62a). As a result, the pile heads of Row F are in compression while those of Row A are in tension. This tension state can deteriorate the overall performance of the pile group and further analyses are needed for verification. The final deformed mesh for the wharf for Case W3N-F is also shown in Figure 7.63 where contour fill shows the longitudinal displacement.

Figure 7.64 and Figure 7.65 show the response profiles for Pile A3 & F1 (see Figure 7.3c). The axial forces and the bending moments were calculated by using SAP 2000 (CSI 2005). In this crude representation, the profile of pile displacement (along the centerline of the constituting brick elements) was applied to an equivalent beam-column element model. The front pile (Pile A3) is seen to undergo significant tension (Figure 7.64) while the back pile (Pile F1) experiences large compression (Figure 7.65).

For comparison, the final deformed meshes for Cases W3N-C & W3N-M are shown in Figure 7.66 and Figure 7.67 respectively. The finer meshes (Figure 7.59 and Figure 7.67) result in larger deformations due to the added flexibility.

Figure 7.68 shows the stress ratio distribution for Case W3N-F before and after shaking. Those for Cases W3N-C & W3N-M are shown in Figure 7.69 and Figure 7.70. The maximum stress ratio after shaking is about 0.91, 0.88 and 0.89 for Cases W3N-F, W3N-M and W3N-C, respectively.

Figures 7.71-7.73 display the shear stress-strain responses at different depths for locations A, B and C, respectively for Case W3N-F. These responses are quite similar to the 2D simulations (Figures 7.31-7.33). The large shear strain excursions in Figures 7.31-7.33 correspond to the big "jumps" in the displacement time histories as shown in Figures 7.55-7.57.

The other responses of Cases W3N-C & W3N-M are quite similar and are listed in Appendix B (Figures B.25-B.32 for Case W3N-C and Figures B.33-B.40 for Case W3N-M).

7.5.4 Parallel Performance

The execution time measurements are listed in Table 7.4 for nonlinear analyses and Table 7.5 for linear analyses. As we can see, the time expended on the initialization phase is insignificant compared to that of the overall analysis. Most of the time in the initialization phase is spent on the FE model input and formation of the adjacency structure for these high fidelity meshes. The multilevel nested dissection ordering using METIS is relatively fast and less than 4 seconds are needed to order the high fidelity 10,028 elements mesh with 142,332 degrees of freedom (Table 7.4).

The times spent on the LHS formation, the RHS formation and the numerical factorization per step are listed in Table 6.1 for nonlinear analyses and Table 6.1 for linear analyses.

Table 7.1: Material properties for cohesive soils

Soil type	Medium Clay	Very Stiff Clay
Shear Modulus (kPa)	$8. \times 10^4$	4.86×10^5
Bulk Modulus (kPa)	9.73×10^5	5.91×10^6
Cohesion (kPa)	44.	225.
Mass Density (kg/m^3)	1.55×10^3	$2. \times 10^3$
Poisson's Ratio	0.46	0.46

Table 7.2: Material properties for piles

Simulation Cases	2D simulation	3D simulation
Young's Modulus (kPa)	6.711×10^6	2.237×10^7
Mass Density above ground surface (kg/m^3)	0.72×10^3	2.4×10^3
Poisson's Ratio	0.3	0.3

Table 7.3: Wharf system simulations

Simulation case	With/Without wharf	Dimension	Analysis type	Total number of elements	Total number of equations
C2L (**C**lay, **2**D, **L**inear)	Without wharf	2D plane strain	Linear	648	5,450
C2N (**C**lay, **2**D, **N**onlinear)	Without wharf	2D plane strain	Nonlinear		
W2L (**W**harf, **2**D, **L**inear)	With wharf	2D plane strain	Linear	683	5,840
W2N (**W**harf, **2**D, **N**onlinear)	With wharf	2D plane strain	Nonlinear		
W3L-C (**W**harf, **3**D, **L**inear, **C**oarse mesh)	With wharf	3D	Linear	2,081	32,238
W3N-C (**W**harf, **3**D, **N**onlinear, **C**oarse mesh)	With wharf	3D	Nonlinear		
W3L-M (**W**harf, **3**D, **L**inear, **M**edium size mesh)	With wharf	3D	Linear	5,424	79,434
W3N-M (**W**harf, **3**D, **N**onlinear, **M**edium size mesh)	With wharf	3D	Nonlinear		
W3L-F (**W**harf, **3**D, **L**inear, **F**ine mesh)	With wharf	3D	Linear	10,028	142,332
W3N-F (**W**harf, **3**D, **N**onlinear, **F**ine mesh)	With wharf	3D	Nonlinear		

Table 7.4: Execution time measurements for 3D nonlinear analyses of the wharf system (supercomputer: Datastar).

Case		W3N-C	W3N-M	W3N-F
Total number of elements		2,081	5,424	10,028
Total number of equations		32,238	79,434	142,332
Number of processors used		16	64	64
Execution time measurements (time in seconds)				
Initialization phase	FE model input	4.5	40.2	134.4
	Formation of adjacency structure	3.7	9.8	18.2
	Multilevel nested dissection ordering (using METIS)	0.7	1.9	3.9
	Elimination tree setup and postordering	0.1	0.2	0.3
	Symbolic factorization	0.5	1.3	2.3
	Solver inter-processor communication setup	1.8	6.6	11.8
	Matrix storage and solver indexing setup	1.0	1.3	2.1
	Total on initialization phase	12.8	62.6	175.4
Nonlinear solution phase	LHS formation	902.7	2,534.7	3,261.2
	RHS formation	1,706.0	2,341.8	3,686.5
	Stress update	114.5	196.2	275.2
	Numerical factorization	2,526.5	5,980.6	12,742.0
	Forward and backward solves	640.3	2,940.6	5,260.5
	Total on solution phase	6,649.8	20,594.7	42,862.0
Total execution time		6,662.7	20,657.5	43,037.4

Table 7.5: Execution time measurements for 3D linear analyses of the wharf system (supercomputer: Datastar).

Case		W3L-C	W3L-M	W3L-F
Total number of elements		2,081	5,424	10,028
Total number of equations		32,238	79,434	142,332
Number of processors used		16	64	128
Execution time measurements (time in seconds)				
Initialization phase	FE model input	4.5	40.1	134.2
	Formation of adjacency structure	3.7	9.7	18.2
	Multilevel nested dissection ordering (using METIS)	0.7	1.9	3.9
	Elimination tree setup and postordering	0.1	0.2	0.3
	Symbolic factorization	0.5	1.3	2.4
	Solver inter-processor communication setup	1.8	7.2	14.9
	Matrix storage and solver indexing setup	1.0	1.3	1.1
	Total on initialization phase	12.8	63.0	177.3
Nonlinear solution phase	LHS formation	1.7	2.7	3.9
	RHS formation	465.5	369.9	484.6
	Stress update	41.3	36.2	30.5
	Numerical factorization	4.1	5.7	7.8
	Forward and backward solves	140.9	423.9	1,813.6
	Total on solution phase	914.6	2,255.5	7,138.5
Total execution time		927.4	2,318.7	7,316.1

Table 7.6: Timing details of the nonlinear solution phase for 3D nonlinear analyses of the wharf system (time in seconds; supercomputer: Datastar).

Case	Number of processors		LHS formation	RHS formation	Stress update	Numerical factorization	Forward and backward solves
W3N-C	16	Time	902.7	1,706.0	114.5	2,526.5	640.3
		Number of times performed	627	11556	2348	627	8883
		Time per step	**1.44**	**0.15**	**0.05**	**4.03**	**0.07**
W3N-M	64	Time	2,534.7	2,341.8	196.2	5,980.6	2,940.6
		Number of times performed	1165	19677	4620	1165	14461
		Time per step	**2.18**	**0.12**	**0.04**	**5.13**	**0.20**
W3N-F	64	Time	3,261.2	3,686.5	275.2	12,742.0	5,260.5
		Number of times performed	1005	22520	4511	1005	17503
		Time per step	**3.24**	**0.16**	**0.06**	**12.68**	**0.30**

Table 7.7: Timing details of the solution phase for 3D linear analyses of the wharf system (time in seconds; supercomputer: Datastar).

Case	Number of processors		LHS formation	RHS formation	Stress update	Numerical factorization	Forward and backward solves
W3L-C	16	Time	1.7	465.5	41.3	4.1	140.9
		Number of times performed	1	4000	2000	1	2000
		Time per step	**1.70**	**0.12**	**0.02**	**4.10**	**0.07**
W3L-M	64	Time	2.7	369.9	36.2	5.7	423.9
		Number of times performed	1	4000	2000	1	2000
		Time per step	**2.70**	**0.09**	**0.02**	**5.70**	**0.21**
W3L-F	128	Time	3.9	484.6	30.5	7.8	1,813.6
		Number of times performed	1	6000	2000	1	4000
		Time per step	**3.90**	**0.08**	**0.02**	**7.80**	**0.45**

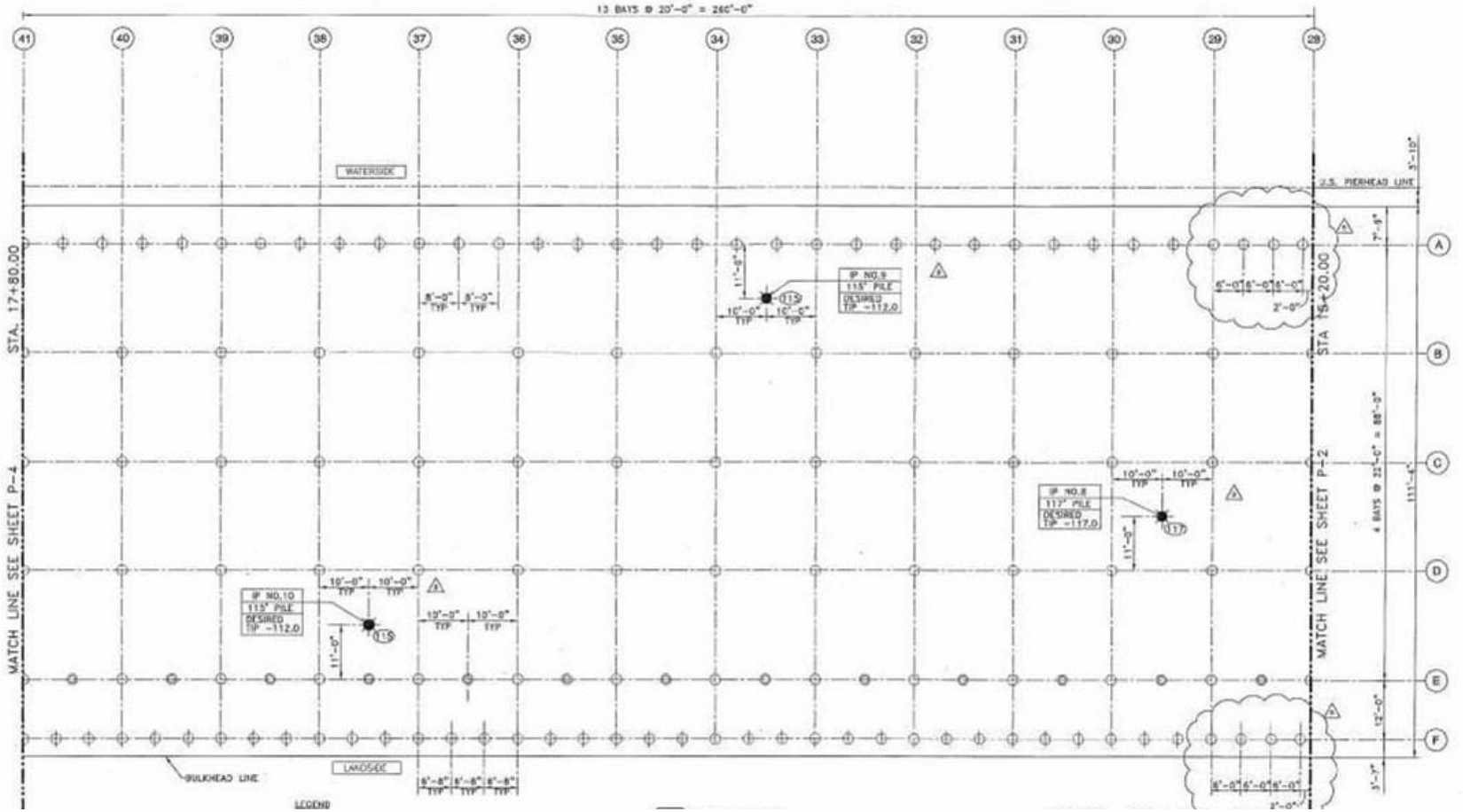

Figure 7.1: Plan view of the Berth 100 Container Wharf at Port of Los Angeles (Arulmoli 2005).

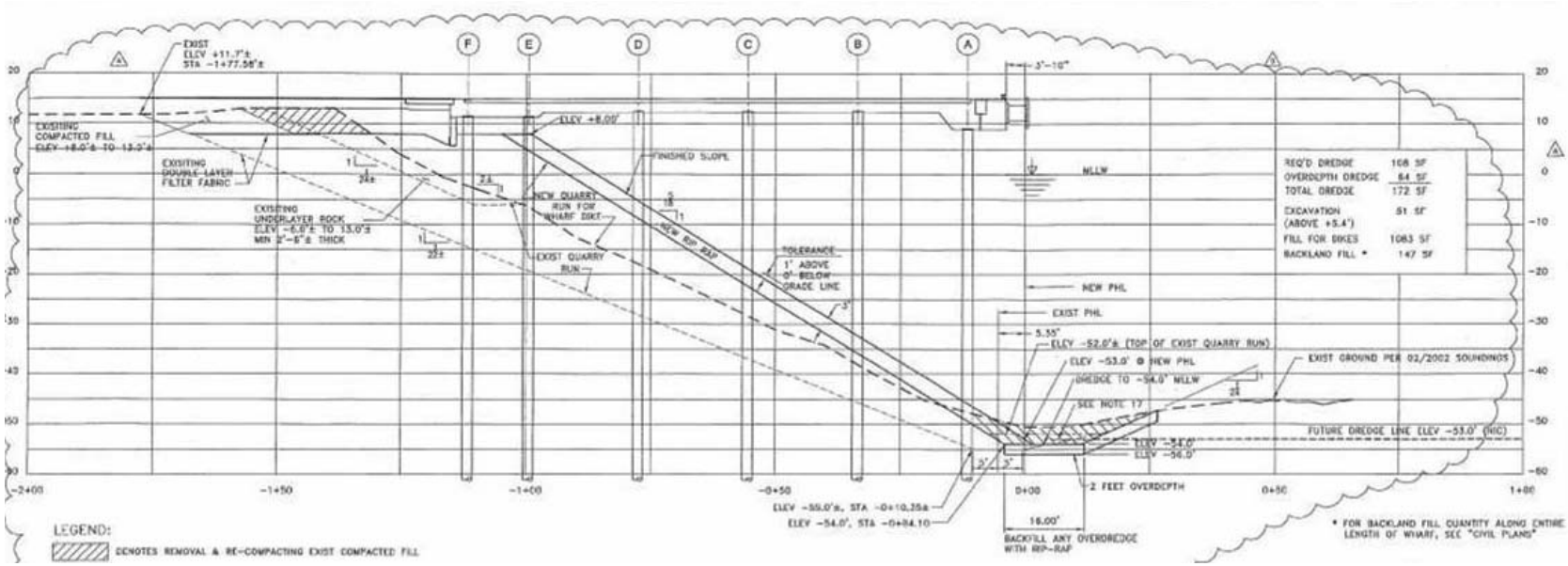

Figure 7.2: Cross-section of the Berth 100 Container Wharf at Port of Los Angeles (Arulmoli 2005).

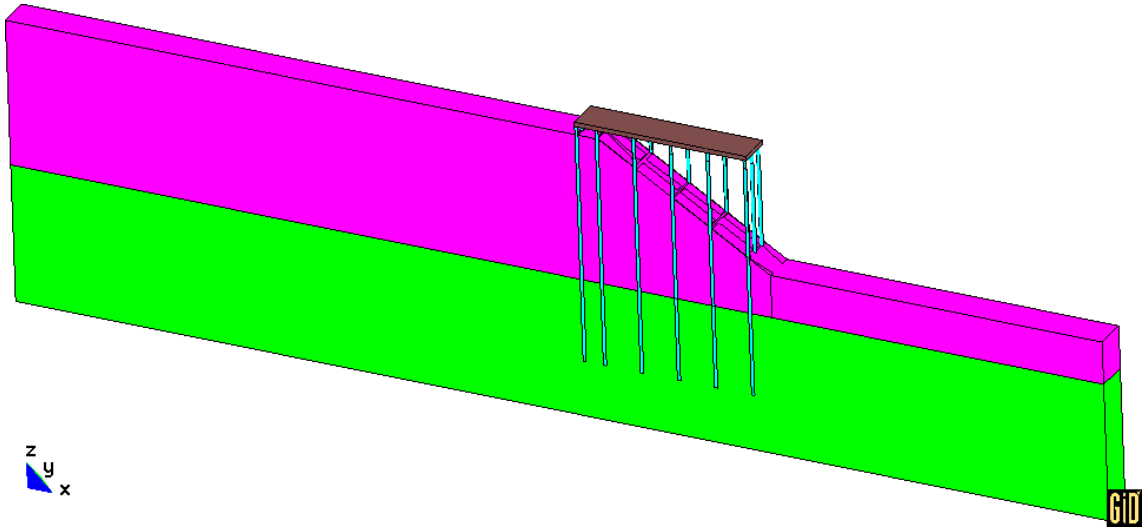

(a) Isometric view

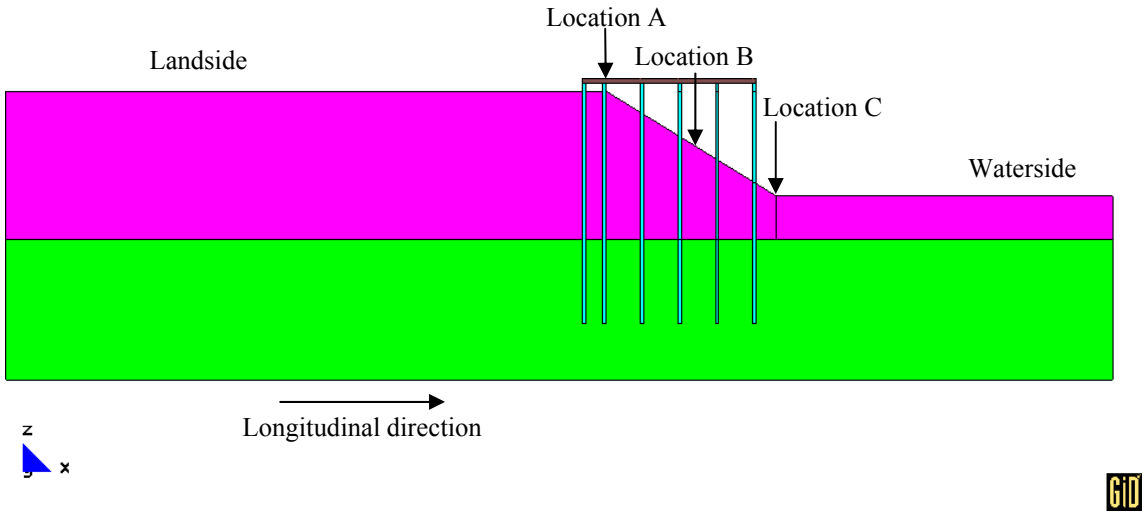

(b) Elevation view

Figure 7.3: Simplified pile-supported wharf model (upper soil layer: Medium Clay; lower layer: Very Stiff Clay).

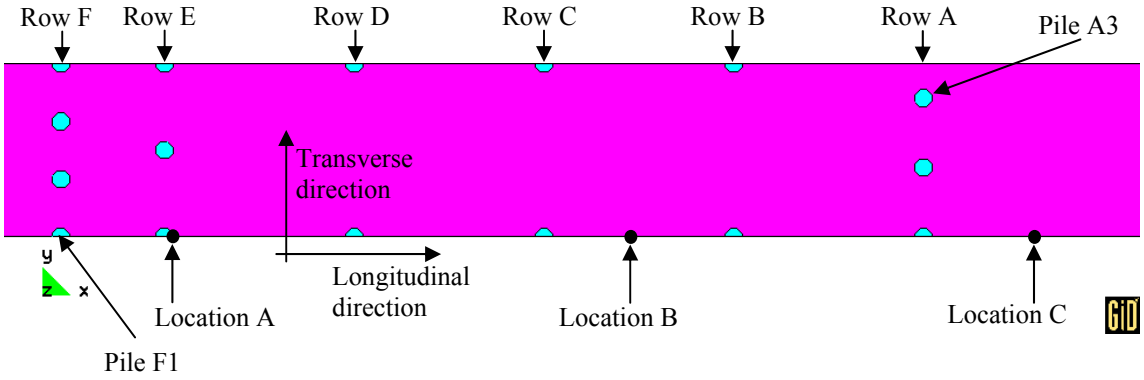

(c) Pile group layout (plan view)

Figure 7.3: (continued).

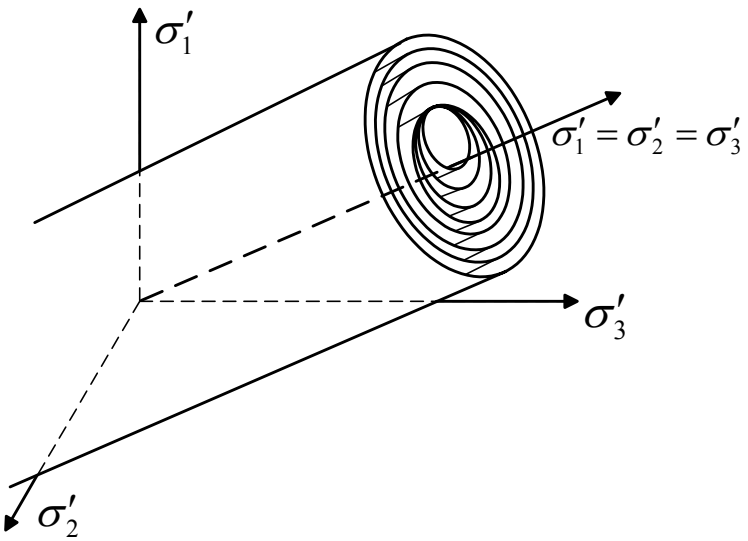

(a) Von Mises multi-surface.

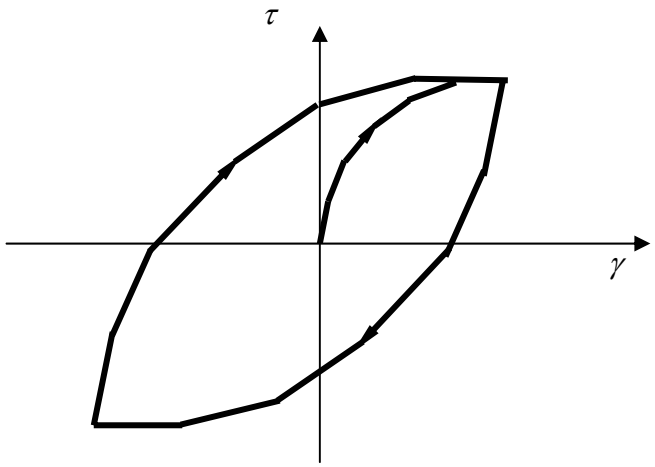

(b) Hysteretic shear response.

Figure 7.4: Von Mises multi-surface kinematic plasticity model (Yang 2000; Yang et al. 2003).

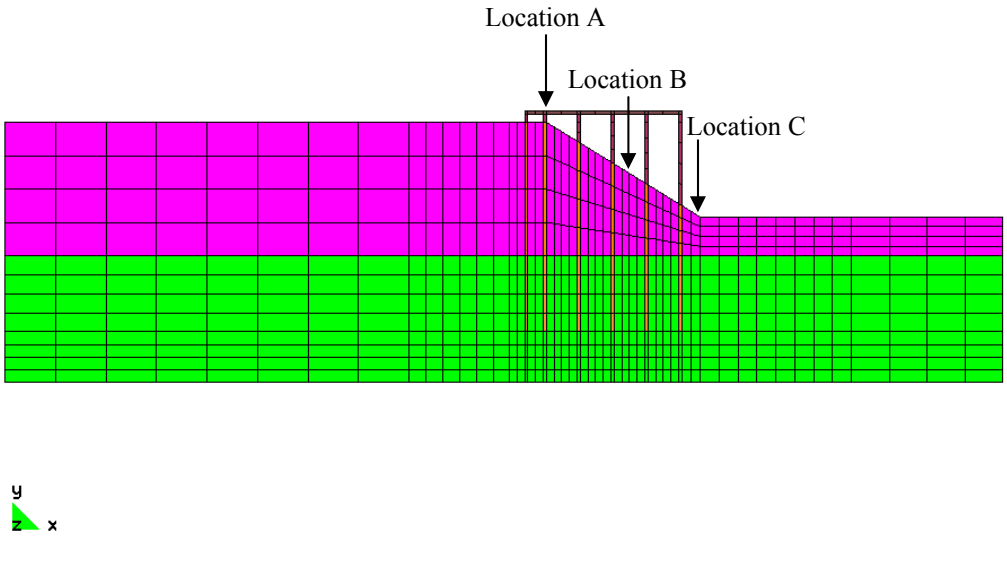

Figure 7.5: FE mesh of 2D plane strain wharf model (Cases W2L & W2N).

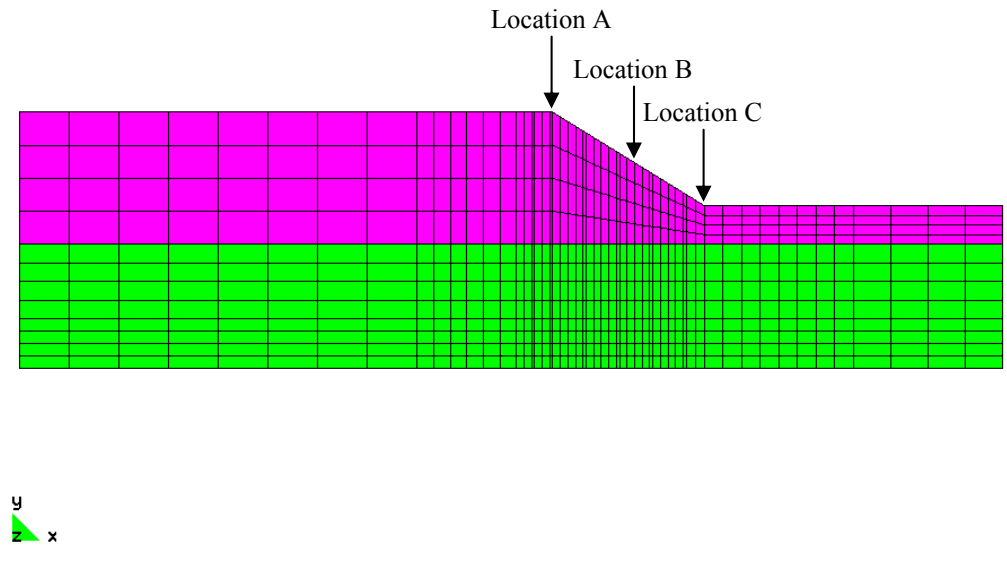

Figure 7.6: FE mesh of 2D plane strain model without wharf (Cases C2L & C2N).

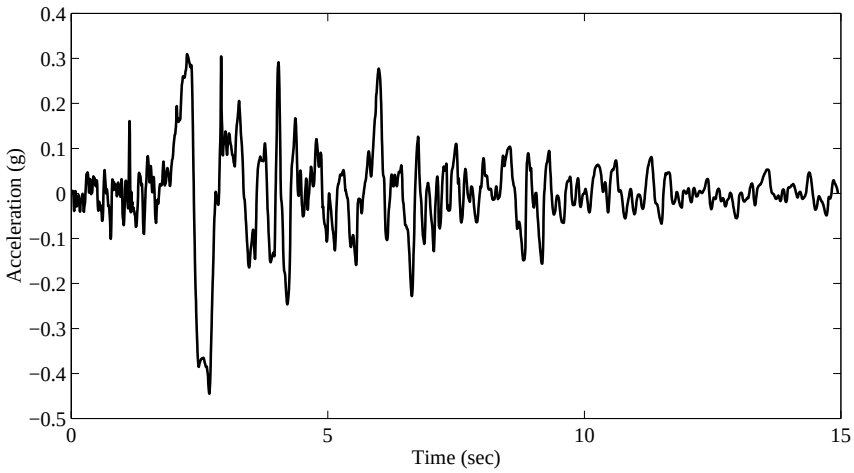

Figure 7.7: Base input motion.

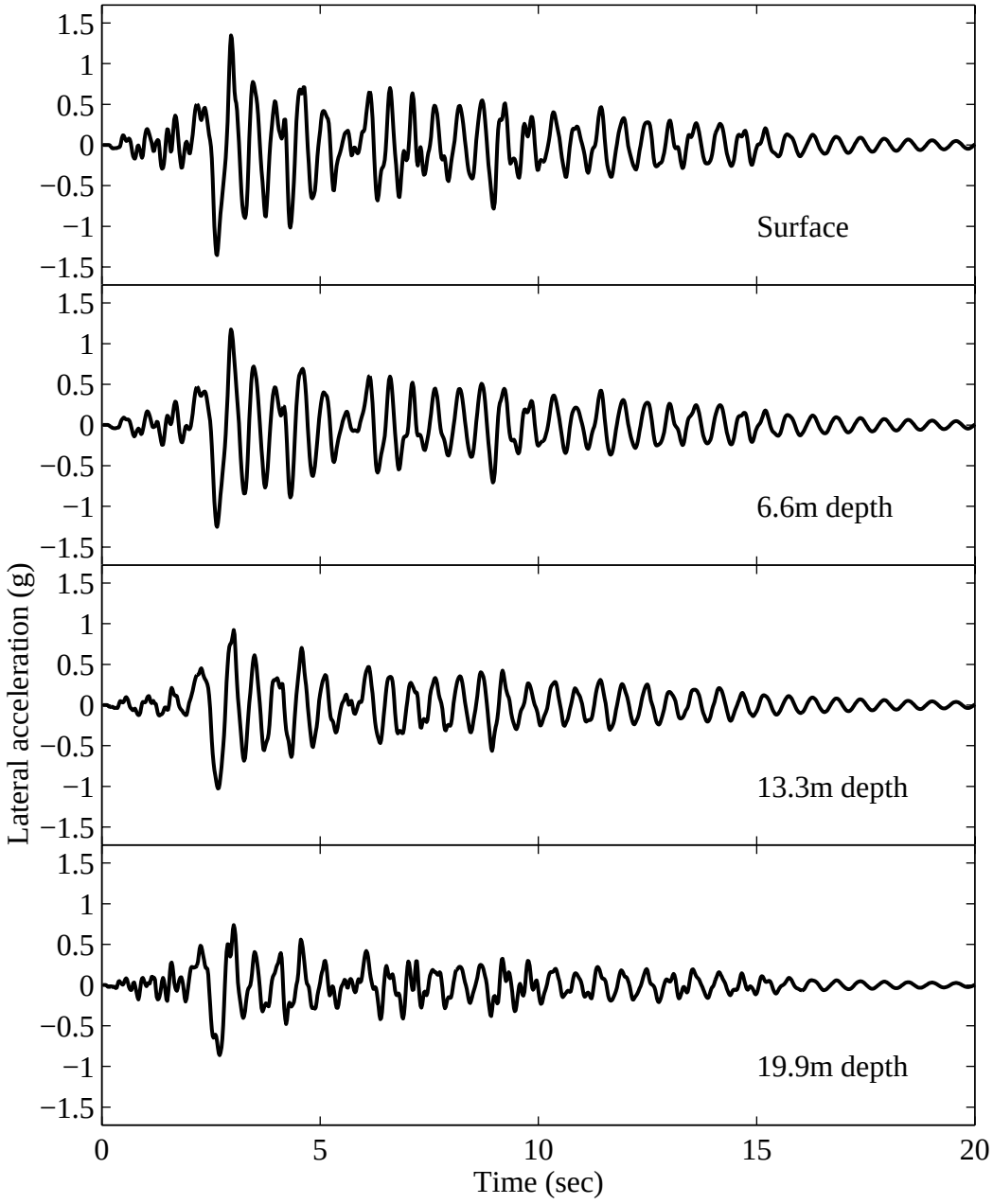

Figure 7.8: Lateral input motion specified at the far left-side/landside of the models (upper soil layer) in the linear analyses.

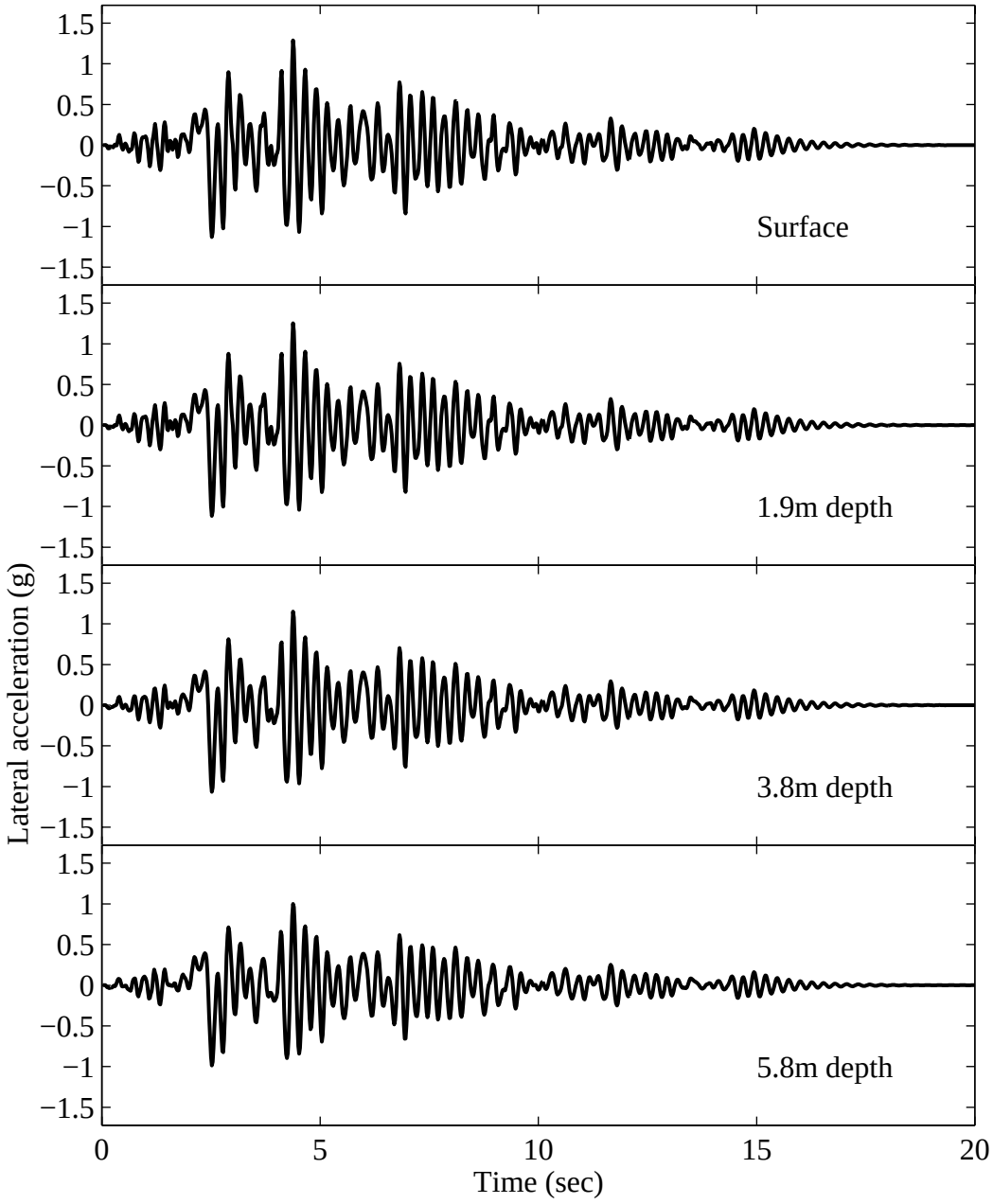

Figure 7.9: Lateral input motion specified at the far right-side/waterside of the models (upper soil layer) in the linear analyses.

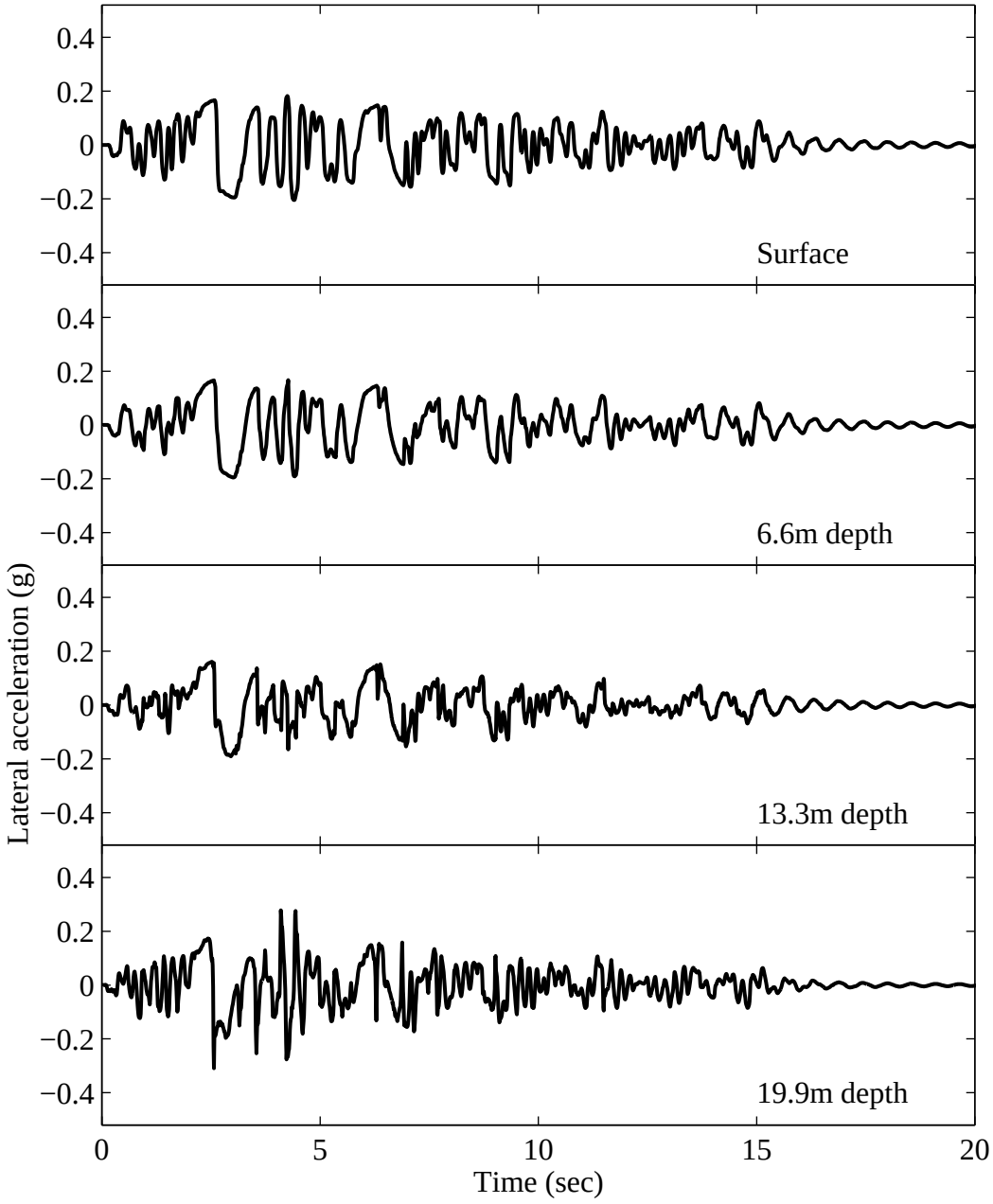

Figure 7.10: Lateral input motion specified at the far left-side/landside of the models (upper soil layer) in the nonlinear analyses.

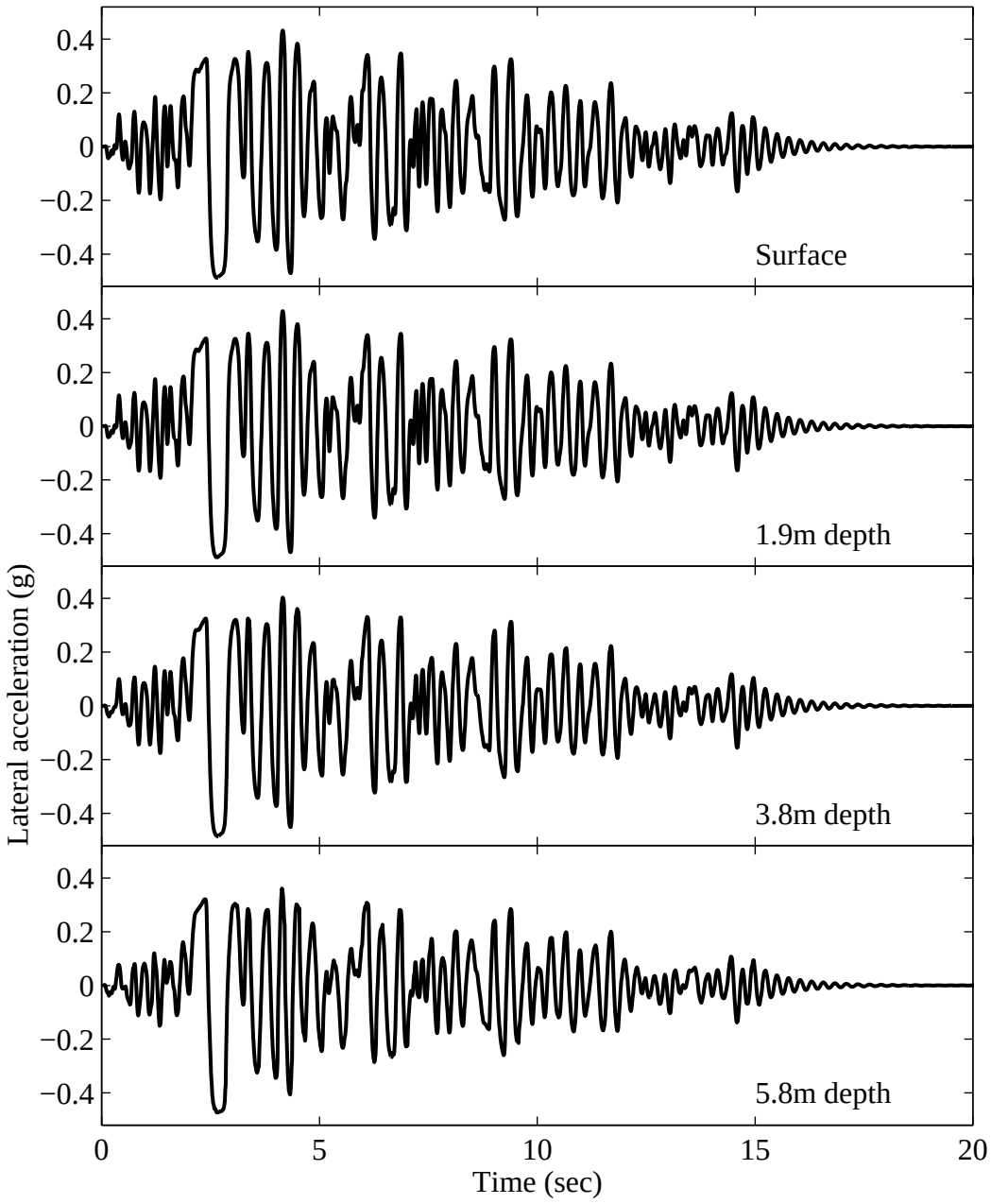

Figure 7.11: Lateral input motion specified at the far right-side/waterside of the models (upper soil layer) in the nonlinear analyses.

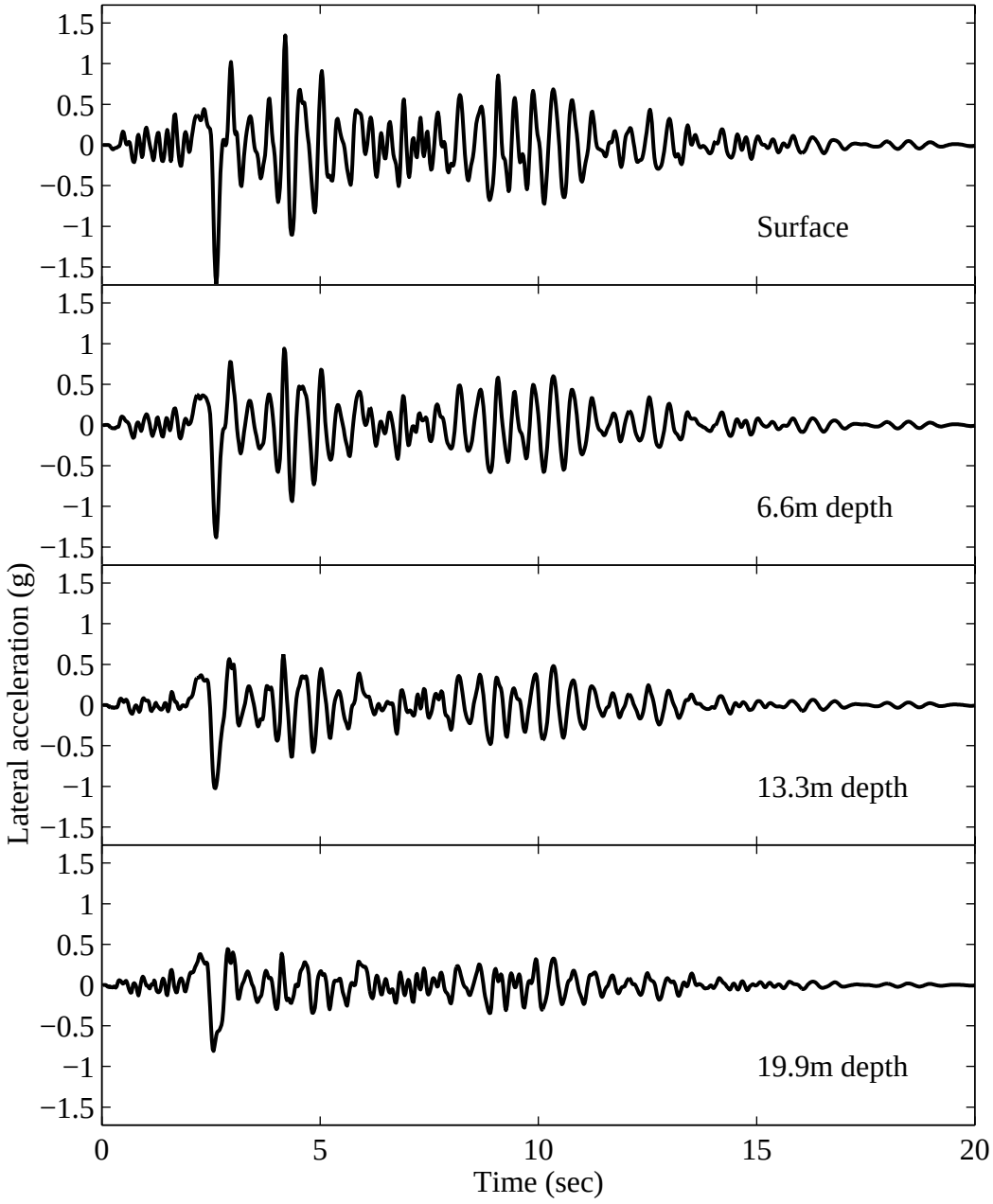

Figure 7.12: Lateral acceleration time histories at Location A for Case W2L.

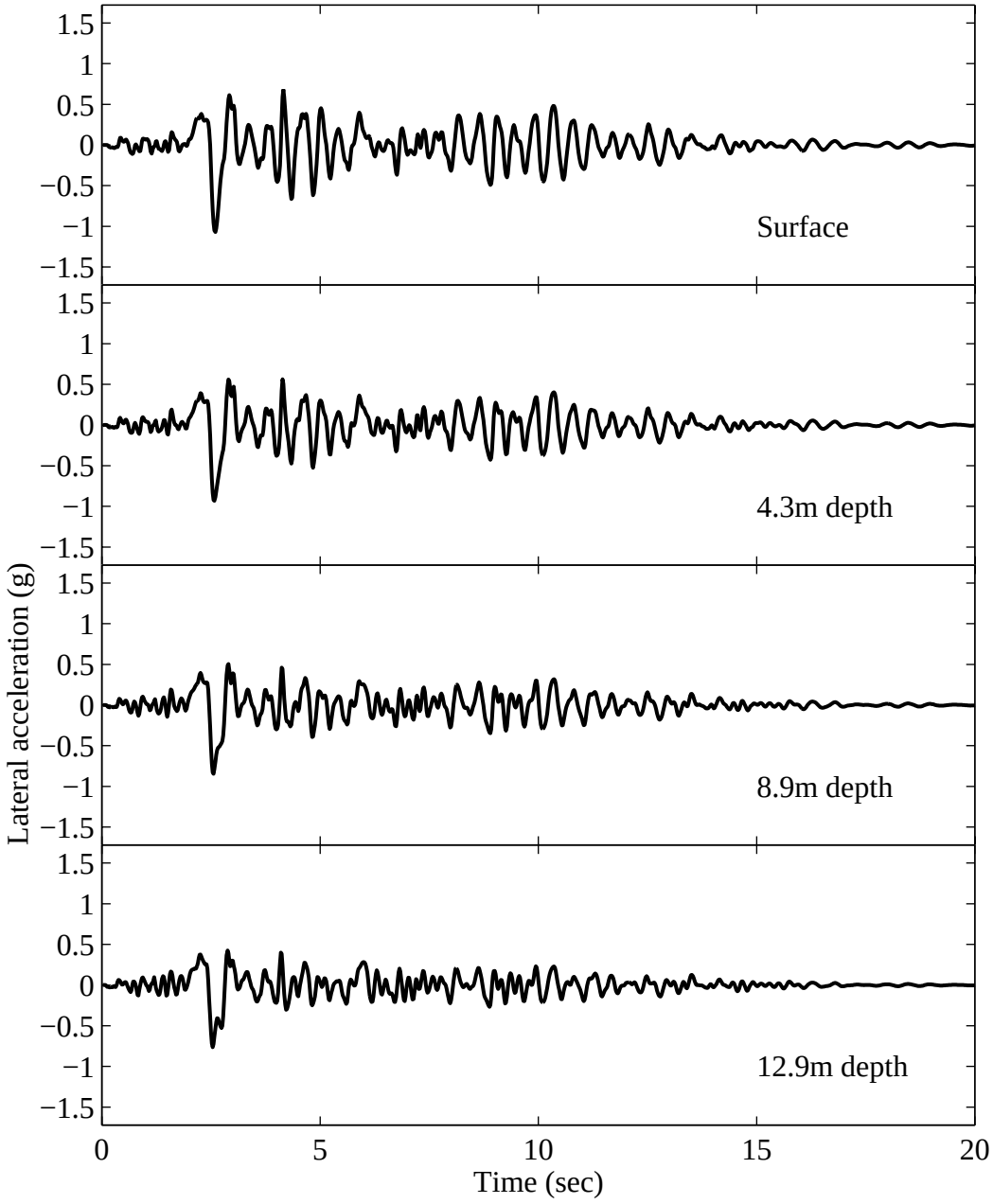

Figure 7.13: Lateral acceleration time histories at Location B for Case W2L.

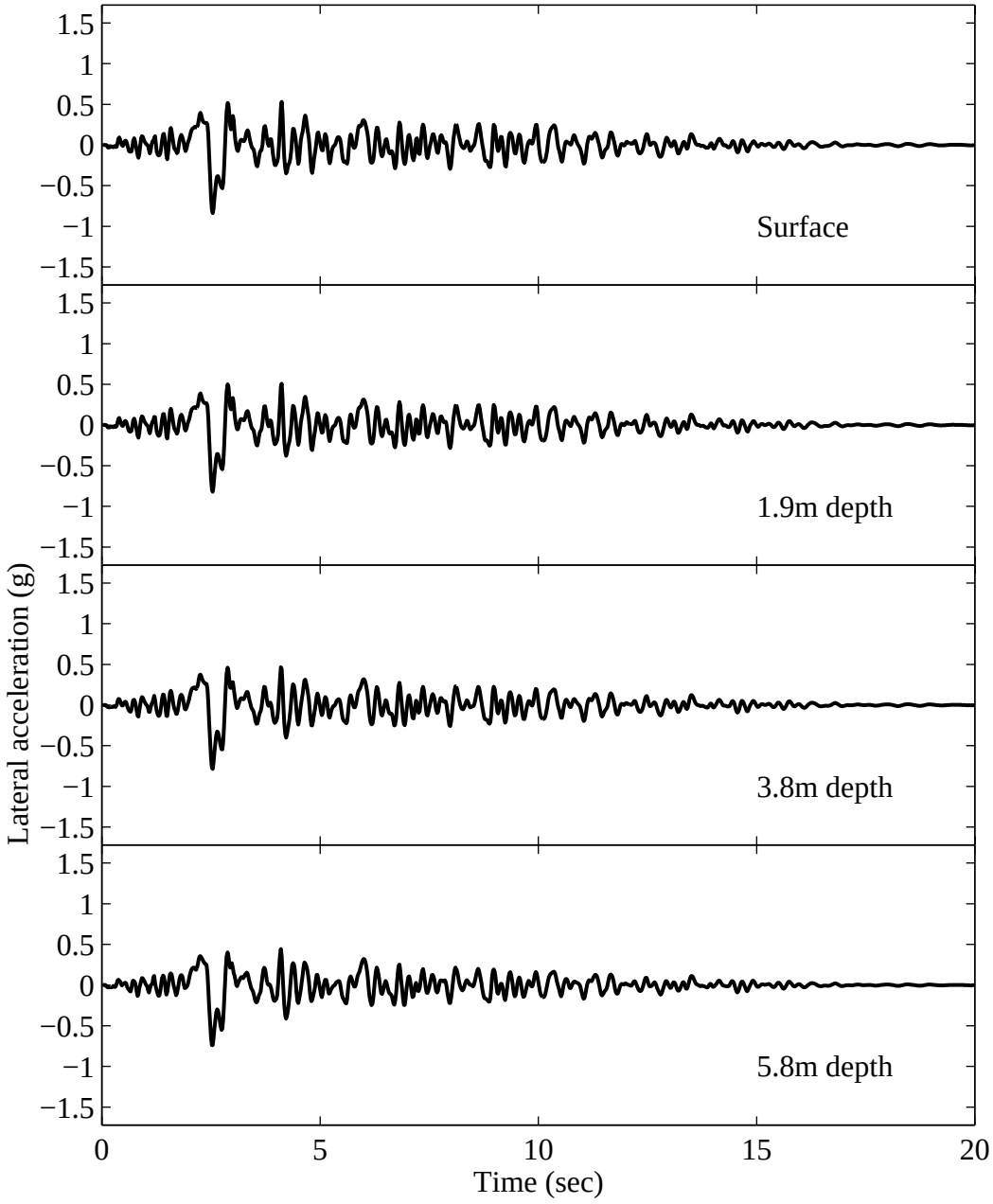

Figure 7.14: Lateral acceleration time histories at Location C for Case W2L.

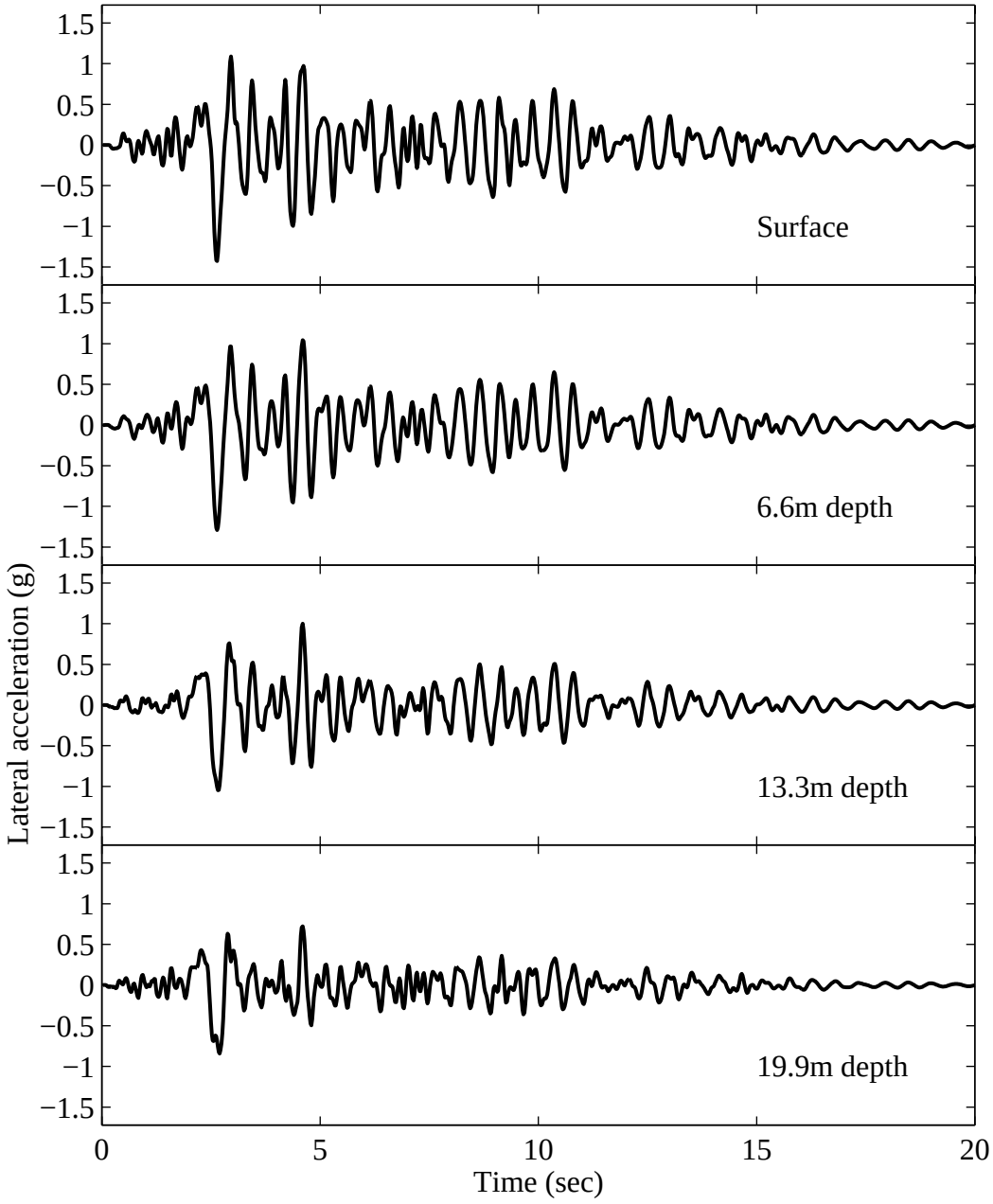

Figure 7.15: Lateral acceleration time histories at free field for the landside for Case W2L.

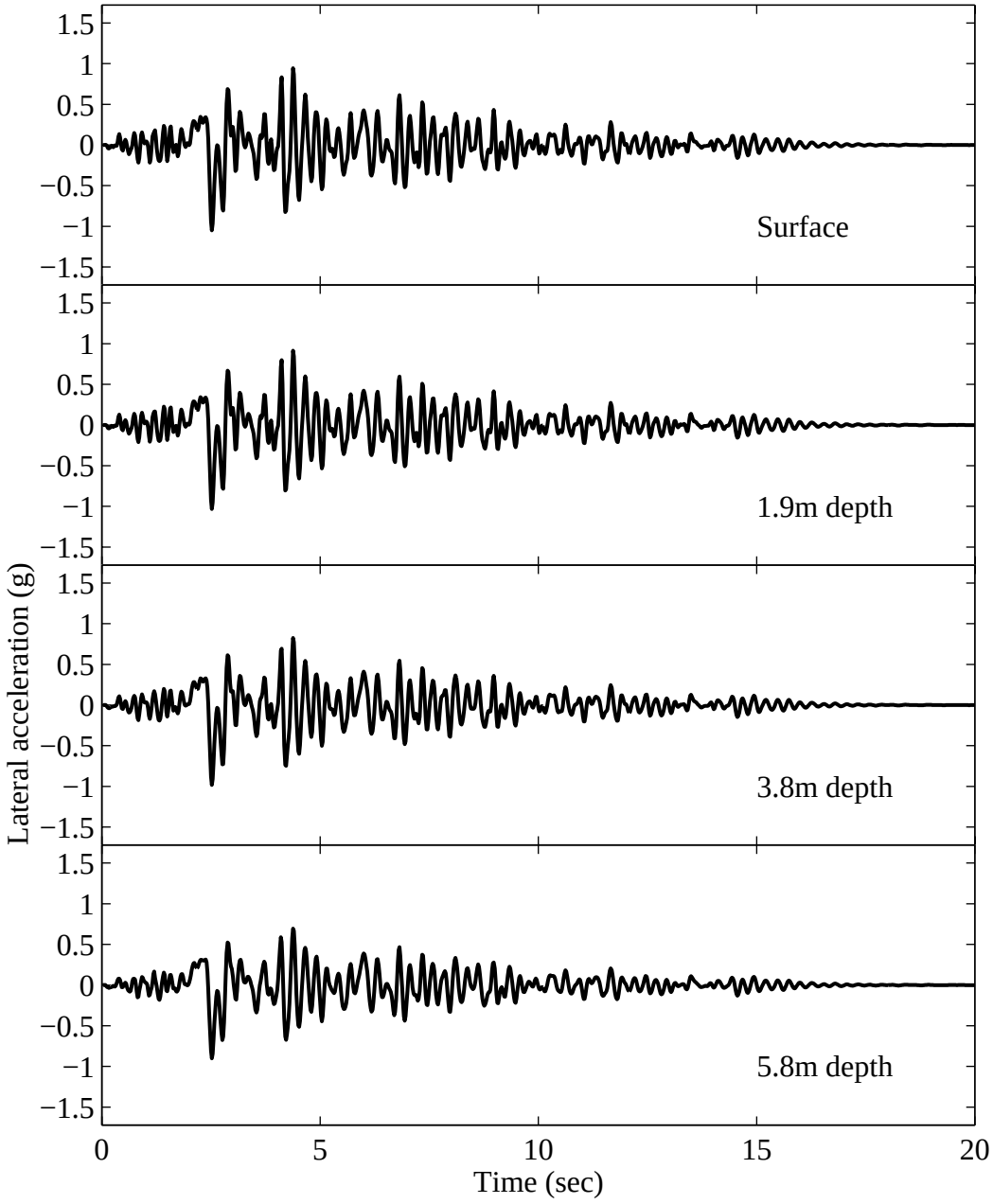

Figure 7.16: Lateral acceleration time histories at free field for the waterside for Case W2L.

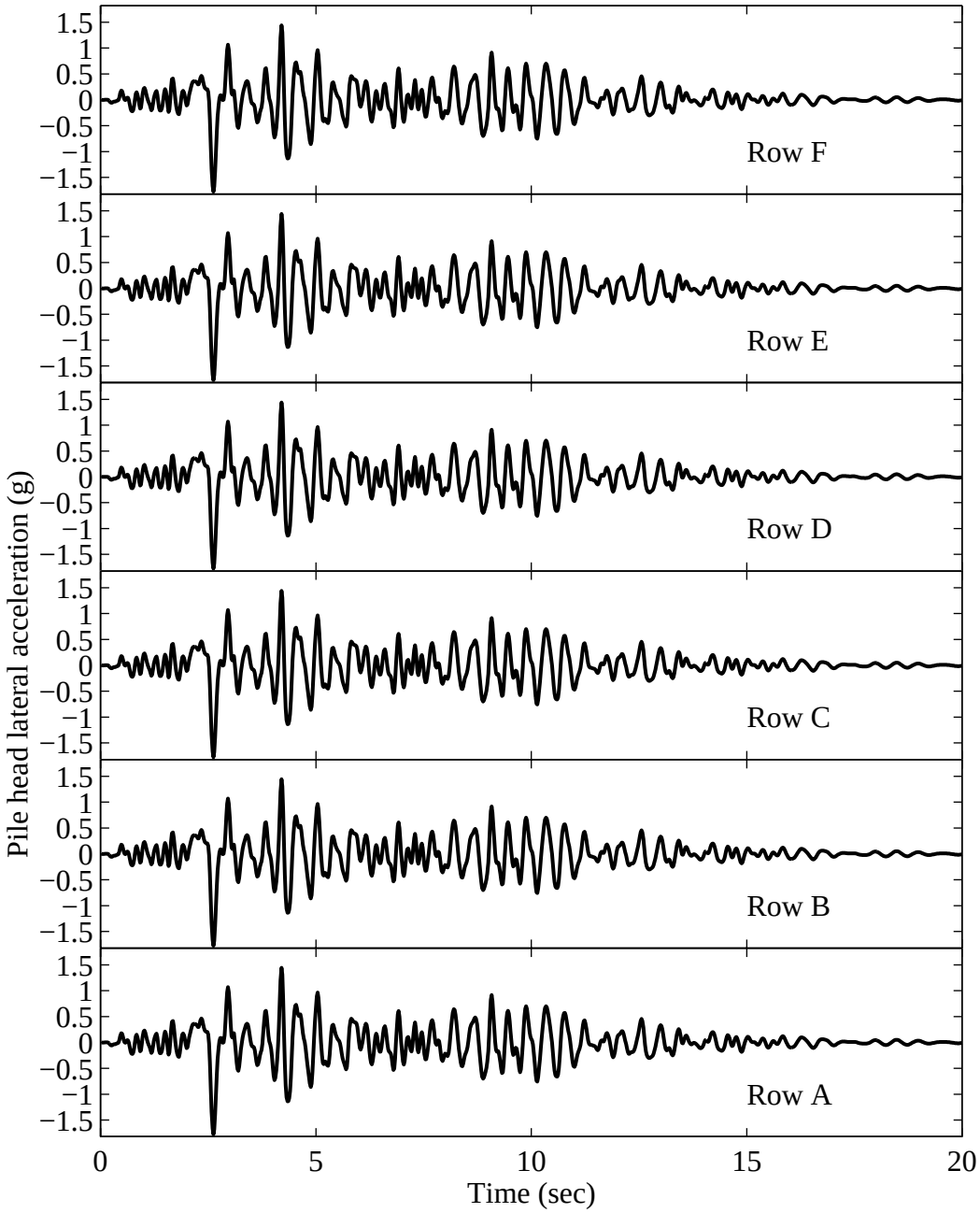

Figure 7.17: Lateral acceleration time histories of pile heads for Case W2L.

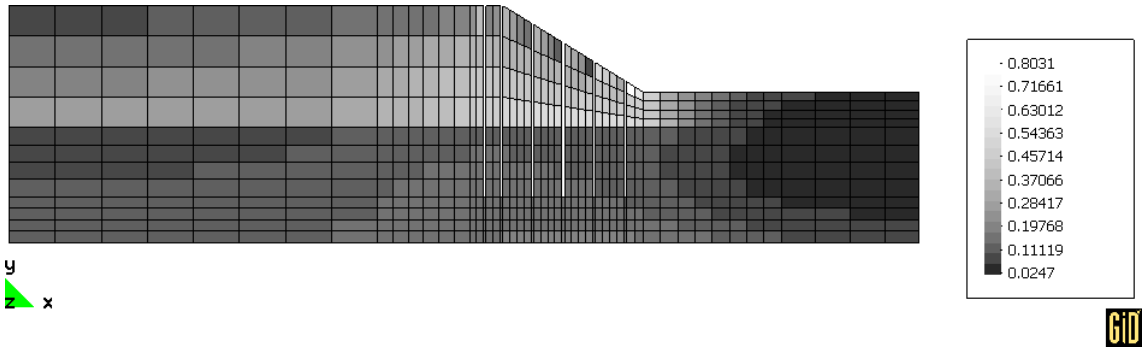

(a) Before shaking (elevation view)

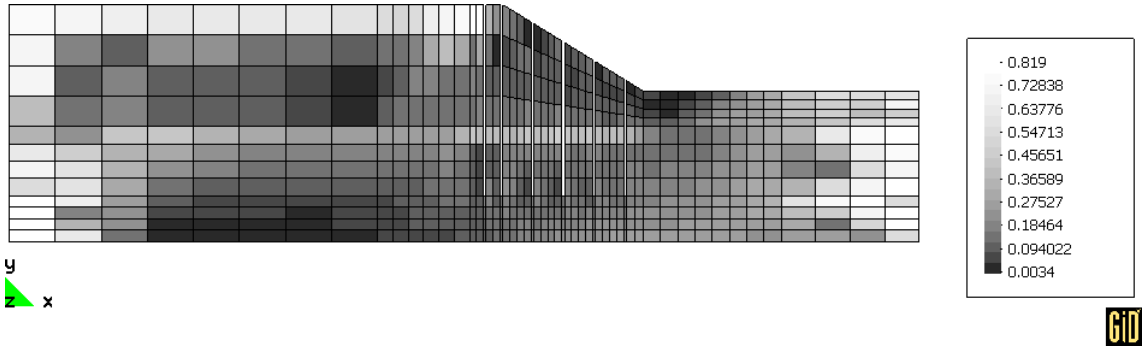

(b) After shaking (elevation view)

Figure 7.18: Stress ratio distribution before and after shaking for Case W2L.

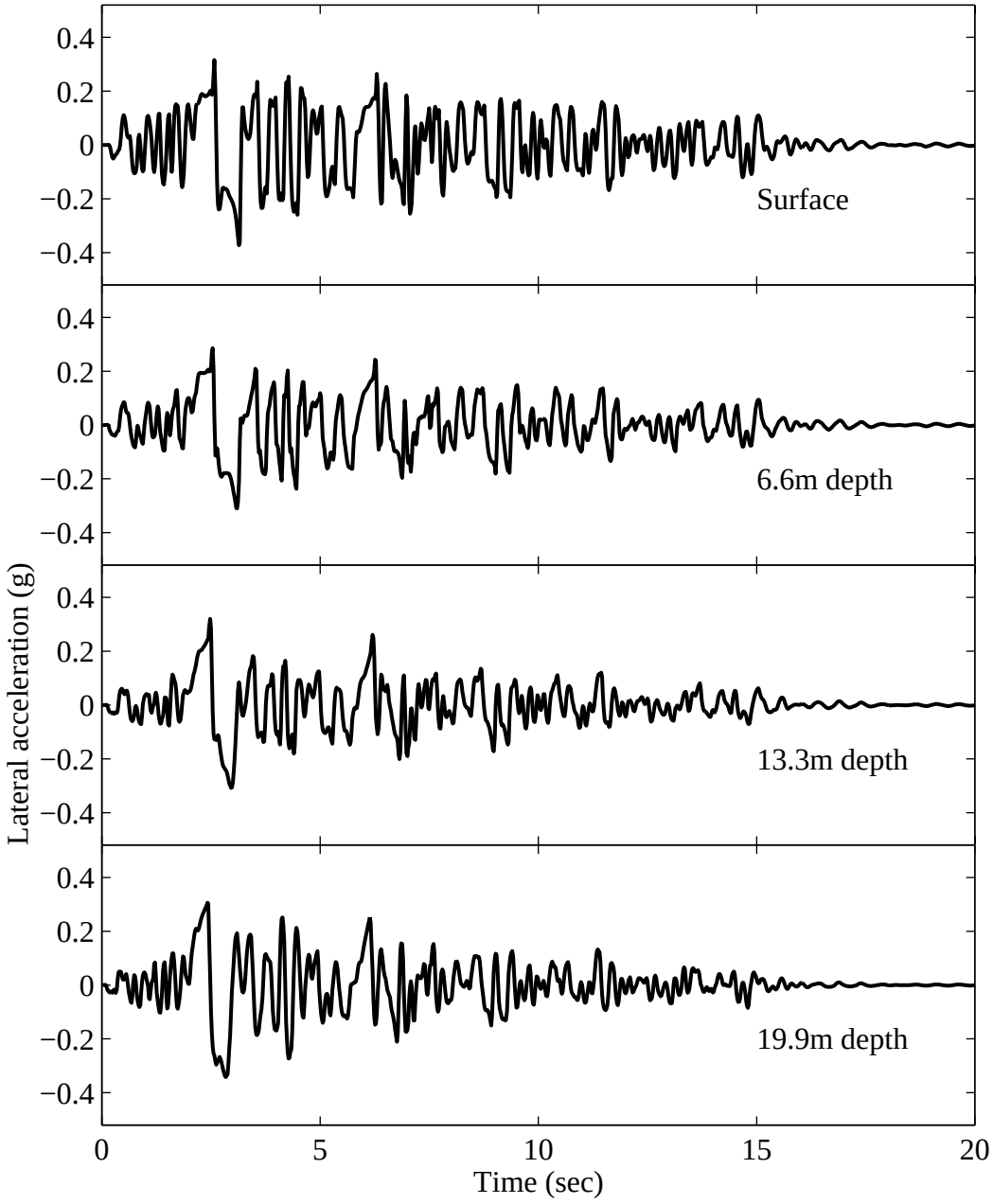

Figure 7.19: Lateral acceleration time histories at Location A for Case W2N.

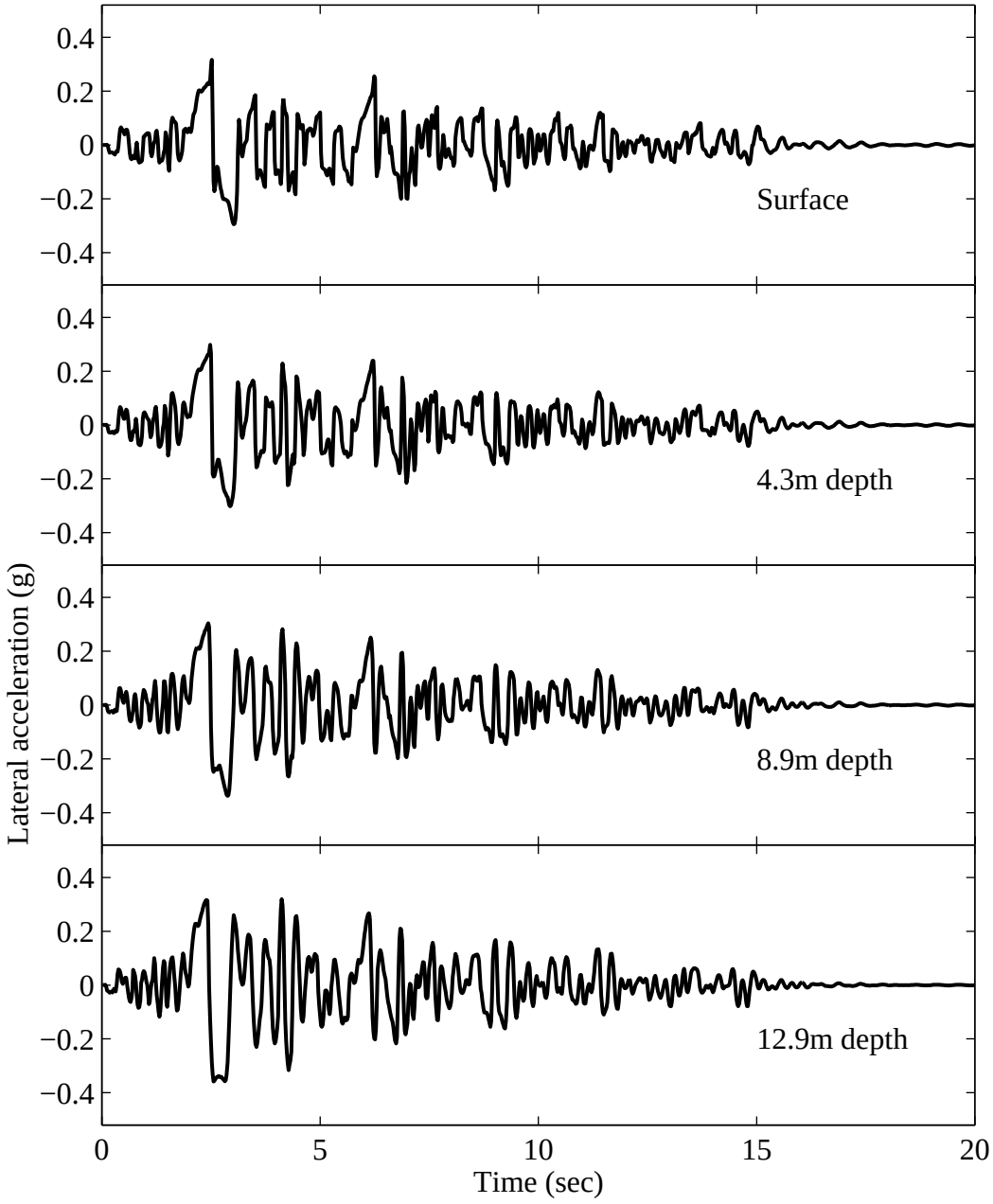

Figure 7.20: Lateral acceleration time histories at Location B for Case W2N.

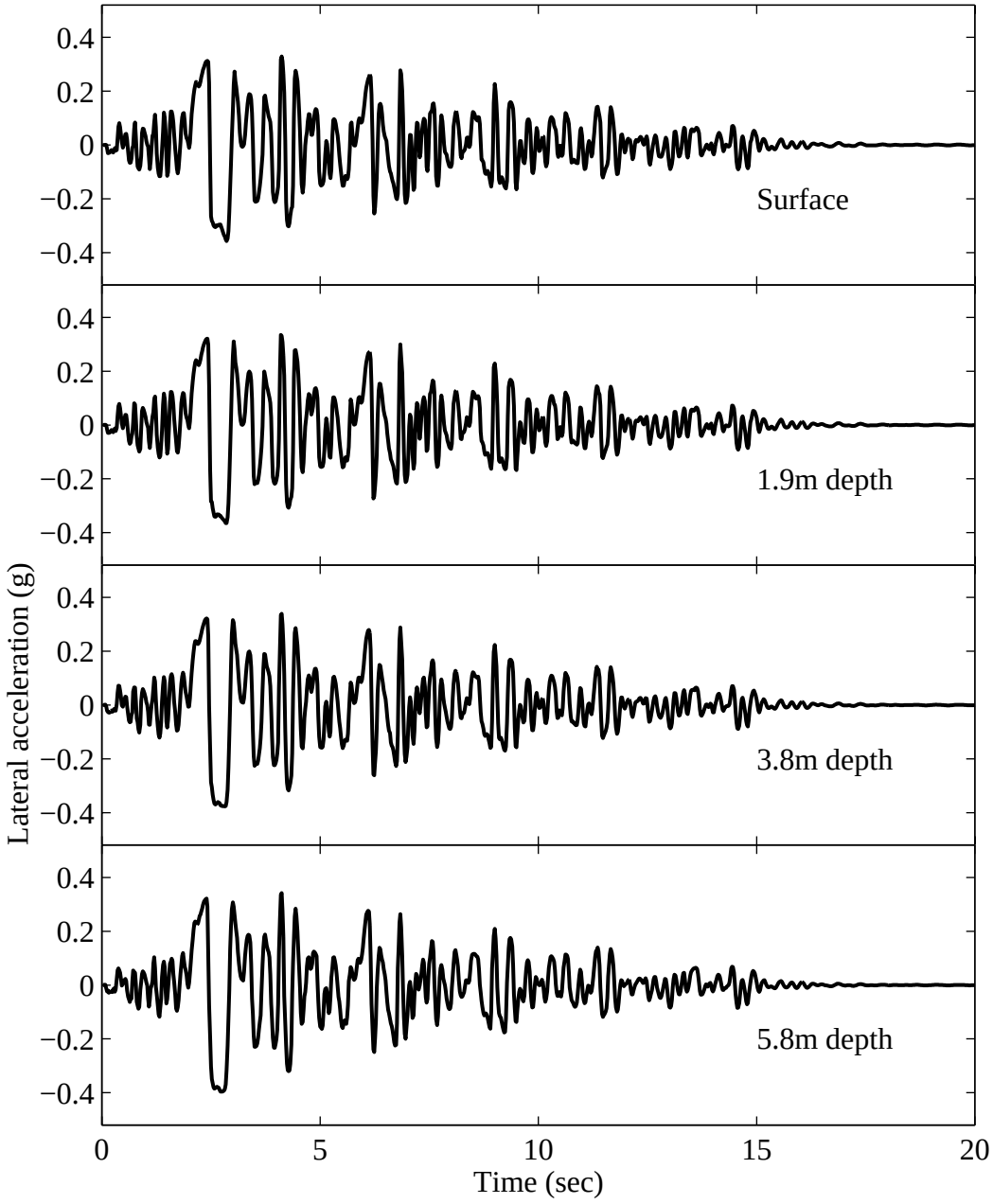

Figure 7.21: Lateral acceleration time histories at Location C for Case W2N.

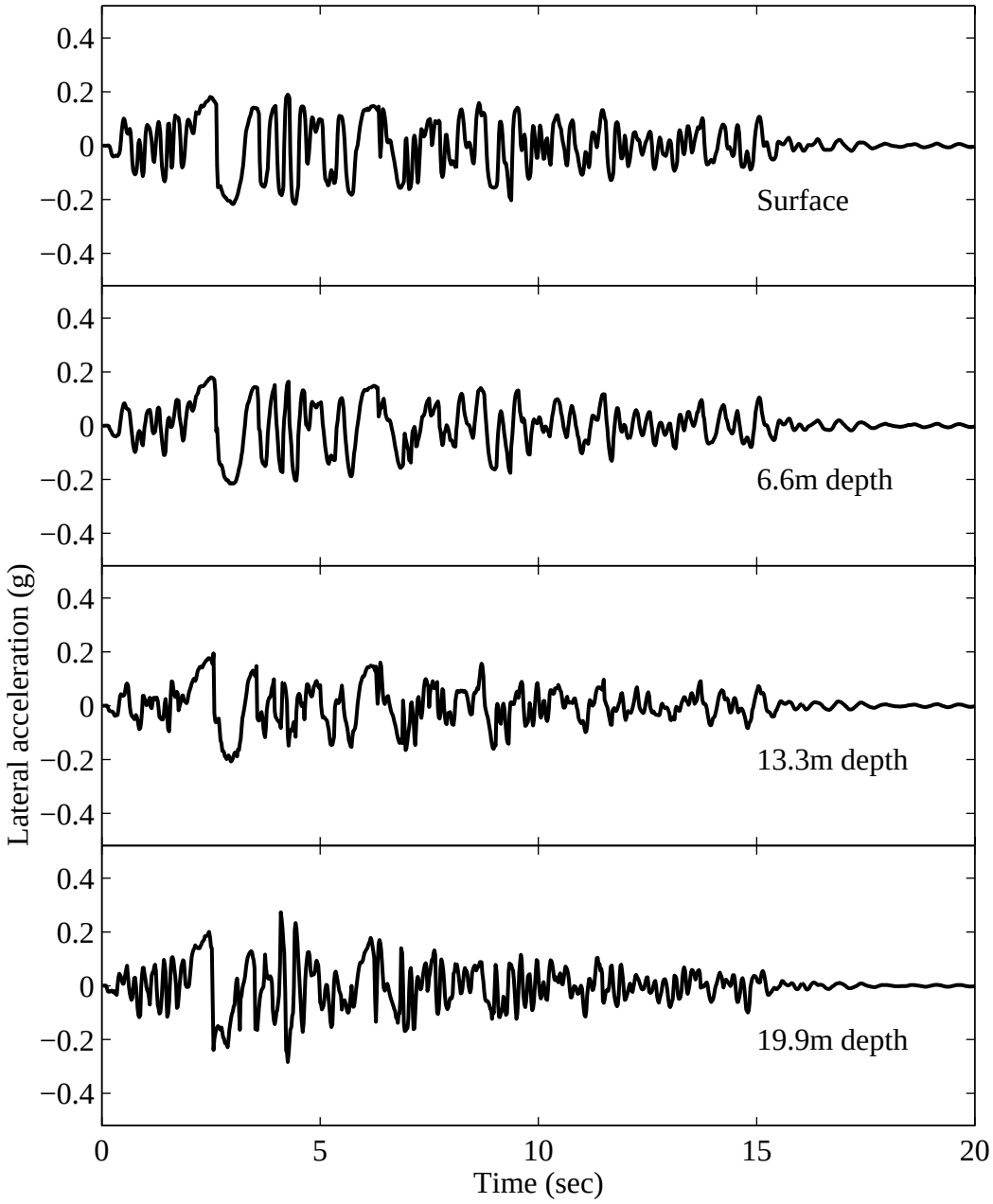

Figure 7.22: Lateral acceleration time histories at free field for the landside for Case W2N.

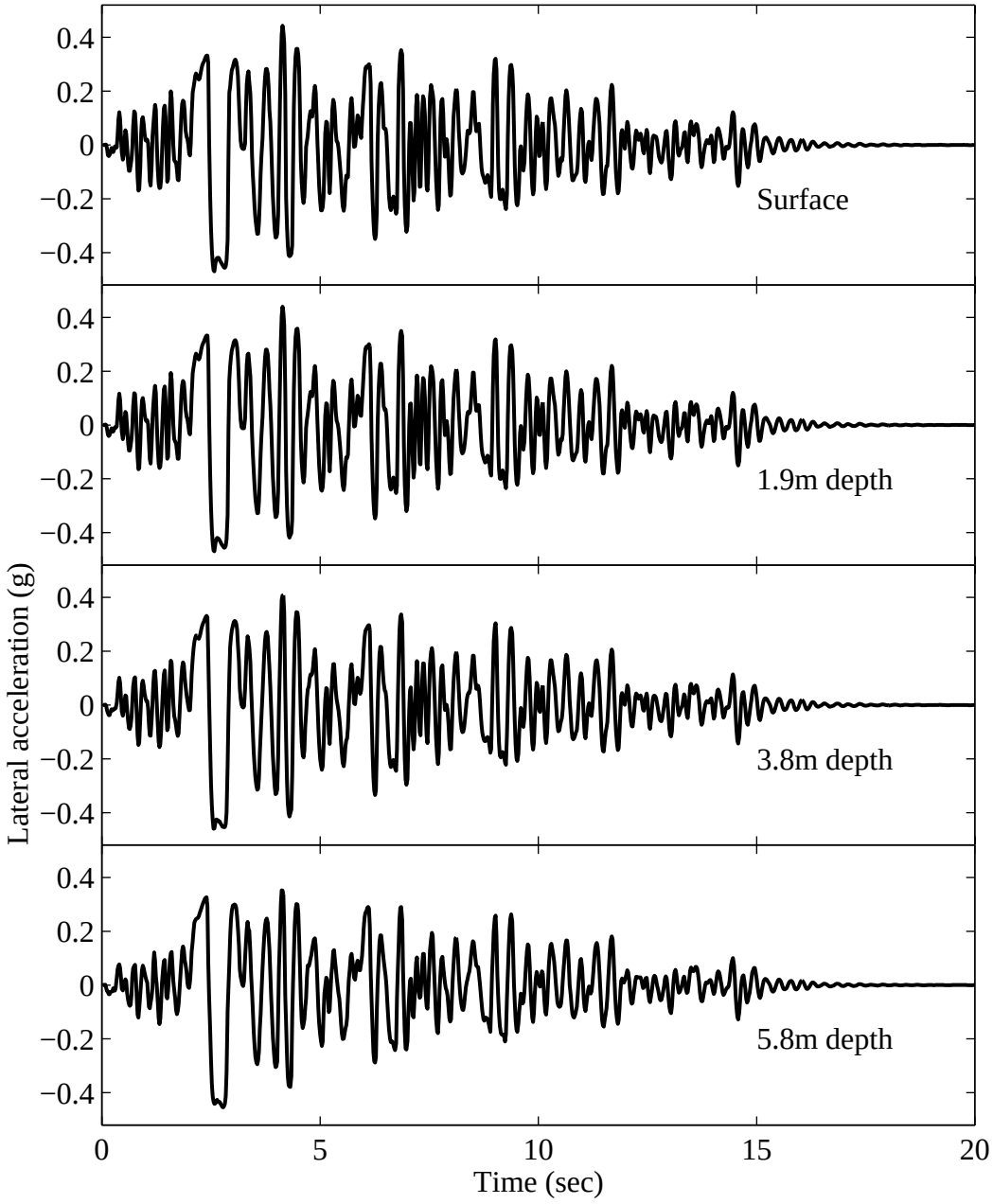

Figure 7.23: Lateral acceleration time histories at free field for the waterside for Case W2N.

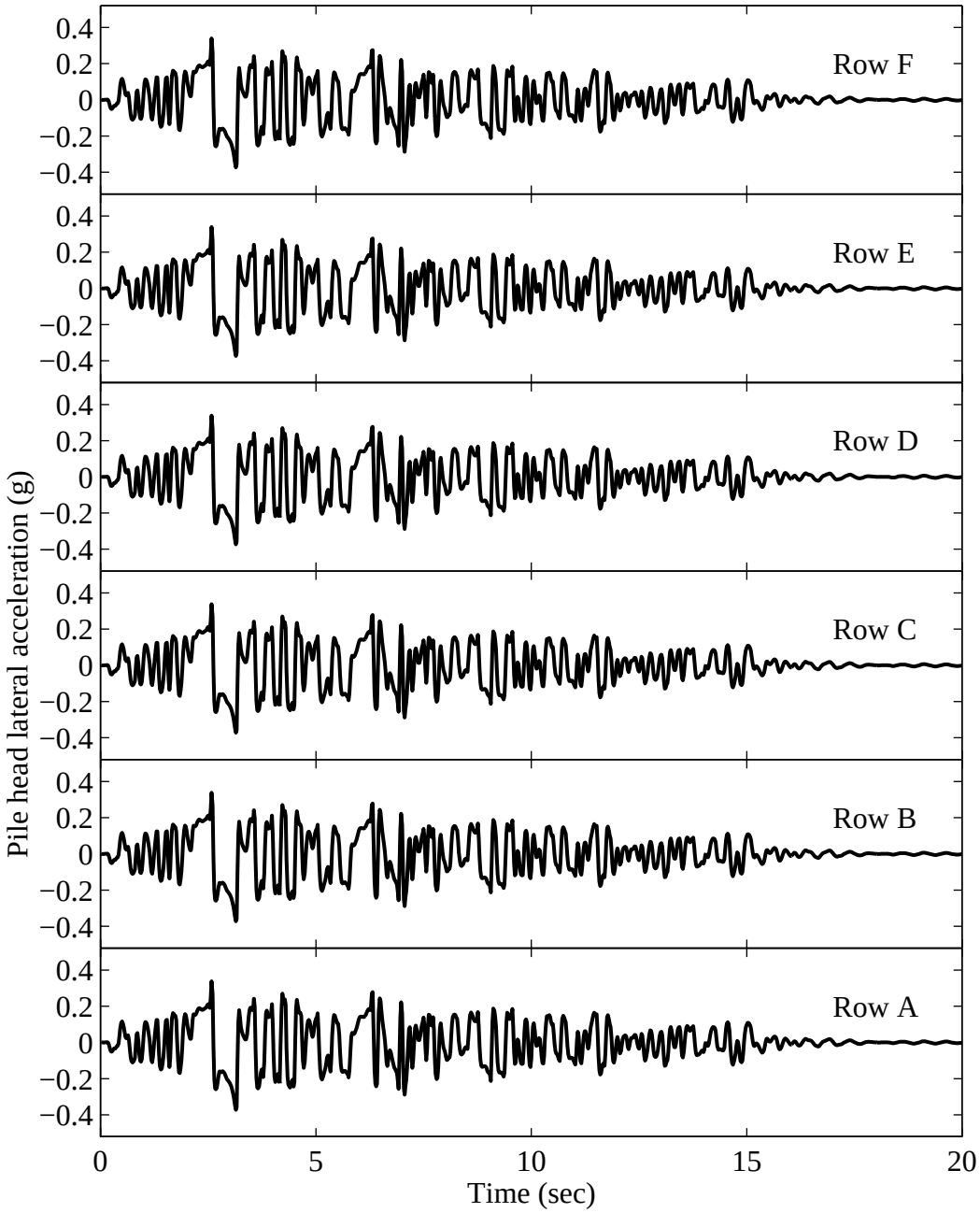

Figure 7.24: Lateral acceleration time histories at pile heads for Case W2N.

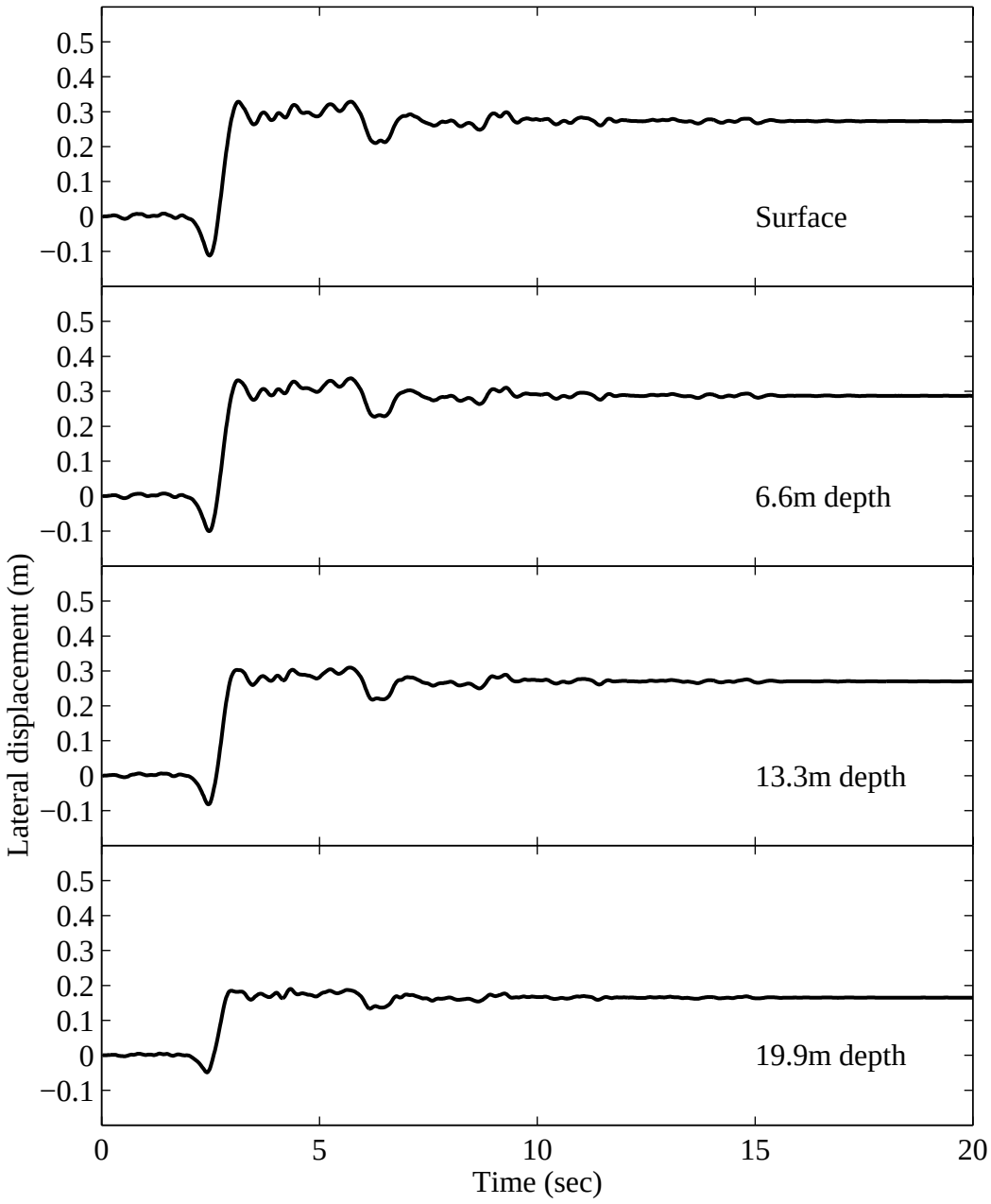

Figure 7.25: Lateral displacement time histories at Location A for Case W2N.

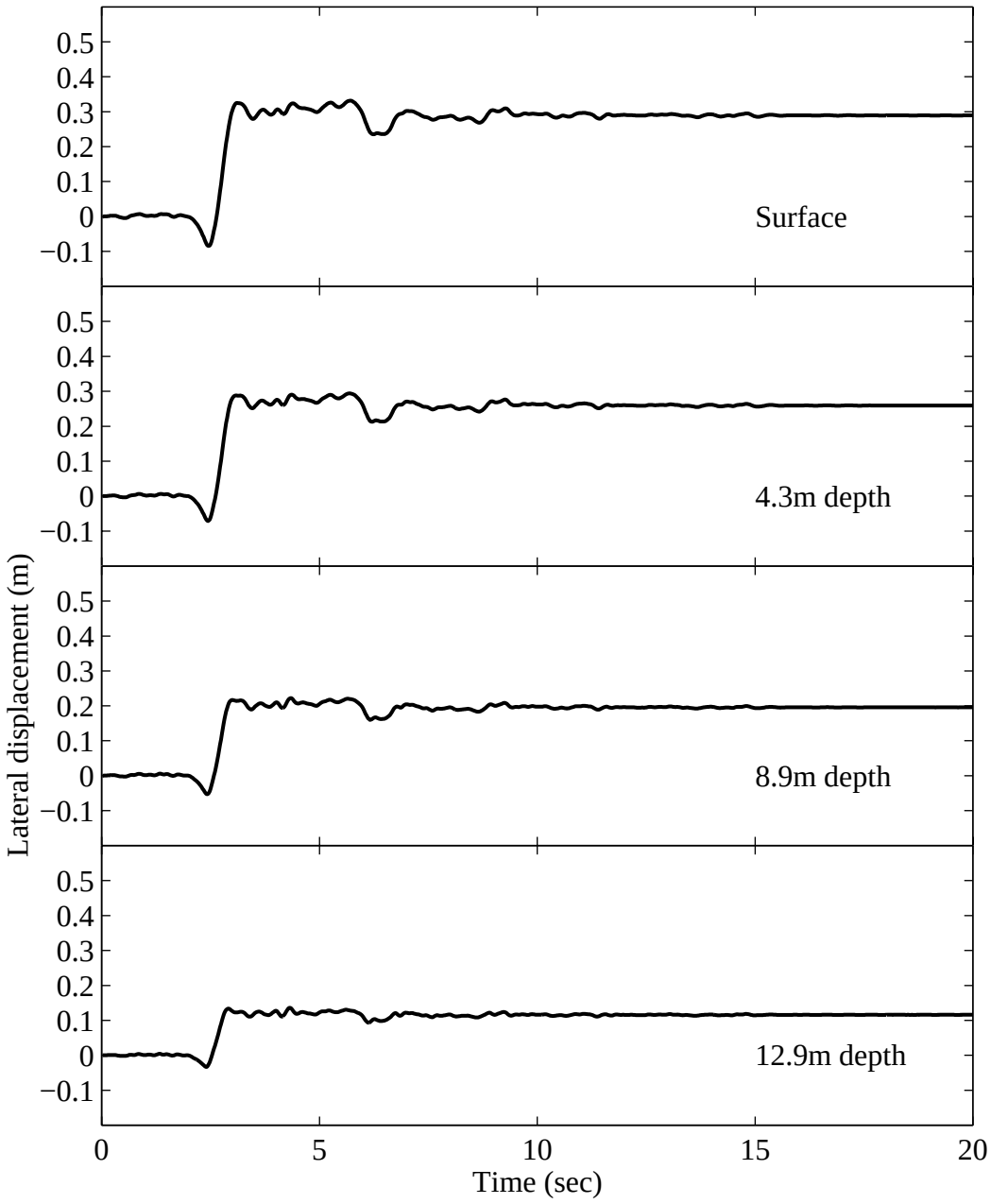

Figure 7.26: Lateral displacement time histories at Location B for Case W2N.

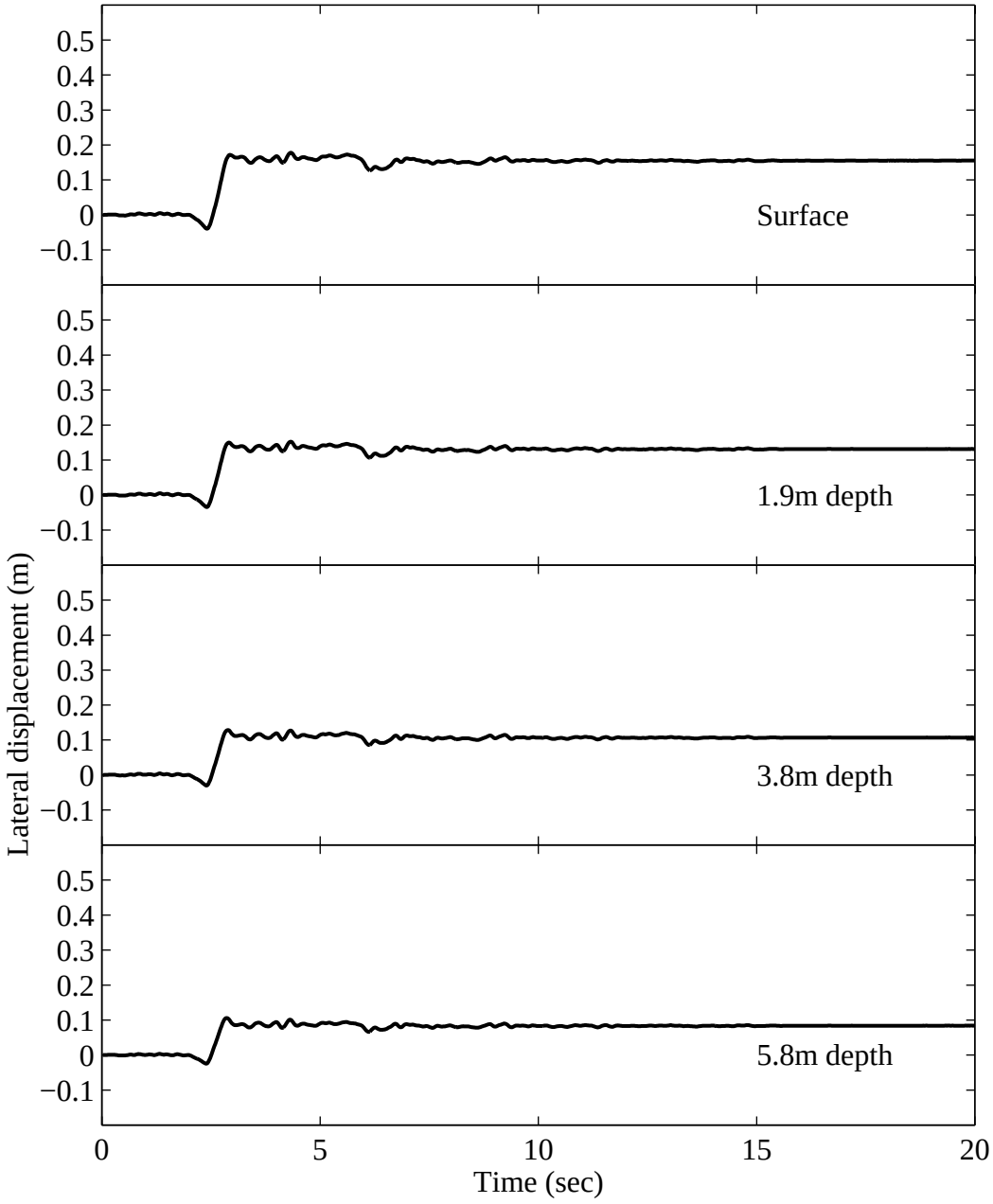

Figure 7.27: Lateral displacement time histories at Location C for Case W2N.

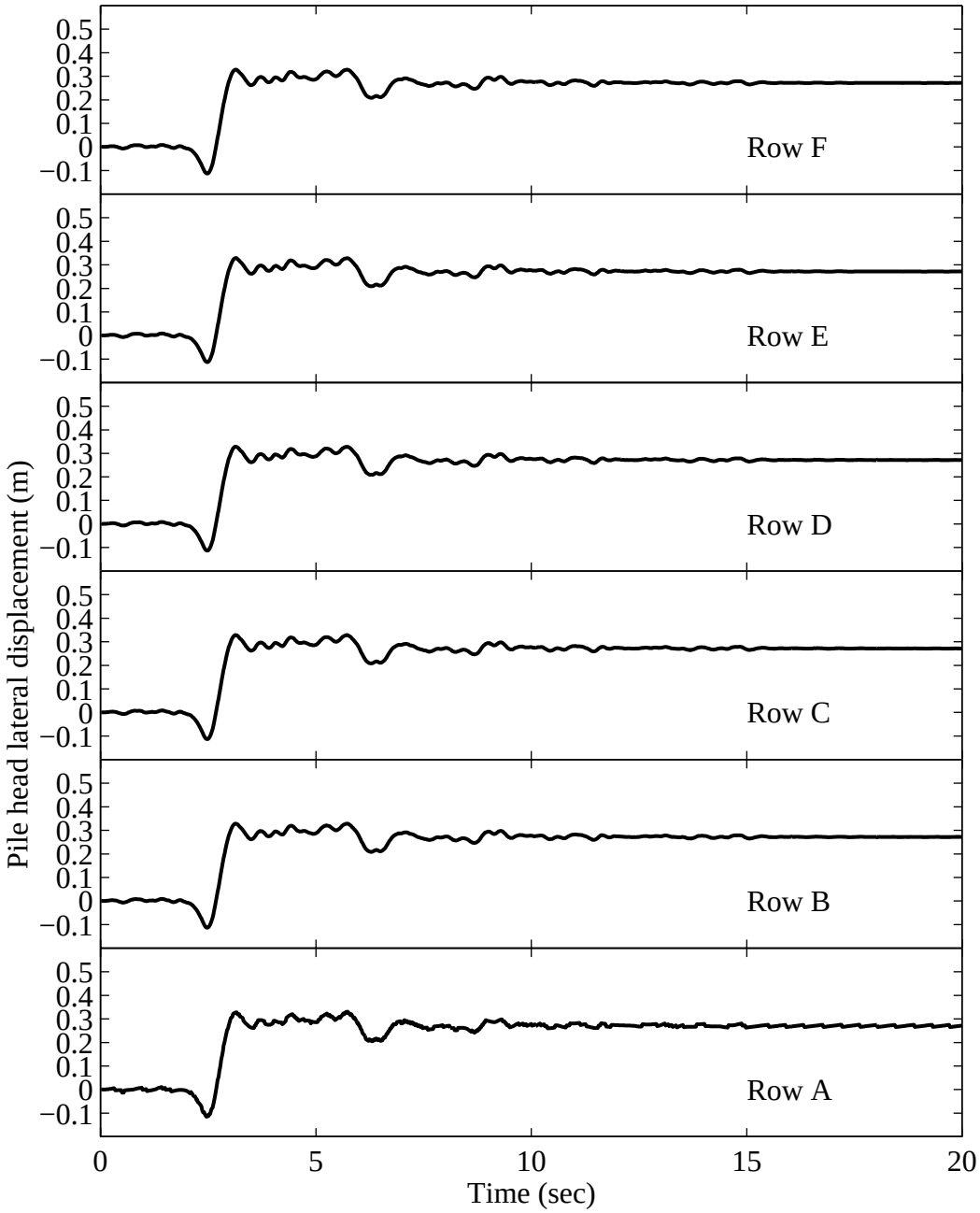

Figure 7.28: Lateral displacement time histories at pile heads for Case W2N.

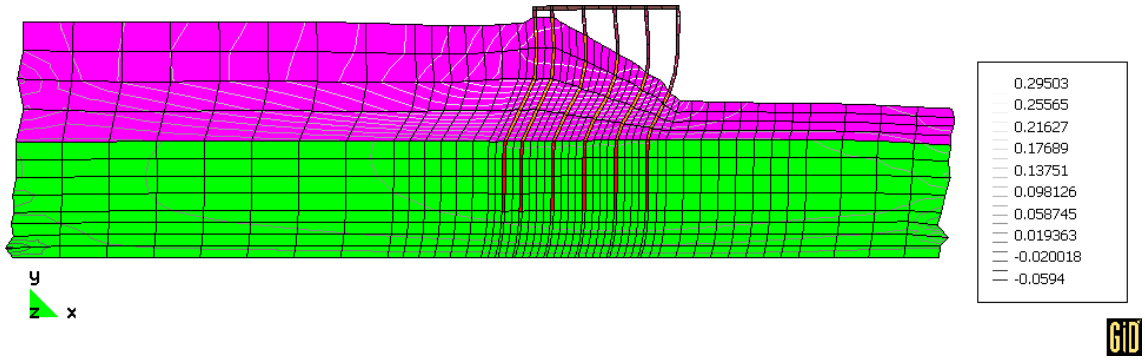

Figure 7.29: Final deformed mesh (factor of 30; contour lines show lateral displacement; unit: m) for Case W2N (elevation view).

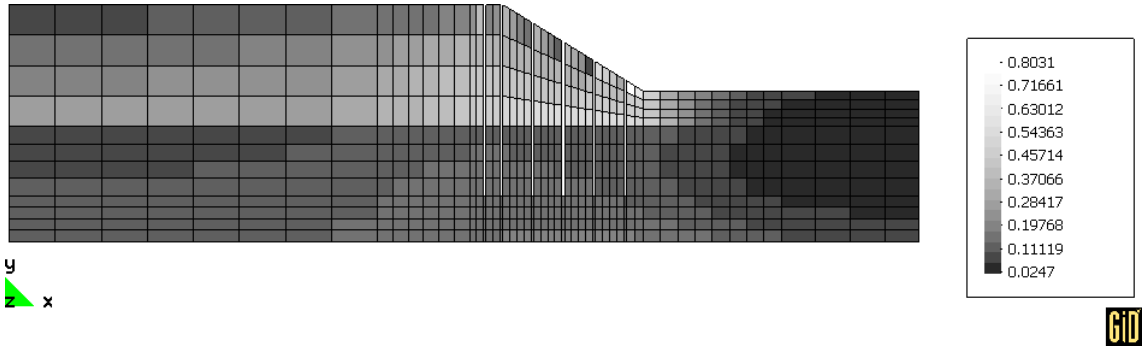

(a) Before shaking (elevation view)

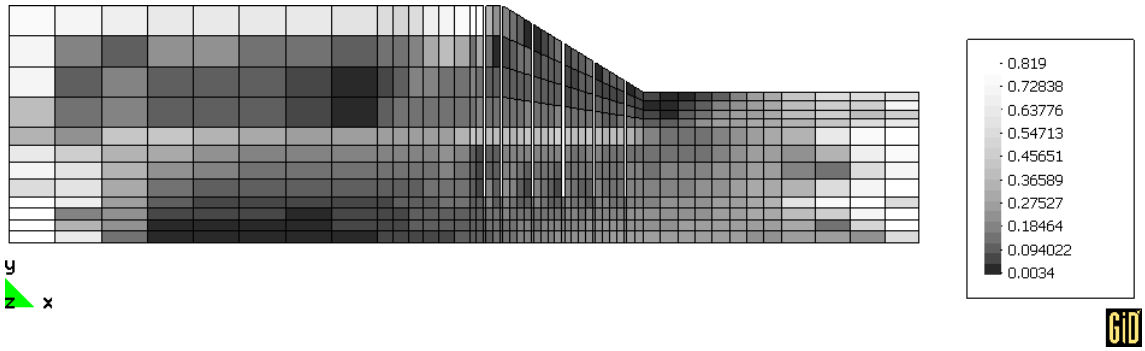

(b) After shaking (elevation view)

Figure 7.30: Stress ratio distribution for Case W2N before and after shaking.

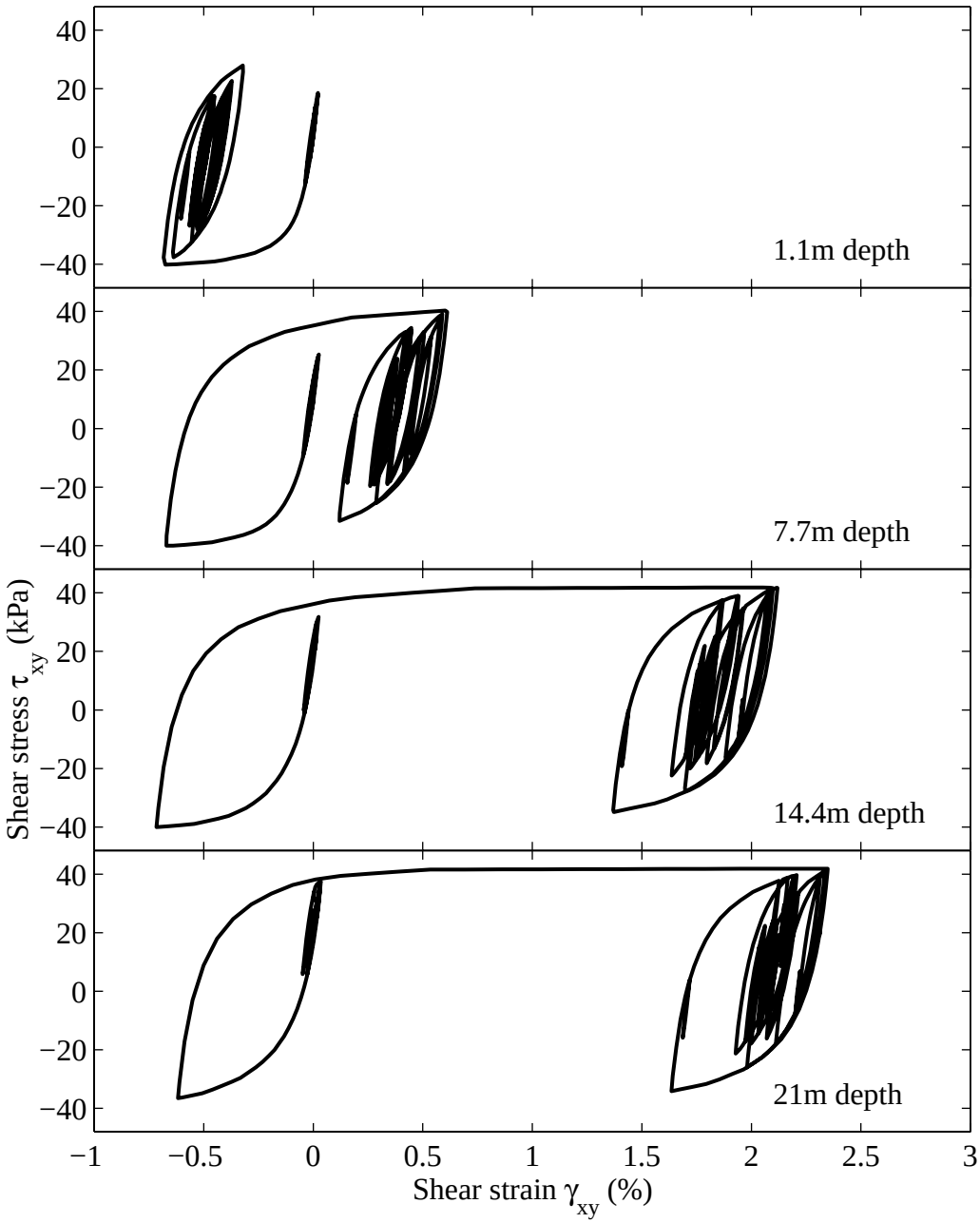

Figure 7.31: Shear stress-strain response at Location A for Case W2N.

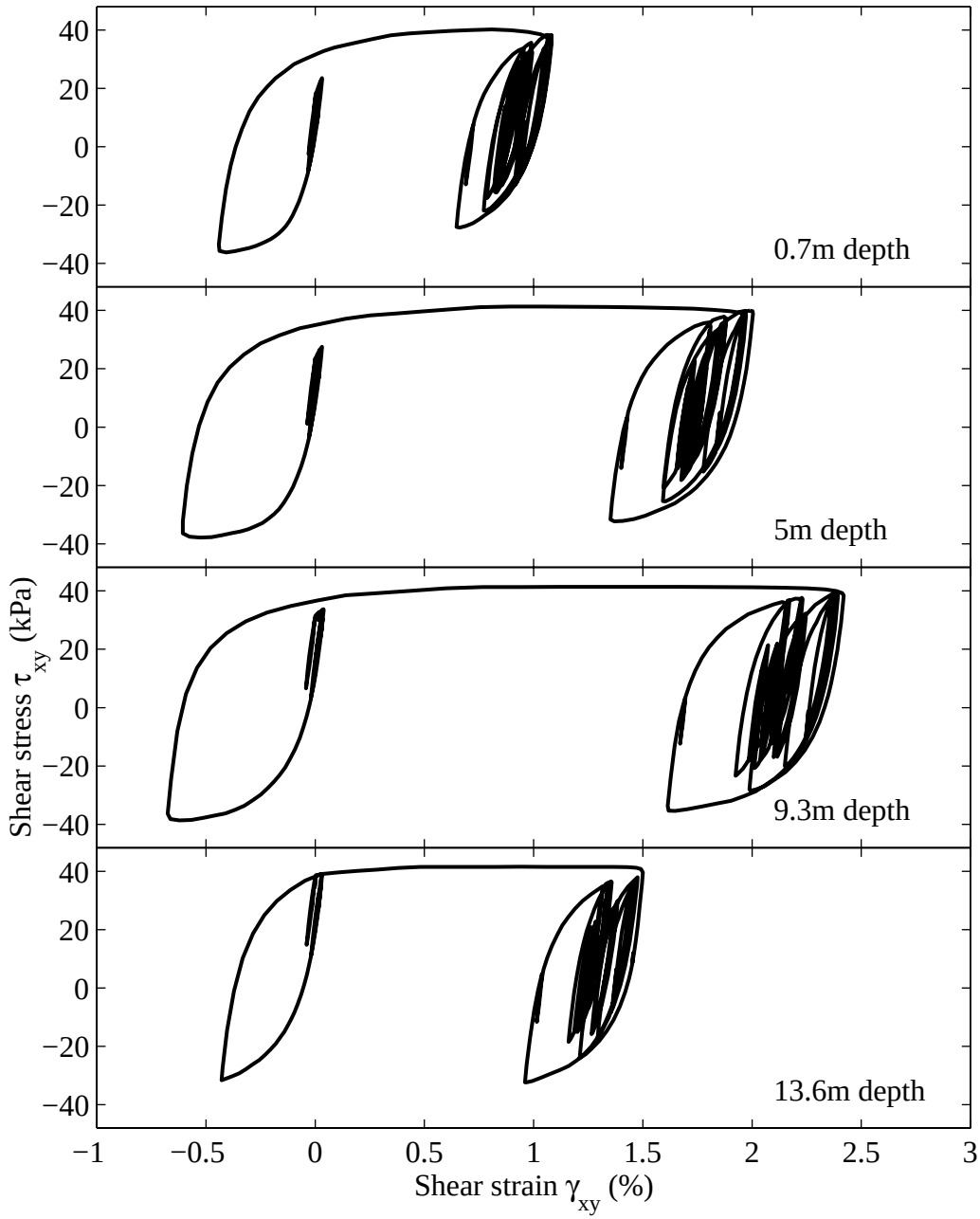

Figure 7.32: Shear stress-strain response at Location B for Case W2N.

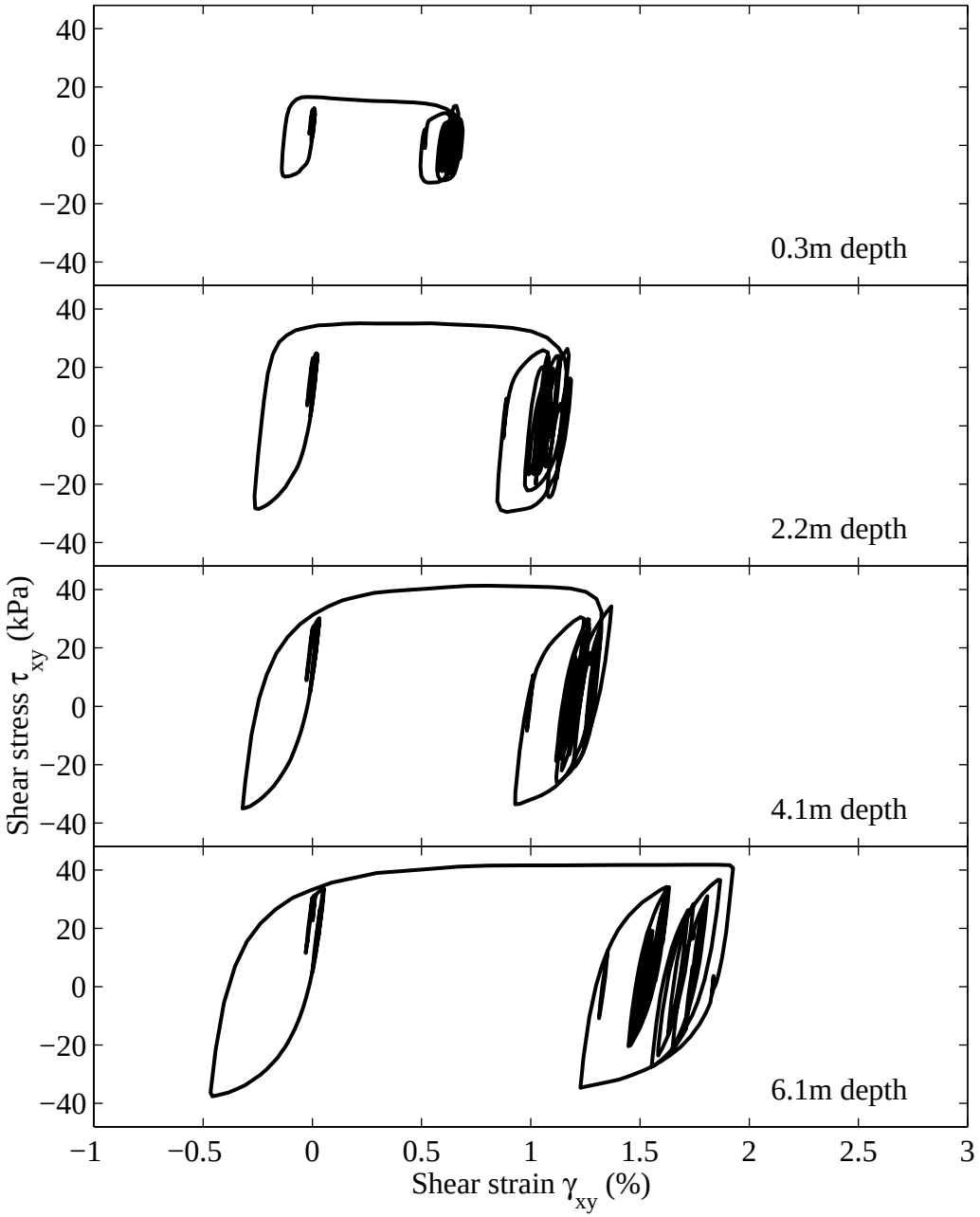

Figure 7.33: Shear stress-strain response at Location C for Case W2N.

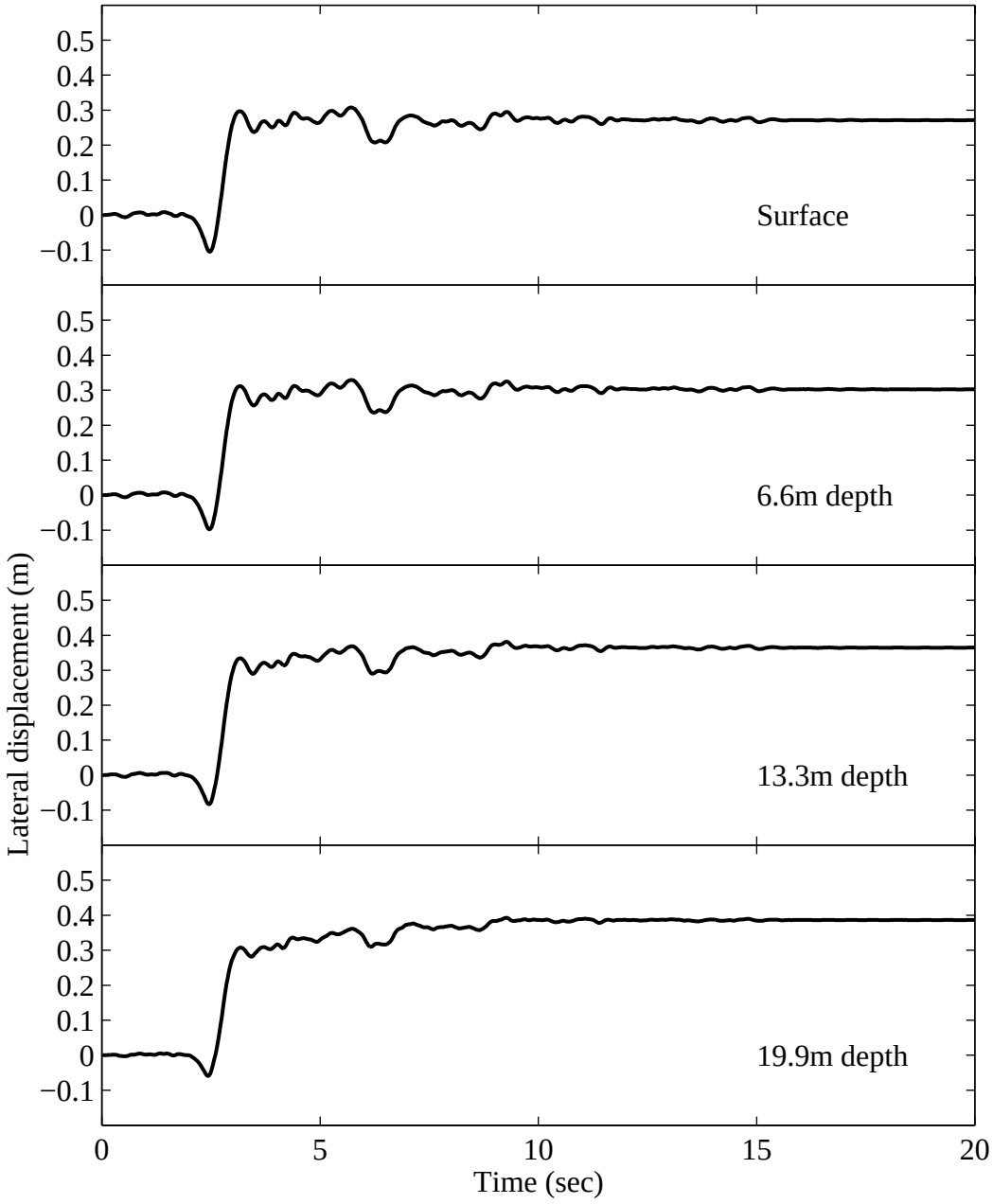

Figure 7.34: Lateral displacement time histories at Location A for Case C2N.

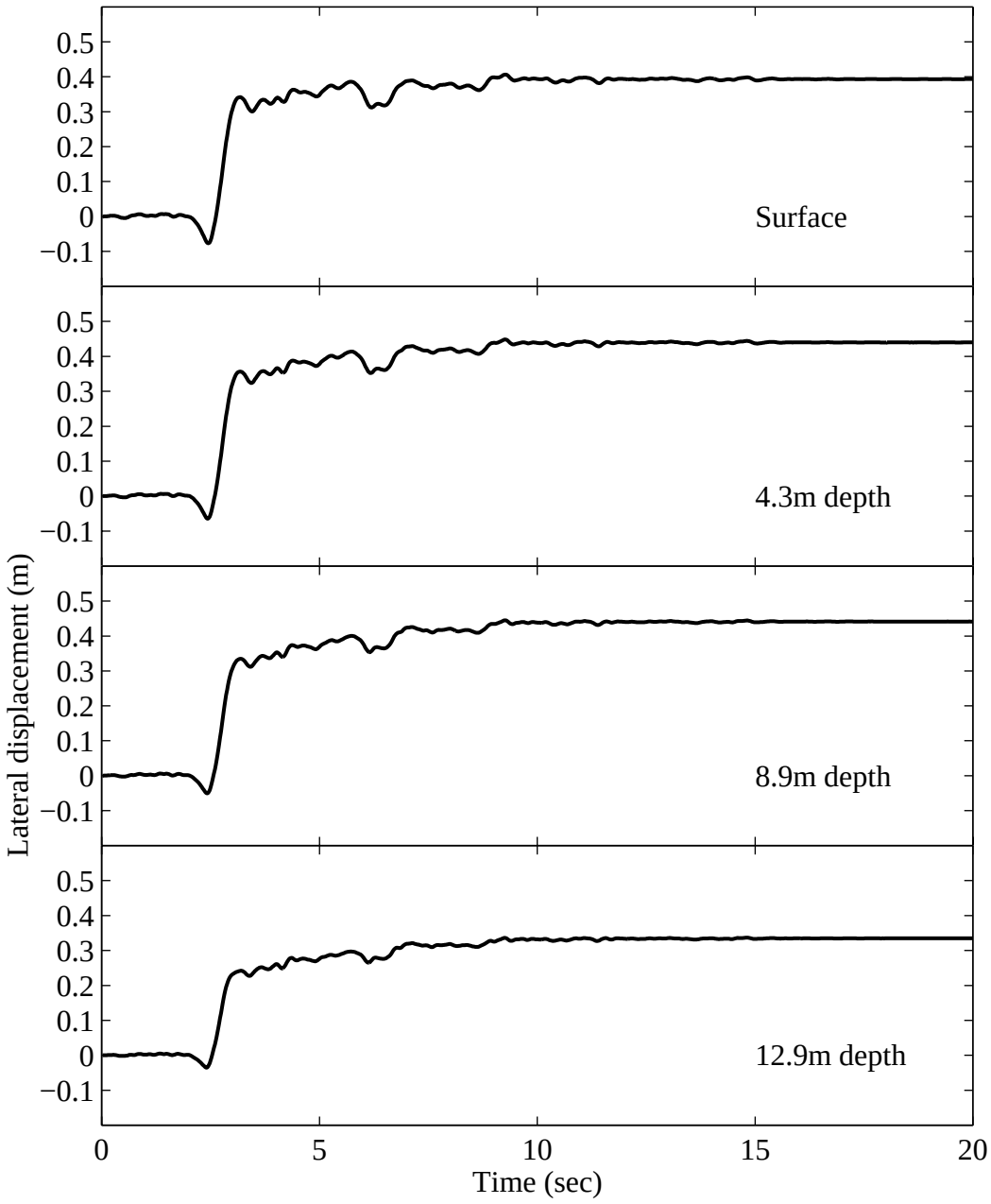

Figure 7.35: Lateral displacement time histories at Location B for Case C2N.

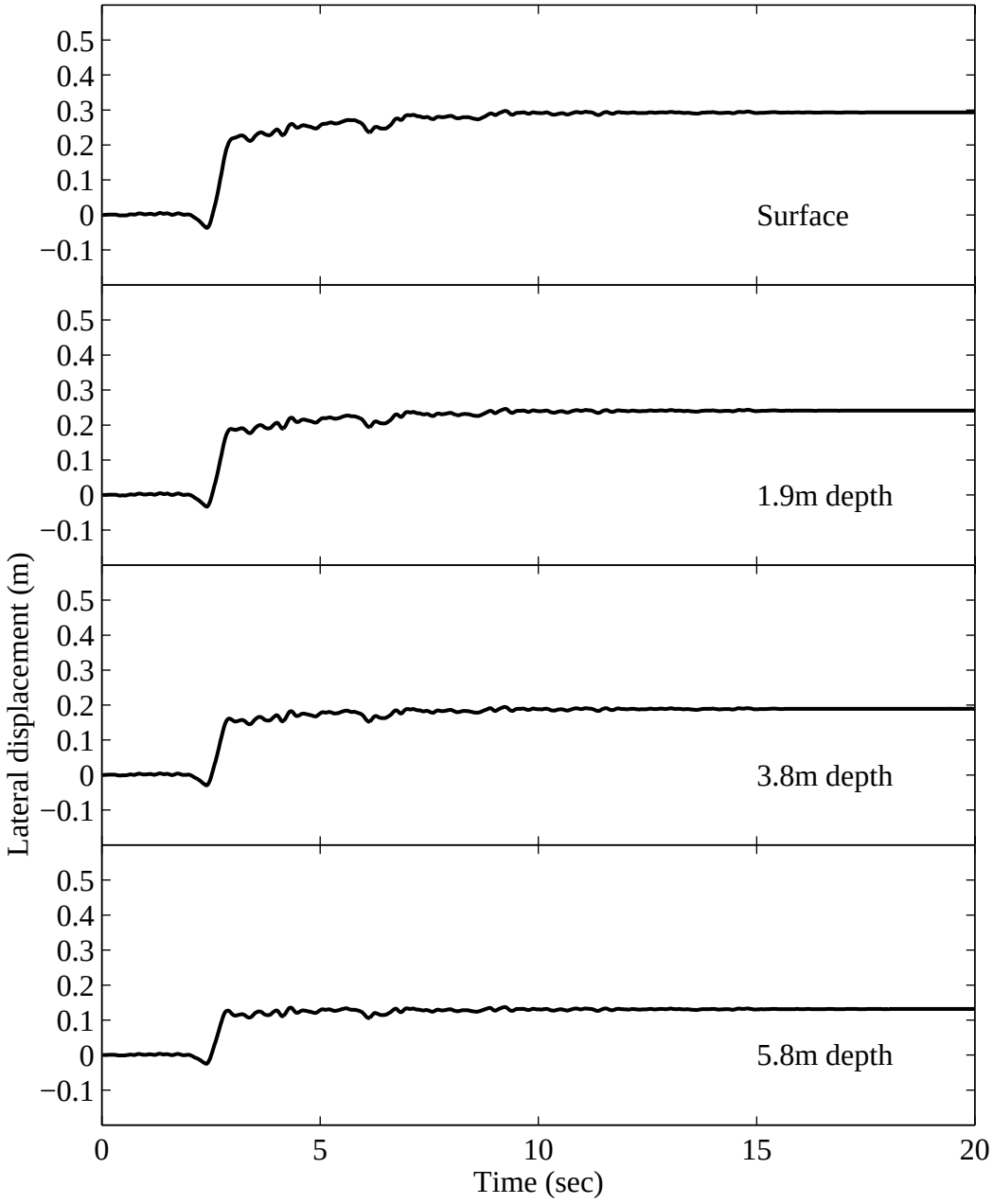

Figure 7.36: Lateral displacement time histories at Location C for Case C2N.

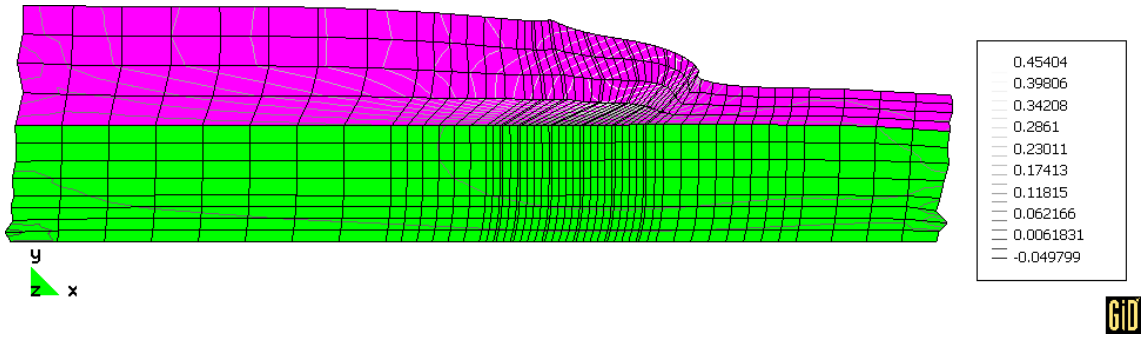

Figure 7.37: Final deformed mesh (factor of 30; contour lines show lateral displacement; unit: m) for Case C2N (elevation view).

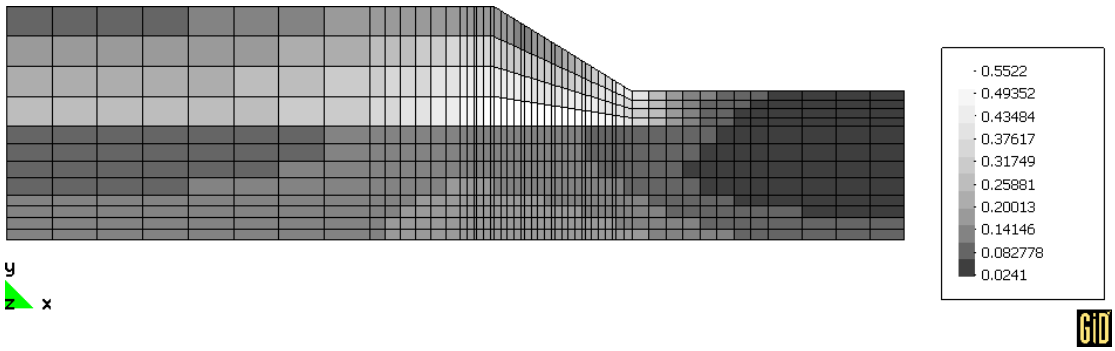

(a) Before shaking (elevation view)

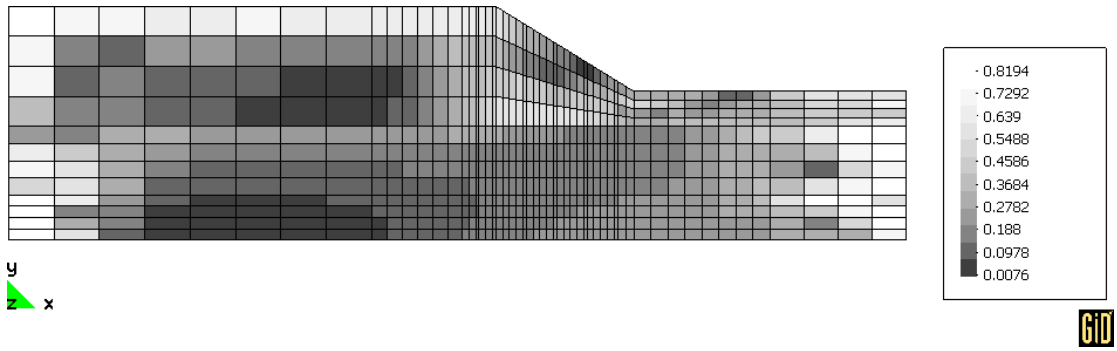

(b) After shaking (elevation view)

Figure 7.38: Stress ratio distribution for Case C2N before and after shaking.

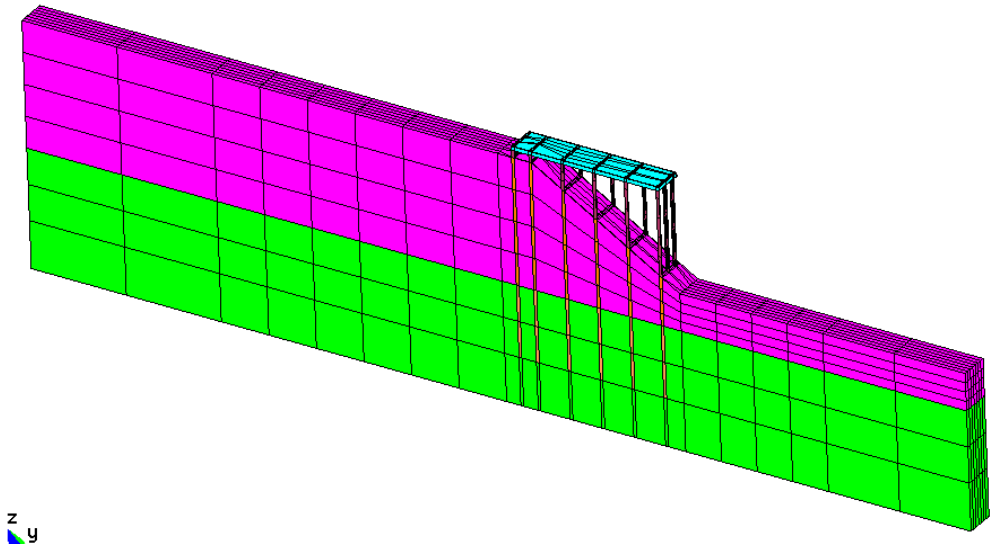

(a) Cases W3L-C & W3N-C

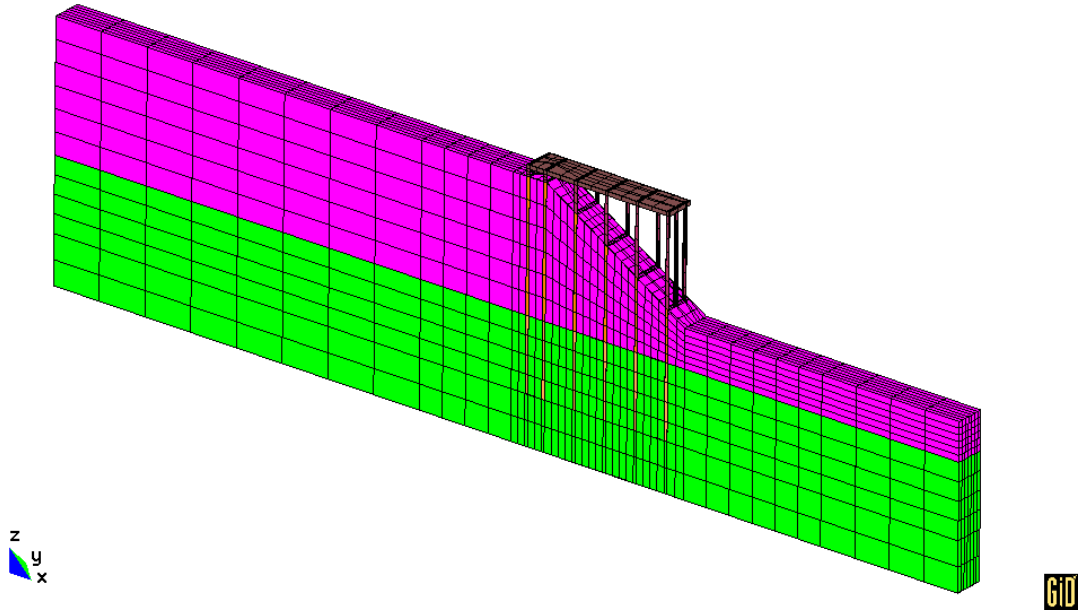

(b) Cases W3L-M & W3N-M

Figure 7.39: FE meshes of 3D wharf simulations (isometric view).

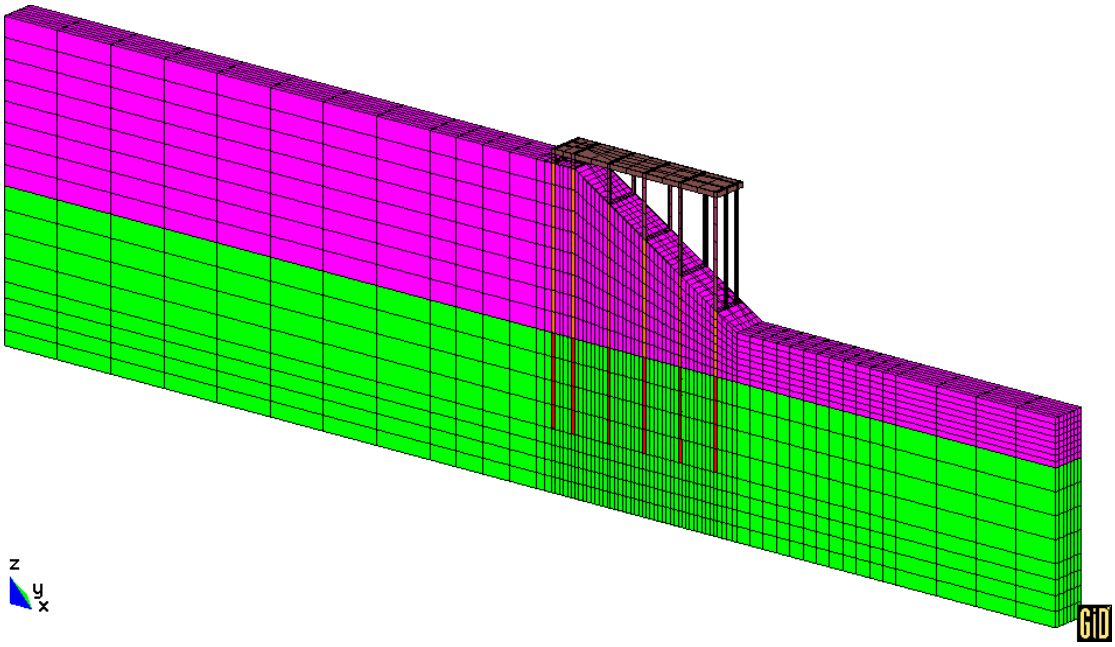

(c) Cases W3L-F & W3N-F

Figure 7.39: (continued).

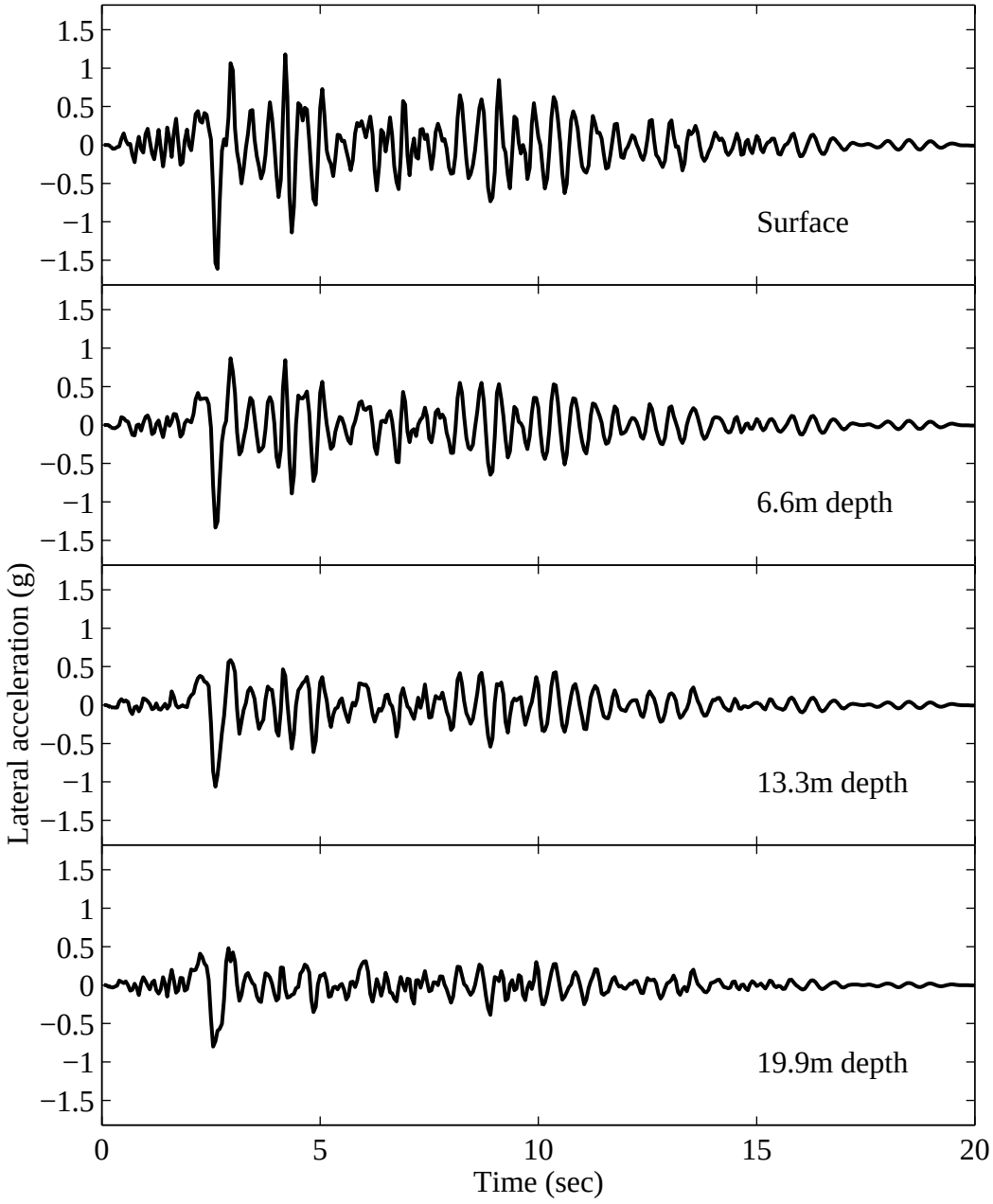

Figure 7.40: Longitudinal acceleration time histories at Location A for Case W3L-F.

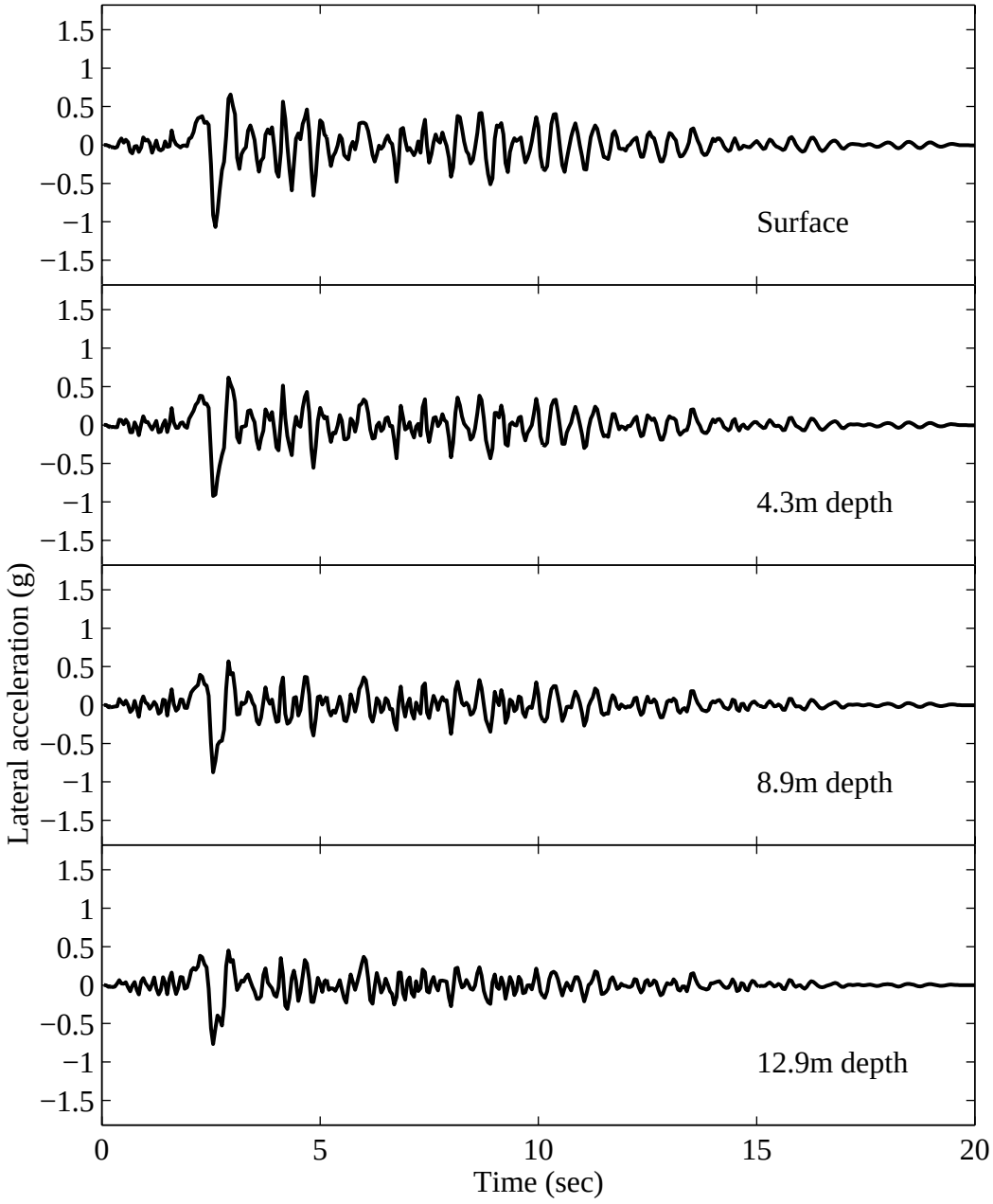

Figure 7.41: Longitudinal acceleration time histories at Location B for Case W3L-F.

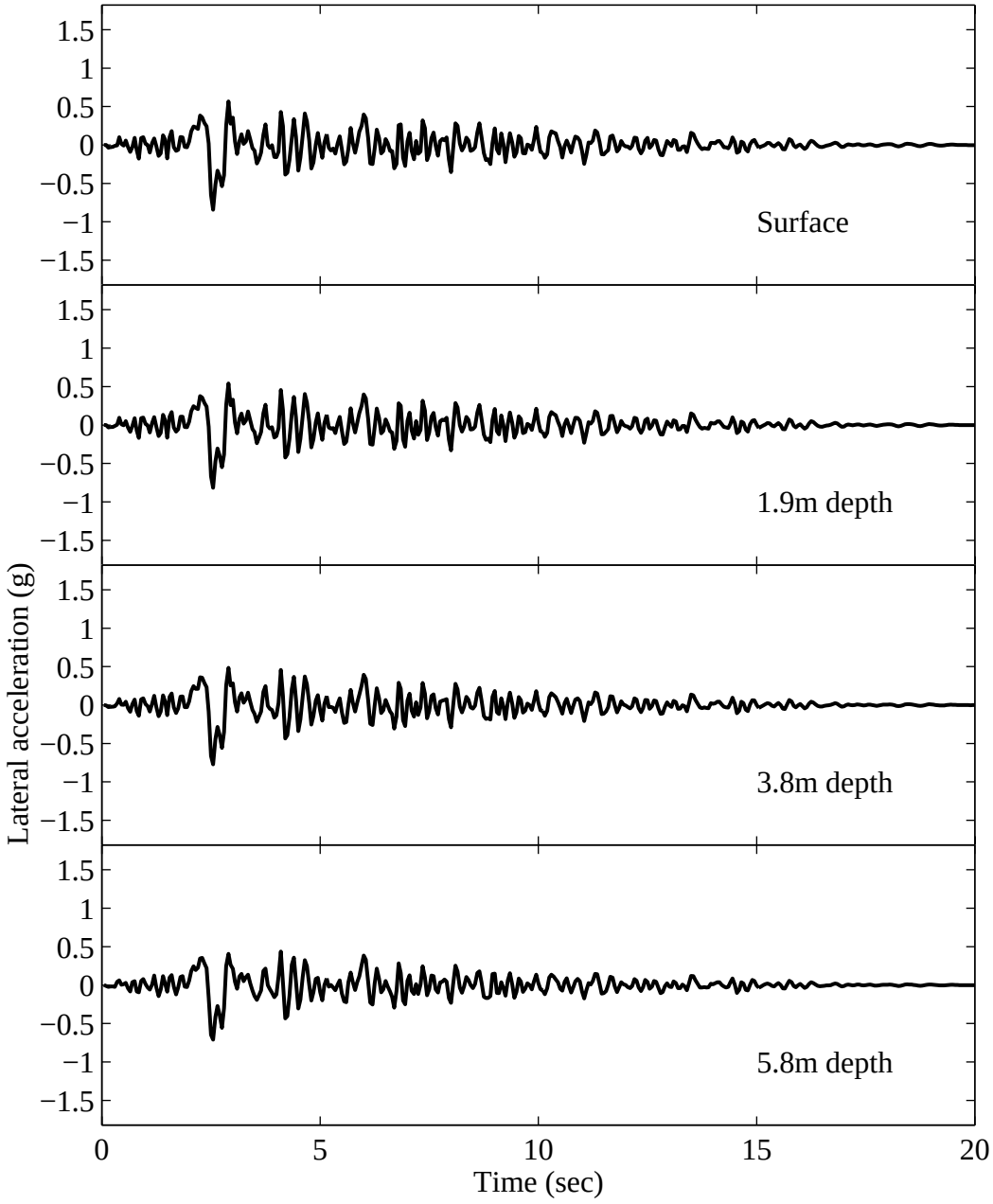

Figure 7.42: Longitudinal acceleration time histories at Location C for Case W3L-F.

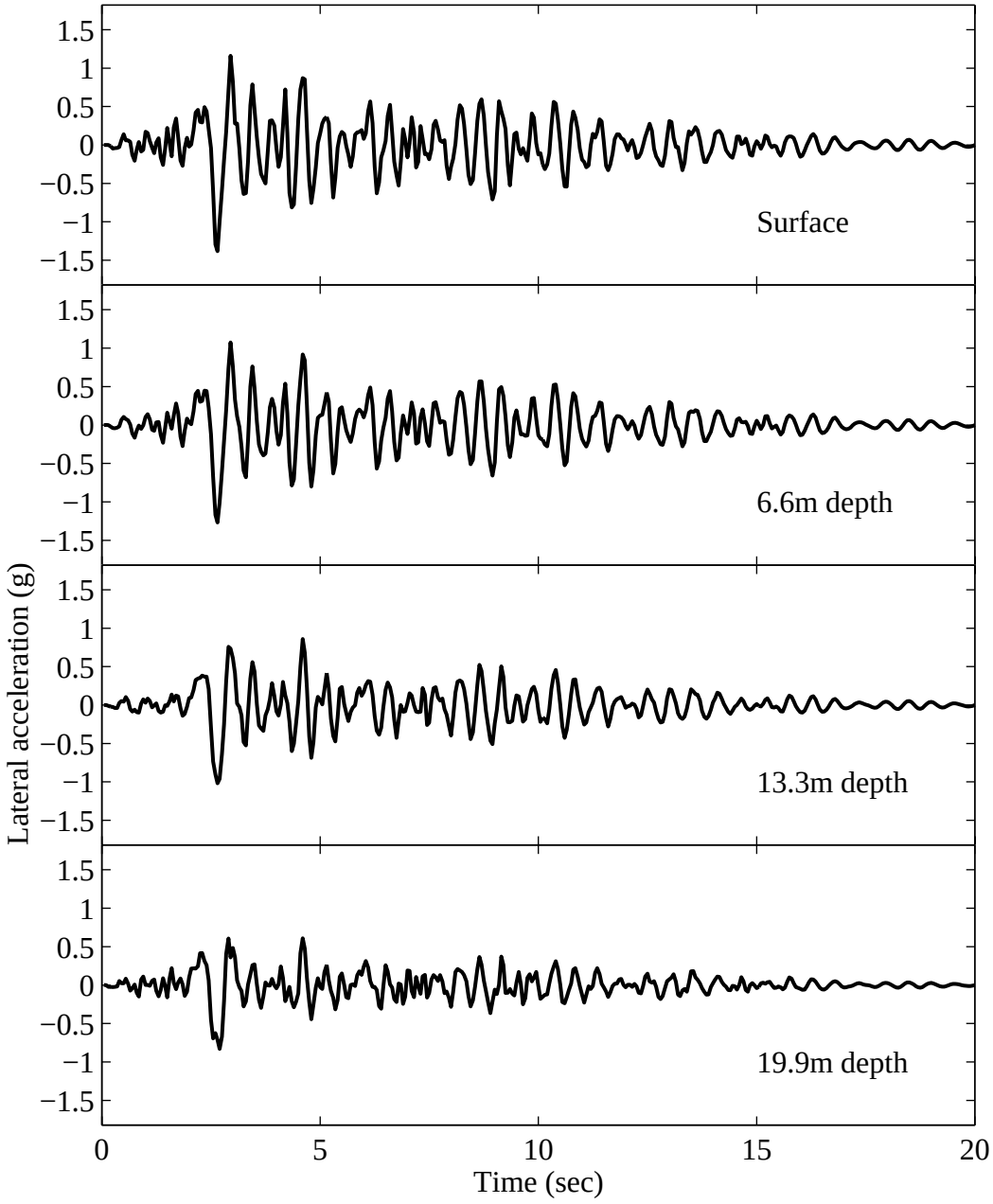

Figure 7.43: Longitudinal acceleration time histories at free field for the landside for Case W3L-F.

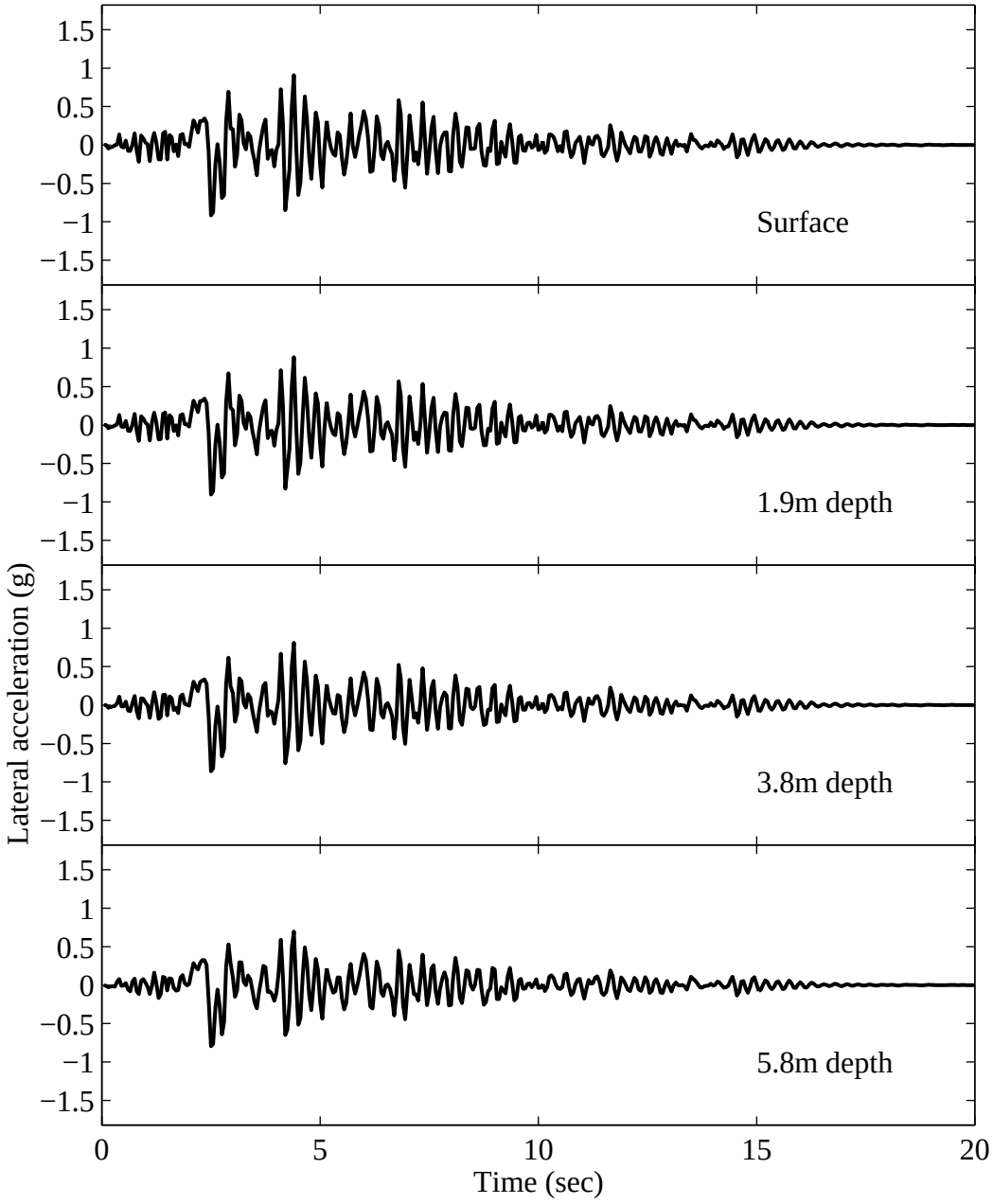

Figure 7.44: Longitudinal acceleration time histories at free field for the waterside for Case W3L-F.

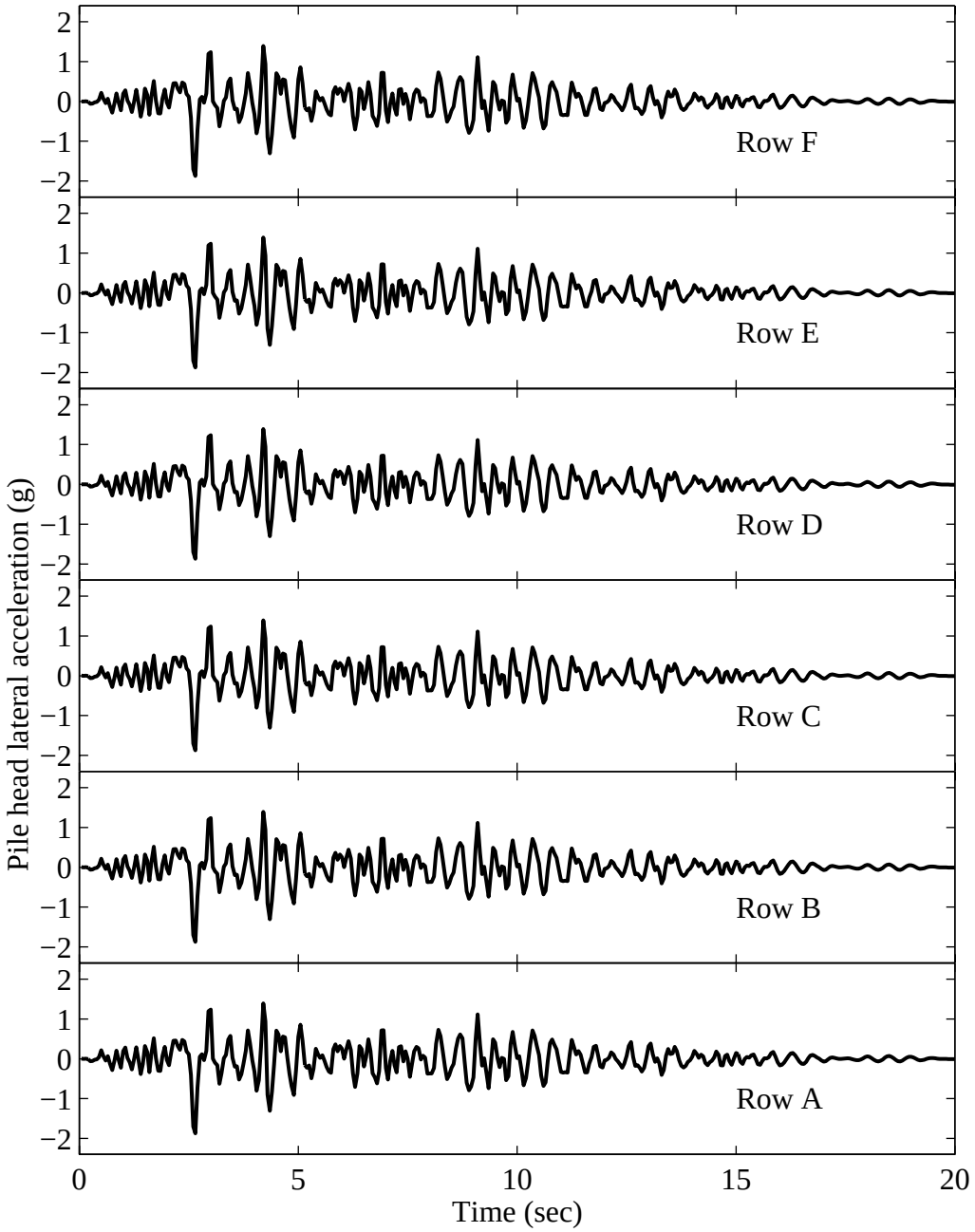

Figure 7.45: Longitudinal acceleration time histories of pile heads for Case W3L-F.

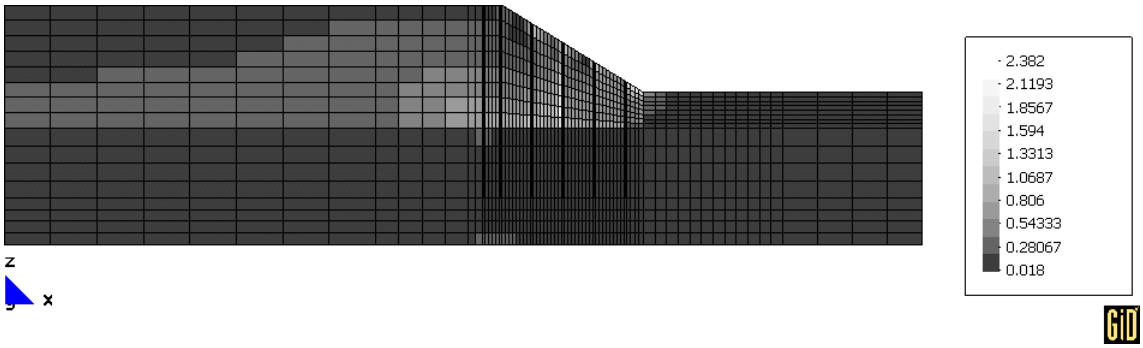

(a) Before shaking (elevation view)

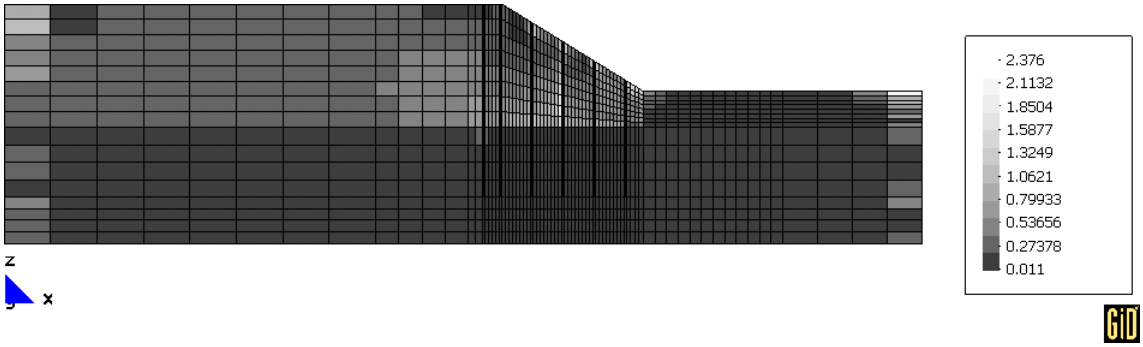

(b) After shaking (elevation view)

Figure 7.46: Stress ratio distribution (side view) before and after shaking for Case W3L-F.

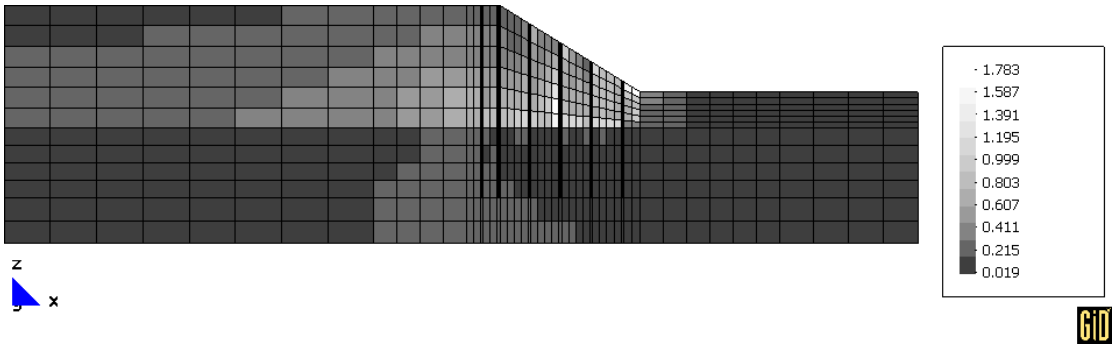

(a) Before shaking (elevation view)

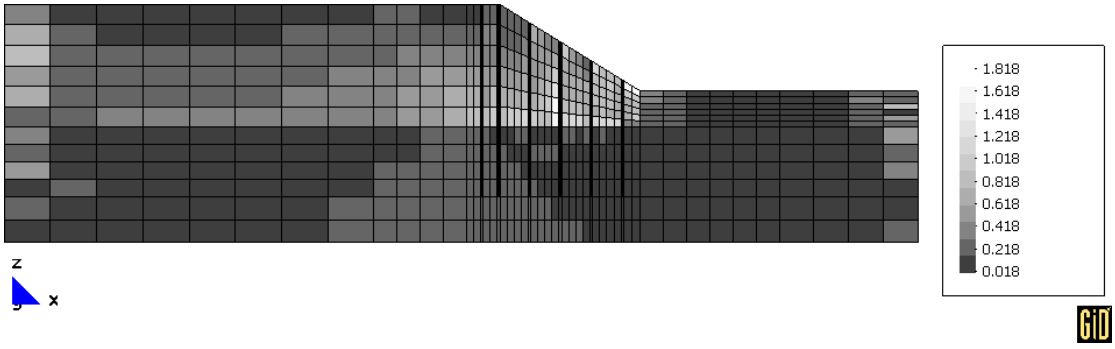

(b) After shaking (elevation view)

Figure 7.47: Stress ratio distribution (side view) before and after shaking for Case W3L-M.

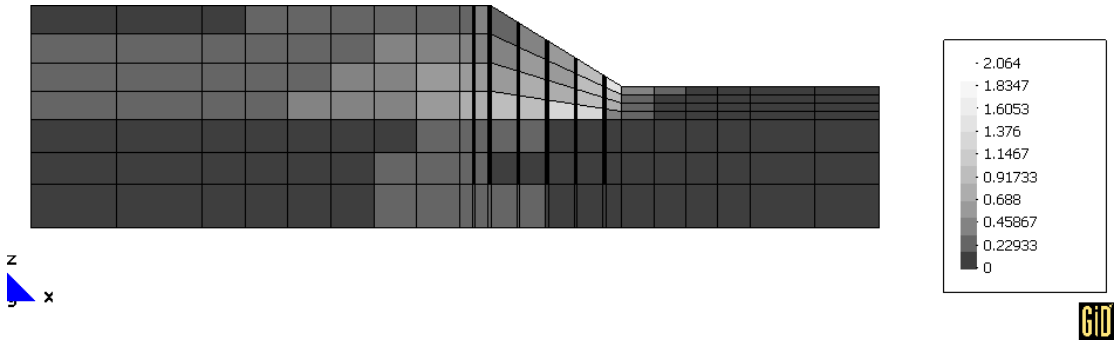

(a) Before shaking (elevation view)

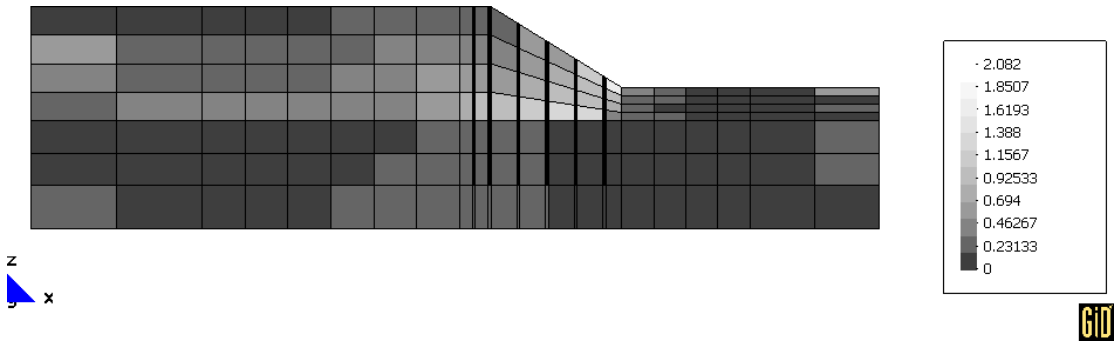

(b) After shaking (elevation view)

Figure 7.48: Stress ratio distribution (side view) before and after shaking for Case W3L-C.

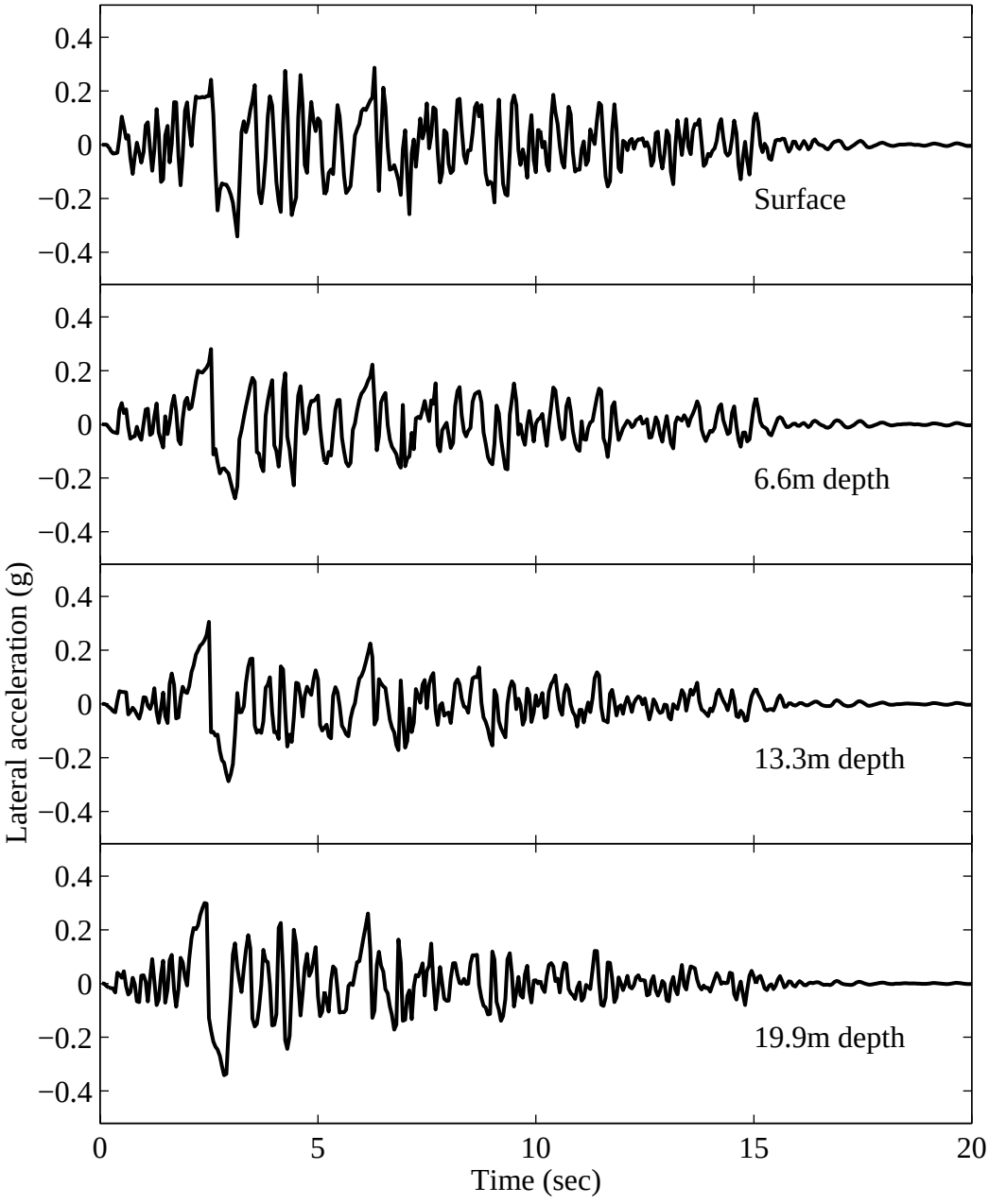

Figure 7.49: Longitudinal acceleration time histories at Location A for Case W3N-F.

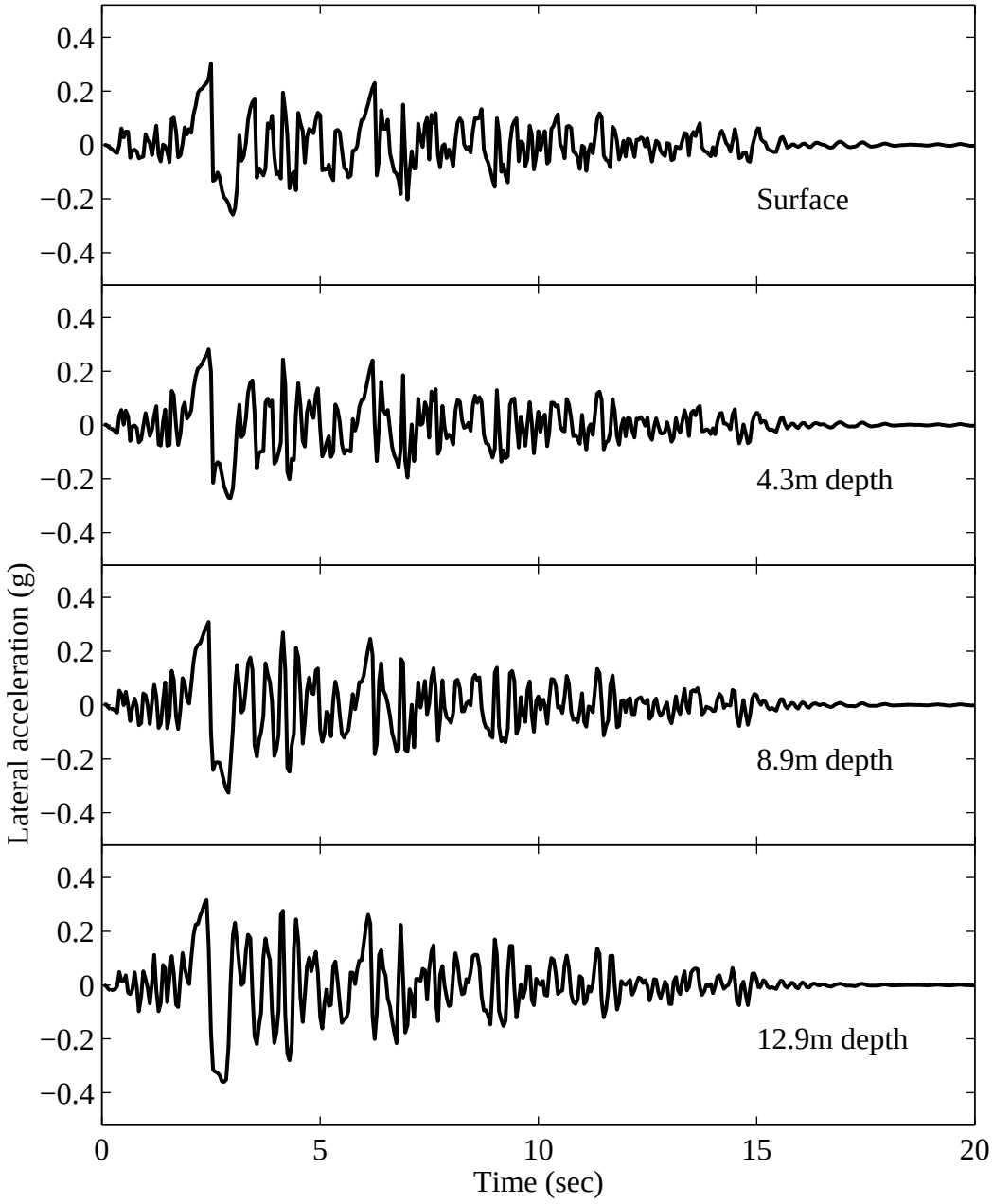

Figure 7.50: Longitudinal acceleration time histories at Location B for Case W3N-F.

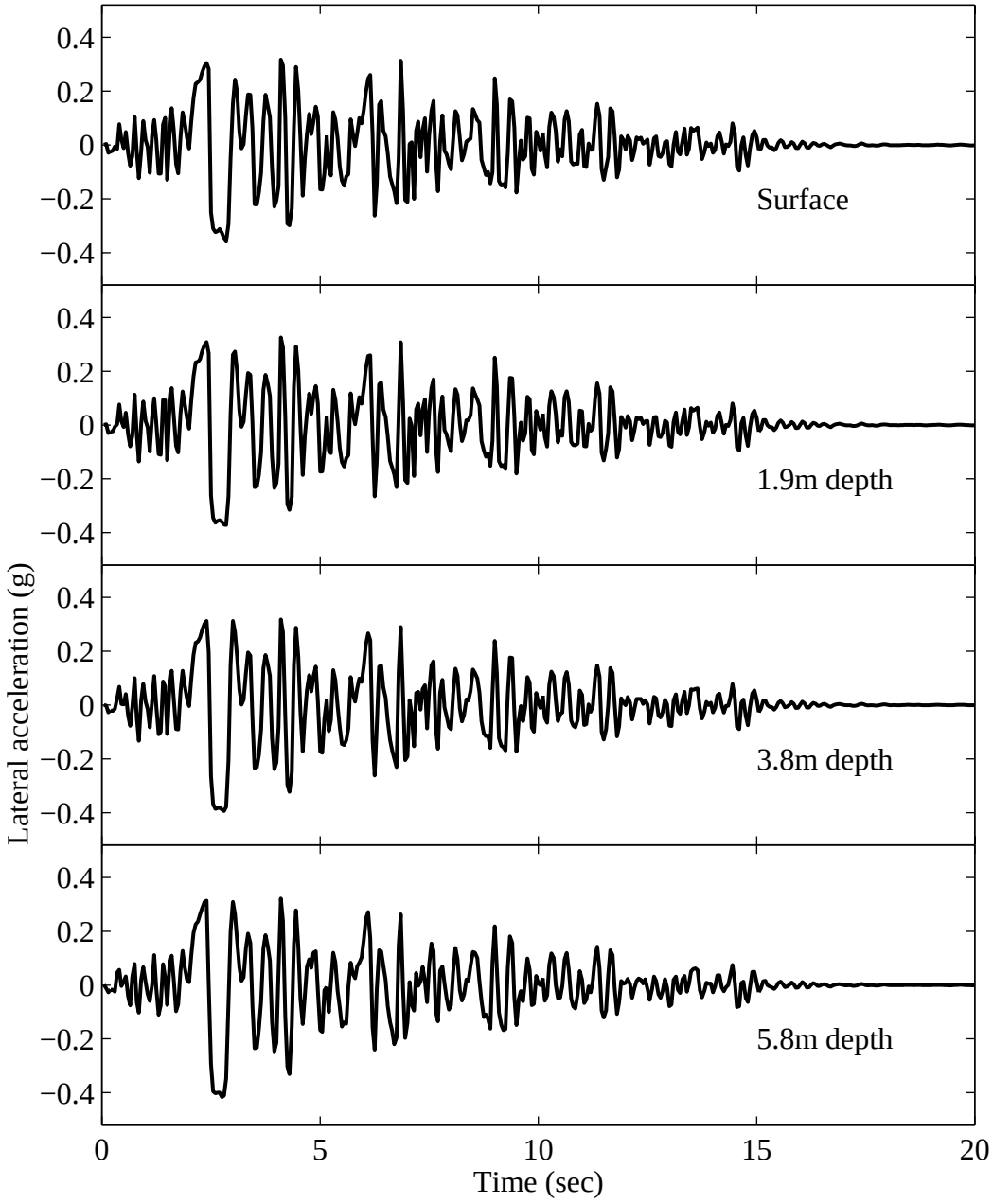

Figure 7.51: Longitudinal acceleration time histories at Location C for Case W3N-F.

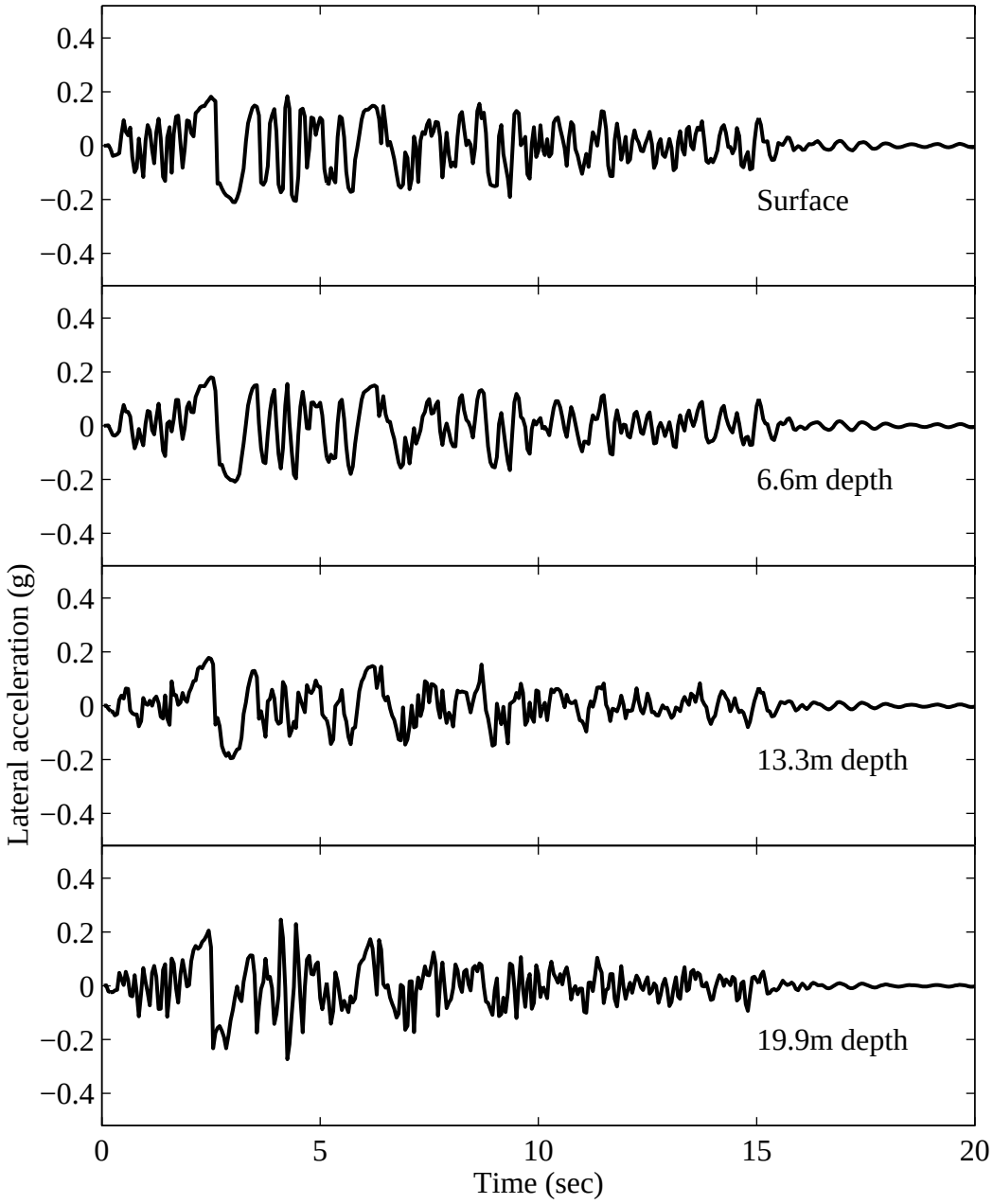

Figure 7.52: Longitudinal acceleration time histories at free field for the landside for Case W3N-F.

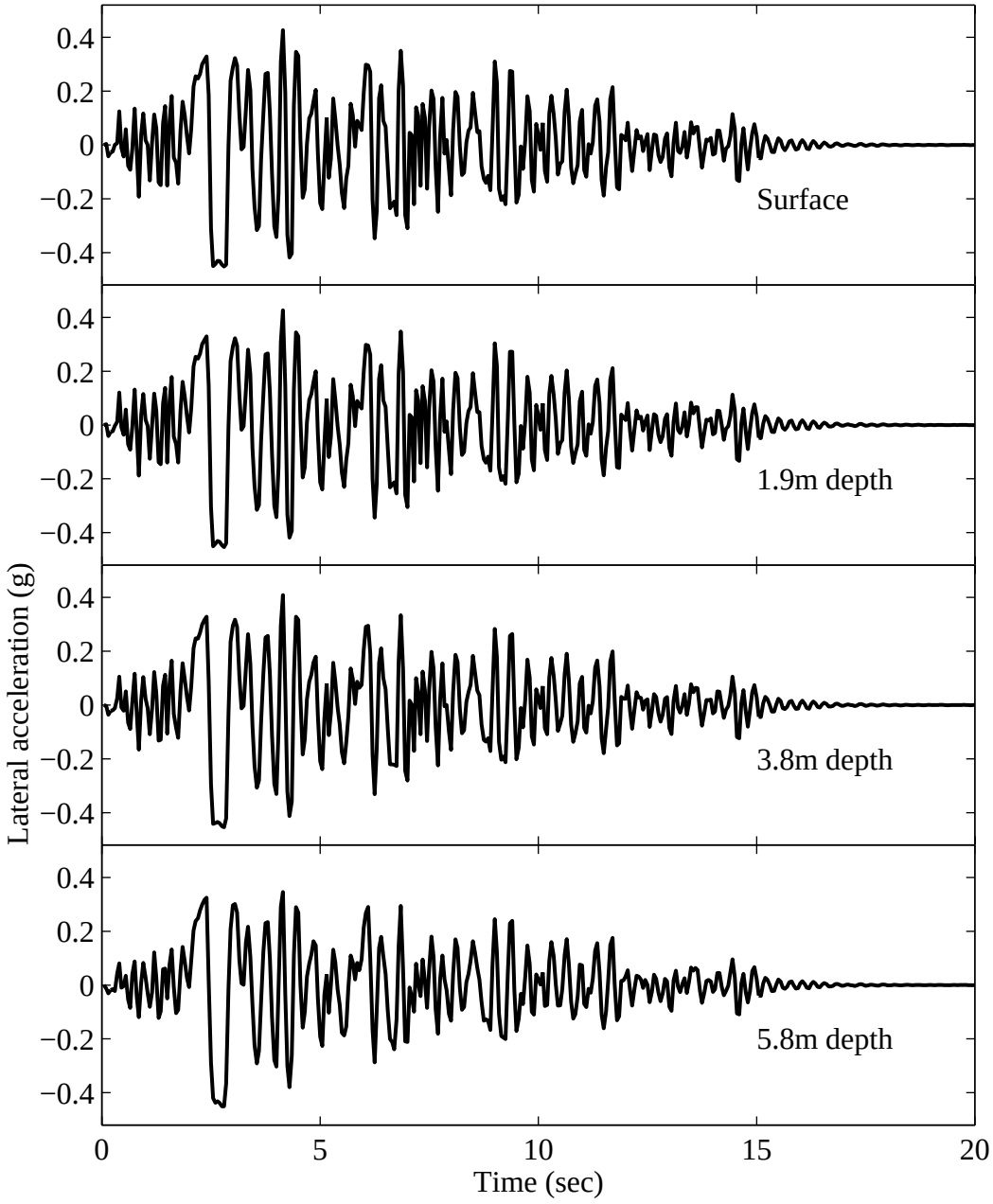

Figure 7.53: Longitudinal acceleration time histories at free field for the waterside for Case W3N-F.

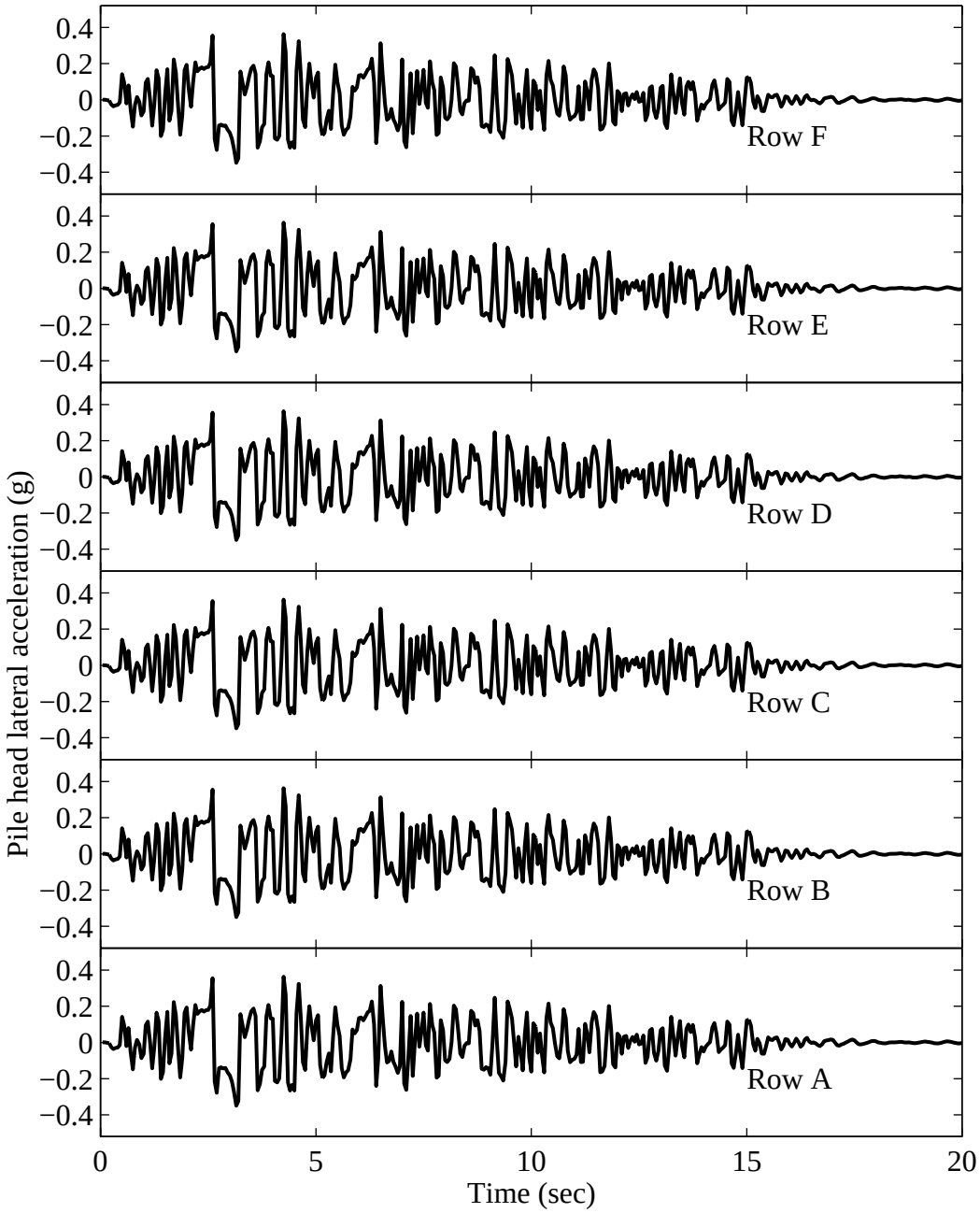

Figure 7.54: Longitudinal acceleration time histories at pile heads for Case W3N-F.

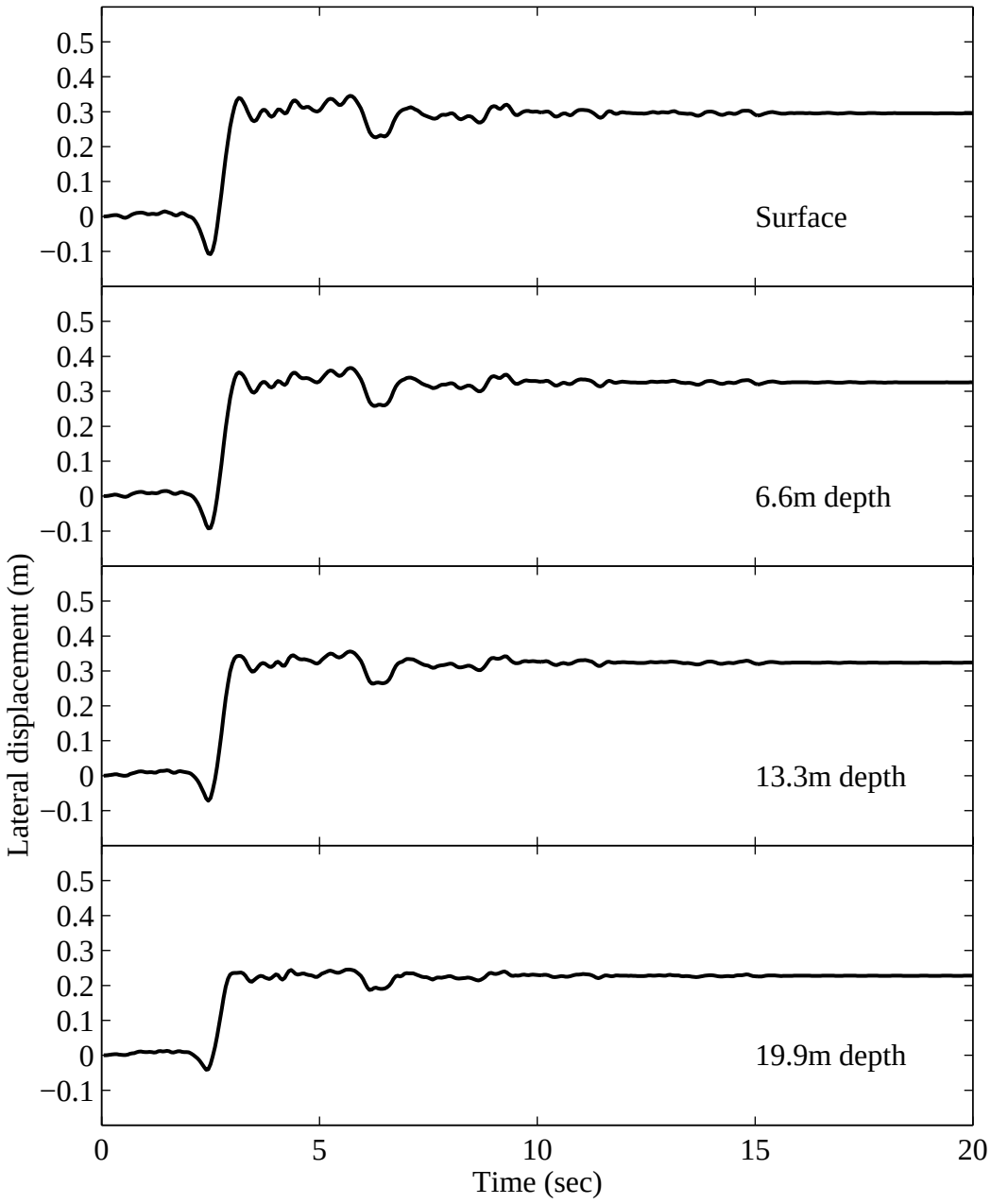

Figure 7.55: Longitudinal displacement time histories at Location A for Case W3N-F.

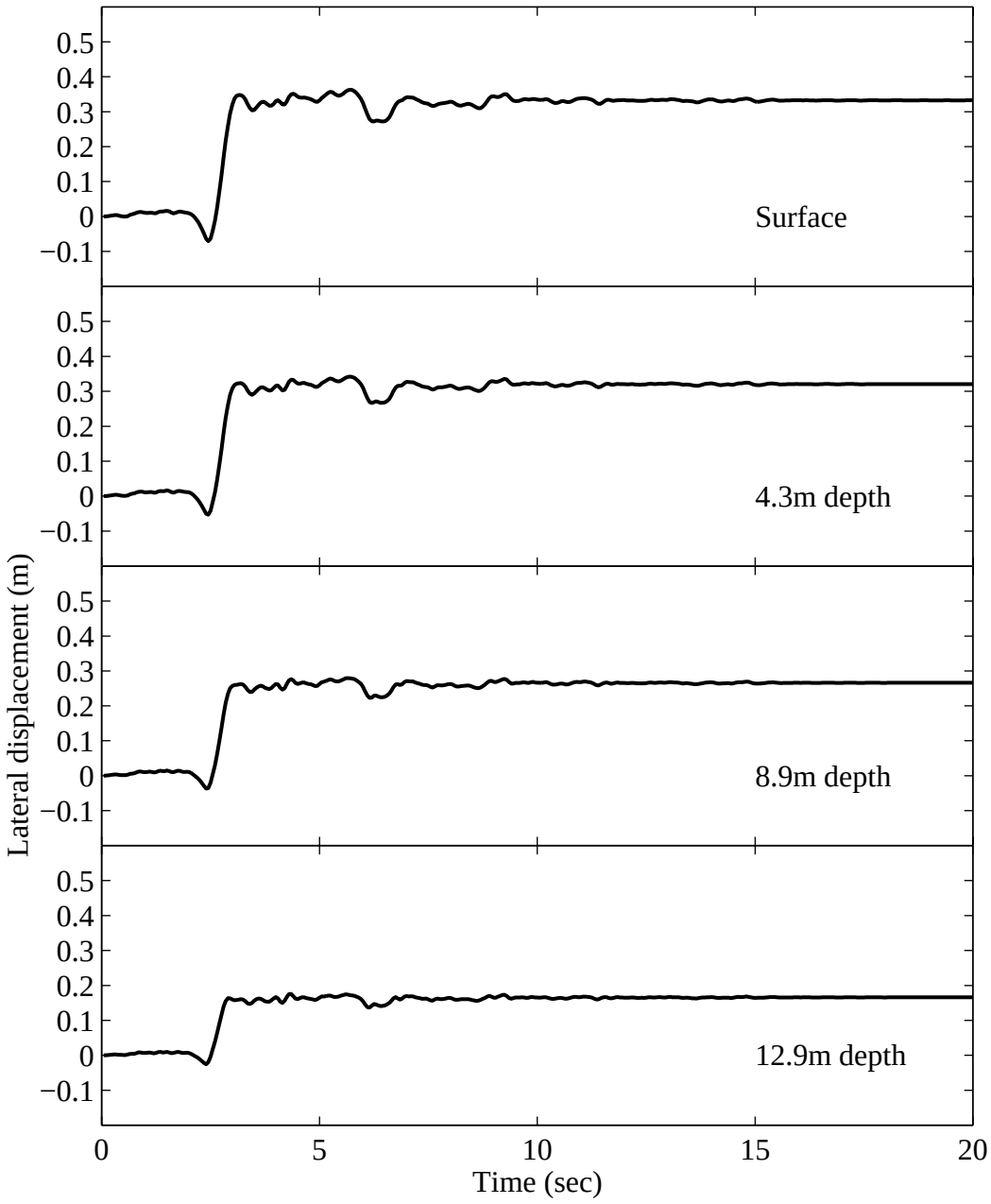

Figure 7.56: Longitudinal displacement time histories at Location B for Case W3N-F.

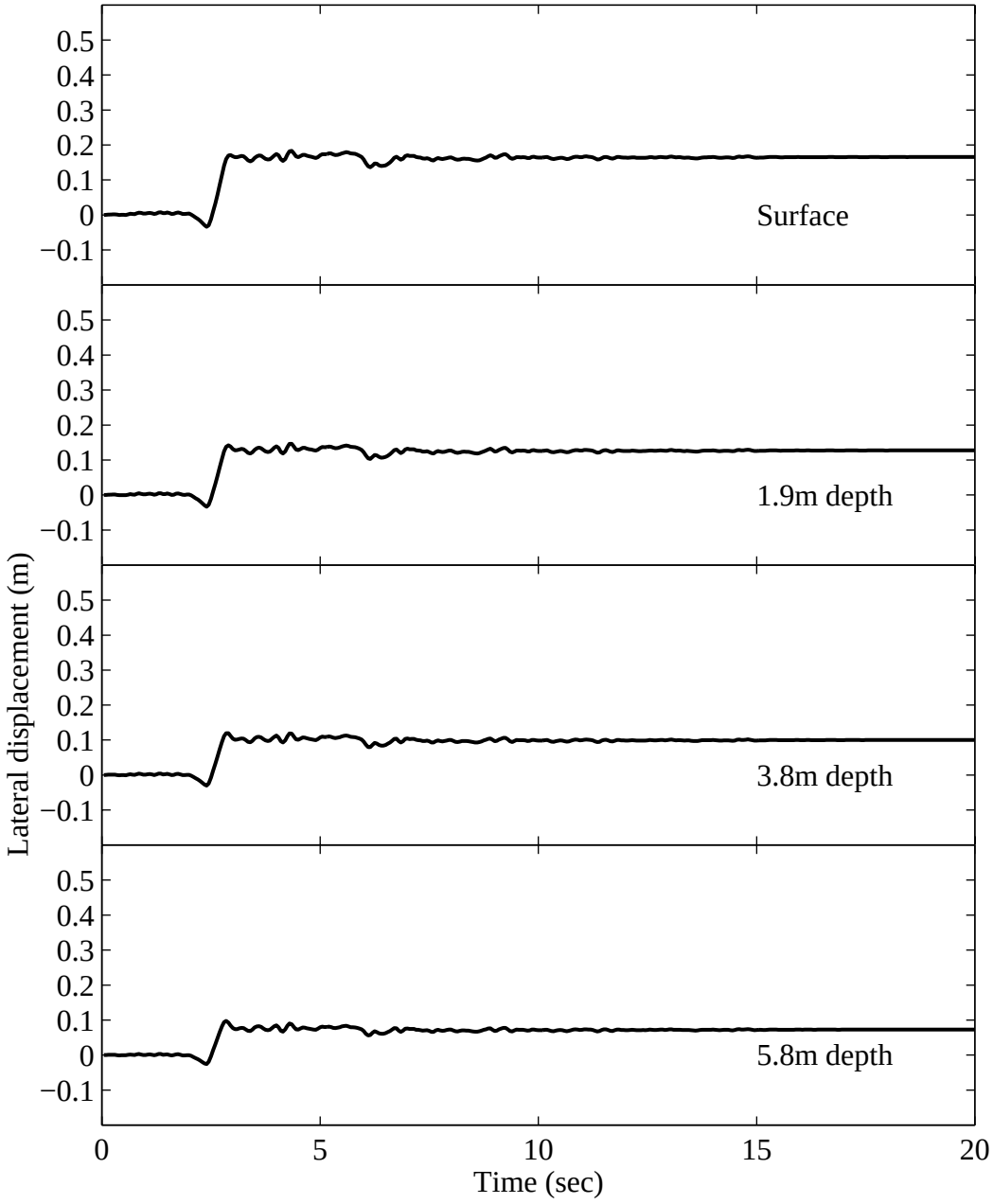

Figure 7.57: Longitudinal displacement time histories at Location C for Case W3N-F.

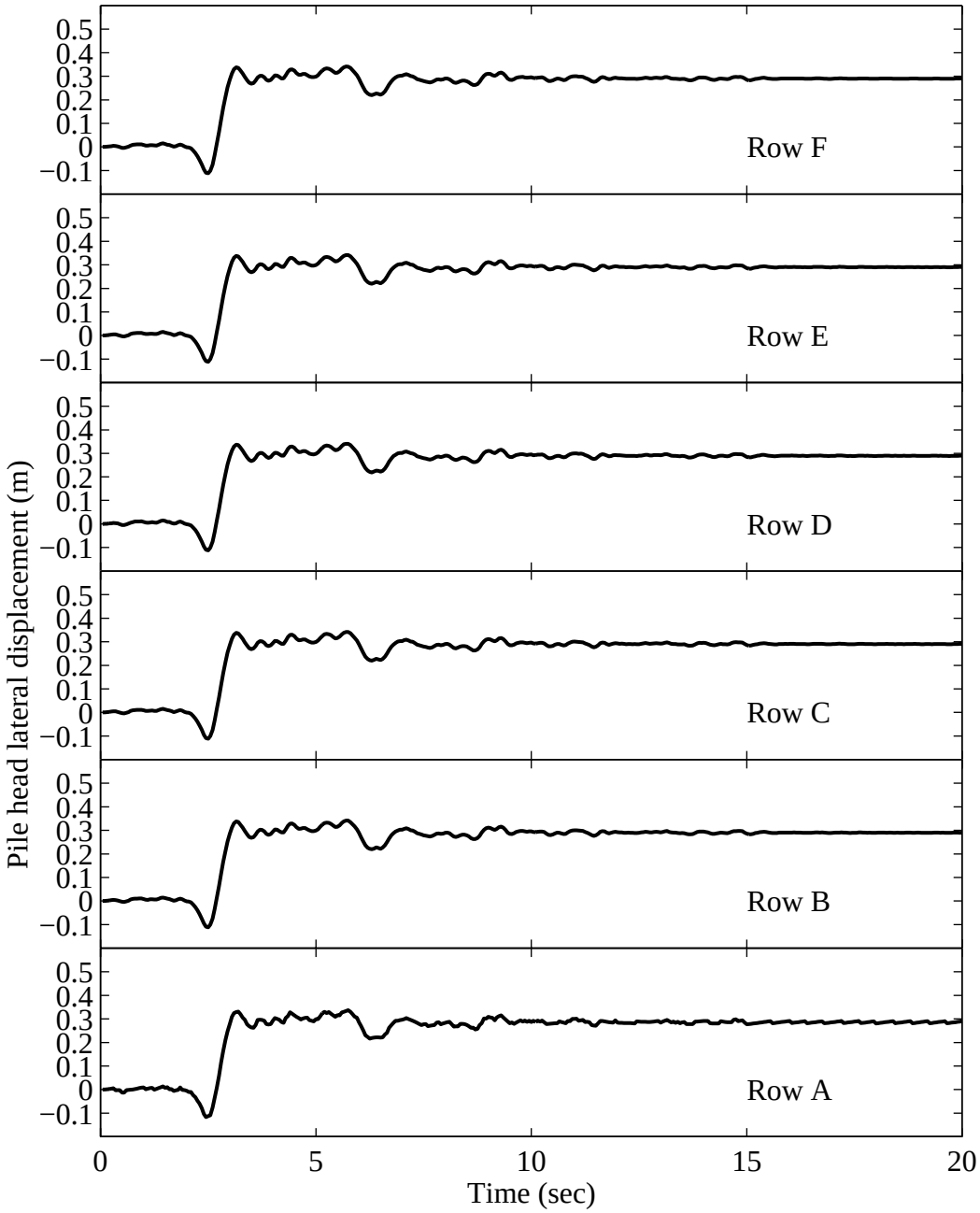

Figure 7.58: Longitudinal displacement time histories at pile heads for Case W3N-F.

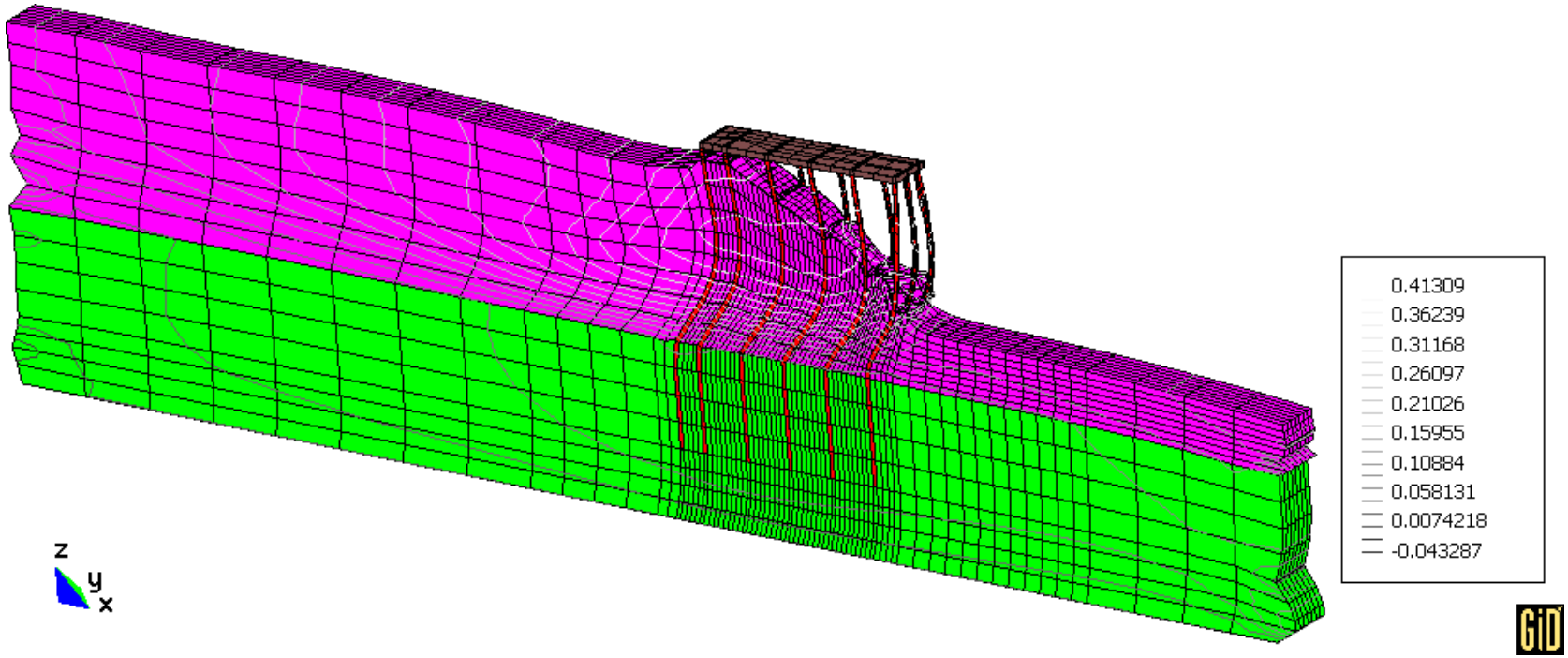

(a) Isometric view

Figure 7.59: Final deformed mesh (factor of 30; contour lines show the longitudinal displacement in meters) for Case W3N-F.

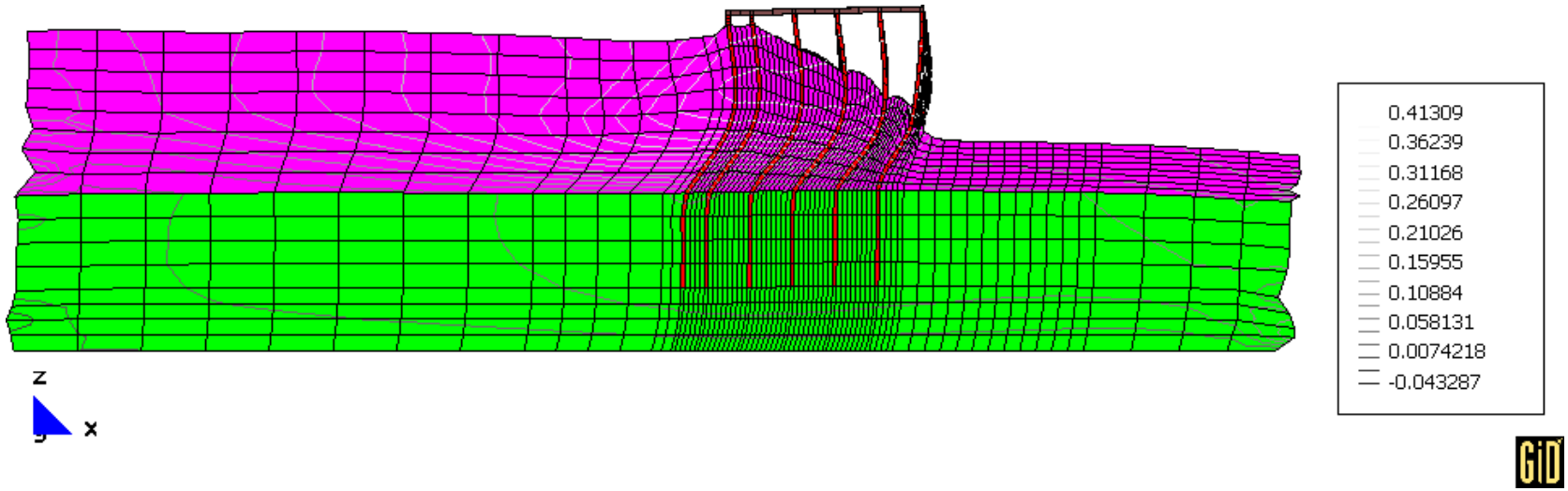

(b) Elevation view

Figure 7.59: (continued).

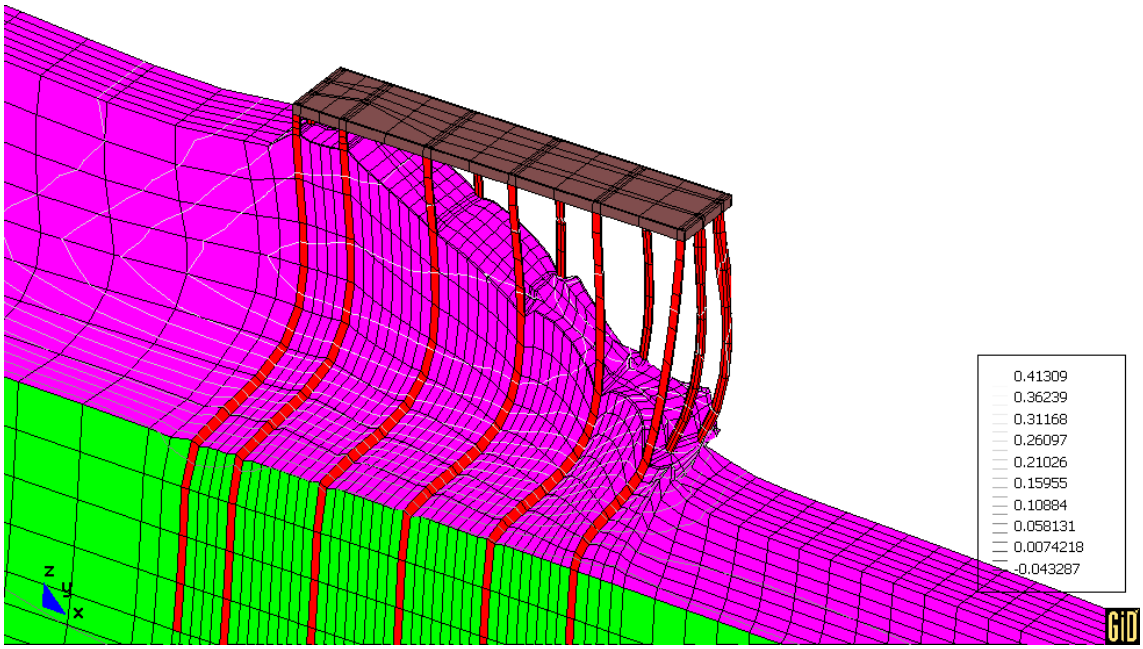

Figure 7.60: Close up of final deformed mesh (factor of 30) for Case W3N-F (isometric view).

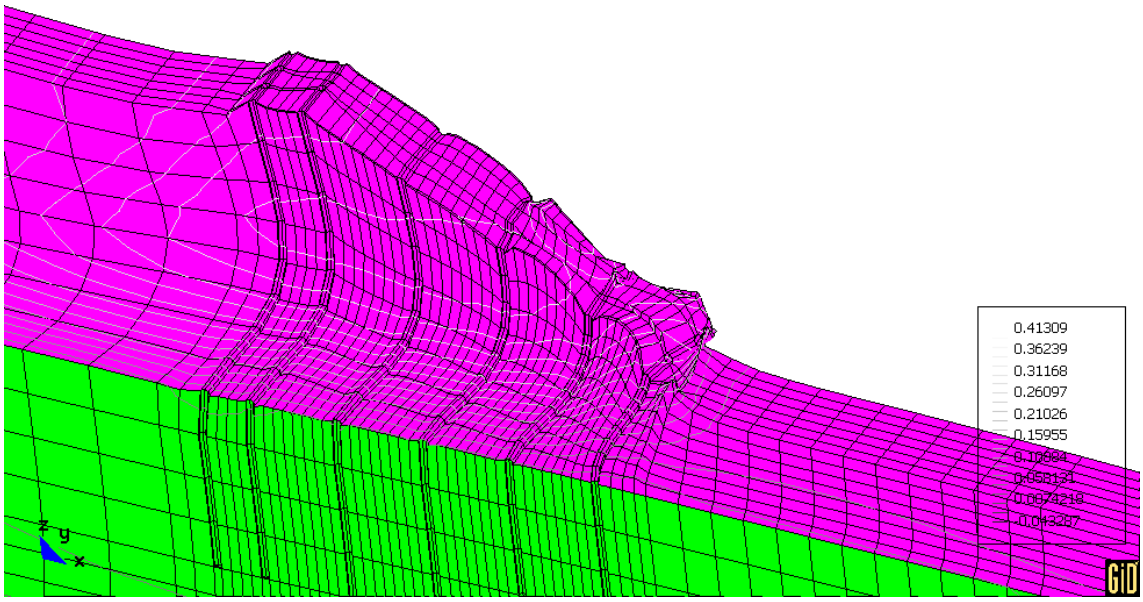

(a) Isometric view

(b) Plan view

Figure 7.61: Close up of final deformed mesh (factor of 30; contour lines show longitudinal displacement in meters) of the slope section for Case W3N-F.

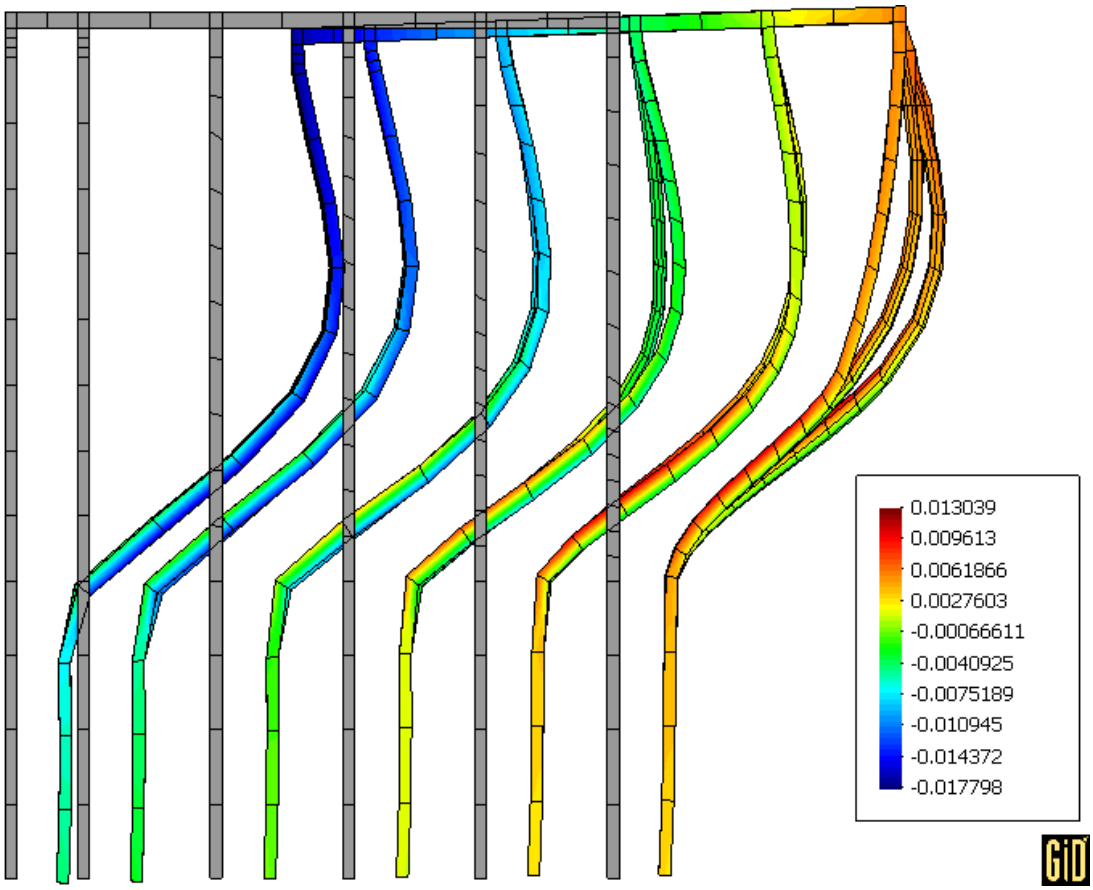

(a) Elevation view

Figure 7.62: Contour fill of the final vertical displacement of the wharf (factor of 50; unit: m) for Case W3N-F.

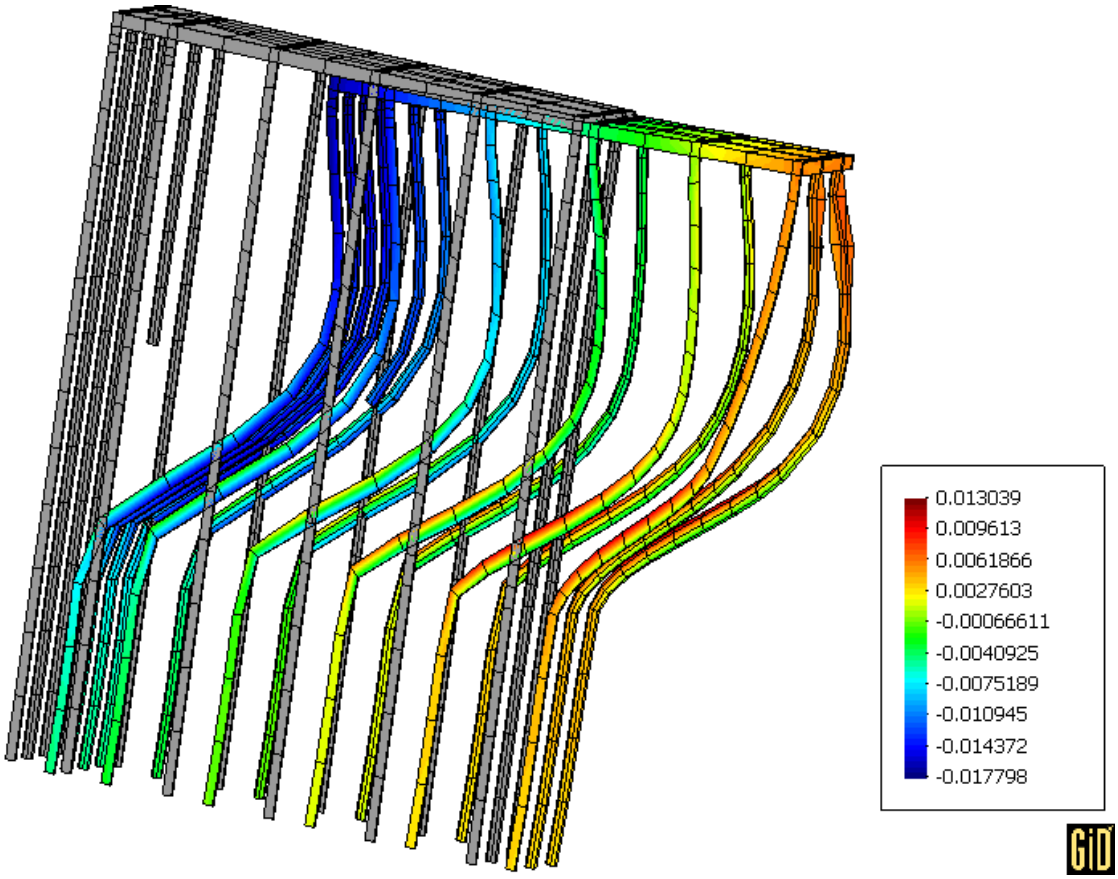

(b) Isometric view

Figure 7.62: (continued).

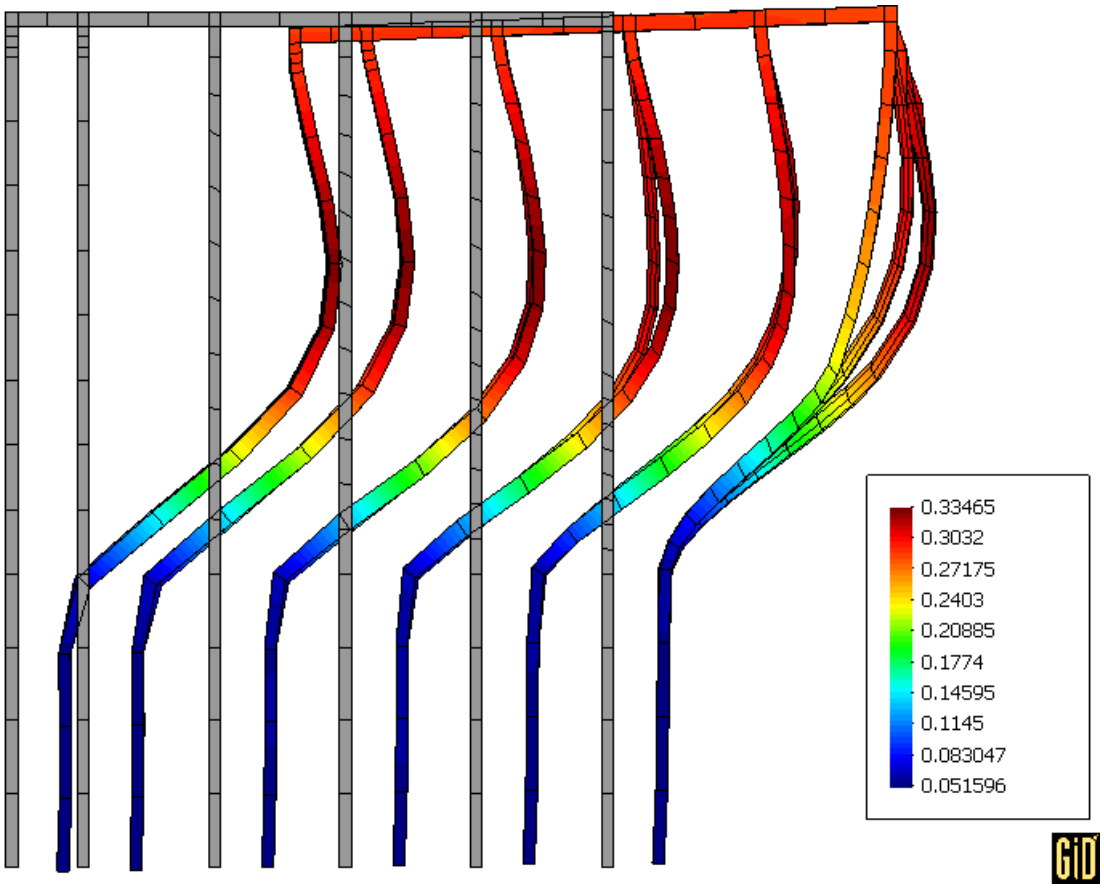

(a) Elevation view

Figure 7.63: Contour fill of the final longitudinal displacement of the wharf (factor of 50; unit: m) for Case W3N-F.

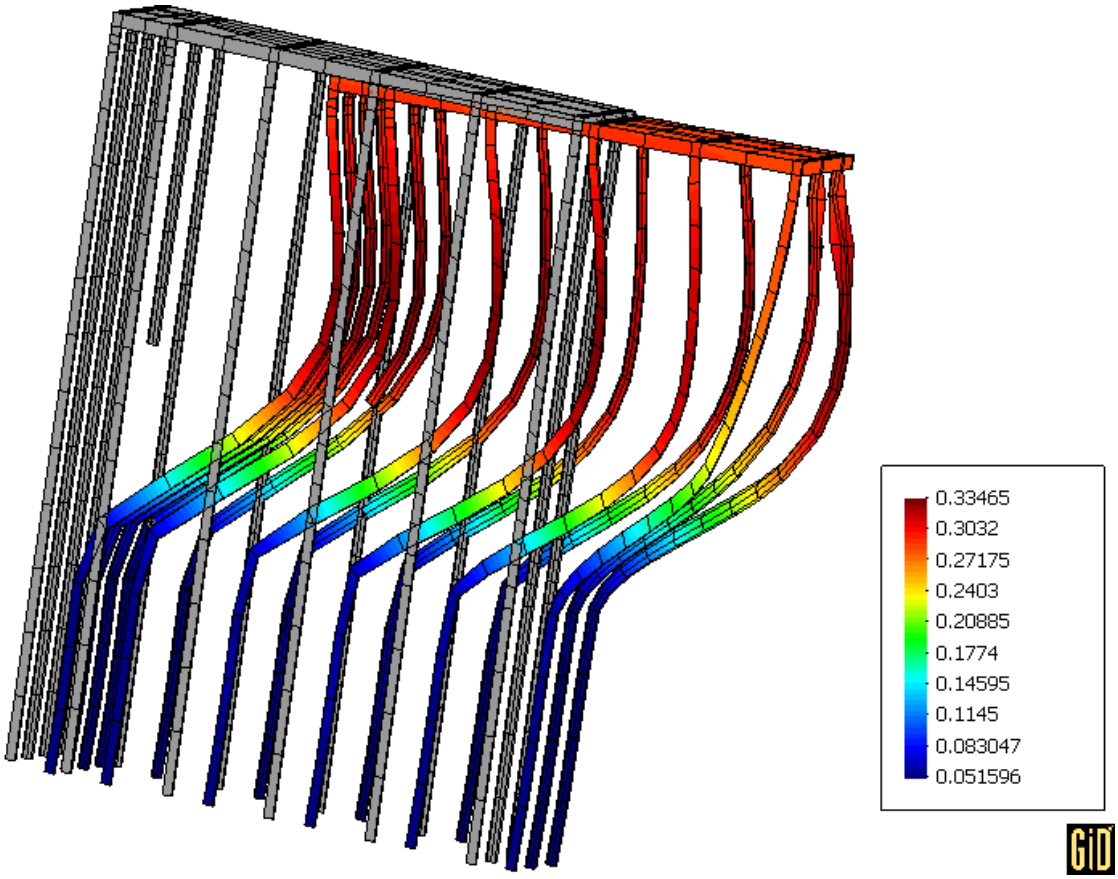

(b) Isometric view

Figure 7.63: (continued).

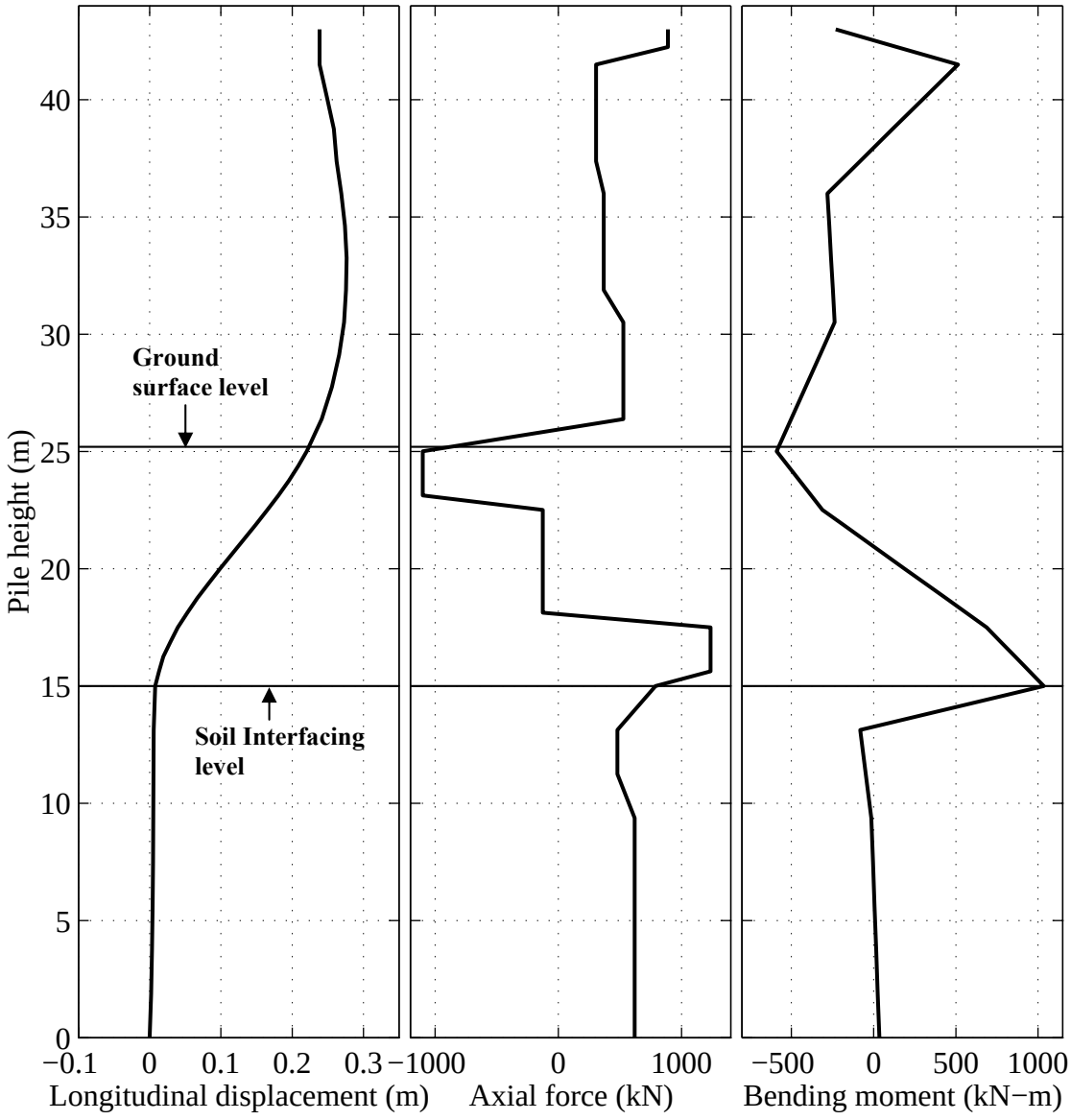

Figure 7.64: Response profiles for pile A3 (see Figure 7.3) for Case W3N-F.

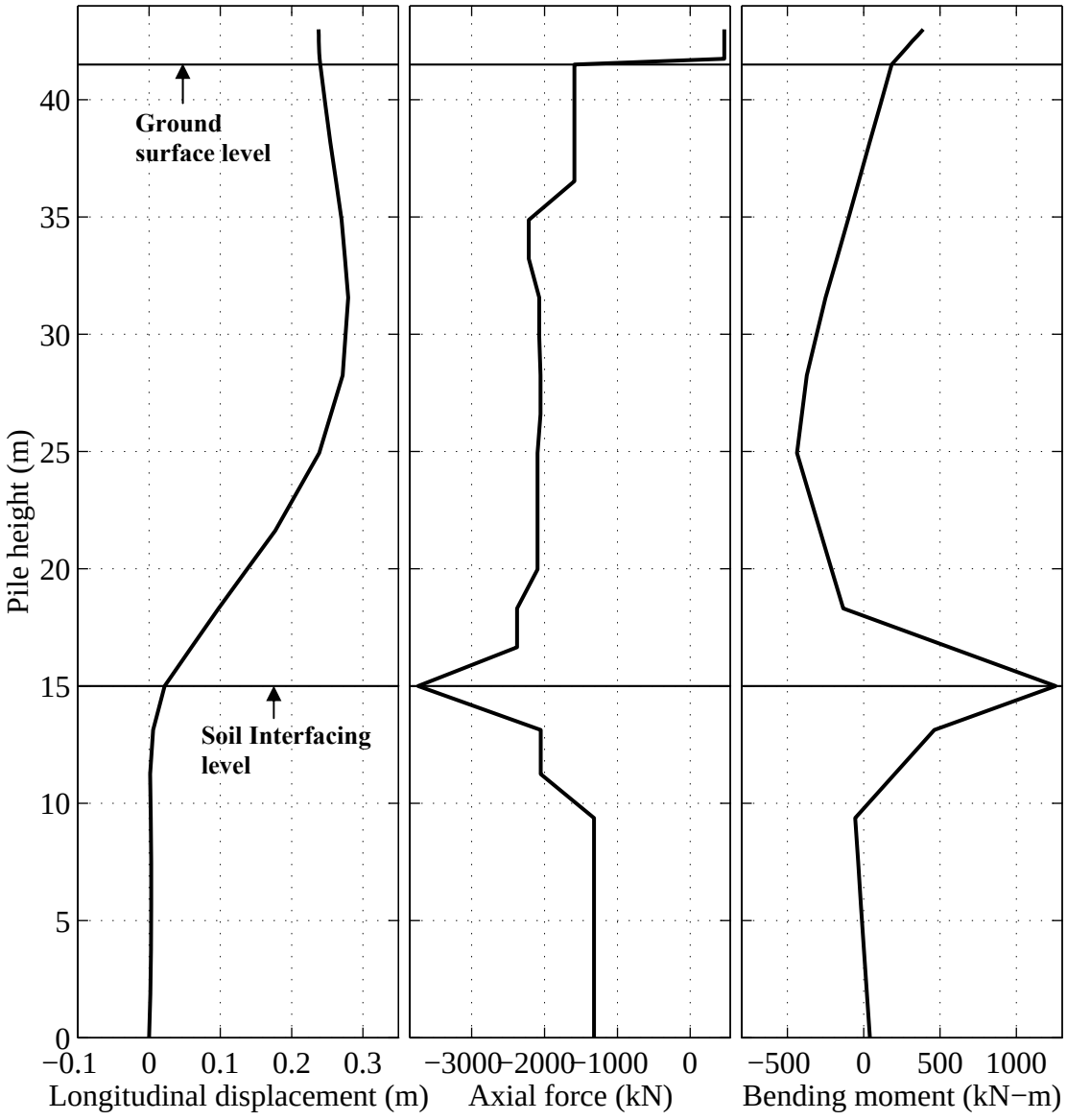

Figure 7.65: Response profiles for pile F1 (see Figure 7.3) for Case W3N-F.

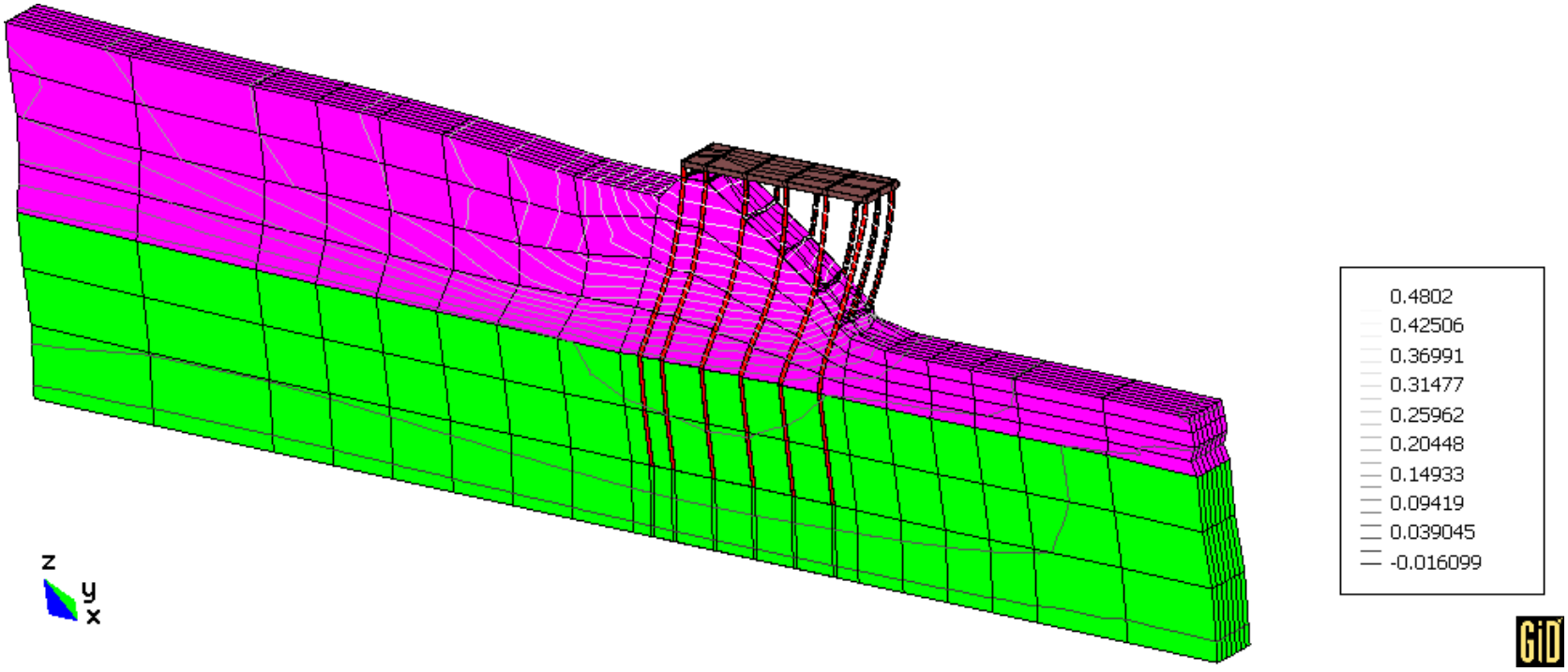

(a) Isometric view

Figure 7.66: Final deformed mesh (factor of 30; contour lines show the longitudinal displacement in meters) for Case W3N-C.

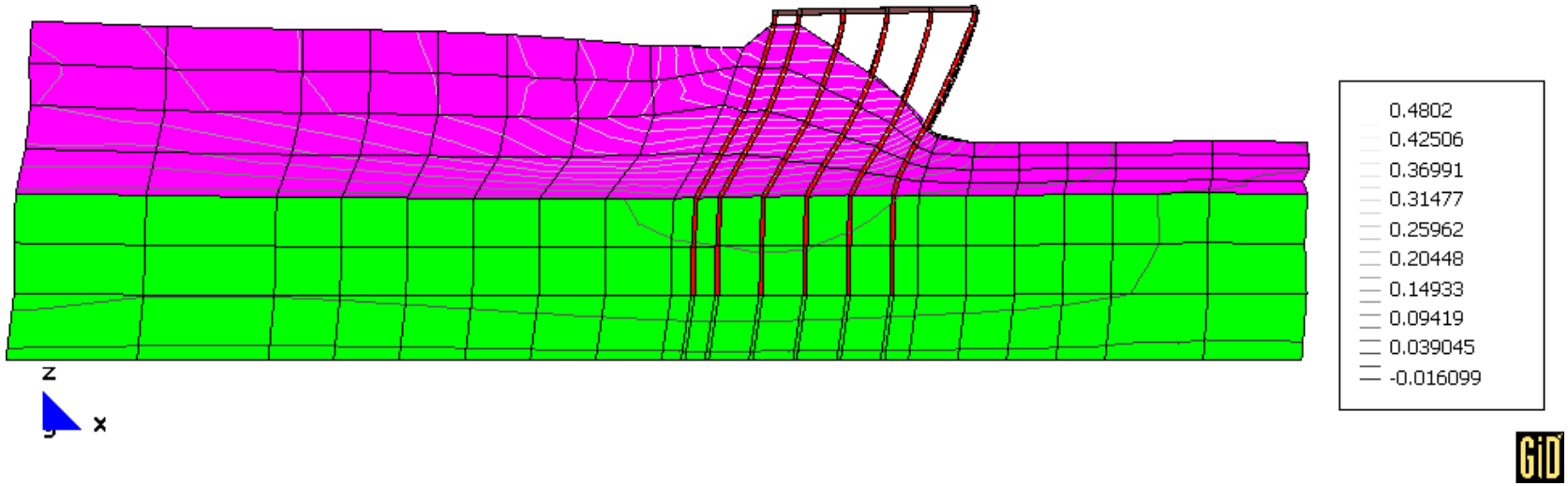

(b) Elevation view

Figure 7.66: (continued).

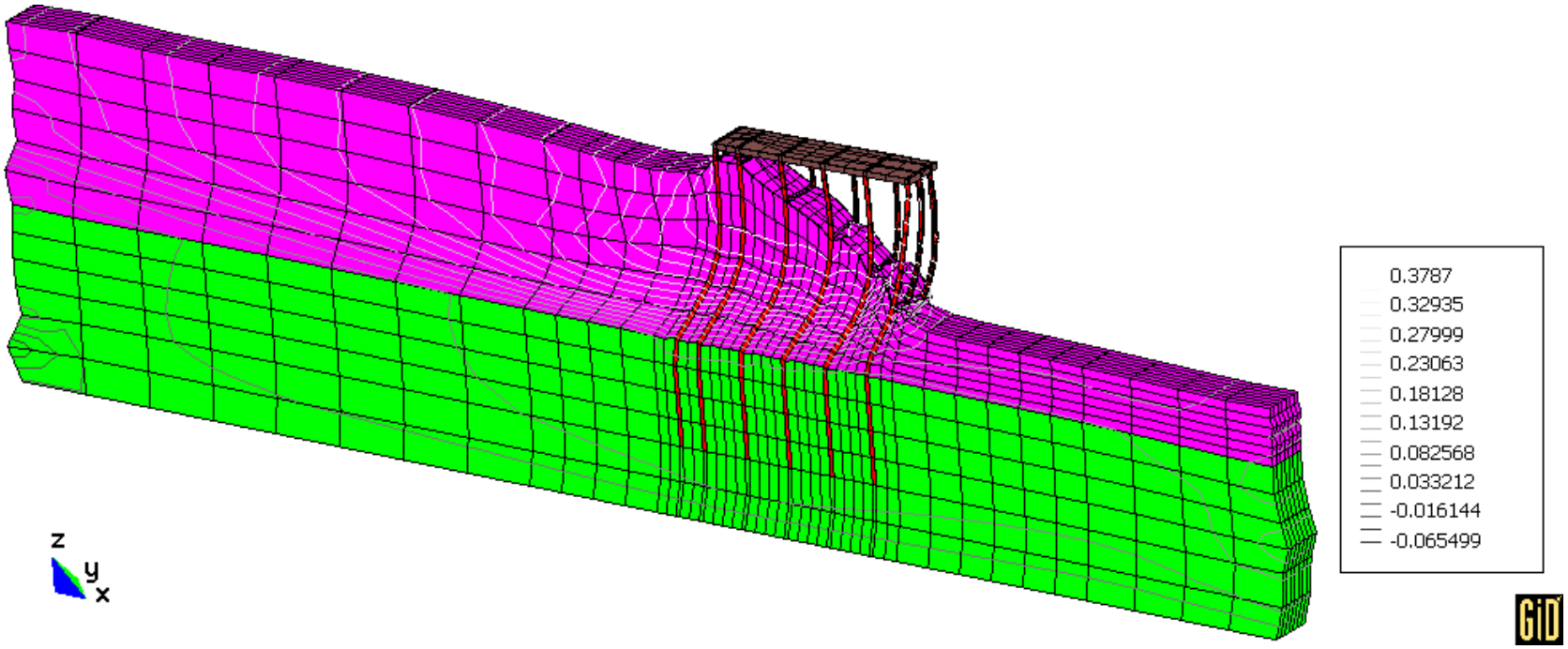

(a) Isometric view

Figure 7.67: Final deformed mesh (factor of 30; contour lines show the longitudinal displacement in meters) for Case W3N-M.

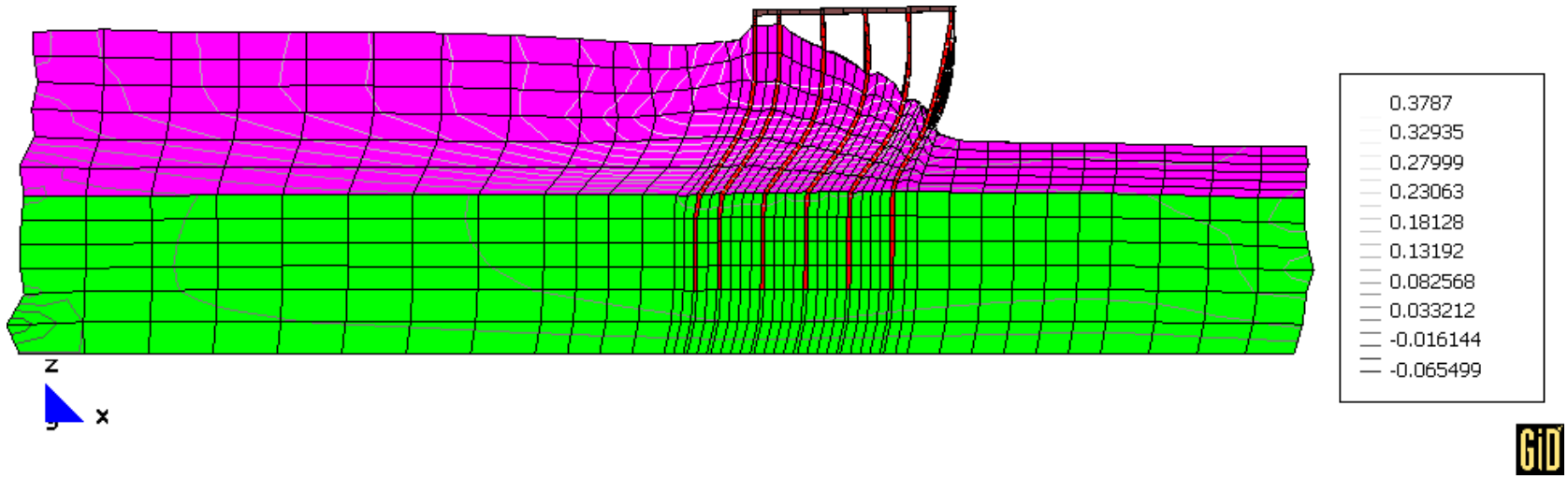

(b) Elevation view

Figure 7.67: (continued).

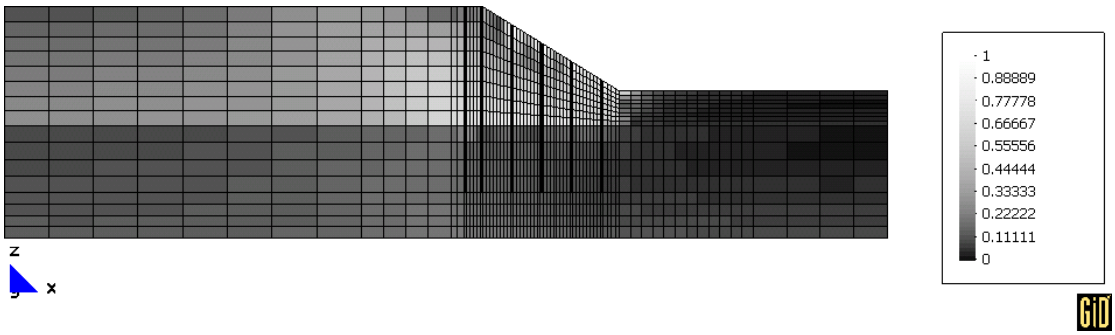

(a) Before shaking (elevation view)

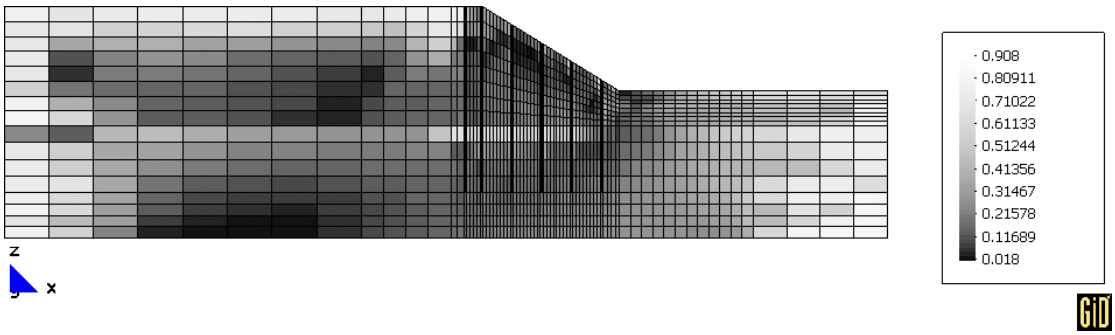

(b) After shaking (elevation view)

Figure 7.68: Stress ratio distribution for Case W3N-F before and after shaking.

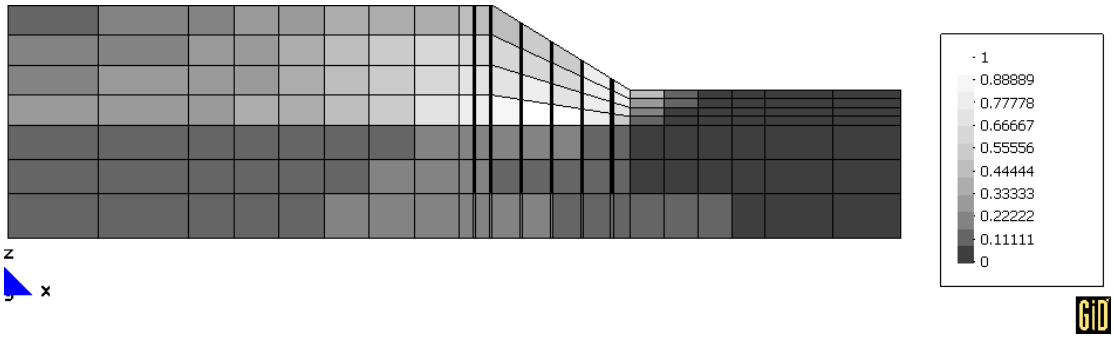

(a) Before shaking (elevation view)

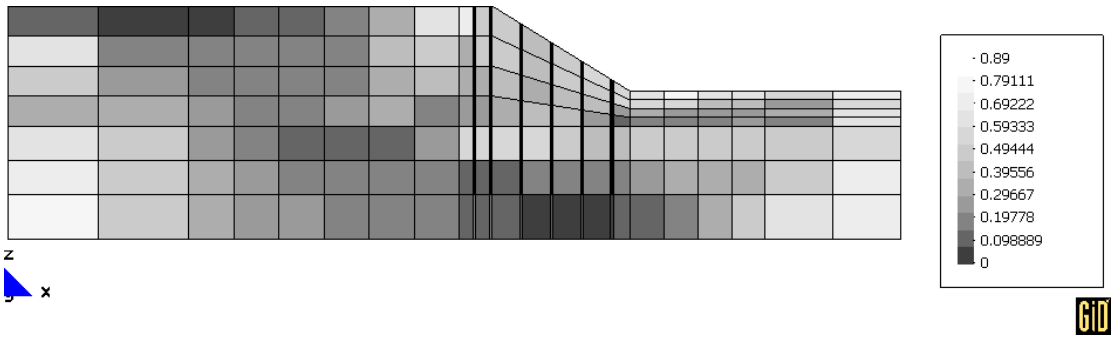

(b) After shaking (elevation view)

Figure 7.69: Stress ratio distribution for Case W3N-C before and after shaking.

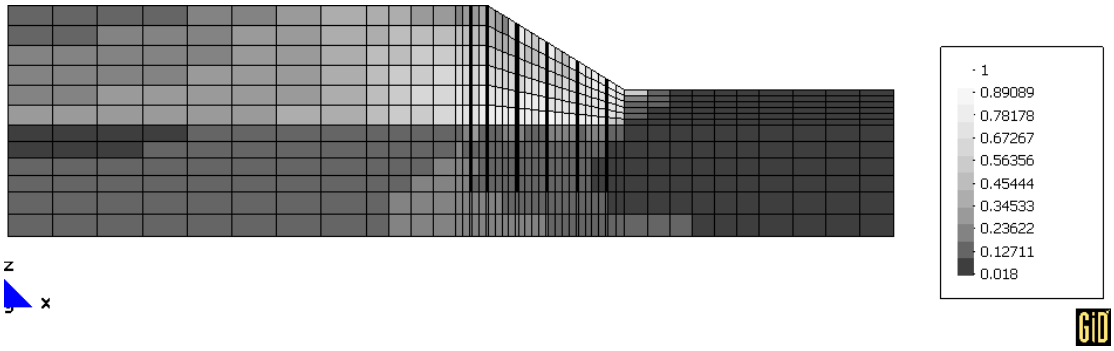

(a) Before shaking (elevation view)

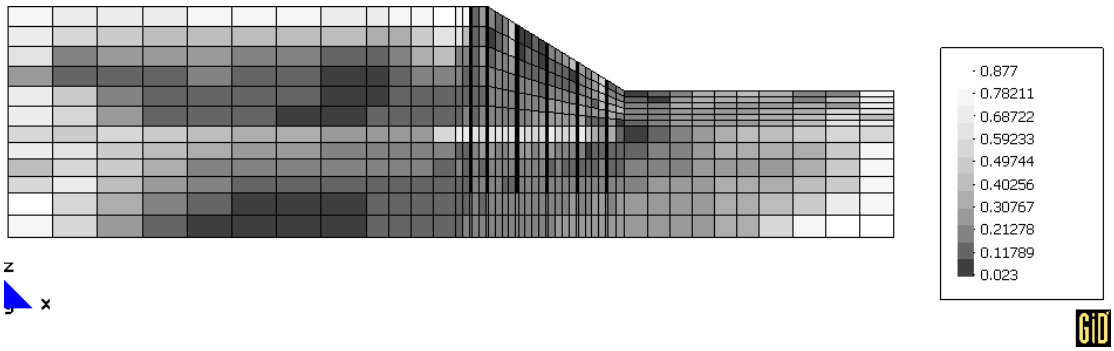

(b) After shaking (elevation view)

Figure 7.70: Stress ratio distribution for Case W3N-M before and after shaking.

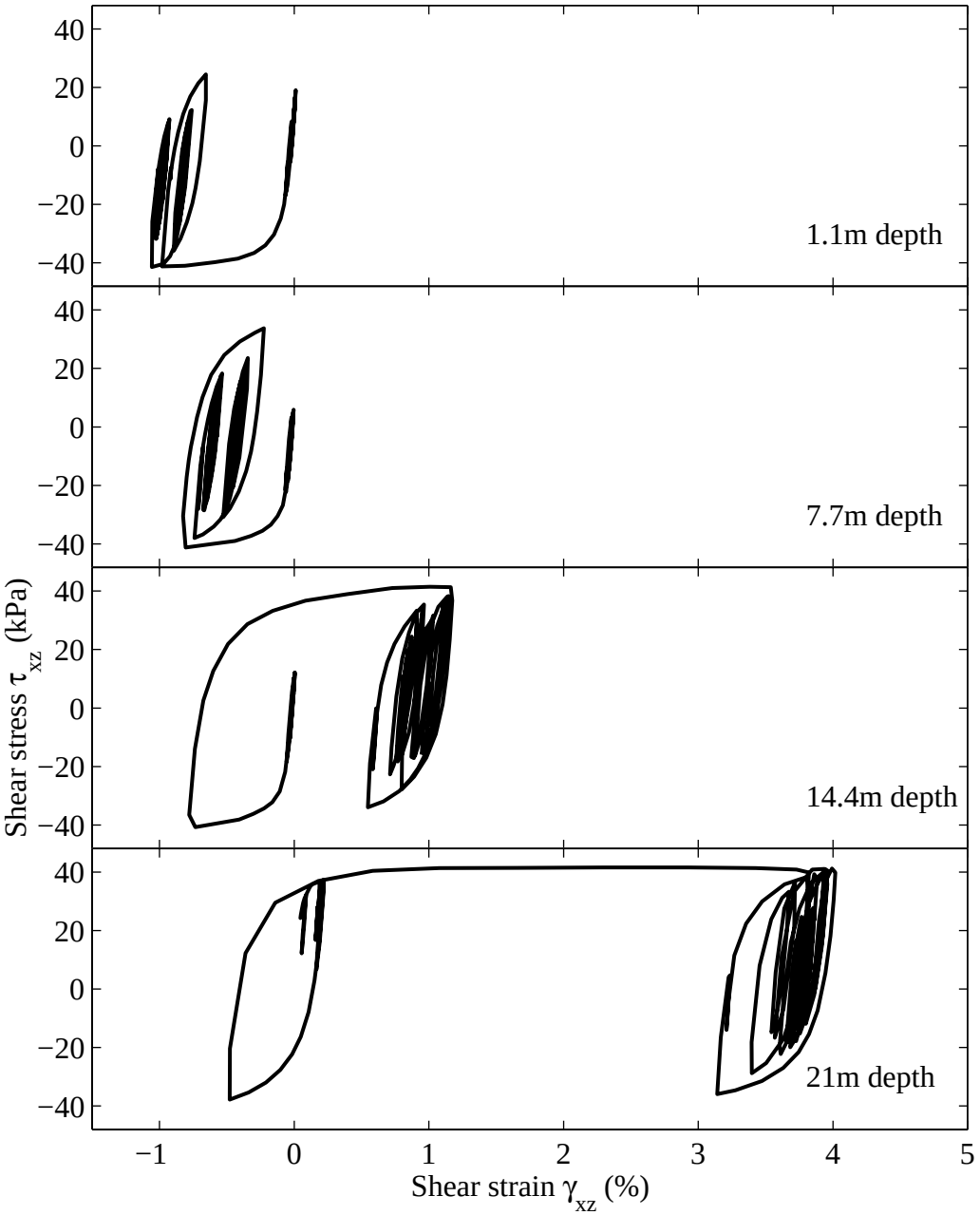

Figure 7.71: Shear stress-strain response at Location A for Case W3N-F.

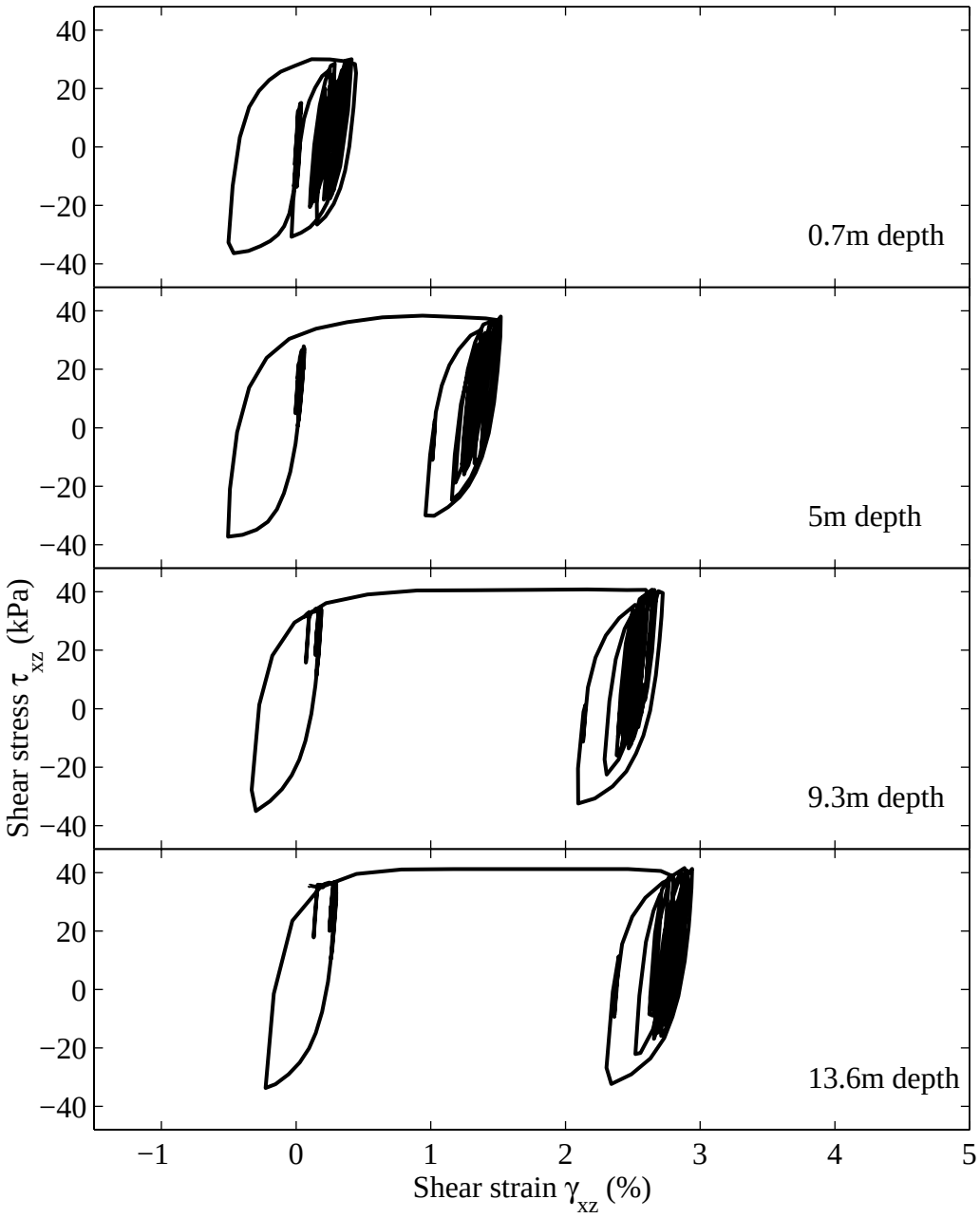

Figure 7.72: Shear stress-strain response at Location B for Case W3N-F.

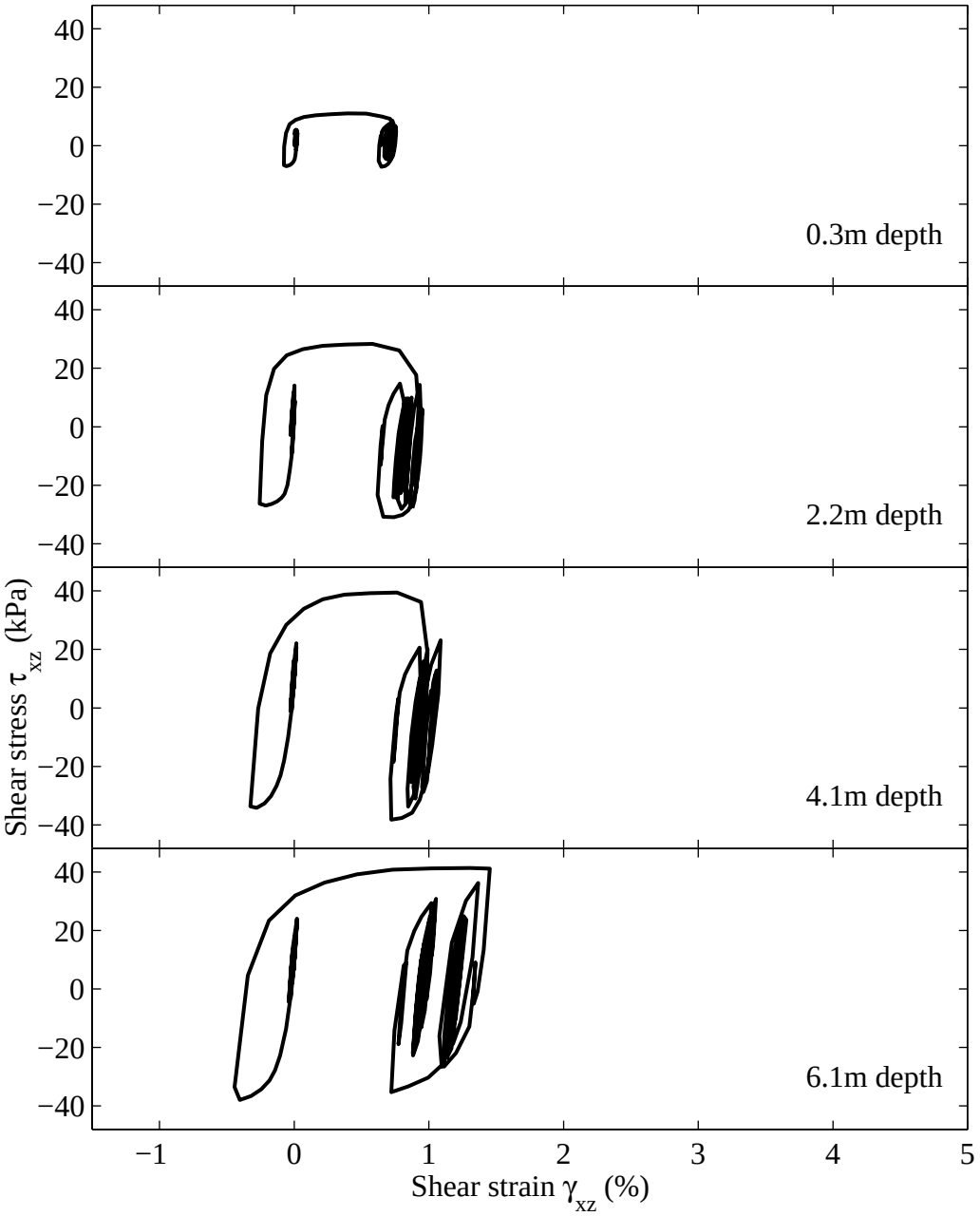

Figure 7.73: Shear stress-strain response at Location C for Case W3N-F.

Chapter 8 User Interfaces for Parallel Simulation

8.1 Introduction

Experience from past strong earthquakes worldwide has distinguished soil liquefaction as one of the main causes of structural damage (Seed et al. 1990; JGS 1996, 1998; Ansal et al. 1999). In recent years, a number of computer programs have been developed for assessing earthquake-induced nonlinear ground response including liquefaction effects (e.g. DYSAC2 (Muraleetharan et al. 1988), DYNAFLOW (Prevost 1998), SUMDES2D (Li et al. 2000), CYCLIC (Elgamal et al. 2002b)). However, even with great advances in computational capabilities, usage of these programs is still relatively limited. One main reason is that the underlying soil constitutive models usually require a large number of input parameters (10–20 typically for each soil material type), and a lengthy calibration process. In addition, analysis of large amounts of data generated from these simulations demands efficient tools. Consequently, a user-friendly interface for convenient pre- and post-processing is essential (Yang et al. 2004b).

Much time and effort is expended today in building an appropriate FE mesh, particularly for 3D simulation. Preparation of data files is a step that requires careful attention to detail. Debugging can consume many weeks or even months. A minor oversight or misinterpretation might go undetected leading to erroneous results. Numerical opportunities for such errors abound. The need to address this challenge cannot be overstated.

Commercial computer codes usually offer powerful pre- and post-processing capabilities, which increase efficiency and reduce the chance for error. Currently, the tools for creating such user-friendly interfaces are becoming commonplace, allowing specialized numerical codes to be more easily utilized. Windows-based coding techniques allow for broad usage on a world-wide scale.

Scenario-specific user-friendly interfaces, though potentially restrictive, can significantly alleviate this problem allowing for high efficiency and much increased confidence. A graphical user interface (GUI) would be useful not only for simulation of small size problems on one-single processor (e.g., a PC) but also for analyses of parallel large-scale modeling on a multiprocessor workstation (e.g., a 8-processor Linux Cluster).

This chapter presents a framework of the simulation environment for seismic analysis for scenario-specific geotechnical problems.

8.2 Parallel FE Simulation Environment with User Interfaces

Figure 8.1 shows a network-based system architecture of a collaborative environment for distributive simulation (Peng and Law 2002, 2004) of ParCYCLIC. Using a user-friendly interface, users build their model, run the analysis and then view the output. The model is submitted through a local network to a Linux cluster parallel computer for analysis and the result is sent back to the client computer for the users to view it.

A user-interface platform usually includes an input interface and an output interface. The input interface allows the user to define a model by making selections and entering numbers or text. Mesh generation is performed by a preprocessor upon the

completion of the input phase. The main purpose of the output interface is for the user to conveniently visualize and manipulate the simulation results.

The following sections will discuss a series of user interfaces developed to conduct seismic analysis for 2D plane-strain (CyclicTP), 2D earth dams (CyclicED), 1D site response (Cyclic1D), and 3D pile response (CyclicPL). Building on the CYCLIC/ParCYCLIC computational platform, these GUIs are developed to facilitate pre- and post-processing of simulation data. Through this interface, a few mouse clicks allow definition of geometry and material properties, and thereafter permit visualization of the results. Such an interface will allow wide usage, practically permitting all interested practicing engineers to benefit from the research outcomes.

In current implementations, the analysis engine resides in the same computer as the user interfaces (and thus the serial version CYCLIC is employed). As for large scale models, the generated input files are sent to supercomputers for analysis (thus ParCYCLIC is employed as the analysis engine) and the results are sent back for visualization. However, it is straightforward to connect the analysis engine (thus ParCYCLIC is employed) installed in the Linux cluster to the client user interfaces since input files for CYCLIC and ParCYCLIC are essentially the same.

All of the user interfaces were developed using Microsoft Foundation Class Library (MFC) Version 6.0, within the Microsoft Visual C++ development environment. MFC is an extensive framework for general-purpose GUI application development in an object-oriented programming style (Kruglinski et al. 1998; Prosise 1999).

8.3 CyclicTP: A 2D Seismic Analysis Tool for Shallow Foundations

CyclicTP is intended primarily as an analysis tool for surface loads on saturated ground, under liquefaction-induced seismic excitation scenarios. Excitation is prescribed along the mesh base as total dynamic lateral motion. The lateral mesh borders undergo shear-beam type motions (equal motion of lateral boundaries is enforced). The program allows execution of linear analysis (with viscous damping) to allow users more basic insight, before exercising the plasticity-based nonlinear soil compatibilities.

8.3.1 Input Interface of CyclicTP

In CyclicTP, a FE model is defined by specifying (Figure 8.2): (1) the dimension and material properties of the footing; (2) soil strata; (3) Rayleigh viscous damping coefficients; and (4) base seismic excitation.

1) Soil Strata

A complete definition for each soil type requires about 15 modeling constants in the core FE code. Considering the large number of constants involved, we have pre-defined model parameters for typical soil types in the CyclicTP input interface (Figure 8.3). Definition of these constants was based partially on an intensive calibration phase, and partially on data from the available literature.

The pre-defined materials fall into two main categories (Table 8.1): cohesionless and cohesive. For cohesionless materials, it is known that relative density and permeability are among the most influential parameters controlling nonlinear stress-strain behavior and liquefaction response (Kramer 1996). Therefore, four cohesionless

soil types were defined to cover a wide range of relative densities: loose (representative of relative densities between 15 and 35%), medium (35-65%), medium-dense (65-85%), and dense (85-100%). Furthermore, each of the four types is associated with three different permeability coefficients (representative of silt, sand and gravel, respectively), resulting in a total of 12 materials. For cohesive materials (Table 8.1), there are three types based on shear strength: soft, medium, and stiff clay (J_2 plasticity cyclic model).

These representative properties (Table 8.1) attempt to embody the inevitable inaccuracies associated with measurement, testing, and standard site investigation procedures. However, the definition of these properties (e.g., for use in liquefaction analysis) lacks acceptance and needs scrutiny (e.g., via a peer review process), and in this regard remains of only limited value. Nevertheless, such pre-defined soil properties are: 1) indicators of ranges for values of the different parameters, 2) collectively as a set, allow the constitutive model to reproduce a response bracketed by observations (and some validation) based on the underlying employed data sets (from full-scale downhole array measurements, sample laboratory testing, and centrifuge testing data sets).

2) Viscous Damping

In CyclicTP, damping is mostly generated from soil nonlinear hysteretic response. Additional Rayleigh-type viscous damping may be assigned either by directly specifying two Rayleigh damping coefficients, or by way of specifying two damping ratios at two different frequencies (Chopra 2001). After these coefficients are defined, the corresponding damping ratio curve is portrayed as a function of frequency in a

dialog window (Figure 8.4). This useful visual feature allows the user to define interactively the desired dependence of damping on frequency.

3) Input Motion

Base seismic excitation can be defined by either of the following two methods (Figure 8.2):

i) Via a built-in input motion library. This library includes near-fault soil surface motions as well as long-duration rock outcrop motions recorded during past strong earthquakes worldwide, as described in detail in http://peer.berkeley.edu/research/motions/ (where these motions are available for downloading).

ii) 'U-Shake', a user-defined input motion. The user can select a pre-defined input motion file. This file will be screened to ensure valid formatting.

The amplitude of the input motion can be scaled by a factor ranging from 0.01 to 1.0. In addition, if '1g sinusoidal motion' is chosen, the user must specify excitation frequency and number of cycles.

8.3.2 Output Interface of CyclicTP

Many users are interested in response time histories at a particular depth (e.g. ground surface). Such time histories include acceleration, displacement, excess pore pressure, shear stress, and shear strain (Figure 8.6). In CyclicTP, the user can view all these histories for any desired depth at any horizontal location in one window (Figure

8.7). Moreover, the user can: (1) save any of these histories as a figure (images in Graphics Interchange Format or GIF), and (2) select any of these histories to be included in a report (Section 8.3.3).

In addition to time histories of individual variables, the user can also view animations of the deformed mesh, horizontal displacement, vertical displacement, excess pore pressure, excess pore pressure ratio, octahedral shear stress and effective confinement (Figure 8.6). An example of animating deformed mesh contour fill is shown in Figure 8.8.

The following software packages were employed in implementing the CyclicTP interfaces: (1) interactive X-Y plots are generated using PtPlot (http://ptolemy.eecs.berkeley.edu), an open source plotting tool written in Java language (Lee et al. 2001), and (2) all images (GIF files) are created using the freeware GNUPLOT (http://gnuplot.info).

8.3.3 Report Generator

Instead of keeping all model input/output data in many separate files, a convenient option is to write a report that includes all desired information about the simulation. Using the report generator function in the CyclicTP output interface, a customized report can be created in Microsoft Word or Rich Text Format (RTF) for further modification. While the Word file format is most convenient for computers using a Windows operating system, the RTF format is compatible with many other operating systems including Unix and Macintosh.

The report generator window allows the inclusion of any portion of the model input/output information described above. In the resulting report, input model parameters are listed in tables, whereas the simulation results are presented as GIF images.

The report generator was implemented using an application interfacing technique known as Automation (developed by Microsoft Corporation). Automation allows a developer to take advantage of existing software, by directly incorporating its content and functionality into his/her own applications (Prosise 1999). Microsoft provides the Microsoft Word Object Library, which contains all necessary functions for creating a Word file. Using the Automation technique, one can access the member functions of this library from within the Visual C++ environment, in order to create a new Word document and insert text, tables, and figures into it.

8.4 CyclicED: A 2D Seismic Simulation Environment for Earth Dams

After the 1971 San Fernando Earthquake, extensive reevaluation and remediation of earth dams took place, and the number of seismically unsafe dams was substantially reduced. Nevertheless, of over 110,000 dams in the U.S. (Association of State Dam Safety Officials ASDSO 1992), 30% are more than 50 years old by now (Tschantz 1985), and many are in need of repair. Moreover, reevaluation is necessary in areas where previously undiscovered faults have been found and where known faults have been reclassified (United States Committee on Large Dams USCOLD 1999).

The formidable task of periodical reassessment of a large number of dams calls for efficient procedures that can reliably identify potential damage states and prioritize

risks associated with each dam. However, the development of performance and risk assessment tools for earth dams is still at a preliminary stage (Elgamal et al. 2002a; United States Society on Dams USSD 2003; Yang et al. 2004a).

In view of the above, a seismic simulation environment for earth dams, CyclicED, was developed (Figure 8.9 and Figure 8.10).

8.4.1 Model Builder of CyclicED

The model builder allows the user to build an earth dam FE model by specifying the geometry of the dam shell, the dam core and the foundation involved (Figure 8.9). One special feature implemented in CyclicED is to allow the user to define the water table levels on the upstream and downstream sides of the earth dam. Therefore, liquefaction problems of any water table level in the reservoir can be simulated in CyclicED.

8.4.2 Output Interface of CyclicED

Most features implemented in CyclicED (Figure 8.10) are quite similar to those in CyclicTP. Please refer to Section 8.3 for more details.

8.5 Cyclic1D: A 1D Earthquake Liquefaction Analysis Tool

For the purpose of structural design, it is often assumed that (Kramer 1996): 1) near ground surface, earthquakes result in lateral shear waves propagating predominantly in the vertical direction, and 2) the soil material is laterally uniform. Under such conditions, it is sufficient to study the behavior of a one-dimensional (1D)

soil column (either level or inclined) deforming as a shear beam, subjected to earthquake motion exerted at the base. This is the basis of the well-known computer program SHAKE (Schnabel et al. 1972; Idriss and Sun 1992), a widely used tool in practice. SHAKE can simulate mildly nonlinear site amplification in level ground with adequate accuracy, but does not address the important situation of liquefaction. This is due to the fact that SHAKE employs degraded but linear elastic properties for soil response.

Cyclic1D is a seismic analysis tool for conducting simulations of nonlinear seismic ground response including liquefaction. Such simulations provide critical information for earthquake-resistant structural design in seismically active areas.

8.5.1 Model Builder of Cyclic1D

In the model builder (Figure 8.11), the user defines a FE model by specifying: (1) the soil profile of interest; (2) material composition of the profile; (3) Rayleigh viscous damping coefficients; and (4) base seismic excitation. All of these features are similar to CyclicTP. Please refer to Section 8.3 for more details.

8.5.2 Output Interface of Cyclic1D

The output interface includes response time histories at a particular depth (e.g. ground surface). Such time histories include acceleration (and its response spectrum and Fourier spectrum), displacement, excess pore pressure, shear stress, and shear strain (Figure 8.12).

In addition to time histories of individual variables, the user can also view the maximum and final values of these variables along the model depth (i.e. response profile or response envelope, Figure 8.13). These response profiles help the user appreciate overall performance of the model. Similarly, all model input/output data can be placed into a report by using an automatic report generator (Figure 8.14).

Again, most of the features implemented in Cyclic1D are quite similar to those in CyclicTP. Please refer to Section 8.3 for more details.

8.6 CyclicPL: A 3D Seismic Analysis Tool for Single Pile in a Half-space

CyclicPL is a special purpose user-friendly interface (Figure 8.15) allowing convenient studies of 3D seismic (earthquake) and/or push-over pile analyses.

8.6.1 Model Builder of CyclicPL

CyclicPL includes a pre-processor for: 1) definition of the pile geometry and material properties, 2) definition of the 3D spatial soil domain, 3) definition of the boundary conditions and input excitation or push-over analysis parameters, and 4) selection of soil materials from an available menu of cohesionless and cohesive soil materials (Figure 8.16). CyclicPL also allows users to control soil parameters (Figure 8.16) such as yield strength (S_u) for instance, making the definition of properties as simple as the user wishes and the situation demands. The selection of soil materials was discussed in Section 8.3.

Definition of pile dimension and material properties is an important part in CyclicPL. In this interface, pile cross section can be circular or square. The interface can

generate meshes for piles in slopes, knowing that this problem is one of great significance (Figure 8.17). Options of quarter mesh, half mesh and full mesh (Figure 8.18) are available for use (to reduce computational effort depending on the situation at hand). In addition, CyclicPL allows for simulations for any size of pile diameter. In this regard, it can be used for analysis of large diameter shafts, an extremely involved modeling problem, for which p-y type (L-Pile style) analyses may be more difficult to calibrate.

It is important to note that CyclicPL is not only meant to conduct complex analyses, but can be used for simple and insightful configurations. In either case, the problem definition and program execution might actually be as convenient as using simplified programs such as L-Pile for instance. The outcome no doubt will be a great complement to insights from programs such as L-Pile, but actually will also allow for studying configurations that far exceed those possible by p-y logics.

8.6.2 Output Interface of CyclicPL

The output interface of CyclicPL allows the user to view the deformed mesh and the response time histories. In addition, pile response such bending moment and deflection profiles can be viewed in CyclicPL. Other features implemented in CyclicPL (Figure 8.10) are also quite similar to those in CyclicTP. Please refer to Section 8.3 for more details.

8.7 Summary

In an attempt to increase efficiency and reduce the chance for error, a series of user-friendly interfaces have been developed to facilitate use of otherwise complicated computational environments with numerous (often vaguely defined) input parameters. These user interfaces provide libraries of pre-defined material properties and input motions, tools for viewing computational results, and automated report generation capabilities. The effort is a first step in the direction of allowing for more convenient exposure and utilization of such computational tools. A peer review process is needed to verify and provide further credibility to the pre-defined structural and soil model parameters and the resulting responses.

Table 8.1: Representative set of basic material parameters (data based on Seed and Idriss (1970), Holtz and Kovacs (1981), Das (1983), and Das (1995)) (Elgamal et al. 2004).

Cohesionless Soils	Shear wave velocity* at 10m depth (m/s)	Friction angle (degrees)	Possion's ratio	Mass density (kg/m^3)
Loose	185	29	0.4	$1.7x10^3$
Medium	205	31.5	0.4	$1.9x10^3$
Medium-dense	225	35	0.4	$2.0x10^3$
Dense	255	40	0.4	$2.1x10^3$
Cohesive Soils	Shear wave velocity (m/s)	Undrained shear strength (kPa)	Possion's ratio	Mass density (kg/m^3)
Soft clay	100	18.0	0.4	$1.3x10^3$
Medium clay	200	37.0	0.4	$1.5x10^3$
Stiff clay	300	75.0	0.4	$1.8x10^3$

* Shear wave velocity of cohesionless soils in proportion to $(p_m)^{1/4}$ where p_m is effective mean confinement.

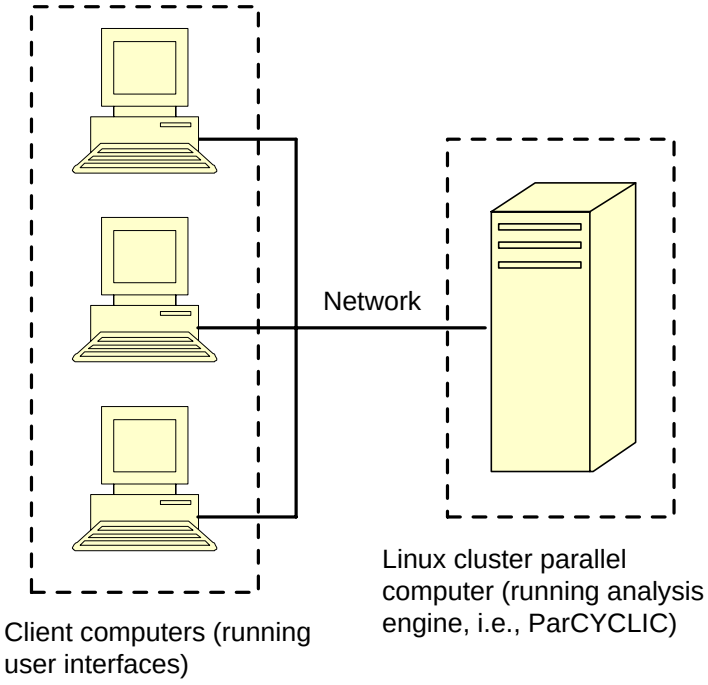

Figure 8.1: Architecture of network-based computing.

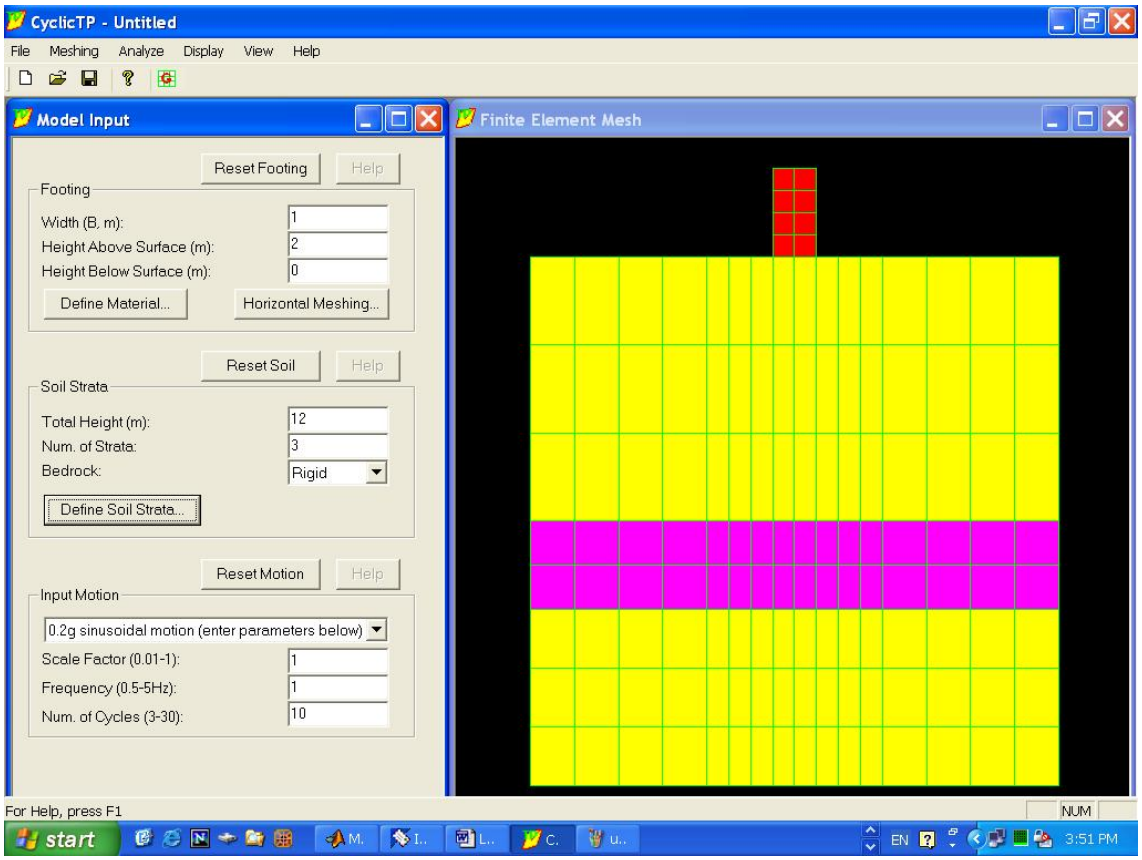

Figure 8.2. CyclicTP user interface.

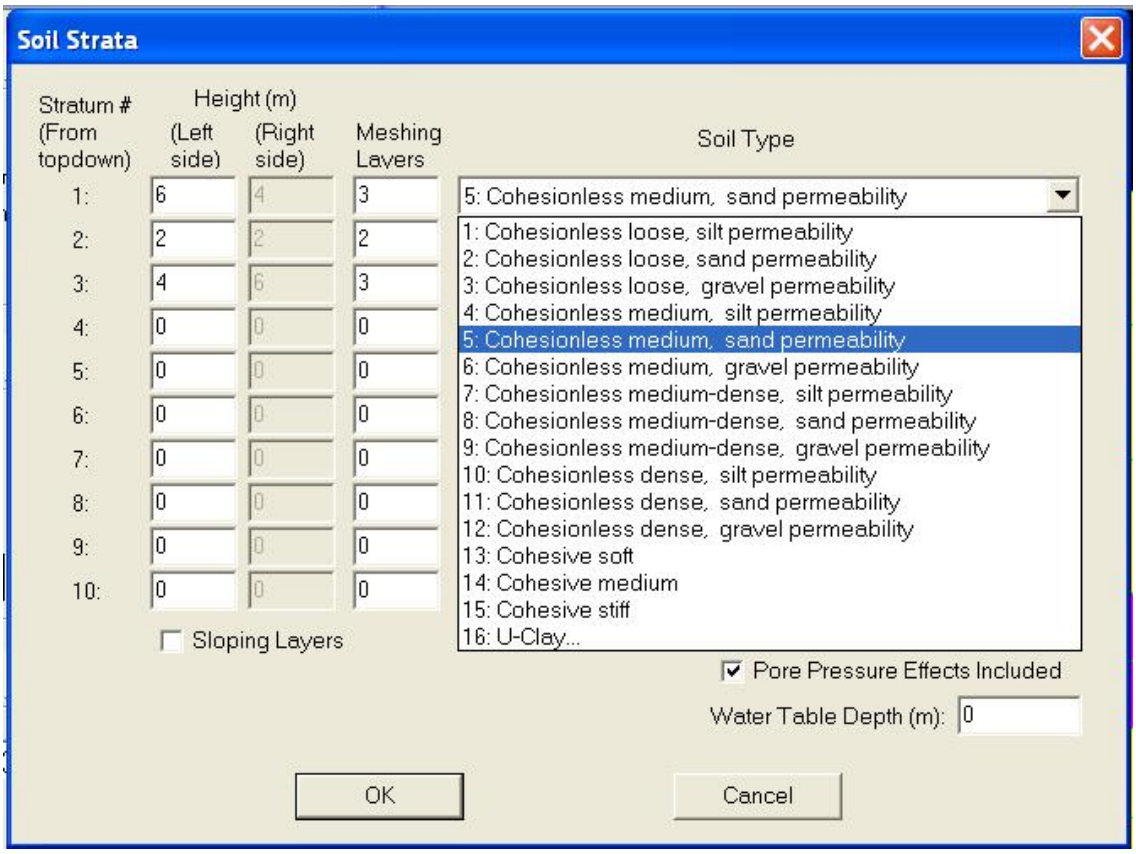

Figure 8.3. User dialog window for defining soil material properties.

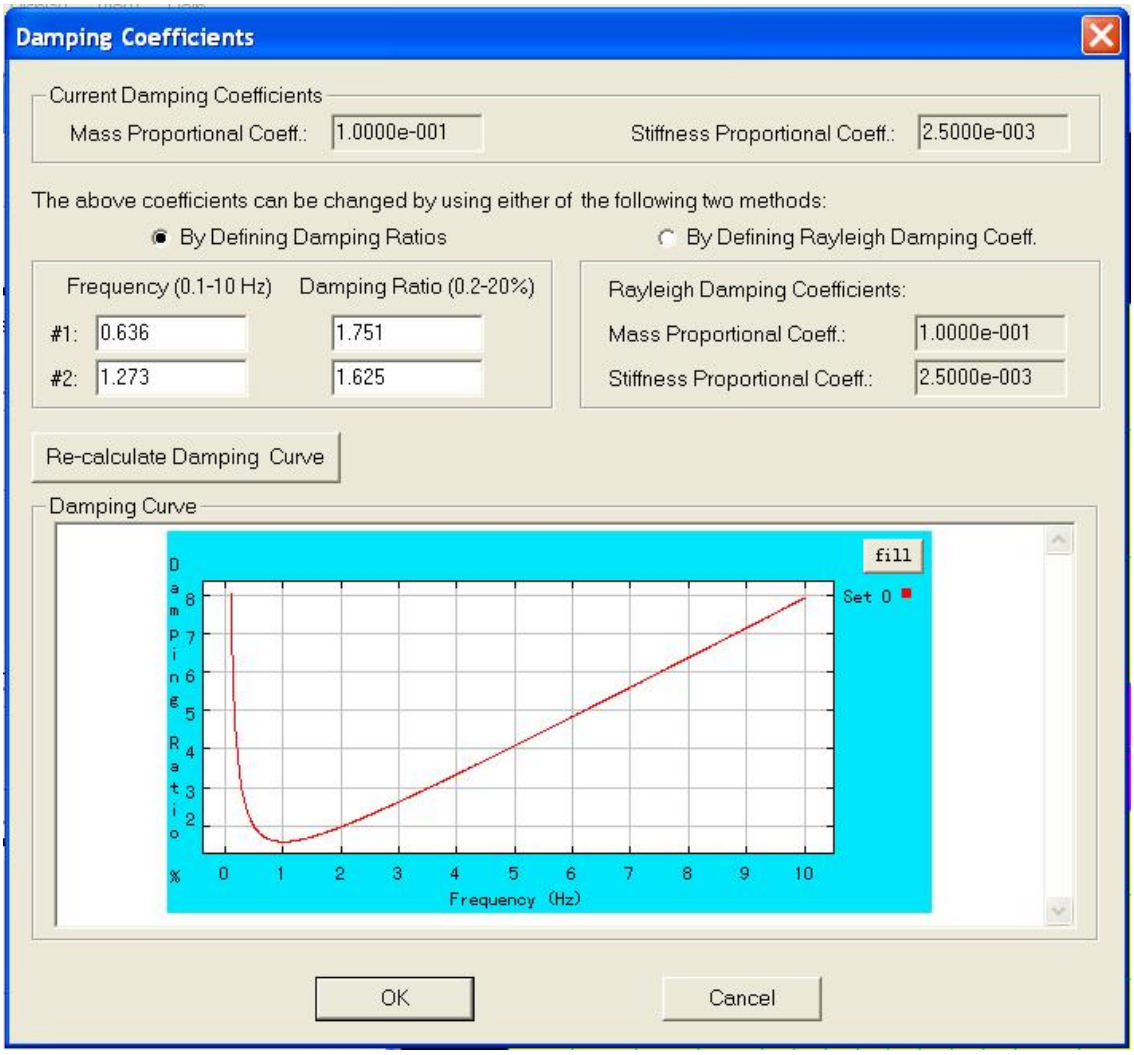

Figure 8.4: User dialog window for defining Rayleigh damping coefficients and viewing damping ratio curve as a function of frequency.

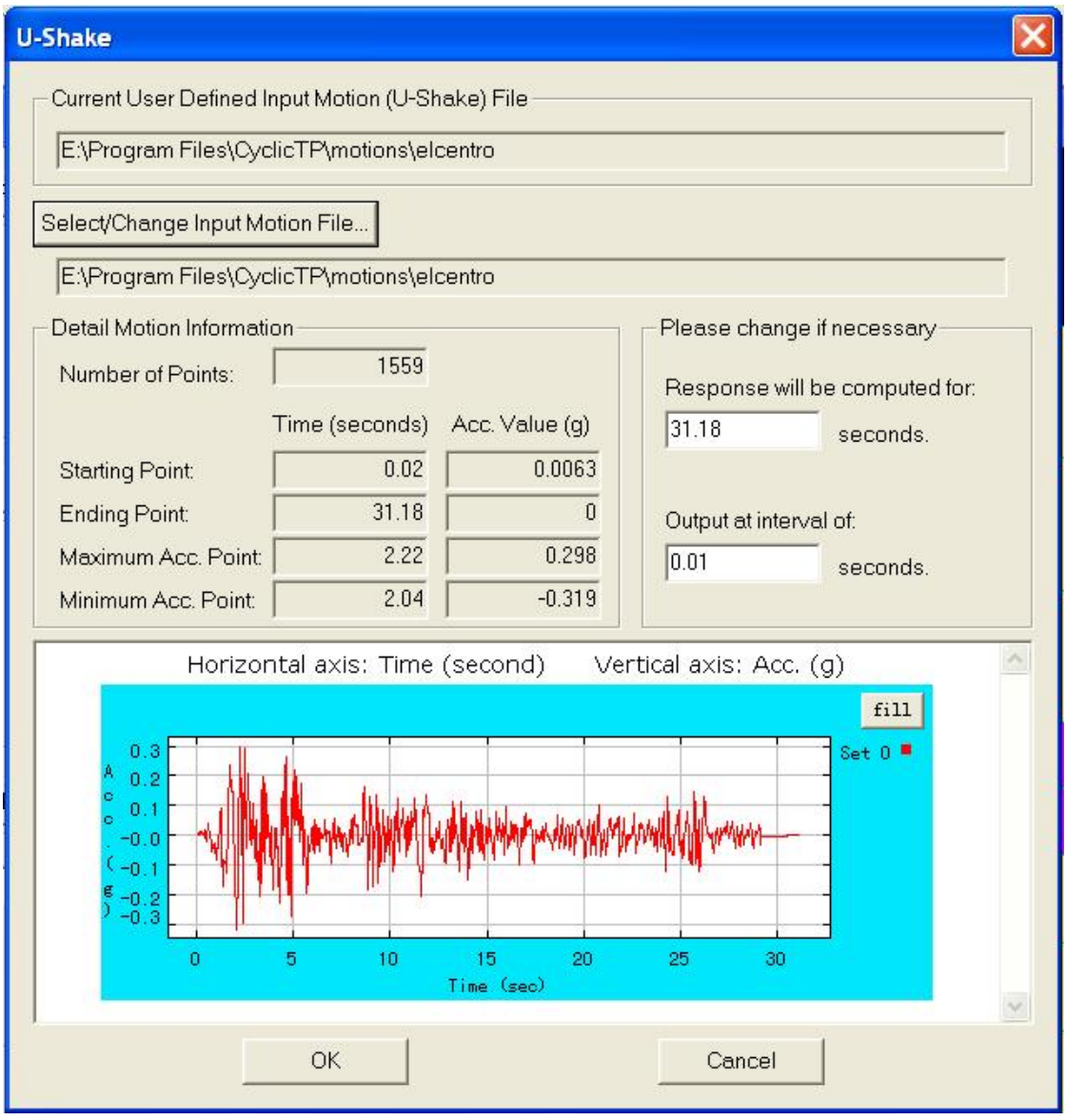

Figure 8.5: User dialog window for defining U-shake (user-defined input motion).

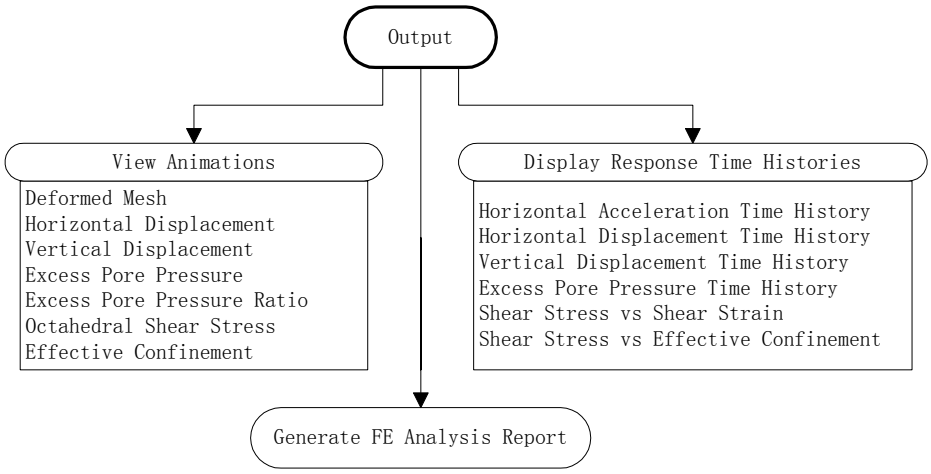

Figure 8.6: CyclicTP output interfaces.

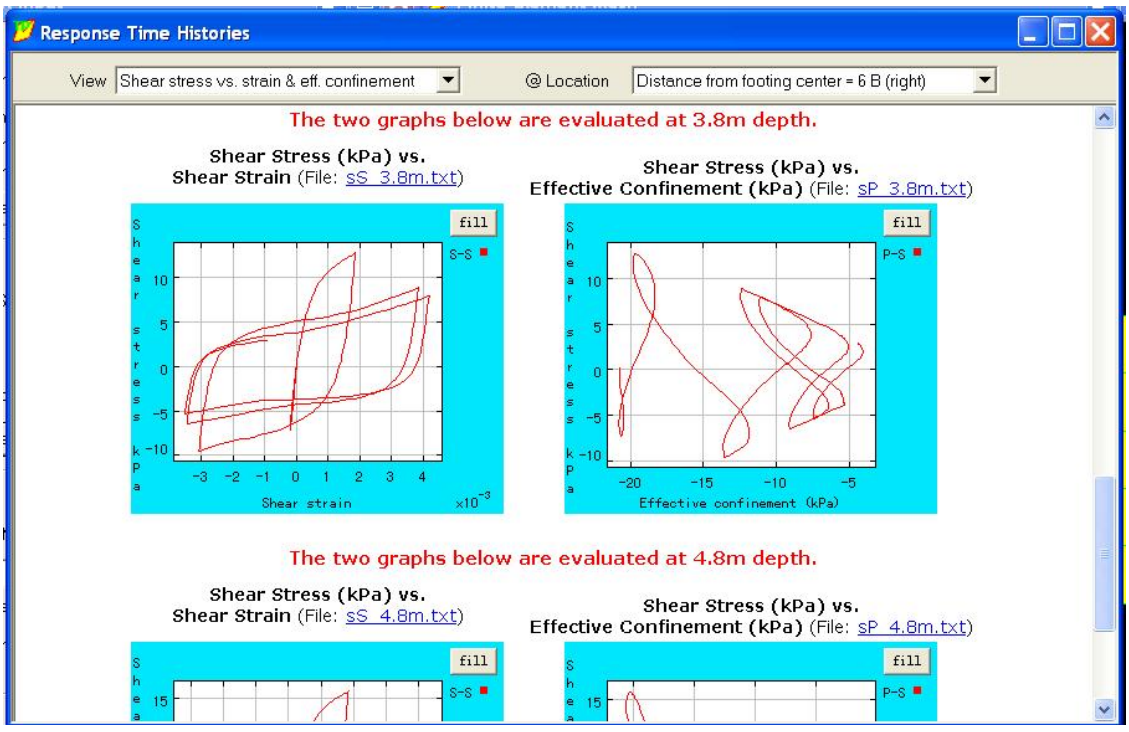

Figure 8.7: Sample graphical output for response time histories in CyclicTP.

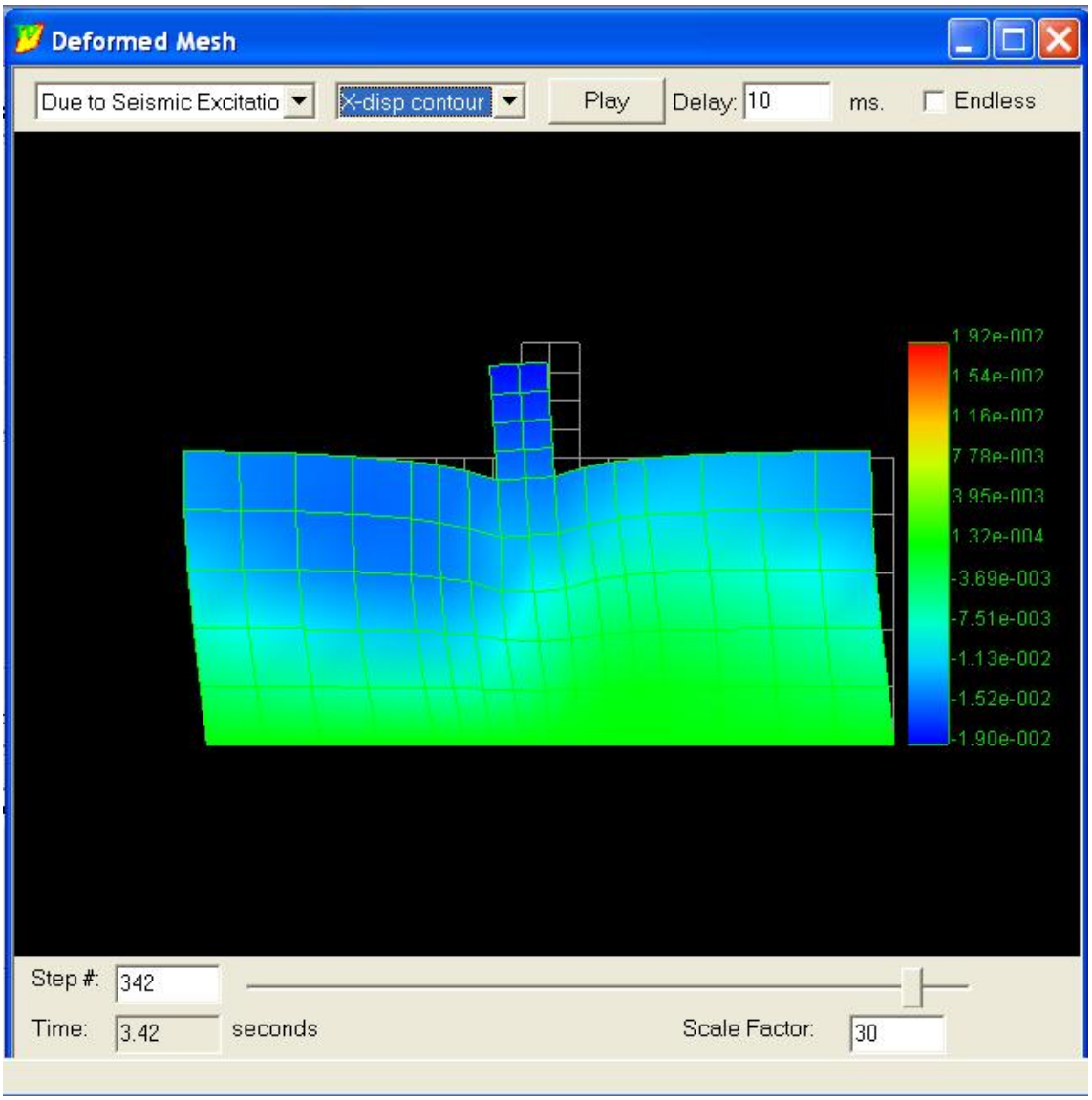

Figure 8.8: Animation display of deformed mesh in CyclicTP.

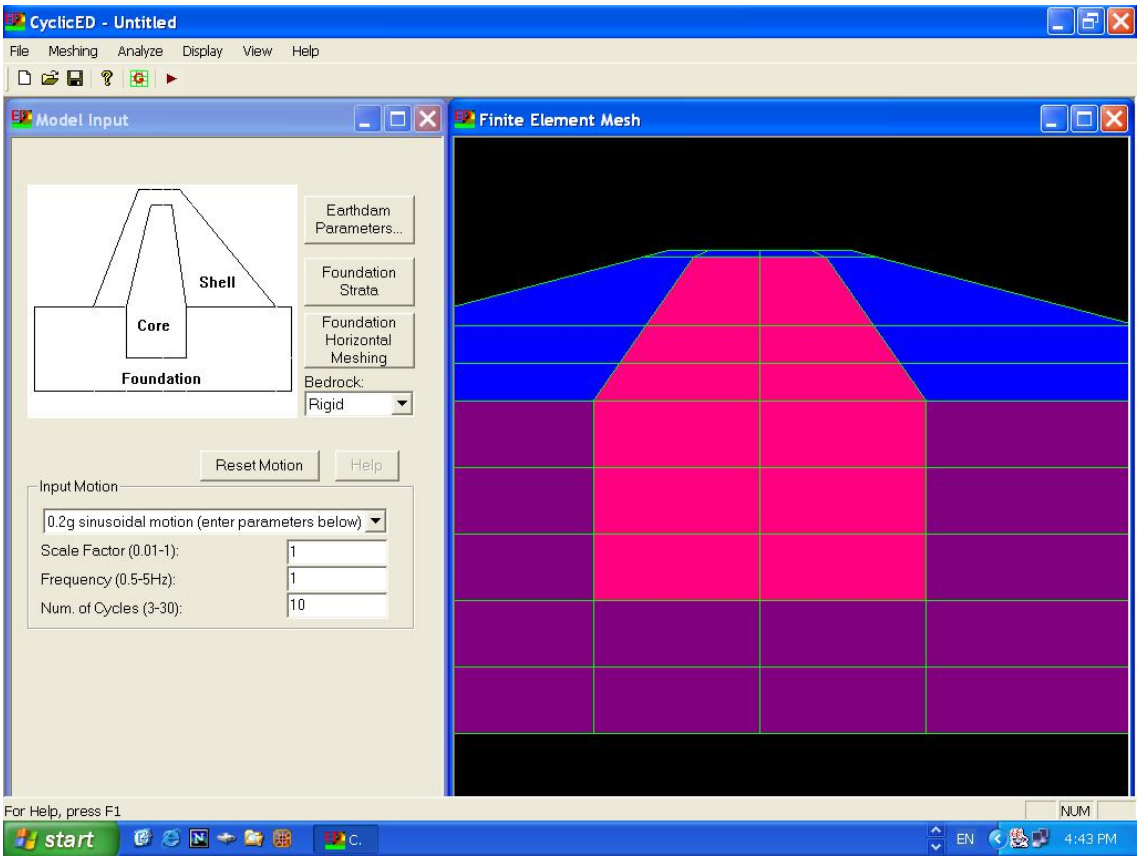

Figure 8.9: CyclicED model builder.

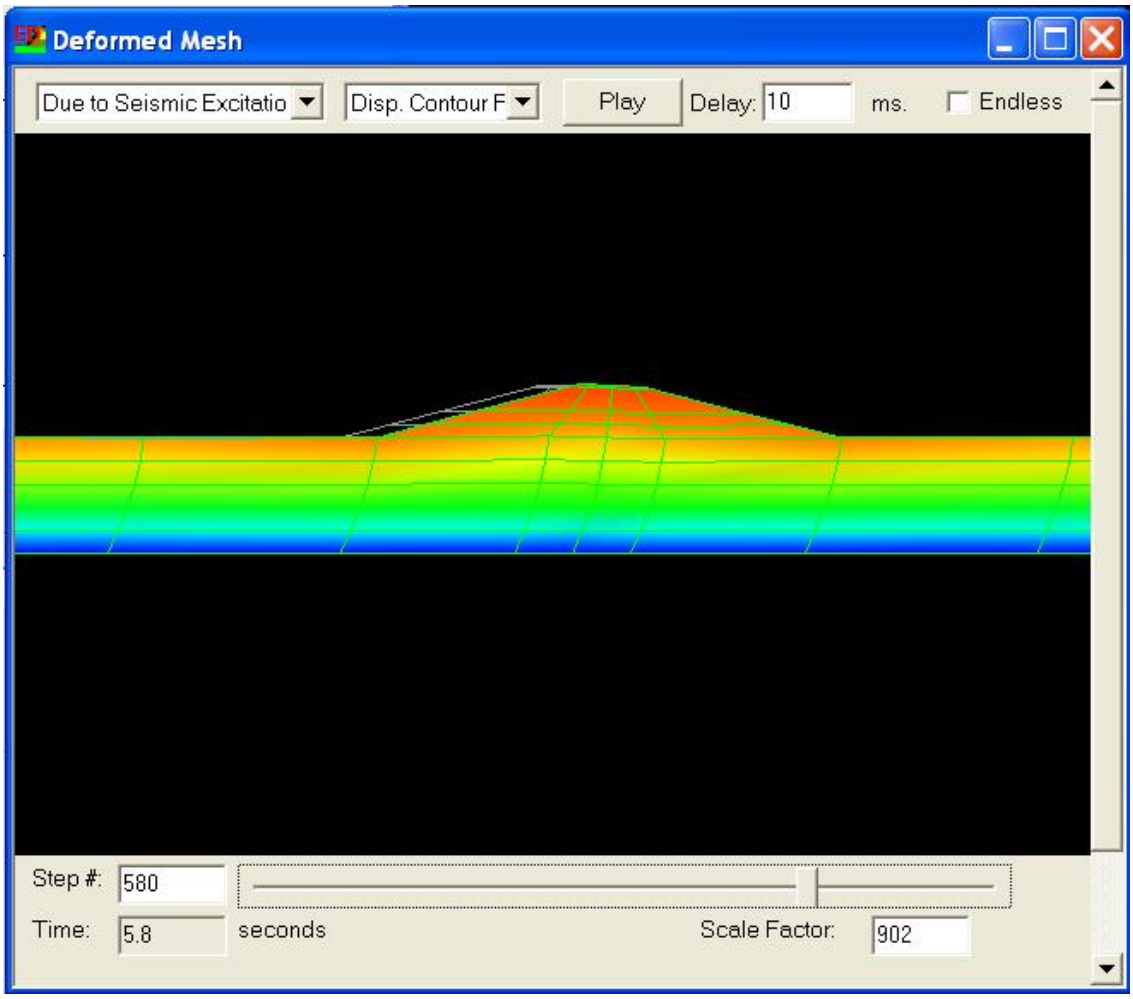

Figure 8.10: Deformed mesh in CyclicED.

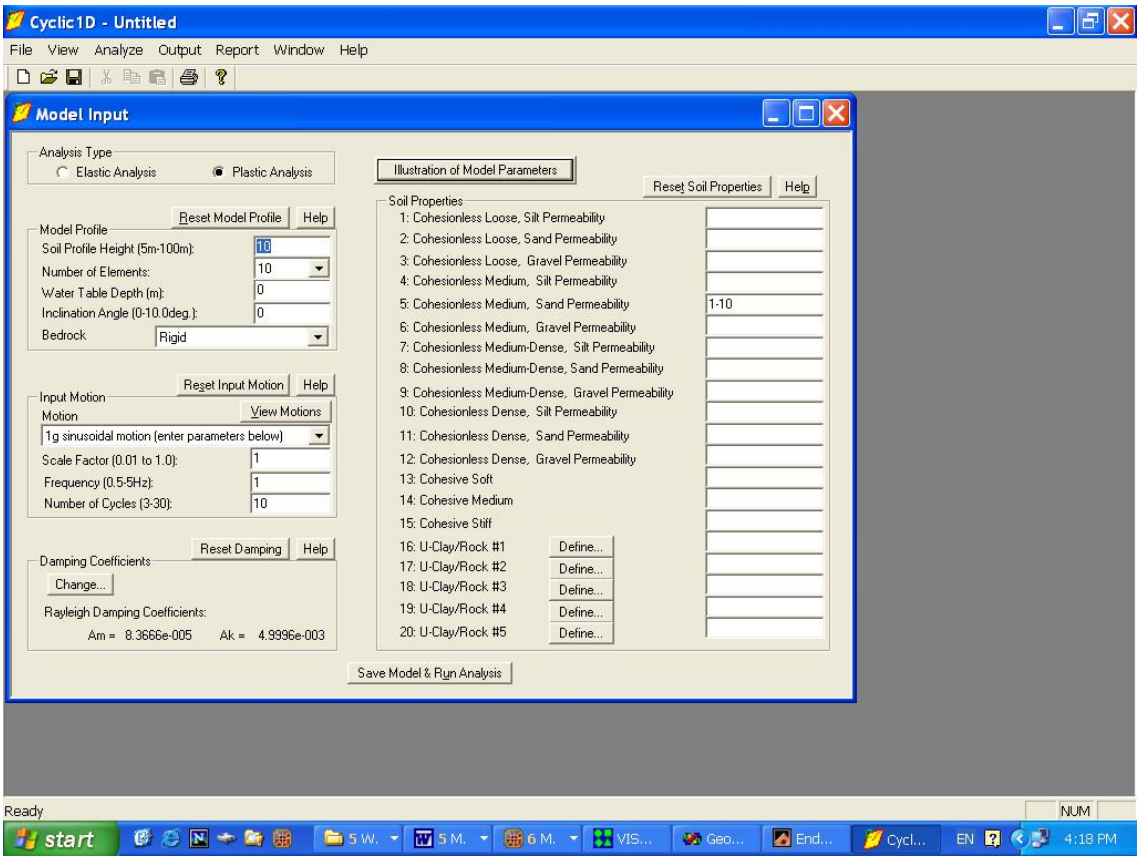

Figure 8.11: Cyclic1D model builder.

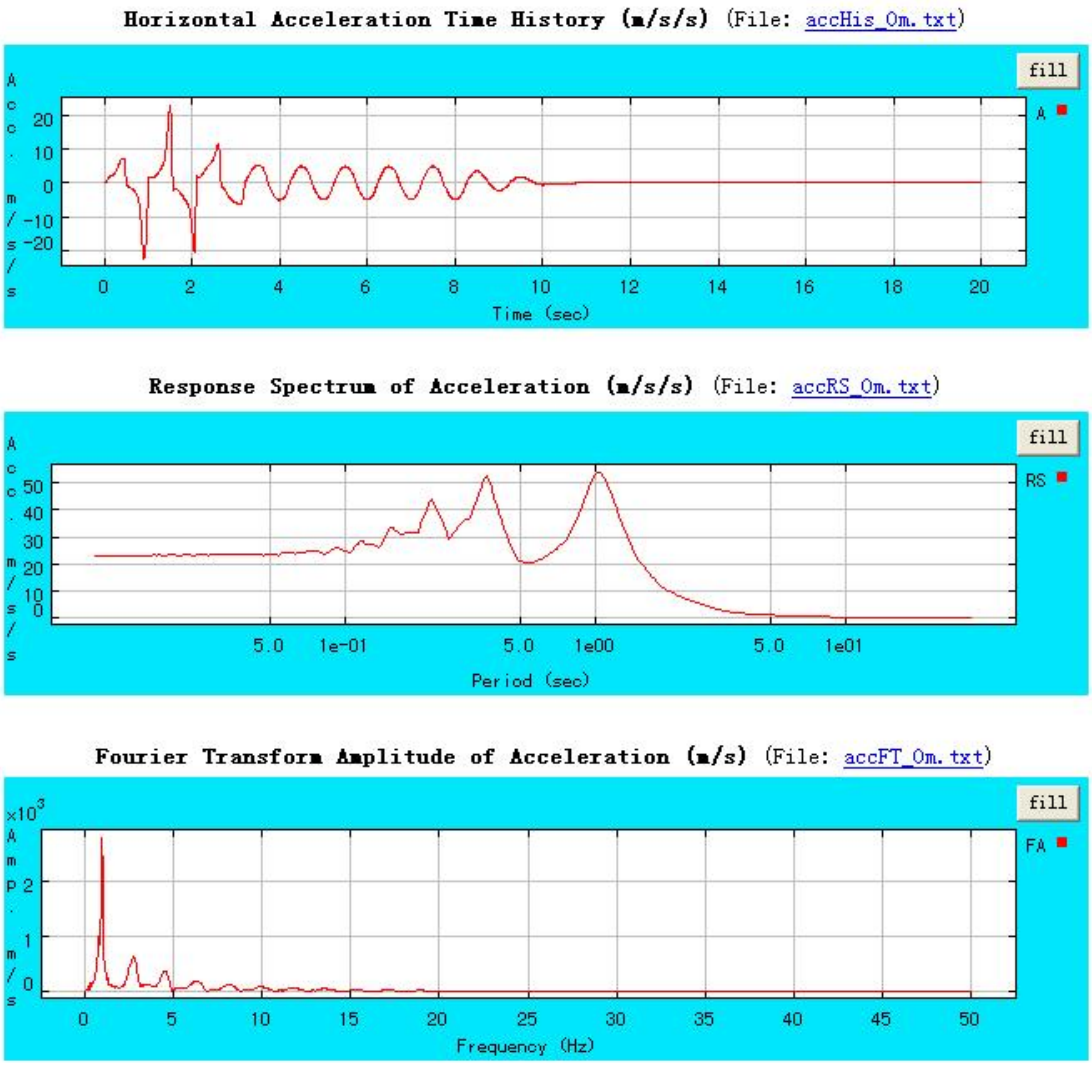

Figure 8.12: Sample graphical output for response time histories in Cyclic1D.

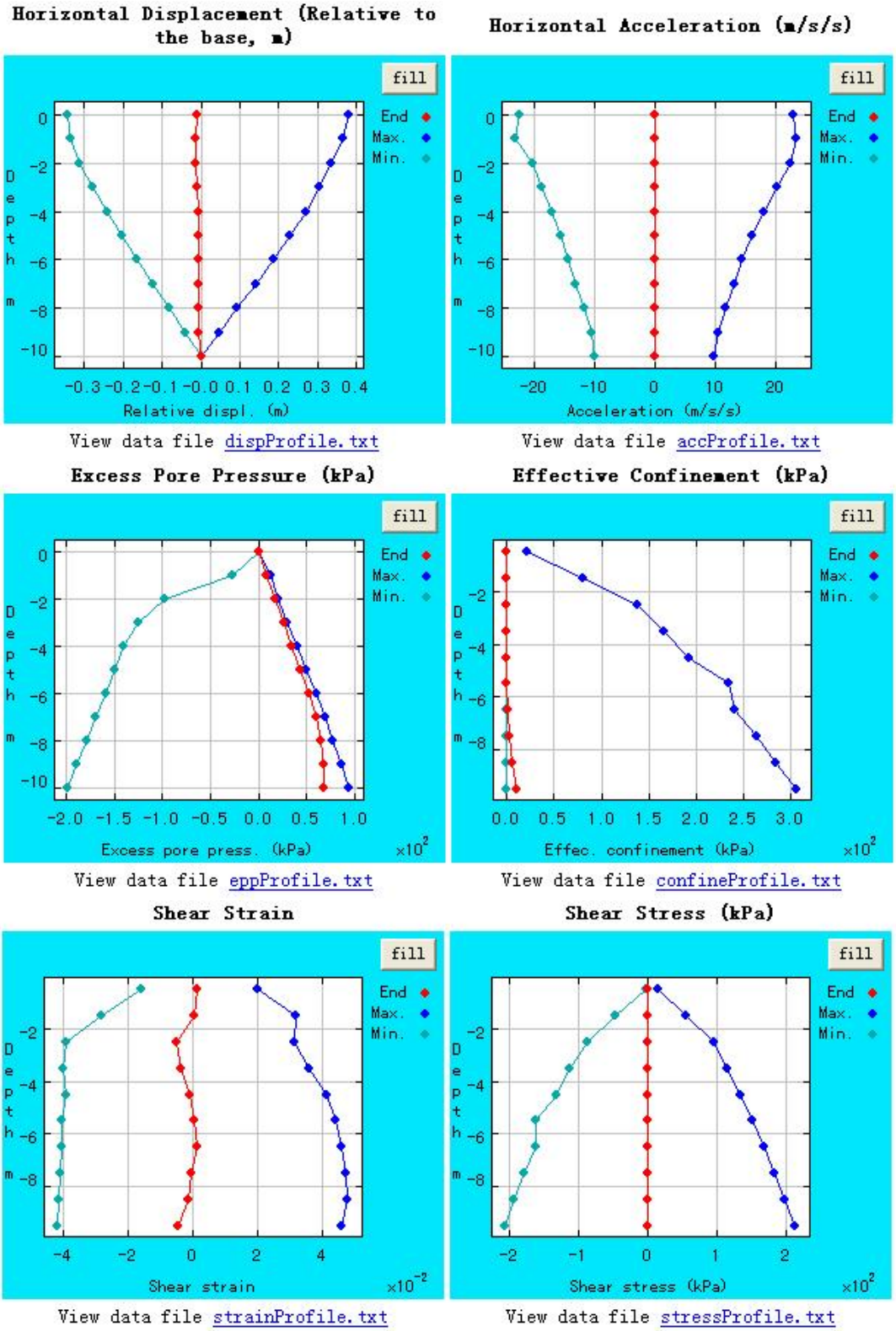

Figure 8.13: Sample graphical output for response profiles in Cyclic1D.

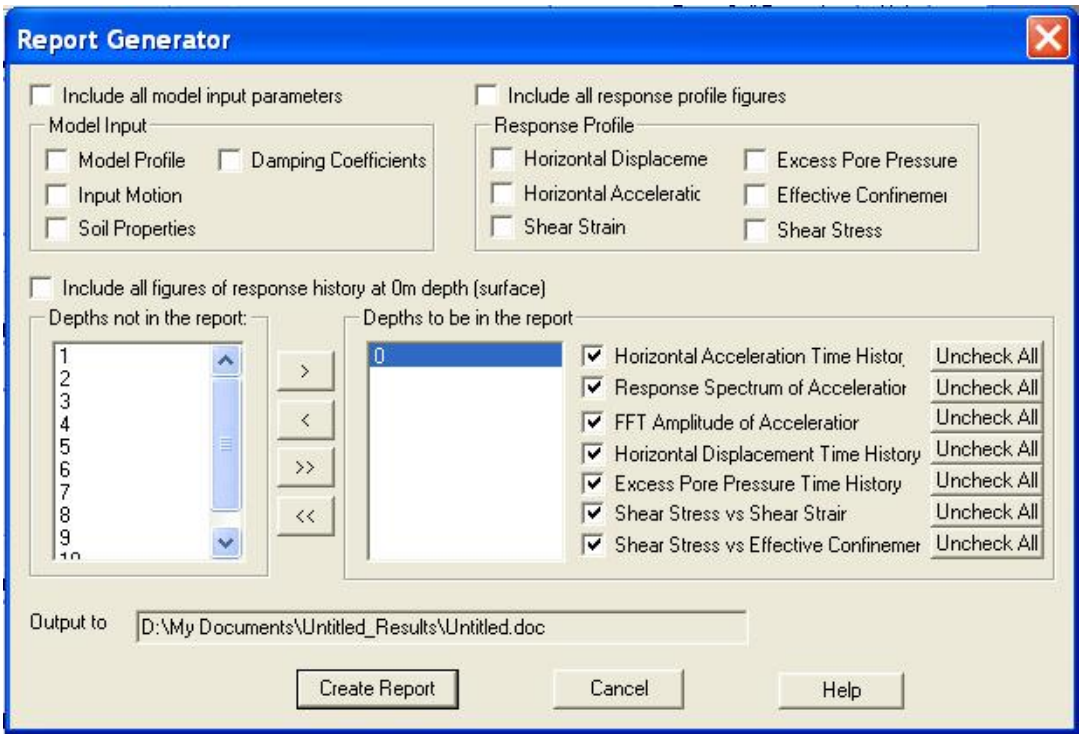

Figure 8.14: Report generator in Cyclic1D.

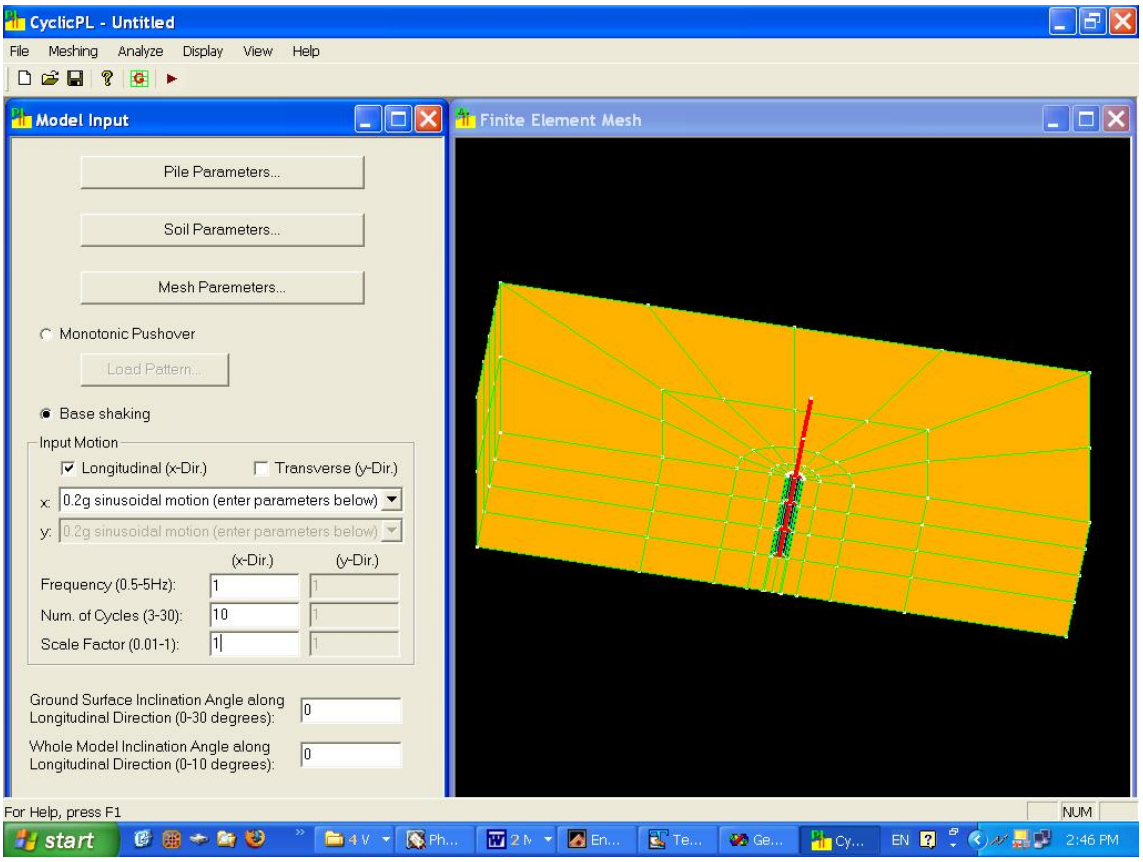

Figure 8.15: CyclicPL user interface (the mesh shows a circular pile in level ground (view of ½ mesh employed due to symmetry for uni-directional lateral loading)).

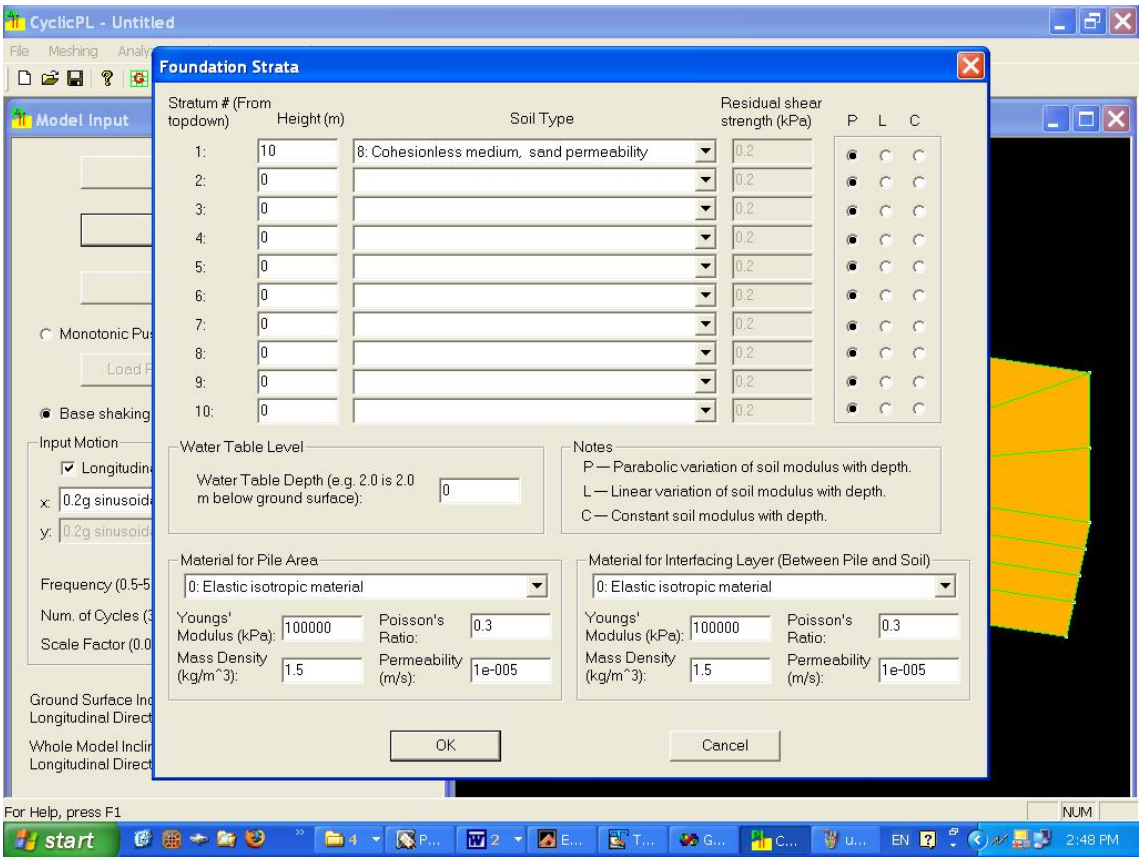

Figure 8.16: Definition of foundation/soil properties in CyclicPL.

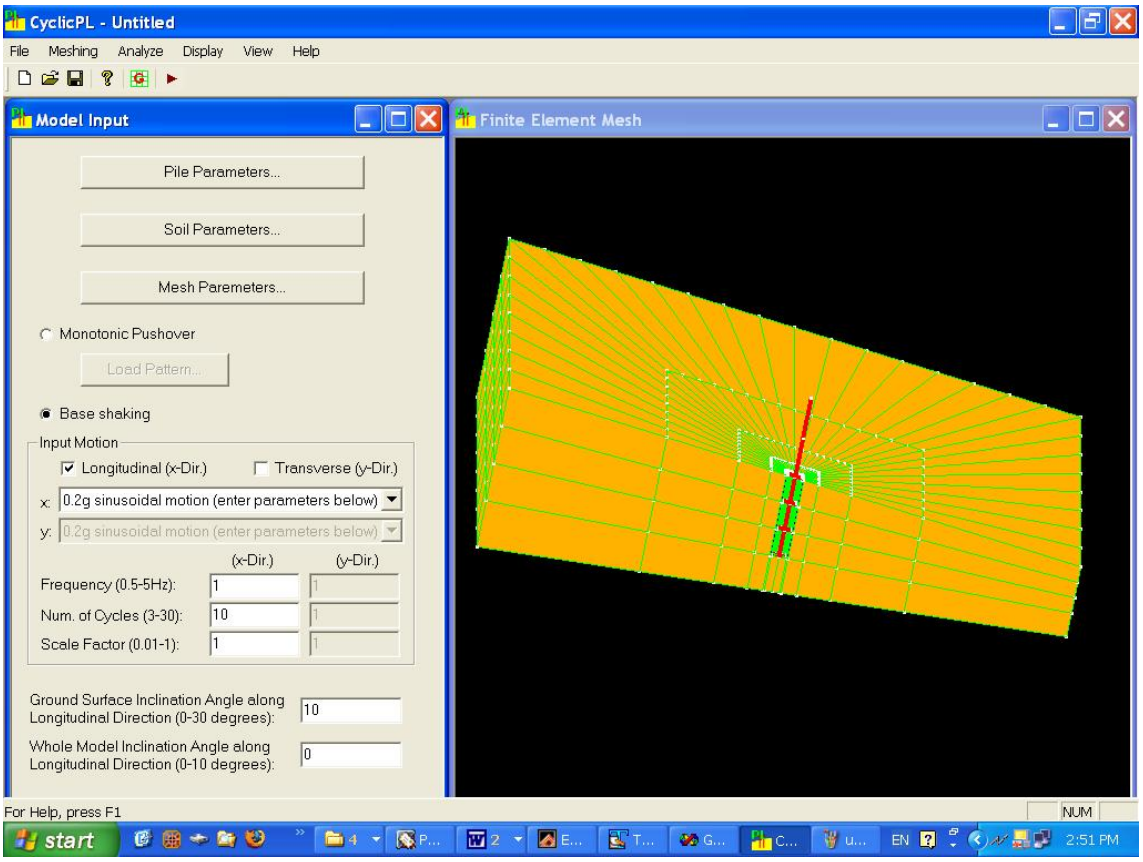

Figure 8.17: Square pile in slope: filled view of ½ mesh due to symmetry.

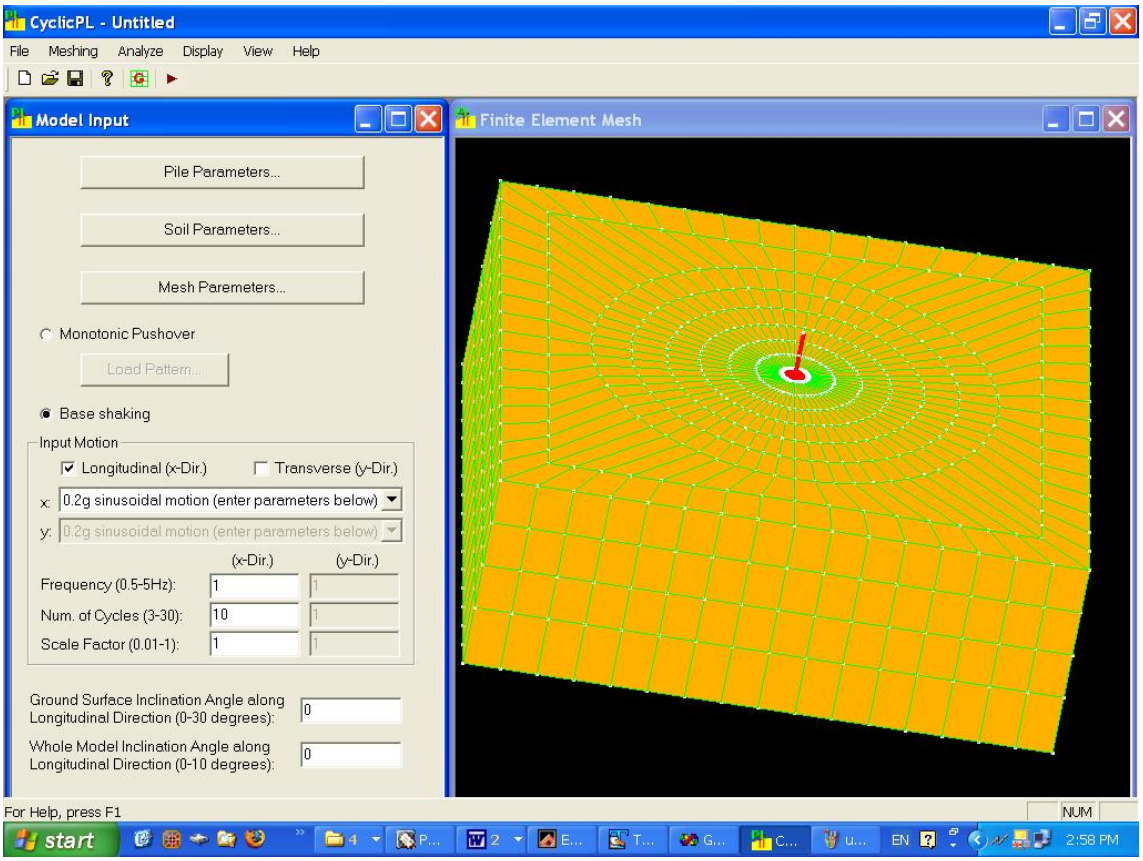

Figure 8.18: Filled view of fine 3D full-mesh (for combined x-y loading) in CyclicPL.

Chapter 9 Summary and Suggestions for Future Research

9.1 Summary

A parallel nonlinear FE program, ParCYCLIC, was developed to conduct simulations of earthquake ground/structure response including liquefaction scenarios. In ParCYCLIC, finite elements are employed within an incremental plasticity, coupled solid-fluid formulation. A constitutive model developed for the simulation of liquefaction-induced deformations is a main component of this analysis framework. Extensive calibration of ParCYCLIC has been conducted based on results from experiments and full-scale response of earthquake simulations involving ground liquefaction.

The solution strategy in ParCYCLIC is based on a parallel sparse solver (Law and Mackay 1993). Several improvements have been made to the original parallel sparse solver. An automatic domain decomposer was developed to partition the FE mesh so that the workload on each processor is more or less evenly distributed and the communication among processors is minimized. METIS routines (Karypis and Kumar 1997) were incorporated in ParCYCLIC to perform domain decomposition, and the internal nodes of each sub-domain were ordered using Multilevel Nested Dissection among other ordering strategies. Due to the deployment of the automatic domain decomposer, the input files for ParCYCLIC are easy to prepare. No information for processor assignment of nodes and elements is needed, and the input essentially has the same format as that for the sequential program CYCLIC.

In addition, a parallel data structure was introduced to store the matrix coefficients. There are three different data structures for storing these coefficients: one for the principal block submatrices associated with the column blocks assigned to a single processor, one for the principal block submatrices associated with column blocks shared by multiple processors, and one for the row segments in column blocks.

An enhancement to the original parallel solver is the processor communication interface. The original solver was designed for running on Intel supercomputers such as the hypercube, the Delta system and the Intel Paragon; and the message-passing routines were written using the Intel NX library (Pierce and Regnier 1994). Communication in ParCYCLIC was written in MPI (Snir and Gropp 1998), making ParCYCLIC more portable to run on a wide range of parallel computers and workstation clusters.

Large-scale experimental results for 3D geotechnical simulations including shallow foundation settlement studies and pile-supported wharf system modeling have been presented to demonstrate the capability and performance of ParCYCLIC. Simulation results demonstrated that ParCYCLIC is suitable for large-scale geotechnical/structural simulations.

Calibrated FE simulations are increasingly providing a reliable environment for modeling liquefaction-induced ground deformation. Effects on foundations and super-structures may be assessed and associated remediation techniques may be explored, within a unified framework. Current capabilities of such a FE framework are demonstrated via a simple 3-dimensional (3D) series of simulations. High-fidelity 3D numerical simulations using ParCYCLIC conducted on parallel computers were shown to provide more accurate estimates of liquefaction-induced foundation settlements.

A series of scenario-specific user-friendly interfaces were also developed to allow for high efficiency and much increased confidence. Such user-friendly interfaces are useful not only for simulation of small size problems on one-single processor (e.g., a PC machine) but also for parallel large-scale modeling on a multiprocessor workstation (e.g., a 8-processor Linux Cluster).

9.2 Main Conclusions and Observations

9.2.1 Numerical Algorithm Performance and Efficiency

The automatic domain decomposer implemented in ParCYCLIC was able to provide load balancing among processors. Usage of ParCYCLIC is essentially as easy as that of the serial code due to the deployment of the automatic domain decomposer.

The serial version of the Multilevel Nested Dissection algorithm for ordering of the FE nodes is rather fast (it takes less than 1 minute to order a model with 1 million degrees of freedom on a 1.5GHz IBM Power4 processor). In this regard, the parallel version of the Multilevel Nested Dissection algorithm may not be necessary for nonlinear modeling of geotechnical problems (similar to the ones studies herein).

The computation time spent on the initialization phase, including the FE model input, constitutive model preparation and solver initialization, is insignificant compared to the entire nonlinear analysis. Less than 5% of the total execution time is spent on the initialization phase for modeling a system with 20,000 degrees of freedom. In this regard, parallelization of a serial nonlinear FE code should be focused on the nonlinear solution phase (solving of the system of linear equations).

It is found that ParCYCLIC, which employs a direct solution scheme, remains scalable to a large number of processors (e.g., 64 or more). In addition, ParCYCLIC can be used to simulate large-scale problems, which would otherwise be infeasible using single-processor computers due to the limited memory. The parallel computational strategies employed in ParCYCLIC are general and can be adapted to other similar applications without difficulties.

9.2.2 Soil-Foundation System Response

High drainage was found to be effective in reducing liquefaction-induced settlement of a shallow foundation. In the investigated scenario, high permeability right under the foundation only, immediately reduced settlement by more than 50%. The zone treated by compaction was relatively little consequence.

The dynamic soil-structure interaction of a pile-supported wharf system is a complex process. Large-scale modeling on parallel computers can provide a better understanding of its seismic behavior. It was found that 3D modeling may shed more light than 2D plane strain modeling in simulating a wharf system.

9.3 Suggestions for Future Research

1) Currently ParCYCLIC can run efficiently on parallel computers. For a distributed environment, ParCYCLIC has to be re-engineered. A new multi-task SPMD (Single-Program Multiple-Data) program model will be needed for a cluster of PCs and workstations (some may have multiprocessors).

Furthermore, a hybrid direct/iterative solution strategy will be needed for a heterogeneous network of PCs and workstations.

2) The efficient parallel sparse symmetric solver can be extended for unsymmetric matrix situations.

3) The implemented solid-fluid coupled formulation assumes small deformation and small displacements. However, liquefaction phenomena often result in large deformation and large displacements. A FE implementation based on large deformation and large displacement assumptions (e.g., Total Lagrangian or Updated Lagrangian formulation) is believed to render more stable numerical performance and more accurate predictions.

4) 3D 20-node brick elements are currently crudely employed for the structural elements (e.g., piles). However, beam elements are more appropriate for pile foundations for instance. Adding beam elements, especially with nonlinear capabilities would be very useful.

5) An interactive web environment that supports simulations of 2D and 3D models utilizing a distributed/parallel computing environment will be very helpful. In this environment, a library of predefined 2D/3D meshes should be included for commonly encountered geotechnical problems. Users should be able to modify the mesh attributes or even submit their own meshes. Viewing of the results should be facilitated by the ever advancing 3D visualization tools.

Appendix A Procedure for Constructing Shape Functions for 3D 8-27 Node Brick Elements

Referred to Figure 2.4, the local node numbering pattern for a 3D brick element is as follows:

Nodes 1- 4: Lower surface, counterclockwise

Nodes 5 - 8: Upper surface, counterclockwise

Nodes 9 - 12: Mid-sides of edges 1-2, 2-3, 3-4, 4-1

Nodes 13 - 16: Mid-sides of edges 5-6, 6-7, 7-8, 8-5

Nodes 17 - 20: Mid-sides of edges 1-5, 2-6, 3-7, 4-8

Nodes 21 - 26: Mid-face nodes on +r, +s, +t, -r, -s, -t

Node 27: Centroid node

The procedure to construct shape functions for 3D 8-27 node brick element is as follows:

Step 1: Construct basic three-dimensional quadratic shape functions (where N_i represents the shape function of Node i, ξ, η and ζ are three normalized coordinates):

$$N_1 = \frac{1}{8}(1-\xi)(1-\eta)(1-\zeta) \qquad N_5 = \frac{1}{8}(1-\xi)(1-\eta)(1+\zeta)$$

$$N_2 = \frac{1}{8}(1+\xi)(1-\eta)(1-\zeta) \qquad N_6 = \frac{1}{8}(1+\xi)(1-\eta)(1+\zeta)$$

$$N_3 = \frac{1}{8}(1+\xi)(1+\eta)(1-\zeta) \qquad N_7 = \frac{1}{8}(1+\xi)(1+\eta)(1+\zeta)$$

$$N_4 = \frac{1}{8}(1-\xi)(1+\eta)(1-\zeta) \qquad N_8 = \frac{1}{8}(1-\xi)(1+\eta)(1+\zeta)$$

$$N_9 = \frac{1}{4}(1-\xi^2)(1-\eta)(1-\zeta) \qquad N_{13} = \frac{1}{4}(1-\xi^2)(1-\eta)(1+\zeta)$$

$$N_{10} = \frac{1}{4}(1+\xi)(1-\eta^2)(1-\zeta) \qquad N_{14} = \frac{1}{4}(1+\xi)(1-\eta^2)(1+\zeta)$$

$$N_{11} = \frac{1}{4}(1-\xi^2)(1+\eta)(1-\zeta) \qquad N_{15} = \frac{1}{4}(1-\xi^2)(1+\eta)(1+\zeta)$$

$$N_{12} = \frac{1}{4}(1-\xi)(1-\eta^2)(1-\zeta) \qquad N_{16} = \frac{1}{4}(1-\xi)(1-\eta^2)(1+\zeta)$$

$$N_{17} = \frac{1}{4}(1-\xi)(1-\eta)(1-\zeta^2) \qquad N_{21} = \frac{1}{2}(1+\xi)(1-\eta^2)(1-\zeta^2)$$

$$N_{18} = \frac{1}{4}(1+\xi)(1-\eta)(1-\zeta^2) \qquad N_{22} = \frac{1}{2}(1-\xi^2)(1+\eta)(1-\zeta^2)$$

$$N_{19} = \frac{1}{4}(1+\xi)(1+\eta)(1-\zeta^2) \qquad N_{23} = \frac{1}{2}(1-\xi^2)(1-\eta^2)(1+\zeta)$$

$$N_{20} = \frac{1}{4}(1-\xi)(1+\eta)(1-\zeta^2) \qquad N_{24} = \frac{1}{2}(1-\xi)(1-\eta^2)(1-\zeta^2)$$

$$N_{25} = \frac{1}{2}(1-\xi^2)(1-\eta)(1-\zeta^2)$$

$$N_{26} = \frac{1}{2}(1-\xi^2)(1-\eta^2)(1-\zeta)$$

$$N_{27} = (1-\xi^2)(1-\eta^2)(1-\zeta^2)$$

Step 2: Modify basic shape functions for Nodes 21-26 to account for omitted nodes (set $N_i = 0$ for the omitted nodes i):

$N_{21} = N_{21} - 0.5\ N_{27}$

$N_{22} = N_{22} - 0.5\ N_{27}$

$N_{23} = N_{23} - 0.5\ N_{27}$

$N_{24} = N_{24} - 0.5\ N_{27}$

$N_{25} = N_{25} - 0.5\ N_{27}$

$N_{26} = N_{26} - 0.5\ N_{27}$

Step 3: Modify basic shape functions for Nodes 9-20 to account for omitted nodes (set $N_i = 0$ for the omitted nodes i):

$N_9 = N_9 - 0.5\ (N_{25} + N_{26}) - 0.25\ N_{27}$

$N_{10} = N_{10} - 0.5\ (N_{21} + N_{26}) - 0.25\ N_{27}$

$N_{11} = N_{11} - 0.5\ (N_{22} + N_{26}) - 0.25\ N_{27}$

$N_{12} = N_{12} - 0.5\ (N_{24} + N_{26}) - 0.25\ N_{27}$

$N_{13} = N_{13} - 0.5\ (N_{25} + N_{23}) - 0.25\ N_{27}$

$N_{14} = N_{14} - 0.5\ (N_{21} + N_{23}) - 0.25\ N_{27}$

$N_{15} = N_{15} - 0.5\ (N_{22} + N_{23}) - 0.25\ N_{27}$

$N_{16} = N_{16} - 0.5\ (N_{24} + N_{23}) - 0.25\ N_{27}$

$N_{17} = N_{17} - 0.5\ (N_{24} + N_{25}) - 0.25\ N_{27}$

$N_{18} = N_{18} - 0.5\ (N_{25} + N_{21}) - 0.25\ N_{27}$

$N_{19} = N_{19} - 0.5\ (N_{21} + N_{22}) - 0.25\ N_{27}$

$N_{20} = N_{20} - 0.5\ (N_{22} + N_{24}) - 0.25\ N_{27}$

Step 4: Modify basic shape functions for Nodes 1-8 to account for omitted nodes (set $N_i = 0$ for the omitted Nodes i):

$N_1 = N_1 - 0.5\ (N_{17} + N_9 + N_{12}) - 0.25\ (N_{26} + N_{25} + N_{24}) - 0.125\ N_{27}$

$N_2 = N_2 - 0.5\ (N_{18} + N_{10} + N_9) - 0.25\ (N_{26} + N_{21} + N_{25}) - 0.125\ N_{27}$

$N_3 = N_3 - 0.5\ (N_{19} + N_{11} + N_{10}) - 0.25\ (N_{26} + N_{21} + N_{22}) - 0.125\ N_{27}$

$N_4 = N_4 - 0.5\ (N_{20} + N_{12} + N_{11}) - 0.25\ (N_{26} + N_{24} + N_{24}) - 0.125\ N_{27}$

$N_5 = N_5 - 0.5\ (N_{17} + N_{13} + N_{16}) - 0.25\ (N_{23} + N_{24} + N_{25}) - 0.125\ N_{27}$

$N_6 = N_6 - 0.5\ (N_{18} + N_{14} + N_{13}) - 0.25\ (N_{23} + N_{25} + N_{21}) - 0.125\ N_{27}$

$$N_7 = N_7 - 0.5\ (N_{19} + N_{15} + N_{14}) - 0.25\ (N_{23} + N_{21} + N_{22}) - 0.125\ N_{27}$$

$$N_8 = N_8 - 0.5\ (N_{20} + N_{16} + N_{15}) - 0.25\ (N_{23} + N_{24} + N_{22}) - 0.125\ N_{27}$$

Appendix B Figures of Wharf Simulation Results

This appendix lists figures of the results for the wharf simulations discussed in Chapter 7.

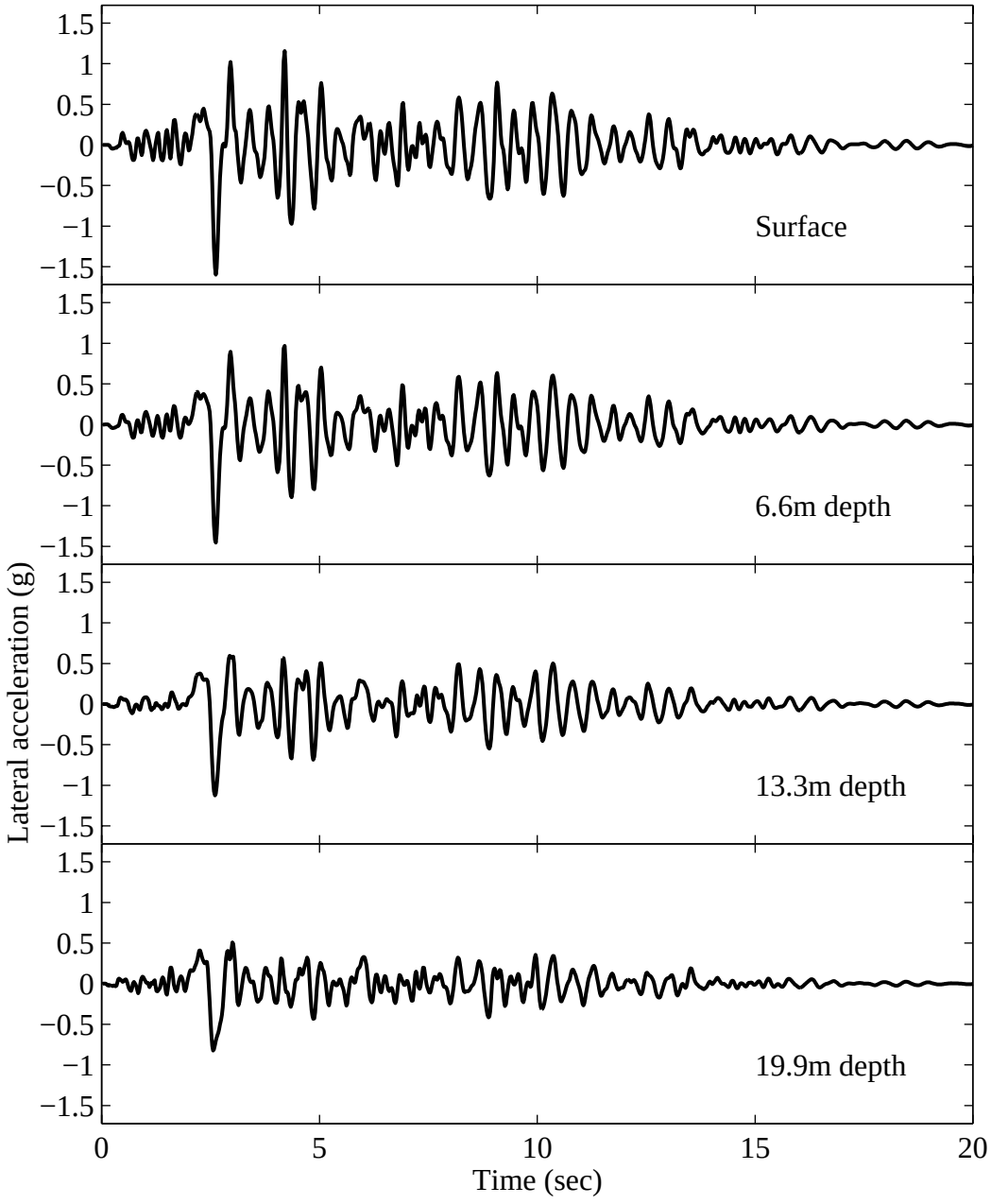

Figure B.1: Lateral acceleration time histories at Location A for Case C2L.

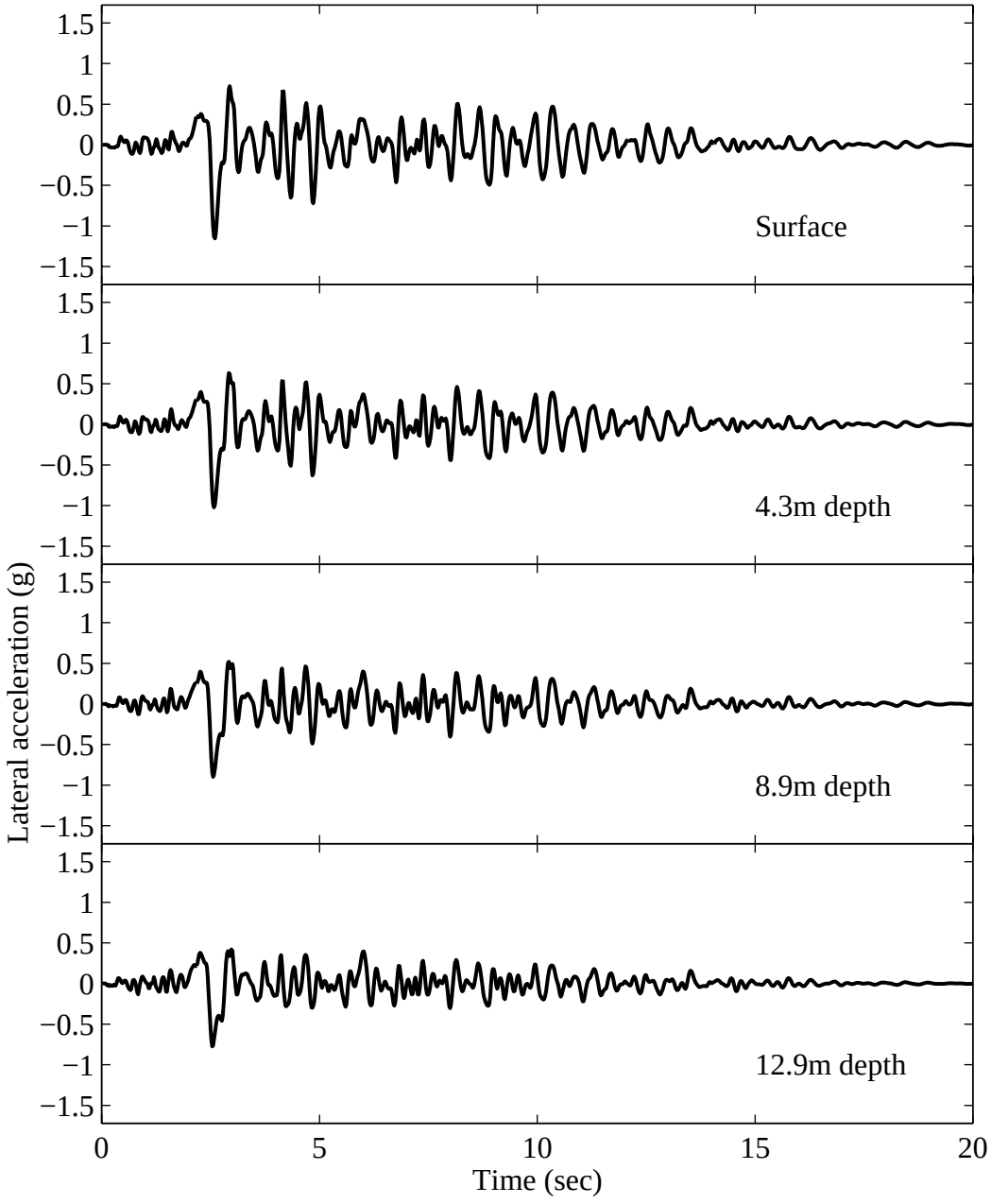

Figure B.2: Lateral acceleration time histories at Location B for Case C2L.

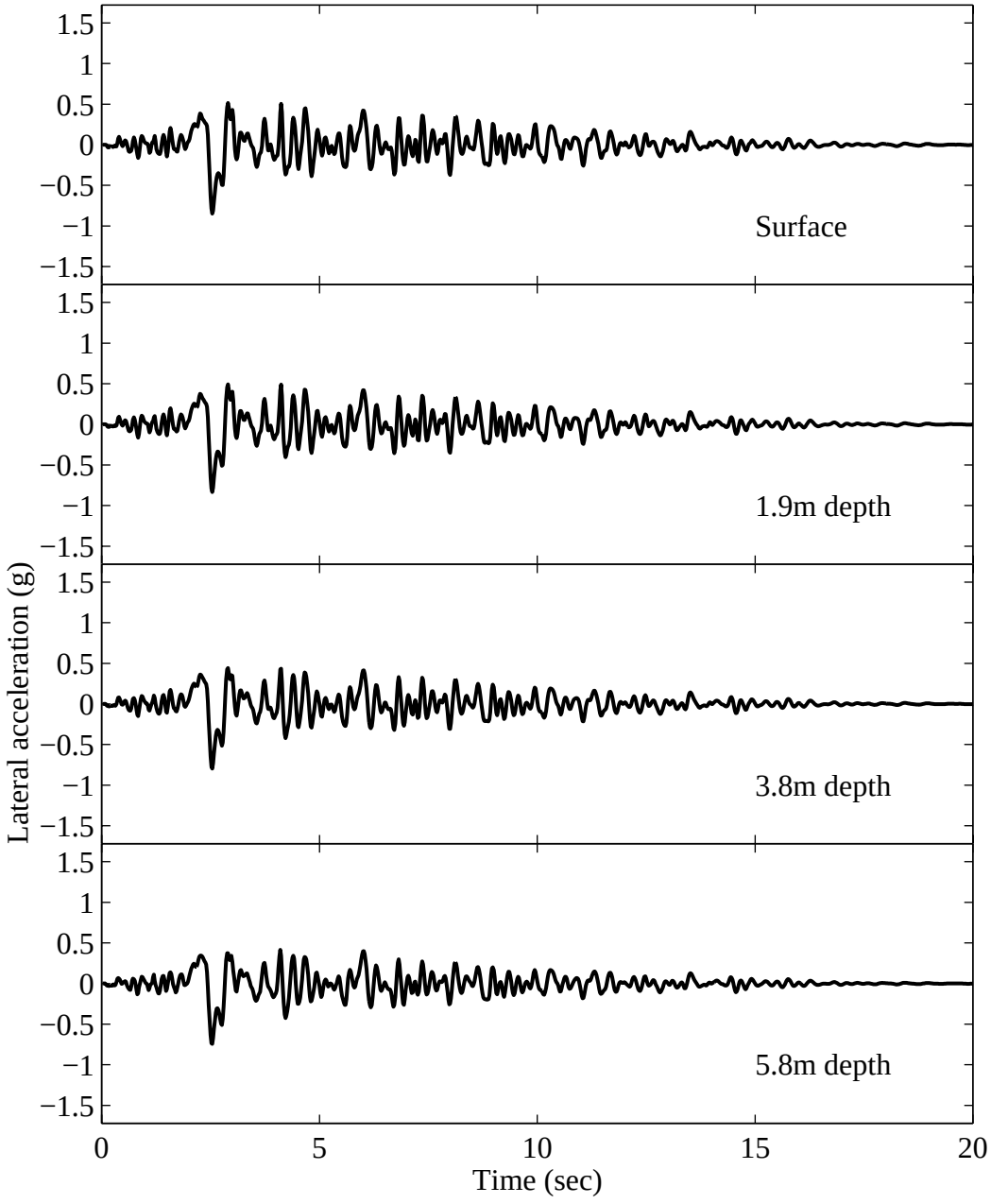

Figure B.3: Lateral acceleration time histories at Location C for Case C2L.

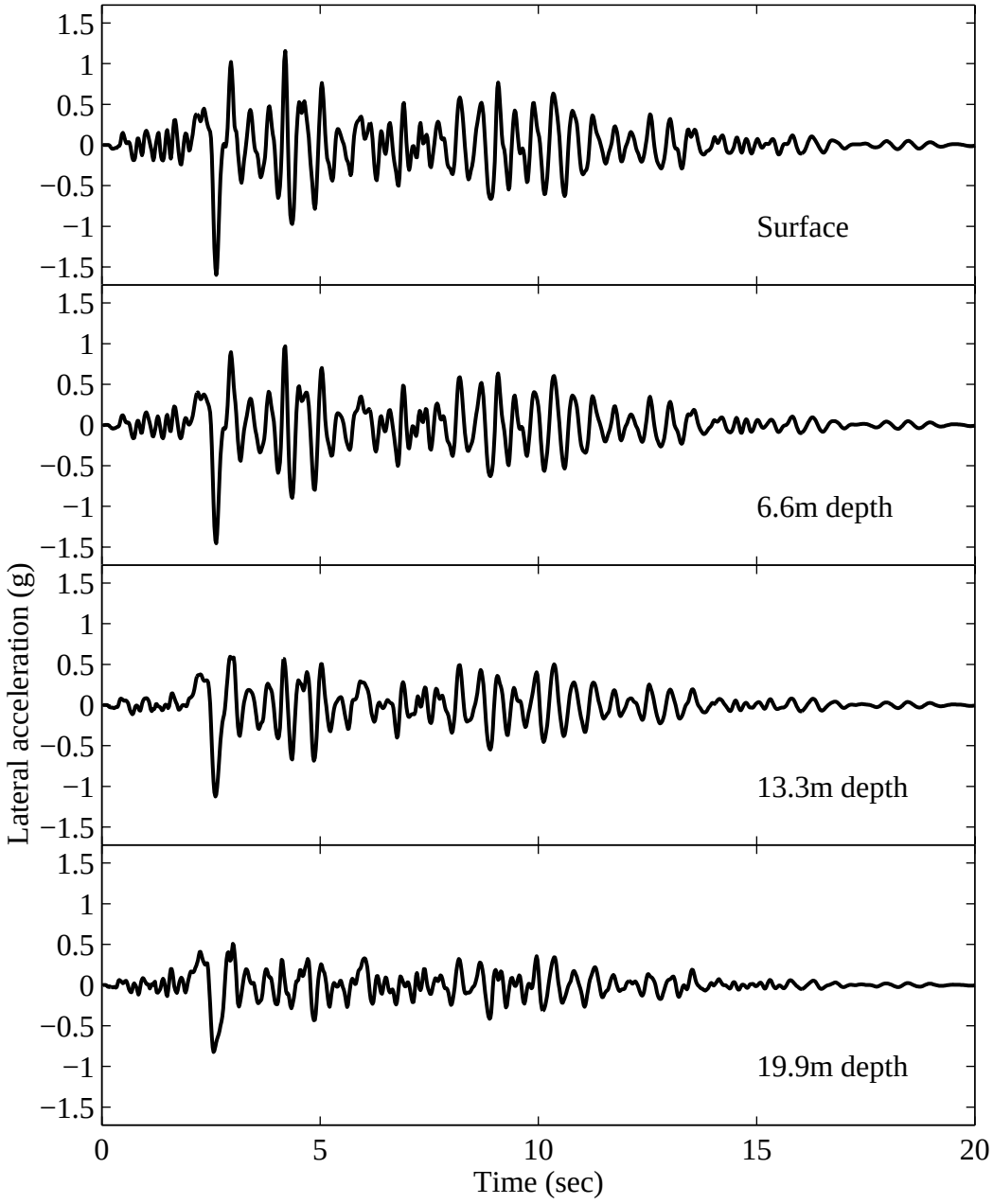

Figure B.4: Lateral acceleration time histories at free field for the landside for Case C2L.

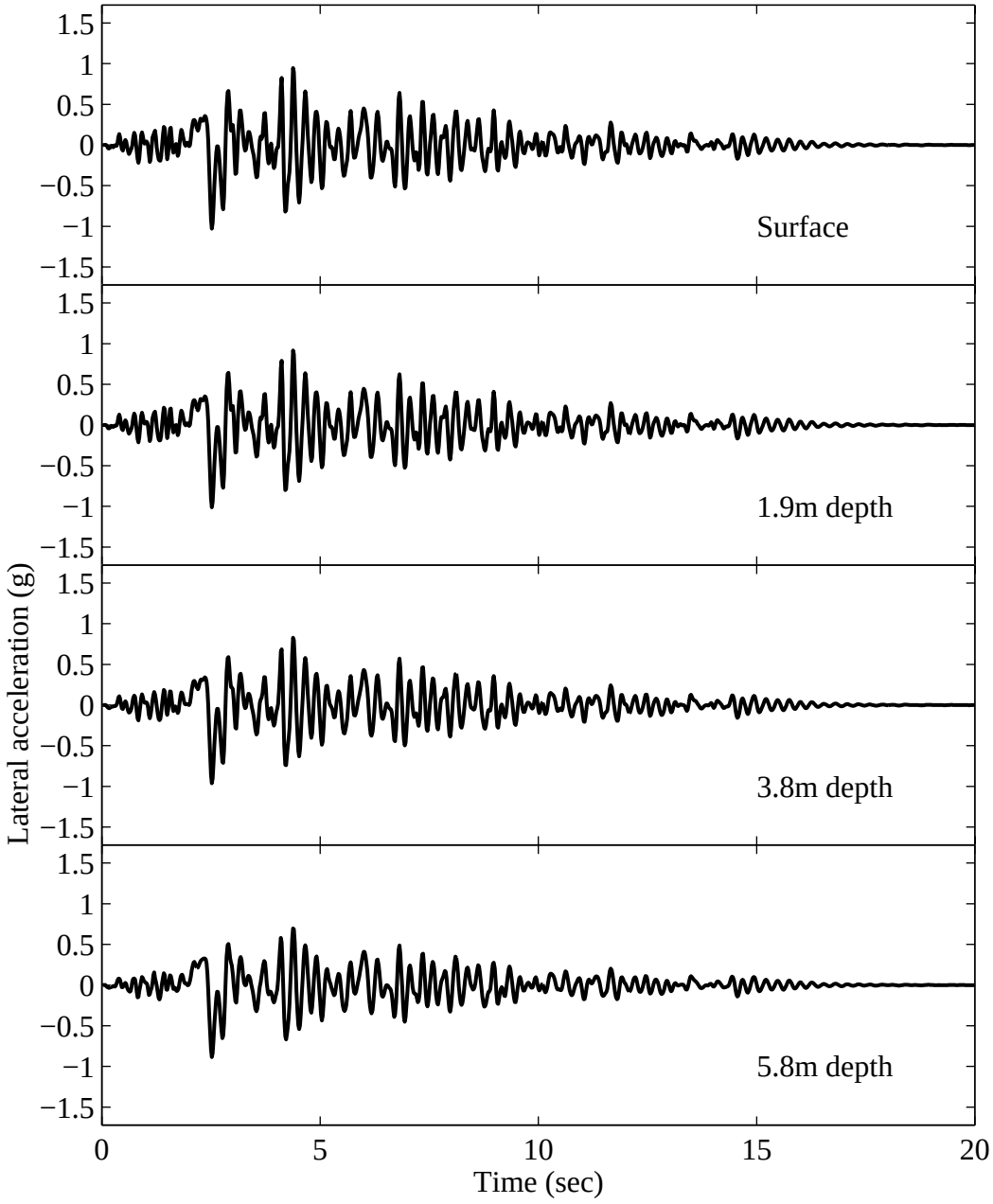

Figure B.5: Lateral acceleration time histories at free field for the waterside for Case C2L.

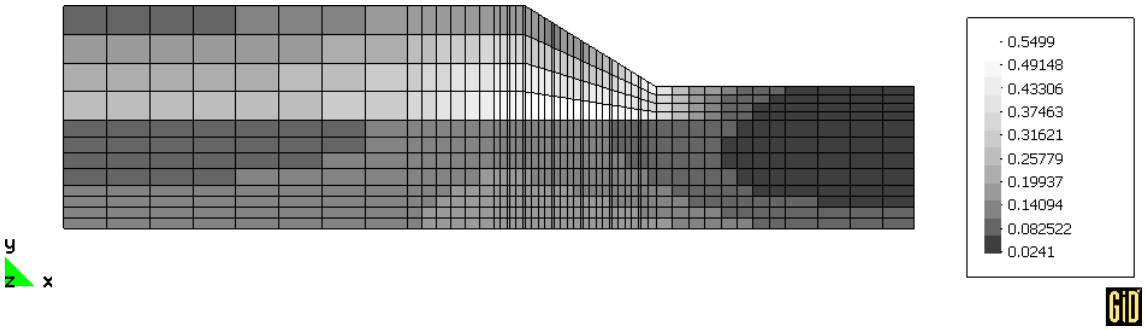

(a) Before shaking (elevation view)

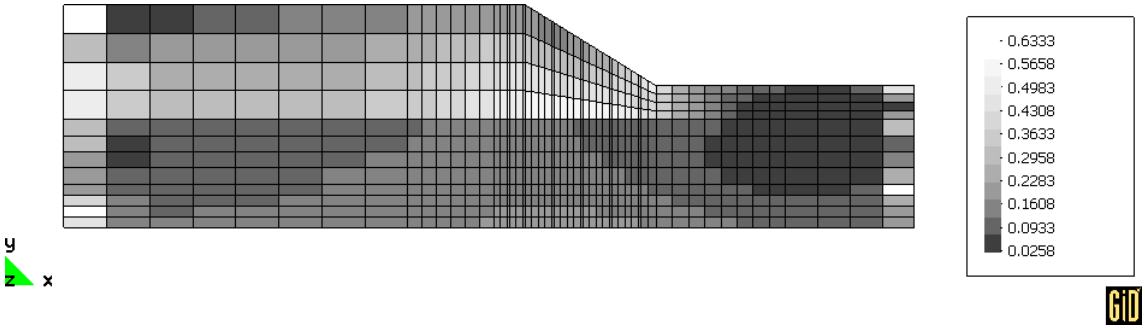

(b) After shaking (elevation view)

Figure B.6: Stress ratio distribution before and after shaking for Case C2L.

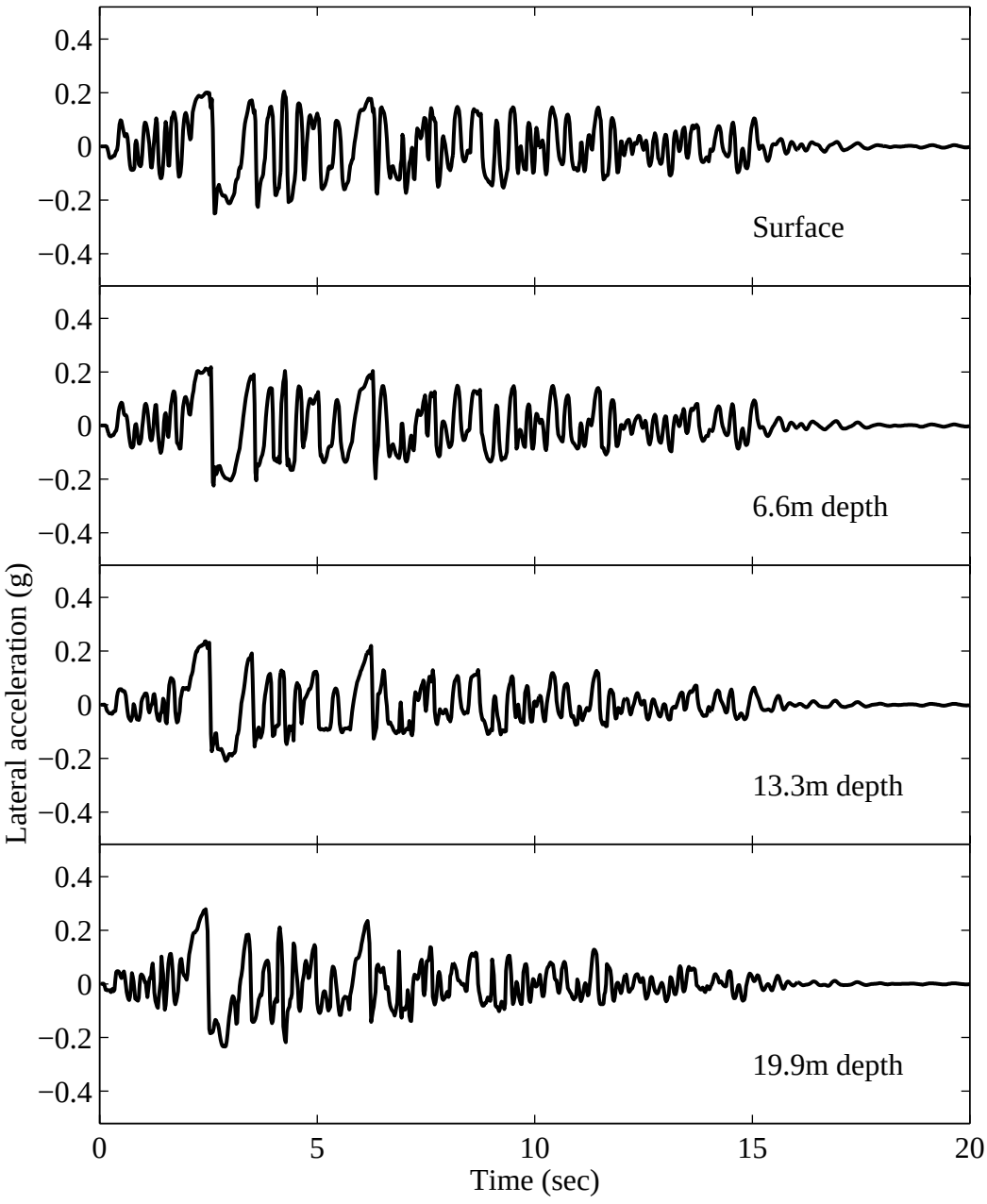

Figure B.7: Lateral acceleration time histories at Location A for Case C2N.

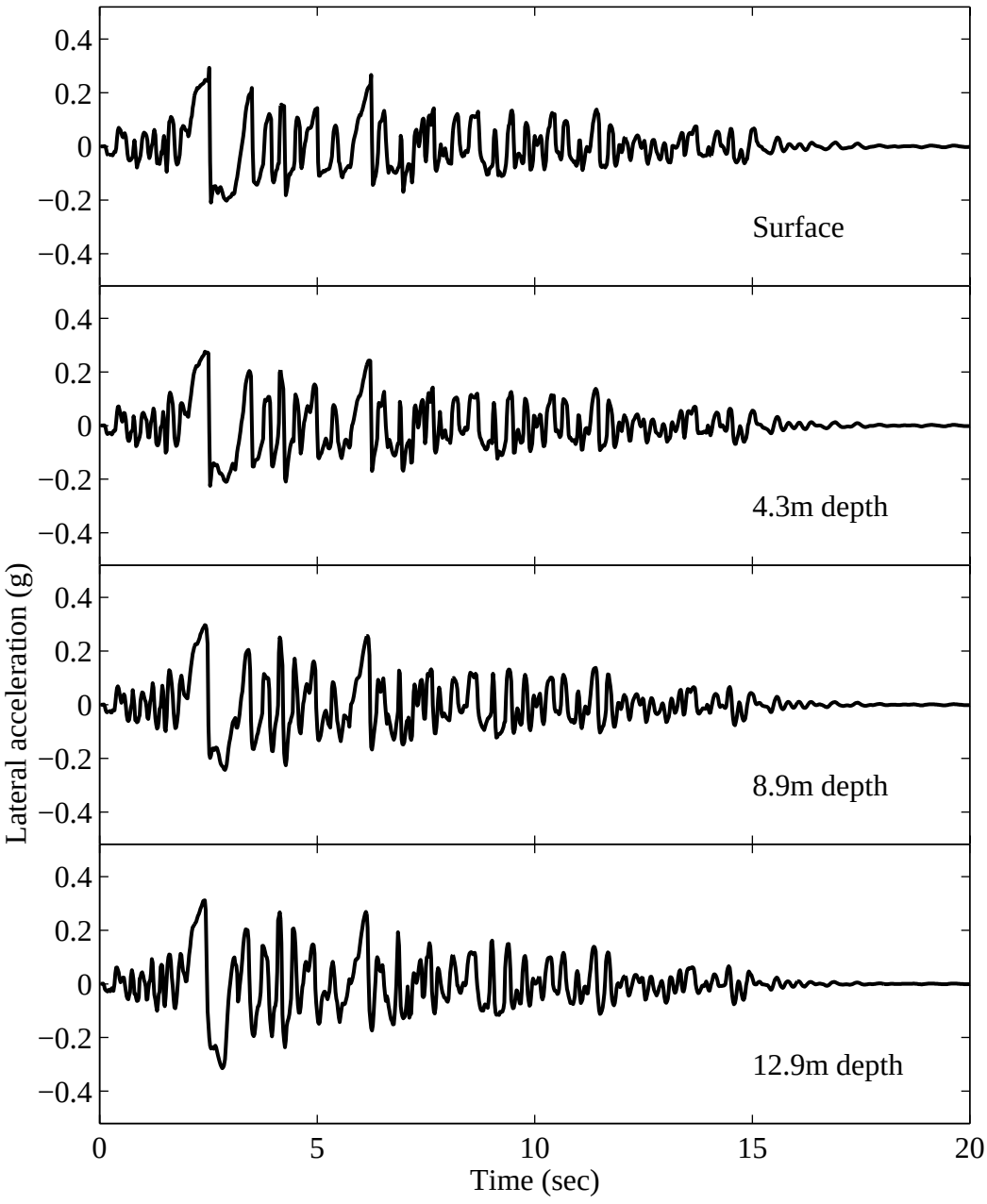

Figure B.8: Lateral acceleration time histories at Location B for Case C2N.

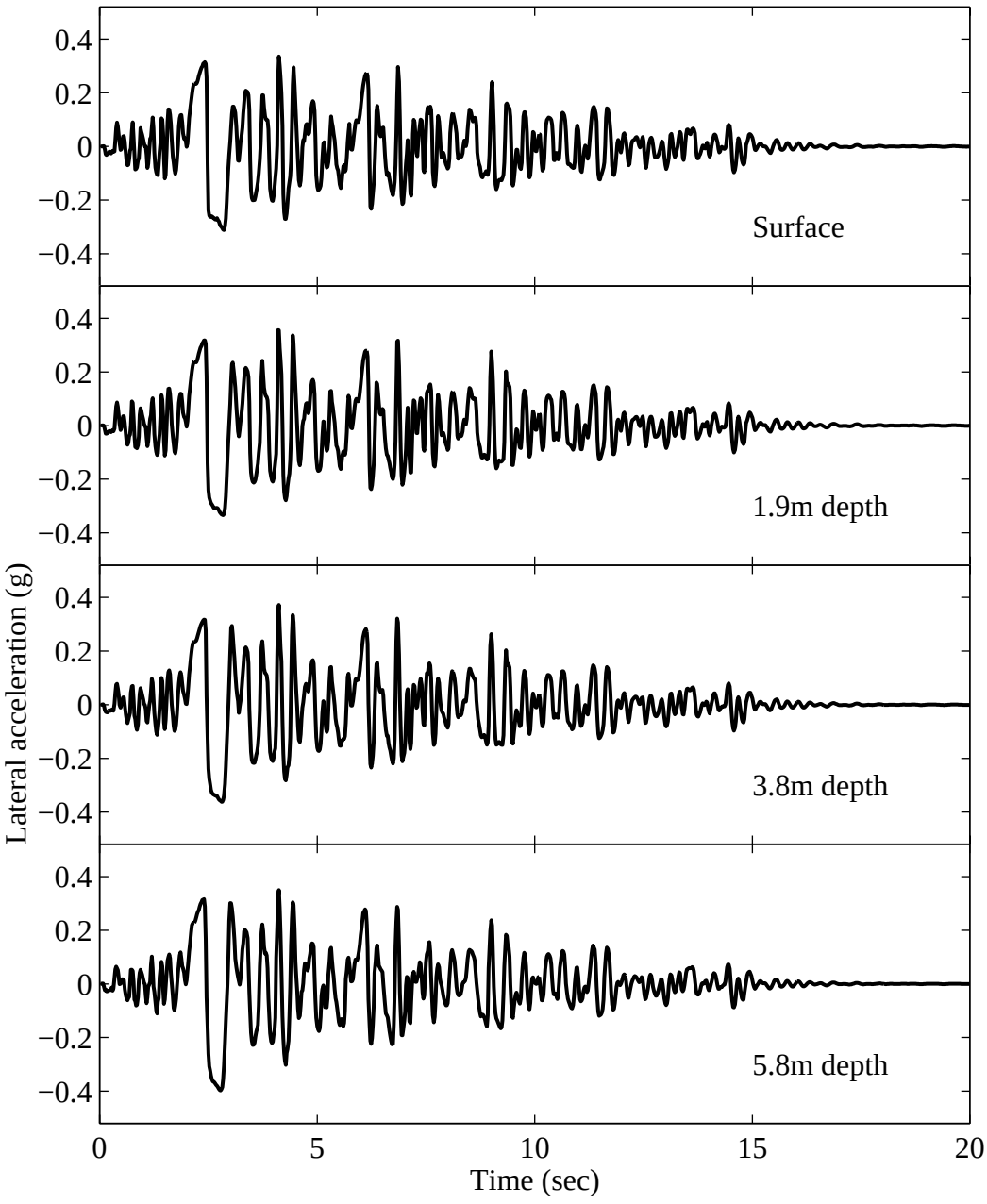

Figure B.9: Lateral acceleration time histories at Location C for Case C2N.

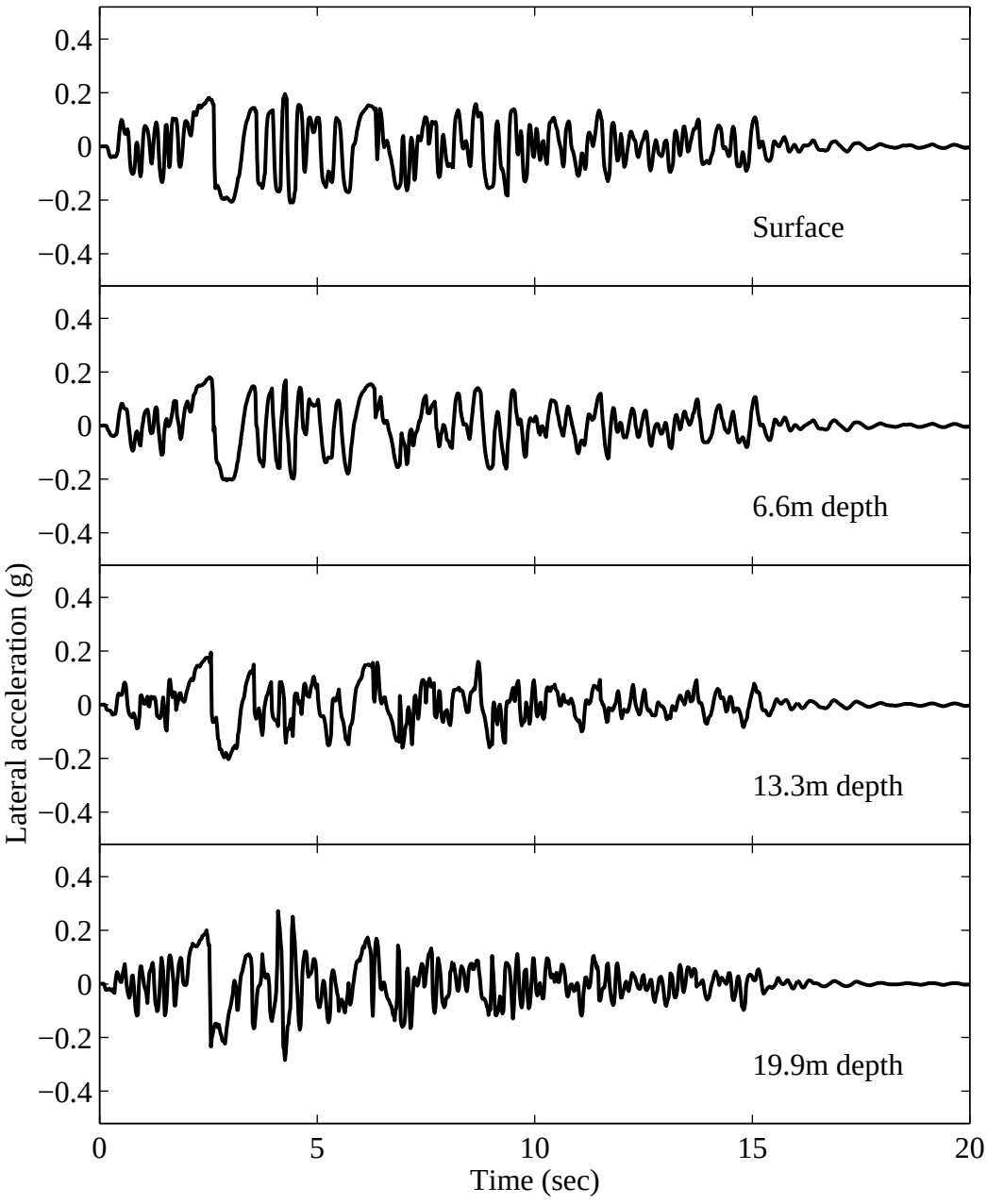

Figure B.10: Lateral acceleration time histories at free field for the landside for Case C2N.

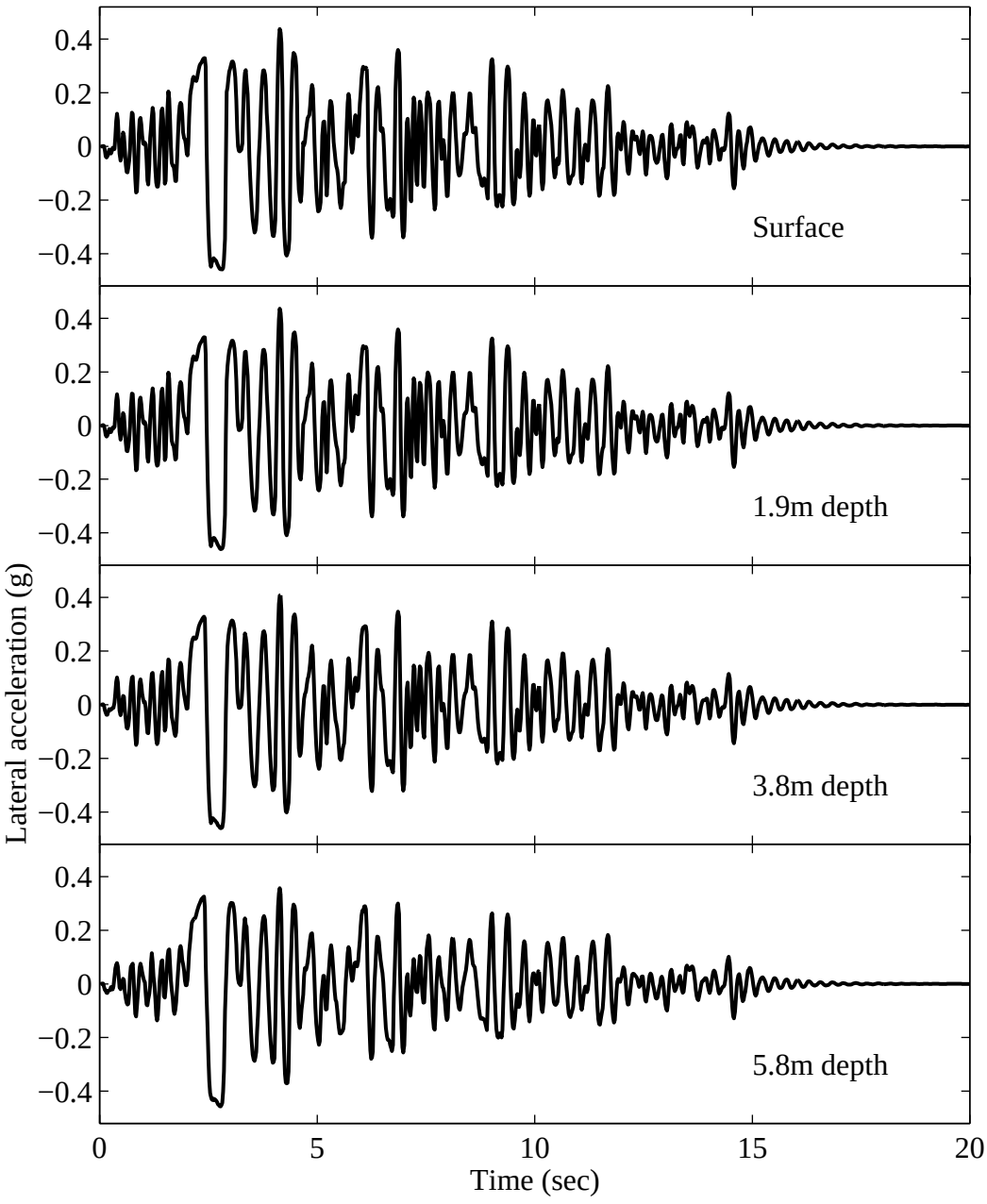

Figure B.11: Lateral acceleration time histories at free field for the waterside for Case C2N.

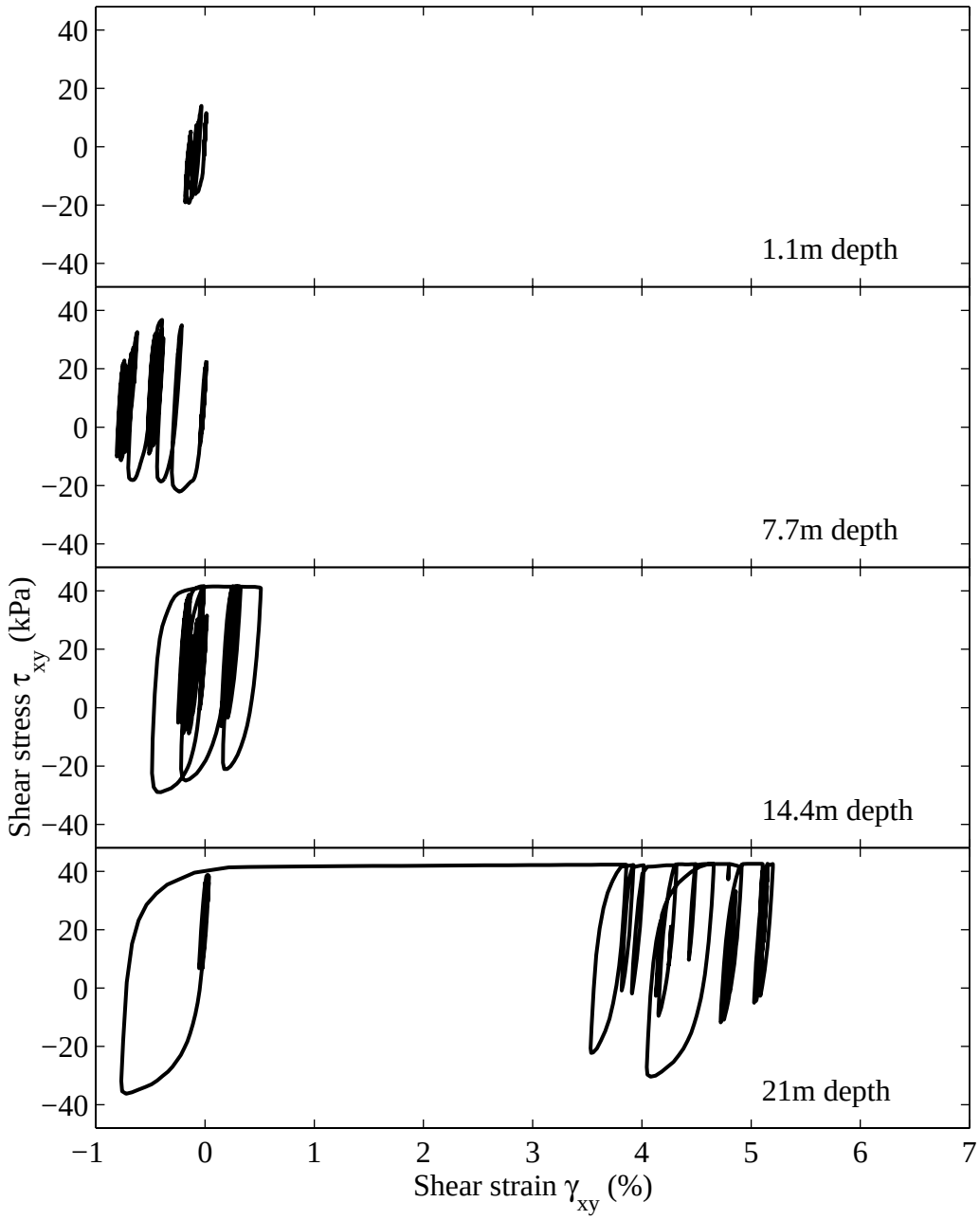

Figure B.12: Shear stress-strain response at Location A for Case C2N.

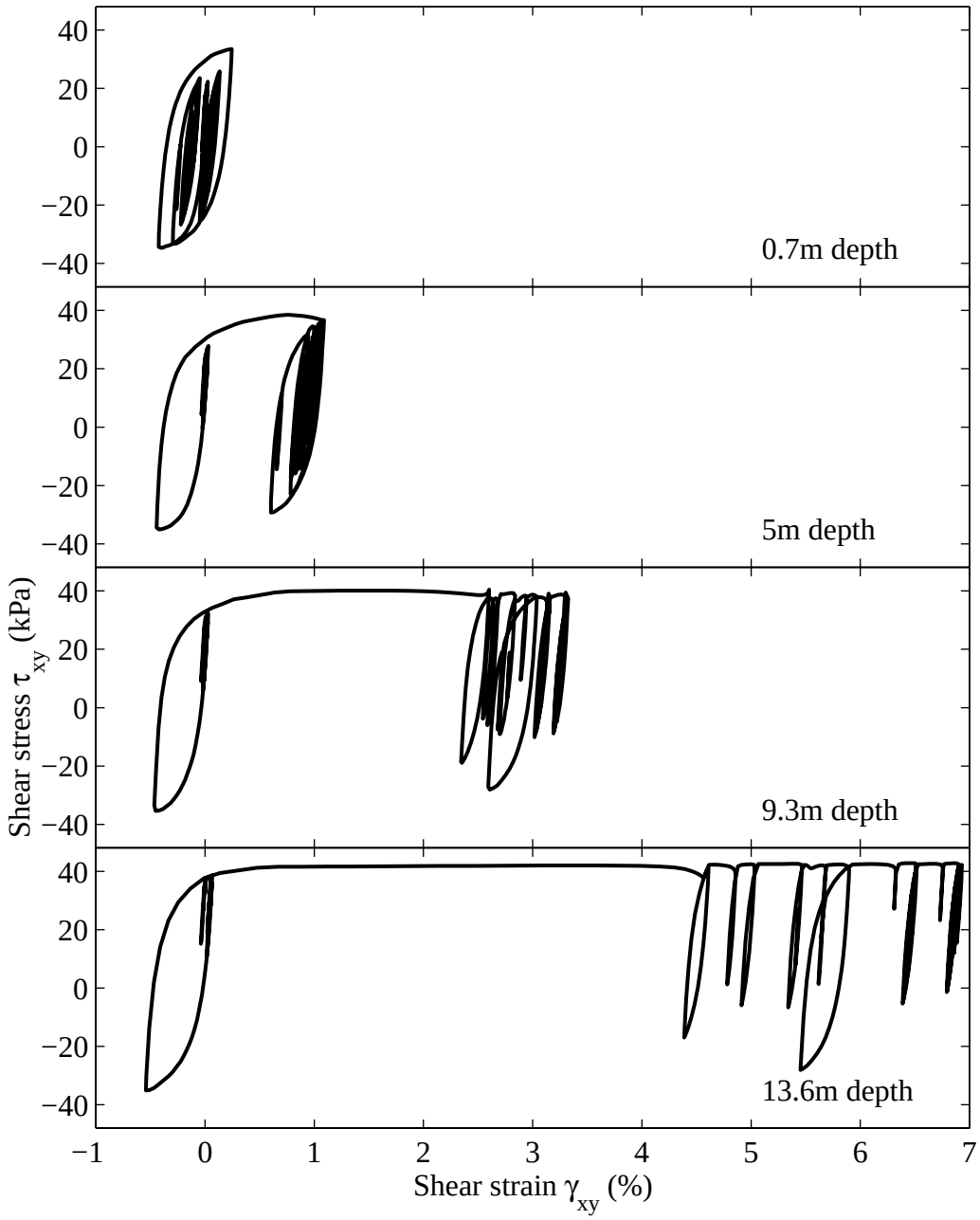

Figure B.13: Shear stress-strain response at Location B for Case C2N.

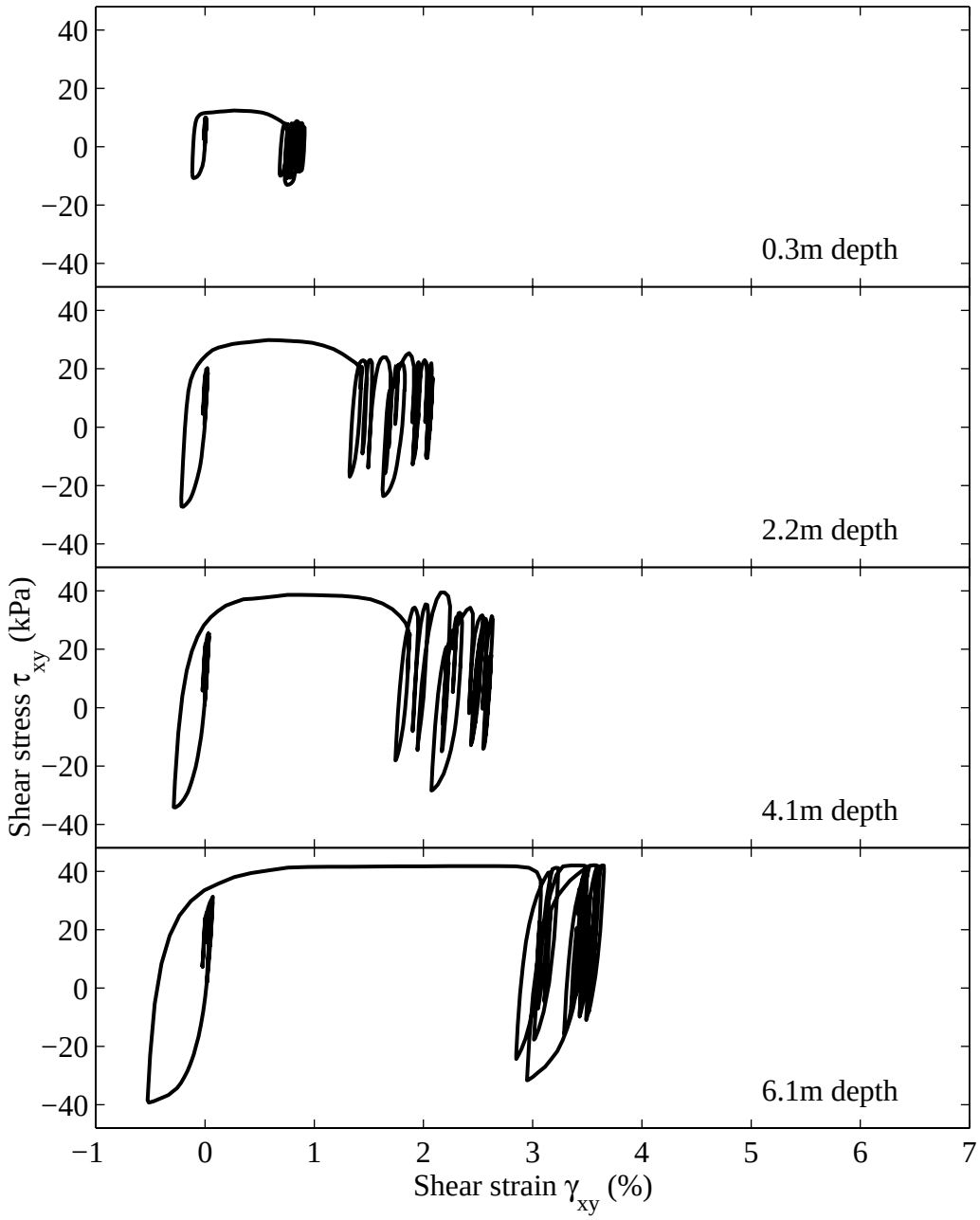

Figure B.14: Shear stress-strain response at Location C for Case C2N.

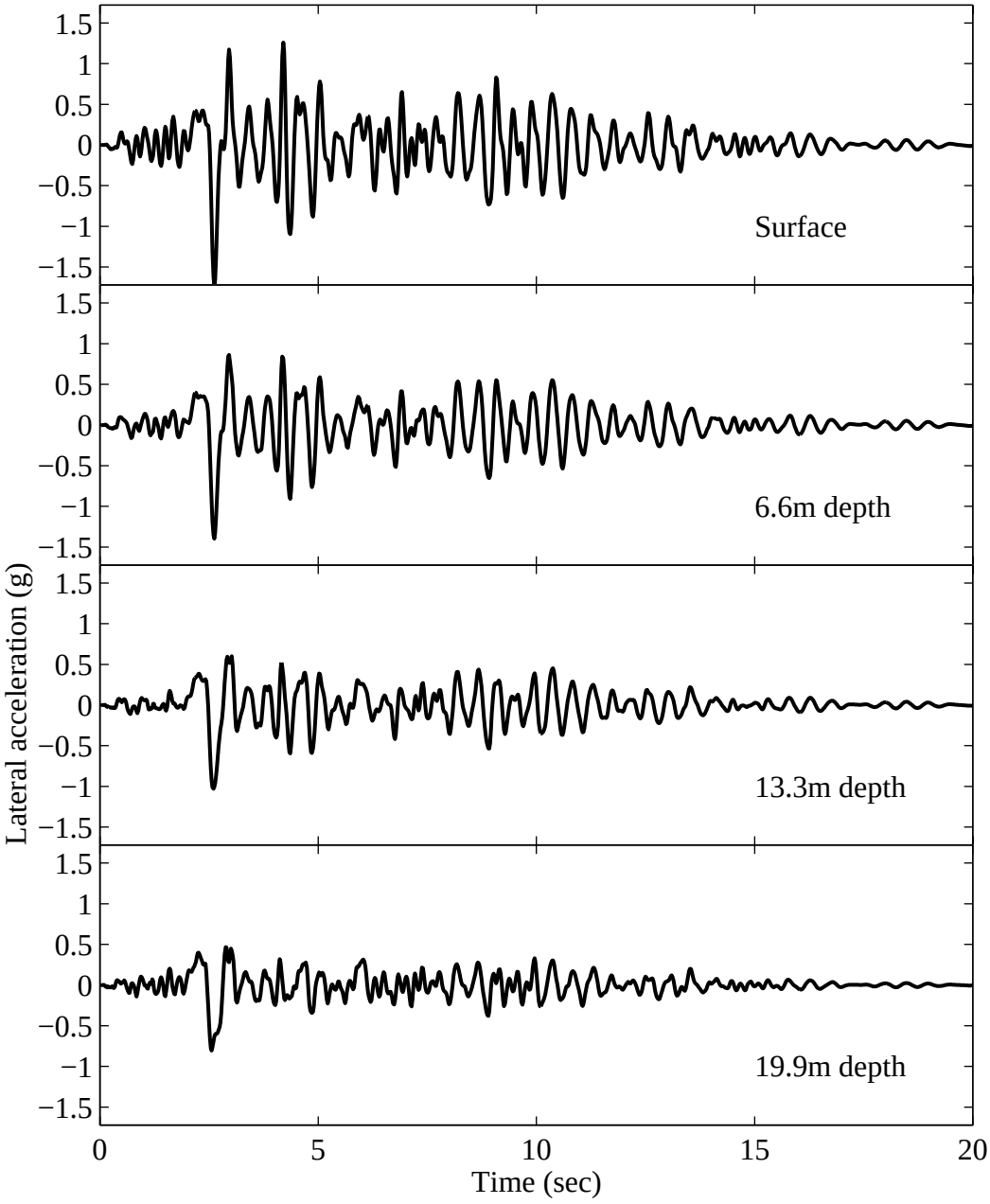

Figure B.15: Longitudinal acceleration time histories at Location A for Case W3L-C.

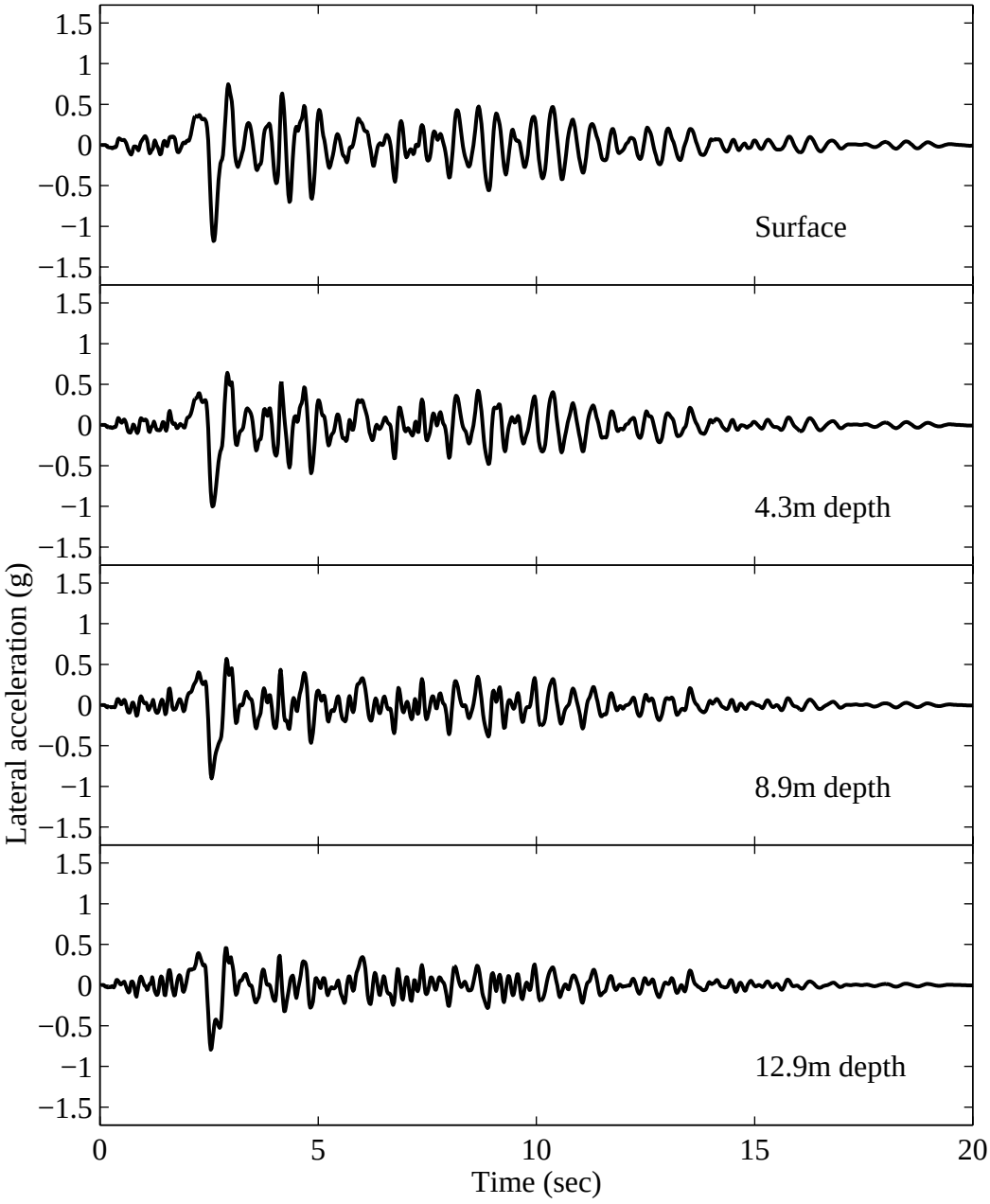

Figure B.16: Longitudinal acceleration time histories at Location B for Case W3L-C.

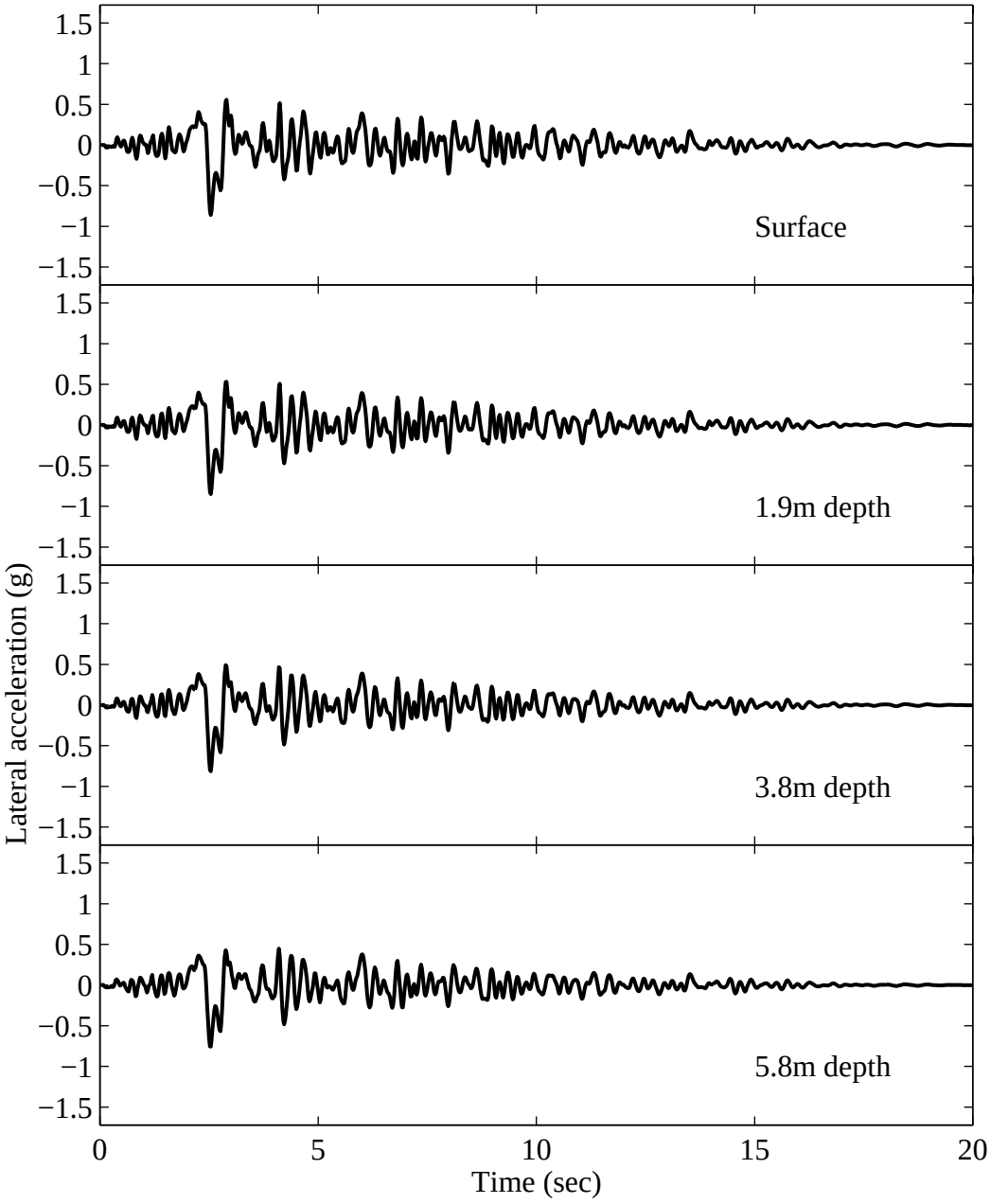

Figure B.17: Longitudinal acceleration time histories at Location C for Case W3L-C.

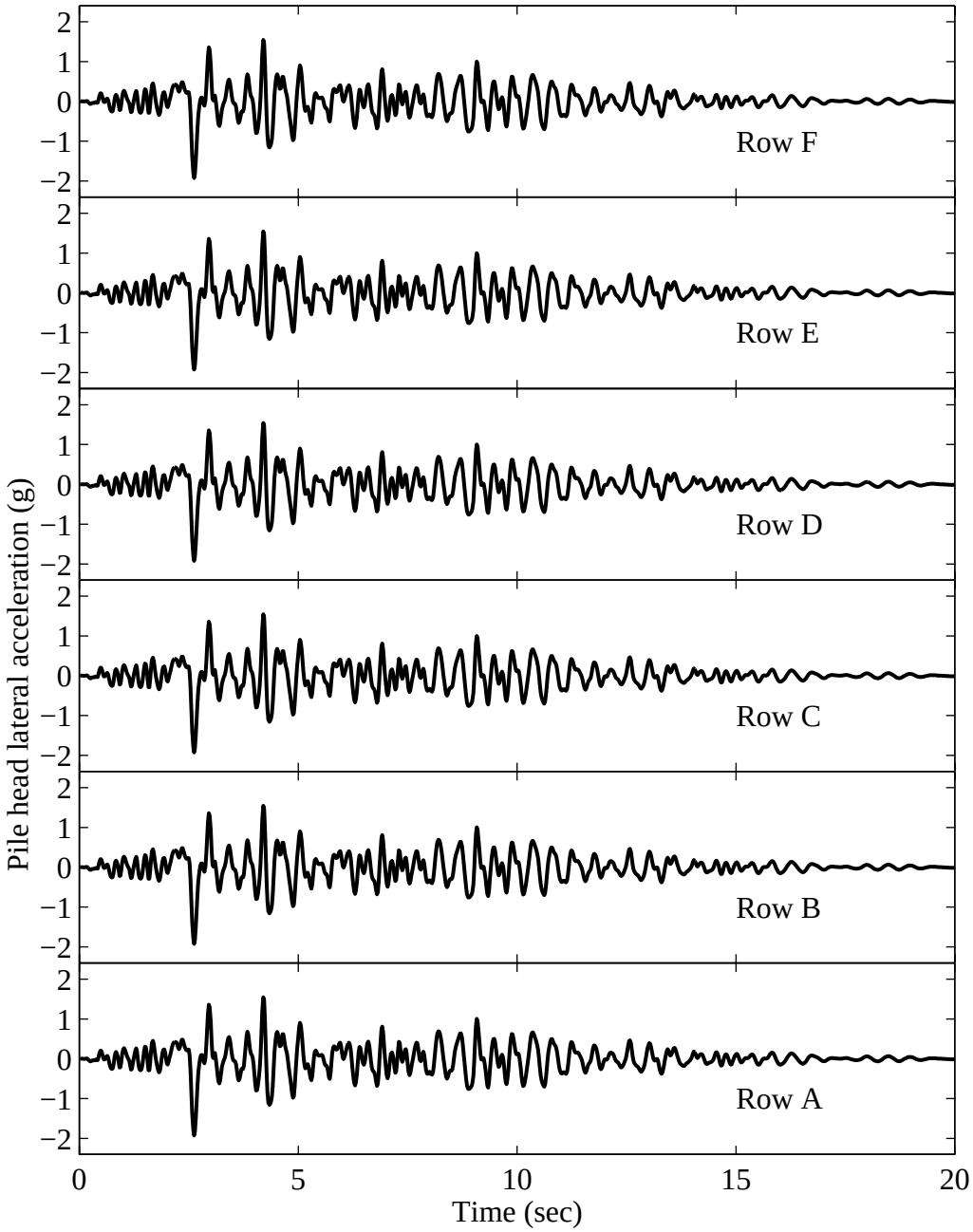

Figure B.18: Longitudinal acceleration time histories at the pile heads for Case W3L-C.

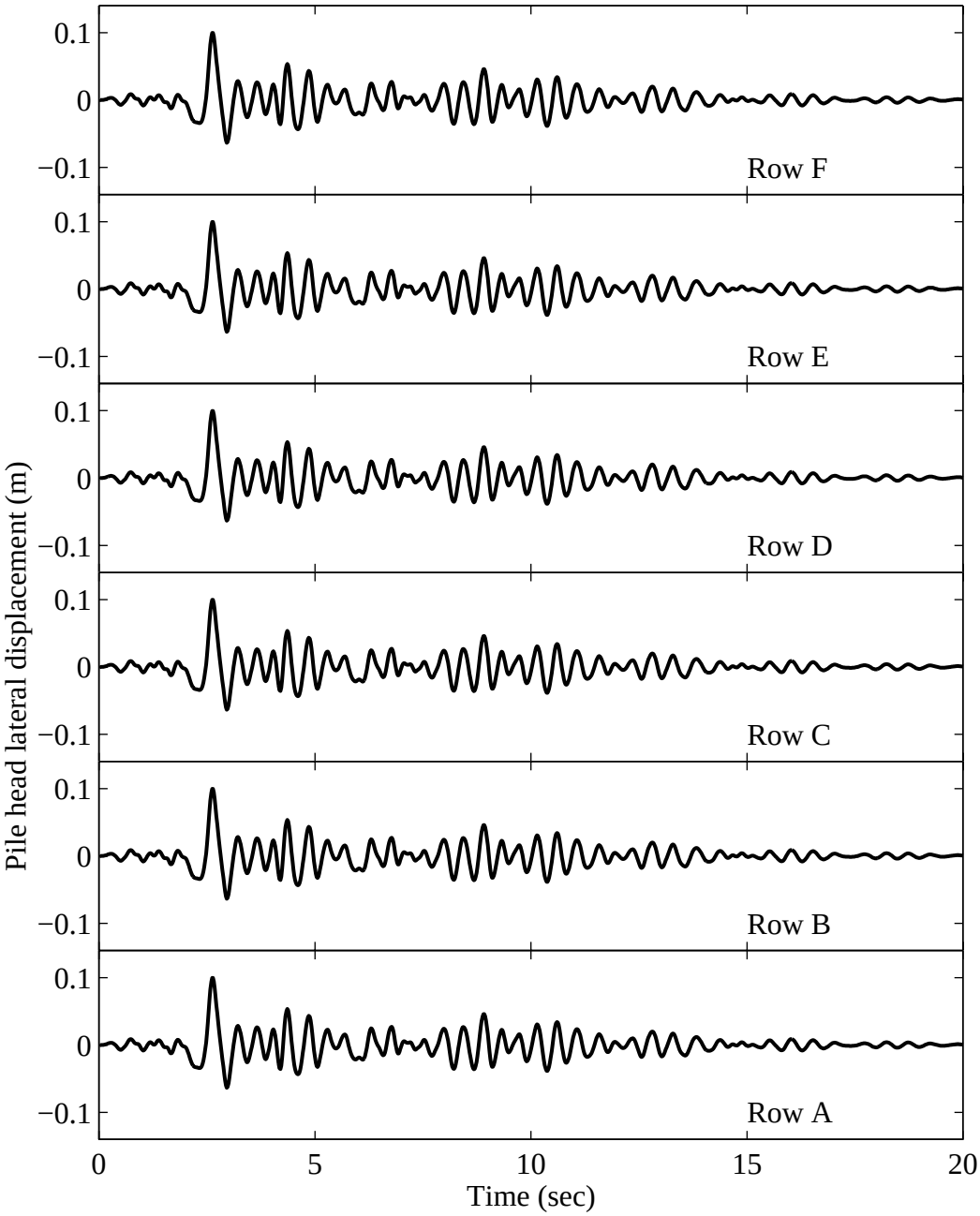

Figure B.19: Longitudinal displacement time histories at the pile heads for Case W3L-C.

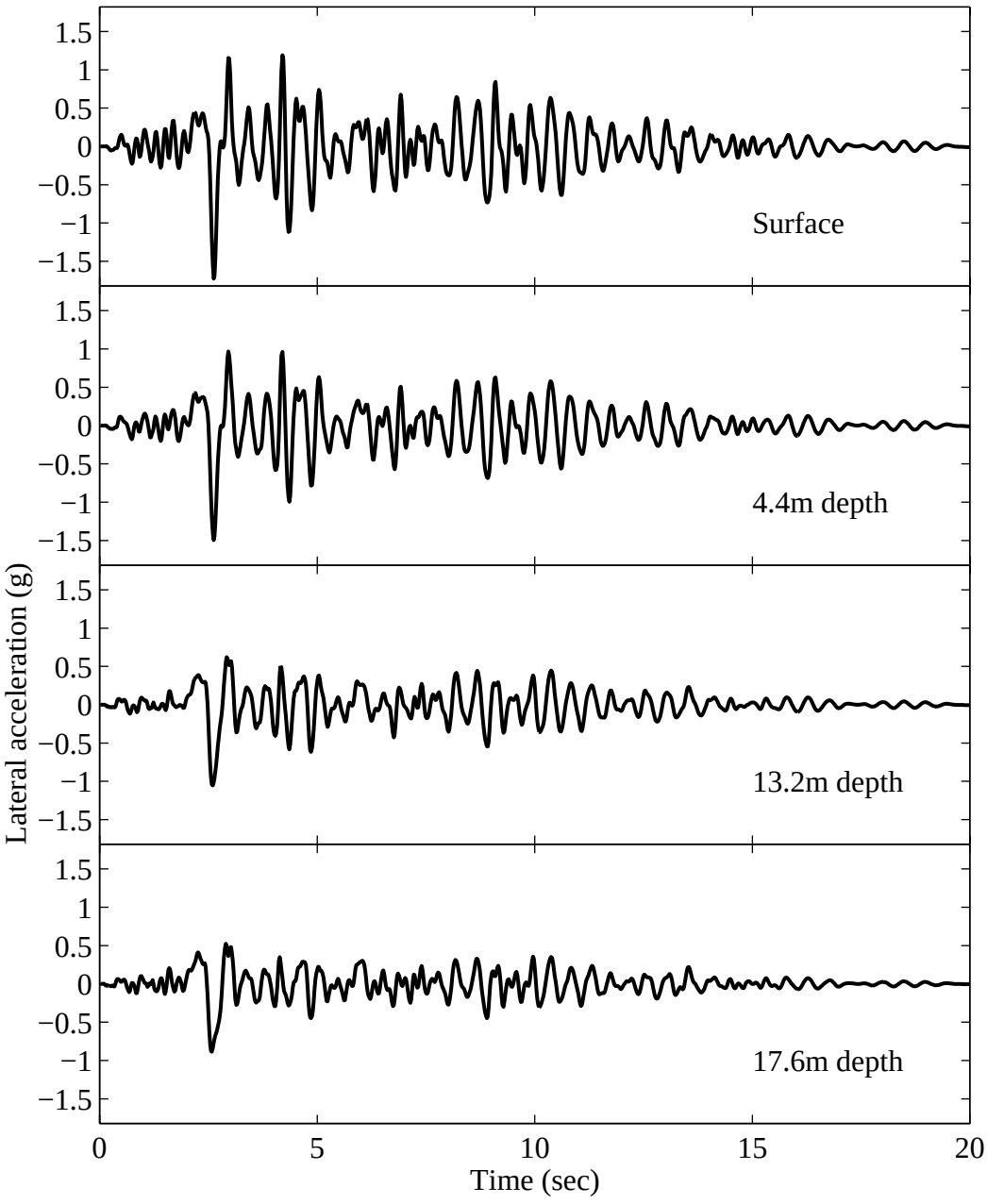

Figure B.20: Longitudinal acceleration time histories at Location A for Case W3L-M.

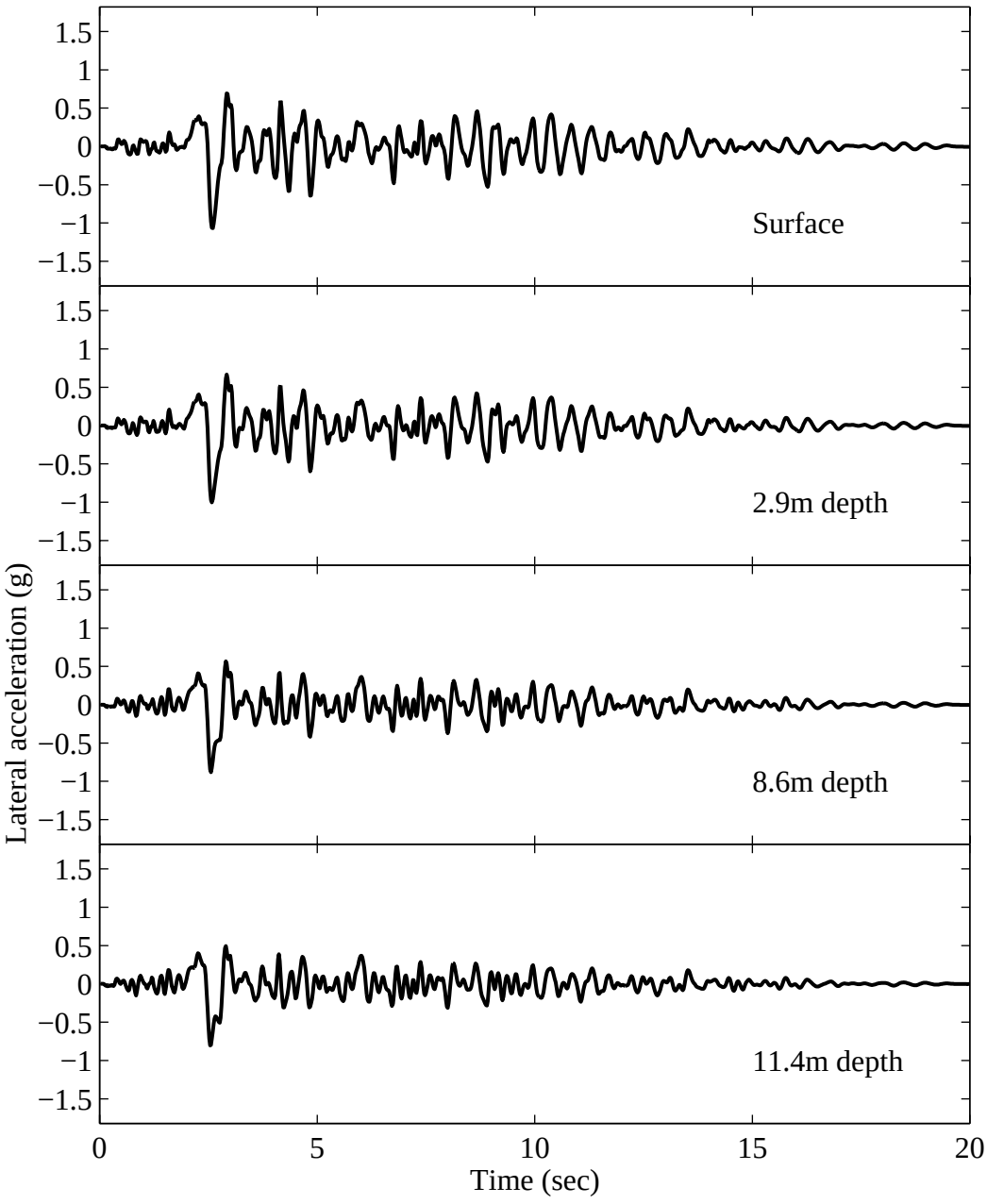

Figure B.21: Longitudinal acceleration time histories at Location B for Case W3L-M.

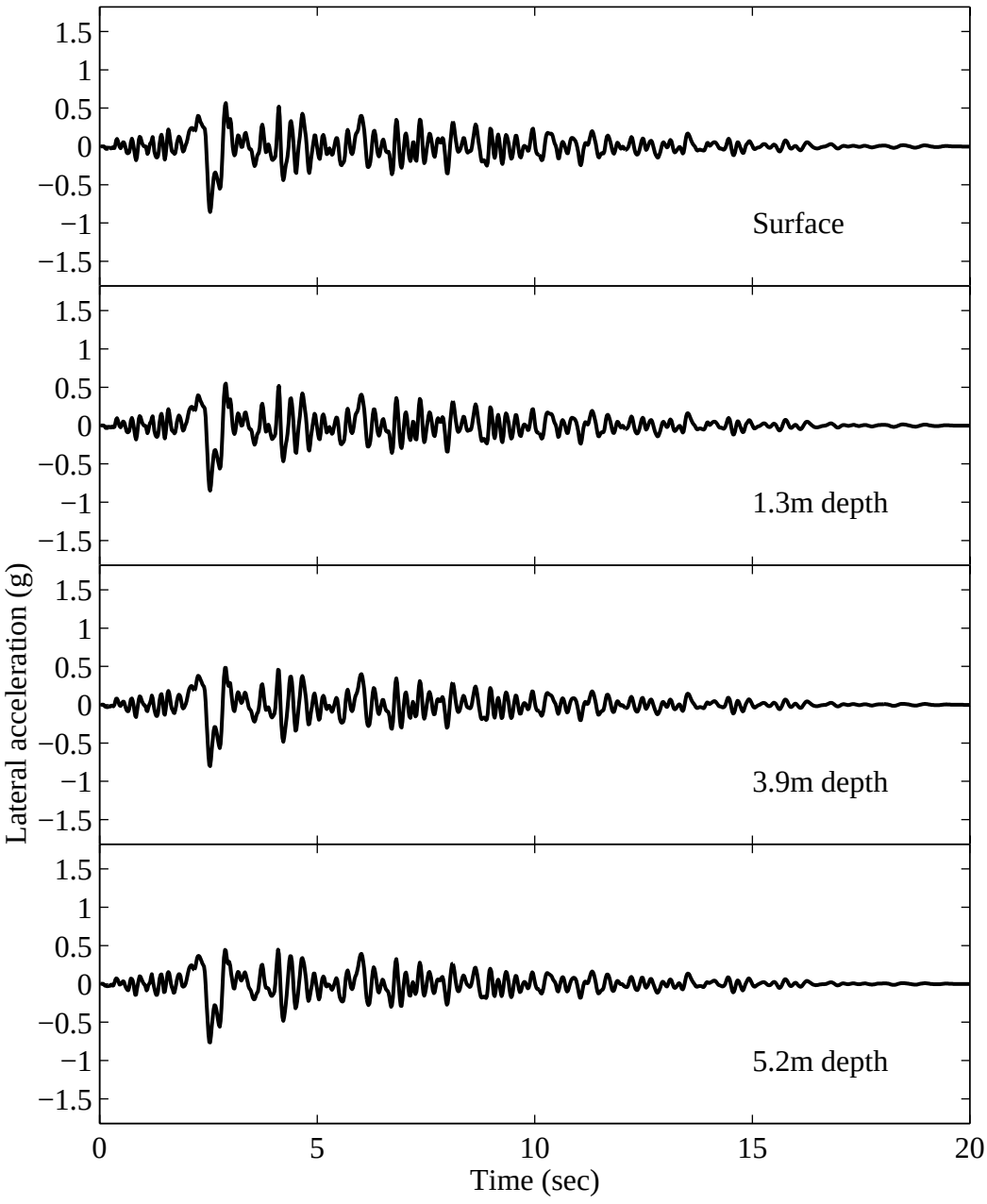

Figure B.22: Longitudinal acceleration time histories at Location C for Case W3L-M.

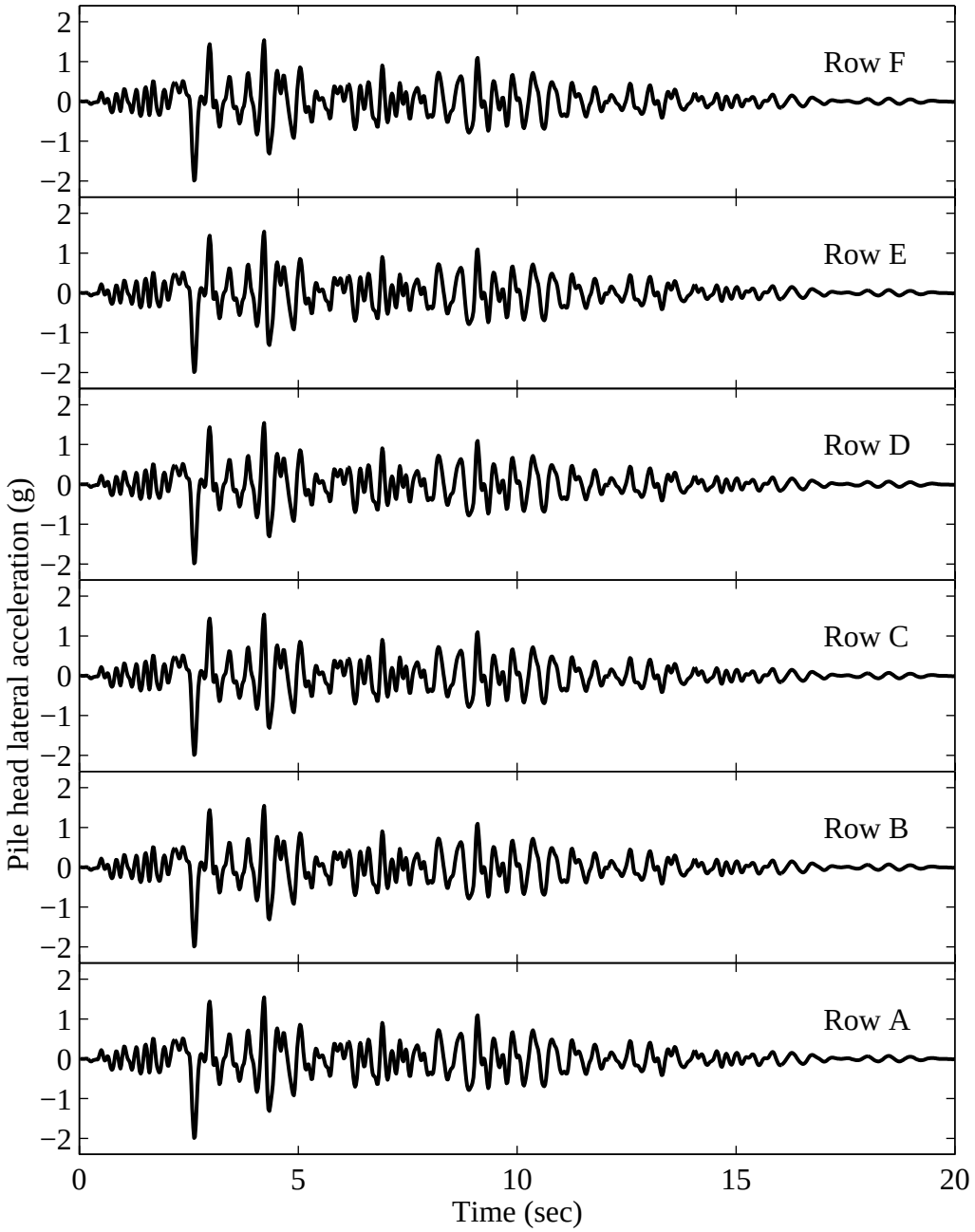

Figure B.23: Longitudinal acceleration time histories at the pile heads for Case W3L-M.

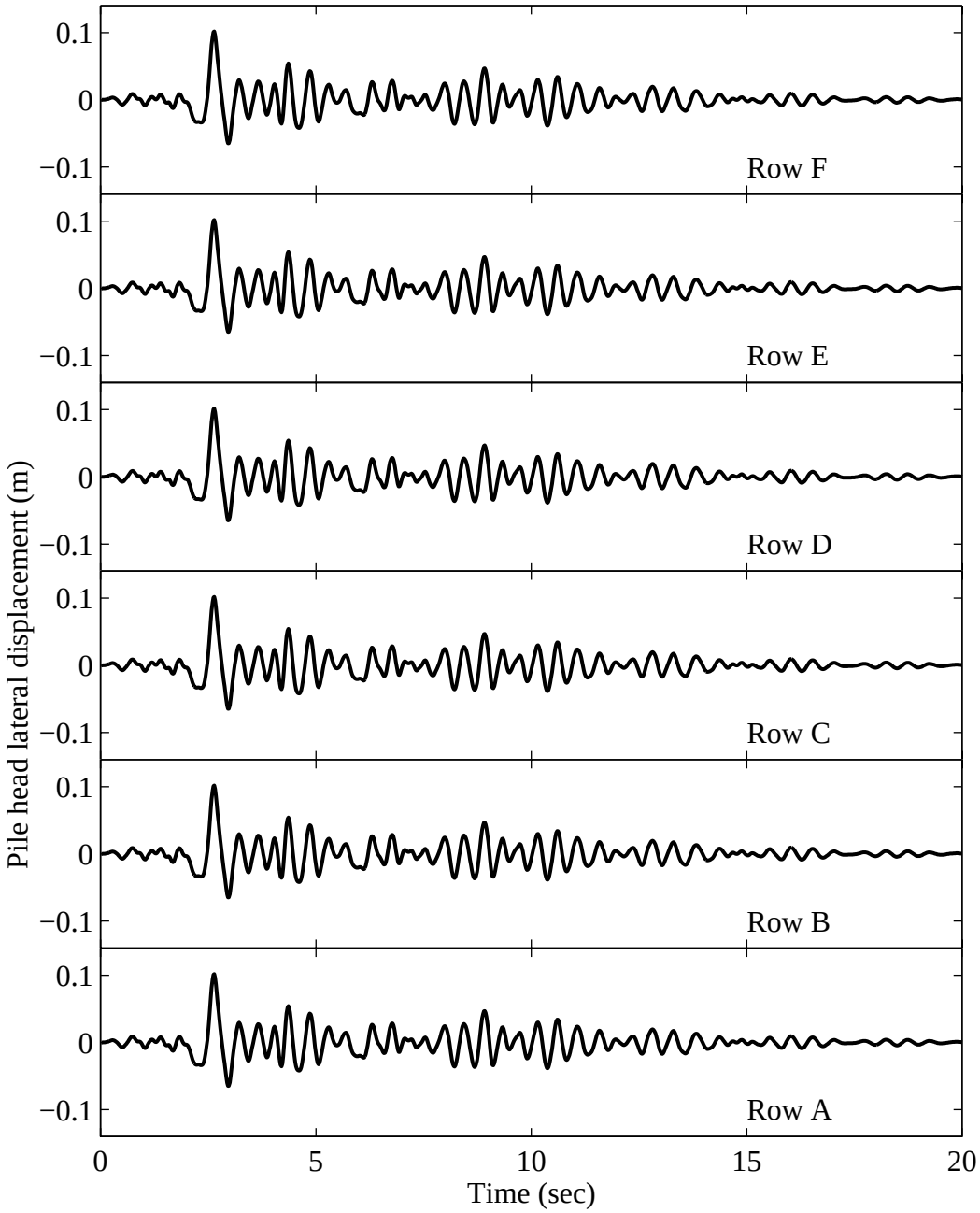

Figure B.24: Longitudinal displacement time histories at the pile heads for Case W3L-M.

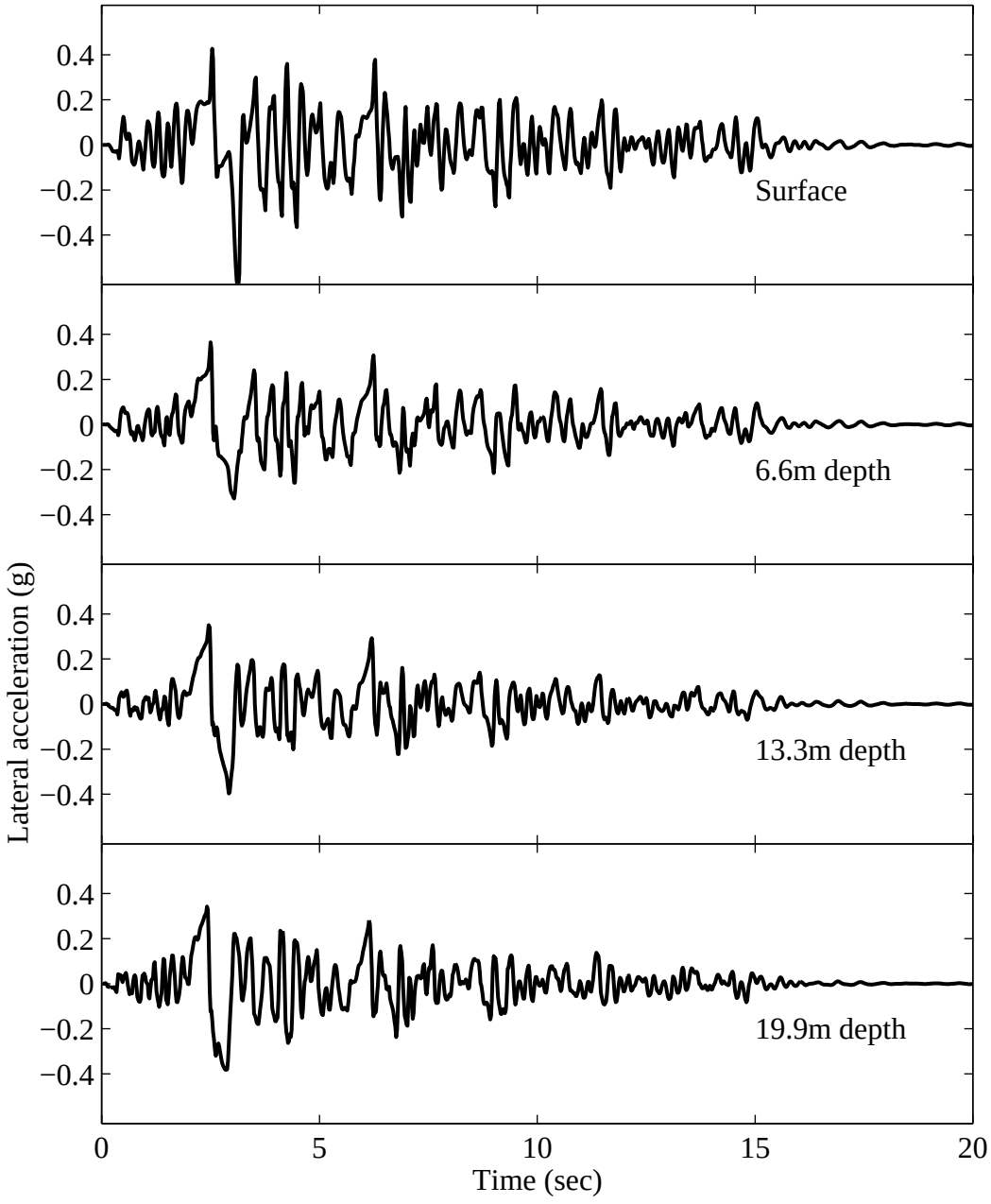

Figure B.25: Longitudinal acceleration time histories at Location A for Case W3N-C.

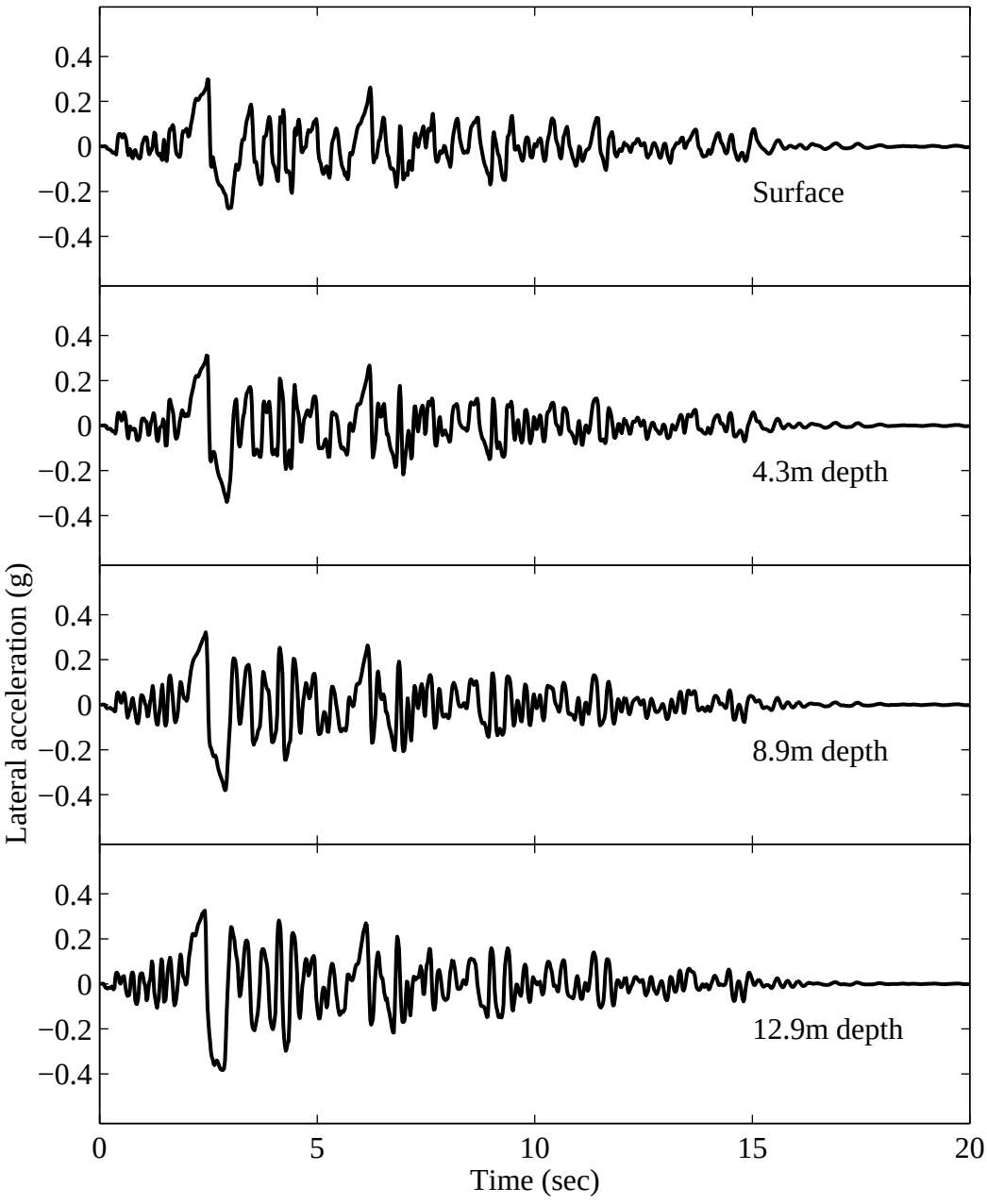

Figure B.26: Longitudinal acceleration time histories at Location B for Case W3N-C.

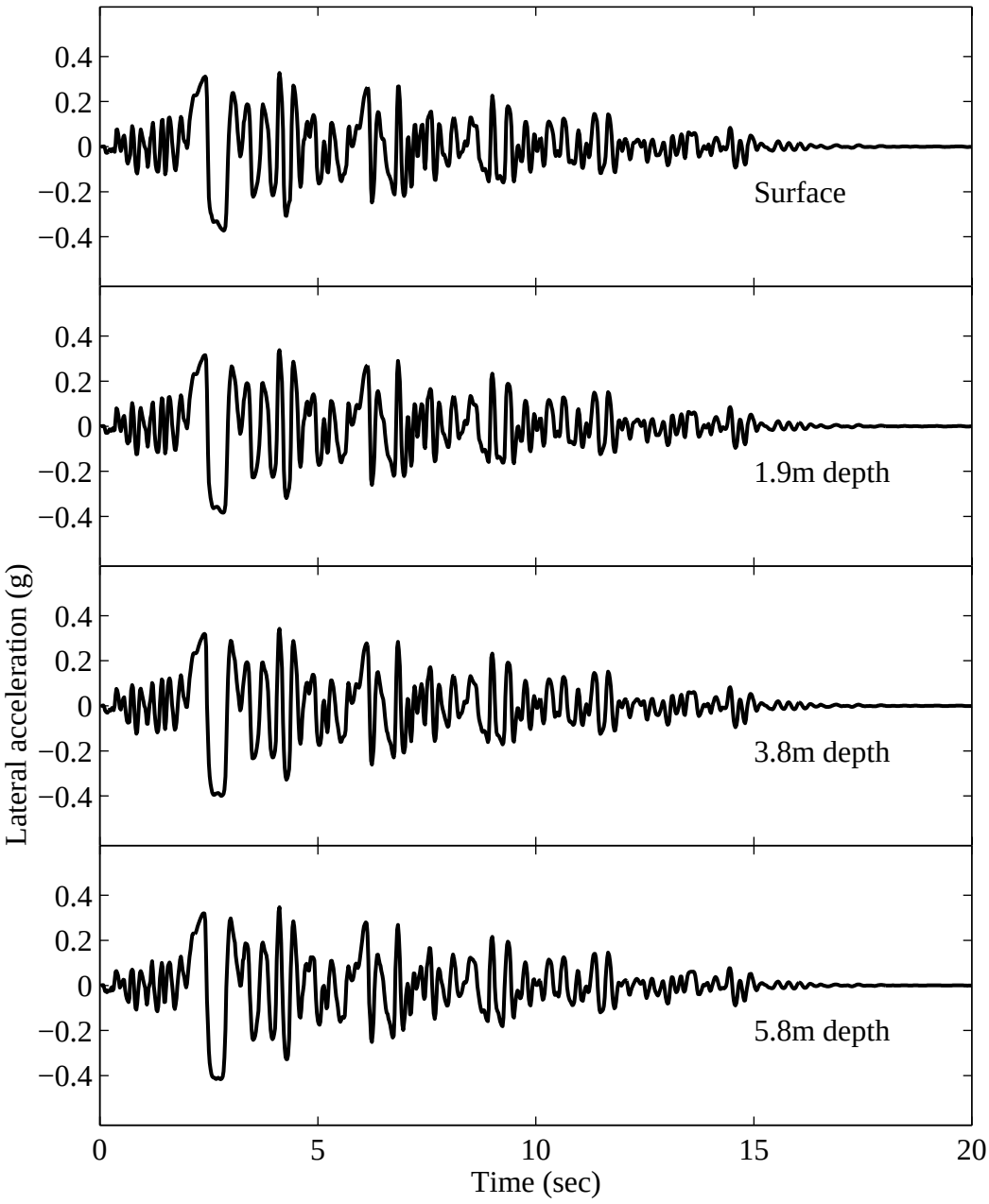

Figure B.27: Longitudinal acceleration time histories at Location C for Case W3N-C.

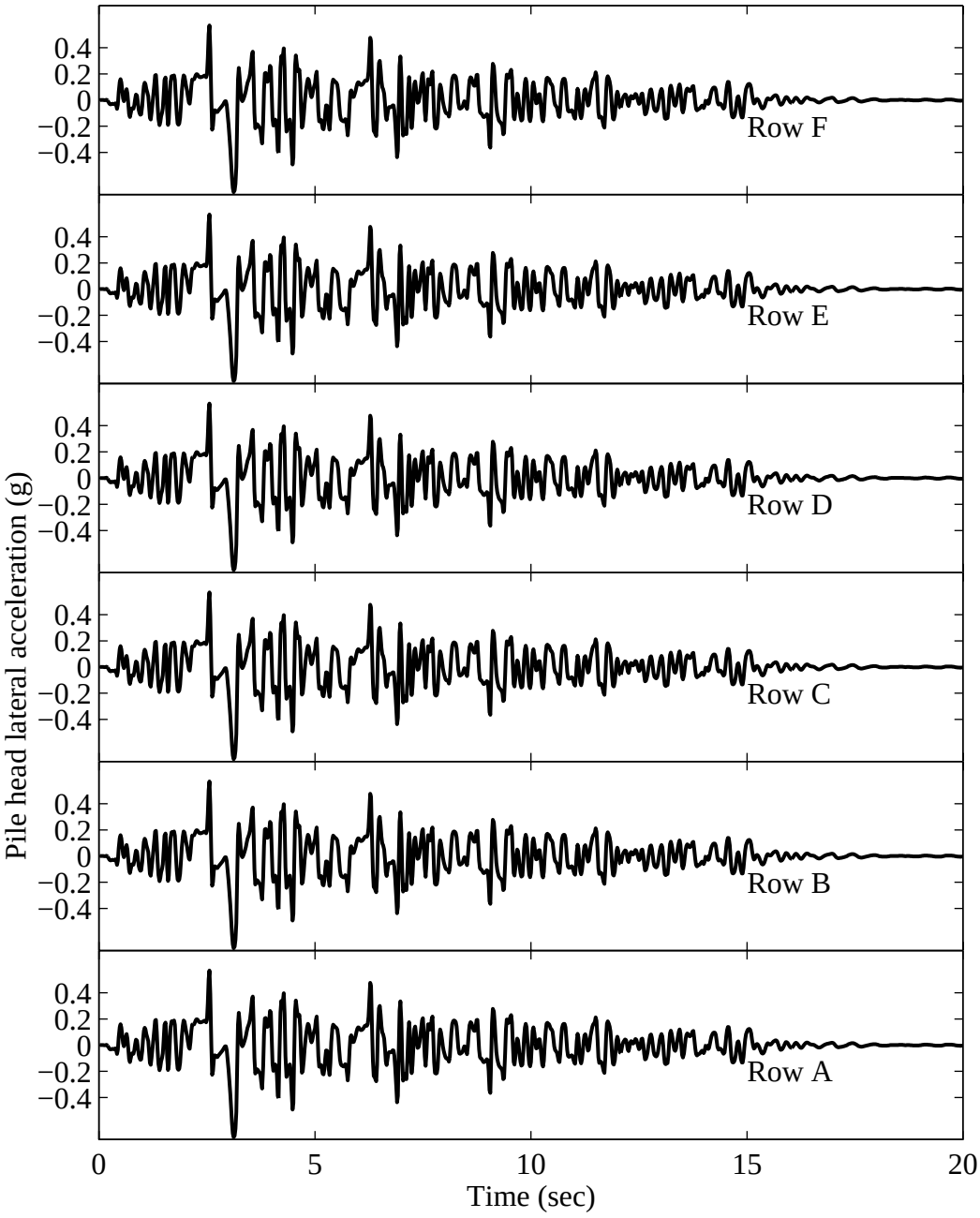

Figure B.28: Longitudinal acceleration time histories at the pile heads for Case W3N-C.

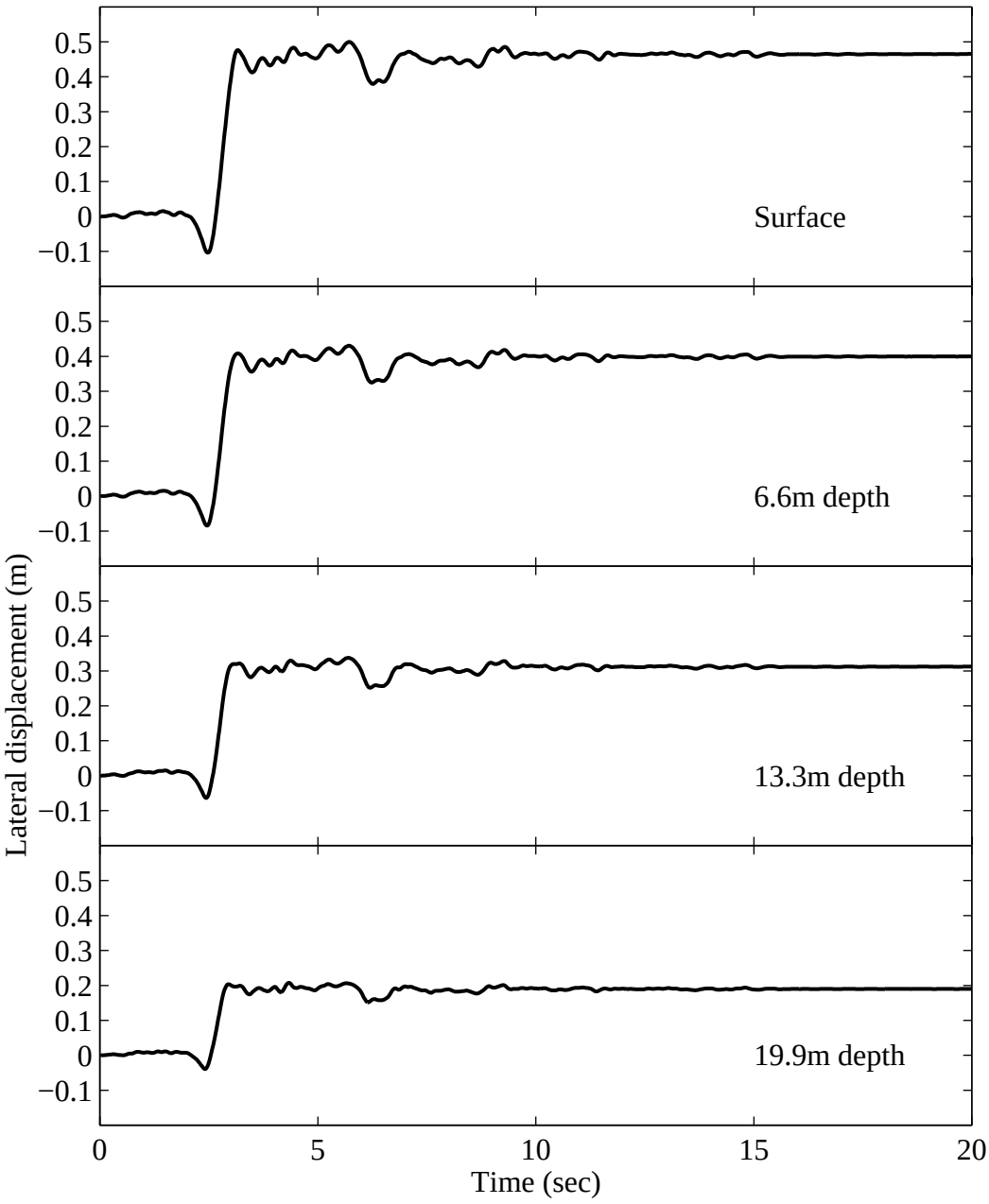

Figure B.29: Longitudinal displacement time histories at Location A for Case W3N-C.

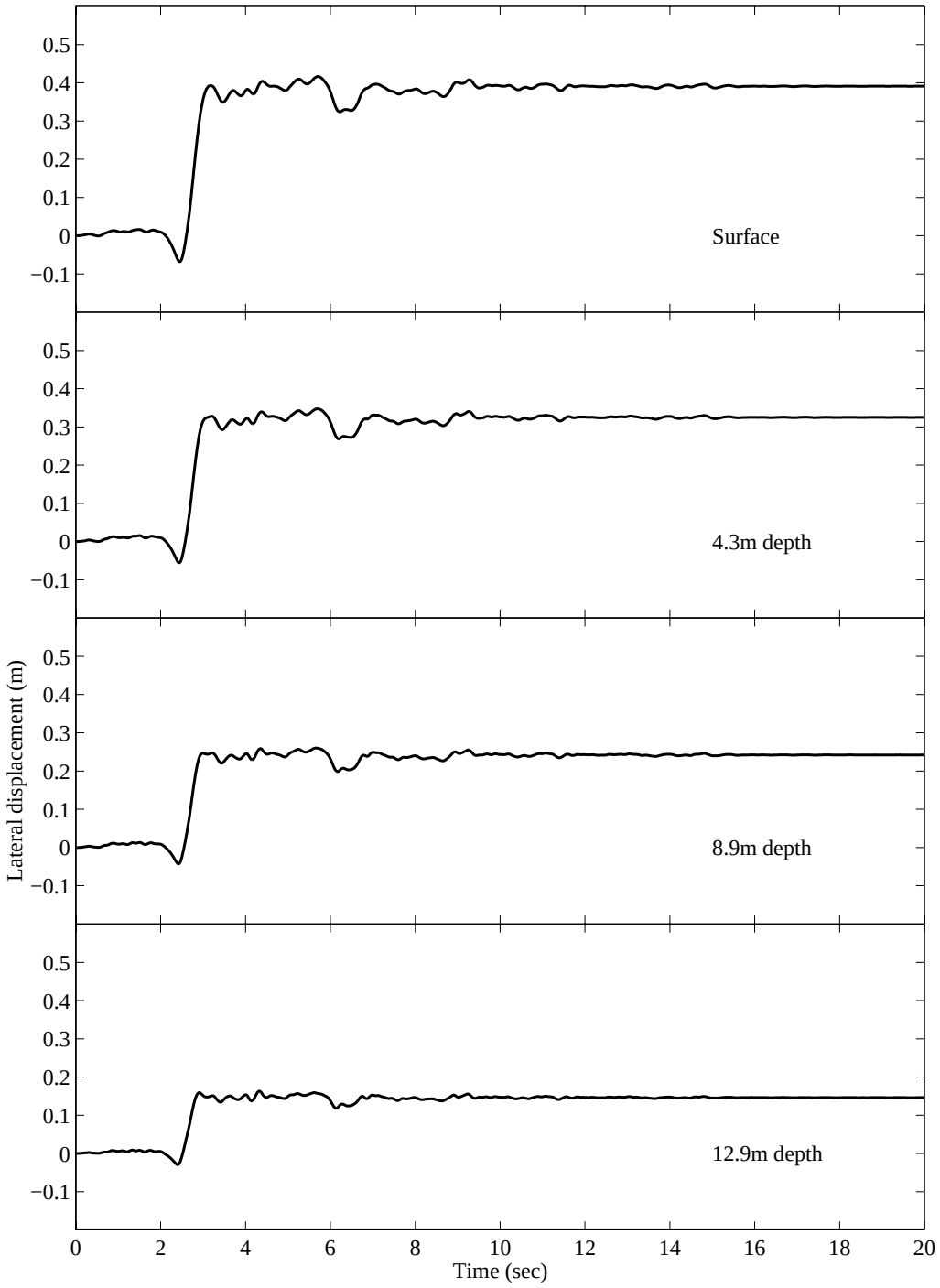

Figure B.30: Longitudinal displacement time histories at Location B for Case W3N-C.

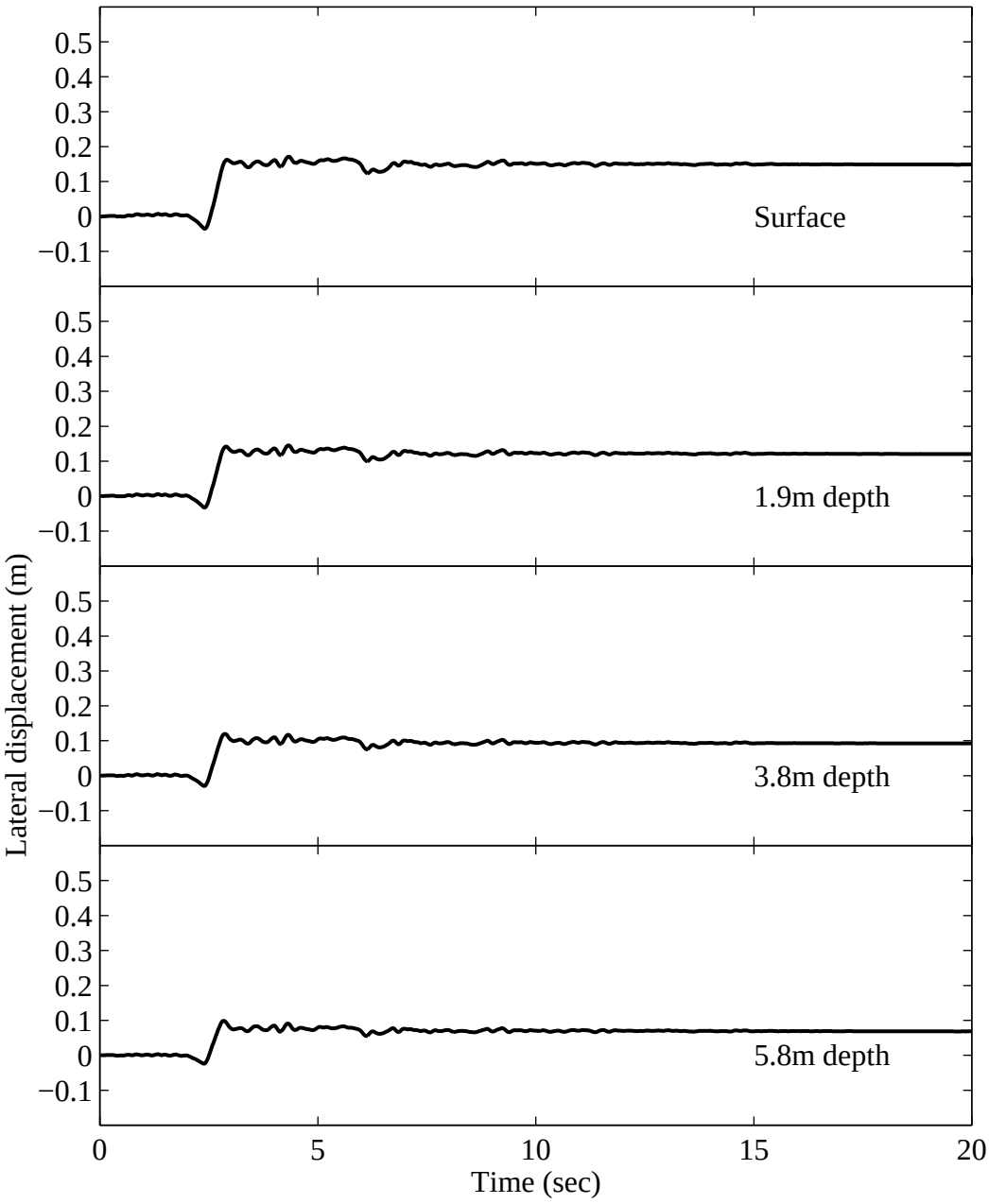

Figure B.31: Longitudinal displacement time histories at Location C for Case W3N-C.

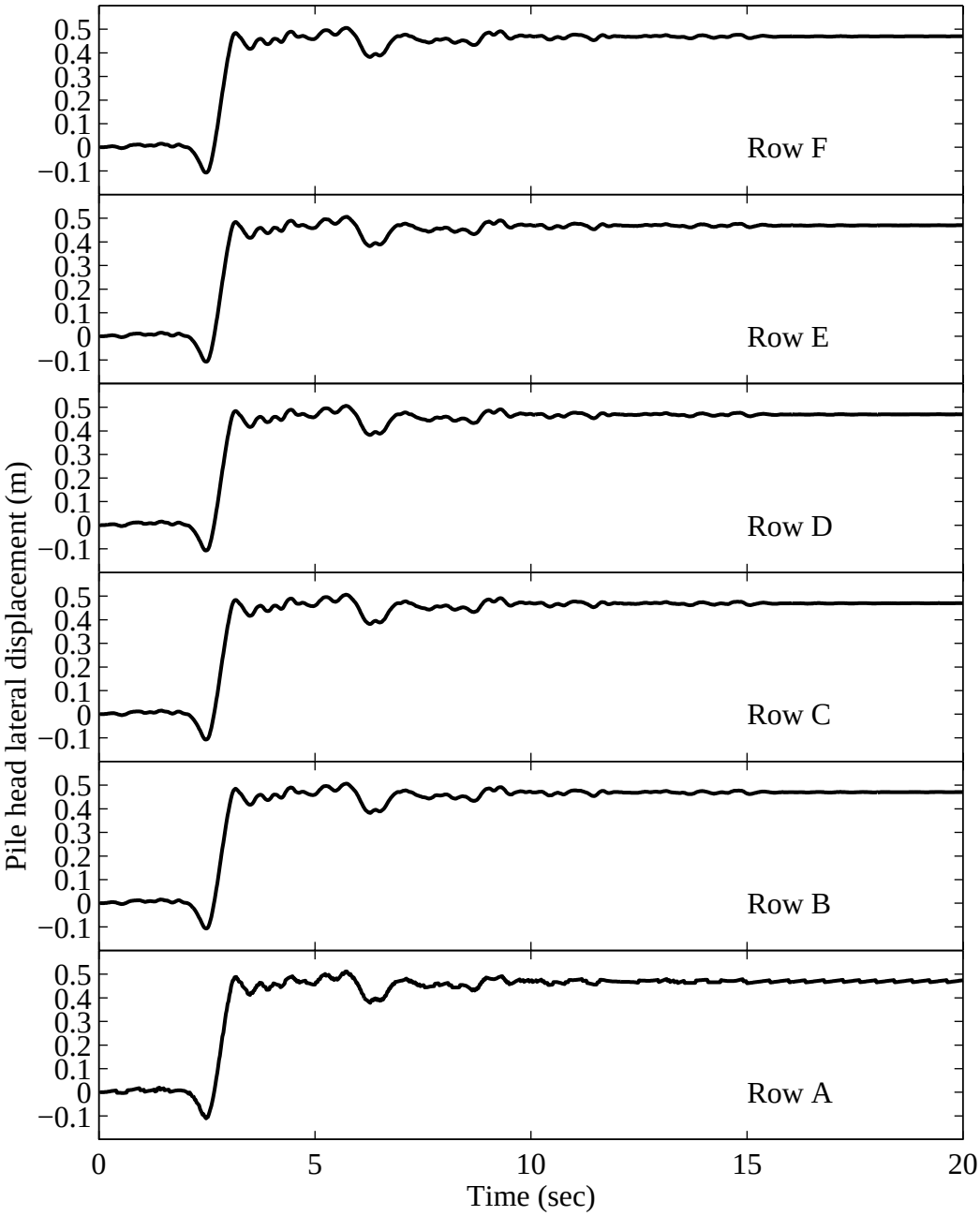

Figure B.32: Longitudinal displacement time histories at the pile heads for Case W3N-C.

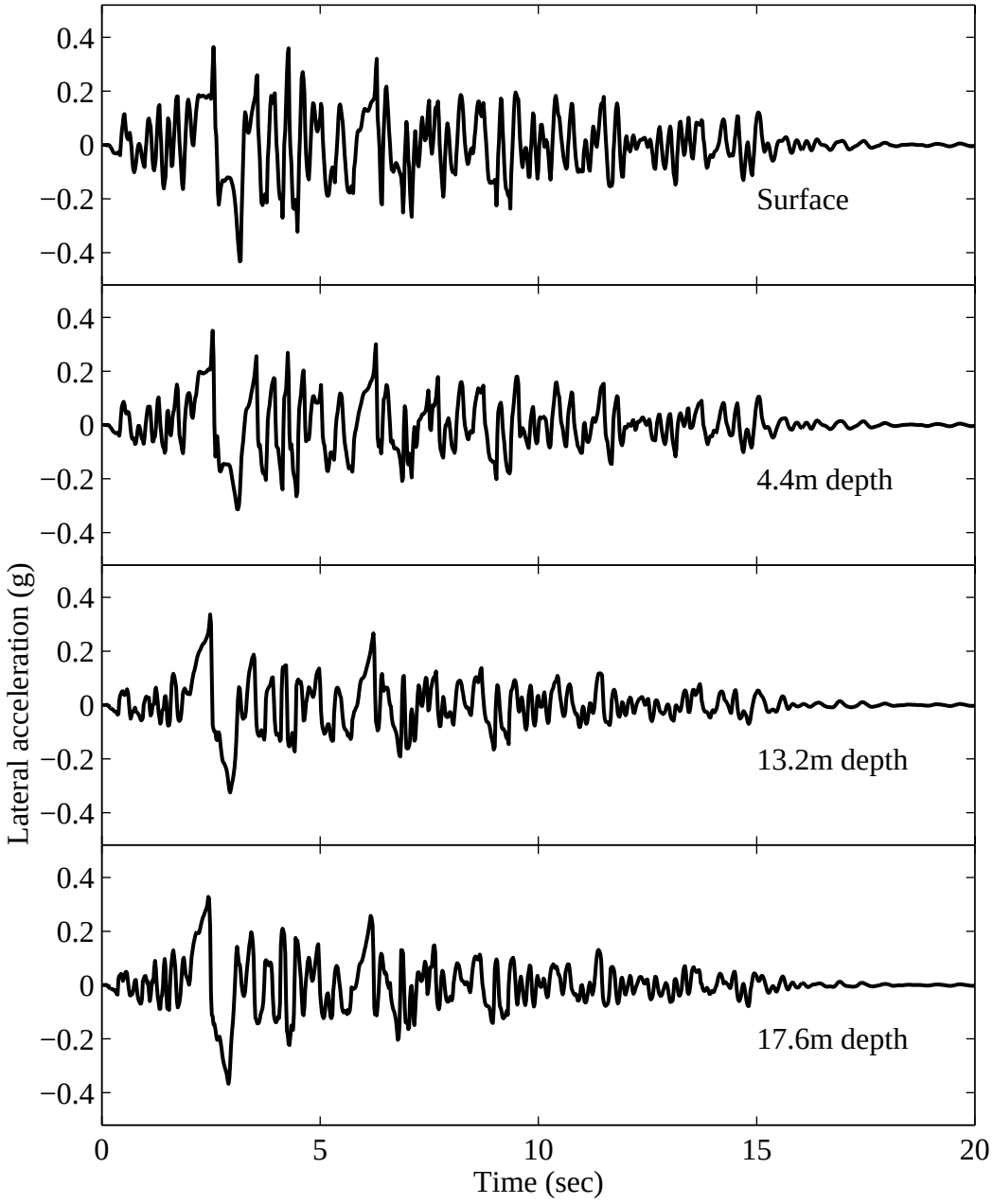

Figure B.33: Longitudinal acceleration time histories at Location A for Case W3N-M.

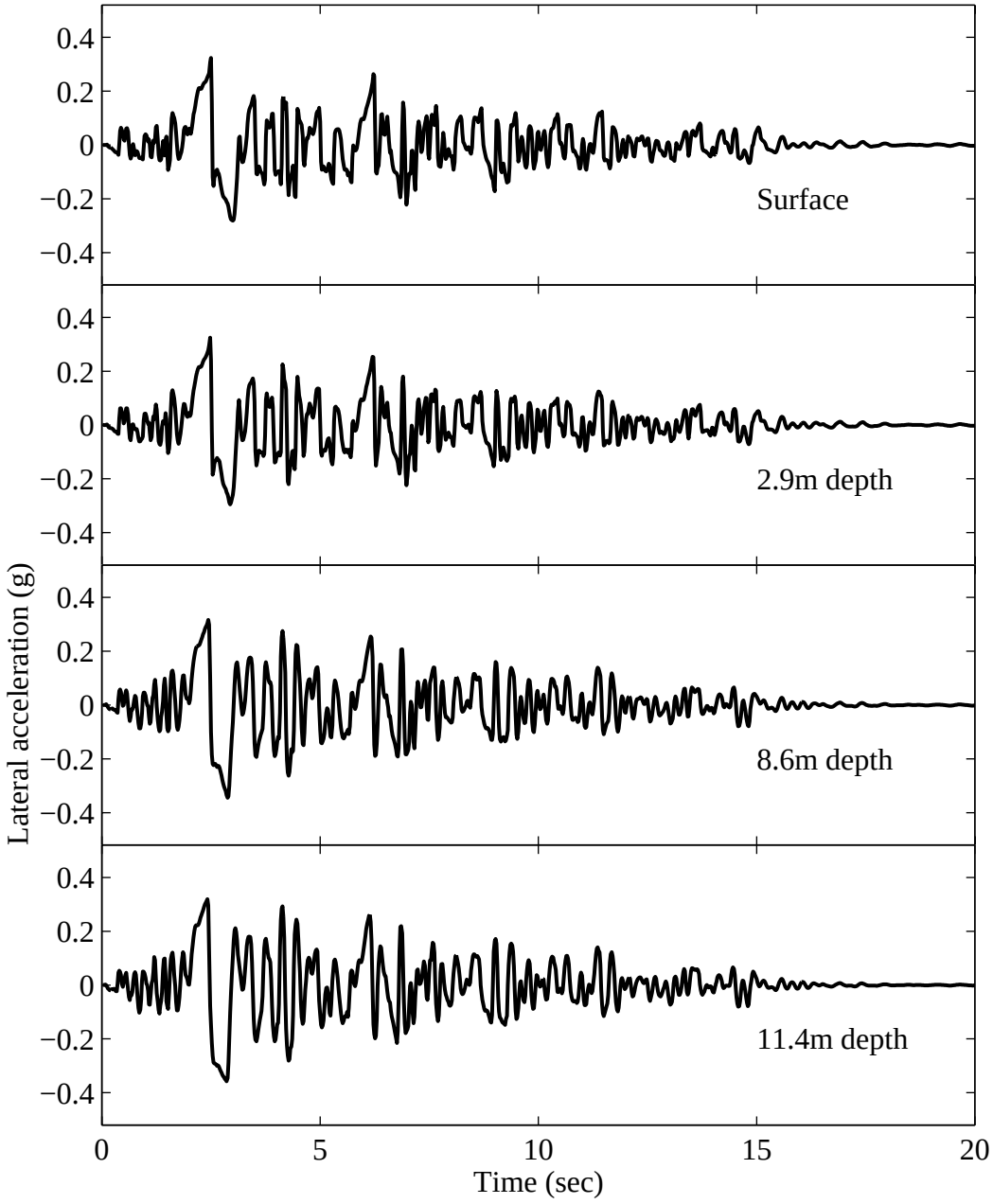

Figure B.34: Longitudinal acceleration time histories at Location B for Case W3N-M.

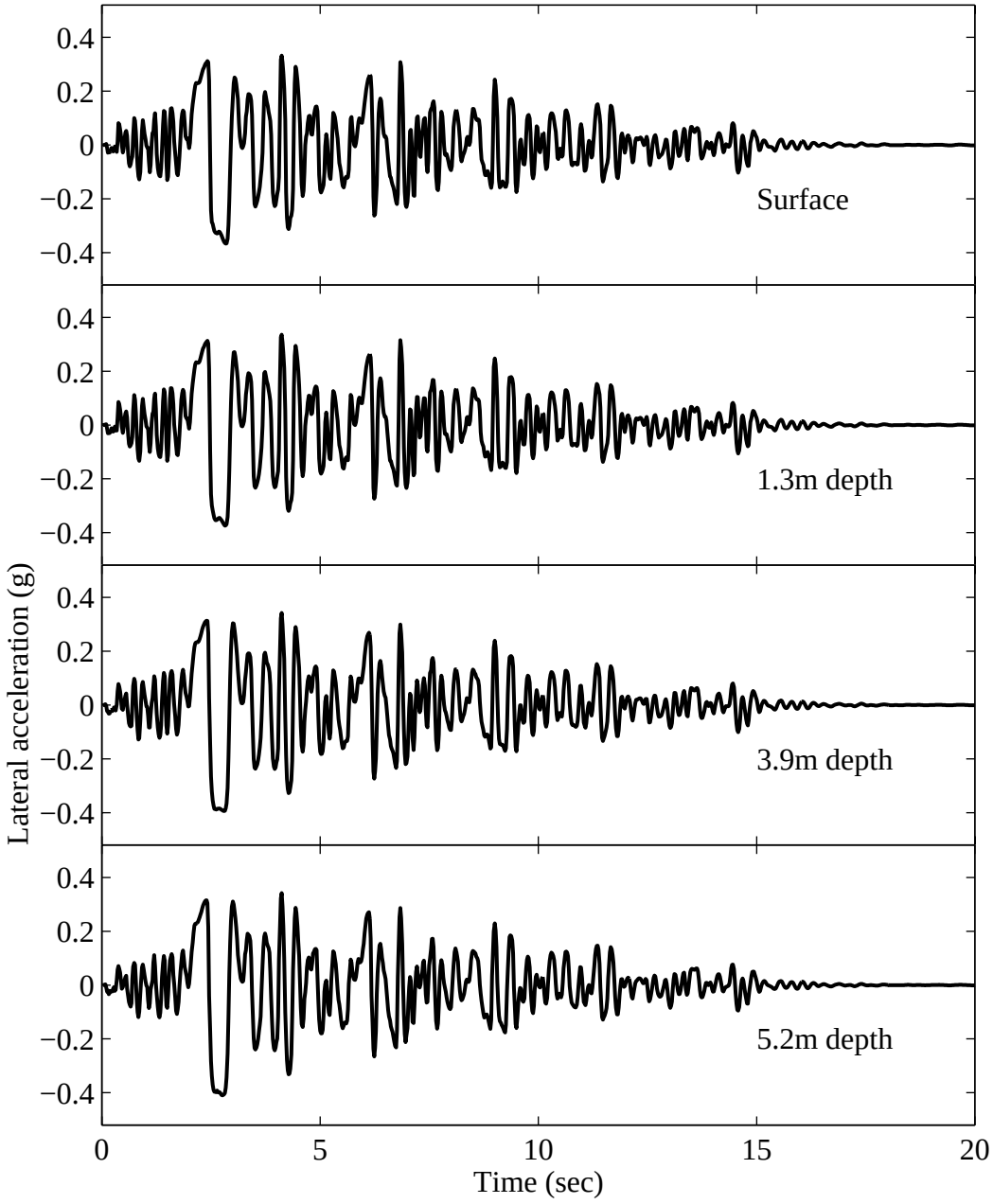

Figure B.35: Longitudinal acceleration time histories at Location C for Case W3N-M.

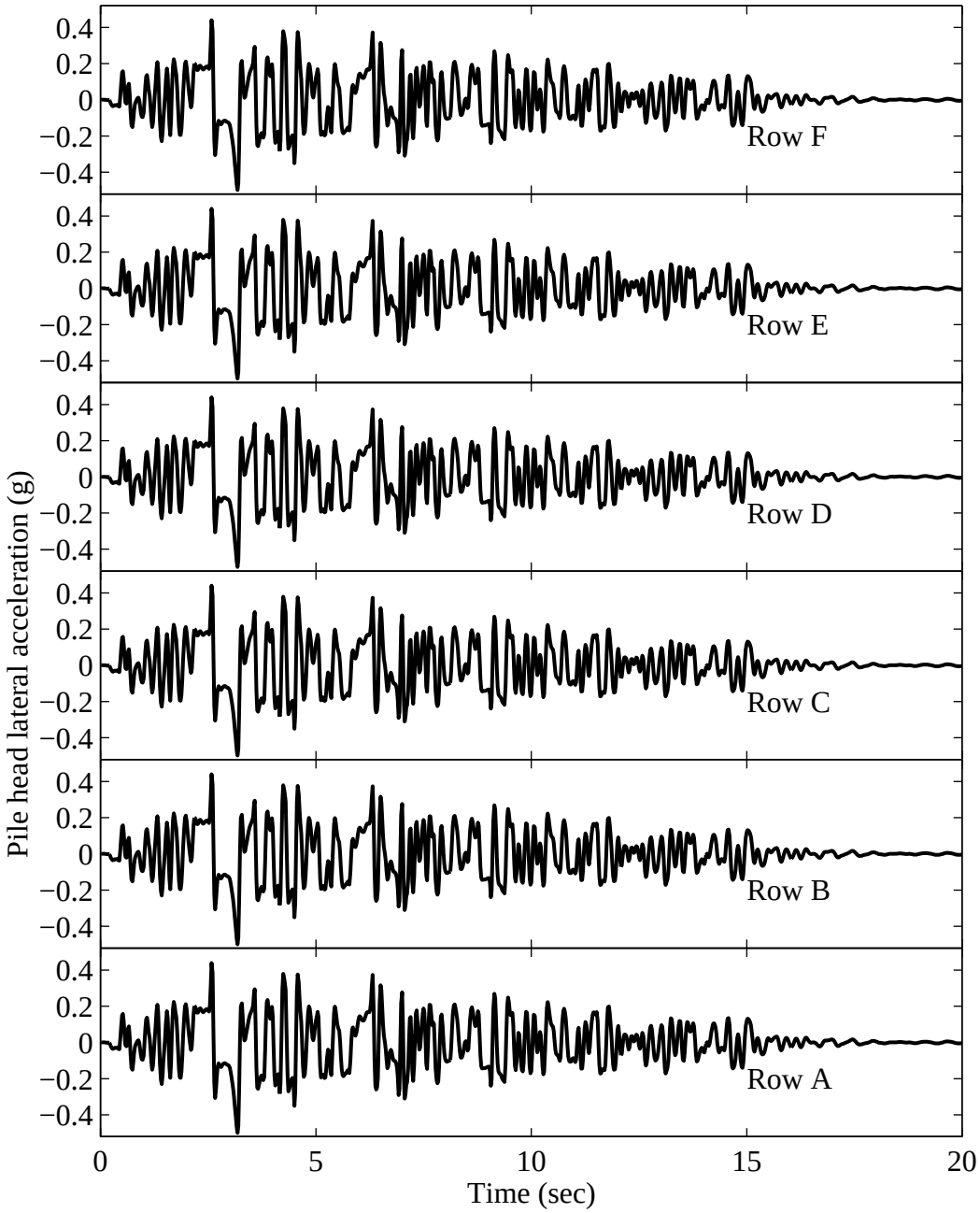

Figure B.36: Longitudinal acceleration time histories at the pile heads for Case W3N-M.

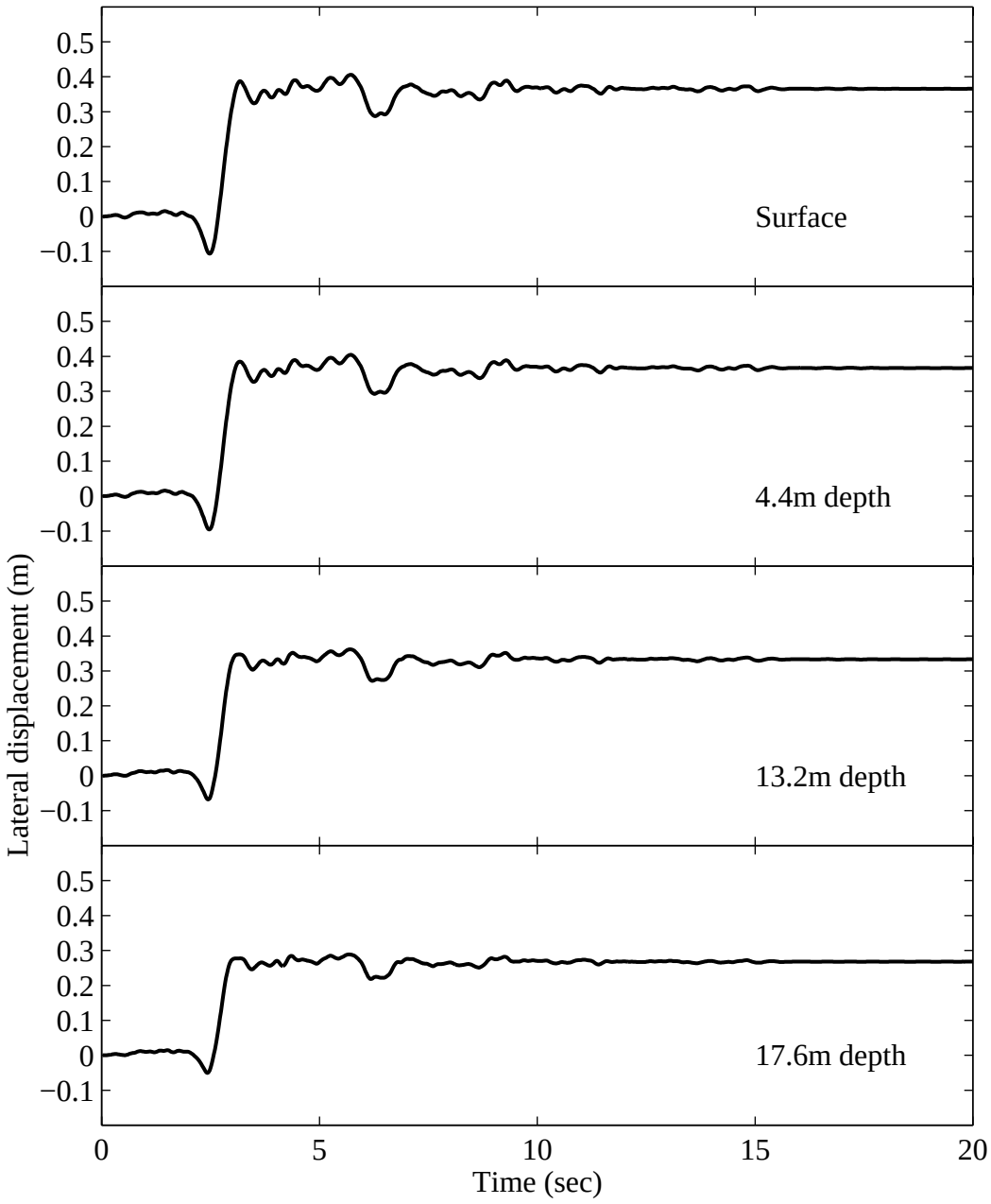

Figure B.37: Longitudinal displacement time histories at Location A for Case W3N-M.

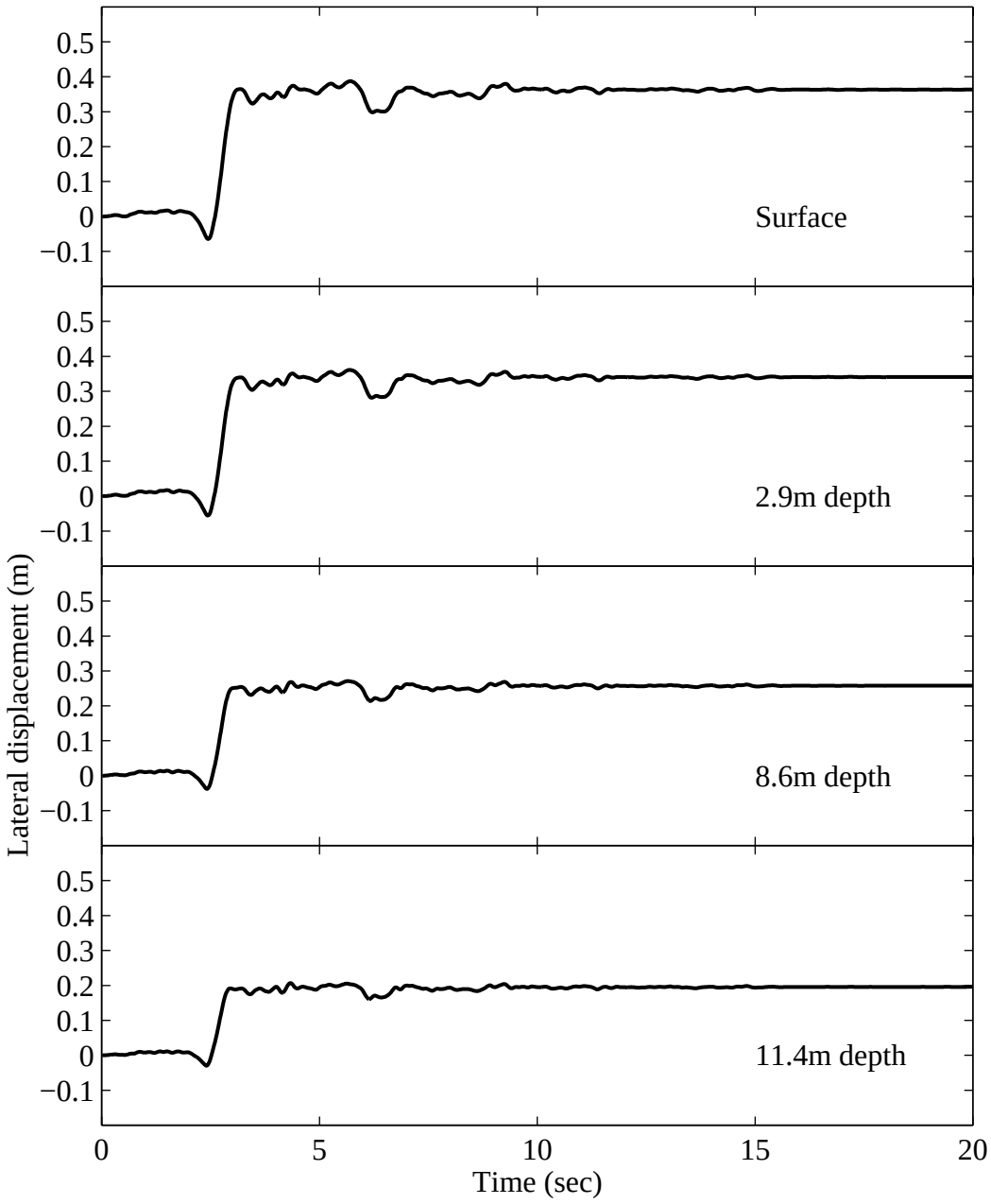

Figure B.38: Longitudinal displacement time histories at Location B for Case W3N-M.

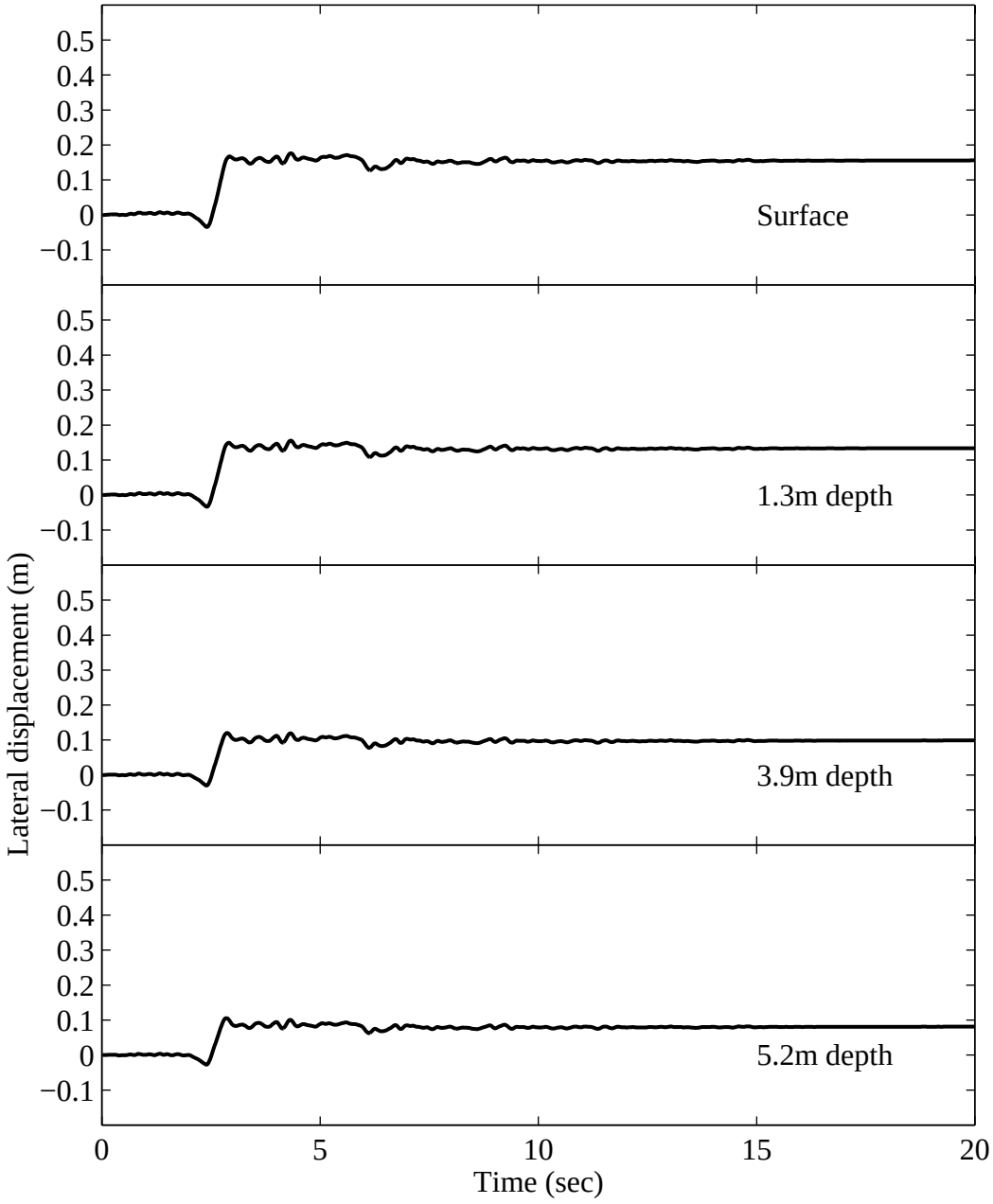

Figure B.39: Longitudinal displacement time histories at Location C for Case W3N-M.

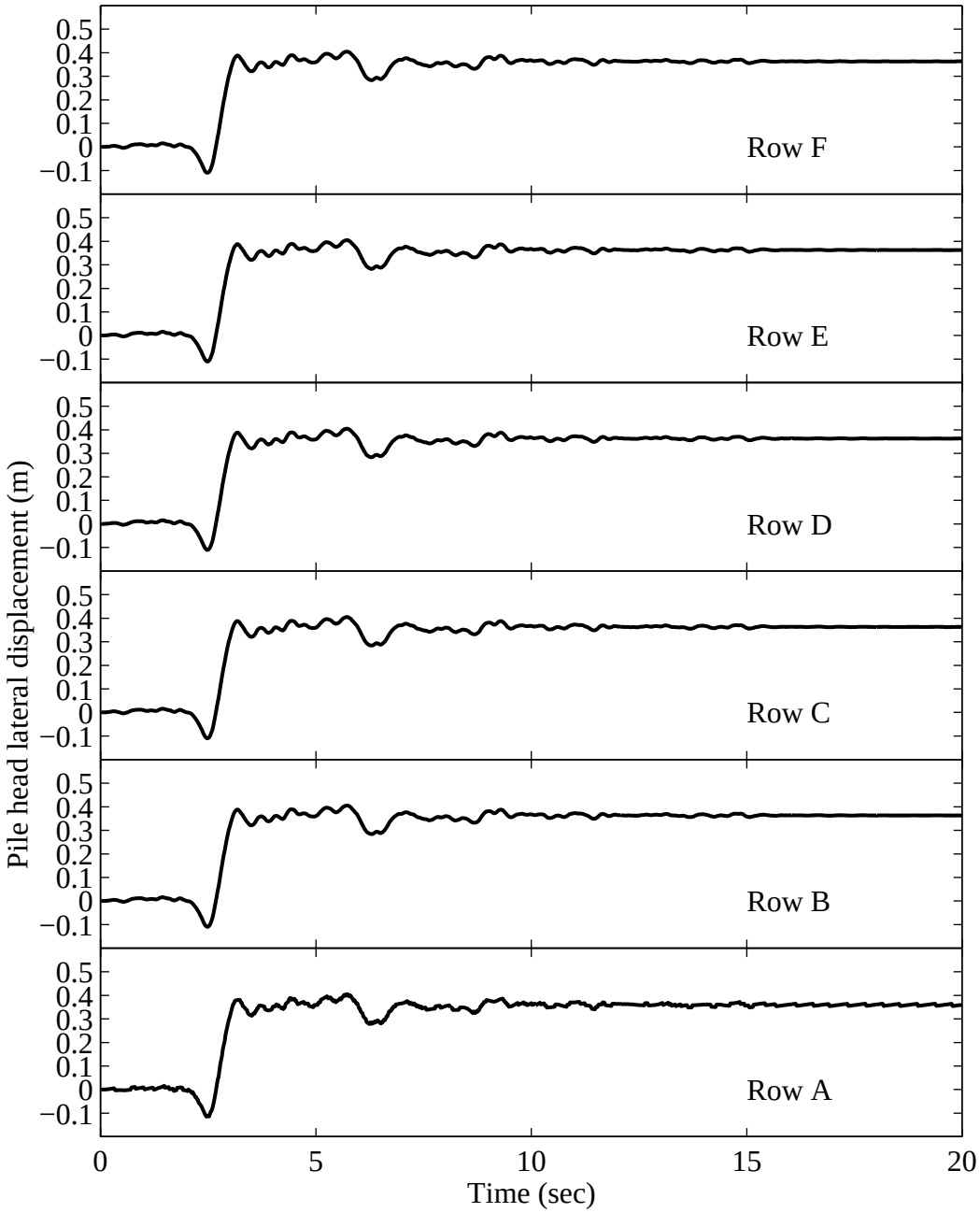

Figure B.40: Longitudinal displacement time histories at the pile heads for Case W3N-M.

Bibliography

Abdoun, T. (1997). "Modeling of Seismically Induced Lateral Spreading of Multi-Layered Soil and Its Effect on Pile Foundations," Ph.D. Thesis, Dept. of Civil Engineering, Rensselaer Polytechnic Institute, Troy, New York.

Abdoun, T., and Doubry, R. (2002). "Evaluation of Pile Foundation Response to Lateral Spreading." *Soil Dynamics and Earthquake Engineering*, 22(9-12), 1069-1076.

Adachi, T., Iwai, S., Yasui, M., and Sato, Y. (1992). "Settlement of Inclination of Reinforced Concrete Buildings in Dagupan City Due to Liquefaction During 1990 Philippine Earthquake." *Proceedings of the 10th World Conference on Earthquake Engineering*, A. A. B. (ed.), Madrid, Spain, July 19-25, 2, 147-152.

Adalier, K. (1992). "Post-liquefaction Behavior of Soil Systems," MS Thesis, Dept. of Civil Engineering, Rensselaer Polytechnic Institute, Troy, NY.

Adalier, K., Elgamal, A.-W., and Martin, G.R. (1998). "Foundation Liquefaction Countermeasures for Earth Embankments." *Journal of Geotechnical and Geoenvironmental Engineering*, 124(6), 500-517.

Adalier, K., and Elgamal, A.-W. (2002). "Seismic Response of Adjacent Dense and Loose Saturated Sand Columns." *Soil Dynamics and Earthquake Engineering*, 22(2), 115-127.

Adalier, K., Elgamal, A., Meneses, J., and Baez, J. I. (2003). "Stone Column as Liquefaction Countermeasure in Non-plastic Silty Soils." *Soil Dynamics and Earthquake Engineering*, 23(7), 571-584.

Adams, M. F. (1998). "Multigrid Equation Solvers for Large Scale Nonlinear Finite Element Simulations," Ph.D. Thesis, Department of Civil Engineering, University of California, Berkeley.

Aluru, N. R. (1995). "Parallel and Stabilized Finite Element Methods for the Hydrodynamic Transport Model of Semiconductor Devices," Ph.D. Thesis, Department of Civil Engineering, Stanford University, Stanford, CA.

Amdahl, G.M. (1968). "The Validity of the Single-Processor Approach to Achieving Large-scale Computing Capabilities." *Proceedings of the American Federation of Information Processing Society*, Atlantic City, NJ, April 18-20.

Amestoy, P.R., Duff, I.S., and L'Excellent, J.-Y. (2000). "Multifrontal Parallel Distributed Symmetric and Unsymmetric Solvers." *Computer Methods in Applied Mechanics and Engineering*, 184(2-4), 501-520.

Ansal, A., Bardet, J.P., Barka, A., Baturay, M.B., Berilgen, M., Bray, J., Cetin, O., Cluff, L., Durgunoglu, T., Erten, D., Erdik, M., Idriss, I.M., Karadayilar, T., Kaya, A., Lettis, W., Olgun, G., Paige, W., Rathje, E., Roblee, C., Stewart, J., and Ural, D. (1999). "Initial Geotechnical Observations of the November 12, 1999, Duzce Earthquake, A Report of the Turkey-US Geotechnical Earthquake Engineering Reconnaissance Team."

Aoyama, Yukiya, and Nakano, Jun. (1999). *RS/6000 SP: Practical MPI Programming*, Intenational Business Machines Corporation (IBM).

Arduino, P., Kramer, S., and Baska, D. (2001). "UW-Sand: A Simple Constitutive Model for Liquefiable Soils." *Books of Abstract, 2001 Mechanics and Materials Summer Conference*, San Diego, CA, June 27-29, 108.

Arulanandan, K., and Scott, R.F. (1993). "Verification of Numerical Procedures for the Analysis of Soil Liquefaction Problems." Conference Proceedings, Volume 1, Balkema, Davis, CA.

Arulanandan, K., and Scott, R.F. (1994). "Verification of Numerical Procedures for the Analysis of Soil Liquefaction Problems." Conference Proceedings, Volume 2, Balkema, Davis, CA.

Arulmoli, K., Muraleetharan, K.K., Hossain, M.M., and Fruth, L.S. (1992). "VELACS: Verification of Liquefaction Analyses by Centrifuge Studies, Laboratory Testing Program, Soil Data Report." *Report*, The Earth Technology Corporation, Project No. 90-0562, Irvine,CA.

Arulmoli, K. (2005). Personal Communication.

Ashford, S. A., Rollins, K. M., Bradford, S. C., Weaver, T. J., and Baez, J. I. (2000). "Liquefaction Mitigation Using Stone Columns Around Deep Foundations: Full-Scale Test Results." Soil Mechanics 2000, Transportation Research Record No. 1736, Transportation Research Board (TRB), Washington D.C., 110-118.

Association of State Dam Safety Officials ASDSO. (1992). "Compilation of National Dam Inventory Data." Lexington, KY.

Baez, J. I., and Martin, G. R. (1993). "Advances in the Design of Vibro Systems for the Improvement of Liquefaction Resistance." *Symposium of Ground Improvement*, Vancouver Geotechnical Society, Vancouver, BC.

Bao, H., Bielak, J., Ghattas, O., O'Hallaron, D.R., Kallivokas, L.F., Shewchuk, J. R., and Xu, J. (1998). "Large-scale Simulation of Elastic Wave Propagation in Heterogeneous Media on Parallel Computers." *Computer Methods in Applied Mechanics and Engineering*, 152(1-2), 85-102.

Bardet, J.P., Huang, Q., and Chi, S.W. (1993). "Numerical Prediction for Model No. 1." *Proceedings of the International Conference on the Verification of Numerical Procedures for the Analysis of Soil Liquefaction Problems*, K. Arulanandan, Scott, R.F. (Eds.), Balkema, Netherlands, Vol. 1, 67-86.

Bardet, J.P., Oka, F., Sugito, M., and Yashima, A. (1995). "The Great Hanshin Earthquake Disaster." *Preliminary Investigation Report*, Department of Civil Engineering, University of Southern California, Los Angeles, CA.

Bielak, J., Xu, J., and Ghattas, O. (1999). "Earthquake Ground Motion and Structural Response in Alluvial Valleys." *Journal of Geotechnical and Geoenvironmental Engineering*, 125(5), 404-412.

Bielak, J., Hisada, Y., Bao, H., Xu, J., and Ghattas, O. (2000). "One- Vs Two- or Three-Dimensional Effects in Sedimentary Valleys." *Proceedings of 12th World Conference on Earthquake Engineering*, New Zealand, February.

Biot, M. A. (1962). "The Mechanics of Deformation and Acoustic Propagation in Porous Media." *Journal of Applied Physics*, 33(4), 1482-1498.

Borja, R.I., Chao, H.Y., Montans, F., and Lin, C.H. (1999a). "Nonlinear Ground Response at Lotung LSST Site." *Journal of Geotechnical and Geoenvironmental Engineering*, 125(3), 187-197.

Borja, R.I., Chao, H.Y., Montans, F., and Lin, C.H. (1999b). "SSI Effects on Ground Motion at Lotung LSST Site." *Journal of Geotechnical and Geoenvironmental Engineering*, 125(9), 760-770.

Borja, Ronaldo I. (2004). "Incorporating Uncertainties in Nonlinear Soil Properties into Numerical Models." *Proceedings of the International Workshop on Uncertainties in Nonlinear Soil Properties and their Impact on Modeling Dynamic Soil Response*, Pacific Earthquake Engineering Research Center (PEER), Berkeley, CA, March 18-19.

Bray, Jonathan D., Sancio, Rodolfo B., Riemer, Michael, and Durgunoglu, H. Turan. (2004). "Liquefaction Susceptibility of Fine-Grained Soils." *Proceedings of the 11th International Conference on Soil Dynamics and Earthquake Engineering*, D.Doolin, A.Kammerer, T. Nogami, R. B. Seed, and I. T. (eds.), Berkeley, CA, January 7-9, 1, 655-662.

Casagrande, A. (1975). "Liquefaction and Cyclic Deformation of Sands -- A Critical Review." *Proceedings of the 5th Pan-American Conference on Soil Mechanics and Foundation Engineering*, Buenos Aires, Argentina.

Castro, G., and Poulos, S.J. (1977). "Factors Affecting Liquefaction and Cyclic Mobility." *Journal of Geotechnical Engineering Division*, 103(GT6), 501-516.

Chan, A.H.C. (1988). "A Unified Finite Element Solution to Static and Dynamic Problems in Geomechanics," PhD Thesis, University College of Swansea, U. K.

Chopra, A.K. (2001). *Dynamics of Structures (2nd Edition)*, Upper Saddle River: Prentice Hall.

CIMNE. (1999). *GiD Reference Manual*, http://gid.cimne.upc.es, International Center for Numerical Methods in Engineering, Barcelona, Spain.

Conte, Joel P., Vijalapura, P. K., and Meghella, M. (2003). "Consistent Finite-Element Response Sensitivity Analysis." *Journal of Engineering Mechanics*, 129(12), 1380-1393.

CSI. (2005). "SAP2000." http://www.csiberkeley.com/, Berkeley, CA.

Das, B.M. (1983). *Advanced Soil Mechanics*, Taylor and Francis Publisher, Washington, DC.

Das, B.M. (1995). *Principles of Foundation Engineering*, PWS Publishing Co., Boston, MA.

Davis, C.A., and Bardet, J.P. (1996). "Performance of Two Reservoirs during the 1994 Northridge Earthquake." *Journal of Geotechnical Engineering*, 122(8), 613-622.

Desai, C.S., and Christian, J.T. (1977). *Numerical Methods in Geotechnical Engineering*, McGraw Hill Book Co., New York.

Desai, C.S., and Siriwardane, H.J. (1984). *Constitutive Laws for Engineering Materials: With Emphasis on Geologic Materials*, Prentice Hall, Inc., Englewood Cliffs, New Jersey.

Desai, C.S. (2000). "Evaluation of Liquefaction Using Disturbed State and Energy Approaches." *Journal of Geotechnical and Geoenvironmental Engineering*, 126(7), 618-631.

Dickenson, Stephen E., and McCullough, Nason J. (2005). "Modeling the Seismic Performance of Pile Foundations for Port and Coastal Infrastructure." Seismic Performance and Simulations of Pile Foundations in Liquefied and Laterally Spreading Ground, Geotechnical Special Publication No. 145, Edited by R. Boulanger and K. Tokimatsu, 173-191.

Dobry, R., and Taboada, V.M. (1994a). "Possible Lessons from VELACS Model No. 2 Results." *Proceedings of the International Conference on the Verification of Numerical Procedures for the Analysis of Soil Liquefaction Problems*, K. Arulanandan and R. F. Scott, Balkema, Rotterdam, 2, 1341-1352.

Dobry, R., and Taboada, V.M. (1994b). "Experimental Results of Model No.2 at RPI." *Proceedings of the International Conference on the Verification of Numerical Procedures for the Analysis of Soil Liquefaction Problems, Vol. 2*, Aarulanandan K, Scott RF eds., Rotterdam: Balkema, 2, 1341-1352.

Dobry, R., Taboada, V., and Liu, L. (1995). "Centrifuge Modeling of Liquefaction Effects During Earthquakes." *Proceedings of the 1st International Conference On Earthquake Geotechnical Engineering, IS-Tokyo*, K. Ishihara, Balkema, Rotterdam, Tokyo, Japan, November 14-16, 3, 1291-1324.

Donahue, Matthew J., Dickenson, Stephen E., Miller, Thomas H., and Yim, Solomon C. (2005). "Implications of the Observed Seismic Performance of a Pile-Supported Wharf for Numerical Modeling." *Earthquake Spectra*, 21(3), 617-634.

EERI. (2000). "Kocaeli. Turkey, Earthquake of August 17, 1999 Reconnaissance Report." *Earthquake Spectra 16, Supplement A*, Earthquake Engineering Research Institute (EERI).

EERI. (2001). "Chi-Chi, Taiwan, Earthquake of September 21, 1999, Reconnaissance Report." *Earthquake Spectra 17, Supplement A*, Earthquake Engineering Research Institute (EERI).

Elgamal, A., Parra, E., Yang, Z., and Adalier, K. (2002a). "Numerical Analysis of Embankment Foundation Liquefaction Countermeasures." *Journal of Earthquake Engineering*, 6(4), 447-471.

Elgamal, A., Yang, Z., and Parra, E. (2002b). "Computational Modeling of Cyclic Mobility and Post-Liquefaction Site Response." *Soil Dynamics and Earthquake Engineering*, 22(4), 259-271.

Elgamal, A., Yang, Z., Parra, E., and Ragheb, A. (2003). "Modeling of Cyclic Mobility in Saturated Cohesionless Soils." *International Journal of Plasticity*, 19(6), 883-905.

Elgamal, A.-W., Zeghal, M., Taboada, V., and Dobry, R. (1996). "Analysis of Site Liquefaction and Lateral Spreading Using Centrifuge Testing Records." *Soils and Foundations*, Japanese Geotechnical Society.

Elgamal, Ahmed, Lai, Tao, Yang, Zhaohui, and He, Liangcai. (2001). "Dynamic Soil Properties, Seismic Downhole Arrays and Applications in Practice." *Proceedings of the 4th International Conference on Recent Advances in Geotechnical Earthquake Engineering and Soil Dynamics*, S. P. (Ed.), San Diego, CA, March 26-31.

Elgamal, Ahmed, Lu, Jinchi, and Yang, Zhaohui. (2004). "Data Uncertainty for Numerical Simulation in Geotechnical Earthquake Engineering." *Proceedings of the International Workshop on Uncertainties in Nonlinear Soil Properties and their*

Impact on Modeling Dynamic Soil Response, Pacific Earthquake Engineering Research Center (PEER), Berkeley, CA, March 18-19.

Farhat, Charbel. (1988). "A Simple and Efficient Automatic FEM Domain Decomposer." *Computers and Structures*, 28(5), 579-602.

Finn, W.D.L., Lee, K.W., and Martin, G.R. (1977). "An Effective Stress Model for Liquefaction." *Journal of Geotechnical Engineering Division*, 103.

Flynn, M.J. (1966). "Very High Speed Computing Systems." *Proc. IEEE*, 12, 1901-1909.

Garatani, K., Nakajima, K., Okuda, H., and Yagawa, G. (2001). "Three-dimensional Elasto-static Analysis of 100 Million Degrees of Freedom." *Advances in Engineering Software*, 32(7), 511-518.

George, A., Heath, M. T., Liu, J., and Ng, E. (1986). "Solution of Sparse Positive Definite Systems on a Shared-Memory Multiprocessor." *International Journal of Parallel Programming*, 15(4), 309-328.

George, A., Heath, M.T., Liu, J., and Ng, E. (1989). "Solution of Sparse Positive Definite Systems on a Hypercube." *Journal of Computational and Applied Mathematics*, 27, 129-156.

George, Alan. (1971). "Computer Implementation of the Finite Element Method," Ph.D. Thesis, Computer Science Department, Stanford University, Stanford, CA.

George, Alan, and Liu, Joseph W. (1981). *Computer Solution of Large Sparse Positive Definite*, Prentice-Hall, Inc.

Gu, Quan, and Conte, Joel P. (2003). "Convergence Studies in Nonlinear Finite Element Response Sensitivity Analysis." *Proceedings of the 9th International Conference on Applications of Statistics and Probability in Civil Engineering*, Berkeley, California, July 6-9.

Gullerud, Arne S., and Dodds, Robert H. (2001). "MPI-based Implementation of a PCG solver using an EBE Architecture and Preconditioner for Implicit, 3-D Finite Element Analysis." *Computers and Structures*, 79(5), 553-575.

Gummadi, L.N.B., and Palazotto, A.H. (1997). "Nonlinear Finite Element Analysis of Beams and Arches Using Parallel Processors." *Computers and Structures*, 63, 413-428.

Hamada, M. (1991). "Damage to Piles by Liquefaction-induced Ground Displacements." *Proceedings of the 3rd US Conference Lifeline Earthquake Engineering, ASCE*, Los Angeles, 1172-1181.

Hausler, Elizabeth A. (2002). "Influence of Ground Improvement on Settlement and Liquefaction: A Study Based on Field Case History Evidence and Dynamic Geotechnical Centrifuge Tests," PhD Thesis, Department of Civil Engineering, University of California, Berkeley, CA.

Heath, M.T., Ng, E., and Peyton, B.W. (1991). "Parallel Algorithms for Sparse Linear Systems." Parallel Algorithms for Matrix Computations, SIAM, Philadelphia, 83-124.

Herndon, B., Aluru, N., Raefsky, A., Goossens, R. J. G., Law, K. H., and Dutton, R. W. (1995). "A Methodology for Parallelizing PDE Solvers: Applications to Semiconductor Device Simulation." *the Seventh SIAM Conference on Parallel Processing for Scientific Computing*, San Francisco, CA.

Hisada, Y., Bao, H., Bielak, J., Ghattas, O., and O'Hallaron, D.R. (1998). "Simulations of Long-period Ground Motions During the 1995 Hyogoken-Nanbu (Kobe) Earthquake Using 3D Finite Element Method." *Proceedings of the 2nd International Symposium on Effect of Surface Geology on Seismic Motion*, Yokohama, Japan, December, 59-66.

Holtz, R.D., and Kovacs, W.D. (1981). *An Introduction to Geotechnical Engineering*, Prentice Hall, Englewood Cliffs, NJ.

Holzer, T. L., Youd, T. L., and Hanks, T. C. (1989). "Dynamics of Liquefaction During the 1987 Superstition Hills, California, Earthquake." *Science*, 244, 56-59.

Hughes, Thomas J.R. (1987). *The Finite Element Method: Linear Static and Dynamic Finite Element Analysis*, Prentice-Hall, Inc.

Iai, S. (1991). "A Strain Space Multiple Mechanism Model for Cyclic Behavior of Sand and Its Application." *Earthquake Engineering Research Note No. 43*, Port and Harbor Research Institute, Ministry of Transport, Japan.

Iai, S. (1998). "Seismic Analysis and Performance of Retaining Structures." *Proc. Geotech. Earthq. Engng. Soil Dyn. III*, P. Dakoulas, Yegian, M. and Holtz., R. D., Eds., Geotechnical Special Publication No. 75, 2, 1020-1044.

Idriss, I.M., and Sun, J.I. (1992). *User's Manual for SHAKE91*, Department of Civil and Environmental Engineering, University of California, Davis, CA.

Ishihara, K., Tatsuoka, F., and Yasuda, S. (1975). "Undrained Deformation and Liquefaction of Sand under Cyclic Stresses." *Soils and Foundations*, 15(1), 29-44.

Ishihara, K., Alex, A., Acacio, and Towhata, I. (1993). "Liquefaction-Induced Ground Damage in Dagupan in the July 16, 1990 Luzon Earthquake." *Soils and Foundations*, 33(1), 133-154.

Iwan, W.D. (1967). "On a Class of Models for the Yielding Behavior of Continuous and Composite Systems." *J. Appl. Mech.*, ASME 34, 612-617.

Jeremic, B., Runesson, K., and Sture, S. (1999). "A Model for Elastic-plastic Pressure Sensitive Material Subjected to Large Deformations (Invited Paper)." *International Journal of Solids and Structures*, 36(32-32), 4901-4918.

Jeremic, Boris. (2004). "Geowulf: http://sokocalo.engr.ucdavis.edu/~jeremic/GeoWulf/." University of California, Davis, Davis, CA.

JGS. (1996). Special Issue on Geotechnical Aspects of the January 17, 1995 Hyogoken-Nanbu Earthquake, Soils and Foundations (Tokyo, Japan), Japanese Geotechnical Society.

JGS. (1998). Special Issue on Geotechnical Aspects of the January 17, 1995 Hyogoken-Nanbu Earthquake, No. 2, Soils and Foundations (Tokyo, Japan), Japanese Geotechnical Society.

Ju, S. H. (2004). "Three-Dimensional Analyses of Wave Barriers for Reduction of Train-Induced Vibrations." *Journal of Geotechnical and Geoenvironmental Engineering*, 130(7), 740-748.

Karypis, G., and Kumar, V. (1997). *METIS, a Software Package for Partitioning Unstructured Graphs, Partitioning Meshes and Computing Fill-Reducing Ordering of Sparse Matrices*, Technical Report, Department of Computer Science, University of Minnesota.

Karypis, George, and Kumar, Vipin. (1998a). "METIS Version 4.0: A Software Package For Partitioning Unstructured Graphs, Partitioning Meshes, and Computing Fill-Reducing Orderings of Sparse Matrices." Department of Computer Science and Engineering, University of Minnesota, Minneapolis, MN.

Karypis, George, and Kumar, Vipin. (1998b). "A Fast and High Quality Multilevel Scheme for Partitioning Irregular Graphs." *SIAM Journal on Scientific Computing*, 20(1), 359-392.

Karypis, George, and Kumar, Vipin. (1998c). "Multilevel k-way Partitioning Scheme For Irregular Graphs." *Journal for Parallel and Distributed Computing*, 48(1), 96-129.

Kishida, H. (1966). "Damage to Reinforced Concrete Buildings in Niigata City with Special Reference to Foundation Engineering." *Soils and Foundations*, 6(1), 71-88.

Kokusho, T. (1999). "Water Film in Liquefied Sand and Its Effect on Lateral Spread." *Journal of Geotechnical and Geoenvironmental Engineering*, 125(10), 817-826.

Kondner, R.L. (1963). "Hyperbolic Stress-Strain Response: Cohesive Soils." *Journal of the Soil Mechanics and Foundations Division*, 89(SM1), 115-143.

Kramer, S.L. (1996). *Geotechnical Earthquake Engineering*, Prentice Hall, Upper Saddle River, NJ.

Kramer, Steven L., and Elgamal, Ahmed. (2001). "Modeling Soil Liquefaction Hazards for Performance-Based Earthquake Engineering." *PEER Report 2001/13*, Pacific Earthquake Engineering Research Center (PEER), Berkeley, CA.

Kruglinski, D. J., Shepherd, G., and Wingo, S. (1998). *Programming Microsoft Visual C++, Fifth Edition*, Microsoft Press, Redmond, WA.

Krysl, P., and Belytschko, T. (1998). "Objected-oriented Parallelization of Explicit Structural Dynamics with PVM." *Computers and Structures*, 66, 259-273.

Krysl, P., and Bittnar, Z. (2001). "Parallel Explicit Finite Element Solid Dynamics with Domain Decomposition and Message Passing: Dual Partitioning Scalability." *Computers and Structures*, 79, 345-360.

Lacy, S. (1986). "Numerical Procedures for Nonlinear Transient Analysis of Two-phase Soil System," Ph.D. Thesis, Princeton University, NJ.

Lambe, T.W., and Whitman, R.V. (1969). *Soil Mechanics*, John Wiley & Sons, New York.

Law, K H. (1994). "Large Scale Engineering Computations on Distributed Memory Parallel Computers and Distributed Workstations." *NSF Workshop on Scientific Supercomputing, Visualization and Animation in Geotechnical Earthquake Engineering and Engineering Seismology*, Carnegie-Mellon University, Pittsburgh, PA.

Law, K.H., and Mackay, D.R. (1993). "A Parallel Row-oriented Sparse Solution Method for Finite Element Structural Analysis." *International Journal for Numerical Methods in Engineering*, 36, 2895-2919.

Law, Kincho H. (1986). "A Parallel Finite Element Solution Method." *Computers and Structures*, 23(6), 845-858.

Law, Kincho H., and Fenves, Steven J. (1986). "A Node-Addition Model for Symbolic Factorization." *ACM Transactions on Mathematical Software*, 12(1), 37-50.

Law, Kincho H. (2004). Personal Communication.

Lee, E.A., Davis, J., Hylands, C., Janneck, J., Liu, J., Liu, X., S., Neuendorffer, Sachs, S., Stewart, M., Vissers, K., Whitaker, P., and Xiong, Y. (2001). "Overview of the

Ptolemy Project." Department of Electrical Engineering and Computer Science, University of California, Berkeley.

Li, X.S., and Dafalias, Y.F. (2000). "Dilatancy for Cohesionless Soils." *Geotechnique*, 50(4), 449-460.

Li, X.S., Ming, H.Y., and Cai, Z.Y. (2000). "Constitutive Modeling of Flow Liquefaction and Cyclic Mobility." Computer Simulation of Earthquake Effects. ASCE Geotechnical Special Publication, vol. 110, K. Arulanandan, Anandarajah, A., Li, X.S., ed., 81-98.

Li, Xiaoye S., and Demmel, James W. (1998). "Making Sparse Gaussian Elimination Scalable by Static Pivoting." *SC98: High Performance Networking and Computing Conference*, Orlando, FL.

Lipton, R. J., Rose, D. J., and Tarjan, R. E. (1979). "Generalized Nested Dissection." *SIAM Journal on Numerical Analysis*, 16(1), 346-358.

Liu, Joseph W. H. (1990). "The Role of Elimination Trees in Sparse Factorization." *SIAM Journal on Matrix Analysis and Applications*, 11(1), 134-172.

Liu, Joseph W. H. (1991). "A Generalized Envelope Method for Sparse Factorization by Rows." *ACM Transactions on Mathematical Software*, 17(1), 112-129.

Liu, L., and Dobry, R. (1997). "Seismic Response of Shallow Foundation on Liquefiable Sand." *Journal of Geotechnical and Geoenvironmental Engineering*, 123(6), 557-567.

Lu, Jinchi, He, Liangcai, Yang, Zhaohui, Abdoun, Tarek, and Elgamal, Ahmed. (2004). "Three-Dimensional Finite Element Analysis of Dynamic Pile Behavior in Liquefied Ground." *Proceedings of the 11th International Conference on Soil Dynamics and Earthquake Engineering*, D.Doolin, A.Kammerer, T. Nogami, R. B. Seed, and I. T. (eds.), Berkeley, CA, January 7-9, 1, 144-148.

Mackay, D.R., Law, K.H., and Raefsky, A. (1991). "An Implementation of A Generalized Sparse/Profile Finite Element Solution Method." *Computer and Structure*, 41(4), 723-737.

Mackay, D.R. (1992). "Solution Methods for Static and Dynamic Structural Analysis on Distributed Memory Computers," Ph.D. Thesis, Department of Civil Engineering, Stanford University.

Malvick, E. J., Kutter, B. L., Boulanger, R. W., and Feigenbaum1, H. P. (2004). "Post-shaking Failure of Sand Slope in Centrifuge Test." *Proceedings of the 11th International Conference on Soil Dynamics and Earthquake Engineering*, D.Doolin, A.Kammerer, T. Nogami, R. B. Seed, and I. T. (eds.), Berkeley, CA, Jan. 7-9, 2.

Manzari, M.T., and Dafalias, Y.F. (1997). "A Critical State Two-surface Plasticity Model for Sands." *Geotechnique*, 49(2), 252-272.

Manzari, Majid. (2004). "Large Deformation Analysis in Liquefaction Problems." *Proceedings of the 17th ASCE Engineering Mechanics Division Conference*, Newark, Delaware, June 13-16.

Margetts, L. (2002). "Parallel Finite Element Analysis," PhD Thesis, University of Manchester, Manchester.

Matsui, T., and Oda, K. (1996). "Foundation Damage of Structures." Soils and Foundations, 189-200.

McCullough, Nason J., Dickenson, Stephen E., and Schlechter, Scott M. (2001a). "The Seismic Performance of Pile Supported Wharf Structures." *Proceedings of the ASCE Ports 2001 Conference*, Norfolk, VA, April.

McCullough, Nason J., Schlechter, Scott M., and Dickenson, Stephen E. (2001b). "Centrifuge Modeling of Pile-Supported Wharves for Seismic Hazards." *Proceedings of the 4th International Conference on Recent Advances in Geotechnical Earthquake Engineering and Soil Dynamics Conference*, San Diego, CA, March 26-31.

McKenna, F. (1997). "Object Oriented Finite Element Analysis: Frameworks for Analysis Algorithms and Parallel Computing," PhD Thesis, Department of Civil Engineering, University of California, Berkeley, CA.

McKenna, F., and Fenves, G.L. (2001). "OpenSees Manual." PEER Center, http://opensees.berkeley.edu.

Mizuno, H. (1987). "Pile Damage During Earthquakes in Japan (1923-1983)." *Proceedings of the Session on Dynamic Response of Pile Foundations*, T. N. (ed.), ASCE, Atlantic City, April 27, 53-77.

Mroz, Z. (1967). "On the Description of Anisotropic Work Hardening." *Journal of Mechanics and Physics of Solids*, 15, 163-175.

Muraleetharan, K.K., Mish, K.D., C., Yogachandran, and Arulanandan, K. (1988). "DYSAC2: Dynamic Soil Analysis Code for 2-Dimensional Problems." Computer Code, Department of Civil Engineering, University of California, Davis, California.

Neapolitan, Richid, and Naimipour, Kumarss. (1998). *Foundations of Algorithms Using C++ Pseudocode, Second Edition*, Jones & Bartlett Pub.

Nikishkov, G.P., Kawka, M., Makinouchi, A., Yagawa, G., and Yoshimura, S. (1998). "Porting an Industrial Sheet Metal Forming Code to a Distributed Memory Parallel Computer." *Computers and Structures*, 67, 439-449.

Ohsaki, Y. (1966). "Niigata Earthquake, 1964 Building Damage and Soil Condition." *Soils and Foundations*, 6(2), 14-37.

Park, I.J., and Desai, C.S. (2000). "Cyclic Behavior and Liquefaction of Sand Using Disturbed State Concept." *Journal of Geotechnical and Geoenvironmental Engineering*, 126(9).

Parra, E. (1996). "Numerical Modeling of Liquefaction and Lateral Ground Deformation Including Cyclic Mobility and Dilation Response in Soil Systems," PhD Thesis, Department of Civil Engineering, Rensselaer Polytechnic Institute, Troy, NY.

Parra, E., Adalier, K., Elgamal, A.-W., Zeghal, M., and Ragheb, A. (1996). "Analyses and Modeling of Site Liquefaction Using Centrifuge Tests." *Proceedings of the 11th World Conference on Earthquake Engineering*, Acapulco, Mexico, June 23-28.

Pastor, M., and Zienkiewicz, O.C. (1986). "A Generalized Plasticity Hierarchical Model for Sand under Monotonic and Cyclic Loading." *Proceedings of the 2nd International Conference on Numerical Models in Geomechanics*, G. N. Pande, Van Impe, W.F. (Eds.), 131-150.

Pecker, A., Prevost, J. H., and Dormieux, L. (2001). "Analysis of Pore Pressure Generation and Dissipation in Cohesionless Materials During Seismic Loading." *Journal of Earthquake Engineering*, 5(4), 441-464.

Peng, Jun. (2002). "An Internet-Enabled Software Framework for the Collaborative Development of a Structural Analysis Program," Ph.D. Thesis, Department of Civil Engineering, Stanford University.

Peng, Jun, and Law, Kincho H. (2002). "A Prototype Software Framework for Internet-Enabled Colloborattive Development of a Structural Analysis Program." *Engineering with Computers*, 18(1), 38-49.

Peng, Jun, D. Liu, and Law, Kincho H. (2003). "An Online Data Access System for a Finite Element Program." *Advances in Engineering Software*, 34(3), 163-181.

Peng, Jun, and Law, Kincho H. (2004). "Building Finite Element Analysis Programs in Distributed Services Environment." *Computers and Structures*, 82(22), 1813-1833.

Peng, Jun, Lu, Jinchi , Law, Kincho H. , and Elgamal, Ahmed. (2004). "ParCYCLIC: Finite Element Modeling of Earthquake Liquefaction Response on Parallel Computers." *International Journal for Numerical and Analytical Methods in Geomechanics*, 28(12), 1207-1232.

PIANC. (2001). *Seismic Design Guidelines for Port Structures*, International Navigation Association Working Group No. 34, A.A. Balkema.

Pierce, Paul, and Regnier, Greg. (1994). "The Paragon Implementation of the NX Message Passing Interface." *the Scalable High Performance Computing Conference (SHPCC94)*, Knoxville, TN.

Prevost, J.H. (1985). "A Simple Plasticity Theory for Frictional Cohesionless Soils." *Soil Dynamics and Earthquake Engineering*, 4(1), 9-17.

Prevost, J.H. (1989). "DYNA1D, A Computer Program for Nonlinear Seismic Site Response Analysis: Technical Documentation." *Technical Report NCEER-89-0025*, National Center for Earthquake Engineering Research, State University of New York at Buffalo.

Prevost, J.H. (1998). *DYNAFLOW User's Manual*, Department of Civil Engineering and Operations Research, Princeton University.

Prosise, J. (1999). *Programming Windows with MFC, Second Edition*, Microsoft Press, Redmond, WA.

Ragheb, Ahmed M. (1994). "Numerical Analysis of Seismically Induced Deformations In Saturated Granular Soil Strata," PhD Thesis, Department of Civil Engineering, Rensselaer Polytechnic Institute, Troy, NY.

Romero, M.L., Miguel, P.F., and Cano, J.J. (2002). "A Parallel Procedure for Nonlinear Analysis of Reinforced Concrete Three-Dimensional Frames." *Computers and Structures*, 80, 1337-1350.

Schnabel, P.B., Lysmer, J., and Seed, H.B. (1972). "SHAKE: A Computer Program for Earthquake Response Analysis of Horizontally Layered Sites." *Report No. EERC 72-12*, Earthquake Engineering Research Center, University of California, Berkeley, CA.

Scott, R.F., and Zuckerman, K.A. (1972). "Sandblows and Liquefaction." *The Great Alaska Earthquake of 1964-engineering Publication 1606*, National Academy of Sciences, Washington, D.C.

SDSC. (2003). *Blue Horizon User Guide*, http://www.npaci.edu/BlueHorizon/, San Diego, CA.

SDSC. (2004). *DataStar User Guide*, http://www.npaci.edu/DataStar/, San Diego, CA.

Seed, H.B., and Idriss, I.M. (1967). "Analysis of Soil Liquefaction: Niigata Earthquake." *Journal of Soil Mechanics and Foundations Division*, 93(3), 83-108.

Seed, H.B., Lee, K.L., Idriss, I.M., and Makdisi, F.I. (1975). "The Slides on the San Fernando Dams during the Earthquake of February 9, 1971." *Journal of Geotechnical Engineering Division*, 101(7), 651-688.

Seed, H.B., Seed, R.B., Harder, L.F., and Jong, H.L. (1989). "Re-evaluation of the Slide in the Lower San Fenando Dam in the 1971 San Fenando Earthquake." *Report No. UCB/EERC-88/04*, University of California, Berkeley, CA.

Seed, H.B. , and Idriss, I.M. (1970). "Soil Moduli and Damping Factors for Dynamic Response Analyses." *Report EERC 70-10*, Earthquake Engineering Research Center, University of California, Berkeley, CA.

Seed, R.B., Dickenson, S.E., Riemer, M.F., Bray, J.D., Sitar, N., Mitchell, J.K., Idriss, I.M., Kayen, R.E., Kropp, A., Hander Jr., L.F., and Power, M.S. (1990). "Preliminary Report on the Principal Geotechnical Aspects of the October 17, 1989, Loma Prieta Earthquake." *Report No. UCB/EERC-90/05*, Earthquake Engineering Research Center, University of California, Berkeley, CA.

Shao, C., and Desai, C.S. (2000). "Implementation of DSC Model and Application for Analysis of Field Pile Tests Under Cyclic Loading." *International Journal for Numerical and Analytical Methods in Geomechanics*, 24(6), 601-624.

Sharp, Michael K., Dobry, Ricardo, and Abdoun, Tarek. (2003). "Liquefaction Centrifuge Modeling of Sands of Different Permeability." *Journal of Geotechnical and Geoenvironmental Engineering*, 129(12), 1083-1091.

Sitar, N. (1995). "Geotechnical Reconnaissance of the Effects of the January 17, 1995, Hyogoken-Nanbu Earthquake Japan." *Report No. UCB/EERC-95/01*, Earthquake Engineering Research Center, CA.

Smith, I.M., and Margetts, L. (2002). "Parallel Finite Element Analysis of Coupled Problems." Numerical Models in Geomechanics, Rome, Italy.

Snir, Marc, and Gropp, William. (1998). *MPI: The Complete Reference*, MIT Press, Boston, MA.

Taboada, V.M. (1995). "Centrifuge Modeling of Earthquake-Induced Lateral Spreading in Sand Using a Laminar Box," PhD Thesis, Rensselaer Polytechnic Institute, Troy, NY.

Tan, T.S., and Scott, R.F. (1985). "Centrifuge Scaling Considerations for Fluid-Particle Systems." *Geotechnique*, 35(4), 461-470.

Tinney, W. F., and Walker, J. W. (1967). "Direct Solutions of Sparse Network Equations by Optimally Ordered Triangular Factorization." *Proceedings of the IEEE*, 55(11), 1801-1809.

Tokimatsu, K., Midorikawa, S., Tamura, S., Kuwayama, S., and Abe, A. (1991). "Preliminary Report on the Geotechnical Aspects of the Philippine Earthquake of July 16, 1990." *Proceedings of the 2nd International Conference on Recent Advances*

in Geotechnical Earthquake Engineering and Soil Dynamics, University of Missouri-Rolla, 1, 357-364.

Tokimatsu, K., Kojima, H., Kuwayama, S., and Midorikawa, S. (1994). "Liquefaction-Induced Damages to Buildings in 1990 Luzon Earthquake." *Journal of Geotechnical Engineering*, 120(2), 290-307.

Tokimatsu, K., and Aska, Y. (1998). "Effects of Liquefaction-Induced Ground Displacements on Pile Performance in the 1995 Hyogoken-Nambu Earthquake." Soils and Foundations, 163-178.

TOP500. (2005). "Top 500 Supercomputers: http://www.top500.org.",

Tschantz, B.A. (1985). "Report on Review of State Non-Federal Dam Safety." Department of Civil Engineering, University of Tennessee.

United States Committee on Large Dams USCOLD. (1999). "Updated Guidelines for Selecting Seismic Parameters for Dam Projects." USCOLD Committee on Earthquakes, Denver, CO.

United States Society on Dams USSD. (2003). "White Paper on Dam Safety Risk Assessment." USSD Committee on Earthquakes, Denver, CO.

Werner, S.D. (1998). *Seismic Guidelines for Ports*, ASCE Technical Council Lifeline Earthquake Engineering, Reston, VA.

Wilkinson, Barry, and Allen, Michael. (1999). *Parallel Programming: Techniques and Applications Using Networked Workstations and Parallel Computers*, Prentice-Hall, Inc., Upper Saddle River, NJ.

Yan, Liping, Arulmoli, Kandiah, Weismair, Max, Aliviado, Ray, and PoLam, Ignatius. (2004). "Seismic Soil-Structure Interaction Analyses of an Underwater Bulkhead and Wharf System." *Proceedings of the Geo-Trans 2004*, M. Yegian and E. K. (eds.), Los Angeles, July 27-31.

Yang, Z. (2000). "Numerical Modeling of Earthquake Site Response Including Dilation and Liquefaction," PhD Thesis, Department of Civil Engineering and Engineering Mechanics, Columbia University, New York, NY.

Yang, Z., and Elgamal, A. (2002). "Influence of Permeability on Liquefaction-Induced Shear Deformation." *Journal of Engineering Mechanics*, 128(7), 720-729.

Yang, Z., Elgamal, A., and Parra, E. (2003). "A Computational Model for Cyclic Mobility and Associated Shear Deformation." *Journal of Geotechnical and Geoenvironmental Engineering*, 129(12), 1119-1127.

Yang, Zhaohui. (2002). "Development of Geotechnical Capabilities into OpenSees Platform and their Applications in Soil-Foundation-Structure Interaction Analyses," PhD Thesis, Department of Civil Engineering, University of California, Davis, CA.

Yang, Zhaohui, and Elgamal, Ahmed. (2004). "A Multi-Surface Plasticity Sand Model Including the Lode Angle Effect." *Proceedings of the 17th ASCE Engineering Mechanics Conference*, U. of Delaware, Newark, DE, June 13-16.

Yang, Zhaohui, Elgamal, Ahmed, Adalier, Korhan, and Sharp, Michael K. (2004a). "Earth Dam on Liquefiable Foundation and Remediation: Numerical Simulation of Centrifuge Experiments." *Journal of Engineering Mechanics*, 130(10), 1168-1176.

Yang, Zhaohui, Lu, Jinchi, and Elgamal, Ahmed. (2004b). "A Web-Based Platform for Computer Simulation of Seismic Ground Response." *Advances in Engineering Software*, 35(5), 249-259.

Yoshimi, Y., and Tokimatsu, K. (1977). "Settlement of Buildings on Saturated Sand During Earthquakes." *Soils and Foundations*, 17(1), 23-38.

Youd, T. L., and Holzer, T. L. (1994). "Piezometer Performance at the Wildlife Liquefaction Site." *Journal of Geotechnical Engineering*, 120(6), 975-995.

Youd, T.L., Hansen, C., and Bartlett, S. (1999). "Revised MLR Equations for Predicting Lateral Spread Displacement." Technical Report MCEER-99-0019, *Proceedings of the 7th US-Japan Workshop on Earthquake Resistant Design of Lifeline Facilities and Countermeasures against Liquefaction*, T. D. O'Rourke, Bardet, J.P., Hamada, M. (Eds.), 99-114.

Zeghal, M, and Elgamal, A. (1994). "Analysis of Site Liquefaction Using Earthquake Records." *Journal of Geotechnical Engineering*, 120(6), 996-1017.

Zienkiewicz, O. C., Chan, A. H. C., Pastor, M., Paul, D. K., and Shiomi, T. (1990). "Static and Dynamic Behavior of Soils: A Rational Approach to Quantitative Solutions: I. Fully Saturated Problems." *Proceedings of the Royal Society London, Series A, Mathematical and Physical Sciences*, 429, 285-309.

Zienkiewicz, O.C., Chan, A.H.C., Pastor, M., Schrefler, B.A., and Shiomi, T. (1999). *Computational Geomechanics with Special Reference to Earthquake Engineering*, John Wiley & Sons, Inc.